



Les régions HII de la galaxie irrégulière NGC 4449 avec SITELLE

Mémoire

Justine Giroux

Maîtrise en physique - avec mémoire
Maître ès sciences (M. Sc.)

Québec, Canada

Les régions H II de la galaxie irrégulière NGC 4449 avec SITELLE

Mémoire

Justine Giroux

Sous la direction de:

Carmelle Robert, directrice de recherche
Laurent Drissen, codirecteur de recherche

Résumé

Les galaxies irrégulières naines renferment de multiples mystères quant à leur fonctionnement et à leur évolution. Malgré ces énigmes, elles sont très importantes pour comprendre l'évolution de l'Univers, puisque certains scénarios cosmologiques suggèrent qu'elles constituaient les bases fondamentales de la fusion hiérarchique des galaxies.

La galaxie irrégulière naine NGC 4449 est la candidate parfaite pour étudier avec une haute résolution les comportements des galaxies du début de l'Univers, à cause de sa forte ressemblance avec celles-ci. Des données prises avec une haute résolution spatiale et spectrale sont utilisées pour obtenir de l'information à l'échelle des amas stellaires individuels, tout comme à l'échelle de la galaxie entière. Il est donc possible de relier les mécanismes de formation stellaire globaux de la galaxie aux propriétés morphologiques, chimiques, et cinématiques des régions de formation stellaire récente.

Dans ce mémoire, la théorie des galaxies naines et irrégulières est explorée, en se concentrant particulièrement sur les propriétés reliées à la formation stellaire. Les caractéristiques de la galaxie irrégulière naine NGC 4449, qui constitue le sujet de cette étude, sont ensuite détaillées. Ses régions H II, régions de gaz ionisé associées aux amas stellaires jeunes, sont subséquemment détectées et étudiées de manière statistique, pour en apprendre plus sur l'activité de formation stellaire et l'histoire évolutive de NGC 4449. Cette étude fait partie du grand programme SIGNALS, visant l'étude de l'évolution des galaxies qui utilise les données acquises à l'aide de l'instrument SITELLE au CFHT.

Abstract

Dwarf irregular galaxies still hold multiple mysteries regarding their behaviours and evolution. However, they are crucial systems to understand the evolution of the Universe, as they represent the fundamental building blocks of hierarchical galaxy fusion in certain cosmological scenarios.

The dwarf irregular galaxy NGC 4449 is the perfect candidate to study, with a high resolution, the behaviours of the galaxies at the beginning of the Universe, due to its strong resemblance with them. High spatial and spectral resolution data is used to obtain information on the stellar cluster scale, as well as on the scale of the entire galaxy. It is thus possible to link the global star formation mechanisms of the galaxy to the morphological, chemical, and kinematical properties of the recent star formation regions.

In this work, the theory of the dwarf and irregular galaxies, especially regarding their properties related to the stellar formation, is explored. The characteristics of the dwarf irregular galaxy NGC 4449, the subject of this study, are detailed thereafter. Its H II regions, regions of ionised gas associated to young stellar clusters, are then detected and statistically studied to gain more insight on the star-forming activities and the evolution of NGC 4449. This study is part of the SIGNALS large program, which aims to study the evolution of galaxies in the nearby Universe, by using data from the SITELLE instrument at the CFHT.

Table des matières

Résumé	ii
Abstract	iii
Table des matières	iv
Liste des tableaux	v
Liste des figures	vi
Remerciements	ix
Avant-propos	x
Introduction	1
1 NGC 4449 et les galaxies naines en contexte	3
1.1 Galaxies naines	3
1.2 Formation stellaire	6
1.3 NGC 4449	14
1.4 Méthodologie	31
2 HII Regions in the Irregular Galaxy NGC 4449 with SITELLE	33
2.1 Avant-propos	33
2.2 Résumé	33
2.3 Abstract	34
2.4 Introduction	34
2.5 Observations, Data Reduction, and Emission Line Measurements	39
2.6 Emission Regions Measurements	46
2.7 Results and Analysis	61
2.8 Conclusions	111
References	114
Appendices	120
Conclusion	265
Bibliographie	270

Liste des tableaux

2.1	Observing parameters of the SITELLE data of NGC 4449	40
2.2	Detected emission regions with the highest H α surface brightness	78
2.3	Line ratios of region 467	107
F.1	Morphological parameters of the emission regions	140
F.2	Uncorrected flux values of the emission regions in the catalogue	167
F.3	Corrected flux values with the local background of the emission regions in the catalogue	190
F.4	Corrected flux values of the emission regions in the catalogue	215
F.5	Kinematical and chemical parameters of the emission regions in the catalogue .	238

Liste des figures

1.1	Image en couleur de NGC 4449	16
2.1	Colour image of NGC 4449	41
2.2	H α flux map	42
2.3	Kinematics maps	43
2.4	Examples of the detected emission regions	50
2.5	Example of an H II region's integrated spectrum	52
2.6	Spatial distribution of the emission regions with their H α luminosity value	55
2.7	Global stellar absorption spectrum of the stellar populations	56
2.8	Comparaison of the emission region's flux with and without a global stellar absorption correction	57
2.9	Comparaison of the stellar absorption correction methodologies	58
2.10	Spatial distribution of the emission regions with their extinction value	60
2.11	Extinction map	60
2.12	Radial profile of the emission region's extinction	61
2.13	H α luminosity function	63
2.14	H α luminosity function uncorrected and corrected for extinction	67
2.15	H α luminosity function of the two main morphological features of NGC 4449	68
2.16	Size distribution	70
2.17	Size distribution of the two main morphological features of NGC 4449	73
2.18	Spatial distribution of the emission regions with their radius	74
2.19	Spatial distribution of the emission regions with their eccentricity	75
2.20	Correlation between the H α luminosity of the emission regions, their radius, and their velocity dispersion	77
2.21	Correlation between the luminosity of the emission regions, their size, and their velocity dispersion of the two main morphological regions of NGC 4449	79
2.22	BPT diagrams of the detected emission regions	83
2.23	BPT diagrams of the local background regions	84
2.24	BPT diagrams of the emission regions without any flux corrections	85
2.25	Spatial distribution of the detected emission regions with their distance from the H II region limit in the BPT diagrams	86
2.26	BPT diagrams of the detected emission regions with their velocity dispersion	87
2.27	BPT diagrams of the detected emission features of the two main morphological regions of NGC 4449	88
2.28	Examples of detected emission regions compared to the distribution of the H α flux, SN2 continuum level, and SN1 continuum level	89
2.29	Examples of our detected emission regions with the LEGUS star clusters' age	90
2.30	Examples of our detected emission regions with the LEGUS star clusters' mass	92

2.31 Metallicity map	94
2.32 Spatial distribution of the emission regions with their metallicity value	96
2.33 Radial profile of the emission region's metallicity	97
2.34 Spatial distribution of the emission regions with their velocity and velocity dispersion	100
2.35 Spectra of the H α line for each pixel in the region of the potential inflow/outflow	102
2.36 Location and spectrum of the base of the potential inflow/outflow	103
2.37 Location and spectrum of region 283	104
2.38 Spectrum of the young supernova remnant J1228+441	107
2.39 Spatial distribution of the predicted object type for the emission regions	110
2.40 BPT diagrams of the emission regions with their predicted object type	110
A.1 Flux maps obtained by fitting the lines in the SN3 datacube	120
A.2 Flux maps obtained by fitting the lines in the SN1 and SN2 datacubes	121
B.1 Median sky spectrum	121
B.2 Sky velocity map	122
C.1 H α amplitude map	123
C.2 Effects of different Laplacian sigma values used for the detection algorithm . .	124
C.3 Effects of different detection box sizes used for the detection algorithm . . .	125
C.4 Effects of different noise sigma values used for the detection algorithm . . .	126
C.5 Effects of different local background box sizes used for the detection algorithm	127
C.6 Effects of different scaling factor values used for the detection algorithm . .	128
C.7 Convergence curve of the number of detections of the artificial H II regions . .	129
D.1 Location of the emission regions detected in the different morphological features of NGC 4449	129
D.2 Location of the four detections used as examples	130
D.3 Examples of detected emission regions with varying eccentricities	131
D.4 Spatial location of the detected GEHRs	132
E.1 Map of the H α /H β line ratio	133
E.2 Map of the [N II] $\lambda\lambda 6583$ /H α line ratio	133
E.3 Map of the [S II] $\lambda\lambda 6716,6731$ /H α line ratio	134
E.4 Map of the [S II] $\lambda\lambda 6716,6731$ /[N II] $\lambda 6583$ line ratio	134
E.5 Map of the [O III] $\lambda 5007$ /H β line ratio	135
E.6 Map of the [O II] $\lambda\lambda 3726,3729$ /H β line ratio	135
E.7 Map of the ([O II] $\lambda\lambda 3726,3729$ + [O III] $\lambda 5007$)/H β line ratio	136
E.8 Map of the [O III] $\lambda 5007$ /[O II] $\lambda\lambda 3726,3729$ line ratio	136
E.9 Map of the [O III] $\lambda 5007$ /[N II] $\lambda 6583$ line ratio	137
E.10 Map of the [O II] $\lambda\lambda 3726,3729$ /[N II] $\lambda 6583$ line ratio	137
E.11 Map of the [S II] $\lambda 6716$ /[S II] $\lambda 6731$ line ratio	138
E.12 Map of the H α equivalent width	138
E.13 Map of the H β equivalent width	138
E.14 Radial profile of the H II region's metallicity in NGC 4449 for the different indicators	139

À Justine du futur.

Remerciements

Je tiens à remercier mes directeurs, Carmelle Robert et Laurent Drissen, de m'avoir supportée tout au long de ma recherche. Je dois aussi remercier tous les étudiants du groupe de recherche pour tous les moments agréables passés ensemble. Il est aussi important de souligner l'impact du mentorat que Laurie Rousseau-Nepton m'a prodigué tout au long de ma maîtrise. Elle fut une inspiration pour moi. Je suis aussi très reconnaissante de l'aide et du support précieux que Carter Rhea m'a apportés. Je veux aussi remercier ma mère de m'avoir encouragé tous les jours à persévérer. Je tiens particulièrement à remercier mon partenaire Philippe-André Luneau qui a rendu mon succès possible.

Avant-propos

Ce mémoire présente la recherche produite lors de ma maîtrise sous la direction de Carmelle Robert et Laurent Drissen. L'article *HII Regions in the Irregular Galaxy NGC 4449 with SITELLE* est le produit qui résulte de ce travail de recherche. J'en possède le statut de première auteure, grâce à ma contribution tant au travail de recherche, qu'à l'élaboration d'algorithmes pour les méthodes développées, à l'analyse des résultats pour la galaxie NGC 4449, et à la rédaction de ce manuscrit. Cet article se trouve au Chapitre 2, inséré sans modifications. Sa circulation entre les coauteurs et soumission se feront après l'évaluation du mémoire.

Introduction

Paradoxalement, les galaxies naines sont les galaxies les plus communes, cependant les chercheurs s'entendent pour dire qu'elles sont les moins comprises. Les galaxies naines soulèvent un intérêt cosmologique très important, puisqu'elles seraient perçues comme les cellules de base pour la fusion hiérarchique des galaxies. Ainsi, comprendre les galaxies naines de l'Univers local permet d'éclaircir les mystères entourant la formation et l'évolution des galaxies après le Big Bang. De plus, les galaxies naines ne possèdent pas de mécanismes de régulation globaux de leur gaz (en lien avec une rotation du disque, des bras, etc.), comme les galaxies spirales. Ainsi, les mécanismes régissant les mouvements du gaz et la formation stellaire ayant lieu dans les galaxies naines peuvent être étudiés de manière plus simple. Par conséquent, mieux comprendre les phénomènes de l'évolution des galaxies naines permet, entre autres, d'émettre des hypothèses visant à expliquer l'origine des mécanismes de la formation stellaire et, de façon générale, l'évolution des galaxies.

Catégorisée comme une galaxie irrégulière magellanique naine (IB(s)m), NGC 4449 est considérée comme un excellent laboratoire pour étudier la formation d'étoiles, en raison de son taux de formation stellaire spectaculairement élevé. Sa proximité permet d'étudier avec une excellente résolution les signatures de formation stellaire récente (c.-à-d. les régions H II). Les interactions passées avec d'autres galaxies causent de fortes perturbations dans le gaz de NGC 4449. Par conséquent, la relation entre la cinématique du gaz et les régions H II peut aussi être explorée en détail.

Les données de la galaxie NGC 4449 ont été obtenues à l'aide du spectromètre imageur SITELLE au Télescope Canada-France-Hawaii dans le cadre du relevé SIGNALS. Le but de ce relevé est d'étudier la formation d'étoiles dans plus de 40 galaxies locales. Ce relevé vise à générer un catalogue systématique et statistiquement significatif de plus de 50000 régions H II. Dans le cadre de ce programme, la recherche présentée ici produit un catalogue de régions H II pour la galaxie NGC 4449, en utilisant les méthodes développées à cet effet. En plus de fournir un catalogue des régions d'émission, cette recherche examine leurs caractéristiques morphologiques, chimiques et cinématiques, tout en essayant d'établir des liens avec les propriétés de leur environnement au sein de la galaxie.

Le Chapitre 1 présente les propriétés reliées aux galaxies irrégulières naines et leur processus

de formation stellaire. Les régions H II y sont aussi abordées plus en détail. En outre, un portrait global de NGC 4449 y est fait. Celui-ci résume les études passées dans différents domaines de longueurs d'onde sur la distribution et la cinématique du gaz de NGC 4449, ses interactions passées, sa formation stellaire, sa métallicité, et ses catalogues de régions H II existants. L'article scientifique résultant de cette recherche est présenté dans la Chapitre 2. Un résumé des résultats et des conclusions tirées de cette recherche est offert à la fin de ce document.

Chapitre 1

NGC 4449 et les galaxies naines en contexte

Les galaxies naines sont d'un intérêt particulier. Elles se distinguent totalement des grandes galaxies classiques, soit les galaxies spirales et elliptiques, par leur absence de morphologie ordonnée et leur contenu varié. Les paramètres physiques décrivant les galaxies irrégulières (p. ex. masse, taille, taux de formation stellaire, métallicité, etc.) peuvent prendre des valeurs dans des plages plus étendues que pour les galaxies massives (Sacchi et al. 2018). Moins d'intérêt leur a été accordé dans le passé comparativement aux galaxies spirales, à cause à leur luminosité généralement plus faible. Avec l'amélioration des instruments d'observation, les galaxies naines sont maintenant de plus en plus étudiées (McConnachie 2012). Grâce à ces instruments, il est possible de constater qu'elles sont omniprésentes dans l'Univers local et surtout au début de l'Univers et très différentes des galaxies spirales, en particulier au niveau de la formation stellaire (Sacchi et al. 2018).

La théorie des galaxies naines et irrégulières sera discutée dans la Section 1.1. Ensuite, les processus de formation stellaire sont résumés dans la Section 1.2. La Section 1.3 présente la galaxie NGC 4449, une galaxie irrégulière formant des étoiles à un taux très élevé ; elle est le sujet du projet d'étude présenté ici. La méthodologie et les objectifs de ce projet sont définis à la Section 1.4.

1.1 Galaxies naines

Malgré la présence fréquente des galaxies naines, leur évolution et les processus de formation stellaire qui les régissent demeurent mystérieux (Sacchi et al. 2018). Les valeurs des paramètres physiques définissant les galaxies naines varient énormément dans la littérature. Cependant, malgré leur grande diversité, les mêmes mécanismes de régulation interne s'y retrouvent et des tendances globales dans leurs comportements peuvent être observés. Elles forment un groupe

bien distinct des autres types de galaxies.

Les galaxies naines possèdent, en moyenne, une masse et une dimension plus petites que les galaxies spirales et elliptiques. Leur luminosité moyenne est aussi plus faible que celle des galaxies massives. La magnitude visuelle absolue qualifiant une galaxie naine n'est pas particulièrement bien définie (McConnachie 2012), mais l'ordre de grandeur standard se trouve entre $M_V \simeq -9$ et $M_V \simeq -18.5$ (Grebel et al. 2003). Généralement, elles possèdent aussi une métallicité plus faible que les galaxies massives (Hensler 2011). Dans tous les cas, les galaxies naines présentent des intervalles de propriétés beaucoup plus variés que les galaxies massives (Sacchi et al. 2018).

Les galaxies naines peuvent être divisées en deux groupes (Hensler 2011 ; Kunth & Östlin 2000) : celles qui ne forment pas d'étoiles, les galaxies naines elliptiques (dE) et les naines sphéroïdales (dSph), et celles qui en forment, les galaxies irrégulières naines (dIrr), dont les naines compactes bleues (*blue compact dwarfs*, BCD) et les naines en sursaut de formation stellaire (*starburst dwarfs*, SBDG). Les galaxies naines dE et dSph sont dominées par une population d'étoiles vieilles et contiennent très peu de gaz, donc elles ne possèdent pas de régions H II. Par opposition, les galaxies dIrr contiennent beaucoup de gaz et forment activement des étoiles, comme en témoigne la présence de régions H II. Sandage & Binggeli (1984) ont observé que les dE sont plus communes dans les amas de galaxies (Hensler 2011). Cependant, hors des amas de galaxies, les dIrr sont le type de galaxies le plus fréquent. Binggeli et al. (1988) concluent que ce comportement souligne un lien avec les interactions.

Ma recherche s'intéresse particulièrement aux galaxies irrégulières naines, dans le but d'étudier leur formation stellaire. Dans la séquence de classification de Hubble, les galaxies irrégulières suivent les galaxies spirales, après les types très tardifs, telles que les Sd et Sm. Leurs différences avec les galaxies spirales ne se limitent pas à leur morphologie ; elles sont généralement plus bleues, plus petites, moins lumineuses, moins massives, plus riches en gaz, moins riches en métaux, et contiennent moins de poussières (Hunter 1997). Leur profil de brillance de surface peut cependant être décrit par une fonction exponentielle (Kunth & Östlin 2000), comme pour les galaxies spirales. En raison de leurs processus de formation stellaire différents des galaxies spirales (discutés plus en détail dans la Section 1.2), certains voient les galaxies irrégulières comme moins évoluées que les galaxies spirales (Hunter 1997). En effet, leur haut contenu en gaz et leur faible abondance en métaux sont une signature que peu de générations d'étoiles ont été produites par ce gaz.

Il existe une grande variété de sous-catégories de galaxies irrégulières, basées sur les structures présentes. Les galaxies irrégulières magellaniques (Im) sont des galaxies irrégulières possédant des ressemblances aux Nuages de Magellan, d'où vient leur nom. Les galaxies Im ne contiennent pas de structure ressemblant aux bras des galaxies spirales ; cependant, elles peuvent posséder une barre. Les galaxies spirales magellaniques (Sm) se situent avant les galaxies Im dans la sé-

quence de classification de Hubble, puisqu'elles possèdent quelques structures ressemblant aux galaxies spirales. En effet, les galaxies Sm contiennent parfois un début de bras, les rendant asymétriques, et dans certains cas une barre, comme le Grand Nuage de Magellan. Cependant, comme pour les galaxies en général, la classification des galaxies irrégulières est basée sur l'inspection visuelle et ces catégories ne sont pas définies clairement par des paramètres physiques quantifiables.

Les galaxies naines sont particulièrement intéressantes du point de vue cosmologique, pour mieux comprendre l'évolution des galaxies à travers l'Univers (Kunth & Östlin 2000). Elles seraient considérées comme les cellules de base dans les scénarios cosmologiques de la fusion hiérarchique des galaxies (Summers et al. 2003), suggérant que les galaxies se seraient assemblées en accrétenant des systèmes plus petits (White & Rees 1978). En effet, ces petites galaxies seraient les premiers endroits dans l'Univers hébergeant de la formation stellaire.

Des galaxies naines sont présentes dans l'Univers local, mais de manière moins fréquente qu'au début de l'Univers. Il est alors fort intéressant d'étudier les galaxies naines proches, ce qui permet des observations à plus haute résolution, pour acquérir une meilleure compréhension du fonctionnement des galaxies au début de l'Univers (Kumari et al. 2017). Ainsi, il est possible de mieux comprendre les processus d'évolution et de mieux expliquer le portrait global de l'Univers local (Summers et al. 2003).

Cependant, malgré leur grand intérêt pour répondre aux questions fondamentales de l'évolution de l'Univers, les galaxies naines demeurent très énigmatiques. En effet, les galaxies spirales sont beaucoup plus étudiées et mieux comprises (Sacchi et al. 2018). Il est connu que les galaxies naines possèdent une plus grande diversité de propriétés chimiques, dynamiques, et de formation stellaire que les galaxies spirales, mais les mécanismes causant de si gros sursauts de formation stellaire dans des systèmes si petits et l'impact de ces sursauts sur l'évolution de la galaxie demeurent actuellement nébuleux (Sacchi et al. 2018).

Certains schémas d'évolution des galaxies suggèrent que plusieurs galaxies naines forment leurs étoiles dans des épisodes stochastiques, qui pourraient être causés par des événements d'accrétion ou de perturbations internes (p. ex. supernovae, vents stellaires à grande échelle, collisions de nuages moléculaires ; Martinez-Delgado et al. 2012). La formation stellaire dans les galaxies naines est discutée plus en profondeur dans la section suivante.

La faible métallicité des galaxies naines (voir Section 1.2.1) permet de les utiliser comme révélateur pour les galaxies de faible métallicité observées à haut décalage spectral (Searle & Sargent 1972). Ceci aide à mieux comprendre, au niveau cosmologique, les processus de formation stellaire qui auraient donné naissance aux galaxies observables aujourd'hui. Ainsi, les galaxies naines sont des objets parfaits pour étudier la formation stellaire dans des conditions de faible métallicité (Cignoni et al. 2018 ; Kumari et al. 2017 ; Kunth & Östlin 2000). L'avantage d'utiliser les galaxies naines faibles en métaux de l'Univers local comme analogues aux

galaxies de l’Univers jeune est qu’elles nous permettent de les observer avec une résolution spatiale supérieure. Alors, ces galaxies permettent de voir avec beaucoup de détails l’activité de formation stellaire dans des conditions extrêmes, de suivre l’évolution des abondances chimiques précisément, et de mieux comprendre leurs rôles dans l’évolution des galaxies (Cignoni et al. 2018).

1.2 Formation stellaire

L’évolution des galaxies est un processus qui dépend de plusieurs facteurs, dont la présence de gaz moléculaire, la dynamique du gaz, l’abondance chimique, et l’environnement galactique (Kumari et al. 2017). Ces facteurs affectent la formation stellaire (Calzetti et al. 2015 ; Kumari et al. 2017) qui, à son tour, modifie les propriétés du gaz.

Les étoiles se forment lors de l’effondrement de nuages de gaz froid (Kumari et al. 2017). Ce gaz froid provient de plusieurs sources : soit il se forme par les processus internes de la galaxie, ou alors il provient d’autres galaxies ou du milieu intergalactique et se retrouve dans la galaxie par accrétion (Combes et al. 2002). Les vents stellaires et les explosions des étoiles en supernovae contribuent à modifier les abondances chimiques et la dynamique du gaz (Maeder 2009). Ces phénomènes influencent à leur tour la formation stellaire en créant potentiellement des zones de densité plus élevée du gaz du milieu interstellaire, ce qui pourrait entraîner l’effondrement d’autres nuages. Des événements de formation stellaire intenses peuvent aussi causer des éjections de matière en lien avec des perturbations dynamiques du milieu interstellaire produites par les supernovae et les vents galactiques (Heckman et al. 1990).

La nucléosynthèse se produisant dans le cœur des étoiles plus massives au cours de leur vie donne lieu à un enrichissement important en métaux (Maeder 2009). Ainsi, lors de leur mort, ce gaz avec une abondance en métaux plus élevée que le gaz qui a formé l’étoile est réinjecté dans le milieu interstellaire. La métallicité du gaz est discuté plus en détail dans la Section 1.2.1.

Lorsque la galaxie accrète du gaz provenant du milieu intergalactique ou de galaxies moins évoluées, il est possible que ce dernier soit plus faible en métaux que le gaz présent dans la galaxie, parce qu’il ne résulte pas de plusieurs générations d’étoiles. Aussi, certaines régions de la galaxie peuvent avoir des concentrations différentes de métaux à cause d’une efficacité de formation stellaire différente. Bref, plusieurs mécanismes internes et externes peuvent créer des inhomogénéités chimiques dans le gaz de la galaxie (Ceverino et al. 2016 ; Cresci et al. 2010 ; Davé et al. 2011 ; Kewley et al. 2010 ; Kumari et al. 2017 ; Sánchez Almeida et al. 2013, 2014, 2015).

L’emplacement de la formation stellaire récente est alors relié aux régions de gaz dense et froid ainsi qu’aux régions cinématiquement perturbées. Elles peuvent être identifiées par des régions de gaz photoionisées par les étoiles massives (c.-à-d. régions H II ; Section 1.2.2) et ionisées par

les chocs du milieu interstellaire, provenant des perturbations causées par l'énergie mécanique produite par les étoiles (Osterbrock 1989).

La théorie des ondes de densité de Lin & Shu (1964) est utilisée pour expliquer la présence de structures spirales où la formation stellaire est active dans plusieurs galaxies spirales. Les ondes de densité entraînent la compression du gaz, engendrant de la formation stellaire (Phillipps 2005 ; Roberts 1969). Pour d'autres spirales, la rotation différentielle avec propagation de la formation stellaire explique mieux leur mode de formation stellaire (Gerola & Seiden 1978). Cependant, ces théories ne s'appliquent pas bien aux galaxies irrégulières, puisqu'elles ne possèdent pas, en général, de mécanismes qui régulent la dynamique de leur gaz à l'échelle globale. Malgré l'absence de tels mécanismes, les galaxies irrégulières forment tout de même des étoiles à des taux comparables à ceux des galaxies spirales (Hunter 1997).

L'absence d'ondes de densité spirales et l'absence de rotation différentielle importante influencent l'évolution des galaxies irrégulières, en modifiant leurs historiques de formation stellaire, comparativement à celles des galaxies plus massives (Cignoni et al. 2018, 2019). Les galaxies plus massives forment la majorité de leurs étoiles dans les premiers ~ 3 Gans de leur existence. Au contraire, les galaxies de faible masse forment leurs étoiles sur l'entièreté du temps cosmique (Cignoni et al. 2018 ; Mateo 1998), probablement de façon discontinue, sous forme d'épisodes de durée et d'intensité variables (Kunth & Östlin 2000 ; Tolstoy et al. 1998). Les taux de formation stellaire des galaxies moins massives sont dispersés dans un intervalle de valeurs plus étendu que celui de galaxies plus massives (Hunter 1997). Effectivement, les galaxies naines peuvent être presque inactives, tout comme extrêmement actives (Cignoni et al. 2018). De la même façon, leurs historiques de formation stellaire sont uniques à chacune d'elles et ne suivent pas de tendances claires lorsque différentes galaxies sont comparées (Cignoni et al. 2018 ; Kunth & Östlin 2000).

L'absence d'ondes de densité et de rotation différentielle rend l'environnement des galaxies irrégulières plus simple que celui des galaxies spirales (Hunter 1997). Ainsi, il est possible d'étudier les mécanismes environnementaux fondamentaux (c.-à-d. de petite échelle) qui influencent la formation stellaire dans ces galaxies (Kunth & Östlin 2000 ; Youngblood & Hunter 1999). Les mécanismes provoquant la formation stellaire dans les galaxies naines peuvent provenir d'événements internes et externes (Cignoni et al. 2018). Les galaxies possèdent intrinsèquement des mécanismes qui régulent la formation stellaire, indépendamment du milieu environnant. La densité du gaz et sa distribution dans la galaxie influencent aussi son taux de formation stellaire (Sacchi et al. 2018). Le taux de formation stellaire actuel est aussi influencé par l'historique de formation stellaire de la galaxie, puisque l'effet de rétroaction des anciennes étoiles (p. ex. explosions de supernovae, vents stellaires) peut avoir un impact considérable sur le gaz interstellaire (El-Badry et al. 2016 ; Leitherer et al. 1992 ; Sacchi et al. 2018). Ces événements peuvent causer de grandes perturbations dans la cinématique du gaz, qui pourraient engendrer potentiellement de la formation stellaire en compressant le gaz ou empêcher la formation

stellaire séquentielle en dispersant le gaz.

La formation stellaire stochastique autopropagée (*Stochastic Self-Propagated Stellar Formation*, SSPSF) est un modèle proposé par Gerola & Seiden (1978), Gerola et al. (1980) et Mueller & Arnett (1976) qui cherche à décrire le processus intrinsèque de formation stellaire des galaxies irrégulières. Celui-ci représente la raréfaction de gaz lors de la création des étoiles, la diffusion locale de matériaux après l'explosion des supernovae, et le transport naturel de gaz au travers de la galaxie. Dans ce paradigme, la galaxie est supposée être une grille contenant plusieurs petites cellules. Les quantités nécessaires au modèle sont propagées entre les cellules et initialement distribuées de façon aléatoire. Les cellules peuvent se trouver dans trois états, représentant des stades physiques de la formation stellaire. Le premier état correspond au matériel susceptible de former des étoiles, puisque ces cellules contiennent de la formation stellaire récente. Ceci implique que des étoiles massives sont présentes ; ainsi, des vents stellaires et des supernovae y sont produits, causant des ondes de chocs dans le gaz. Le deuxième état correspond aux cellules qui contiendront la prochaine génération d'étoiles. Les ondes de chocs des cellules adjacentes causeront, avec une probabilité non nulle, l'effondrement du nuage contenu dans la cellule. Cependant, les cellules adjacentes à cette cellule ne peuvent pas former d'autres étoiles, puisque le gaz disponible pour la formation stellaire a été utilisé par la cellule dans le deuxième état. Ceci correspond au troisième état. Les cellules dans le troisième état doivent y demeurer temporairement, en attendant que le gaz se refroidisse, malgré la présence de chocs.

Donc, la SSPSF suggère qu'une région de formation stellaire induit de la formation stellaire dans les cellules adjacentes par les chocs qu'elle produit dans le milieu interstellaire. Ainsi, la formation stellaire se propage à travers la galaxie. Lors de ses études, Auer (1999) conclut que les ondes de densité ne contribuent pas autant à la formation stellaire que la SSPSF. Le phénomène de SSPSF joue un rôle particulièrement important dans les galaxies naines, qui possèdent peu de rotation dans une structure en disque.

Ainsi, dans une galaxie naine, un événement de formation stellaire peut avoir un impact beaucoup plus important sur son évolution que dans une galaxie massive. En effet, il est possible que sa luminosité soit radicalement modifiée, tout comme la cinématique de son gaz (Cignoni et al. 2018). À cause du faible potentiel gravitationnel de la galaxie, le gaz perturbé par les vents stellaires et les explosions de supernovae pourrait être éjecté de la galaxie, ce qui lui ferait perdre une quantité significative de masse. Ainsi, l'historique de formation stellaire des galaxies naines serait à jamais modifié si elles ne sont pas capable de réaccréter du gaz.

Les mécanismes externes peuvent aussi avoir une énorme influence sur la formation stellaire d'une galaxie. L'accrétion de gaz externe, provenant d'autres galaxies lors d'interactions ou du milieu intergalactique, peut engendrer de la formation stellaire dans la galaxie (Larson & Tinsley 1978). Ainsi, ces mécanismes externes sont particulièrement importants dans le cas des galaxies naines, qui sont très sensibles aux perturbations (Cignoni et al. 2018). En effet,

leur faible masse rend les galaxies naines plus vulnérables aux interactions, à l'afflux de gaz, ou aux collisions avec d'autres galaxies. Plusieurs types d'interactions existent entre les galaxies. Selon divers facteurs (p. ex. la masse des deux systèmes, leur vitesse d'approche, leur angle d'approche), les interactions peuvent donner lieu à des effets de marée, de même qu'à des fusions majeures ou mineures. Notamment, lors d'interactions, l'afflux de gaz peut causer un sursaut de formation stellaire dans la galaxie. Une augmentation par un facteur significatif du taux de formation stellaire en résulte, comparativement au taux typique pour une galaxie de cette masse. Cependant, ces événements ne peuvent pas expliquer tous les sursauts de formation stellaire observés dans les galaxies (Lelli et al. 2014b).

Les galaxies naines sont généralement les victimes lors d'interactions, puisqu'elles sont souvent les objets de masses les plus faibles (Hunter et al. 1999). Leur potentiel gravitationnel n'est pas assez fort pour conserver leur gaz lorsqu'un système plus massif passe trop près d'elles. Cependant, plusieurs cas connus de galaxies naines en interaction avec d'autres galaxies sont documentés. En effet, des galaxies naines accrétant d'autres galaxies naines ont été observées par Annibali et al. (2016), Martinez-Delgado et al. (2012), Sacchi et al. (2016) et Tully et al. (2006). Les interactions entre les galaxies naines et les satellites se font majoritairement par accrétion furtive (Cignoni et al. 2018), soit sans l'accrétion d'étoiles. Donc, Starkenburg et al. (2016) suggèrent que ce type d'interaction pourrait expliquer l'augmentation du taux de formation stellaire observé dans certaines galaxies naines, pour lesquelles aucun signe d'interaction n'est apparent. Les larges halos de gaz H I observés par Ramya et al. (2009) autour de certaines BCD, ne possédant pas d'émission optique, pourraient suggérer que ce type d'accrétion est, en effet, possible.

Stierwalt et al. (2017) concluent que les propriétés et les résultats des interactions naines-naines diffèrent de celles vues entre des galaxies plus massives. Dans les deux types d'interactions, qui peuvent se déclencher à des distances de séparation avoisinant 100 kpc, une augmentation du taux de formation stellaire est observée, à cause de l'afflux de gaz et des chocs qui en résultent. Cependant, une plus grande fraction du rayon viriel est impliquée dans le cas des interactions naines-naines et l'augmentation du taux de formation stellaire est plus grande par un facteur de 1.3, comparativement aux interactions massives-massives (Cignoni et al. 2018; Patton et al. 2013; Stierwalt et al. 2017). Donc, l'impact d'une interaction naine-naine sur la structure globale des galaxies naines concernées est beaucoup plus important que lors d'interactions d'objets plus massifs. Cet impact sur la formation stellaire peut être démontré par le fait que 20 % des galaxies naines en interaction naine-naine, isolées dans leur environnement, sont dans un état de sursaut de formation stellaire, comparativement à 6 % pour les galaxies naines seules (Stierwalt et al. 2017). Ce phénomène pourrait expliquer en partie les mécanismes permettant à de si petits systèmes de vivre des sursauts de formation stellaire, malgré l'absence de mécanismes globaux régulant leur formation stellaire. Ainsi, les interactions entre galaxies naines pourraient jouer un rôle crucial dans le déclenchement d'un sursaut

de formation stellaire (Cignoni et al. 2018).

Malgré la compréhension de certains mécanismes internes et externes de la formation stellaire, plusieurs mystères demeurent (Calzetti et al. 2015). La formation stellaire est bien comprise sur deux échelles spatiales. Différents objets et phénomènes sont étudiés à l'échelle du parsec (p. ex. étoiles individuelles, groupes, et associations d'étoiles) et du kiloparsec (p. ex. la formation stellaire globale à l'échelle galactique). Pour ces deux échelles distinctes, les instruments astronomiques et les défis observationnels requis sont vastement différents. Ainsi, la recherche à ces deux échelles a évolué de manière indépendante. La loi de Schmidt–Kennicutt (Kennicutt & Evans 2012 ; Kennicutt 1989 ; Kennicutt & De Los Reyes 2021 ; Schmidt 1959) est un bon exemple de notre compréhension des mécanismes à grande échelle. Cette loi est considérée comme universelle (c.-à-d. s'appliquant aux galaxies à tout décalage spectral). Elle permet de relier le contenu de gaz de la galaxie à son taux de formation stellaire (Daddi et al. 2010 ; Genzel et al. 2010 ; Kennicutt & Evans 2012). Toutefois, pour les études à l'échelle du parsec, cette relation n'est plus valide (Calzetti et al. 2015). En effet, à une échelle plus petite que $\sim 100\text{--}200\,\text{pc}$, les groupes d'étoiles jeunes ne semblent pas corrélés aux nuages moléculaires (Momose et al. 2010 ; Onodera et al. 2010 ; Schruba et al. 2010). Cette dichotomie entre les deux échelles retarde le développement de nouvelles théories sur la formation stellaire (Hopkins et al. 2013).

Comme mentionné dans la Section 1.1, les galaxies naines ont des propriétés similaires à celles des galaxies du début de l'Univers. Cependant, comme expliqué précédemment, l'environnement galactique a un impact considérable sur l'évolution des galaxies. Évidemment, le portrait galactique au début de l'Univers était considérablement différent de celui observé aujourd'hui. Des amas stellaires géants ($\sim 10^8\,M_\odot$) de la taille du kiloparsec ont été observés dans des galaxies, à un décalage spectral de $z > 1$, par Elmegreen & Elmegreen (2005), Elmegreen et al. (2007, 2009), Förster Schreiber et al. (2011), Genzel et al. (2008, 2011), Guo et al. (2012) et Immeli et al. (2004). Ces amas géants tireraient leur origine des disques galactiques turbulents et riches en gaz et seraient le résultat d'instabilités gravitationnelles (Ceverino et al. 2010, 2012 ; Dekel et al. 2009a ; Elmegreen et al. 2008). D'après Dekel et al. (2009b), Giavalisco et al. (2011) et Kereš et al. (2005), les turbulences dans ces disques proviendraient de l'accrétion de gaz froid. Avec le temps, ces amas géants de formation stellaire migrent vers le centre de leur galaxie (Bournaud et al. 2009 ; Genel et al. 2012 ; Murray et al. 2010), ou peuvent être éjectés de la galaxie par rétroaction gravitationnelle. Ils contribuent ainsi au disque épais par des forces de marées ou en se fusionnant avec le bulbe de leur galaxie hôte (Bournaud et al. 2009 ; Genel et al. 2012 ; Murray et al. 2010). Ces amas ont effectivement été observés à haut décalage spectral ; cependant, ils sont gigantesques et ne sont pas observés dans les galaxies de l'Univers local (Elmegreen et al. 2009), ce qui suggère que les conditions de formation stellaire de l'Univers local ne sont plus propices à la formation de tels amas (Calzetti et al. 2015). Toutefois, les structures agrégées présentes dans les galaxies irrégulières de l'Univers local res-

semblent fortement aux amas géants de formation stellaire observés au début de l’Univers. Par contre, les masses de ces agrégats sont des dizaines de fois plus faibles que celles des amas géants (Elmegreen et al. 2012 ; Elmegreen et al. 2009). Ceci suggère que les processus internes et externes de formation stellaire et les conditions dans lesquelles elle prend place ont changé au cours de l’évolution de l’Univers (Calzetti et al. 2015). Dans tous les cas, les galaxies irrégulières sont d’excellents substituts pour les galaxies du passé et méritent d’être étudiées pour mieux comprendre la formation stellaire à toutes les échelles et l’évolution des galaxies. De plus, les galaxies irrégulières pourraient permettre d’effectuer des liens entre les activités de formation stellaire et les propriétés globales des galaxies (Dobbs et al. 2011, 2014 ; Hopkins et al. 2013).

1.2.1 Métallicité

En astrophysique, la métallicité fait référence à l’abondance chimique d’éléments plus lourds que l’hélium. Ces éléments proviennent en majorité de la nucléosynthèse des étoiles massives. Ils sont produits dans le cœur des étoiles et sont relâchés principalement dans le milieu interstellaire lors des phases terminales de leur vie (Maeder 2009). Ainsi, la concentration de métaux dans le gaz croît de manière monotone en fonction des générations de populations stellaires et la métallicité est parfois utilisée comme indicateur de l’évolution (maturité) de la galaxie, puisqu’elle informe sur le nombre de générations d’étoiles produites avec le gaz. Mais il faut se souvenir que la métallicité peut être modifiée par des mécanismes externes, tels que l’accrétion de gaz lors d’interactions avec d’autres galaxies ou du milieu intergalactique.

La métallicité des galaxies naines est d’un intérêt particulier, en raison de sa relation avec la formation stellaire relativement simple pour ces galaxies (Berg et al. 2012 ; Hunter et al. 1982 ; Izotov et al. 2006 ; Kobulnicky et al. 1999 ; Lequeux et al. 1979 ; McCall et al. 1985 ; Sabbadin et al. 1984). Les trois dernières décennies ont apporté énormément de données par le biais de plusieurs études sur la composition chimique des galaxies naines (Kunth & Östlin 2000). Grâce à ces recherches, une relation claire entre leur faible métallicité et faible masse est mise en évidence (Lequeux et al. 1979). Les galaxies naines ont tendance à être moins riches en métaux que les galaxies géantes. Cependant, à grand décalage spectral, l’existence de grandes protogalaxies massives dépourvues de métaux est spéculée (Kunth & Östlin 2000). Un des intérêts pour l’étude des galaxies irrégulières est de mieux comprendre les processus de formation d’étoiles massives dans du gaz pauvre en métaux, puisque les propriétés de ces étoiles (c.-à-d. population III) sont totalement différentes des étoiles formées dans un milieu contenant des métaux (Maeder 2009). Ainsi, les galaxies naines sont d’excellents laboratoires pour étudier les mécanismes de formation stellaire dans des environnements moins métalliques.

La métallicité du gaz se mesure couramment avec l’abondance relative de l’oxygène et de l’hydrogène ($12 + \log[\text{O}/\text{H}]$). Pour déterminer les indicateurs de métallicité, diverses raies d’émission du gaz sont utilisées, selon le domaine spectral couvert par les instruments obser-

vationnels. Plusieurs méthodes permettent de calibrer ces indicateurs de métallicité (Denicoló et al. 2002 ; Dopita et al. 2016 ; Garnett 1992 ; Kewley & Dopita 2002 ; Kewley & Ellison 2008 ; Kobulnicky et al. 1999 ; Kobulnicky & Kewley 2004 ; Marino et al. 2013 ; Pettini & Pagel 2004 ; Pilyugin & Grebel 2016 ; Zaritsky et al. 1994). La majorité des indicateurs utilisent les raies fortes et sont calibrées empiriquement. La meilleure méthode, dite directe, se base sur une mesure de la température électronique, qui nécessite la raie aurorale $[\text{O III}]\lambda 4363$, très difficile à observer, car elle est beaucoup plus faible que les autres raies d'émission (Kumari et al. 2017).

La métallicité actuelle du milieu interstellaire dans une galaxie peut donc être mesurée à l'aide des régions H II (p. ex. Diaz 1989 ; Marino et al. 2013 ; Rosales-Ortega et al. 2011 ; Sánchez-Menguiano et al. 2016). Ces régions de gaz ionisé permettent de déterminer localement la métallicité du gaz. Ainsi, les variations spatiales des abondances chimiques à travers une galaxie peuvent être étudiées. De plus, les abondances mesurées peuvent servir à contraindre des théories d'évolution chimiques de galaxies ou à obtenir de l'information sur les processus de nucléosynthèse prenant place dans les étoiles. En outre, la métallicité permet d'obtenir de l'information additionnelle sur l'historique de formation stellaire de la galaxie (Espinosa-Ponce et al. 2020).

Un avantage de l'utilisation des régions H II pour la mesure des abondances chimiques est leur présence dans des galaxies à haut décalage spectral et le fait qu'elles sont brillantes (Kunth & Östlin 2000). Cependant, l'utilisation des régions H II comme indicateur de métallicité requiert que les galaxies étudiées forment activement des étoiles.

1.2.2 Régions HII

Le milieu interstellaire fait référence au gaz et à la poussière localisés entre les étoiles dans une galaxie. Le gaz se retrouve sous trois formes : soit sous forme de gaz moléculaire, atomique, ou ionisé. Les étoiles sont formées par l'effondrement de nuages moléculaires. Les masses des étoiles formées par ce nuage suivent globalement une fonction de masse initiale assez standard (Kroupa 2001). Selon leur masse, les étoiles ont des propriétés très différentes, les forçant à fonctionner et à évoluer de manières distinctes. Notamment, les étoiles de type O et B sont considérées comme des étoiles massives ($M_\star \geq 10 M_\odot$; Lee et al. 2009). En raison de leur masse, celles-ci sont chaudes ($T_{\text{eff}} \geq 10\,000\,\text{K}$; Maeder 2009) et utilisent leurs combustibles intensément et rapidement. Par conséquent, elles émettent énormément d'énergie dans le milieu interstellaire et leur temps de vie est très court ($\tau \leq 10\,\text{Mans}$; Maeder 2009). Les étoiles OB produisent ainsi une grande quantité de photons UV qui ionisent le gaz environnant. La recombinaison du gaz ionisé produit, entre autres, de l'émission $\text{H}\alpha$ (Osterbrock 1989). Une région H II est définie comme un volume d'ionisation de gaz d'hydrogène (majoritairement), excité par au moins une étoile massive et jeune ($\leq 15\,\text{Mans}$; Espinosa-Ponce et al. 2020 ; Scowen 1992). Le court temps de vie des étoiles OB permet de tracer la formation stellaire récente via

les régions H II.

Les régions H II possèdent une grande plage de propriétés physiques. Elles peuvent avoir des diamètres allant de quelques parsecs (p. ex. la nébuleuse d'Orion avec ≤ 8 pc ; Anderson et al. 2014) jusqu'à des centaines de parsecs (p. ex. 30 Dorade avec ~ 200 pc, NGC 604 avec ~ 460 pc, et NGC 5471 avec ~ 1 kpc ; García-Benito et al. 2011 ; Lebouteiller et al. 2008 ; Oey et al. 2003). Les plus gros amas stellaires peuvent contenir des milliers d'étoiles. Avec le temps, les étoiles massives contribuent de manière significative à l'énergie mécanique et radiative du milieu interstellaire. La taille des régions H II est aussi reliée à leur âge. Au début, elles sont spatialement très compactes (<1 pc) et prennent de l'expansion au fil du temps (Spitzer 1978 ; Zamora-Avilés et al. 2019). À la fin de leur vie, elles s'éteignent totalement. Les amas stellaires ne coïncident spatialement pas toujours avec le centre des régions H II, puisque celles-ci croissent anisotropiquement dans le milieu interstellaire (Zamora-Avilés et al. 2019). Il est alors très intéressant d'étudier la morphologie des régions H II, leur cinématique, ainsi que les mécanismes impliqués dans la formation des amas, pour mieux comprendre leur évolution et leur impact sur le gaz environnant (Cosens et al. 2022). Elles permettent donc d'observer les interactions complexes entre les étoiles massives et le milieu interstellaire.

La formation stellaire récente indique que rapidement, les étoiles OB restitueront les métaux fraîchement formés dans leurs cœurs, ce qui contribue à l'enrichissement chimique de l'environnement interstellaire local. Ainsi, les régions H II, qui montrent aussi des raies de métaux ionisés, permettent aussi l'étude de l'évolution de la métallicité des galaxies. Globalement, les régions H II ont longtemps été étudiées pour approfondir la compréhension du rôle de la formation stellaire dans l'évolution des galaxies (Gutiérrez et al. 2011).

La raie d'émission H α est l'une des plus fortes émises par les régions H II dans le domaine visible. Ainsi, elle est utilisée pour détecter la présence de régions H II dans les données observationnelles de galaxies proches et lointaines (Youngblood & Hunter 1999). Dans le but d'étudier statistiquement les caractéristiques et les comportements des régions H II, des catalogues de régions H II sont construits. Ceux-ci recueillent, entre autres, les propriétés morphologiques, cinématiques, et chimiques des régions H II. Il est aussi possible de corrélérer ces propriétés avec l'environnement où elles se situent dans la galaxie, mais aussi avec l'environnement dans lequel la galaxie se situe dans l'Univers. Grâce à l'avènement de technologies clefs, telles que les techniques d'imagerie spectrale, des données avec des résolutions spatiales et spectrales plus élevées sont disponibles (Espinosa-Ponce et al. 2020 ; Gutiérrez et al. 2011). Ceci permet de mieux échantillonner les régions H II en atteignant des luminosités plus faibles qu'avant et en résolvant les complexes de régions H II. De plus, les études peuvent couvrir plusieurs raies spectrales. Ainsi, il est possible de produire des analyses statistiques beaucoup plus détaillées du gaz, en mesurant plusieurs paramètres physiques (p. ex. température, densité, source d'ionisation, en plus de sa métallicité ; Osterbrock 1989).

Les mécanismes sous-jacents régulant la formation stellaire des galaxies peuvent être étudiés via la distribution spatiale et la cinématique des régions H II (Hunter 1982). Dans les galaxies possédant des ondes de densité (p. ex. les galaxies spirales), les régions H II tracent la structure des bras spiraux, barres, et anneaux (Baade & Mayall 1951 ; Humphreys 1979 ; Hunter 1982 ; Morgan et al. 1952). Par exemple, les ondes de densité spirales augmentent la compression du gaz dans les bras, ce qui favorise la formation stellaire, donc la présence de régions H II qui ont un temps de vie trop court pour avoir le temps d'être entraînées hors des bras spiraux (Carroll & Ostlie 2006). Par conséquent, dans les galaxies spirales, des populations différentes de régions H II sont observées dans les bras et entre les bras (Knapen et al. 1993 ; Kreckel et al. 2016). Donc, l'étude des régions H II (p. ex. à l'aide de leur fonction de luminosité) permet de mieux comprendre l'influence qu'ont les ondes de densité sur la formation stellaire (Lin & Shu 1964 ; Roberts 1969 ; Toomre 1977 ; Woodward 1976).

L'absence de structures ordonnées et de dynamique globale dans les galaxies irrégulières ne les empêchent pas d'être efficaces pour former des étoiles (Gallagher et al. 1981 ; Huchra 1977 ; Hunter et al. 1982). La distribution spatiale des régions H II dans les galaxies irrégulières diffère de celles observées dans les galaxies spirales. Il est prédict que la distribution des régions H II dans les galaxies irrégulières naines est plus homogène et aléatoire que dans les galaxies avec des ondes de densité spirales, en raison de l'absence de bras spiraux et de barres (Fuentes-Masip et al. 2000a ; Hunter et al. 2018). Dans certains cas, cette formation stellaire peut être causée par des interactions externes (Larson & Tinsley 1978). Cependant, plusieurs autres cas observés ne sont pas reliés à des interactions. Ceci suggère que des mécanismes internes qui régulent la formation stellaire des galaxies irrégulières naines sont aussi possibles (Hunter 1982), comme expliqué plus en détail dans la section précédente.

En étudiant la distribution des régions H II, Elmegreen & Elmegreen (1980) suggèrent, par exemple, que la présence d'une barre dans les galaxies irrégulières magellaniques créerait une compression du gaz, entraînant une activité de formation stellaire plus élevée. Dans les cas sans interaction, certains chercheurs expliquent que les régions de formation stellaire des galaxies irrégulières naines ont tendance à être regroupées en amas hiérarchiques, comme si une seconde génération d'étoiles est induite par la formation de la génération précédente (Dopita et al. 1985 ; Efremov & Elmegreen 1998a,b).

1.3 NGC 4449

Dans cette étude, les régions H II de la galaxie irrégulière naine NGC 4449 sont analysées. NGC 4449 est d'intérêt particulier pour l'étude de l'évolution des galaxies, puisqu'elle est une galaxie irrégulière naine très atypique, avec une forte formation stellaire et une morphologie perturbée. De plus, ses propriétés distinctes de celles des galaxies spirales permettent de comparer ses régions H II avec celles obtenues pour les galaxies spirales incluses dans le programme

SIGNALS (Rousseau-Nepton et al. 2019). En outre, sa proximité offre une résolution spatiale qui facilite la séparation des complexes de régions H II. La résolution spectrale des données permet aussi une étude cinématique des régions H II individuelles. La section suivante décrit les propriétés de cette galaxie, de la distribution de son gaz neutre, et des interactions qu'elle a subies dans le passé. Toutes ses informations permettent de mieux mettre en contexte le choix de l'étude de cette galaxie et les tendances dans les résultats obtenus.

1.3.1 Description générale

NGC 4449 est une galaxie irrégulière naine de type magellanique (IB(s)m ; de Vaucouleurs et al. 1991). Une image de NGC 4449 est présentée à la Figure 1.1. Elle se trouve à une distance de (3.82 ± 0.27) Mpc (Annibali et al. 2008 ; Martinez-Delgado et al. 2012). Certains observent une barre en son centre, et d'autres y voient aussi un début de bras au nord, contenant de la formation stellaire (p. ex. Hill et al. 1994). Cette formation stellaire active semble induire des traits morphologiques caractéristiques, tels que des filaments, des arcs et des boucles au travers de la galaxie en entier (Hunter & Gallagher 1997). Un disque n'est pas particulièrement souligné, vu sa faible vitesse de rotation ($\sim 18 \text{ km s}^{-1}$; Hunter et al. 1998).

NGC 4449 est reconnue pour sa formation stellaire spectaculaire. En effet, son taux de formation stellaire est de $0.47 \text{ M}_\odot \text{ an}^{-1}$ (Hunter et al. 1999 ; Sacchi et al. 2018). Ce taux de formation stellaire est dérivé à l'aide de la luminosité H α totale. Il est surprenant qu'un si petit système ($M_\star \simeq 1.1 \times 10^9 \text{ M}_\odot$; Calzetti et al. 2015 ; Sacchi et al. 2018) forme autant d'étoiles. La densité de taux de formation stellaire de NGC 4449 est de $0.011 \text{ M}_\odot \text{ an}^{-1} \text{ kpc}^{-2}$, en supposant une surface sous le rayon de $R_{25} = 3.6 \text{ kpc}$ (Hunter et al. 1999 ; Sacchi et al. 2018). Elle est considérée comme une des galaxies ayant le sursaut de formation stellaire galactique global, relatif à la masse, le plus fort dans l'Univers local (Martinez-Delgado et al. 2012). Selon Hunter (1997), Hunter et al. (1999) et de Vaucouleurs et al. (1991), NGC 4449 est une des galaxies irrégulières de type magellanique les plus lumineuses et formant le plus d'étoiles.

Une explication possible pour le taux de formation stellaire élevé observé est que des interactions avec d'autres galaxies dans le passé causent un impact sur la dynamique du gaz froid, menant à un sursaut de formation stellaire (Karachentsev et al. 2007 ; Martinez-Delgado et al. 2012).

La masse ($M_\star \simeq 1.1 \times 10^9 \text{ M}_\odot$; Calzetti et al. 2015 ; Sacchi et al. 2018), taille ($R_{\text{opt}} \simeq 3.3 \text{ kpc}$; Lelli et al. 2014a), et magnitude absolue ($M_V = -18.6$; Martinez-Delgado et al. 2012) de NGC 4449 sont similaires à son analogue, le Grand Nuage de Magellan (LMC). Cependant, le taux de formation stellaire extrêmement élevé de NGC 4449 la distingue du LMC (Martinez-Delgado et al. 2012 ; Sacchi et al. 2018). La luminosité de NGC 4449 est 1.4 fois plus élevée que celle du LMC et forme des étoiles 2 fois plus rapidement (Hunter et al. 1999). Comparativement



FIGURE 1.1 – Image en couleur de NGC 4449 créée avec les données de SITELLE. L'image profonde du filtre SN3 est utilisée comme canal rouge, le canal vert correspond à l'image profonde du filtre SN2, et l'image profonde du filtre SN1 est utilisée pour le canal bleu. La carte de flux H α est superposée pour accentuer la couleur rouge des régions H II. Le nord est vers le haut et l'est est vers la gauche. Le champ de vue est de $11' \times 11'$, centré sur les coordonnées RA 12h28m09.8s et DEC +44°05m51.2s. Cette image a été créée par Laurent Drissen.

au LMC, NGC 4449 permet l'étude des propriétés des galaxies irrégulières magellaniques sans être perturbée par les effets de marée d'une galaxie plus massive (Theis & Kohle 2001). La formation stellaire de NGC 4449 est discutée plus en détail dans la Section 1.3.6. Comme il est attendu pour les galaxies irrégulières naines, NGC 4449 a une métallicité considérée comme faible, soit de $12 + \log[\text{O}/\text{H}] \simeq 8.3$ (Annibali et al. 2017; Berg et al. 2012; Cook et al. 2014; Engelbracht et al. 2008; Izotov et al. 2006; Kobulnicky et al. 1999; Lequeux et al. 1979; Marble et al. 2010; Martin 1997; Martinez-Delgado et al. 2012; Sabbadin et al. 1984; Scowen 1992; Skillman et al. 1989). La métallicité de NGC 4449 est explorée à la Section 1.3.7.

Selon certaines définitions, la magnitude absolue de NGC 4449 ne la définirait pas comme une galaxie naine (Martinez-Delgado et al. 2012); cependant, cette limite est très arbitraire et varie grandement dans la littérature. Dans tous les cas, NGC 4449 se comporte comme une

galaxie irrégulière naine ; ainsi, les concepts décrits précédemment s'appliquent.

1.3.2 Observations multispectrales

NGC 4449 fascine les astrophysiciens depuis longtemps par sa beauté complexe ; ainsi, elle a été observée dans plusieurs domaines spectraux par de nombreux télescopes. Entre autres, dans le domaine radio, le gaz H I a été observé avec le *Very Large Array* (Chyzy et al. 2000 ; Walter et al. 2008), et avec l'instrument *SCUBA* au Télescope *James Clerk Maxwell* (Böttner et al. 2003). Le gaz CO a été étudié avec le télescope de 45 m de l'Observatoire radio *Nobeyama* (Sasaki et al. 1990). Son halo de gaz H I est particulièrement grand pour une galaxie irrégulière (Huchtmeier et al. 1981) et montre une rotation opposée entre le centre et les bords (Bajaja et al. 1994). De plus, la polarisation du continuum radio observé avec le *Very Large Array* permet de conclure qu'elle possède un grand champ magnétique ordonné (Chyzy et al. 2000 ; Klein et al. 1996). Un restant de supernova très jeune et lumineux se retrouve dans NGC 4449 (Balick & Heckman 1978 ; Bignell & Seaquist 1983 ; Blair et al. 1983, 1984 ; Lacey et al. 2007 ; Patnaude & Fesen 2003 ; Seaquist & Bignell 1978 ; Summers et al. 2003).

Dans l'infrarouge proche, moyen, et lointain, NGC 4449 a été explorée avec les télescopes spatiaux *Spitzer* (Dale et al. 2009 ; Engelbracht et al. 2008 ; Sheth et al. 2010 ; Werner et al. 2004), *IRAS* (Hunter et al. 1986), *WISE* (Wright et al. 2010), *Planck* (Collaboration et al. 2011), et *Herschel* (Bendo et al. 2012 ; Karczewski et al. 2013 ; Pilbratt et al. 2010). Dans l'infrarouge proche, elle est aussi observée avec le télescope spatial *Hubble* (Böker et al. 1999) et lors de l'étude *2MASS* (Jarrett et al. 2003 ; Skrutskie et al. 2006). Thronson et al. (1987) dérivent une luminosité infrarouge ($10\text{--}150 \mu\text{m}$) de $6.1 \times 10^{42} \text{ erg s}^{-1}$ (corrigée pour la distance supposée dans cette étude) en utilisant le télescope de 0.9 m à l'observatoire aéroporté *Kuiper*. À l'aide des observations du CO, Hunter & Thronson (1996) ont relevé la présence de nuages moléculaires complexes à travers l'entièreté de NGC 4449. À l'aide de l'imageur à champ large *Suprime-Cam* ($34' \times 27'$) au Télescope *Subaru* de 8.2 m, permettant un échantillonage de $0''.202$, l'interaction avec sa galaxie satellite (NGC 4449B), située à une distance projetée de 9 kpc (Rich et al. 2012), est mise en évidence avec les filtres r' et i' (Martinez-Delgado et al. 2012). Avec cette résolution, les étoiles individuelles peuvent être résolues, permettant de mieux comprendre le progéniteur de NGC 4449B et l'interaction s'étant déroulée. Une image très profonde, allant de 3500 Å à 8500 Å, est aussi obtenue pour cette étude avec le télescope de 0.5 m de l'Observatoire à distance *BlackBird*, avec un champ de vue de $31'.3 \times 31'.3$ et un échantillonage de $0''.46$ (Martinez-Delgado et al. 2012). Toloba et al. (2016) concluent que les deux systèmes sont gravitationnellement liés à l'aide des données du spectrographe *DEIMOS* au télescope de 10 m à l'Observatoire *Keck*.

Dans le visible, NGC 4449 a été observée avec le télescope de 3 m à l'Observatoire *Lick* (Hodge 1967) ; avec le télescope de 1.5 m à l'Observatoire *Palomar* (Frei et al. 1996 ; Hodge 1967 ; Scowen 1992) ; avec le télescope de 1.82 m de l'Observatoire d'*Asiago* (Sabbatin & Bianchini

1979) ; avec le télescope de 1.1 m à l'Observatoire *Lowell* (Frei et al. 1996) ; avec le *Vatican Advanced Technology Telescope* (Taylor et al. 2005) ; pour l'étude du *Sloan Digital Sky Survey* (Adelman-McCarthy et al. 2007 ; York et al. 2000) utilisant le télescope de 2.5 m à l'Observatoire *Apache Point* ; pour le *Carnegie Atlas* avec le Télescope *Hooker* à l'Observatoire du *Mont Wilson* (Sandage & Bedke 1994) ; pour, entre autres, l'étude du *Local Volume Legacy* (Cook et al. 2014) avec le télescope de 0.9 m, de 2.1, et de 4 m (avec le spectrographe échelle) à l'Observatoire national de *Kitt Peak* (Cook et al. 2014 ; Hodge & Kennicutt 1983 ; Hunter 1982 ; Kennicutt 1992 ; Kennicutt & Chu 1988) ; avec le spectrographe échelle du télescope de 1.5 m de l'Observatoire du *Mont Hopkins* (Hartmann et al. 1986) ; pour, entre autres, l'étude *GHASP* (Epinat et al. 2008) utilisant le Fabry-Perot au télescope de 1.98 m à l'Observatoire de *Haute Provence* (Crillon & Monnet 1969 ; Epinat et al. 2008) ; avec le Fabry-Perot *PUMA* au télescope de 2.1 m à l'Observatoire astronomique national de *la Sierra de San Pedro Martir* (Valdez-Gutiérrez et al. 2002) ; avec le Fabry-Perot *TAURUS-II* au Télescope *William Herschel* de 4.2 m à l'Observatoire *del Roque de los Muchachos* (Fuentes-Masip et al. 2000b) ; avec le spectrographe à champ intégral *Gemini Multi-Object Spectrograph North* à l'Observatoire *Gemini* (Kumari et al. 2017) ; et avec le spectrographe imageur *SITELLE* au Télescope *Canada-France-Hawaii* (Drissen et al. 2019 ; Rousseau-Nepton et al. 2019). La spectroscopie échelle à fentes longues et Fabry-Perot a permis d'observer des structures dynamiques intéressantes, telles que des bulles en expansion, des coquilles supergéantes, et des filaments avec des vitesses très élevées (Bomans & Weis 2014 ; Hunter & Gallagher 1997). Les données obtenues avec le télescope spatial *Hubble* permettent, entre autres, d'étudier les populations stellaires contenues dans NGC 4449 dans le cadre de l'étude *LEGUS* (Adamo et al. 2017 ; Calzetti et al. 2015 ; Cignoni et al. 2018, 2019 ; Cook et al. 2019 ; Sacchi et al. 2018 ; Whitmore et al. 2020) et d'étudier les régions H II (Gutiérrez & Beckman 2010). Les observations du gaz ionisé révèlent une morphologie très perturbée ; des bulles, coquilles et filaments de gaz H α sont observées (Hunter & Gallagher 1990, 1997). En étudiant les régions H II, Hartmann et al. (1986) concluent que leurs cinématiques très chaotiques seraient associées aux interactions passées de NGC 4449.

Dans l'ultraviolet, NGC 4449 a été imagée avec le *Ultraviolet Imaging Telescope* (Kuchinski et al. 2000) et avec *GALEX* (Dale et al. 2009 ; Martin et al. 2005). L'élargissement des raies d'absorption (O I, Si II, Fe II) suggère de grandes dispersions de vitesses dans le gaz neutre, causées par des turbulences (James et al. 2014).

Dans les rayons X, NGC 4449 a été observée avec les télescopes spatiaux *Einstein* (Blair et al. 1983 ; Fabbiano et al. 1992) ; *ROSAT* (Della Cecca et al. 1997 ; Vogler & Pietsch 1997) ; *Chandra* (Summers et al. 2003 ; Swartz et al. 2011) ; *XMM-Newton* (Feng & Soria 2011 ; Jansen et al. 2001 ; Turner et al. 2001 ; Winter et al. 2006) ; et *Swift* (Burrows et al. 2005 ; Gehrels et al. 2004). Ces études ont identifié des sources d'émission ponctuelles, cohérentes avec des restants de supernovae dans la galaxie, des binaires à rayons X, et des sources à rayons X mous

(Della Ceca et al. 1997; Vogler & Pietsch 1997). L'émission diffuse dans les rayons X de la galaxie est aussi étudiée par Della Ceca et al. (1997) et Vogler & Pietsch (1997), et Summers et al. (2003), concluant qu'elle est spatialement cohérente avec la distribution du gaz H α et H I (Summers et al. 2003).

1.3.3 Gaz neutre

NGC 4449 se distingue des autres galaxies irrégulières par sa distribution de gaz H I particulière (Hunter et al. 1998). Le halo de gaz neutre de NGC 4449 s'étend environ 14 fois plus loin que l'émission visible (Bajaja et al. 1994), qui fait $3.9 \text{ kpc} \times 2.8 \text{ kpc}$ de diamètre (Fuentes-Masip et al. 2000a), corrigé pour la distance utilisée dans cette étude. Comparativement aux autres galaxies naines, cette différence de taille est 3 fois plus grande (Huchtmeier et al. 1981 ; Hunter et al. 1998).

En plus d'être très étendu, le halo de gaz H I présente une morphologie très perturbée, des anneaux géants étranges, des complexes en forme de coquilles, et des filaments qui s'entourent autour de l'émission visible (Hunter et al. 1998). Certains chercheurs attribuent la déformation du halo de H I aux interactions subies dans le passé par NGC 4449, en particulier avec DDO 125, située à une distance projetée de 41 kpc (Hunter et al. 1999), tel que discuté plus en détail dans la Section 1.3.4.

Une autre particularité de gaz H I de NGC 4449 est sa cinématique. Un gradient de vitesse opposé entre la partie interne et externe est observé (Bajaja et al. 1994 ; Hunter et al. 1999 ; Theis & Kohle 2001 ; van Woerden et al. 1975). Un tel phénomène est un indicateur clair d'interaction dans le passé. Dans la partie extérieure de l'enveloppe, un gradient de vitesse, partant du nord vers le sud, peut être remarqué (Bosma 2017). Dans la partie interne, où se situe l'émission visible, la vitesse change de sens pour se superposer avec celle du gaz ionisé (Bosma 2017). Cette vitesse de rotation est faible (18 km s^{-1} ; Hunter et al. 1998), indiquant un faible disque avec une inclinaison de 43° (Valdez-Gutiérrez et al. 2002) avec un angle de position de -60° (Bosma 2017). Lorsque l'étendu complet du halo de gaz H I est considéré, la vitesse maximale de rotation s'élève à $(100 \pm 10) \text{ km s}^{-1}$ (Hunter et al. 1998). Les régions ayant les dispersions de vitesse les plus élevées dans le gaz H I ne coïncident pas avec les régions de formation stellaire (Hunter et al. 1999). Certaines régions de forte dispersion de vitesse se retrouvent dans le halo (Hunter et al. 1999).

1.3.4 Interactions

La morphologie inhabituelle de NGC 4449 est interprétée comme une signature de perturbations externes, en particulier due à des interactions (Cignoni et al. 2018). Ces dernières n'ont pas seulement un impact sur la morphologie de la galaxie, mais aussi, entre autres, sur la formation stellaire et la cinématique du gaz.

Comme mentionné dans la Section 1.3.3, le halo de NGC 4449 est tellement étendu qu'il atteint la galaxie voisine DDO 125 qui est située à une distance projetée de 41 kpc vers le sud-est (Hunter et al. 1999). Selon des simulations numériques, l'approche maximale se serait produite il y a 350 Mans à une distance minimale de 25 kpc (Theis & Kohle 2001 ; Theis 1999). La morphologie inhabituelle observée dans le gaz H_I indiquerait que le gaz n'est pas encore retourné à son état d'équilibre (Cignoni et al. 2018).

Par contre, l'interaction entre NGC 4449 et DDO 125 n'est pas parfaitement claire, puisqu'elles ne sont pas observées en train d'interagir directement. Bien que le gaz H_I de NGC 4449 soit déformé, DDO 125 ne présente aucun signe de perturbation (Hunter & Gallagher 1997). En effet, globalement, le gaz et les propriétés optiques de DDO 125 sont typiques de celles des galaxies irrégulières (Hunter & Gallagher 1997). Après une telle interaction, si forte qu'elle cause autant de perturbations dans NGC 4449, un pont de matière entre les deux galaxies serait attendu. Pourtant, un pont de matière clair n'est pas observé. De plus, DDO 125 possède une masse de gaz H_I relative plus faible ($1 \times 10^8 M_{\odot}$; Fisher & Tully 1981) que celle de NGC 4449 (Hunter et al. 1998). Ainsi, après leur interaction, selon les modèles, DDO 125 aurait perdu 90 % de sa masse pour expliquer la masse des filaments autour de NGC 4449 (Hunter et al. 1998), tel que les observations ne concordent pas bien avec l'existence d'une interaction passée entre NGC 4449 et DDO 125.

Des hypothèses d'interactions entre NGC 4449 et d'autres galaxies ont aussi été émises, pour expliquer sa morphologie perturbée. En effet, un pont de marée stellaire est observé par Karachentsev et al. (2007), Martinez-Delgado et al. (2012), Rich et al. (2012) et Toloba et al. (2016) dans le halo de NGC 4449. Ce pont proviendrait de l'interaction actuelle avec la galaxie satellite NGC 4449B. NGC 4449B est une galaxie naine (dSph) ayant une masse stellaire $M_{\star} < 1 \times 10^8 M_{\odot}$ (Martinez-Delgado et al. 2012). NGC 4449B se situe à une distance projetée de 9 kpc par rapport au centre du noyau de NGC 4449 (Rich et al. 2012). Elle ne semble pas former d'étoiles ni posséder de gaz froid (Martinez-Delgado et al. 2012). Il serait possible que son gaz ait été accrétré par NGC 4449, arrêtant la formation stellaire de NGC 4449B. En effet, seuls des amas globulaires en dissolution sont observés dans les vestiges de NGC 4449B (Odenkirchen et al. 2003). De plus, la morphologie en forme de S de NGC 4449B est caractéristique de galaxies en interaction (Capuzzo Dolcetta et al. 2005 ; Peñarrubia et al. 2009).

Rich et al. (2012) spéculent que les galaxies en sont à leur première rencontre, en se basant sur la morphologie de NGC 4449B et des simulations. L'interaction aurait été provoquée par un passage rapproché il y a 1×10^8 ans. Cette échelle temporelle est cohérente avec le sursaut de formation stellaire présent dans NGC 4449. La métallicité du pont de marée, mesurée par Toloba et al. (2016), suggère que le progéniteur aurait pu être aussi massif que les galaxies naines du Fourneau ou du Sagittaire.

En outre, Annibali et al. (2012) suggèrent qu'un amas globulaire, situé dans deux structures

d'étoiles bleues dans NGC 4449, pourrait être le noyau d'une ancienne galaxie satellite riche en gaz.

NGC 4449, faisant partie du groupe de galaxies CVnI (de Vaucouleurs 1975), les hypothèses d'interactions avec d'autres galaxies sont donc très plausibles (Hunter et al. 1999). La morphologie visible et du gaz froid de NGC 4449 indique clairement que des forces extérieures ont causé des perturbations. Cependant, même avant d'avoir vécu des interactions, NGC 4449 aurait tout de même été une galaxie de type tardif. Hunter et al. (1999) justifient cette hypothèse en se basant sur des indices observationnels. Un premier indice est l'absence de bras spiraux et d'un bulbe central clair, comme typiquement observés dans des galaxies de type plus précoce. Ayant été d'un type morphologique différent dans le passé, NGC 4449 présenterait des fossiles plus évidents de structures galactiques. Il n'est pas impossible qu'une galaxie plus précoce perde ses structures morphologiques lors d'une interaction, cependant, dans ces cas, les interactions sont beaucoup plus violentes. En effet, si NGC 4449 avait subi des interactions si intenses, au point de perdre ses composantes morphologiques, elle présenterait une morphologie globale beaucoup plus perturbée aujourd'hui.

Un deuxième indice est la petite taille visible de NGC 4449. Il est connu que les galaxies de type plus précoce ont tendance à être plus massives, suggérant que NGC 4449 aurait dû perdre beaucoup de masse lors de ses interactions. Cependant, les candidats d'interaction mentionnés précédemment ne sont pas des galaxies très massives qui auraient eu le potentiel gravitationnel requis pour accréter le gaz de NGC 4449, lui donnant un type plus tardif.

Un troisième indice est que la vitesse de rotation faible et la quantité élevée de gaz, en combinaison avec une petite taille, sont incohérents avec la supposition que NGC 4449 ait été de type morphologique plus précoce avant les interactions. De plus, sa faible abondance en oxygène ($1/5 Z_{\odot}$; Hunter & Gallagher 1997) est caractéristique des galaxies de types plus tardifs (Hunter et al. 1999), comme mentionné dans la Section 1.1. L'absence de mécanismes de régulation globaux cause un impact sur l'historique de formation stellaire dans les galaxies naines, qui diffère de celui des galaxies plus massives. L'évolution plus lente des galaxies naines, due à leur masse plus faible, explique leur métallicité plus faible. Ainsi, puisque la métallicité croît de manière monotone dès les premiers 3 Gans (Cignoni et al. 2018) pour une galaxie massive, la métallicité de NGC 4449 n'aurait pas eu le temps de diminuer après l'interaction par l'accrétion de gaz supplémentaire faible en métaux du milieu intergalactique, puisque sa masse doit aussi avoir diminuée pour expliquer le changement de classe morphologique. Néanmoins, si NGC 4449 était une galaxie de type plus précoce avant ses interactions, beaucoup plus de signatures de ce changement et beaucoup plus de perturbations devraient être observées.

Les interactions entre les galaxies sont des facteurs importants pour leur évolution, particulièrement pour les galaxies elliptiques (Hunter et al. 1999). En effet, selon des scénarios cosmologiques, les galaxies elliptiques seraient le résultat d'interactions de galaxies, expliquant

leur présence fréquente dans les amas de galaxies (Dressler 1980). En raison de leur faible masse, les galaxies irrégulières ont tendance à être les victimes des interactions avec de plus gros objets (Hunter et al. 1999). Alors, dans certains cas, elles disparaissent totalement dans le système plus massif. Ainsi, il est rare de pouvoir observer des galaxies irrégulières ayant survécu à des interactions, ce qui rend l'étude de NGC 4449 encore plus pertinente. Hunter et al. (1999) soulignent qu'il est aussi intéressant de voir que même après une interaction, NGC 4449 demeure une galaxie irrégulière qui ne peut pas avoir changé considérablement de type morphologique. Par conséquent, l'étude de la dynamique et de la formation stellaire dans NGC 4449 peut révéler des indices additionnels sur le comportement des galaxies irrégulières ayant subi des interactions.

1.3.5 Cinématique du gaz

Les galaxies irrégulières sont reconnues pour avoir une faible vitesse de rotation, ayant des valeurs plus faibles que la moitié de la vitesse de rotation des galaxies spirales (Hunter & Gallagher 1986). Ceci est, en effet, le cas pour NGC 4449, qui présente très peu de rotation ($\sim 18 \text{ km s}^{-1}$; Hunter et al. 1998). Cependant, les structures galactiques (barre et début de bras) qu'elle présente sont connues pour avoir une influence sur la formation stellaire dans les galaxies spirales (Matteucci 2012). Ainsi, il serait possible qu'elles influencent la cinématique du gaz dans NGC 4449. Néanmoins, comme mentionné par Hunter et al. (1999), il est peu probable que NGC 4449 ait été d'un type morphologique différent avant ses interactions ; par conséquent, il est possible que ces structures morphologiques ne se comportent pas comme des barres et des bras standards de galaxies spirales. Cependant, la divergence de la polarisation atteint des valeurs très faibles dans le côté est de NGC 4449, à la jonction entre la barre et le bras (Chyzy et al. 2000). Ceci pourrait suggérer que la barre et le bras se comportent en effet comme dans une galaxie spirale standard. Par opposition, le gaz du sud de la barre montre beaucoup plus de perturbations et moins de régions H II que la partie nord et pourrait être un effet des interactions passées (Valdez-Gutiérrez et al. 2002).

Quelques recherches se sont concentrées sur la cinématique du gaz ionisé de NGC 4449. La première analyse interférométrique utilisant un Fabry-Perot, conduite par Crillon & Monnet (1969), détermine les vitesses radiales des plus gros complexes de régions H II. Arsenault & Roy (1988) et Fuentes-Masip et al. (2000a), à l'aide d'un interféromètre de Fabry-Perot à balayage, concentrent leurs recherches sur l'étude des dispersions de vitesses supersoniques dans les régions H II brillantes de la barre de NGC 4449 dans le but de les utiliser comme indicateur de distance. Valdez-Gutiérrez et al. (2002) étudient la cinématique de régions H II et du gaz diffus sur l'entièreté de NGC 4449 en utilisant un interféromètre de Fabry-Perot. À l'aide de spectroscopie à fente longue, Hartmann et al. (1986), Hunter & Gallagher (1997), Martin (1998) et Sabbadin et al. (1984) étudient la cinématique des régions H II les plus brillantes, des filaments, et des superbulles.

Des éjections de matière galactiques, appelées *outflows* ou supervents (p. ex. M82 ; Leroy et al. 2015) sont utilisés de manière fréquente pour expliquer l'enrichissement en métaux du milieu intergalactique (López-Cobá et al. 2020). Ces phénomènes ne sont pas rares ; cependant, ils sont particulièrement fréquents dans les galaxies de faible masse (López-Cobá et al. 2020 ; Veilleux et al. 2005). Ils pourraient alors empêcher l'évolution des galaxies naines en atténuant la formation stellaire (Bower et al. 2006 ; Hopkins & Hernquist 2009 ; López-Cobá et al. 2020 ; Silk & Rees 1998). Ces éjections de matière sont souvent reliées à des épisodes de formation stellaire intenses, à cause des chocs cinématiques engendrés par les explosions de supernovae quelques méga-années plus tard, comme expliqué dans la Section 1.2. Ceci explique les supervents galactiques présents dans les galaxies possédant des hauts taux de formation stellaire et en sursaut de formation stellaire (Aguirre et al. 2001 ; Heckman et al. 2000 ; López-Cobá et al. 2020 ; Rupke et al. 2005a,b,c). Une perte de gaz dans les galaxies naines est un processus bien documenté, p. ex. par James et al. (2016), Meurer et al. (1992) et Roy et al. (1991). Ces pertes sont attribuées à plusieurs mécanismes. En effet, les explosions de supernovae (Mac Low & Ferrara 1999) ou les vents stellaires des étoiles massives (Tremonti et al. 2004) peuvent en être responsable (Kumari et al. 2017).

Le processus inverse, appelé *inflow*, est aussi possible, par lequel la galaxie accrète du gaz provenant de l'extérieur. Plusieurs phénomènes peuvent mener à ce genre de scénario. Le plus commun est l'accrétion de gaz extérieur lors d'interactions entre galaxies. Cependant, il est aussi possible qu'une galaxie accrète du gaz dans un environnement isolé. Une source de gaz possible est les filaments cosmiques constituant l'Univers, qui approvisionneraient de gaz primordial la galaxie. Une autre option pourrait être la réaccrétion du gaz éjecté lors d'épisodes de formation stellaire intense. Ce scénario est peu fréquent dans les galaxies de faible masse, puisque leur potentiel gravitationnel n'est pas assez élevé pour contraindre le gaz perturbé par la formation stellaire. Dans certains cas, le halo de gaz neutre retient la matière qui s'était fait éjecter dans le passé (Ott et al. 2005). Des gradients de métallicité positifs sont observés dans d'autres galaxies à différents décalages spectraux et sont expliqués par l'accrétion de gaz primordial (Elmegreen et al. 2016 ; Sánchez Almeida et al. 2014, 2015). Les *inflows* de gaz peuvent causer des inhomogénéités chimiques dans les galaxies (Ceverino et al. 2016). En effet, Cresci et al. (2010) concluent que ce phénomène est la cause des trois gradients de métallicité positifs observés dans leur étude des galaxies supportées par la rotation à des décalages vers le rouge de $z \sim 3$. Sánchez Almeida et al. (2015) suggèrent que certains sursauts de formation stellaire dans des galaxies très pauvres en métaux dans l'Univers local seraient causés par la chute de gaz cosmique primordial (Kumari et al. 2017).

NGC 4449 présente du gaz froid et ionisé fortement chaotique. Les perturbations de son gaz seraient causées par la forte activité de formation stellaire et les interactions passées. Le mouvement très complexe du gaz se traduit par la présence de composantes cinématiques multiples, comme observé par Valdez-Gutiérrez et al. (2002). Ces composantes multiples indiquent que

la vitesse du gaz et que la résolution spectrale des données sont assez élevées pour être capable de discerner des nuages de gaz qui se déplacent à des vitesses différentes, superposés sur la ligne de visée. Plusieurs scénarios peuvent expliquer la présence de mouvements si complexes dans NGC 4449. La présence d'un *outflow* ou d'un *inflow* pourrait expliquer ces observations. Les interactions passées sont aussi une explication très probable.

Summers et al. (2003) et Kumari et al. (2017) suggèrent la présence d'un *outflow* dans NGC 4449. Ce phénomène expliquerait la diminution de métallicité au centre de la galaxie observée par Kumari et al. (2017). Summers et al. (2003) justifient cette hypothèse par une augmentation de la densité de colonne à l'endroit de l'*outflow* potentiel, observé dans les rayons X. De plus, la correspondance morphologique entre H α , H I, et les rayons X consolide cette hypothèse selon eux. Les observations de Valdez-Gutiérrez et al. (2002) montrent que les régions possédant les plus grandes dispersions de vitesse coïncident aussi avec cet *outflow* potentiel.

Avec un disque incliné à 43° (Valdez-Gutiérrez et al. 2002), l'*outflow* potentiel serait vu à l'est, perpendiculaire au disque de la galaxie. Un *outflow* se présenterait dans un spectre comme une superposition de deux raies d'émission de même nature avec des décalages en vitesse différents. Avec une assez bonne résolution spectrale et/ou des vitesses assez différentes, il est possible d'observer plusieurs composantes dans un même spectre. La présence de multiples composantes dans un spectre partant du centre de la galaxie et dans l'axe de l'*outflow* potentiel serait une signature de sa présence. En effet, Valdez-Gutiérrez et al. (2002) observent la présence de doubles composantes dans ses spectres se situant à l'emplacement proposé pour l'*outflow* potentiel.

Plusieurs suggestions par rapport à l'origine de l'*outflow* de NGC 4449 sont émises. Aucune mention de la présence d'un noyau galactique actif (*active galactic nucleus*; AGN) n'est faite. Ainsi pour cette galaxie, il est peu probable que l'*outflow* soit causé par un AGN. Selon Summers et al. (2003), l'*outflow* présent dans NGC 4449 serait causé par des vents stellaires, engendrant un écoulement le long de l'axe mineur, où la pression est plus faible. L'origine de ces vents proviendrait des superamas d'étoiles (Summers et al. 2003). Ces vents transportent de l'énergie et de la matière à l'extérieur de la galaxie, potentiellement jusque dans le milieu intergalactique. La vitesse de rotation faible du gaz au centre de la galaxie ($\sim 18 \text{ km s}^{-1}$; Hunter et al. 1998) indique que la vitesse d'échappement de la galaxie est faible. Cependant, la présence du grand halo de H I pourrait retenir le gaz chaud s'échappant de la galaxie. En effet, ce phénomène a déjà été documenté dans le passé (Westmoquette et al. 2013). De plus, Kumari et al. (2017) soulèvent le fait qu'aucun restant de supernova n'a été détecté près du centre de NGC 4449 par Summers et al. (2003), en utilisant le télescope *Chandra*. En effet, le restant de supernova documenté le plus près du noyau de NGC 4449 se situe à 1' au nord de celui-ci.

Kumari et al. (2017) considèrent aussi le cas d'un *inflow* de gaz à la place d'un *outflow*. Ainsi, l'apport de gaz pauvre en métaux au centre causerait une diminution de la métallicité mesurée en ce point. Dans le cas de NGC 4449, le gaz pourrait provenir d'un *inflow* le long de filaments cosmiques. Par contre, l'accrétion de gaz provenant des interactions passées de NGC 4449 est aussi une explication probable, qui est souvent utilisée pour justifier le sursaut de formation stellaire observé (Karachentsev et al. 2007 ; Lelli et al. 2014b ; Martinez-Delgado et al. 2012). De plus, la concentration plus élevée de gaz atomique, observée sur la carte de H I de Hunter et al. (1998), est interprété par Kumari et al. (2017) comme la source potentielle du *outflow/inflow*, se situant au centre de la galaxie.

Kumari et al. (2017) proposent aussi un mécanisme alternatif pour expliquer le gradient de métallicité positif observé dans leur étude (voir Section 1.3.7). Ce mécanisme se distingue des deux autres suggestions, puisqu'il est indépendant à la présence d'un *outflow/inflow* central. Le mécanisme propose que l'accrétion de gaz préenrichi lors des interactions passées s'est faite par les régions périphériques de NGC 4449 ; ainsi le centre de la galaxie est demeuré plus faible en métaux.

Les conséquences de la présence d'un exode de gaz pourrait être catastrophiques sur NGC 4449 et modifier de manière considérable l'historique de sa formation stellaire (Summers et al. 2003). Le faible potentiel gravitationnel de NGC 4449 la rend fortement sujette à perdre son gaz nouvellement synthétisé par la forte activité de formation stellaire qui créera des supervents galactiques. Cependant, en étudiant la formation stellaire actuelle de NGC 4449 et la cinématique du gaz, Summers et al. (2003) prédisent que NGC 4449 perdrait seulement 0.1 % de sa masse ! Ainsi, NGC 4449 pourra continuer à époustoufler les astrophysiciens encore longtemps.

1.3.6 Formation stellaire

L'existence de NGC 4449 est une des preuves qu'il n'est pas nécessaire de posséder des bras spiraux importants pour former beaucoup d'étoiles (Thronson et al. 1987) ! NGC 4449 contient des populations stellaires complexes et riches, incluant des amas contenant des étoiles jeunes, intermédiaires, et vieilles (Annibali et al. 2011 ; Cignoni et al. 2019 ; Menon et al. 2021). Plusieurs pensent que ses interactions dans le passé sont responsables pour son historique de formation stellaire élaboré (Cignoni et al. 2019 ; Menon et al. 2021). En utilisant le spectre visible global de NGC 4449 et le code de modélisation spectrale **STARLIGHT**, Karczewski et al. (2013) concluent que seulement 1 % de la fraction de masse de NGC 4449 provient de populations stellaires avec un âge de <10 Mans, 20–25 % auraient environ de 100 Mans, et 60–75 % seraient plus vieilles qu'environ 1 Gans.

L'étude des populations stellaires de NGC 4449 tire avantage de sa proximité, qui permet de résoudre les étoiles individuelles pour les analyser de manière plus précise (Sacchi et al. 2018). En utilisant les observations du télescope *Hubble* dans l'UV proche à l'IR proche, dans le cadre

de l'étude *LEGUS* (Calzetti et al. 2015), un catalogue des amas stellaires de NGC 4449 a été produit (Annibali et al. 2011; Whitmore et al. 2020). Celui-ci contient les estimations des âges, masses, tailles, et extinction de ses amas stellaires. L'utilisation de l'UV proche permet de retracer la formation stellaire sur une échelle temporelle 10 fois plus grande que dans le domaine visible avec l'émission H α (Calzetti et al. 2015). Alors que l'UV est sensible aux étoiles massives et aux amas jeunes, l'IR proche permet de mieux voir les étoiles de faible masse.

Dans le passé, les populations stellaires sont étudiées par Bothun (1986), où il détermine l'emplacement des étoiles OB. Bothun (1986), Fuentes-Masip et al. (2000a), Hill et al. (1994), Hunter & Gallagher (1997), Kennicutt et al. (1989), Sasaki et al. (1990) et Scowen (1992) ont étudié le gaz et les étoiles de NGC 4449 pour mieux comprendre les processus de formation stellaire dans les galaxies irrégulières.

Annibali et al. (2008) remarquent que la majorité des populations stellaires plus jeunes que 10 Mans ne se situent pas dans le centre de la barre, près du noyau, ni dans le bras du nord. En effet, la plus grande concentration d'étoiles jeunes se retrouvent dans la partie sud de la barre, où il est possible d'observer une superbulle. Cette région correspond à celle montrant une grande perturbation dans la cinématique du gaz, telle que mentionnée dans la Section 1.3.5.

Reines et al. (2008) détectent 13 amas à émission radio thermale. Ils estiment que ces sources ont un âge de ≤ 5 Mans et une masse stellaire de $\geq 1 \times 10^4 M_{\odot}$. Ces amas représentent les endroits de naissance de la prochaine génération d'étoiles (Sacchi et al. 2018).

Sacchi et al. (2018) observent que la région à l'ouest de l'apex du bras du nord contient une population d'étoiles possédant toutes le même âge (80 Mans à 150 Mans), ce qui suggère qu'elles proviennent toutes du même épisode de formation stellaire, causé par un afflux de nouveau gaz suite à une interaction. De plus, cette région contient un amas de Wolf-Rayet massives, analogue à 30 Dorade dans le LMC. Sokal et al. (2015) concluent que cet amas contiendrait ~ 240 étoiles massives, dont ~ 18 seraient des étoiles Wolf-Rayet. Selon eux, cet amas aurait un âge minimal de ~ 3 Mans, ce qui indiquerait que le matériel natif n'a pas encore été totalement évacué dans le milieu interstellaire.

L'historique de formation stellaire de NGC 4449 a été étudié dans le visible par McQuinn et al. (2010) et Sacchi et al. (2018), et dans l'UV par Cignoni et al. (2018, 2019). Cignoni et al. (2018) suggèrent que l'augmentation du taux de formation stellaire aurait atteint son apogée il y a 10 Mans à 15 Mans. Cignoni et al. (2018) pensent que ce serait le seul événement de formation stellaire majeur dans les derniers 40 Mans et serait maintenant en train de diminuer. Dans son étude de l'historique de formation stellaire, McQuinn et al. (2010) remarquent aussi une diminution dans le taux de formation stellaire de NGC 4449, mais dans les dernières 50 Mans ; ils suggèrent que NGC 4449 serait dans une phase post-sursaut de formation stellaire.

NGC 4449 est un des systèmes formant le plus d'étoiles par unité de masse dans l'Univers local (Lee et al. 2009). En effet, NGC 4449 est souvent considérée comme une galaxie à sursaut de formation stellaire (Sacchi et al. 2018). La définition de galaxie à sursaut de formation stellaire varie d'un auteur à l'autre, selon l'analyse et les données considérés (Sacchi et al. 2018). Certaines définitions sont basées sur la courte durée de l'activité de sursaut et sur le fait que le taux de formation stellaire présent est au moins d'un facteur 2 à 3 plus élevé que le taux de formation stellaire moyen passé (McQuinn et al. 2010). Sacchi et al. (2018) trouvent que la durée du sursaut d'activité de formation stellaire de NGC 4449 est de ~ 20 Mans et que le taux de formation stellaire présent est ~ 4 fois plus élevé que le taux de formation stellaire moyen. Une autre définition considère que la largeur équivalente de l'émission H α soit supérieur à 100 \AA pour la galaxie entière pour la qualifier de galaxie à sursaut de formation stellaire (Lee et al. 2009). La largeur équivalente de l'émission H α pour NGC 4449 est de $\sim 72\text{ \AA}$ selon Sacchi et al. (2018), ce qui signifierait que NGC 4449 ne se qualifie pas comme une galaxie à sursaut de formation stellaire. Cependant, Sacchi et al. (2018) précisent que l'émission H α a une durée de vie très courte, donc elle trace seulement la formation stellaire des derniers ~ 5 Mans. Ceci est plus court que le pic de formation stellaire estimé par Sacchi et al. (2018), qui se situerait entre 5 Mans et 20 Mans. L'augmentation significative de formation stellaire survenue il y a ~ 10 Mans n'est pas considérée comme un vrai sursaut par Sacchi et al. (2018), puisqu'il est seulement un facteur ≤ 4 fois plus élevé que la phase la plus dormante. Selon Sacchi et al. (2018), un régime est considéré en sursaut quand l'augmentation de formation stellaire est au moins 10 fois plus élevée que le taux de formation stellaire moyen, que la durée est courte, et que la phase dormante est significativement plus longue que celle du sursaut. D'après cette définition, Sacchi et al. (2018) ne considèrent pas NGC 4449 comme une galaxie en sursaut de formation stellaire.

1.3.7 Méetallicité

Selon différentes sources, la métallicité globale du gaz ionisé de NGC 4449 est estimée à $12 + \log[\text{O}/\text{H}] \simeq 8.3$. Certaines études possèdent une mesure de la raie d'émission [O III] à 4363 \AA , ce qui permet d'utiliser la méthode directe. Les valeurs de métallicité globale obtenues par cette méthode sont de $12 + \log[\text{O}/\text{H}] = 8.3$ (Lequeux et al. 1979), 8.32 (Skillman et al. 1989), 8.31 ± 0.07 (Martin 1997), > 8.05 (Kobulnicky et al. 1999), 8.31 ± 0.07 (Marble et al. 2010) basé sur les mesures de Hunter et al. (1982), Sabbadin et al. (1984), McCall et al. (1985), Martin (1997), Kobulnicky et al. (1999), et Izotov et al. (2006), 8.26 ± 0.09 (Berg et al. 2012), et 8.32 ± 0.03 (Cook et al. 2014) qui utilisent une des valeurs calculées par Berg et al. (2012). Les études de la métallicité globale n'ayant pas une mesure de la raie 4363 \AA doivent utiliser des calibrateurs empiriques. Sabbadin et al. (1984) utilisent le ratio [O III]/H β et obtiennent une métallicité globale de 8.3. Scowen (1992) utilise aussi le ratio [O III]/H β et calcule l'abondance d'oxygène avec la méthode de Edmunds & Pagel (1984), ce qui résulte en une valeur de métallicité de 8.5 ± 0.1 . Engelbracht et al. (2008) utilisent les calibrateurs de Pilyugin &

Thuan (2005) et Pettini & Pagel (2004) pour obtenir leur valeur de métallicité de 8.23 ± 0.16 .

À l'aide des données du *Sloan Digital Sky Survey*, Izotov et al. (2006) a obtenu une valeur de métallicité de 8.24 ± 0.27 et 8.47 ± 0.02 à l'aide de deux spectres pris à différents endroits dans NGC 4449, en utilisant la méthode directe. Annibali et al. (2017) ont obtenu une métallicité, en utilisant la méthode directe, pour leur échantillon de 6 régions H II une métallicité de 8.37 ± 0.05 et de 8.3 ± 0.1 pour leurs 4 nébuleuses planétaires.

La région H II du centre de NGC 4449 a été étudiée avec le spectrographe à champ intégral *Gemini Multi-Object Spectrograph North* par Kumari et al. (2017). Ils obtiennent une métallicité de 7.88 ± 0.14 , à l'aide de la méthode directe. Un des buts de leur étude était de déterminer s'il est possible d'observer des inhomogénéités chimiques à l'échelle spatiale de 5.5 pc px^{-1} . Cependant, avec la méthode directe, ils concluent que des variations chimiques significatives dans la région centrale de NGC 4449, à l'intérieur de leur champ de vue de $3''.5 \times 5''$ ne sont pas observées. Kumari et al. (2017) extrapolent aussi le comportement de la métallicité en fonction du rayon galactocentrique de NGC 4449 en utilisant des données provenant des études de Böker et al. (2001), Buckalew et al. (2005), Izotov et al. (2006) et Martin (1997). Ils ont ainsi des mesures de métallicité pour quatre endroits à différentes distances du centre de la galaxie. Ceci leur permet de conclure que NGC 4449 présente un gradient de métallicité avec une pente positive, avec des valeurs entre 7.88 ± 0.14 au centre et 8.47 ± 0.02 à $\sim 1.8 \text{ kpc}$ (mesure la plus éloignée utilisée dans leur étude).

Cependant, dans les galaxies spirales, il est connu que la pente du gradient de métallicité est négative (Sánchez et al. 2016). Ceci est causé par le fait que le centre contient plusieurs générations d'étoiles, comparativement aux bords de la galaxie. Dans tous les cas, une pente dans le gradient de métallicité n'est pas nécessairement attendue dans une galaxie irrégulière, puisque la dynamique radiale du gaz et l'historique de formation stellaire diffèrent. Néanmoins, des inhomogénéités chimiques sont attendues dans les galaxies formant des étoiles, causées par l'afflux et l'exode de gaz (Ceverino et al. 2016 ; Cresci et al. 2010 ; Davé et al. 2011 ; Kewley et al. 2010 ; Kumari et al. 2017 ; Sánchez Almeida et al. 2013, 2014, 2015).

1.3.8 Régions HII

Les régions H II de NGC 4449 ont été étudiées à maintes reprises, dans le but de mieux comprendre l'origine de la formation stellaire particulière. Plusieurs catalogues de régions H II dans NGC 4449 existent dans la littérature.

Hodge (1967) a détecté 2000 régions H II dans un relevé de 90 galaxies et produit un atlas des régions H II de 20 galaxies, qui inclut NGC 4449. 81 régions H II sont répertoriées pour NGC 4449 à l'aide des plaques photographiques de l'émission H α du télescope de 3 m à l'Observatoire *Lick* et 48 régions H II sont vues à l'aide du télescope de 1.2 m à l'Observatoire *Palomar* (Hodge 1974 ; Hodge 1967, 1969b). Hodge (1969a) étudie la distribution des régions

H II dans les galaxies irrégulières et utilise 43 régions H II de NGC 4449. Hodge (1983) étudie la distribution de tailles des régions H II dans les galaxies irrégulières, dont NGC 4449.

Crillon & Monnet (1969) ont détecté 51 régions H II dans NGC 4449 avec une photographie monochromatique d'un filtre interférentiel centré sur H α (provenant de leur Fabry-Perot au télescope de 1.98 m de l'Observatoire de *Haute Provence*) dans le but d'étudier la cinématique.

Sabbadin & Bianchini (1979) identifient 252 régions H II dans NGC 4449 en utilisant une image de la raie H α et du continuum à l'aide du télescope de 1.82 m de l'Observatoire d'*Asiago*. À l'aide d'un microscope, ils identifient et mesurent les régions H II pour étudier leur fonction de taille.

Hunter (1982) a étudié la cinématique, la taille, et la distribution des régions H II dans 15 galaxies irrégulières, dont NGC 4449. Des images et des spectres ont été obtenus à l'aide du télescope de 2.1 m à l'Observatoire national de *Kitt Peak* à l'aide du spectrographe échelle au télescope de 4 m.

Hodge & Kennicutt (1983) produisent un atlas contenant 10632 régions H II qui proviennent de 125 galaxies. Les données utilisées sont des images H α provenant du télescope de 0.9 m de l'Observatoire national de *Kitt Peak*. Pour NGC 4449, ils détectent 36 régions H II.

Hartmann et al. (1986) ont observé 35 régions H II dans NGC 4449 en utilisant les données H α et [O III] λ 5007 du spectrographe échelle du télescope de 1.5 m de l'Observatoire du *Mont Hopkins*, dans le but d'étudier leur cinématique.

Les trois régions H II les plus brillantes de 95 galaxies, dont NGC 4449, sont étudiées par Kennicutt & Chu (1988). Kennicutt et al. (1989) ont étudié la fonction de luminosité de 30 galaxies (spirales et irrégulières), en utilisant des photographies photométriques des télescopes de 2.1 m et 0.9 m de l'Observatoire national de *Kitt Peak*. 136 régions H II sont détectées pour NGC 4449. Ils concluent que les régions H II les plus brillantes dans les galaxies irrégulières magellaniques sont ~ 50 fois plus brillantes que celles des galaxies de types plus précoces.

Scowen (1992) détecte 160 régions H II dans NGC 4449, en utilisant des plaques photographiques du *Wide Field FPUEI* au Télescope *Palomar* de 1.5 m. Avec une résolution de $1.190'' \text{ px}^{-1}$, il étudie aussi deux autres galaxies spirales pour comparer les différences de propriétés des régions H II en présence d'ondes de densités spirales.

Fuentes-Masip et al. (2000a) observent la région centrale ($80'' \times 80''$) de NGC 4449 avec l'interféromètre de Fabry-Perot *Taurus II* au Télescope *William Herschel* de 4.2 m à l'Observatoire de *Roque de los Muchachos*. Ils détectent 44 régions H II en utilisant l'émission H α et 24 avec l'émission [O III]. Leur but était de développer une méthode robuste et systématique pour obtenir les paramètres des régions H II dans les galaxies contenant autant de gaz que NGC 4449.

Valdez-Gutiérrez et al. (2002) détectent 101 régions H II en utilisant l'interféromètre de Fabry-

Perot *PUMA* au télescope de 2.1 m de l’Observatoire astronomique national de la *Sierra de San Pedro Martir*. Ils sont les premiers à obtenir des données cinématiques 3D de l’entièreté de NGC 4449 (avec un champ de vue de $10'$). Ils étudient aussi la distribution et la cinématique du gaz diffus dans NGC 4449.

Gutiérrez & Beckman (2010) utilisent les données du *Advanced Camera for Surveys* à bord du Télescope spatial *Hubble*, permettant d’avoir un échantillonnage de 0.93 pc px^{-1} . Ils identifient 273 régions H II dans NGC 4449 et produisent le catalogue le mieux résolu pour l’entièreté de NGC 4449.

Au fil du temps et avec l’avènement des instruments, plusieurs méthodes ont été utilisées pour détecter et mesurer les propriétés physiques des régions H II. Les méthodes cherchent à être justes et applicables à tous types de galaxies, pour produire des études systématiques et comparables entre les différents échantillons.

L’analyse visuelle est la technique qui a permis les premiers catalogues de régions H II et a été utilisée, par exemple, dans les études de Crillon & Monnet (1969), Hodge (1976, 1983), Hodge (1967), Sabbadin & Bianchini (1979), Sandage & Tamman (1974) et Valdez-Gutiérrez et al. (2002). Cette méthode se base sur l’inspection visuelle pour déterminer la position et les dimensions des régions H II. Cependant, cette technique est fortement subjective et dépend du temps d’exposition des données utilisées (Fuentes-Masip et al. 2000a). En effet, Kennicutt (1979) démontre que la technique d’analyse visuelle produit des erreurs stochastiques et systématiques entre les différents chercheurs, même en utilisant les mêmes images.

Ainsi, Kennicutt (1979) propose l’utilisation d’un seuil de tolérance isophotal pour déterminer les tailles des régions H II. Cette méthode est objective, mais ne s’applique pas très bien puisqu’elle ne prend pas en compte les variations locales du gaz diffus ionisé autour des régions H II dans les galaxies, ce qui rend cette technique inutilisable dans les galaxies irrégulières magellaniques selon Fuentes-Masip et al. (2000a).

Gallagher & Hunter (1983) utilisent les gradients d’élargissement des raies d’émission pour déterminer les dimensions des régions H II, puisque les différentes régions H II possèdent habituellement des propriétés cinématiques différentes (Muñoz-Tunon 1994). Cette technique permet de démêler les régions d’émission qui sont près des autres ou qui se superposent (Fuentes-Masip et al. 2000a). Elle s’applique pour des données de spectrographe à fentes longues. Cependant, elle n’aide pas à déterminer la dimension des régions avec une très grande précision (Fuentes-Masip et al. 2000a). Cette méthode est aussi utilisée par Fuentes-Masip et al. (2000a) pour des données provenant de spectrographes à champ intégral. Ils suggèrent l’utilisation de la vitesse et la dispersion de vitesse pour séparer les pixels et les assigner aux différentes régions H II, permettant de mieux séparer les régions H II adjacentes ou qui se superposent.

Gutiérrez et al. (2011) assignent les pixels de chaque région d’émission en se basant sur la

décroissance du flux autour de cette région. Ensuite, pour obtenir la taille de la région, ils convertissent le nombre de pixels en aire.

Cependant, ces techniques ne sont pas toutes adaptées à la quantité de gaz diffus ionisé particulièrement élevé dans NGC 4449. Dans son étude, Scowen (1992) conclut que les techniques de détection automatique appliquées aux galaxies spirales ne fonctionnent pas de manière satisfaisante sur NGC 4449, à cause de son haut niveau de gaz diffus ionisé, forçant l'utilisation de l'identification à la main des régions H II.

Fuentes-Masip et al. (2000a) démontrent aussi que les méthodes traditionnelles pour déterminer les dimensions des régions H II ne peuvent pas s'appliquer dans le cas de NGC 4449, à cause de son haut niveau de gaz diffus ionisé (Munoz-Tunon et al. 1998). Dans son étude, Fuentes-Masip et al. (2000a) utilisent la méthode de la librairie *FOCAS*, permettant d'éviter la subjectivité des méthodes précédentes. Cette méthode trouve les maxima locaux dans la carte d'émission pour déterminer les centroïdes des régions d'émission, en s'assurant qu'ils soient supérieurs à l'émission de fond locale et que la région contienne assez de pixels. Cette méthode est similaire à celle proposée par Kennicutt (1979), mais avec un seuil de tolérance isophotal variable pour chacune des régions d'émissions, ce qui permet plus de flexibilité pour prendre en compte l'émission locale du gaz diffus ionisé.

Dans le but d'améliorer les catalogues de régions H II existants pour NGC 4449, des données spectroscopiques à haute résolution de l'entièreté de la galaxie sont nécessaires. Ceci permettrait de mieux séparer les régions H II du gaz diffus, d'étudier la distribution spatiale des régions H II, et de comparer les propriétés des régions H II en fonction des régions morphologiques de la galaxie pour obtenir de l'information supplémentaire sur son historique de formation stellaire. Les abondances chimiques des régions H II pourraient aussi être étudiées, tout comme leurs variations à travers la galaxie et leur relation avec la cinématique du gaz.

1.4 Méthodologie

L'étude dans ce mémoire se base sur les données de la galaxie NGC 4449 obtenues en mars 2022 et en octobre 2021 à l'aide de l'instrument SITELLE (Spectro-Imageur à Transformée de Fourier pour l'Étude en Long et en Large des raies d'Émission ; Drissen et al. 2019), un spectromètre-imageur à transformée de Fourier, au Télescope Canada-France-Hawaii. SITELLE possède un champ de vue de $11' \times 11'$, ce qui permet de couvrir la galaxie au complet. L'échantillonnage des données est de $0.321'' \text{ px}^{-1}$, donc de $5.9 \text{ pc } \text{px}^{-1}$ lorsque la distance de NGC 4449 ((3.82 ± 0.27) Mpc ; Annibali et al. 2008 ; Martinez-Delgado et al. 2012) est prise en compte. Les trois filtres SN sont utilisés pour couvrir neuf raies d'émission fortes, de $[\text{O II}]\lambda 3727$ à $[\text{S II}]\lambda 6731$. La résolution spectrale R du filtre contenant la raie H α est de 4741, permettant aussi une étude relativement détaillée de la dynamique du gaz ionisé.

Les régions d'émissions sont détectées de manière systématique à l'aide d'outils développés à cette fin (Savard et al. *in prep.*). La carte du laplacien de l'amplitude de la raie H α est utilisée pour détecter les pics d'émission. Ensuite, un seuil de tolérance est appliqué pour retirer les pics dans le bruit. La région d'émission associée à chaque pic est ensuite déterminée en combinant une zone d'influence et un profil gaussien 2D des pixels avoisinant les pics. Les spectres contenus dans la région d'émission sont intégrés et le flux des différentes raies d'émission est obtenu, en tenant compte de l'alignement des filtres, de l'émission diffuse, et des populations stellaires, ainsi que de l'extinction.

Il est alors possible d'étudier les propriétés morphologiques, chimiques, et cinématiques des régions d'émissions de la galaxie NGC 4449. La fonction de luminosité, la fonction de taille, les diagrammes BPT, et la métallicité sont mesurés. Les variations spatiales au travers de la galaxie de ces paramètres et l'historique de formation stellaire sont alors étudiées, tel que présenté dans le chapitre suivant.

Chapitre 2

HII Regions in the Irregular Galaxy NGC 4449 with SITELLE

2.1 Avant-propos

Ce chapitre présente l'article que j'ai écrit durant ma maîtrise, et qui sera soumis au journal scientifique *Monthly Notices of the Royal Astronomical Society*. Cet article a pour titre original : *HII Regions in the Irregular Galaxy NGC 4449 with SITELLE*. Cet article a été composé par moi-même puis a été révisé par mes superviseurs. Il sera lu par les autres coauteurs après l'évaluation du mémoire. Plus spécifiquement, j'ai écrit certaines parties du code pour la modélisation spatiale et spectrale des régions H II en collaboration avec Gabriel Savard. J'ai aussi créé un outil d'analyse des propriétés physiques des régions H II, qui est disponible et utilisé par plusieurs étudiants qui possèdent des données SITELLE et des chercheurs de SIGNALS. J'ai réalisé l'analyse détaillée des régions H II de la galaxie NGC 4449, en appliquant les outils que mes pairs et moi avons développés. Ce chapitre reprend donc brièvement les principes de base développés précédemment dans le Chapitre 1, avant de décrire les données et la méthode employée pour l'analyse, et d'exposer les résultats obtenus pour NGC 4449. Les coauteurs Gabriel Savard, Sébastien Vicens et Étienne Massé ont contribué au développement des outils de détection et d'analyse des régions H II. Les coauteurs Carmelle Robert et Laurent Drissen sont mes superviseurs et ont contribué par leurs conseils et commentaires à ce travail. Les coauteurs Laurie Rousseau-Nepton, René Pierre Martin et Philippe Amram sont des investigateurs principaux dans le relevé SIGNALS, dont NGC 4449 fait partie. Par convention, leur nom est ajouté à la liste de coauteurs.

2.2 Résumé

Dans cet article, les régions d'émission optiques de la galaxie irrégulière NGC 4449 sont étudiées, en lien avec le programme d'étude SIGNALS avec SITELLE, dans le but de gagner

une meilleure compréhension de son historique de formation stellaire. Le taux de formation stellaire élevé dans cette galaxie et sa proximité (~ 4 Mpc), en font une candidate idéale pour l'étude, avec une résolution spatiale de 5.9 pc, des régions H II individuelles. Des observations hyperspectrales couvrant toute la galaxie ont été obtenues avec une résolution spectrale R entre 1000 et 4700 de 363 nm à 685 nm, couvrant les raies d'émission fortes provenant du gaz ionisé. La résolution élevée permet une mesure juste de la vitesse et de la dispersion de vitesse, aussi bien que la résolution de composantes doubles dans les spectres. Un catalogue de 535 régions d'émission est fourni, incluant, entre autres, le flux des raies d'émission, la vitesse, l'extinction et la métallicité. Celui-ci permet une analyse statistiquement significative de la fonction de luminosité, de la fonction de taille, des diagrammes BPT, et de la distribution de métallicité des régions. Un gradient de métallicité de $12 + \log[\text{O}/\text{H}] \simeq 8.3$ dans le centre, à $12 + \log[\text{O}/\text{H}] \simeq 8.2$ dans le nord est observé. La cinématique complexe du gaz pourrait indiquer la présence d'un afflux/exode de matière. Cette information est un ingrédient clef pour améliorer notre compréhension des mécanismes sous-jacents et de la dynamique globale se produisant dans NGC 4449.

2.3 Abstract

In this paper, optical emission line regions of the irregular galaxy NGC 4449 are studied as part of the SIGNALS survey using SITELLE, with the goal of gaining a better understanding of its stellar formation history. The high star-forming rate of this galaxy and its proximity (~ 4 Mpc) makes it an ideal target to study in details with a spatial resolution of 5.9 pc, the individual H II regions. Hyperspectral observations over the whole galaxy have been obtained with a spectral resolution R between 1000 and 4700 from 363 nm to 685 nm, covering the strong emission lines from the ionized gas. The high resolution enables accurate velocity and velocity dispersion measurements, as well as separating double components in the spectra. A catalogue of 535 emission regions is provided, including their emission lines' flux, dimensions, velocity, extinction, and metallicity. It allows for a statistically significant study of the emission regions' luminosity function as well as a size function, BPT diagrams and metallicity distribution of the regions. A metallicity gradient from $12 + \log[\text{O}/\text{H}] \simeq 8.3$ in the centre to $12 + \log[\text{O}/\text{H}] \simeq 8.2$ in the north is observed. The complex motion of the gas could indicate the presence of an inflow/outflow. This information is a key ingredient to improve our understanding of the underlying mechanisms and global dynamics occurring in NGC 4449.

2.4 Introduction

Dwarf galaxies are the most common morphological type of galaxies in the universe, yet paradoxically the least understood (Sacchi et al. 2018). Their evolution and the star formation processes that occur within them remain obfuscated. It is known that the local environment of

galaxies, the distribution and density of their gas, as well as their star formation history affect their current star formation rate (SFR; Calzetti et al. 2015; Kumari et al. 2017). External events, such as tidal interactions, major mergers, and gas accretion, and internal processes are known to modify the star formation in galaxies (Lelli et al. 2014b). These occurrences have been found to lead to a starburst phase in which the star formation activity is multiplied by a significant factor compared to the typical star-forming rates for a given galaxy mass. However, not all starburst can be explained by these phenomena, especially in the case of dwarf irregulars (dIrr).

In the case of dwarf irregular galaxies, the star formation is believed to occur in stochastic episodes, which could be caused by accretion events (Martinez-Delgado et al. 2012) as well as by timely events triggered by internal perturbations (*e.g.* supernovae, large-scale stellar winds, molecular clouds collisions). The absence of spiral density waves and the lack of differential rotation in these galaxies impacts their evolution by not regulating their star formation activity at a global-scale like it is the case of the more massive spiral galaxies (Cignoni et al. 2018, 2019). As a result, massive galaxies tend to form most of their stars in the first ~ 3 Gyr, compared to low mass galaxies, which form stars over ranges of time covering the entirety of the cosmic time (Cignoni et al. 2018). On the other hand, the absence of global motions in dIrr make them ideal target to study other environmental factors that impacts the stellar formation efficiency (Youngblood & Hunter 1999).

Metallicity in dwarf galaxies is of particular interest (Berg et al. 2012; Hunter et al. 1982; Izotov et al. 2006; Kobulnicky et al. 1999; Lequeux et al. 1979; McCall et al. 1985; Sabbadin et al. 1984). The global low-metallicity observed at high redshift can be similar to the metallicity of dwarfs (Kunth & Östlin 2000). Therefore, smaller galaxies become even more important in the cosmological picture of our understanding of the star-formation process since they are ideal targets to study low-metallicity conditions. In a way, they act as analogues of the early galaxies, while being local and well-resolved. As a result, they offer a unique laboratory to see in great detail the star formation activity in these critical conditions, to track more precisely the evolution of the chemical abundances, and to understand their role in galaxy evolution (Cignoni et al. 2018).

Regions containing young massive stars are often identified through their H α emission, which is used as a proxy for recent stellar formation (Youngblood & Hunter 1999). Referred as H II regions, they have long been studied to further our understanding of the role of star formation in galactic evolution (*e.g.* Anderson et al. 2014; Buckalew & Kobulnicky 2006; Espinosa-Ponce et al. 2020; Feinstein 1997; Fuentes-Masip et al. 2000a; González Delgado & Pérez 1997; Gutiérrez & Beckman 2010; Gutiérrez et al. 2011; Hakobyan et al. 2007; Hodge 1974, 1983; Hodge & Kennicutt 1983; Hodge et al. 1989a; Hodge 1967, 1969a,b; Hunter 1982; Kennicutt & Hodge 1980; Kennicutt et al. 1989; Knapen et al. 1993; MacKenty et al. 2000; Rand 1992; Rozas et al. 1996, 2000, 1999; Santoro et al. 2022; Scowen 1992; Thilker et al. 2002; Youngblood

(*e.g.* Hunter 1999). Providing insights into the intricate interactions between massive stars and the interstellar medium (ISM), H II regions are part of a short lived cycle in which massive stars contribute significantly to the mechanical and radiative energy inputted into the ISM as well as to the local chemical enrichment (Leitherer et al. 1992). In order to statistically study their characteristics and behaviours, catalogues of H II regions can be very useful, including their morphological, chemical, and kinematic properties, that can then be correlated with the galaxy's environmental properties. With the advancement of key technologies such as spectral imaging techniques, higher-spatial and -spectral resolution data can be obtained, allowing a better sampling of H II regions (*e.g.* reaching lower luminosity than ever before and separating H II region complexes) and gathering more precise spectral information over a wider variety of spectral lines (Espinosa-Ponce et al. 2020; Rousseau-Nepton et al. 2019; Santoro et al. 2022).

This study investigates the dwarf irregular galaxy NGC 4449 (IB(s)m; de Vaucouleurs et al. 1991), as seen in Figure 2.1, which is located at a distance of (3.82 ± 0.27) Mpc (Annibali et al. 2008; Martinez-Delgado et al. 2012). According to different sources across the literature, the global metallicity of the gas in NGC 4449 is estimated near $12 + \log[\text{O}/\text{H}] = 8.3$ using mainly the direct method with the 4363\AA line (Annibali et al. 2017; Berg et al. 2012; Cook et al. 2014; Engelbracht et al. 2008; Izotov et al. 2006; Kobulnicky et al. 1999; Lequeux et al. 1979; Marble et al. 2010; Martin 1997; Sabbadin et al. 1984; Scowen 1992; Skillman et al. 1989).

The mass ($M_\star \simeq 1.1 \times 10^9 M_\odot$; Calzetti et al. 2015; Sacchi et al. 2018), size ($R_{\text{opt}} \simeq 3.3$ kpc Lelli et al. 2014a), and absolute magnitude ($M_V = -18.6$ Martinez-Delgado et al. 2012) of NGC 4449 are very similar to the well known Large Magellanic Cloud (LMC), a similar irregular galaxy. However, NGC 4449's extremely high SFR density distinguishes it from the LMC (Sacchi et al. 2018). In the nearby Universe, NGC 4449 is considered to be one of the strongest galaxy-wide starburst (Martinez-Delgado et al. 2012).

In the literature, NGC 4449's SFR ($0.47 M_\odot \text{ yr}^{-1}$) has been derived from the total H α luminosity, corresponding to a SFR density of $0.011 M_\odot \text{ yr}^{-1} \text{ kpc}^{-2}$ over the area under a radius $R_{25} = 3'2$ or 3.6 kpc (Hunter et al. 1999; Sacchi et al. 2018). In comparison, NGC 4449 is 1.4 times more luminous and forms stars twice as rapidly as the LMC, despite their similarities. A possible cause of the high SFR observed in NGC 4449 was proposed by Karachentsev et al. (2007) and Martinez-Delgado et al. (2012). Their studies suggested that past interactions with other galaxies had an impact on the dynamics of NGC 4449 cold gas content, leading to starbursts.

NGC 4449 contains a giant H I halo about 14 times bigger than its optical counterpart (Bajaja et al. 1994). This is considerably more extended than what is typically observed in irregular galaxies (Huchtmeier et al. 1981). The halo extends to the nearby dwarf galaxy, DDO 125, located south-east at a distance of 41 kpc (Hunter et al. 1999). Simulations of an encounter between these two galaxies have predicted that the closest approach occurred 350 Myr ago at

a minimum distance of 25 kpc (Theis 1999). This interaction is believed to be responsible for the strong warp in the H_I halo (Bajaja et al. 1994). The halo also displays peculiar giant rings, shell-shaped complexes, and filaments (Hunter et al. 1999) and complex distributions of clouds and streamers are also observed wrapping around the galaxy (Hunter et al. 1998). Observations reveal that the H_I envelope has opposite velocity gradients in its inner and outer parts, which is interpreted as a clear signature of past gas accretion (Bajaja et al. 1994; Hunter et al. 1999; Theis & Kohle 2001; van Woerden et al. 1975). The inner part of the H_I gas, with a diameter of 4 kpc, rotates in the same direction as the optical part of the galaxy. The regions with the highest velocity dispersion in the H_I gas are observed mostly outside of the stellar formation regions and, in some cases, outside of the bright parts of the optical galaxy (Hunter et al. 1999). This peculiar H_I gas distribution really sets NGC 4449 apart from the typical isolated irregular galaxies (Hunter et al. 1998).

The disturbed H_I gas is consistent with interactions with an external perturbing body as evidenced by the fact that the gas has not returned to its equilibrium state (Cignoni et al. 2018). Yet, according to Hunter & Gallagher (1997), NGC 4449's closest neighbour DDO 125 does not show any signs of perturbation. Its global gas and optical properties are consistent with the typical ones observed in irregular galaxies. Furthermore, no clear bridge has been observed between NGC 4449 and DDO 125. Due to the lower relative H_I gas mass of DDO 125 ($1 \times 10^8 M_{\odot}$; Fisher & Tully 1981), it is expected that 90 % of the gas mass should have been lost, to account for the mass of the observed streamers around NGC 4449 (Hunter et al. 1998). In opposition to the observations previously mentionned, simulations are able to reproduce the interaction between the two galaxies, which could indicate that it is plausible (Theis & Kohle 2001; Theis 1999).

Others have also hypothesised interactions with additional galaxies. A stellar tidal stream in the halo of NGC 4449 is believed to be the result of an ongoing interaction with a dSph galaxy NGC 4449B (Karachentsev et al. 2007; Martinez-Delgado et al. 2012; Rich et al. 2012; Toloba et al. 2016). NGC 4449B lies at a projected distance of 9 kpc from the nucleus of NGC 4449 (Rich et al. 2012). It has a stellar mass $M_{\star} < 1 \times 10^8 M_{\odot}$, does not show signs of star formation, and does not contain cold gas (Martinez-Delgado et al. 2012). NGC 4449B has a strong S-shaped morphology, which is expected for interacting galaxies (Capuzzo Dolcetta et al. 2005; Peñarrubia et al. 2009). However, this shape had only yet been observed in dissolving globular clusters (Odenkirchen et al. 2003). It is speculated that it is NGC 4449B's first encounter with NGC 4449 (Rich et al. 2012). The pericentric passage of NGC 4449B is estimated to have occurred 1×10^8 yr ago. The time-scale of the interaction is consistent with the hypothesis that the encounter is related to the present epoch of star formation observed in NGC 4449. Toloba et al. (2016) measured the metallicity of the stream and suggests that the progenitor could have been as massive as the Fornax or Sagittarius dwarf galaxies.

Additionally, Annibali et al. (2012) have proposed that a globular cluster belonging to

NGC 4449 could have been the nucleus of a former gas-rich satellite galaxy, that has been tidally disrupted by NGC 4449, because it is sitting in two tails of blue stars (Annibali et al. 2012).

Based on a spectroscopic study in the visible part of the spectrum, Cignoni et al. (2018) concluded that a recent enhancement of the SFR in NGC 4449 peaked between 10 Myr and 15 Myr ago and is now declining. They estimate that this stellar formation enhancement is the only major event in the past 40 Myr and that it is consistent with the strongly disturbed morphology still seen in the H_I gas of NGC 4449, in relation with a merger or a cold flow accretion.

As NGC 4449 is part of the CVnI cloud of galaxies (de Vaucouleurs 1975), past interactions with other galaxies is a highly plausible hypothesis (Hunter et al. 1999). Hunter et al. (1999) analysed the possibility that NGC 4449 was an earlier-type galaxy prior to its interactions. They note that the absence of clear organised galactic structures in NGC 4449 does not support this idea. Indeed, in order to have had such a drastic change in morphological type, from an earlier-type to a later-type galaxy, a very violent interaction would have been required to break the galaxy's structures. If this scenario was the case, it would have left NGC 4449 more perturbed than its current state. The slow rotational speed of the optical part ($\sim 18 \text{ km s}^{-1}$; Hunter et al. 1998), the high level of gas, in combination with the small optical-scale of NGC 4449, and the low metallicity are more inconsistent with a late spiral-type galaxy progenitor.

External interactions and mergers between galaxies are important factors in their evolution, especially for elliptical galaxies (Hunter et al. 1999). However, irregular galaxies are rather seen as the victims of such interactions and the ones to disappear into larger systems (Hunter et al. 1999). Therefore, it is rare to observe irregular galaxies which have survived such interactions. It is interesting to see that even after one of many interactions, NGC 4449 remains an irregular galaxy dwarf. Thus, the study of the star formation properties and mechanisms in galaxies is important.

Recent stellar formation may be studied through H II regions. Whereas different H II region populations are expected in the arms and inner arms of spiral galaxies (Knapen et al. 1993; Kreckel et al. 2016), the H II regions distribution of dwarf irregular galaxies is expected to be spatially homogeneous, due to the absence of important global gas motions (Fuentes-Masip et al. 2000a). NGC 4449's H II regions have long been studied (*e.g.* Crillon & Monnet 1969; Fuentes-Masip et al. 2000a; Gutiérrez & Beckman 2010; Hartmann et al. 1986; Hodge & Kennicutt 1983; Hodge 1969a,b; Hunter 1982; Kennicutt et al. 1989; Sabbadin & Bianchini 1979; Scowen 1992; Valdez-Gutiérrez et al. 2002).

The data presented here for NGC 4449 have been obtained with SITELLE at the Canada-France-Hawaii Telescope, as part of the SIGNALS program (Rousseau-Nepton et al. 2019).

The goal of this survey is to study the star formation in ~ 40 star-forming nearby galaxies with a high spatial resolution (on average ~ 20 pc). It aims to produce a statistically significant and systematic catalogue of more than 50000 H II regions in different environments. This paper provides an H II regions catalogue for NGC 4449, using the detection methodology described by Savard et al. (in prep.), with the goal of investigating their morphological, chemical, and kinematical properties within the galaxy.

The data are presented in Section 2.5, describing the observations, their reduction, the emission line measurement, and the refined calibrations. The procedure to detect the emission regions is summarised in Section 2.6, the analysis is detailed in Section 2.7, with a discussion on the global morphological, chemical, and kinematical properties of the emission regions. The conclusions from this work are presented in Section 2.8.

2.5 Observations, Data Reduction, and Emission Line Measurements

2.5.1 Observations

NGC 4449 was observed, with SITELLE, an imaging Fourier transform spectrometer (Drissen et al. 2019) at the Canada-France-Hawaii Telescope (PI: Laurie Rousseau-Nepton). The observations are centred at RA 12h28m09.8s and DEC $+44^{\circ}05\text{m}51.2\text{s}$. SITELLE’s field of view (FoV) of $11' \times 11'$ encompasses the whole optical disc of NGC 4449. With SITELLE’s mean pixel-scale of $0''.321$, the resulting sampling for NGC 4449 is 5.9 pc px^{-1} .

The SN1, SN2, and SN3 filters have been used. These filters cover the strong emission lines $[\text{O II}]\lambda\lambda 3726,3729$, $\text{H}\beta$, $[\text{O III}]\lambda\lambda 4959,5007$, $\text{H}\alpha$, $[\text{N II}]\lambda\lambda 6548,6583$, and $[\text{S II}]\lambda\lambda 6716,6731$. Table 2.1 gives a summary of the observing parameters. The SN2 and SN3 datacubes were taken in March 2020 during the same night, with a seeing of $0''.96$ and $0''.93$, respectively. The SN1 datacube was acquired in October 2021 (after a newly aluminised mirror), with a seeing of $1''.11$. Each filter has a total exposure time of about 3 h, excluding the overheads of 3.8 s per step.

2.5.2 Data Reduction

SITELLE’s raw datacubes each contain over 4 million interferograms, which are converted into spectra using ORBS (Martin et al. 2015, 2021), SITELLE’s fully parallelised reduction software. This software takes into account bias, flats, sky transparency, Fourier transform, wavenumber calibration with an He laser, and the flux calibration (with the standard stars GD 108 and P177D in the case of NGC 4449).

Figure 2.1 shows the SITELLE deepimage of NGC 4449. This image was obtained by adding the datacubes’ deepframe (sum of all the datacube’s interferograms) for all three filters and

Table 2.1 – Observing parameters of the SITELLE data of NGC 4449.

	SN1	SN2	SN3
Observation ID	2598262	2477185	2475286
Spectral range [Å]	3626-3856	4798-5132	6477-6850
Observing date	2021-10-19	2020-03-05	2020-03-05
Exposure time/step [s]	59.0	45.5	13.3
Number of steps	172	219	842
Total exposure time [h]	2.82	2.77	3.11
Spectral resolution R	965	943	4741
Seeing [arcsec]	1.11	0.96	0.93

superimposing the H α flux map (shown in Fig. 2.2), to emphasize the star forming regions. This image highlights very well the star formation activity of NGC 4449.

2.5.3 Emission Line Measurements

The measurement of the emission lines for each pixel (with no binning) in each datacube is done with SITELLE’s dedicated pipeline ORCS (Martin et al. 2015, 2021). Emission lines are fitted using a sincgauss model (*i.e.* a combination of a sinc function, to account for SITELLE’s instrument line function, with a Gaussian distribution, to account for the velocity dispersion). The velocity and broadening of all the lines in the same filter are approximated to be the same, to help constrain the fit. Since the seeing variation is very small (*i.e.* less than a pixel; see Table 2.1) between the three datacubes, spatial smoothing is not applied to the datacubes prior to the lines measurement. The natural unit of the SITELLE instrument is in wavenumbers. However the figures in this paper are displayed in wavelengths. It is important to note that this has been done purely for convenience and that the fits of the emission lines have been done in wavenumbers, as the conversion into wavelengths causes distortions to the line profiles. ORCS returns maps for the amplitude, flux, continuum, velocity, and velocity dispersion, with their respective uncertainties, for all the lines. Throughout this paper, the S/N is defined as the amplitude of the emission line divided by the noise in the cube, which is obtained from regions without emission, outside the galaxy, as described in Savard et al. (in prep.).

The flux map of the H α emission line is presented in Figure 2.2, the other emission lines’ flux maps ([N II] $\lambda\lambda$ 6548,6583 and [S II] $\lambda\lambda$ 6716,6731 from the SN3 filter, [O III] $\lambda\lambda$ 4959,5007 and H β from the SN2 filter, and [O II] $\lambda\lambda$ 3726,3729 from the SN1 filter) are shown in Figures A.1 and A.2 (Appendix A). Emission regions are visible over the entire body of the galaxy. Many of these are H II regions, but the filamentary structures of the emission also suggests the presence of diffuse ionized gas (DIG).

The velocity (top panel) and velocity dispersion (bottom panel) maps are shown in Fig-



Figure 2.1 – Colour image of NGC 4449 created using SITELLE data. The deepframe of the SN3 filter is used as the red channel, the green channel corresponds to the SN2 filter’s deepframe, and the SN1 filter’s deepframe is used as the blue channel. The H α flux map is superimposed in red to highlight the H II regions. North is up, and East is left. The FoV is $1' \times 11'$, centred on RA 12h28m09.8s and DEC $+44^{\circ}05m51.2s$.

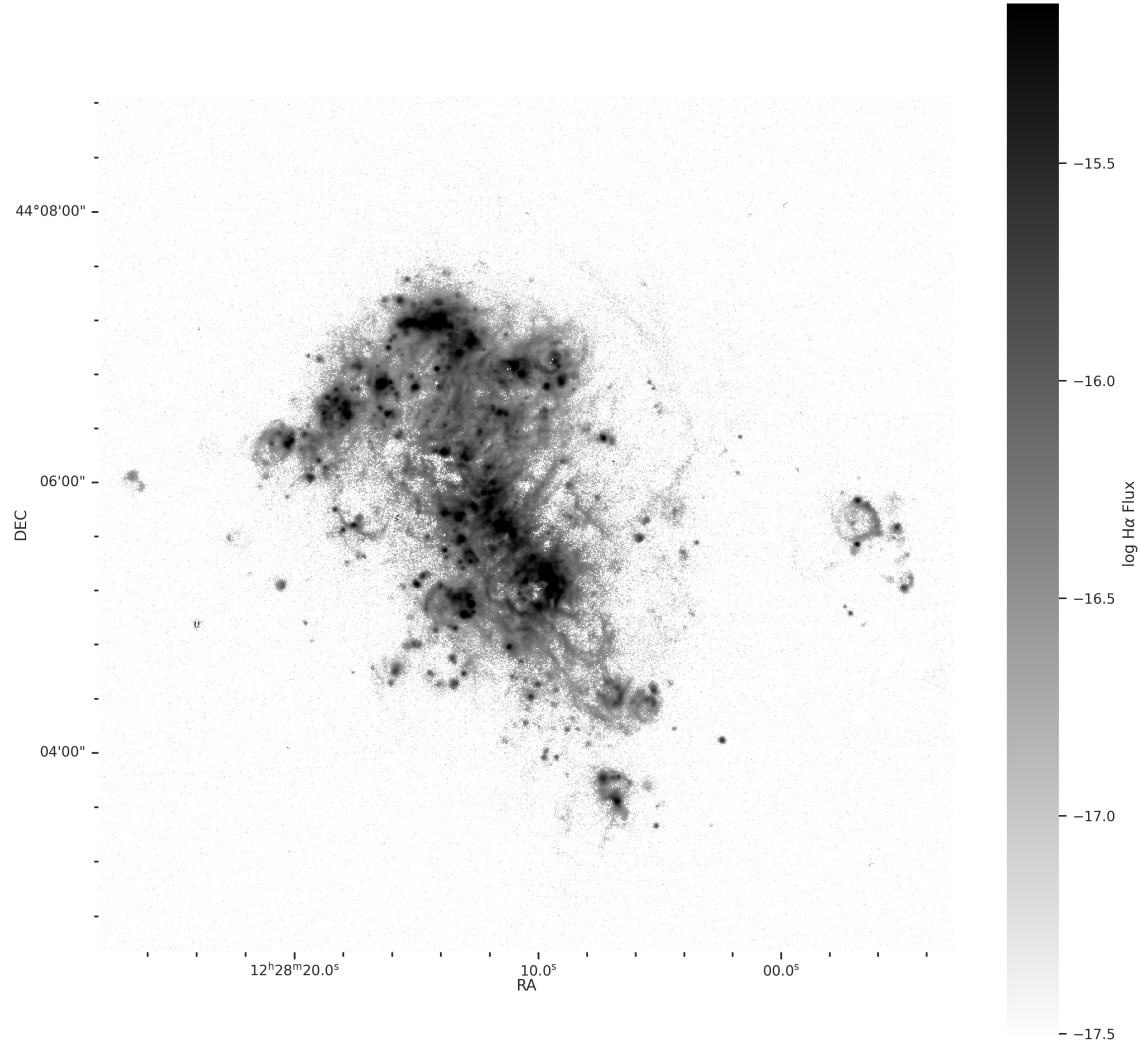


Figure 2.2 – H α flux map in log-scale. Corrections for the global stellar absorption and for the extinction are not applied. Only the sky background correction is done (as described in Section 2.5.4). The pixels with a H α S/N inferior to 1 are not shown.

ure 2.3 and discussed in Section 2.7.9. The minimal velocity dispersion measured is around 15 km s^{-1} , which confirms that the S/N of the spectra are high enough to measure accurately, as SITELLE’s limit is 5 km s^{-1} (Martin et al. 2016).

To obtain the emission lines maps, further operations have been done, as described in the following subsections.

2.5.4 Sky Subtraction

A sky background spectrum is subtracted automatically by ORCS (Martin et al. 2015, 2021) from each spectrum, before fitting its emission lines. This sky spectrum is obtained away from the galaxy, where no object is seen, in order to avoid contamination. The median spectrum

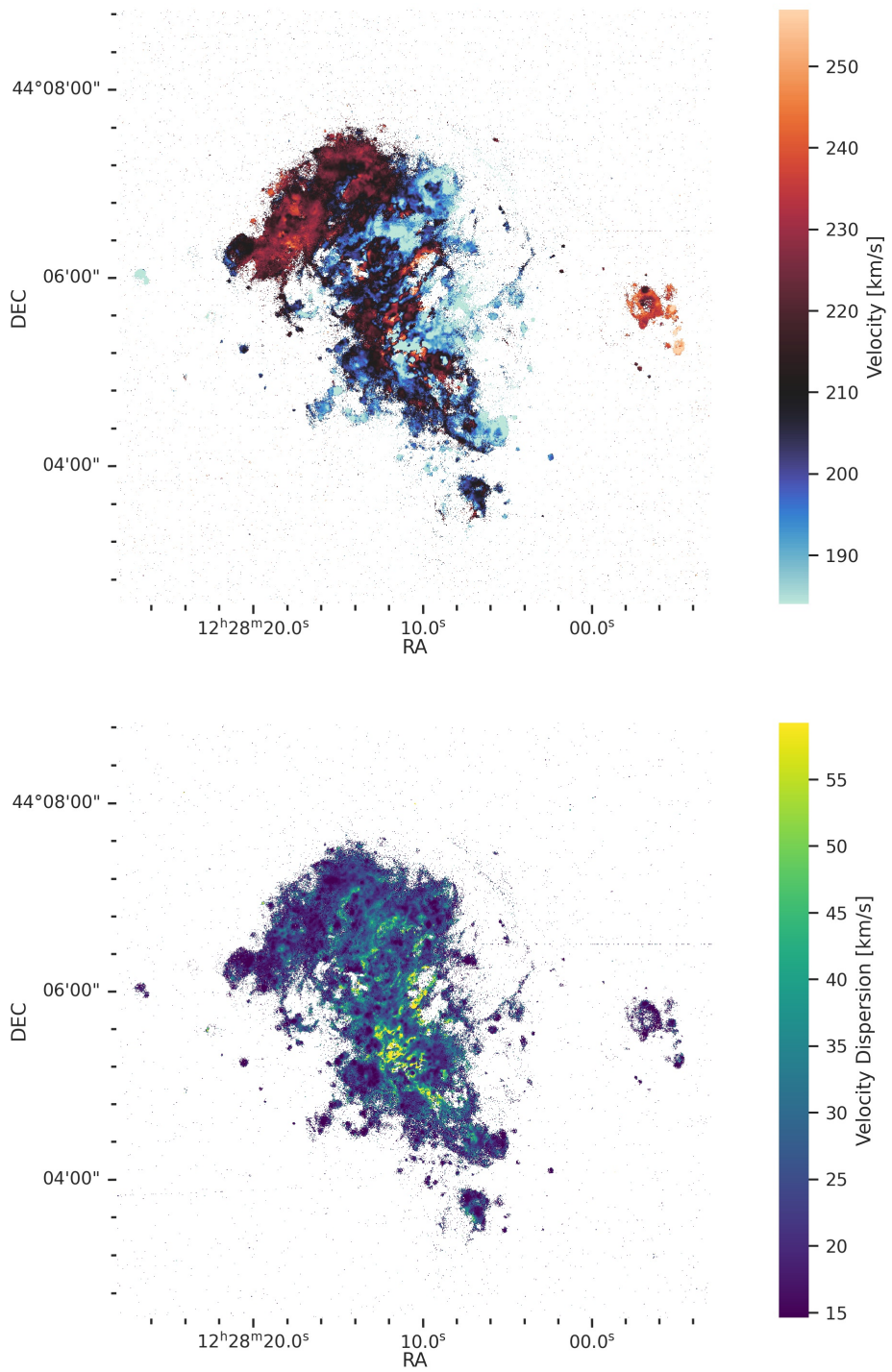


Figure 2.3 – Velocity map (top) and velocity dispersion map (bottom). The values are calculated with the SN3 emission lines. The OH sky line have been used to refine the velocity calibration and the heliocentric correction has been applied. The pixels with a H α S/N inferior to 1, a relative velocity error inferior to 4, and a background value below 2σ are removed.

sampled in a circular region with a \sim 150 pc radius, centred at RA 12h28m34.7s and DEC $+44^{\circ}05\text{m}46.5\text{s}$ is used. The sky spectrum is presented in Figure B.1 (in Appendix B).

2.5.5 Wavenumber Calibration

Since the laser datacube used for the wavenumber calibration is not observed simultaneously with the galaxy, some minor distortions in the spectra may remain (Martin et al. 2016). In the case of the SN3 filter, with many strong emission lines and the higher spectral resolution (see Table 2.1) adopted for the study of the ionized gas dynamics, this effect may be corrected to reach a precision for an absolute velocity measurement of less than 2 km s^{-1} . In order to refine the wavenumber calibration, the centroid of OH sky emission lines present in the SN3 filter is measured following the ORCS procedure described in Martin et al. (2018). The sky velocity map (shown in Fig. B.2) displays a small variation from -82.5 km s^{-1} to -84.5 km s^{-1} from one side of the galaxy to the other. The final SN3 velocity map obtained here for NGC 4449 takes into account this variation as well as the heliocentric correction of 4.5 km s^{-1} . The average heliocentric velocity, integrated over the main body of the galaxy observed with SITELLE, is 209 km s^{-1} , which is very close to the $(207 \pm 4) \text{ km s}^{-1}$ value obtained from the neutral hydrogen with the *Green Bank Radio Telescope* (Schneider et al. 1992).

The wavenumber calibration of the SN2 and SN1 filter may not be refined as done for the SN3 filter, as they do not contain strong OH lines. On the other hand, their spectral resolution is too low to require such precision and they are not used to study the gas dynamics. Nevertheless, since the SN2 datacube is used to study the stellar absorption (see Section 2.6.7), its velocity map is compared to the SN3 velocity map. The difference between the SN3 and the SN2 velocity map is about 60 km s^{-1} with a standard deviation of about 15 km s^{-1} . This is not considered significant for the study of the stellar absorption, thus no correction is applied for the SN2 filter.

2.5.6 Flux Calibration

To validate our flux calibration in the SN3 filter, the H α +[N II] image obtained by Calzetti et al. (2018) with the *Bok Telescope* is used as comparison. The continuum-subtracted calibrated flux from the main body of the galaxy in this image is $2.88 \times 10^{-11} \text{ erg s}^{-1} \text{ cm}^{-2}$, while the SITELLE value, obtained by summing the flux of the H α and the two [N II] emission-line maps produced by ORCS, is $2.61 \times 10^{-11} \text{ erg s}^{-1} \text{ cm}^{-2}$. Using the planetary nebulae catalogue provided by Annibali et al. (2017), the flux calibration in the SN2 filter is validated. The average relative disparity between the measured [O III] $\lambda 5007$ flux for their planetary nebulae labelled PN-1, PN-2, PN-3, and PN-5 is 6 %. The H II regions catalogue provided by Annibali et al. (2017) is used for the flux calibration of the SN1 filter, as the planetary nebulae are not visible in the SITELLE datacube. The average relative disparity between the measured [O II] $\lambda 3727$ flux for their six H II regions is 3 %. These comparisons are in agreement and the

SITELLE’s 10 % limit estimated for its flux calibration is therefore confirmed here for all three filters.

2.5.7 Astrometry

Using field stars present in the datacube as reference points, an Euclidean isometry is computed to correct their alignment with regard to each other. The transformation’s parameters are obtained using the singular value decomposition algorithm from `numpy` (Harris et al. 2020) to compute the translation and rotation parameters with respect to the alignment of the reference points (*i.e.* the field stars in the SN3 filter).

The selected field stars are located in the centre of the datacube to avoid areas affected by distortions in the edges of the field of view. As the galaxy is located in the centre of the datacube’s field of view, distortion correction is not necessary for this object.

The interpolation of the values in the maps required to align them does not affect the values obtained in this study. The only maps that required to be aligned with one another are the line ratio maps, as presented in Section 2.7.5. These maps are only used to qualitatively study the global and local variations of the line ratios. Hence, the interpolation have little effect on the behaviour observed. However, not aligning the maps, and thus requiring some of the values to be interpolated, would have a greater effect on the trends observed in these maps, as some of the cubes have a shift of multiple pixels between them. Especially at the local-scale (*e.g.* individual H II regions), such a shift would cause false patterns to emerge, leading to inaccurate conclusions.

For the case of the measured fluxes for the individual emission regions, as described in Section 2.6.3, the flux values are not interpolated. A mask is generated for each regions, using the H α flux map, and the Euclidean transformation is applied to the mask, in order to fetch the proper spectra, without having to do any modifications to the datacube. Thereby, the flux values presented in the emission region catalogue (Appendix F), used in the luminosity function (Section 2.7.1), the luminosity – size – velocity dispersion correlation (Section 2.7.3), the BPT diagrams (Section 2.7.6), the metallicity analysis (Section 1.2.1), and the study of the nature of the objects (Section 2.7.12) are not interpolated.

2.5.8 Star Removal

Foreground stars present on the line of sight are identified using *GAIA Data Release 3rd Catalog* (Brown et al. 2021). From this list, only the objects with a parallax are considered, and their position is refined using `DAOStarfinder` (Stetson 1987). As very few field stars are located near NGC 4449, they do not pose a problem to this study. Masking them avoids false identifications in our detection routine (Section 2.6.1) and the contamination of the background estimates of the emission regions studied (Section 2.6.3).

2.6 Emission Regions Measurements

NGC 4449 contains a very high density of emission regions entangled with an important amount of DIG escaping the H II regions (Malumuth et al. 1986; Munoz-Tunon 1994). This causes additional challenges when detecting and measuring the integrated parameters of the H II regions; modelling and assigning the pixels that belong to each H II region is more difficult due to the high level of DIG. Although several approaches have been used in the past to detect H II regions, such as visual analysis (Hodge 1976, 1983; Sabbadin & Bianchini 1979; Sandage & Tamman 1974), isophotal threshold (Kennicutt 1979), and emission line width gradients (Gallagher & Hunter 1983), these techniques fail to achieve satisfactory results in the case of NGC 4449, but perform well on spiral galaxies. Thus, systematically detecting H II regions in NGC 4449 is notoriously difficult (Fuentes-Masip et al. 1995; Fuentes-Masip et al. 2000b; Scowen 1992).

The emission regions catalogue is build using the algorithm described by Savard et al. (in prep.). This algorithm was built to detect the centroids of emission regions (Section 2.6.1), to determine the spatial extent of these regions (Section 2.6.2) and then to integrate their emission lines taking into account the local background (Section 2.6.3). Uncertainties associated to this procedure are described in Section 2.6.4. The luminosity threshold of the detections is studied in Section 2.6.5. The validation steps applied to the resulting detections are detailed in Section 2.6.6. A discussion of the global absorption lines from the galaxy’s stellar population is presented in Section 2.6.7 and is taken into account for the extinction within each pixel in Section 2.6.8.

2.6.1 Emission Peak Detection

The Laplacian map of the H α amplitude is used, without the absorption and extinction corrections, to identify the local maxima, which corresponds to the centroids of the regions. The H α amplitude map used is shown in Figure C.1. A `Laplacian sigma` of 1.5 is used here to take into account the seeing of the data. A `detection box size` of 5 px \times 5 px is selected to get the emission peaks. This size is best to take into account the relatively high spatial resolution of the data. The effects of different values of the `Laplacian sigma` and the `detection box size` are shown in Figures C.2 and C.3, respectively. Figure C.2 shows the detections, within a 5 px \times 5 px `detection box size` and using the same threshold parameters (next paragraph), using a `Laplacian sigma` of 1 (top panel), 1.5 (middle panel), and 2 (bottom panel). The four areas used as examples are centred on region 527 (top left), region 420 (top right), region 175 (bottom left), and region 123 (bottom right); the location of these areas in the galaxy is shown in Figure D.2. As seen, the `Laplacian sigma` value modifies the location of the detected peaks, as the Gaussian distribution convoluted with the H α amplitude map has a greater spatial extent. The faint peaks become more blurred and are not detected when the `Laplacian sigma` increases, thus decreasing the number of emission regions detected. Figure C.3 shows

the detection using a `detection box size` of $3\text{ px} \times 3\text{ px}$ (top panel), $5\text{ px} \times 5\text{ px}$ (middle panel), and $7\text{ px} \times 7\text{ px}$ (bottom panel). The `detection box size` prevents peaks too close to each other from being detected, as these individual emission regions cannot be properly resolved, due to the distance of the galaxy and the seeing.

Next, the detection level was applied to select the emission peaks above the noise level and to avoid weaker peaks in diffuse structures. This was done using a `noise sigma` of 3, a `local background box` of $40\text{ px} \times 40\text{ px}$, and a `scaling factor` of 1.6. These parameters were experimentally determined to optimise the output of the detection algorithm for this target. Figure C.4 shows the detection using a `noise sigma` value of 2 (top panel), 3 (middle panel), and 4 (bottom panel). As the `noise sigma` value increases, less regions on the outskirts of the galaxy are detected, as they are fainter and similar to the noise level around the galaxy. Figure C.5 shows the detection using a `local background box` value of $30\text{ px} \times 30\text{ px}$ (top panel), $40\text{ px} \times 40\text{ px}$ (middle panel), and $50\text{ px} \times 50\text{ px}$ (bottom panel). As the `local background box` size increases, more emission regions in large-scale structures, such as filaments, are detected. In order to reduce the detection of DIG regions, the `local background box` size may not be too big. Figure C.6 shows the detection using a `scaling factor` value of 1 (top panel), 1.6 (middle panel), and 2 (bottom panel). The `scaling factor` allows to finetune the detected regions, as its value increases, less faint emission regions are detected.

In general, detecting faint objects in the vicinities of very bright objects is challenging, as the emission of the former is prone to being associated to the latter. However, not detecting these faint H II regions will only influence the lower end of the luminosity function (see Section 2.7.1). These regions are not expected to be included in the fit of the slope of the luminosity function and the global shape of the luminosity function is not expected to be affected (Kennicutt et al. 1989; Knapen et al. 1993; Rand 1992).

The selected parameters are very strict and limit the detection to only the bright emission regions. This choice enables us to study objects that are considered very likely to be H II regions. Still, it is important to note that some H II regions are missing from the detection and some regions included in the detection are not H II regions, but diffuse emission regions (see Sections 2.7.6 and 2.7.12). Although this catalogue is not exhaustive, with 535 emission regions, due to these inherent biases, it is considered a good statistical sample including all bright H II regions. The impact of its incompleteness is discussed later in this section.

2.6.2 Spatial Fitting

The surrounding pixels (inside a 50 pc radius) are assigned to a specific peak (detected local maxima), in order to define a zone of influence, where a 2D Gaussian will be fitted, to set the

emission region domain. The pixels used to define the zone of influence are selected based on:

$$\text{region}(p_{ij}) = \operatorname{argmax}_n \frac{F_{\text{H}\alpha,n}}{\|c_n - p_{ij}\|^2}, \quad (2.1)$$

where $F_{\text{H}\alpha,n}$ is the H α flux of the n -th detected emission region's centroid c_n and p_{ij} corresponds to the position of the pixel studied to assign to $\text{region}(p_{ij})$, as described in Savard et al. (in prep.). One pixel belongs to a single peak. Thus, overlapping fluxes from multiple regions are not separated with this algorithm.

The maximum radius of 50 pc used for the zone of influence is considered to encompass the bigger H II regions possibly seen at the distance of NGC 4449. Some zones of influence are made of multiple spatially disconnected components, due to the behaviour of the pixel assignment algorithm (*e.g.* when faint emission regions are detected close to very bright ones). The pixels disconnected from the core component (the component containing the peaks of the emission region) are removed by using the connected component labelling algorithm from `scikit-image` (Walt et al. 2014).

The emission region detection tool used in this study (Savard et al. in prep.) has been developed to detect local maxima, therefore, various H II region topologies, such as rings and filaments, which are frequent in nearby galaxies (Gutiérrez et al. 2011) will be seen as multiple local maxima that will be separated by the algorithm, although they do not correspond to distinct H II regions, but only variations in the gas density. Thus, odd-shaped H II regions may not be considered as a single H II regions, due to the nature of the algorithm. In all cases, this method provides the most physically meaningful results, as it ensures most of the H II regions detected are associated with a different excitation source. Overall, this method is uniform with the one used by the other SIGNALS' studies: Massé et al. (in prep.), Rousseau-Nepton et al. (2018), and Savard et al. (in prep.).

The high level of DIG and multiple filaments found in NGC 4449 make the disentanglement from H II regions difficult during the detection. The parameters used in the detection algorithm try to minimize the false detections and only keep clearly defined emission regions. The downside of this approach is that small, diffuse, low luminosity H II regions might be missing in the final catalogue, which would affect the luminosity function (see Section 2.7.1). The remaining false detections (DIG and filaments) may not be filtered out by using BPT diagrams (see Section 2.7.6). Due to the proximity of NGC 4449, another challenge encountered in the detection process was disentangling the H II region complexes. The spatial resolution allows to resolve individual H II regions, but the highly chaotic ISM dynamic in NGC 4449 causes complex structures in the H II regions, which makes the simple algorithmic approach to not always be accurate.

2D Gaussian distributions (compactly supported within 3σ) are fitted to the flux map of each region's zones of influence. This delimits the domain of the flux for each region. A 2D

Gaussian fit is used, instead of a 1D profile modelling a sphere (based on the Strömgren model; Strömgren 1939), because of the high spatial resolution allowed by the SITELLE data used. The 2D Gaussian model also includes a plane, to model the background emission coming from the adjacent regions and the diffuse ionized gas. The region's domain is limited to the 3σ radius of the 2D Gaussian model, which is considered to be the physical size of the region and contain most of the flux emitted by the region. The 2D fit parameters obtained are later used to analyse the morphology of the emission regions (Section 2.7.2) and to integrate the emission line flux from the regions (Section 2.6.3).

This supposes that the luminosity profile of the detected emission regions is a 2D Gaussian. For isolated H II regions, this assumption is valid (Fuentes-Masip et al. 1995). However, in other contexts, it is not always the case, as seen in Figure 2.4. Figure 2.4 shows a few examples of the emission regions detected, their centroids, and their spatial extent. The location of these examples is shown on the galaxy on Figure D.2. The contours in teal in Figure 2.4 correspond to the final domains (*i.e.* the intersection of the zone of influence and the fitted 2D Gaussian profile) of the emission regions (their centroids are marked by a teal cross).

2.6.3 Spectral Fitting

The spectrum of the pixels included in the emission region's domain (*i.e.* the intersection of the zone of influence and 3σ of the 2D Gaussian profile, as described in Section 2.6.2) are summed and fitted using the ORCS library. Because of the omnipresence of DIG in NGC 4449, it is crucial to correct the flux values of each detected regions for background emission. The background region corresponds to the pixels within 3σ and 9σ of the 2D Gaussian profile and the region's domain. The same fitting process is applied to the background region. It also excludes the pixels from other regions' domain. The pixels with a continuum S/N inferior to 1 are also excluded from the background region. This allows for a statistically significant sample of spectra within the background domain to correct the flux value of the emission region. Instead of summing the spectra from the background region (as done for the emission region's spectra), the median spectrum is used, so as to get a better estimate of the flux, and reduce bias with extreme variations within the sample of spectra from the background domain. This background spectrum takes into account the local background diffuse emission as well as the local stellar population (if not already removed from the datacubes, see Section 2.6.7).

The flux values obtained from the ORCS fit of the region's spectrum and background's spectrum are subtracted for each line. This attempts to separate the emission by the H II regions from the one of the superposing DIG along the line of sight. This technique assumes a constant and uniform DIG emission from the surroundings of the H II region. As discussed by Zurita et al. (2004), it is difficult to properly correct for this effect, but an effort is made to take into account a local value. Thus, this approximation is deemed acceptable. As mentioned by Gutiérrez et al. (2011), correcting for the superposing DIG emission in NGC 4449 is

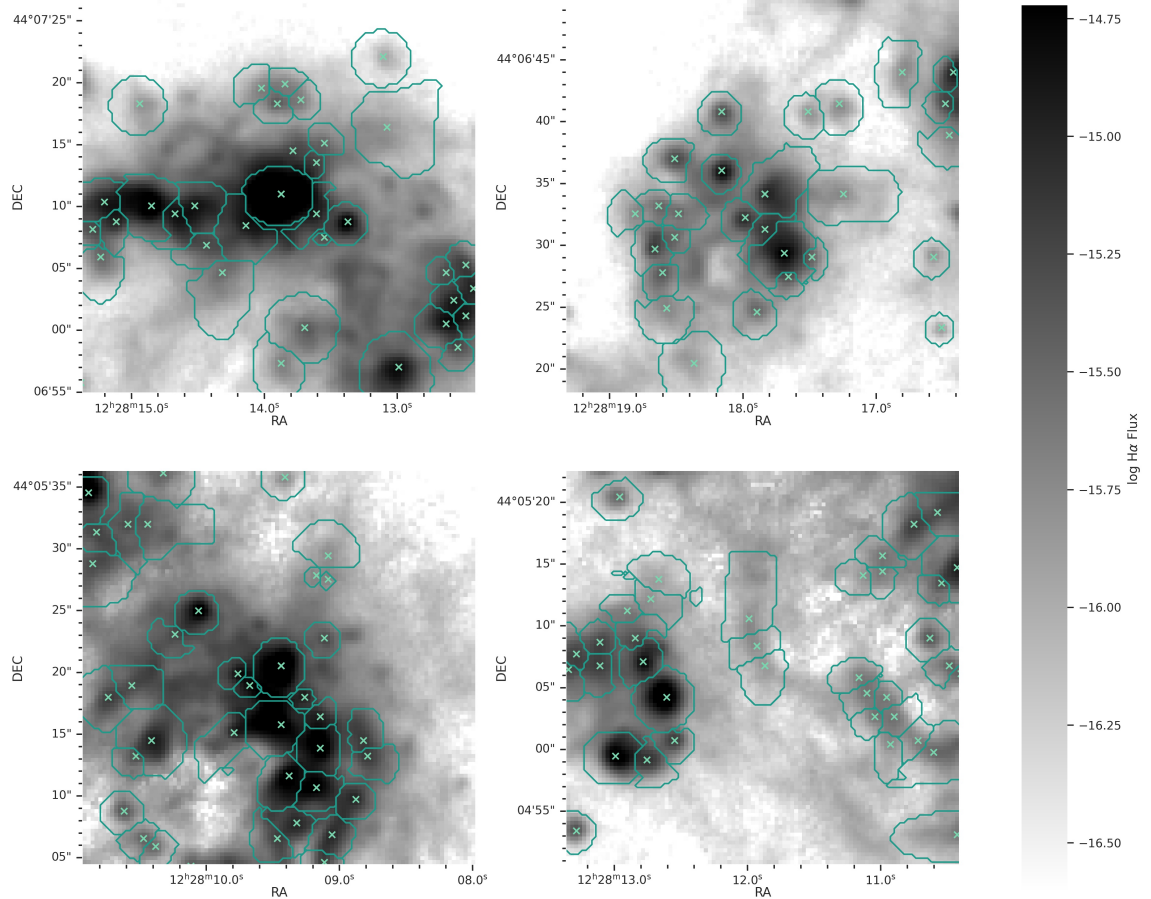


Figure 2.4 – Examples of the emission regions detected with the algorithm created by Savard et al. (in prep.). The peak detection is done with a `Laplacian sigma` of 1.5, a `detection box size` of $5\text{ px} \times 5\text{ px}$, a `noise sigma` of 3, a `local background box` of $40\text{ px} \times 40\text{ px}$, and a `scaling factor` of 1.6 (as described in Section 2.6.1). The centroids of the regions are marked by a teal cross. The contours in teal correspond to the intersection of the zone of influence and the fitted 2D Gaussian profile (at 3σ), as described in Section 2.6.2, for each region. The top left plot is centred on region 527, at RA 12h28m03.4s and DEC +44°05m15.5s. Region 527 is located at the apex of the northern arm. The top right plot is centred on region 420, at RA 12h28m06.9s and DEC +44°04m33.6s. Region 420 is located in the second ring in the northern arm, eastwards of the apex. The bottom left plot is centred on region 175, at RA 12h28m13.6s and DEC +44°06m05.5s. Region 175 is located in a large stellar formation ring, south of the nucleus of the galaxy, in the bar. The bottom right plot is centred on region 123, at RA 12h28m14.9s and DEC +44°05m39.5s. Region 123 is located in a filament expanding from the large stellar formation ring (where region 175 is located), east of the bar, south of the nucleus, between another large stellar formation ring to the east. The location of these plots is shown on the galaxy in Figure D.2. The background image corresponds to the log H α flux map. The aperture size is 597 pc \times 597 pc.

particularly challenging due to its omnipresence throughout the galaxy combined with strong gradients in the observed DIG flux. Attempts of different techniques have been made in the past (Gutiérrez et al. 2011), but this study does not attempt to model the underlying DIG emission to separate it from the H II region.

Figure 2.5 shows the integrated spectrum of region 527 in the three datacubes. This region was chosen to showcase a typical H II region. It corresponds to the region in the top left panel of Figure 2.4, located at the apex of the northern arm of NGC 4449. The top panels show the spatial domain of the H II region (marked by the teal contour), on the $[\text{O II}]\lambda\lambda 3726,3729$ (left), $\text{H}\beta$ (middle), and $\text{H}\alpha$ (right) flux map. The peak of the region is marked by a teal cross. The spectra contained in this domain (teal contour) are summed to produce the integrated spectrum shown in the middle panel in teal. The pink contour in the top panels corresponds to the limit of the background domain. The median spectrum of the background is plotted in the bottom panel in pink. The resulting fits of the spectra are displayed with their corresponding spectrum.

The emission region’s velocity and velocity dispersion are taken from the ORCS fit, without the background subtraction (discussed in Section 2.7.9). In crowded regions where H II regions may overlap, the measured velocity broadening may be overestimated as it contains the emission from multiple H II regions (Fuentes-Masip et al. 1995; Fuentes-Masip et al. 2000b). The wide range of velocity differences between H II regions, often of the order of a few kilometers per second, cannot allow the spectral disentanglement of all overlapping emission. This overlapping of emission is expected to be more prominent in the outskirts of the H II regions (further away from the bright centroid of the region). It is also well known that the physical properties of the H II region change radially (Hippelein 1986; Munoz-Tunon 1994; Sabalisck et al. 1995). Therefore, fitting the integrated spectrum of a region over many spaxels always blends these spatial variations and usually favours the values associated to the brightest spaxels. One could measure the velocity dispersion only in the centroid spectrum to avoid the velocity dispersion blending, as done by Fuentes-Masip et al. (2000b). However, the summed spectrum has a better S/N than only the centroid spectrum, which allows for a more accurate fit. In all cases, these spatial variations are not in the scope of the present paper. Closer galaxies might be more appropriate for this type of investigation.

2.6.4 Uncertainties

Uncertainties for the regions’ parameters are quantified, taking into account the spatial and spectral fit. The spatial fit is repeated 50 times, to allow convergence of the uncertainties estimate, whilst adding random variations on the $\text{H}\alpha$ flux values of the region. The variation in each pixel is sampled from a Gaussian distribution (mean centred on the measured flux value and the standard deviation from ORCS). The median value of the distribution is selected as the spatial fit parameter and the 16th percentiles on each side of the distribution are defined

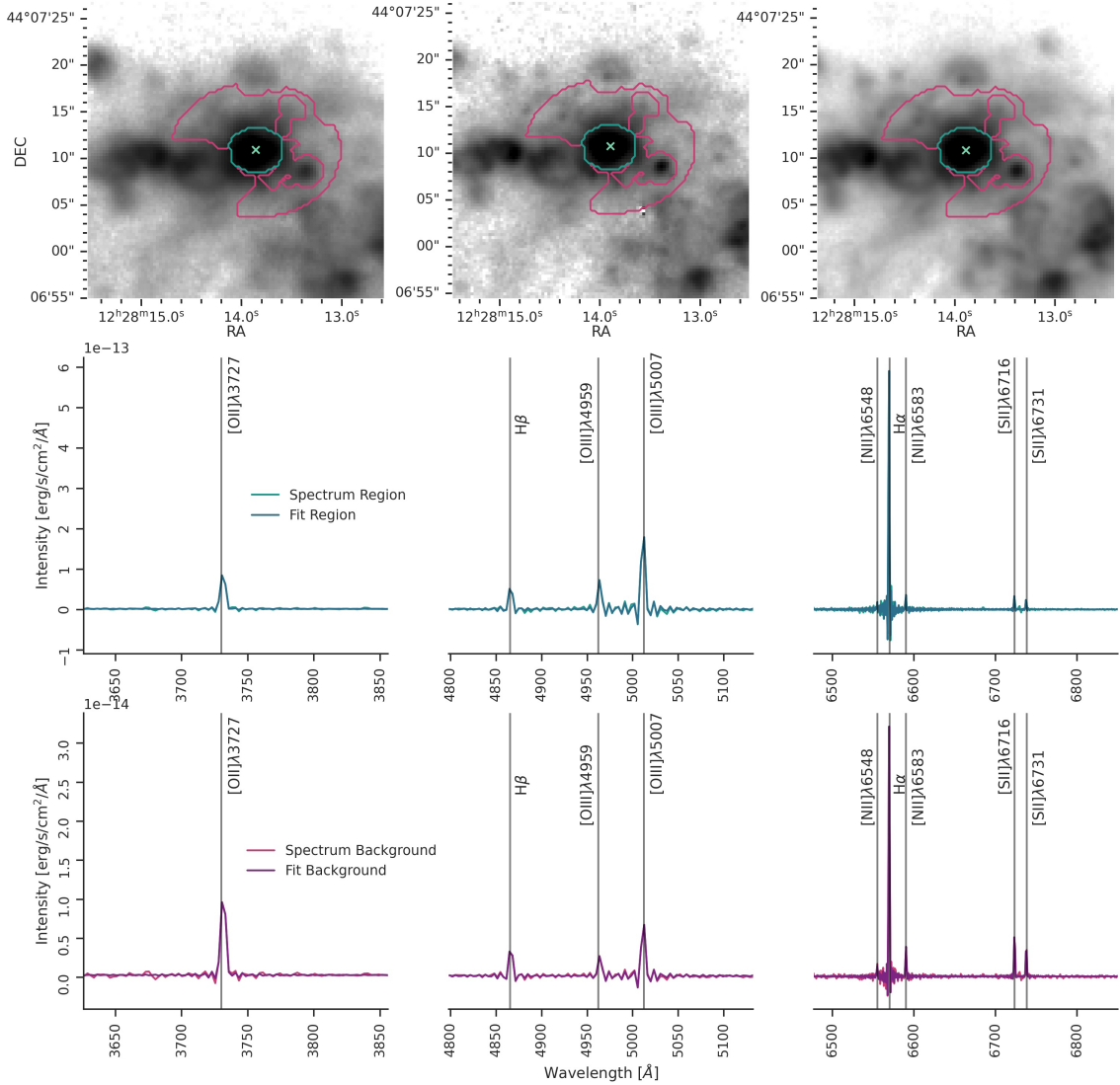


Figure 2.5 – Example of an H II region’s integrated spectrum in the three datacubes (SN1, SN2, and SN3; left to right). This region corresponds to region 527 (as shown in Figure 2.4). The radius of the region’s domain corresponds to about (33.8 ± 0.4) pc. The top row shows the spatial location of the H II region, on the log $[\text{O II}]\lambda\lambda 3726, 3729$ (left), log $\text{H}\beta$ (middle), and log $\text{H}\alpha$ (right) flux maps, with an aperture size of $597 \text{ pc} \times 597 \text{ pc}$. The teal cross corresponds to the peak of the region. The teal contour delimits the boundaries of the H II region’s domain. Its spectrum is shown in the panels of the middle row. The pink contour corresponds to the background domain for this region. The bottom row panels show the resulting median spectrum of the background region (pink contour). The H II region and background spectra are fitted using ORCS as described in Section 2.5.3. The emission lines are labelled and marked with vertical grey lines. The instrumental sinc profile of SITELLE are noticeable, particularly near the emission lines.

as the error. Using a quadratic sum, this error and the median fitting error (which corresponds to the covariance of the fit) are combined to establish the final uncertainty for each parameter. This procedure also prevents from converging to extremely inaccurate parameters that could be caused by outlying pixels poorly fitted due to a low S/N. It is performed for all fitting parameters of the 2D Gaussian and its plane model, allowing throughout propagation of errors in the estimate of the parameters uncertainty.

Note that the uncertainty estimate for the flux also includes uncertainties on the estimated size of the emission region. With the same method used to integrate the flux in the region, the flux is integrated in a radius of $X(\sigma + \Delta\sigma)$ and $X(\sigma - \Delta\sigma)$, where σ is the standard deviation of the 2D Gaussian, used to measure the size of the region (Section 2.6.2) and $\Delta\sigma$ is the uncertainty measured for σ . X is the region's domain size scaling factor, $X = 3$ is used in this study for the emission domain and $X = 9$ for the background domain. This error is combined with the fitting error from ORCS using a quadratic sum.

All uncertainties on the mean values given in this paper are computed as:

$$\Delta\bar{x} = \sqrt{\left(\frac{\sigma_x}{\sqrt{N_x}}\right)^2 + \bar{x}_{\text{err}}^2}, \quad (2.2)$$

where the first term is the distribution mean standard deviation and the second term is the mean of the propagated measuring errors of every datum. Thus, σ_x corresponds to the standard deviation and N_x corresponds to the number of datum in the distribution.

2.6.5 Limit of Detection: Luminosity Threshold

To determine the lowest luminosity value of statistical completeness for the detection of the emission regions in NGC 4449 with the data used in this study, artificial H II regions are injected in the H α amplitude map used for the detection, as described above. Using the same detection parameters as the ones used in Section 2.6.1, the completeness is tested for the detection of 100 artificial H II regions added randomly and uniformly distributed in space over the galaxy. The artificial H II regions are modelled by a 2D Gaussian with a σ value in the x axis randomly sampled from a Gaussian distribution (mean, 1.7 px, and standard deviation, 0.2 px). The y axis value is dependant on the x axis by $\sigma_x * (1 - 0.3 * \text{np.random.random}(1))$. These dimensions are within the average size and eccentricity of detected H II regions. However, the eccentricity is constrained to, on average, 0.7, to avoid inducing multiple detections in the same artificial region.

All the artificial H II regions added to the H α amplitude map have the same amplitude. The process is repeated 1200 times, increasing the amplitude of the artificial H II regions (between 5×10^{-18} erg s $^{-1}$ cm $^{-2}$ Å $^{-1}$ and 1×10^{-14} erg s $^{-1}$ cm $^{-2}$ Å $^{-1}$) each time in order to sample the entire parameter space. The steps between each amplitude is not constant throughout the iterations in order to better model the ranges of high variations. The completeness level is set

at 80%. The completeness convergence is shown in Figure C.7. It corresponds to the lowest luminosity value that can be detected in the noise.

The H II regions in this catalogue are therefore considered incomplete below a luminosity of $\log L_{H\alpha} = 36.6 \pm 0.3$. The incompleteness mostly affects the luminosity function (Section 2.7.1) and is primarily caused by the missing detections of faint emission regions, especially the ones close to bright regions. Another source of incompleteness is the blending between close H II regions that cannot be resolved as distinct objects (Kennicutt et al. 1989).

2.6.6 Rejection of Detections

After fitting all the detections, rejection steps are applied to remove any incorrect or unreliable detections. Regions containing less than 20 pixels in their zone of influence or in their final domain are removed, as they are not considered to be large enough for proper measurement and to physically correspond to an emission region, considering the seeing. An area of 20 pixels corresponds to a circle with a radius of 2.5 pixels, which is close to the seeing limit of the data. It is thus impossible to resolve regions smaller than this radius.

Regions with improperly fitted spectrum are also rejected. The regions where the H α line does not have an emission component (after the local emission background subtraction and the global stellar absorption correction) are not included in the final study. After this quality verification, 535 emission regions remain in the final catalogue, out of the 544 emission regions originally detected.

The final selection of the emission regions for the catalogue is shown in Figure 2.6, superimposed on the H α flux map and colour coded by their H α luminosity. These fluxes are corrected for the global stellar absorption (see Section 2.6.7), for the local background diffuse emission (by using the local background region defined in Section 2.6.3), and for the extinction (see Section 2.6.8). As expected the most luminous H II regions are located in the centre of the galaxy. These regions are the most crowded, suggesting that regions complexes may not be fully resolved.

2.6.7 Underlying Stellar Populations

The local background spectrum created in Section 2.6.3 takes into account the galaxy's (and, in many cases, the cluster's) stellar populations superimposed to the emission regions along with the background diffuse emission. This spectrum is used to correct the emission lines' flux. Nevertheless, another technique is explored in this section to isolate a crude model for the global galaxy's stellar population, that can be useful to study at a pixel-scale, the diffuse emission itself and the extinction.

All spectra are corrected for the presence of continuum and absorption line features coming from the underlying stellar population. To create a stellar population model, spectra selected

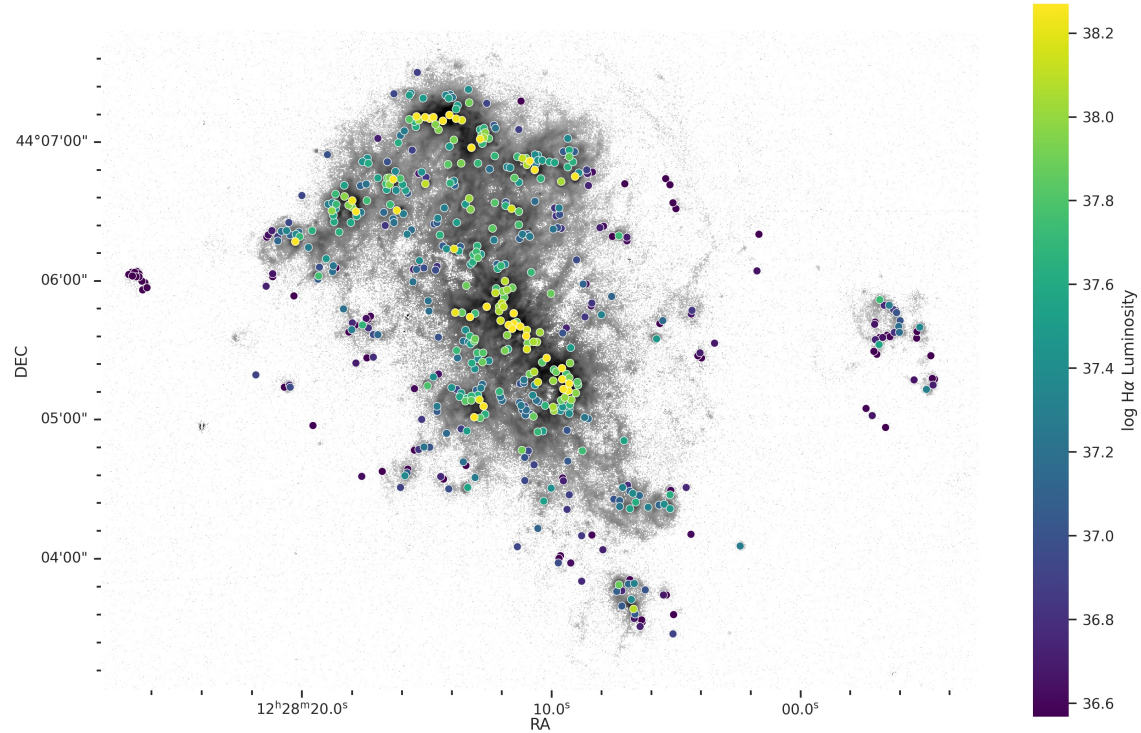


Figure 2.6 – Spatial distribution of the emission regions, colour coded by their H α luminosity value. The regions are superimposed on the log H α flux map, where the pixels with a H α or H β S/N lower than 1 are not shown. The H α luminosity is corrected for the local background diffuse emission, the global stellar absorption, and the extinction.

in the galaxy are summed and used as an input for `ppxf` (a version adapted for SITELLE data), as described by Massé et al. (in prep.). The foreground stars are masked (as described in Section 2.5.8) and the pixels with a SN3 continuum S/N inferior to 3, a SN2 continuum S/N inferior to 1, and a H β flux superior to 5×10^{-18} erg s $^{-1}$ cm $^{-2}$ are removed. Prior to their sum, the remaining pixels are set to rest using a velocity map built by interpolating the SN3 ionized gaz velocity map. The resulting spectrum, containing ~ 17000 pixels with a continuum S/N of 190, is used as an input for `ppxf`. The resulting stellar population model is shown in Figure 2.7. A single combination of stellar populations is considered for the entire galaxy, due to the weak presence of absorption lines in the spectra and the low accuracy of the method used, even if it is not fully inline with the results obtained by Sacchi et al. (2018). Although some emission lines remain in this spectrum, `ppxf` was adapted to take into account the sincgauss profile of the SITELLE instrument for the emission line model. However, in order to not induce further errors in the absorption correction, a more conservative approach is preferred for the correction of the spatial variations of the underlying stellar population, and thus a uniform population is assumed, instead of generating stellar population models for different morphological regions of the galaxy.

The SN3 and SN2 datacubes are corrected by subtracting the stellar population model from

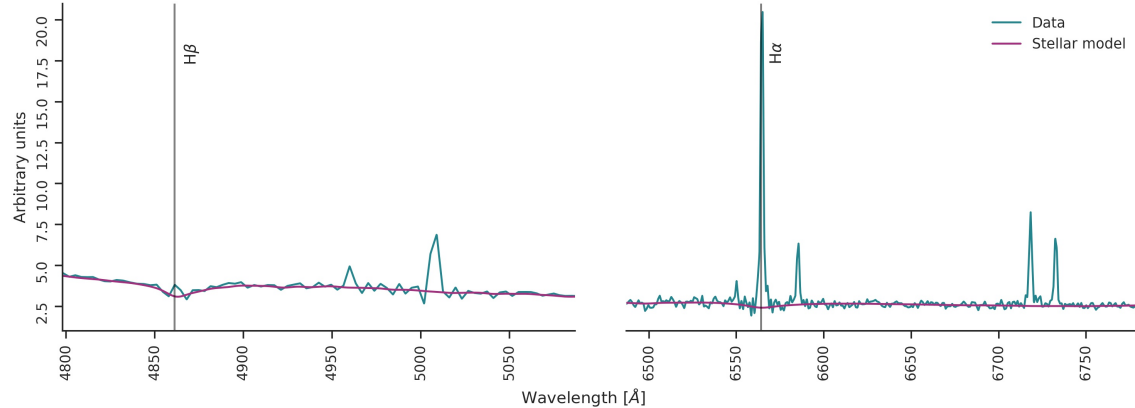


Figure 2.7 – Global stellar absorption spectrum (using only SN2 and SN3) of the stellar populations of NGC 4449 (teal curve) and the resulting model from `ppxf` (pink curve). The H α and H β lines are identified with grey vertical lines.

`ppxf`, after matching their continuum level. The SN1 data, being far from the SN3 and SN2 wavelength range is not used for the analysis with `ppxf`.

The global stellar absorption correction induces multiple uncertainties that are propagated in the emission line fitting described in Section 2.6.3. For instance, it was not possible to create multiple absorption spectra with high enough S/N for `ppxf` for different areas of the NGC 4449 galaxy. It thus assumes a uniform age and metallicity distributions for the underlying old stellar populations. Separating the galaxy into different areas would have resulted in additional uncertainties propagated due to the poor fitting from `ppxf` at low S/N. Nevertheless, since very little absorption is present in NGC 4449 as a whole, this method is deemed sufficient to account for the absorption spectral features for the few spaxels that are the most affected by it, close to the centre of the galaxy.

Additionally, the spectral range of the datacubes used in this study contains very few well-measured absorption lines. The only available absorption line corresponds to the H β line, however, since H α is plagued by emission, it is hard to constrain the `ppxf` fit properly, inducing uncertainties in the width of the absorption lines in the modelled spectrum, based on the stellar population used. Thus, the few absorption lines in the spectral range covered by the data used in this study restrain the accuracy of the model produced by `ppxf` (but see the discussion by Massé et al. (in prep.) for more information).

Globally, the absorption correction is expected to underestimate the absorption in the H α emission line, which would not significantly affect the measured flux values in the present case of NGC 4449, as demonstrated in Figure 2.8. Figure 2.8 compares the measured flux of the detected emission region in order to study the impact of the stellar absorption correction. Figure 2.8 shows the H α (left panel) and H β (right panel) integrated flux values for each region including and excluding the global stellar absorption correction. No other corrections, such as

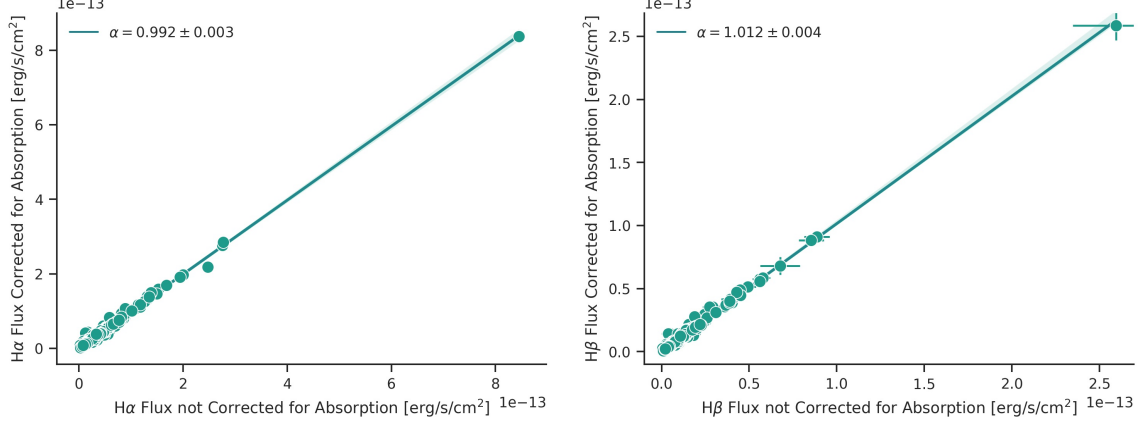


Figure 2.8 – Comparaison of the emission region’s flux with and without a global stellar absorption correction. The left panel shows the impact on the H α flux and the right panel shows the impact on the H β flux. The teal line shows the linear fit, with a slope $\alpha = 0.992 \pm 0.003$ for the H α flux and a slope $\alpha = 1.012 \pm 0.002$ for H β . No other corrections, such as the local background diffuse emission subtraction (described in Section 2.6.3) and the extinction (described in Section 2.6.8), are applied to the flux values.

a local background diffuse emission subtraction (described in Section 2.6.3) and the extinction (described in Section 2.6.8), are applied. The uncertainties of each flux value is obtained from the propagation described in Section 2.6.4. The uncertainty on the fit corresponds to the confidence interval, estimated using a bootstrap method. The slope obtained from the linear regression (teal line) for the H α and H β flux is 0.992 ± 0.003 and 1.012 ± 0.002 , respectively. This indicates that the global stellar absorption correction tends to decrease the H α flux by 0.8% and increase the H β flux by 1.2%. The gain in accuracy of the flux measurement is negligible compared with the uncertainties induced by the method to obtain the global absorption correction and the general methodology used to measure the emission regions in this study. Generally, the H α and H β fluxes obtained from the emission regions calculated with or without the absorption correction are similar.

The impact of the stellar absorption methodology is investigated in Figure 2.9. It compares the integrated H α and H β flux of the emission regions when they are corrected for the local background (containing the local stellar population and diffuse emission; Section 2.6.3) and when the global stellar population model is subtracted from the datacubes prior to calculating the region’s integrated spectrum to apply the correction for the local background diffuse emission (using the background region defined in Section 2.6.3). The method correcting for the local stellar population consists of subtracting the median background’s spectrum to the spectrum of the emission region and then fitting the resulting spectrum to obtain the emission line’s flux values. The flux values obtained using this method are presented in Table F.3. The background spectrum accounts for the underlying stellar population and the DIG emission, without assuming a globally uniform stellar population, like the method using ppxf. However,

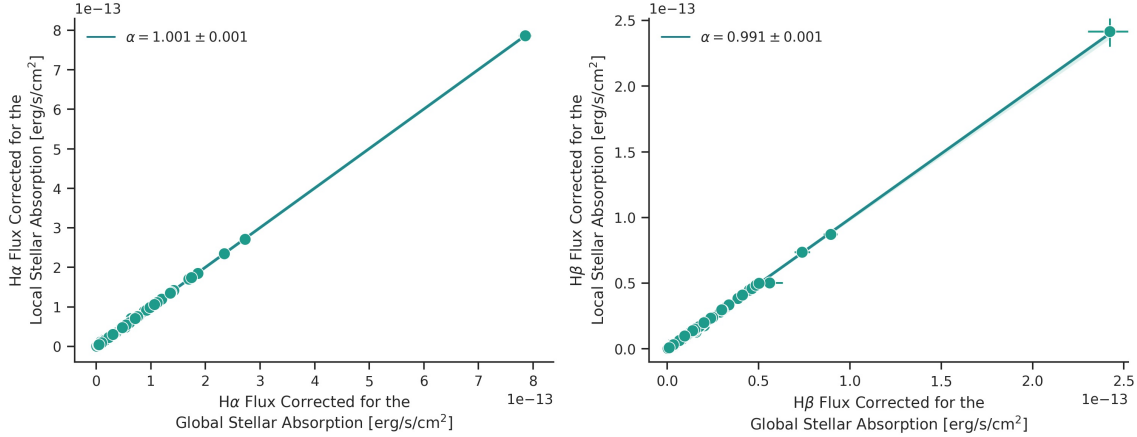


Figure 2.9 – Comparaison of the stellar absorption correction methodologies. The left panel shows the impact on the H α flux and the right panel shows the impact on the H β flux. The teal line shows the linear fit, with a slope $\alpha = 1.001 \pm 0.001$ for the H α flux and a slope $\alpha = 0.991 \pm 0.001$ for H β . The extinction correction is not applied to the flux values.

if the velocity or the velocity dispersion of the background differs from the ones of the region, the spectra subtraction might cause artefacts, leading to inaccurate flux measurements. The extinction correction is not applied to the flux values. The uncertainties of each flux value is obtained from the propagation described in Section 2.6.4. The uncertainty on the fit corresponds to the confidence interval, estimated using a bootstrap method. The slope obtained from the linear regression (teal line) for the H α flux is $\alpha = 1.001 \pm 0.001$ and $\alpha = 0.991 \pm 0.001$ for H β . This indicates that subtracting a local background spectrum to correct for absorption increases the H α flux by 0.1 % and decreases the H β flux by 0.9 % compared to using the global stellar population model from `ppxf` model and subtracting the flux value of the background emission.

Holistically, the absorption correction, regardless of the method employed, has minimal impact on NGC 4449 and the flux values presented in this study. The uncertainties associated to the absorption correction and with the methodology in general are estimated to be greater than the gain in accuracy from the absorption correction per se.

2.6.8 Extinction Correction

For each emission line region and also each pixel, the flux is corrected for dust extinction. The Milky Way extinction is accounted for using:

$$E(B - V) = \frac{A_V}{R_V}, \quad (2.3)$$

where $A_V = 0.053$ mag (according to NED) and $R_V = 3.1$ mag. The python library `pyneb` (Luridiana et al. 2015) and Cardelli et al. (1989) extinction law are used. The intrinsic

extinction is measured, assuming a theoretical ratio of

$$E(B-V) = \frac{2.5}{1.07} \log\left(\frac{F_{H_\alpha}/F_{H_\beta}}{2.87}\right), \quad (2.4)$$

using $A_\lambda = 2.5 \log\left(\frac{I_\lambda}{I_{\lambda_0}}\right)$ and $\frac{E(\beta-\alpha)}{E(B-V)} = 1.07$ as obtained by Cardelli et al. (1989) for their extinction curve. The theoretical ratio of the two main Balmer lines is $\frac{F_{H_\alpha}}{F_{H_\beta}} = 2.87$, as described by Osterbrock (1989), for the theoretical Case B of an H II region, at a temperature of 10 000 K.

Corrected fluxes are presented in the catalogue provided in this study (see Table F.5). All the detected emission regions in this study possess a H β S/N superior to 3, thus the extinction correction is applied to all the regions. The uncertainties from the H α and H β flux measurements are taken into account when correcting all the lines for the intrinsic extinction. This is done by propagating their flux measurement uncertainties onto the corrected lines. The uncertainties from the `pyneb` models also affect the final values.

The extinction value obtained for each emission region is shown in Figure 2.10. The emission regions are represented by the circular markers, placed in their spatial location on the H α flux map.

120 of the 535 emission regions detected have negative A_V values. This might be caused by poorly measured weak H β lines. It may also be due to the fact that the intrinsic extinction correction is calibrated for H II regions. Thus, it is possible that different physical conditions in the DIG regions causes the calculated A_V value to be inaccurate. Another cause might be linked to the assumed theoretical parameters used to calibrate the intrinsic extinction correction for the H II regions. All of these factors might contribute to the negative A_V values calculated for some of the emission regions in this catalogue.

An extinction map, for each pixel, is also shown in Figure 2.11, using the absorption subtracted datacubes directly, but with no correction for the background emission. The pixels with a H α and H β S/N inferior to 3 are not corrected and are not shown in this map. Figure 2.10 and Figure 2.11 are in agreement; higher extinction is seen in the central bar and the northern arm.

The radial variation of the extinction in NGC 4449 is shown in Figure 2.12. The markers represent the detected emission regions. 440 emission regions are used in Figure 2.12, as the ones with a negative A_V value are not included. The galactocentric-distance is computed from the photometric centre, assumed at RA 12h28m11.2s and DEC +44°05m37.9s, with a P.A. of 25° and an inclination of 43°, as used by Valdez-Gutiérrez et al. (2002). The linear regression (teal line) is fitted through the data, resulting in a slope of $(9.7 \pm 0.3) \times 10^{-5} \text{ pc}^{-1}$, indicating that globally the extinction does not vary with regard to the galactic centre of NGC 4449. The uncertainty on the fit corresponds to the confidence interval, estimated using a bootstrap method.

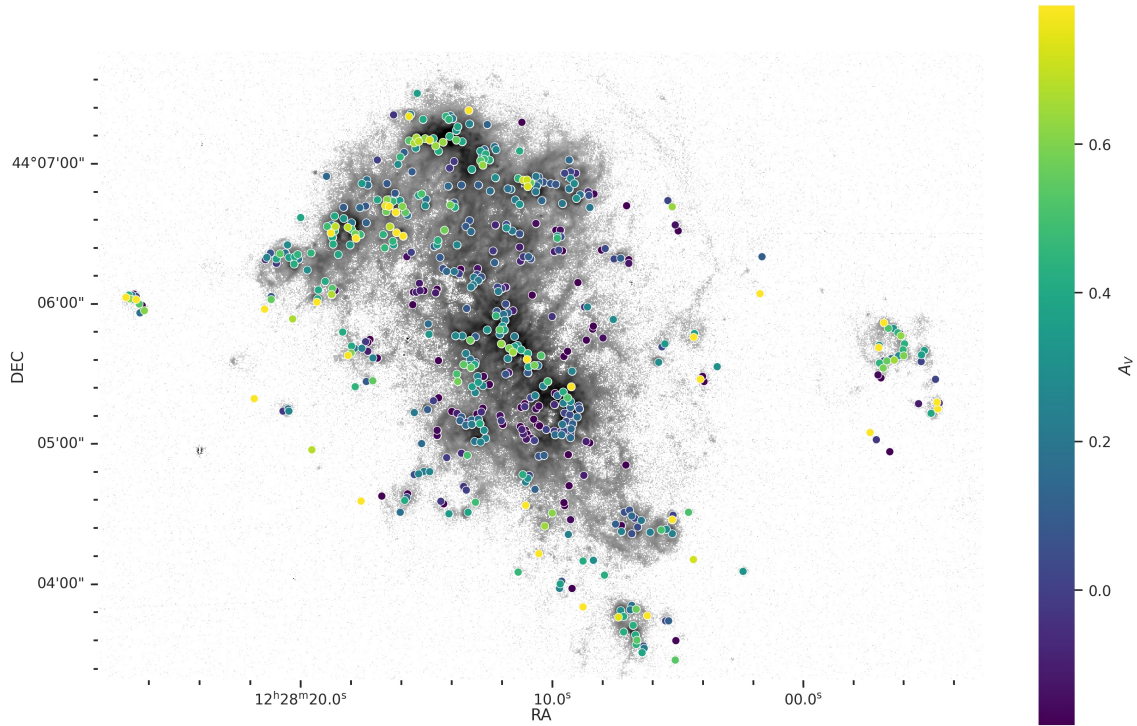


Figure 2.10 – Spatial distribution of the emission regions colour coded with their extinction value. The extinction is obtained using the $\text{H}\alpha$ and $\text{H}\beta$ line ratios and `pyneb`. The line flux have been corrected for the global stellar population and the local background diffuse emission. The HII regions are spatially plotted over the log $\text{H}\alpha$ flux map, where the pixels with a $\text{H}\alpha$ or $\text{H}\beta$ S/N lower than 1 are not shown.

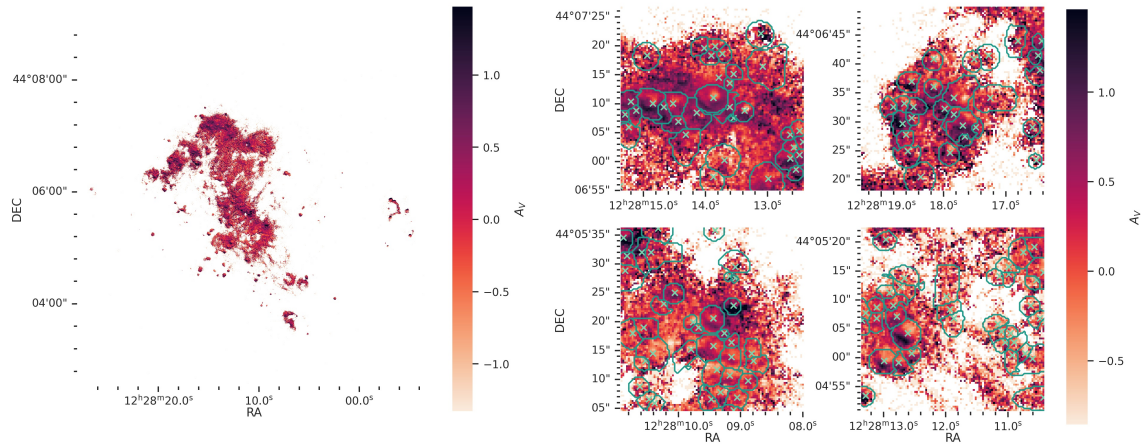


Figure 2.11 – Extinction map of NGC 4449, obtained using the $\text{H}\alpha$ and $\text{H}\beta$ line ratios and `pyneb`. Only the pixels with a S/N for the $\text{H}\alpha$ and $\text{H}\beta$ lines superior to 3 are displayed. The $\text{H}\alpha$ and $\text{H}\beta$ flux maps used to compute the line ratio have been corrected for the global stellar absorption. On the left panel, the entire galaxy is shown. On the right panel, the same areas as in Figure 2.4 (Fig. D.2) are shown. The teal cross indicate the centroid of the regions. The teal contours represent the intersection of the zone of influence and the 2D Gaussian profile for each region. Each panel shows an aperture of $597\text{ pc} \times 597\text{ pc}$.

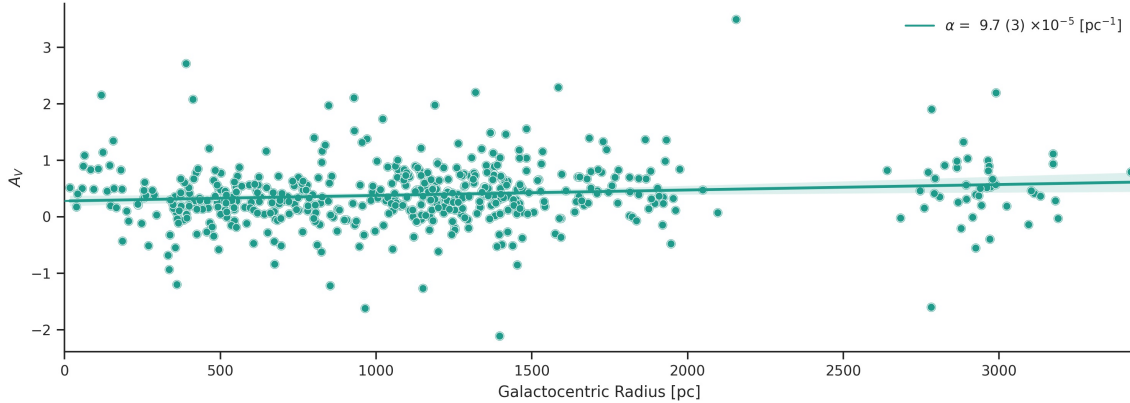


Figure 2.12 – Radial profile of the emission region’s extinction in NGC 4449. The slope obtained from the linear fit (teal line) has a value of $(9.7 \pm 0.3) \times 10^{-5} \text{ pc}^{-1}$. The photometric and dynamic centre is assumed to be at RA 12h28m11.2s and DEC $+44^{\circ}05\text{m}37.9\text{s}$, with a P.A. of 25° and an inclination of 43° (Valdez-Gutiérrez et al. 2002). The emission regions with negative A_V value are not included when calculating the slope.

Globally, as a function of the galactic radius, the extinction value of the emission regions appears to be constant. The same trend is observed by Scowen (1992), using their catalogue of 160 H II regions for NGC 4449. A slight increase in value may be observed at a radius greater than 2.5 kpc, with A_V values spanning a wide range of values. These emission regions are located on the outskirts of the galaxy and may be poorly measured or have different physical properties. The same phenomenon is observed by Scowen (1992). Scowen (1992) also notes that these regions have a low surface brightness and suggests that they could be more dusty than the ones in the main body of the galaxy.

2.7 Results and Analysis

The catalogue with all the detected emission regions in NGC 4449 and the correction parameters mentioned in Section 2.6 is located in Appendix F. The morphology parameters are presented in Table F.1, the raw flux values without corrections are in Table F.2, the flux values corrected for the local background (including the local stellar absorption and diffuse emission, by subtracting the background spectrum; Section 2.6.7) are in Table F.3, the flux values corrected for the local background diffuse emission (using the local background region defined in Section 2.6.3), for the global stellar absorption (Section 2.6.7), and for the extinction (Section 2.6.8) are in Table F.4, and the kinematical and chemical properties (extinction and metallicity) are displayed in Table F.5. In this section, unless stated otherwise, the line flux values used for the detected emission regions are from Table F.4.

The luminosity function is studied in Section 2.7.1 and the size function is presented in Section 2.7.2. The correlation between the luminosity, size, and velocity dispersion is explored in Section 2.7.3. Section 2.7.4 discusses the proximity distance between the regions. The

line ratios for the entire galaxy and the BPT diagrams for the detected emission regions are presented in Section 2.7.5 and Section 2.7.6, respectively. The relation with the young stellar clusters is investigated in Section 2.7.7. The metallicity is discussed in Section 2.7.8. Section 2.7.9 explores the global kinematics of the gas and the emission regions in NGC 4449. The potential inflow/outflow is explored further in Section 2.7.10. Some notable detected objects are presented in Section 2.7.11. The nature of the detected emission regions, using a machine learning algorithm, is investigated in Section 2.7.12.

2.7.1 Luminosity Function and Star Formation Rate

The luminosity function of all the emission regions in this catalogue is presented in Figure 2.13. The bright end of the luminosity function is fitted using a power law:

$$N(L) dL = AL^\alpha dL, \quad (2.5)$$

where $N(L) dL$ corresponds to the number of emission regions with a luminosity between L and $L + dL$. The luminous end of the luminosity function, presented in Figure 2.13, is modelled with a linear fit. The range of the fit spans from the median luminosity value plus 0.2, $\log(L_{1/2}) + 0.2 = (37.50 \pm 0.04) + 0.2$, shown by the vertical line, up to the most luminous H II region $\log(L_{\max}) = 39.30 \pm 0.03$. The added 0.2 value to the median ensures that only the monotonically decreasing part is fitted and is done for coherence with the methodology used by Rousseau-Nepton et al. (2018), in order to compare the slopes obtained. The slope obtained here is $\alpha = -1.08 \pm 0.07$. This slope is thought to be influenced by the morphological type of galaxies, with mean values ranging from -2.3 for Sab-Sb galaxies to -1.75 for Irr galaxies (Kennicutt et al. 1989). The value obtained in this study does not fall in the typical range of values expected for an irregular galaxy, but in the past, this type of study was limited to only a few bright H II region complexes per galaxy.

Kennicutt et al. (1989), using the 0.92 m telescope at the *Kitt Peak National Observatory*, with a field of view of $15'$ and a nominal angular resolution of $2''$, found slopes for irregular galaxies ranging from -1.9 to -1.6 , with the slope $\alpha = -1.48$ for NGC 4449. This in turn suggests that NGC 4449 contains more luminous H II regions than other irregular galaxies. It is also believed to be related to the abnormally high proportion of H II regions with a supersonic velocity dispersion present in NGC 4449 (Fuentes-Masip et al. 2000a).

The brightest H II region measured by Kennicutt et al. (1989) has a luminosity of $\log(L_{\max}) = 39.8$, which is superior to the brightest H II region in this study. Their study found 136 H II regions, which emit a total luminosity of $2.2 \times 10^{40} \text{ erg s}^{-1}$, a value comparable to the one obtained in our study of $(2.197 \pm 0.005) \times 10^{40} \text{ erg s}^{-1}$. H II regions are better resolved here (due to the higher spatial resolution), which allows both a better sampling of the lower end of the luminosity function and the disentangling of close neighbours, affecting the measured slope of their luminosity function.

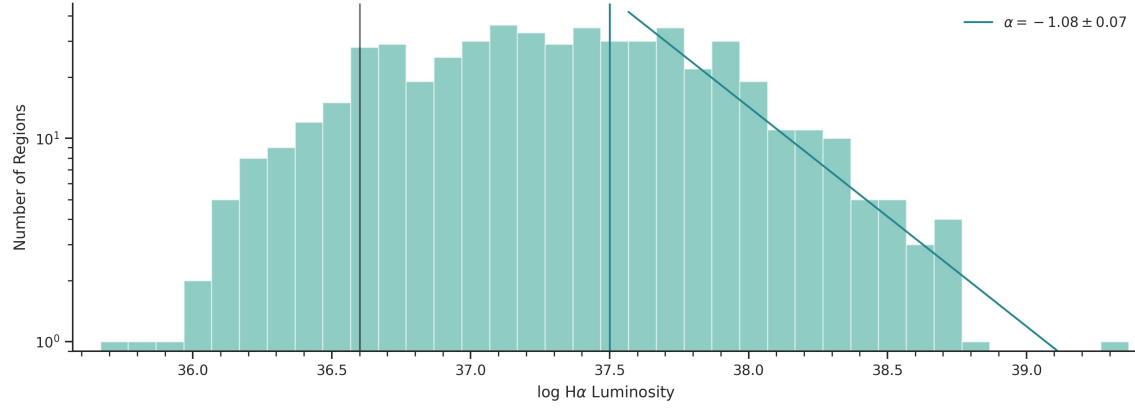


Figure 2.13 – $\text{H}\alpha$ luminosity function for all the emission regions. The vertical teal line corresponds to the median value plus 0.2 of the distribution, which is $\log(L_{1/2}) + 0.2 = (37.50 \pm 0.04) + 0.2$ and corresponds to the beginning of the range for the fit. The fit ends at the maximum value, which is $\log(L_{\max}) = 39.30 \pm 0.03$. The slope of the linear fit obtained from the luminous end of the distribution is -1.08 ± 0.07 . The fit corresponds to the teal line. The grey vertical line corresponds to the completeness limit, located at $\log L_{H\alpha} = 36.6 \pm 0.3$ (as described in Section 2.6.5).

The data used by Kennicutt et al. (1989) has a nominal angular resolution of $2''$, which was further degraded in order to homogenise the resolution of all the images in their sample. Consequently, their low resolution, in combination to the high level of crowding from the H II regions in NGC 4449, would lead to overestimating the luminosity and size of the H II regions. In turn, this would result in a flatter slope for the luminosity function.

Valdez-Gutiérrez et al. (2002) obtained the slope $\alpha = (-1.93 \pm 0.02)$, using a sample of 101 H II regions in NGC 4449, obtained with the *PUMA* Fabry-Perot, which has a pixel size of $0''.58\text{px}^{-1}$. Fuentes-Masip et al. (2000a) obtained (with a spatial-scale of $0''.26\text{px}^{-1}$) a slope $\alpha = -1.9$, using a sample of 44 H II regions located in the central $80'' \times 80''$ field of the galaxy. The discrepancy with our slope value may be caused by the difference in samples of H II regions, as the number of detected emission regions and their location varies greatly between their studies and ours. Using only H II regions from the central part of the galaxy might bias the slope, as discussed further down (Fig. 2.15).

However, using data from the *Hubble Space Telescope*, resulting in a spatial-scale of $0''.05\text{px}^{-1}$ (0.93 pc px^{-1}), Gutiérrez et al. (2011) detected 273 H II regions. Gutiérrez et al. (2011) obtained a slope of $\alpha = -1.43$, which is more negative than the slope obtained in our study. The fit done by Gutiérrez et al. (2011) ranges from $\log(L) = 37.0$ to $\log(L) = 38.5$, which excludes the brightest bin ($\log(L_{\max}) = 38.85$). The second most luminous H II region in this catalogue corresponds to region 175 (which is shown in Figure 2.4) and has a $\text{H}\alpha$ luminosity $\log(L) = (38.83 \pm 0.03)$, which corresponds to the highest luminosity bin of Gutiérrez et al. (2011). Their fit starts at a lower luminosity than the one in our study, because they

are able to resolve and disentangle smaller H II regions, shifting the start of the monotonically decreasing part of the distribution to lower luminosities. This probably explains their steeper slope compared to ours. However, the argument that the slope obtained in our study is considerably less negative than the previous ones (Fuentes-Masip et al. 2000a; Kennicutt et al. 1989; Valdez-Gutiérrez et al. 2002) due to resolving the smaller H II regions and disentangling the complexes better because of the higher spatial resolution and improved detection methodology does not hold with Gutiérrez et al. (2011), as their spatial resolution greatly superior to the data used in this study.

Globally, the gain in the number of emission regions detected and the accuracy of their detection is attributed to the automatic method developed by Savard et al. (in prep.). It enables a rigorous and unbiased detection of the emission regions, compared to the visual analysis technique. Therefore, the different slope value obtained in our study may be assigned to the novel methodology used to detect emission regions.

Our estimate for the total H α luminosity of all the emission regions is $(2.197 \pm 0.005) \times 10^{40}$ erg s $^{-1}$, whilst our total H α luminosity of NGC 4449 is $(4.3 \pm 0.2) \times 10^{40}$ erg s $^{-1}$. The total flux of the galaxy is obtained by fitting the binned spectrum, from all the pixels in the galaxy. The Galactic extinction correction is applied to the total flux of the galaxy, as it is done by Kennicutt et al. (1989). This means that $(50 \pm 5)\%$ of the H α luminosity in NGC 4449 comes from the H II regions. This is lower than expected for an irregular galaxy (Kennicutt et al. 1989). Similar results for NGC 4449 are obtained by Kennicutt et al. (1989), where the H II region's H α luminosity is 2.2×10^{40} erg s $^{-1}$ and the total H α luminosity of the galaxy is 4.5×10^{40} erg s $^{-1}$, resulting in an H II region H α luminosity proportion of 48 %. The percentage obtained in our study includes the value of Kennicutt et al. (1989) in its confidence interval. Also, the total luminosity of the H II regions measured in this study contains the value of Kennicutt et al. (1989) in its confidence interval. This confirms that the detected emission regions from our study are, in nature, similar to the ones detected by Kennicutt et al. (1989), but the higher spatial resolution allows to disentangle them more, resulting in lower luminosities for each H II regions. The difference in the percentage comes from the difference in the total luminosity of the galaxy.

Valdez-Gutiérrez et al. (2002) detected 101 regions, which results in a total H α luminosity from H II regions of 2.54×10^{40} erg s $^{-1}$. The total H α luminosity of the galaxy value used in their study is 6.6×10^{40} erg s $^{-1}$ from Hunter et al. (1999), resulting in 38 % of the H α luminosity coming from the H II regions.

With their sample of 273 H II regions, Gutiérrez et al. (2011) obtained a total H α luminosity from H II regions of 1.45×10^{40} erg s $^{-1}$. This value is considerably lower than the one from Kennicutt et al. (1989), Valdez-Gutiérrez et al. (2002), and our study due to the fact that the H II regions are better resolved. The total luminosity of NGC 4449 used by Gutiérrez et al.

(2011) is $3.15 \times 10^{40} \text{ erg s}^{-1}$, which results in a luminosity coming from the H II regions of 46 %. This value is included in the confidence interval of the value obtained in this study, even though the total luminosity of the H II regions and the galaxy is not.

Disregarding differences between our method and the work of Kennicutt et al. (1989) and Valdez-Gutiérrez et al. (2002) and Gutiérrez et al. (2011), the values for the percentage of luminosity originating from the emission regions are in close agreement confirming the unusual discrepancy in the fraction of the H II region's luminosity over the total luminosity for an irregular galaxy. If the H II region population of NGC 4449 is normal, this confirms that NGC 4449 contains an abnormal amount of DIG emission relative to star forming regions compared to other galaxies of different morphological types, as suggested by Kennicutt et al. (1989). However, Zurita et al. (2004) found that for mid-type spirals (Sb-Sc) galaxies, half of the H α emission originates from the H II regions and the other half from the DIG emission (Gutiérrez et al. 2011), which would be consistent with the results obtained in this study and the previous ones.

To estimate the impact of the incompleteness of the H II regions detection on the total H α luminosity attributed to the H II regions, the sum of the H α luminosity of all low luminosity H II regions ($<1 \times 10^{37} \text{ erg s}^{-1}$, as used in Kennicutt et al. 1989) is compared to the total H α luminosity of all H II regions. A value of $(3.717 \pm 0.006)\%$ is found, which is consistent with others result for late-type galaxies. In Kennicutt et al. (1989), it was found that the proportion of luminosity coming from the faint H II regions in late-type galaxies is about 5–10 %. When using the luminosity limit determined in Section 2.6.5, the sum of the H α luminosity of all low luminosity H II regions ($<4 \times 10^{36} \text{ erg s}^{-1}$), corresponds to $(0.891 \pm 0.009)\%$ of the total H α luminosity of all H II regions.

The discrepancies between the values obtained by this study and the comparable study of Gutiérrez et al. (2011) for the number of detected H II regions, the luminosity function slope, and the total H α luminosity of the H II regions are interesting. The higher number of emission regions detected in our study might be the cause of the flatter slope, as the emission regions are more divided into lower luminosity regions and DIG regions are also included. However, the higher spatial resolution of the data used by Gutiérrez et al. (2011) results in a more accurate estimation of the number of H II regions actually contained in NGC 4449. A slight difference may be expected due to the field of view of the data used in our study, which covers the entire optical body of the galaxy and its outskirts, yet a $\sim 50\%$ increase in the number of H II regions may not be caused by this effect. Nevertheless, even though the total luminosity for the H II regions and the galaxy measured in our study are quite different from the values obtained by Gutiérrez et al. (2011), the ratio between the two values is not too far off. Thus, the small discrepancy could be explained by the fact that our catalogue also includes DIG regions.

The total SFR of the galaxy is calculated using the total H α luminosity from the galaxy, as described by Kennicutt (1998). A total SFR value of $(0.34 \pm 0.02) M_{\odot} \text{ yr}^{-1}$ is obtained, which is lower than the value from Hunter et al. (1999), $0.47 M_{\odot} \text{ yr}^{-1}$, also derived from the H α luminosity. Karczewski et al. (2013) obtained an average SFR of $0.28 M_{\odot} \text{ yr}^{-1}$ and $0.42 M_{\odot} \text{ yr}^{-1}$, assuming a stellar initial mass function from Kroupa and Salpeter, respectively. On the other hand, Hill et al. (1998) obtained a higher SFR value of $0.51 M_{\odot} \text{ yr}^{-1}$. Using *GALEX Ultraviolet Imaging Survey* far-UV data, Lee et al. (2009) obtained $0.94 M_{\odot} \text{ yr}^{-1}$ (corrected for dust attenuation), and Lee et al. (2011) obtained $0.453 M_{\odot} \text{ yr}^{-1}$. Hunter & Gallagher (1986) obtained a SFR of $0.7 M_{\odot} \text{ yr}^{-1}$ using the H α luminosity with a Salpeter initial mass function. Hunter & Gallagher (1986) also obtained a similar value using the infrared luminosity, indicating that the infrared-emitting dust is also heated by the emission of the new OB stars and that the dust is not significantly heated by the older star population (Thronson et al. 1987). Thronson et al. (1987) obtained a SFR of $1.5 M_{\odot} \text{ yr}^{-1}$, using far-infrared luminosity, which is also not in agreement with the value obtained in this study. In general, the SFR derived in our study tends to be lower than the value obtained from previous studies, however differences are expected when comparing SFR from other spectral domaines.

The extinction correction calculated in Section 2.6.8 has a considerable impact on the absolute value of the H α flux. Figure 2.14 displays a comparison of the luminosity function on the H α luminosity of the H II regions without the extinction correction (pink distribution) compared to the extinction corrected H α luminosity (blue distribution). The extinction corrected H α luminosity distribution is the same as the one displayed in Figure 2.13, but is shown again in Figure 2.14 to help the comparison. The slope obtained from the luminous end of the uncorrected distribution (pink line) is -1.15 ± 0.09 (based on 198 regions), whilst the slope of the linear fit obtained with the corrected distribution (blue line) is -1.08 ± 0.07 (based on 179 regions). The maximum luminosity value of the uncorrected distribution is $\log(L_{\max}) = 39.165 \pm 0.006$ and $\log(L_{\max}) = 39.30 \pm 0.03$ for the corrected distribution.

The luminosity of the emission regions is studied based on their location within the galaxy in order to investigate differences due to galactic structures or the star formation history. The two most striking morphological features in NGC 4449 are the central bar and the northern arm. The regions included in each morphological category are presented in Figure D.1. The boundaries of the morphological features are arbitrarily selected, while including enough emission regions to allow for a statistical study of the differences between the populations. 126 emission regions are contained in the central bar and 190 are contained in the northern arm. The difference in luminosity of the H II regions located in the central bar and the northern arm is first studied with by comparing their luminosity functions. Figure 2.15 shows the luminosity function for the central bar (orange) and for the northern arm (teal) distributions, with their corresponding median luminosity plus 0.2 and ends at the maximal luminosity value. The central bar has a slope -1.1 ± 0.4 (based on 63 regions) and the northern arm has a slope of

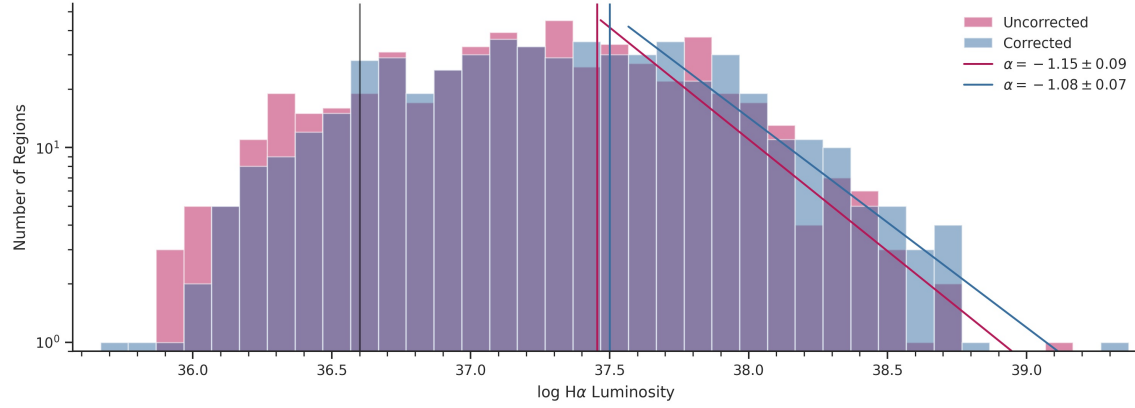


Figure 2.14 – $H\alpha$ luminosity function of all the emission regions detected in NGC 4449, uncorrected (pink) and corrected (blue) for the extinction. The median value (pink vertical line) for the uncorrected distribution is $\log(L_{1/2}) + 0.2 = (37.455 \pm 0.005) + 0.2$ and $\log(L_{1/2}) + 0.2 = (37.50 \pm 0.04) + 0.2$ for the corrected distribution (blue vertical line). The maximum luminosity value of the uncorrected distribution is $\log(L_{\max}) = 39.165 \pm 0.006$ and $\log(L_{\max}) = 39.30 \pm 0.03$ for the corrected distribution. The slope of the linear fit obtained from the luminous end of the uncorrected distribution (pink line) is $\alpha = -1.15 \pm 0.09$. The slope of the linear fit obtained from the luminous end of the corrected distribution (blue line) is $\alpha = -1.08 \pm 0.07$. 198 regions are used to fit the uncorrected distribution, whilst 179 are used for the corrected fit. The grey vertical line corresponds to the completeness limit (as described in Section 2.6.5), located at $\log L_{H\alpha} = 36.6 \pm 0.3$.

-0.8 ± 0.1 (based on 95 regions).

A Kolmogorov–Smirnov test is conducted to determine if the $H\alpha$ luminosity of the populations of the H II regions located within the central bar are statistically different from the one in the northern arm. Using a significance level of 0.05, the obtained p-value of 2.52×10^{-5} confirms that the luminosity of the regions in the central bar are statistically different to those in the northern arm. The different slopes of the two populations could indicate differences in the mechanism for the gas compression, the initial mass function of the massive stars, total mass of the young stellar clusters, or different global time-scales of the star formation process. The central bar contains more of the bright H II regions than in the northern arm, which contains more of the faint H II regions.

Giant extragalactic H II regions (GEHRs) are defined as H II regions with an average $H\alpha$ luminosity of the order of 1×10^{39} erg s $^{-1}$, a diameter greater than 100 pc, an ionized gas mass between $1 \times 10^4 M_\odot$ and $1 \times 10^5 M_\odot$, an average density of 1×10^{10} cm $^{-3}$, and a population of 100 to 200 ionizing stars (Fuentes-Masip et al. 2000a; Kennicutt 1984; Kennicutt 1988). However, this study was conducted on only six irregular galaxies (including NGC 4449), which does not result in a statistically robust sample. Kennicutt et al. (1989) suggested that irregular galaxies contain more GEHRs than earlier-type galaxies. Irregular galaxies have thicker discs that produce less sheer, which would permit clouds to build-up their mass (Larson 1983),

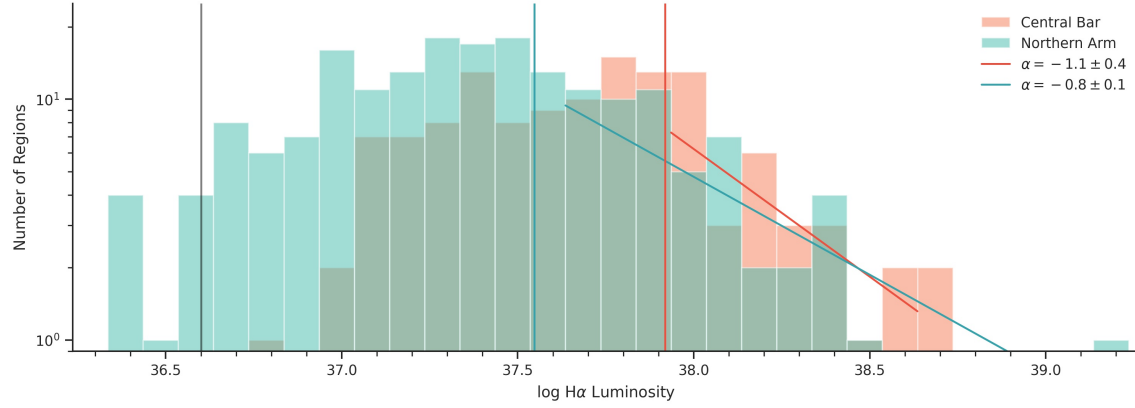


Figure 2.15 – $\text{H}\alpha$ luminosity function of the two main morphological features of NGC 4449. The orange distribution corresponds to the regions in the central bar and the teal are the regions in the northern arm. The vertical lines correspond to the median value plus 0.2, which is where the fit starts. The central bar’s fit (orange line) begins at $\log(L_{1/2}) + 0.2 = (37.72 \pm 0.03) + 0.2$ (orange vertical line) and stops at $\log(L_{\max}) = 38.70 \pm 0.01$, whilst the northern arm’s fit (teal line) begins at $\log(L_{1/2}) + 0.2 = (37.347 \pm 0.004) + 0.2$ (teal vertical line) and stops at $\log(L_{\max}) = 39.165 \pm 0.006$. The slope $\alpha = -1.1 \pm 0.4$ is obtained for the central bar and a slope $\alpha = -0.8 \pm 0.1$ is obtained for the northern arm. The grey vertical line corresponds to the completeness limit (as described in Section 2.6.5), located at $\log L_{H\alpha} = 36.6 \pm 0.3$.

and consequently, more massive H II regions could emerge from such clouds (Larson 1983). Nevertheless, Youngblood & Hunter (1999) instead conclude that GEHRs are more rare in Im galaxies than Sc. Their study uses 29 nearby non-interacting Im-type galaxies (excluding NGC 4449), resulting in a more representative sample.

In this study, only one H II region has a luminosity greater than $1 \times 10^{39} \text{ erg s}^{-1}$, which corresponds to region 527. The region can be seen in the centre of the top left panel of Figure 2.4 (and in Figure D.2). It corresponds to the brightest H II region of the catalogue produced in this study, with a luminosity of $(2.0 \pm 0.1) \times 10^{39} \text{ erg s}^{-1}$. However, its diameter is $(67.5 \pm 0.9) \text{ pc}$, which does not fit into the definition of a GEHR. It is also observed that GEHRs have supersonic velocity dispersion ($\sigma_v \geq 12.85 \text{ km s}^{-1}$), compared to smaller H II regions (Fuentes-Masip et al. 2000b; Smith & Weedman 1970, 1971). Region 527 has a velocity dispersion of $(19.1 \pm 0.2) \text{ km s}^{-1}$.

2.7.2 Morphology

A major caveat in the method used to measure the morphology of the emission regions is that the 2D Gaussian fit (described in Section 2.6.2) is assumed to properly fit all the regions. At the distance of NGC 4449, it is not clear that a perfect sphere represents well most H II regions. The radius of the regions is defined as three times the standard deviation of the 2D Gaussian fit in both axes, and the eccentricity is derived from it. This definition does not take into account the intersection between the zone of influence and the 2D Gaussian spatial fit,

which is done to constrain the emission region's domain and avoid shared pixels. The flux of the emission region is obtained from the intersection of these spatial restrictions. However, the region's morphology is only defined by the 2D Gaussian fit. This results in the radius of regions being bigger than the actual dimensions used to define the region. Thus, the regions with the biggest radius are not necessarily the ones containing the most pixels. This problem particularly affects the regions that have not been properly fitted by the 2D Gaussian (*e.g.* due to the lack of pixels for the fit or that the flux distribution is not measured well by a 2D Gaussian model). Other methods to calculate the morphological features could be used to avoid this issue, *e.g.* using the number of pixels in the intersection of the zone of influence and the 2D Gaussian spatial fit as the area and projecting it on a circle to estimate a radius, or using the Chebyshev norm. In all cases, the 2D morphological information is lost. Using the number of pixels as a measurement of the area also suffers from fundamental issues. The zone of influence accretes pixels that are not associated to other regions until it reaches a maximal radius of 50 pc. Thus, regions that are not properly fitted by the 2D Gaussian model and are fairly isolated will contain a lot of pixels, compared the regions in crowded are, where their zone of influence was assigned only a few pixels.

Another major caveat in the size measurement of the H II regions in NGC 4449 is the ubiquitous presence of DIG in the galaxy. The strong DIG emission surrounding the H II regions underestimates their size, as the measured luminosity profile does not decrease as far as the real luminosity profile due to the high underlying DIG emission which raises the baseline. Thus, only the bright central part of the H II region can be seen and is considered in the luminosity profile fitting (Fuentes-Masip et al. 2000a; Munoz-Tunon et al. 1998). To overcome this issue, Fuentes-Masip et al. (2000a) and Valdez-Gutiérrez et al. (2002) subtract the DIG background prior to measuring the sizes. However, this is not done in this study.

The size distribution of H II regions has long been studied in irregular galaxies (Hodge 1983; Hodge et al. 1994a, 1989a; Hodge & Lee 1990; Hodge et al. 1989b, 1994b; Miller & Hodge 1994; Strobel et al. 1991; Youngblood & Hunter 1999). Size functions of H II regions are typically represented by an exponential function:

$$N(D) dD = N_0 e^{-D/D_0} dD, \quad (2.6)$$

where $N(D) dD$ represents the number of H II regions with sizes between D and $D + dD$ and D_0 corresponds to the characteristic diameter (van den Bergh 1981; Hodge 1983; Hodge 1987). Although theoretically, an exponential distribution is expected, observationally the distribution is better described by a Gamma distribution. Because small H II regions cannot be detected, due to the limitation from the sampling and the seeing, a monotonically decreasing distribution, like the exponential, cannot properly represent the observed distribution. The distance between the H II regions and their relative intensities with the neighbouring H II regions also cause difficulties in their detections. To better model the undersampled region of

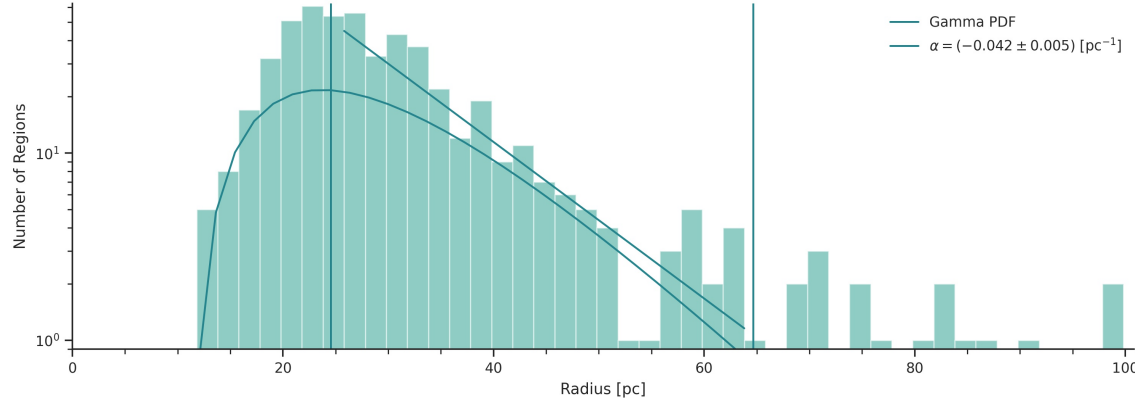


Figure 2.16 – Size distribution of all the H II regions detected in NGC 4449. The full teal curve corresponds to the probability density function of the Gamma fit of the distribution with the fitting parameters: shape = 2.88, loc = 11.07, scale = 6.71. The teal line corresponds to the exponential fit converging with $\alpha = (-0.042 \pm 0.005) \text{ pc}^{-1}$ for the decreasing part of the distribution with, ranging between the two vertical teal lines, corresponding to $(24.5 \pm 0.5) \text{ pc}$ and $(65 \pm 2) \text{ pc}$. The error of the slope parameter corresponds to the standard deviation.

the small-sized H II regions, the generalisation of the exponential distribution (*i.e.* the Gamma distribution) is used.

To allow comparison of the typical slope fitted with an exponential function, the fit of the Gamma distribution is used to obtain the range of the monotonically decreasing part of the size distribution. The range fitted by the exponential function starts at the maximum of Gamma fit and ends at 3σ of the Gamma distribution. The Gamma distribution is fitted using the `scipy` method as well as the linear regression used to fit the exponential distribution (Virtanen et al. 2020).

Figure 2.16 shows the size distribution of the H II regions detected in this study. The size of the H II regions corresponds to the radius, measured using the geometrical mean of 3σ of the 2D spatial Gaussian fits (Section 2.6.2) in the x and y axis. H II regions with a radius superior to 100 pc are removed from the plot for clarity, as they turn out to be outliers (weak and poorly fitted regions), leaving 525 emission regions. A slope value of $\alpha = (-0.042 \pm 0.005) \text{ pc}^{-1}$ and a characteristic diameter of $2''.6 \pm 0''.3$ are obtained.

Rousseau-Nepton et al. (2018) obtained a slope for the size distribution of $\alpha = (-0.016 \pm 0.001) \text{ pc}^{-1}$ for NGC 628, a spiral (SA(s)c) galaxy at 9 Mpc (NED), which results in a characteristic diameter of $6''.7 \pm 0''.4$. The slope value obtained for NGC 4449 is larger than the one obtained for NGC 628 by Rousseau-Nepton et al. (2018), but the characteristic diameter of NGC 4449 is smaller than the one of NGC 628. Sabbadin & Bianchini (1979) have also compared the size distribution for NGC 4449 and NGC 628, showing slopes consistent with the ones obtained in this study and by Rousseau-Nepton et al. (2018). As mentioned in Rousseau-Nepton et al. (2018), the significance of this slope is unclear. van den Bergh (1981)

proposed that the size distribution could represent a universal law for all galaxy types. van den Bergh (1981) indicated that the two biggest H II regions in NGC 4449 are larger than the size predicted by Equation 2.6. As shown in Figure 2.16, there are 26 H II regions detected in this study that are larger than (65 ± 2) pc (including the H II regions with a radius superior to 100 pc not shown in Figure 2.16), which is where the fit ends and thus is considered larger than the predicted distribution.

The radius values of the emission regions in our study range from (12 ± 5) pc (region 528) to (99 ± 2) pc (region 408), when emission regions with a radius superior to 100 pc are not considered. The H II regions catalogue of NGC 4449 realised by Valdez-Gutiérrez et al. (2002) has H II regions with radii ranging from 19.4 pc to 92.2 pc whilst the regions of Fuentes-Masip et al. (2000a) have radii from ~ 13 pc to more than 100 pc for the nucleus of the galaxy. Sabbadin & Bianchini (1979) have radii from ~ 12 pc to ~ 50 pc for their catalogue of 252 H II regions. All these studies have comparable radius values to the ones presented in this catalogue, except the upper limit of Sabbadin & Bianchini (1979), which is smaller than the ones obtained by Fuentes-Masip et al. (2000a) and Valdez-Gutiérrez et al. (2002) and our study.

The mean radius value obtained in our study is (33 ± 2) pc. The mean radius value obtained by Valdez-Gutiérrez et al. (2002) and Fuentes-Masip et al. (2000a) are (44.6 ± 15.8) pc and 65 pc, respectively. Sabbadin & Bianchini (1979) found the mean radius to be near 25–30 pc. Hunter (1982) found a mean radius of 45 pc for NGC 4449. The mean radius of the emission regions detected in our study is comparable to the value obtained by Valdez-Gutiérrez et al. (2002), within uncertainties and close to the one obtained by Sabbadin & Bianchini (1979). The study of Fuentes-Masip et al. (2000a) only considers 44 H II regions in the central region of NGC 4449, thus their statistics might be less reliable and biased by the galactic feature in which the H II regions are located. The same phenomenon explains the discrepancy with the value of Hunter (1982), which had a catalogue of only 46 H II regions. Obtaining a lower mean radius is expected, since the data used in this study has a better angular resolution and may also include DIG regions. However, the sizes obtained by Valdez-Gutiérrez et al. (2002) and Fuentes-Masip et al. (2000a) are expected to be greater than the ones obtained in this study, as they have removed the DIG background in order to more precisely measure the H II regions' sizes. The strong DIG emission is known to underestimate the dimensions (Fuentes-Masip et al. 2000a; Muñoz-Tunón et al. 1998; Valdez-Gutiérrez et al. 2002). Thus, it is consistent to obtain a value similar to Sabbadin & Bianchini (1979), which did not remove the DIG background.

The characteristic radius obtained in our study is (27 ± 2) pc. Valdez-Gutiérrez et al. (2002) found a characteristic radius of (15 ± 1) pc. To compare with other studies, the characteristic diameter is computed, resulting in a value of $2''.6 \pm 0''.3$. Valdez-Gutiérrez et al. (2002) obtained a characteristic diameter of $1''.73 \pm 0''.1$, and of $1''.6$ by Fuentes-Masip et al. (2000a). Larger values are obtained by van den Bergh (1981) ($3''.2$), Sabbadin & Bianchini (1979) ($6''.2$), and

Hodge (1983) ($5''$). Valdez-Gutiérrez et al. (2002) explained the discrepancies between the two groups of values by the fact that they (and Fuentes-Masip et al. 2000a) subtracted the DIG from the galaxy before detecting and measuring the H II regions. It is consistent that the underlying DIG emission would make the H II regions appear bigger. This DIG correction applied by Valdez-Gutiérrez et al. (2002) and Fuentes-Masip et al. (2000a) explains their smaller characteristic diameter value. As the DIG is not subtracted from the galaxy in our study, it is expected that the characteristic diameter has sizes similar to the values of the second (*i.e.* the studies of van den Bergh 1981; Hodge 1983; Sabbadin & Bianchini 1979). It is also important to note that the studies from Hodge (1983) and Sabbadin & Bianchini (1979) contain H II regions from the entire galaxy, unlike the study from Fuentes-Masip et al. (2000a). The size distribution might vary based on their location within the galaxy. Furthermore, the size of the measured emission regions is also affected by the spatial sampling and the seeing, thus an accurate comparison is challenging.

In order to study possible differences in the H II region population characteristics depending on their location in the most obvious morphological structures of the galaxy, we first compared position and size of the regions as shown on Figure 2.17. The two main structures of interest are specifically the central bar and the northern arm of the galaxy. Therefore, regions included in each of the morphological structures were defined as shown in Figure D.1. Again here, the H II regions with a radius superior to 100 pc are excluded from the size analysis, leaving 123 H II regions in the central bar and 187 H II regions in the northern arm. A size function is produced for both sets on Figure 2.17, where the orange distribution and fit curve correspond to the central bar population and the teal distribution and fit curve correspond to the northern arm distribution.

The characteristic radii estimated for the central bar and the northern arm population are (77 ± 10) pc and (34 ± 3) pc, respectively. These correspond to characteristic diameters of $4''7 \pm 0''5$ and $2''8 \pm 0''3$, respectively. A mean radius in the central bar of (37 ± 3) pc and (31 ± 2) pc for the northern arm are obtained. The mean radius obtained by Fuentes-Masip et al. (2000a), of 65 pc, is closer to the mean radius of the central bar population than the northern arm population, which may be due to the fact that their study only included 44 H II regions located in the central part of the galaxy.

A Kolmogorov–Smirnov test is conducted to determine if the populations of the H II regions located in the northern arm and central bar are statistically different in size. Using a significance level of 0.05, the obtained p-value (0.44) cannot reject the hypothesis that the two morphological regions have the same size distributions for their H II regions.

Comparing slopes of size distributions is complex as the parameters are strongly dependant on the definition used of the size characterisation. Visual estimate of sizes is less reliable than the values obtained using isophotal measurements (Fuentes-Masip et al. 2000b). Yet, these

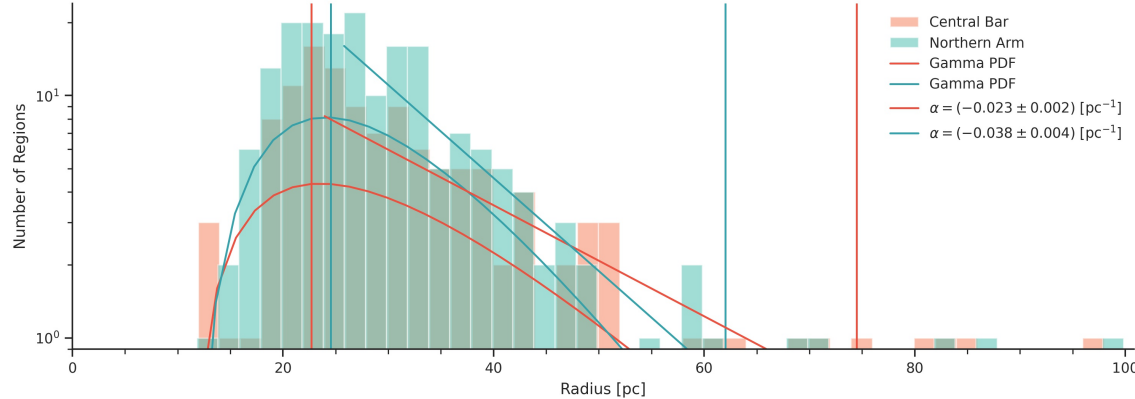


Figure 2.17 – Size distribution of the H II regions located in the central bar (orange) and of the northern arm (teal) of NGC 4449. The H II regions associated with each of these galactic structures are shown on Figure D.1. The full orange and teal curves correspond to the probability density function of the Gamma fit for the distribution of the H II regions in the central bar and the northern arm with fitting parameters: shape = 2.40, loc = 10.87, scale = 9.01 and shape = 3.19, loc = 10.99, scale = 5.97, respectively. The corresponding lines show the exponential fit of the decreasing part of the distribution of the H II regions with $\alpha = (-0.023 \pm 0.002) \text{ pc}^{-1}$ and of $\alpha = (-0.038 \pm 0.004) \text{ pc}^{-1}$, respectively. The range for the fit is indicated by the vertical lines of the associated colour, from $(22.7 \pm 0.6) \text{ pc}$ to $(74 \pm 2) \text{ pc}$ and from $(24.5 \pm 0.5) \text{ pc}$ to $(62 \pm 2) \text{ pc}$, respectively.

methods are not as well constrained as the technique used in this study with the 2D Gaussian profile fitting. Even though H II regions are modelled as spheres, they are not always observed as such (as seen in Figure 2.4).

Figure 2.18 shows the spatial distribution of the H II regions, colour coded by their radius. There appears to be no strong correlation between the spatial location of the emission region and its radius.

The area of the emission regions is defined as the number of pixels included in both the intersection of the zone of influence (as described in Section 2.6.1) and the 3σ limit of their 2D Gaussian spatial fit (as described in Section 2.6.2), multiplied by the area covered by a pixel. This definition allows to account for peculiar morphology of the emission regions. For NGC 4449, the sampling for the SITELLE instrument is 5.9 pc px^{-1} , resulting in an area per pixel of $35.6 \text{ pc}^2 \text{ px}^{-1}$. The average area of the emission regions is 4318 pc^2 (which is equivalent to an average number of 121 px). It must be noted that the radius definition contains less information compared to initially 2D fitted axes, as it reduces the 2D information to a 1D value. One could investigate the distribution of the 2D parameters as a whole to avoid this simplification. A method of studying the relationship between the dimensions of both major and minor axes is by using the excentricity.

In order to study the variations in radius within an emission region, the eccentricity is calcu-

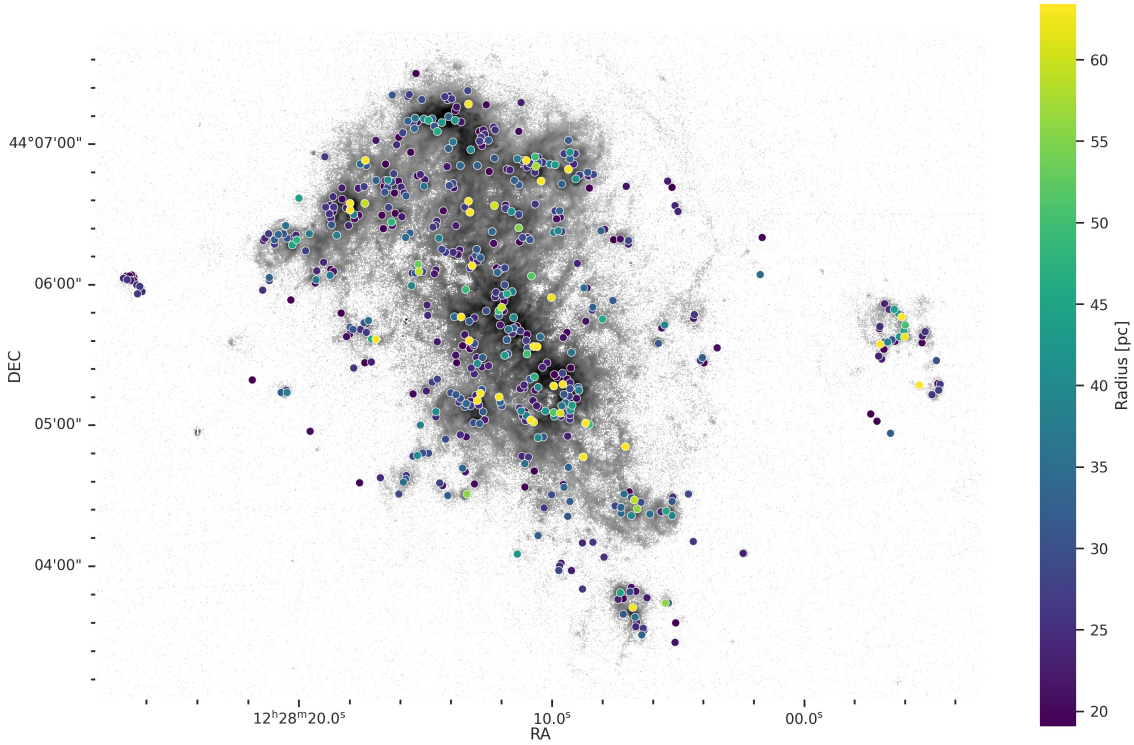


Figure 2.18 – Spatial distribution of the emission regions, colour coded by their radius. The regions are superimposed on the log H α flux map, where the pixels with a H α or H β S/N lower than 1 are not shown.

lated with the equation:

$$E = \frac{\sqrt{|\sigma_x^2 - \sigma_y^2|}}{\|(\sigma_x, \sigma_y)\|_{\infty}}, \quad (2.7)$$

where σ_x and σ_y are the standard deviation of the major and minor axes of the 2D Gaussian fit. An example for different eccentricity values is shown in Figure D.3. The blue contour shows the zone of influence and the pink contour shows the 2D Gaussian fit. It is possible to see ten examples of detected emission regions with different measured eccentricities. The emission regions with a higher eccentricity tend to be structures resembling more filaments than classical H II regions. Crowding, ISM inhomogeneity, shocks and instrumental effects can all contribute to the diversity of the morphologies observed in emission regions.

In this study, the detected emission regions with an eccentricity below 0.2 are considered circular; 41 regions are considered to be circular. The average eccentricity of the regions is 0.56 ± 0.08 , where the uncertainty corresponds to the standard error of the mean distribution. This eccentricity suggests that most regions do not always fall in the classical case of a sphere and that many of them irregularly expand in 3D space, due to crowding and higher gas density in their surrounding environment. The average eccentricity in the central bar is 0.62 ± 0.07 and 0.56 ± 0.08 in the northern arm, hinting at spatial differences between the two morphological

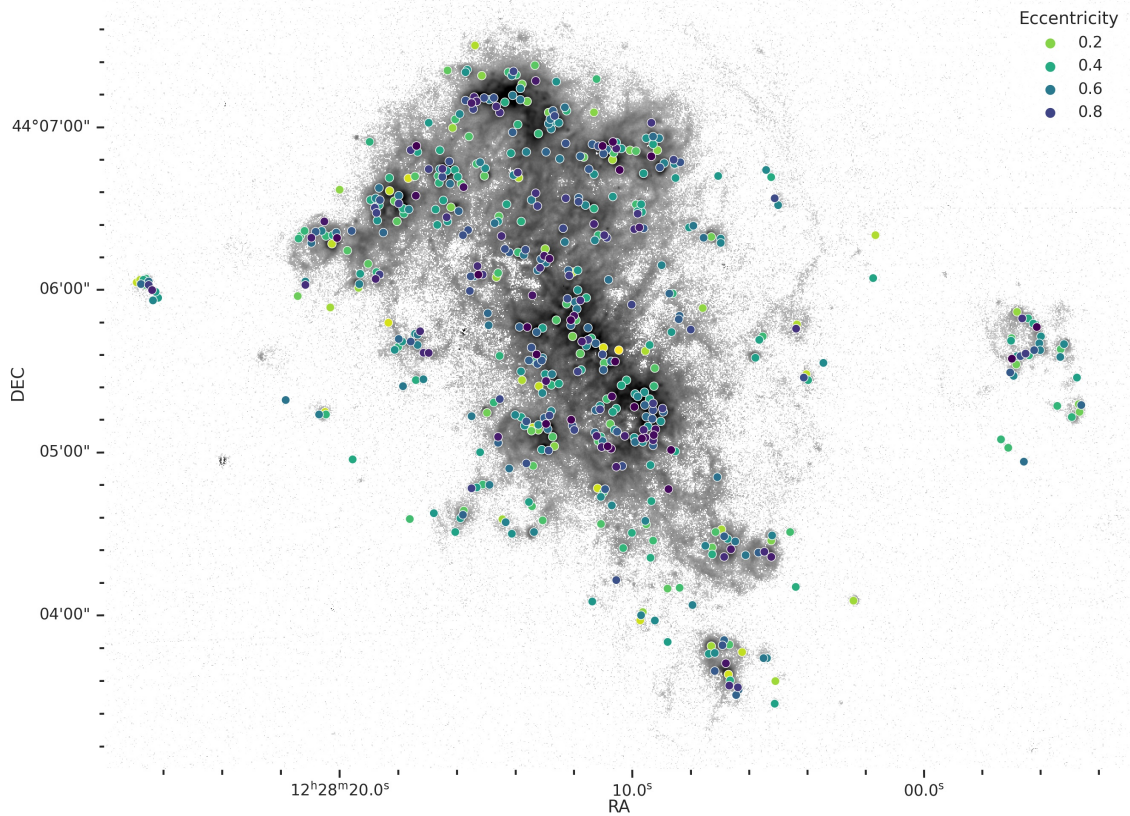


Figure 2.19 – Spatial distribution of the emission regions, colour coded by their eccentricity. The regions are superimposed on the log H α flux map, where the pixels with a H α or H β S/N lower than 1 are not shown.

features of the galaxy. Figure 2.19 shows the spatial distribution of the eccentricity of the emission regions. No clear correlation between the location in the galaxy of the emission region and its eccentricity can be observed. The regions in the central bar and the northern arm have the same average eccentricity as the average eccentricity for all the emission regions, thus no variation is observed for the large morphological features of the galaxy. However, the regions on the outskirts of the galaxy seem to have lower eccentricities, which is expected, as the regions are less crowded and less gas is present to perturb the morphology of the emission region. The ubiquity of the DIG in NGC 4449, more prominently visible in the outskirts of the galaxy (due to the lower density of H II regions), could suggest that more eccentric emission regions would be observed. Yet, this does not seem to be the case. Thus it appears that circular and compact H II regions and filament emission regions are uniformly distributed within the galaxy.

2.7.3 Luminosity – Size – Velocity Dispersion Correlation

The velocity dispersion of the H II regions in NGC 4449 has been studied in the past as well as its correlation to the luminosity and size of the emission region (*e.g.* Chávez et al. 2014;

Fuentes-Masip et al. 2000b; Gallagher & Hunter 1983; Hippelein 1986; Melnick 1977; Melnick et al. 1988, 1987; Roy et al. 1986; Rozas et al. 1998; Terlevich & Melnick 1981; Valdez-Gutiérrez et al. 2002; Zaragoza-Cardiel et al. 2015).

Figure 2.20 shows the distribution of the H α luminosity as a function of the radius of the emission region, colour coded by the velocity dispersion. The regions with a radius superior to 100 pc and a H α luminosity superior to 1×10^{39} erg s $^{-1}$ are removed, leaving 524 regions displayed in Figure 2.20. No obvious correlations between the H α luminosity, the radius, and the velocity dispersion are observed. As expected, the very faint H II regions detected are of smaller sizes, since their ionizing sources emit a smaller number and less energetic ionizing photons. Also, the large and faint regions could be affected by the detection of DIG filaments. A caveat in our methodology is that all the local maxima are detected and treated as independent emission regions. Consequently, possible diffuse emission regions with filaments containing multiple local maxima could be measured as different emission objects, resulting in the detection of small radii and low luminosity regions. An example of that effect may be seen on the bottom right panel in Figure 2.4, for region 123. Another caveat stems from the measurement of the velocity dispersion, which includes a component from the underlying DIG. As described in Section 2.6.3, the local background spectrum of each region is fitted and the flux values are then subtracted from the ones measured for the region. This methodology does not allow to correct for the emission line broadening induced by the background gas superimposed to the emission region. Thus, the velocity dispersion may be overestimated for some of the detected emission regions. However, since the DIG is suspected to originate mostly from the H II regions in NGC 4449 and lie spatially close, they are expected to have similar kinematics, thus it is unlikely that the impact on the velocity dispersion measurement is major.

Small faint regions tend to have a lower velocity dispersion. This is also expected for low mass H II regions which contain only one or a few B type stars, injecting less mechanical energy in the ISM than for their brighter counterpart. Also, small and faint regions might be associated to diffuse emission over a small area of the galaxy. As such, the gas' kinematic is more locally measured, thus measuring correlated components. Also, as blended emission from crowded regions is not separated, the velocity dispersion might be overestimated in dense areas, since the measurements include velocity components from multiple object. This is supported by Figure 2.34 (bottom panel), where the emission regions with the largest velocity dispersion are located in the central bar of the galaxy, where the crowding is very high.

As suggested by Rousseau-Nepton et al. (2018), a lack of extended-high luminosity emission regions might indicate a physical maximal size of their domain. Multiple mechanisms could explain this correlation between the H α luminosity and compactness of the H II regions, which are discussed into more details by Rousseau-Nepton et al. (2018).

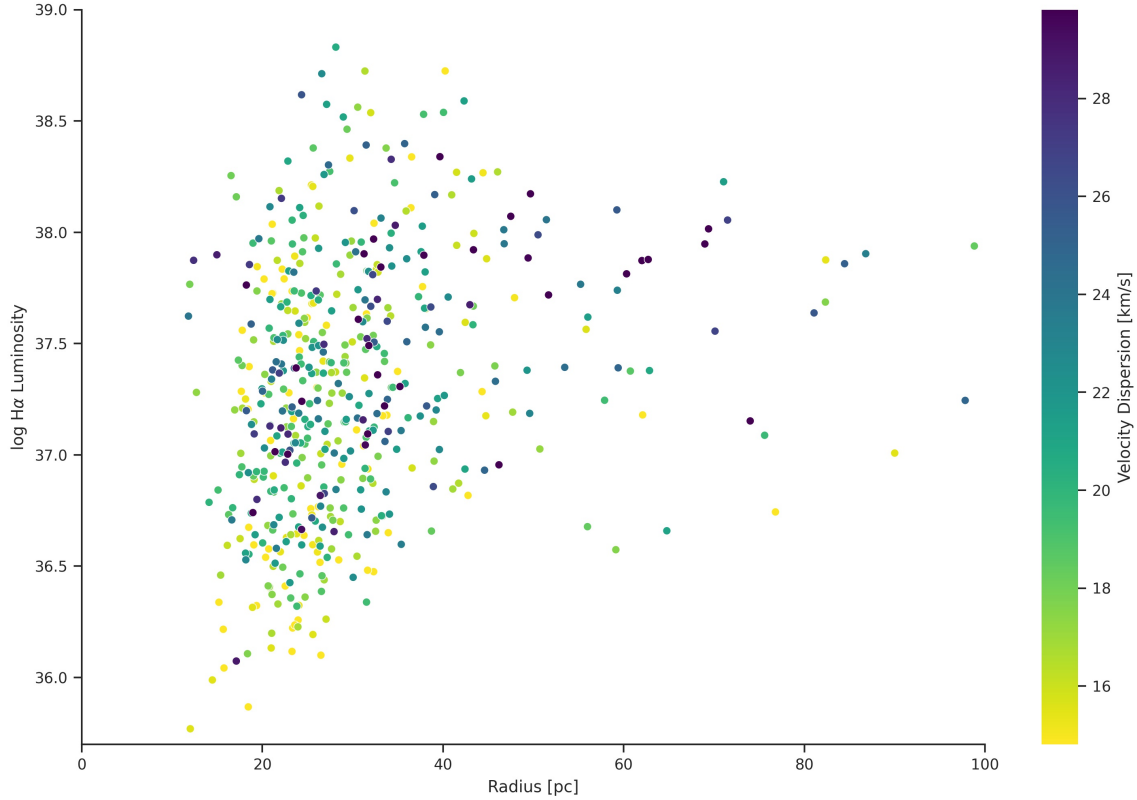


Figure 2.20 – Correlation between the H α luminosity of the emission regions with regard to their radius, colour coded by the velocity dispersion of the region. The regions with a radius superior to 100 pc and a H α luminosity superior to 1×10^{39} erg s $^{-1}$ are removed.

Arsenault & Roy (1988), Arsenault et al. (1990), Dyson (1979), Fuentes-Masip et al. (2000b), Hippelein (1986), Melnick (1979), Melnick et al. (1987), Roy et al. (1986), Rozas et al. (1998), Skillman & Balick (1984), Tenorio-Tagle et al. (1993), and Terlevich & Melnick (1981) have all studied the correlations between the size, luminosity, and velocity dispersion in H II regions. Amongst them, Fuentes-Masip et al. (2000b) note that the luminosity and size versus velocity dispersion relationship only holds for nebulae with a surface brightness superior to 2×10^{35} erg s $^{-1}$ pc $^{-2}$ and a supersonic ($\sigma \geq 12.85$ km s $^{-1}$; Smith & Weedman 1970) single component H α emission line. In our catalogue, only five emission regions have a H α surface brightness superior to this value (regions 175, 234, 238, 399, and 527), with their corresponding values displayed in Table 2.2. Their velocity dispersion is supersonic. The spatial location of these regions are shown in Figure D.4. As it can be seen in the right panel of Figure D.4, their high surface brightness is not caused by missed detections in crowded regions. No linear relationship is observed, like found by most of the past studies. Nevertheless, as mentioned by Rousseau-Nepton et al. (2018), this relationship may be better described by the equation of the Strömgren model (Strömgren 1939).

In order to study the variations between the morphological structures in the galaxy, the

Table 2.2 – Detected emission regions with a H α surface brightness greater than $2 \times 10^{35} \text{ erg s}^{-1} \text{ pc}^{-2}$.

ID	H α Surface Brightness [erg s $^{-1}$ pc $^{-2}$]	Velocity Dispersion [km s $^{-1}$]	Radius [pc]
175	(2.7 ± 0.2)	(20.6 ± 0.2)	(28.1 ± 0.4)
234	(2.2 ± 0.2)	(25.8 ± 0.3)	(24.3 ± 0.6)
238	(2.3 ± 0.3)	(22.7 ± 0.4)	(26.6 ± 0.6)
399	(2.1 ± 0.2)	(18.1 ± 0.2)	(16.6 ± 0.1)
527	(5.6 ± 0.4)	(19.1 ± 0.2)	(33.8 ± 0.4)

luminosity of the emission regions is compared to their size for the regions located in the central bar and the northern arm in Figure 2.21. Regions are colour coded by their velocity dispersion. No obvious pattern amongst the emission regions' luminosity, size, and velocity dispersion is observed in the two galaxy morphological structures studied. Nevertheless, some trends are present. For example, the central bar seems to contain more of the bright compact regions. The regions in the northern arm tend to be fainter and more extended than the ones in the central bar. The regions in the central bar with the highest velocity dispersion is region 310, with a velocity dispersion of $(40.7 \pm 0.8) \text{ km s}^{-1}$, whereas in the northern arm, the region with the highest velocity dispersion is region 451, with a velocity dispersion of $(35.8 \pm 0.3) \text{ km s}^{-1}$. The average velocity dispersion in the central bar is $(24.1 \pm 0.7) \text{ km s}^{-1}$, with a standard deviation of 5.6 km s^{-1} , whilst the average velocity dispersion in the northern arm is $(19.5 \pm 0.5) \text{ km s}^{-1}$, with a standard deviation of 3.9 km s^{-1} . It is consistent with the central bar being more crowded. It is also possibly due to a different star formation efficiency and history in the central bar. As previously mentioned, the velocity dispersion might be overestimated due to the crowding, which is more prevalent in the central bar. The central bar also contains a higher level of star formation compared to the northern arm, which will inject a lot of mechanical energy in the ISM.

For all emission regions, regardless of their location in the galaxy, the average velocity dispersion is $(20.4 \pm 0.7) \text{ km s}^{-1}$, with a standard deviation of 5.3 km s^{-1} . The velocity dispersion of the emission regions in the central bar thus has on average a higher velocity dispersion than the regions in the rest of the galaxy. More can be seen on the velocity dispersion variations due to the spatial location in Figure 2.34 (bottom panel) in Section 2.7.9.

2.7.4 Distance between Regions

The proximity between the emission regions is studied by measuring the distance between a region's peak and the peak of the closest neighbouring region. The median value in NGC 4449 of this proximity distance is $(42 \pm 3) \text{ pc}$. The median value for the second and third closest neighbouring emission region is $(67 \pm 3) \text{ pc}$ and $(95 \pm 3) \text{ pc}$ respectively. This proximity distance was also studied by Rousseau-Nepton et al. (2018) for 4285 emission regions of NGC 628. For

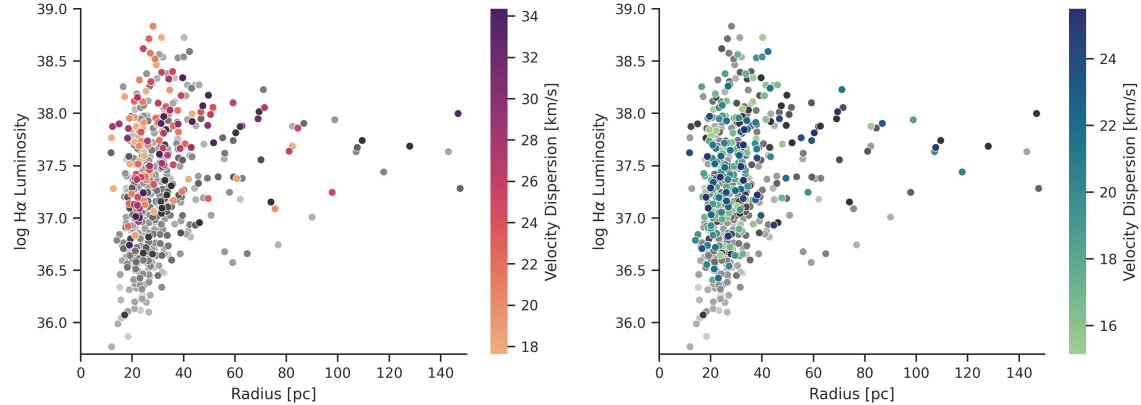


Figure 2.21 – Correlation between the luminosity of the emission regions with regard to their size, colour coded by the velocity dispersion of the region. In the left panel, the coloured regions correspond to the ones included in the central bar. In the right panel, the coloured regions correspond to the ones included in the northern arm. The regions in shades of grey represent the regions located elsewhere in the galaxy. The location of the regions included in each morphological category is shown in Figure D.1.

the regions in the inner part of the galaxy ($R_G < 6.5$ pc), the median value for the closest peak was found at 110.0 pc, the second-closest peak at 159.5 pc, and the third-closest peak at 198.6 pc. For regions in the outer part of the galaxy ($R_G > 6.5$ pc), the median value was found at 115.5 pc, the second-closest peak at 168.3 pc and the third-closest peak at 211.0 pc. Since NGC 628 is located at a distance of 9 Mpc (NED), resulting in a spatial resolution of 35 pc (Rousseau-Nepton et al. 2018), the emission regions have been resolved at a larger scale, which explains the discrepancy between the median proximity distance for NGC 628 compared to NGC 4449. Nevertheless, this discrepancy could be physical, since their galactic type is different (IB(s)m for NGC 4449 and SA(s)c for NGC 628).

Hunter (1982) measured a median distance between all the H II regions and their nearest neighbour of 170 pc for NGC 4449, which is considerably higher than the value obtained in our study. The average and standard deviation of the distance between all the emission regions to their nearest neighbour is 62 pc and 94 pc. Hunter (1982) obtained values of 180 pc and 85 pc, respectively. However, Hunter (1982) used a sample of 46 H II regions and had a spatial resolution of $0''.55\text{px}^{-1}$ (corresponding to $\sim 10 \text{ pc px}^{-1}$, with the assumed distance of NGC 4449 used in this study). Hence, it is expected that the distance between the nearest neighbours measured by Hunter (1982) is higher than the one in this study, as they likely detected the very bright H II regions' complexes, thus augmenting the distance between each complex. Due to their limited sample of only the very bright H II regions' complexes, their measures do not include the faint H II regions between the bright complexes. However, the proximity distance measured in this study may be overestimated as the catalogue contains DIG emission regions, thus the measured proximity distance is not only between H II regions.

The median proximity distance between the emission regions within the two galactic structures are (38 ± 3) pc and (42 ± 3) pc, in the central bar and the northern arm, respectively. To validate the statistical difference between the two morphologies, a Kolmogorov–Smirnov test is conducted. Using a significance level of 0.05, the obtained p-value of (0.0158) rejects the hypothesis that the two morphological structures have the same distribution of distances between closest neighbours. Although the median distances are not extremely different, it might still suggest a different stellar formation history or physical phenomenon that could lead to these differences, including the distribution of the molecular clouds and their structures.

The spatial variations in the proximity distance between the H II regions (either with regard to the galactocentric radius for the spiral galaxy or morphological features for the irregular galaxy) may suggest that large-scale phenomena might affect the location and efficiency of the star formation activity. Further studies on the proximity distance between H II regions and the relation with their environment is required to draw more conclusions.

However, it is possible to observe in the spatial distribution of the detected H II regions (see Figure 2.6 for the global distribution and Figure 2.4 for closer examples) that some H II regions are not all randomly distributed. Some appear to fall in lines or arcs, as observed by Hunter (1982). This local phenomenon could suggest that star formation may trigger neighbouring star formation (Hunter 1982).

A caveat of the tests conducted in this study is that detected emission regions are independent, regardless of their own morphology (symmetrical and asymmetrical bubble, expanding shell/rings or filaments), as described in Section 2.6.1. As regions showing expanding shell/rings or filaments are fundamentally correlated, they are expected to lie closer together with similar properties than distinct H II regions.

2.7.5 Global and Local Line Ratios

Maps of the line ratios are computed for the entire galaxy, to study the ionized gas properties on the global-scale and are displayed in Appendix E. Pixels with a low S/N (< 3) for the lines involved are excluded from these maps. The SN2 and SN3 lines have been corrected for the global stellar absorption (Section 2.6.7), whilst the $[\text{O II}]\lambda\lambda 3726,3729$ line has not been corrected. The extinction correction has been applied to all lines using the value obtained for each pixel. The left panels of the figures show the entire galaxy and the right panels show the four areas used as examples, to study how the line ratios vary withing the emission regions. The centroids of the emission regions are marked with a teal cross and their domain are delimited with a teal contour, for reference.

The $\text{H}\alpha/\text{H}\beta$ map is shown in Figure E.1. This line ratio is used to calibrate the internal extinction correction. Thus as expected, it is pretty constant throughout the galaxy after correction.

The $[\text{N II}]\lambda 6583/\text{H}\alpha$ map is shown in Figure E.2. This ratio is often used to separate H II regions from the DIG; it is higher in DIG regions, outside of the detected H II regions (Elwert & Dettmar 2005; Haffner et al. 1999). For example, region 123 (bottom right panel of the right panel of Fig. E.2) confirms the suspicion that this region (and the regions surrounding it) is likely a DIG filament. As observed by Rousseau-Nepton et al. (2018), the $[\text{N II}]\lambda 6583/\text{H}\alpha$ ratio can vary greatly within a 100 pc distance (about 17 pixels in this study).

The $[\text{S II}]\lambda\lambda 6716,6731/\text{H}\alpha$ map is shown in Figure E.3. Again, it is expected that the $[\text{S II}]\lambda\lambda 6716,6731/\text{H}\alpha$ ratio is higher in the DIG. Globally, the same trends as in Figure E.2 are observed. However, above region 420 (top right panel to the right of Fig. E.3), a region displays very high $[\text{S II}]\lambda\lambda 6716,6731/\text{H}\alpha$ ratio, whilst its $[\text{N II}]\lambda 6583/\text{H}\alpha$ ratio (Fig. E.2) is quite low. The local minima of $[\text{S II}]\lambda\lambda 6716,6731/\text{H}\alpha$ are strongly correlated with the detected peaks. This map could be used to identify supernovae remnants, to further investigate the various objects in NGC 4449. An attempt is made in Section 2.7.12.

The $[\text{S II}]\lambda\lambda 6716,6731/[\text{N II}]\lambda 6583$ map (Fig. E.4) illustrates slight variations within individual regions (right panel): it decreases in the centre of emission regions. As suggested by Levesque et al. (2010) and Rousseau-Nepton et al. (2018), with a higher spatial resolution, the ionization structure of the H II regions might be observable.

The $[\text{O III}]\lambda 5007/\text{H}\beta$ map is shown in Figure E.5, indicating a higher concentration in the centre of individual regions (right panel). Some detected emission regions show a very low $[\text{O III}]\lambda 5007/\text{H}\beta$ ratio. Others show a very high $[\text{O III}]\lambda 5007/\text{H}\beta$ ratio, but skewed from its centroid, *e.g.* region 175 (bottom left panel of the right panel of Fig. E.5). This map could be used to identify planetary nebulae, to further investigate the various objects in NGC 4449. An attempt is made in Section 2.7.12. On the other hand, the $[\text{O II}]\lambda\lambda 3726,3729/\text{H}\beta$ map (Fig. E.6) displays a correlation with the local minima and the centroids of the emission regions. The $([\text{O II}]\lambda\lambda 3726,3729 + [\text{O III}]\lambda 5007)/\text{H}\beta$ map is shown in Figure E.7. It appears to vary a great extent in the spatial dimension, like some of the other line ratios. Yet, the centroids of the detected regions do not coincide as well as some of the other lines with the local minima of this ratio.

The $[\text{O III}]\lambda 5007/[\text{O II}]\lambda\lambda 3726,3729$ map is shown in Figure E.8, estimating the amount of gas in each ionization state. Contrarily to most of the studied line ratios (except the $[\text{O III}]\lambda 5007/\text{H}\beta$ ratio), the centroids of the emission regions correlate with the local maxima of this line ratio. The morphology of the intense $[\text{O III}]\lambda 5007/[\text{O II}]\lambda\lambda 3726,3729$ regions is not circular in all cases and does not necessarily follow the morphology of the region defined with the $\text{H}\alpha$ emission (teal contours).

The $[\text{O III}]\lambda 5007/[\text{N II}]\lambda 6583$ map (Fig. E.9) follows a similar distribution as the $[\text{O III}]\lambda 5007/[\text{O II}]\lambda\lambda 3726,3729$ ratio (*i.e.* the local maxima coincide with the centroids of the detected emission regions), but fewer local maxima are globally observed. The

$[\text{O II}]\lambda\lambda 3726,3729/[\text{N II}]\lambda 6583$ map (Fig. E.10) shows a similar distribution as the $([\text{O II}]\lambda\lambda 3726,3729 + [\text{O III}]\lambda 5007)/\text{H}\beta$ ratio. Globally, the local minima do not coincide with the centroids of the emission regions.

The $[\text{S II}]\lambda 6716/[\text{S II}]\lambda 6731$ map is shown in Figure E.11. This ratio appears to be constant throughout the galaxy. No variation is observed within the individual emission regions (right panel of Fig. E.11). This ratio is a proxy to the density and would indicate that it is globally constant.

The $\text{H}\alpha$ and $\text{H}\beta$ equivalent widths are also presented in Figure E.12 and Figure E.13, respectively. They have been measured by dividing the flux map by the continuum map of the respective filter (SN2 for $\text{H}\beta$ and SN3 for $\text{H}\alpha$). High equivalent width values could indicate the presence of young stellar clusters underneath emission regions. The very high values of the equivalent width of both emission lines, which coincide with some of the detected emission regions, could be used to further study the nature of the detected emission regions. A more detailed knowledge of the underlying stellar population is required in order to gain additional information.

2.7.6 BPT diagrams

As originally defined by Baldwin et al. (1981), BPT diagrams of $\log([\text{O III}]/\text{H}\beta)$ versus $\log([\text{N II}]/\text{H}\alpha)$ and $\log([\text{O III}]/\text{H}\beta)$ versus $\log([\text{S II}]/\text{H}\alpha)$ are studied, in order to better understand the physical properties of the gas and the mechanisms responsible for its ionization. These diagrams for the emission regions in NGC 4449 are presented in Figure 2.22. The integrated flux is corrected for the local background emission (as described in Section 2.6.3), the global stellar absorption (Section 2.6.7) and for the extinction (Section 2.6.8). The top panels show each detected emission region, colour coded by their value of the $\text{H}\alpha$ flux. The bottom panels show the density of points of the emission regions. The Kauffmann et al. (2003) and the Kewley et al. (2001) curves are plotted, separating the H II regions, composite regions, shock regions, and AGNs.

Figure 2.22 shows that most of the emission regions detected lie within the typical photoionization zone of the diagrams. This confirms that most of the detected emission regions are in fact photoionized regions, including H II regions and photoionized DIG.

The chaotic kinematics in NGC 4449 might explain the regions that fall above the Kewley et al. (2001) curve, as they may be caused by mechanical shocks in the ISM originating from supernovae, stellar winds, or expanding H II regions (Kumari et al. 2017). Indeed, it is possible to see some regions located between the Kauffmann et al. (2003) curve and the Kewley et al. (2001) curve, which would suggest that these regions have shocks signatures.

Most of the DIG emission in NGC 4449 is suspected to originate from the H II regions, as the

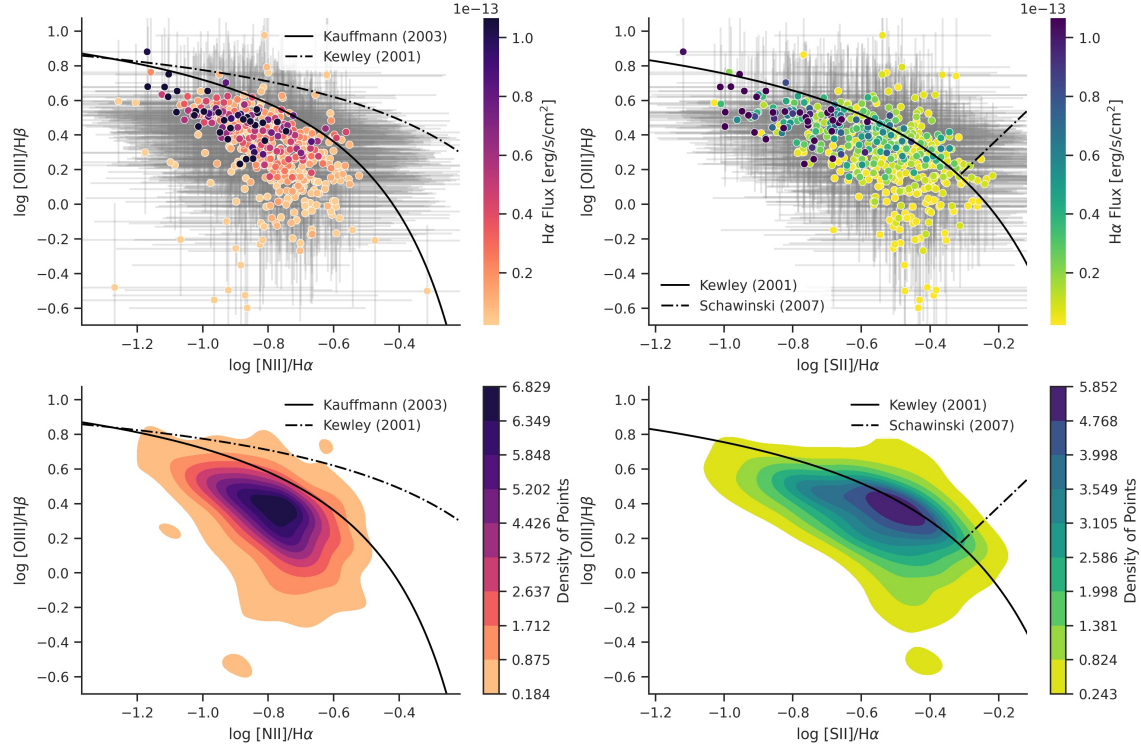


Figure 2.22 – BPT diagrams of the corrected integrated flux of the detected emission regions. The top panels show each detected emission region, colour coded by their $H\alpha$ flux value. The regions with the highest $H\alpha$ flux values are placed on top. The error bars correspond to the uncertainties of the flux measurements, described in Section 2.6.4. The bottom panels show the density of points associated with the distribution of points in the panel above it. On the left panels, the Kauffmann et al. (2003) curve is plotted in solid black and the Kewley et al. (2001) curve in dashed black. On the right panels, the Kewley et al. (2001) curve is plotted in solid black and the Schawinski et al. (2007) curve is plotted in dashed black.

line ratios of the background emission (within the domain used to subtract the background emission) also lie under the H II region’s line in the BPT diagrams and globally in the same region as the H II regions themselves. BPT diagrams of the local background regions, associated to every emission region, is presented in Figure 2.23. Each marker represents the flux values of a local background region, colour coded by their $H\alpha$ flux value. This background flux corresponds to the correction applied to each emission region and is obtained using the procedure described in Section 2.6.3. The spectra fitted to obtain the background region flux has been corrected for the global stellar absorption, as described in Section 2.6.7. However, no extinction correction is applied (described in Section 2.6.8), as it is calibrated for H II regions and thus would assume that the DIG region has the same physical properties. Also, the extinction correction would have a low impact on Figure 2.23, as ratios of nearby lines (in the spectrum) are considered. The background regions are sorted to show the regions with the higher $H\alpha$ flux values on top. The black curves are the same as in Figure 2.22.

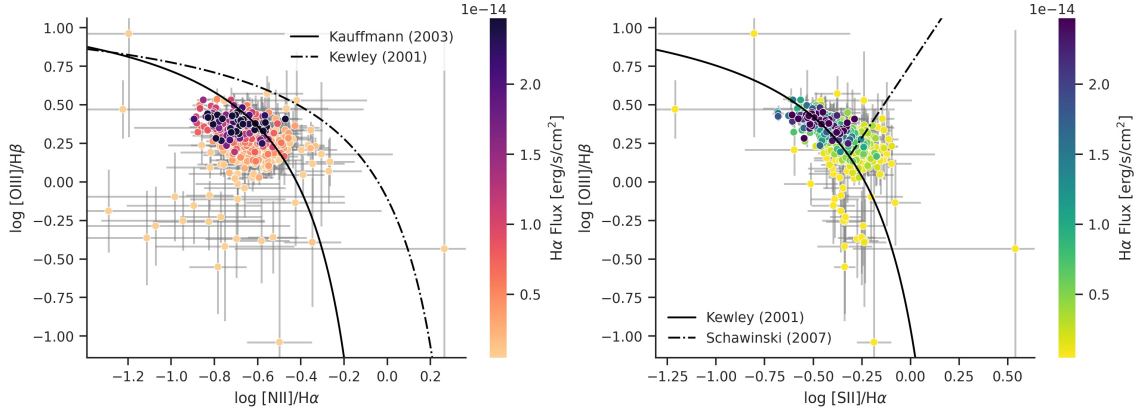


Figure 2.23 – BPT diagrams of the integrated flux of the local background regions, colour coded with their H α flux values. The flux is corrected for the global stellar absorption (Section 2.6.7). The regions with the highest H α flux values are placed on top. The error bars correspond to the uncertainties of the flux measurements, described in Section 2.6.4. The black curves are the same as in Figure 2.22.

Figure 2.23 shows that the background regions, which contain DIG, have a wider range of chemical properties than the emission regions shown in Figure 2.22. As expected, the H α flux is generally lower than the emission regions shown in Figure 2.22. Globally, regardless of the larger spread of chemical properties found in the DIG emission, the trend is similar as the one for the emission regions. The majority of regions fall in the same interval of chemical ratios, when disregarding the few outliers. The relationship with the H α flux value is the same for the DIG and the emission regions; the regions with the strongest H α emission lie close to the Kauffmann et al. (2003) (left panel) and Kewley et al. (2001) curve (right panel). It is thus possible to conclude that the majority of the DIG in NGC 4449 originates from the H II regions. It also implies that disentangling the DIG regions from the emission regions in Figure 2.22 may not be effectively done using the chemical properties of the regions.

To investigate further the impact of the corrections applied to the flux on the resulting BPT diagrams, Figure 2.24 shows the BPT diagrams without any correction (for the local background diffuse emission, the global stellar absorption, or the extinction). Overall, these BPT diagrams are very similar to those with all the corrections (Fig. 2.22), confirming the small impact of the stellar population on the emission lines and the similar physical properties and origin between the DIG and the H II regions.

Figure 2.25 aims to study the spatial location in the galaxy of the emission regions with regard to their position in the BPT diagram. To do so, the distance from the H II region limit in the BPT diagrams of Figure 2.22 (Kauffmann et al. (2003) curve for the [O III] versus [N II] plot and Kewley et al. (2001) curve for the [O III] versus [S II] plot) is computed. The minimal Euclidean distance is used as the metric. It is possible to see that most of the emission regions that fall far from the limit of the H II region regime in the BPT diagrams are located on the

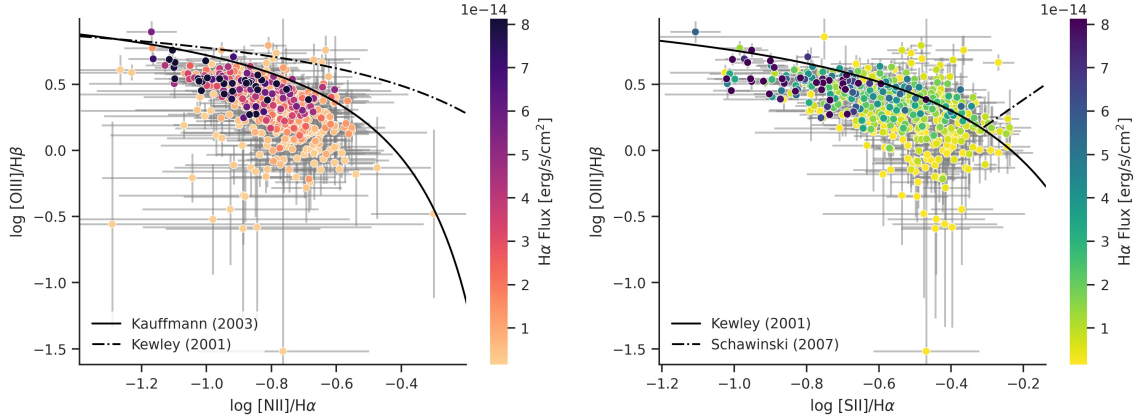


Figure 2.24 – BPT diagrams of the integrated flux of the detected emission regions without any flux corrections applied, colour coded with their $H\alpha$ flux values. The regions with the highest $H\alpha$ flux values are placed on top. The error bars correspond to the uncertainties of the flux measurements, described in Section 2.6.4. The black curves are the same as in Figure 2.22.

outskirts of the galaxy. Their difference from the standard $H\text{ II}$ regions might be due to their physical nature. It might also be due to a lower quality of the measurements in these regions, as the emission from these regions is lower (as seen in Figure 2.6 for the $H\alpha$ flux). These regions are less well modelled spatially as they lie closer to the background and have a lower S/N for the spectral fitting.

It is also possible to observe some variations within the galaxy. The regions in the central bar, especially near the nucleus, have a very small distance from the $H\text{ II}$ regions curves, meaning that they lie near the shift between the $H\text{ II}$ region and composite regime. This might be caused by the high degree of shock, due to their higher level of crowding. Furthermore, a cluster of emission regions at the apex of the northern arm appears to lie far from the $H\text{ II}$ regions curves in the BPT diagram, which could indicate a very different conditions for the gas and stellar clusters (chemical composition, age, etc.) for this spatial region. Yet, the cluster of regions adjacent to them indicates a very close proximity to the $H\text{ II}$ regions curve. Thus, this strong variation could be caused by inexact measurements of weaker lines.

Shocks are believed to have a strong impact on the evolution of the star forming clouds, affecting their SFR and efficiency of star formation (Kumari et al. 2017). Hence, the velocity dispersion of the emission regions is studied, in order to understand the underlying ionization mechanisms better. The BPT diagrams colour coded by their velocity dispersion value are shown in Figure 2.26. It is possible to observe that the regions of higher velocity dispersion fall closer to the limit of the $H\text{ II}$ regions regime. It is expected that the velocity dispersion is higher in the DIG regions, as they undergo more shocks. On the other hand, high luminosity $H\text{ II}$ regions are expected to be young and/or very massive and therefore contain strong stellar winds. This could explain their positions so close to the limit of the photoionization regime. It

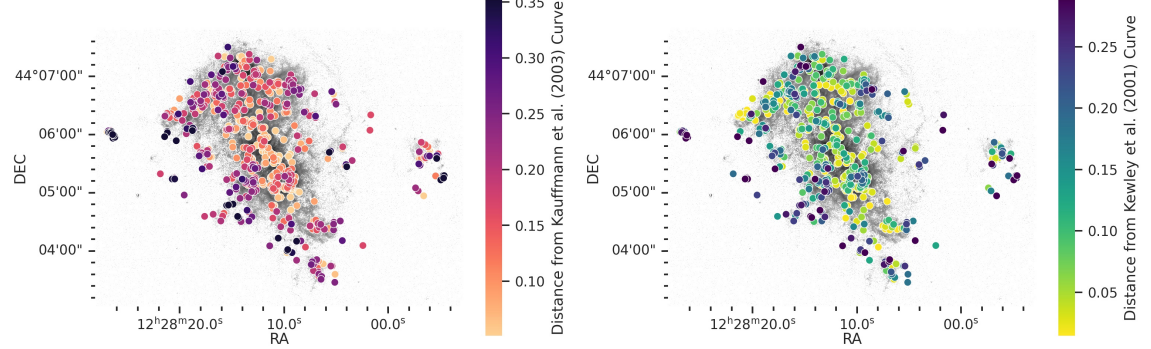


Figure 2.25 – Spatial distribution of the detected emission regions, colour coded by their distance from the H II region limit in the BPT diagrams (shown in Figure 2.22). The left panel shows the distances in the $\log([\text{O III}]/\text{H}\beta)$ versus $\log([\text{N II}]/\text{H}\alpha)$ BPT diagram with the Kauffmann et al. (2003) curve, whilst the right panel shows the distances in the $\log([\text{O III}]/\text{H}\beta)$ versus $\log([\text{S II}]/\text{H}\alpha)$ BPT diagram with the Kewley et al. (2001) curve. The regions are superimposed on the $\log \text{H}\alpha$ flux map, where the pixels with a $\text{H}\alpha$ or $\text{H}\beta$ S/N lower than 1 are not shown.

is thus unclear if the regions with a high velocity dispersion near the photoionization regime's limit are H II regions or DIG regions.

In Figure 2.26, only a few emission regions fall in the shock regime region of the BPT diagrams. Some of these tend to have a high velocity dispersion (especially in the $[\text{O III}]/[\text{S II}]$ BPT diagram), similar to the ones that lie at the limit of the photoionization regime. Their high velocity dispersion could indicate that they are related to DIG regions experiencing shocks or the results of the strong stellar winds. However, similarly to the conclusion obtained by Kumari et al. (2017), no obvious correlation seems to exist between the regions that lie above the H II region regime.

The velocity dispersion of emission regions located in high levels of DIG may be overestimated. The procedure to correct for the underlying local background emission (described in Section 2.6.3) subtracts the integrated flux values of the emission region and its local background, rather than the spectra. Thus, no correction is applied to the velocity dispersion to remove the emission line broadening caused by the underlying DIG.

To further investigate differences in the star formation process, the BPT diagrams of the regions included in the central bar (top panels) and the northern arm (bottom panels) are separated and presented in Figure 2.27. For the $[\text{O III}]$ versus $[\text{N II}]$ BPT diagram, the regions in the central bar (top left panel) of the galaxy seem to fall closer to the H II region limit, shown by the Kauffmann et al. (2003) curve, than the regions in the northern arm (bottom left panel). Regarding the $[\text{O III}]$ versus $[\text{S II}]$ BPT diagram, the regions in the central bar (top right panel) are more compactly clustered when reaching the higher $\log([\text{S II}]/\text{H}\alpha)$ values, compared to the regions in the northern arm (bottom right panel). These differences might

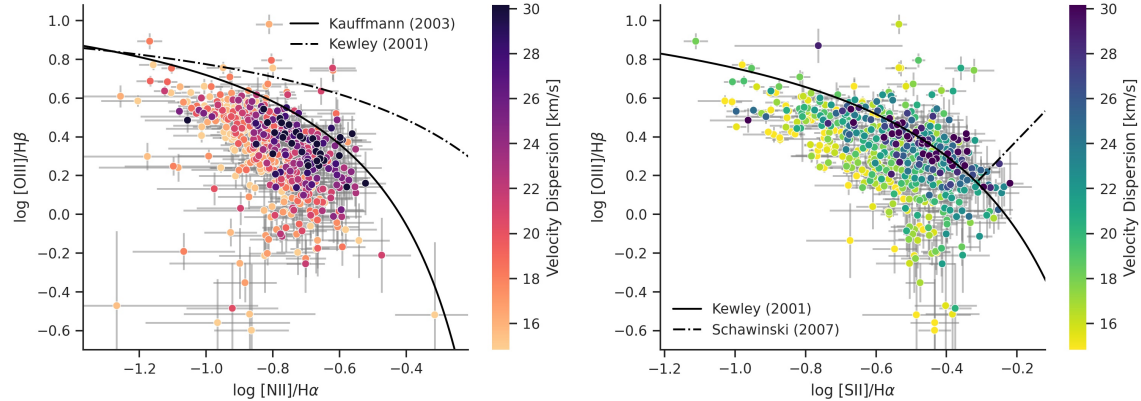


Figure 2.26 – BPT diagrams of the corrected integrated flux of the detected emission regions, colour coded with their measured velocity dispersion values. The regions with the highest velocity dispersion values are placed on top. The error bars correspond to the uncertainties of the velocity dispersion for the fit. The black curves are the same as in Figure 2.22.

indicate a higher contamination by the DIG component (although these fluxes are corrected for the local background diffuse emission) or a difference in the characteristics of the two H II region populations, *e.g.* in the age and metallicity of the regions.

2.7.7 Young Stellar Clusters

H II regions emerge from the interaction between ionizing OB stars and the ISM, thus an attempt to study the young stellar populations is made here. Figure 2.28 shows the detections in three areas of the galaxy, used as examples in Figure 2.4. The detected regions are superimposed to the H α flux map (left panels), the SN2 filter continuum (middle panels) and the SN1 filter continuum (right panels). This allows for a direct comparison of the behaviour of visible clusters accompanying the H α emission.

Depending on the ISM emission surrounding a region and the age of the stellar cluster, an H II region or a cluster may be seen or not, and if both are seen, they may not be perfectly superposed with each other (Zamora-Avilés et al. 2019). As it can be observed, for example with some regions below the region 175 (bottom panels), the centroid of the detected H II regions do not coincide with the centroid of the star cluster on the continuum maps. When comparing the continuum maps to the H α flux, it is in some cases possible to resolve multiple star clusters under a large H II region, as is the case for example with the region at the bottom right of region 527 (top panels), region 420, which clearly includes two very large star clusters (middle panels), and the region below region 175 (bottom panels). Nevertheless, these clusters could be older, and not contributing to the ionizing photons budget.

Region 527 is known to be an emerging Wolf-Rayet massive star cluster, containing ~ 240 massive stars, of which ~ 18 are Wolf-Rayet stars (Sokal et al. 2015). A minimal age of ~ 3 Myr

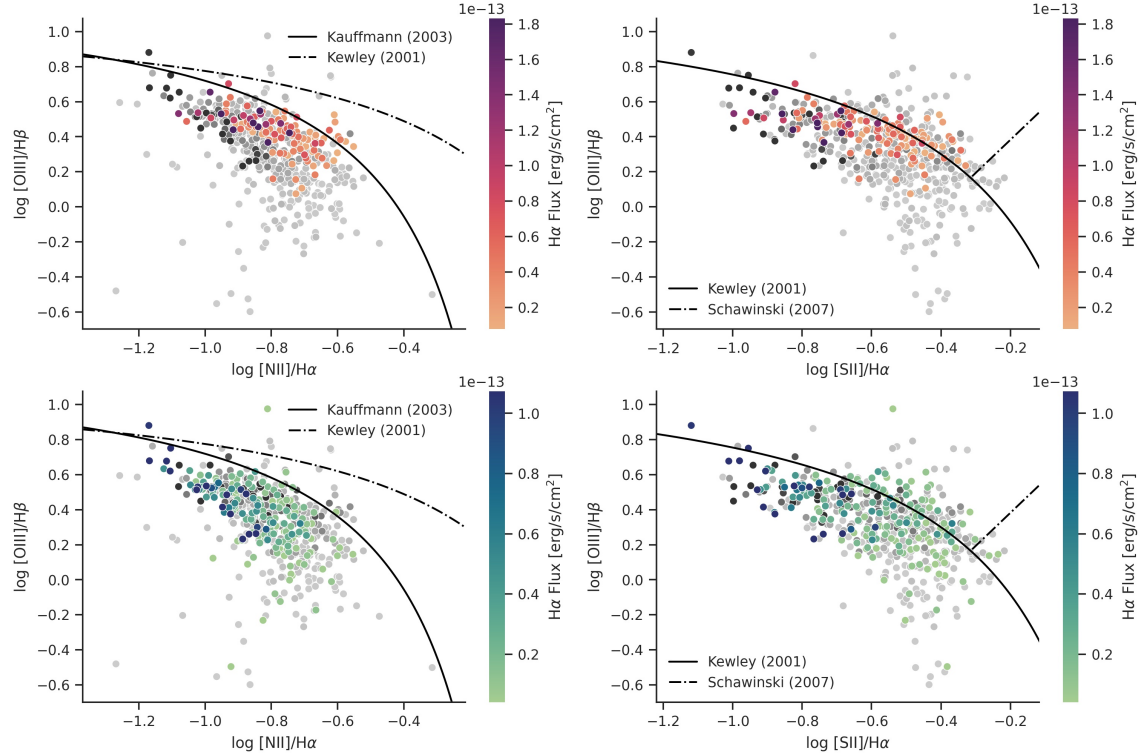


Figure 2.27 – BPT diagrams of the corrected integrated flux of the detected emission regions in the central bar (top panels) and the northern arm (bottom panels). The grey regions correspond to the distribution of all the H II regions, regardless of their location in the galaxy. This superposition allows to compare where the H II regions in the morphological feature fall on the BPT diagram with regard to the overall distribution. The morphological categories are shown in Figure D.1. The colour of each detected emission region corresponds to their H α flux value. The regions with the highest H α flux value are placed on top. The black curves are the same as in Figure 2.22.

has been estimated by Sokal et al. (2015), indicating that it would not have evacuated all its natal material yet. It is believed that this corresponds to the young evolutionary stage of a super star cluster, which would be analogous to 30 Doradus in the LMC (Sacchi et al. 2018; Sokal et al. 2015).

Using the global optical spectrum and the spectral fitting STARLIGHT code, Karczewski et al. (2013) concluded that only 1% of the mass fraction in NGC 4449 originates from the stellar population with an age of <10 Myr, 20–25% around 100 Myr, and 60–75% around >1000 Myr. McQuinn et al. (2010) studied the star formation history in NGC 4449 and noticed a decline in the average activity in the past 50 Myr.

The LEGUS project (Calzetti et al. 2015) uses images from the *Hubble Space Telescope* from the near UV to the near IR to study the stellar clusters in nearby galaxies. The catalogue of stellar clusters provided by Adamo et al. (2017) considers Padova stellar population templates

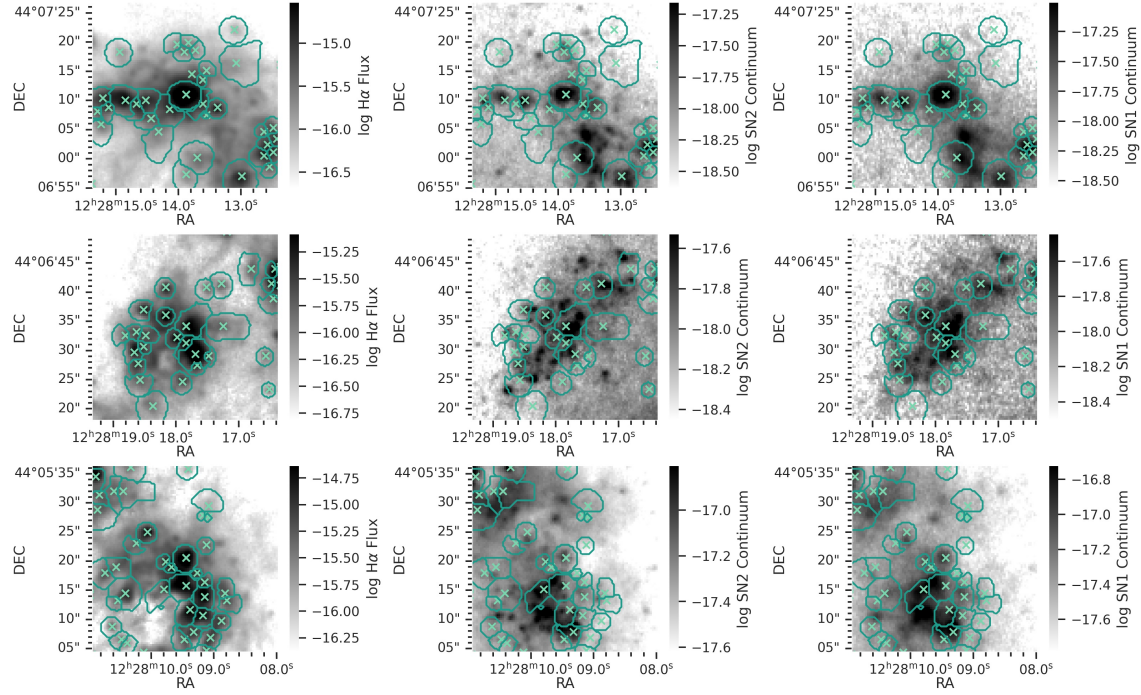


Figure 2.28 – Examples of detected emission regions superimposed on the $\text{H}\alpha$ flux map (left column), the SN2 continuum (middle column) and the SN1 continuum (right column). All the maps are in log-scale. The teal crosses indicate the centroid of the regions and the teal contours show the domain of each region. The central region in the three rows (top to bottom) corresponds to region 527, region 420, and region 175. These area correspond to three of those shown in Figure D.2, with their location in the galaxy shown in Figure D.2. The aperture size is $597 \text{ pc} \times 597 \text{ pc}$.

with the averaged aperture correction method to model the properties (*e.g.* age, mass, and extinction) of the stellar clusters for NGC 4449. This catalogue contains a total 2853 star clusters, of which 975 are selected using quality checks and deemed to have precise enough parameters for this study. Note that these star clusters have been studied by Annibali et al. (2011), Cignoni et al. (2018, 2019), Sacchi et al. (2018), and Whitmore et al. (2020). NGC 4449 is regarded as the best sampled dwarf galaxy of the study (Menon et al. 2021), as it has a complex and rich stellar population, including some young, intermediate, and old star clusters (Annibali et al. 2011; Cignoni et al. 2019). It is hypothesised that its past interactions are responsible for its intricate star formation history (Cignoni et al. 2019; Menon et al. 2021).

The location of the LEGUS star clusters is compared here with our emission regions. Figure 2.29 shows the detected emission regions in the three areas, centred on region 527, 420, and 175, with the LEGUS star clusters overlayed, as circles, colour coded by their estimated age. The periwinkle star clusters are <20 Myr, the chartreuse are between [20, 100] Myr and the scarlet are >100 Myr.

The LEGUS star clusters coincide well with the regions of high SN3 continuum and most

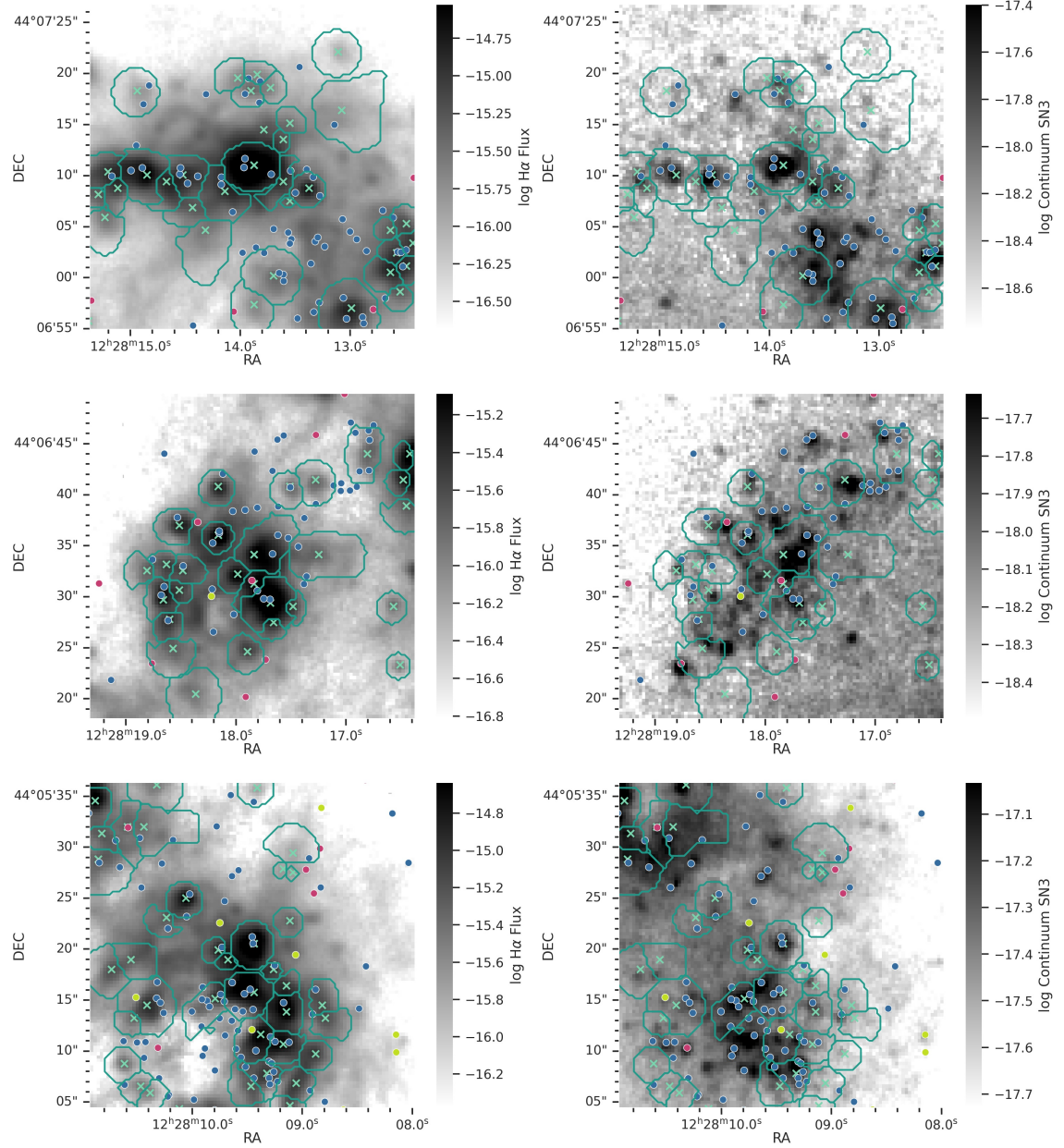


Figure 2.29 – Examples of our detected emission regions with the LEGUS star clusters, superimposed on the $\text{H}\alpha$ flux map (left column) and the SN3 filter continuum (right column). All the maps are in log-scale. The LEGUS star clusters are marked with a circle, colour coded by their estimated age: the periwinkle star clusters are <20 Myr, the chartreuse are between [20, 100] Myr, and the scarlet are >100 Myr. The teal crosses mark the centroids of the detected emission regions from this study and the teal contours delimit their region. The central region in the first row corresponds to region 527; in the second row, region 420; and in the third row, region 175. These area correspond to three of those shown on Figure D.2, with their location in the galaxy shown on Figure D.2. The aperture size is 597 pc \times 597 pc.

of our detected emission regions. 38 % of our detected emission regions contain at least one LEGUS star cluster. Also, 40 % of the LEGUS star clusters are located in detected emission regions. Some emission regions even contain multiple star clusters. On average, the emission regions that contain a LEGUS star cluster, contain 1.85 star clusters. For example, regions 159 and 416 even contains up to 7 star clusters. The centroids of the emission regions do not necessarily coincide with the detected stellar cluster, as H II regions grow anisotropically (Zamora-Avilés et al. 2019).

LEGUS detects more stellar clusters than H II regions detected in this study, due to the use of near UV data, as it allows to trace back older stellar formation 10 times longer than H α (Calzetti et al. 2015). Stars of intermediate mass are able to be detected, as they emit near UV, but do not ionize the ISM.

The median age of the LEGUS star clusters located in H II regions is 5 Myr. The median age of the LEGUS star clusters with no emission region is 10 Myr. A Kolmogorov–Smirnov test is conducted in order to confirm that the age distribution of the LEGUS star clusters with and without emission regions is statistically different. Using a significance level of 0.05, the obtained p-value of 1.89×10^{-15} allows the rejection of the hypothesis that the two distributions are the same.

Differences in the LEGUS star clusters distribution and our two defined morphological structures of the galaxy is studied. 288 LEGUS stellar clusters are located in the central bar and 44 % of them are superposed to an emission region. 360 LEGUS stellar clusters are in the northern arm and 48 % of them are superposed to an emission region. In both cases, the H II regions with star clusters in the central bar and in the northern arm, contain on average 2 of these. The median age of the star clusters located in the central bar is 10 Myr, compared to 6 Myr in the northern arm. The median age of the star clusters superposed to emission regions in the central bar is 10 Myr, compared to 5 Myr in the northern arm. A Kolmogorov–Smirnov test is conducted in order to confirm that the age distributions of the LEGUS star clusters located in emission regions in the central bar and the northern arm are statistically different. Using a significance level of 0.05, the obtained p-value is 0.0287 allows the rejection of the hypothesis that the two distributions are the same. However, Annibali et al. (2008) showed that most of the stellar population with ages below 10 Myr do not reside in the centre of the bar (near the nucleus) nor in the northern arm. A very high concentration is located at the southern end of the bar, in the super bubbles (Annibali et al. 2008).

Figure 2.30 shows the detected emission regions in the areas centred on region 527, 420, and 175, with the LEGUS star clusters overlayed as circles, colour coded by their estimated mass. The periwinkle star clusters are $<1 \times 10^4 M_\odot$, the chartreuse are between $[1 \times 10^4, 1 \times 10^5] M_\odot$, and the scarlet are $>1 \times 10^5 M_\odot$.

The median mass of the LEGUS star clusters superposed with emission regions is $2.37 \times$

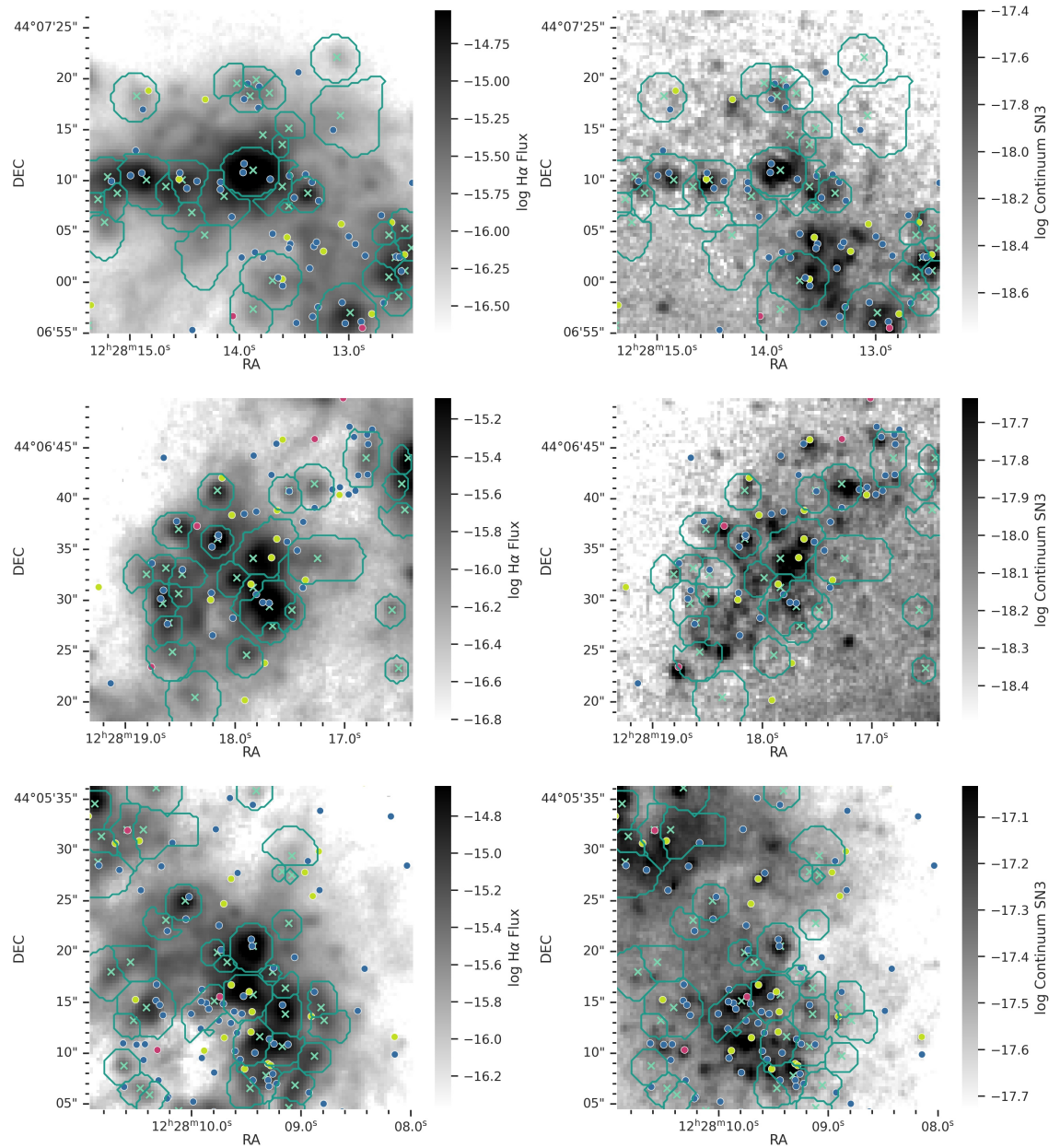


Figure 2.30 – Examples of our detected emission regions with the LEGUS star clusters, superimposed on the $\text{H}\alpha$ flux map (left column) and the SN3 filter continuum (right column). All the maps are in log-scale. The LEGUS star clusters are marked with a circle, colour coded by their estimated mass: the periwinkle star clusters are $<1 \times 10^4 M_\odot$, the chartreuse are between $[1 \times 10^4, 1 \times 10^5] M_\odot$, and the scarlet are $>1 \times 10^5 M_\odot$. The teal crosses mark the centroids of the detected emission regions from this study and the blue contours delimit their region. The central region in the first row corresponds to region 527; in the second row, region 420; and in the third row, region 175. These area correspond to three of those shown on Figure D.2, with their location in the galaxy shown on Figure D.2. The aperture size is $597 \text{ pc} \times 597 \text{ pc}$.

$10^3 M_{\odot}$, compared to $3.91 \times 10^3 M_{\odot}$ for the ones that are not in emission regions. The median mass of the LEGUS star clusters included in H II regions in the central bar is $4.61 \times 10^3 M_{\odot}$, compared to $1.72 \times 10^3 M_{\odot}$ for the ones located in the northern arm. This is significant, hence the mass (more than the age) may be an important factor for the stellar formation activity.

2.7.8 Metallicity

The absence of the weak auroral $[\text{O III}]\lambda 4363$ emission line from the filters used in this study prevents the use of the direct method to estimate the chemical abundances. Thus, an indirect method must be used, even though these types of methods are considered less reliable (Arora et al. 2021; Kumari et al. 2017).

Metallicity of the gas is calculated using the $N2O2$ indicator, calibrated according to the work of Pilyugin & Grebel (2016). Uncertainties on the metallicity are arithmetically propagated to take into account the uncertainties on the emission regions' integrated flux measurement of each line. Regions with uncertainties above 2σ of the metallicity error distribution, which corresponds to a metallicity with an uncertainty superior to 0.1, are removed for further analysis. Also, the regions with a metallicity value outside of 3σ of the metallicity distribution are removed, as they are considered outliers. Regions with a S/N value inferior to 3 for any of the measured lines are removed. In addition, a S/N lower limit for the $\text{H}\alpha$ line is set to 20. Using these restrictions, 471 of the 535 regions have their metallicity estimated. The $N2O2$ indicator is very sensitive to the extinction, however, the extinction correction (described in Section 2.6.8) is considered precise enough to provide accurate results with this calibrator.

Figure 2.31 shows the metallicity of the entire galaxy, calculated for each pixel. Pixels with a S/N lower than 1 are removed and only the pixels corrected for global stellar absorption and extinction are shown. It is also important to note that the $[\text{O II}]\lambda 3727$ line is not corrected for the stellar absorption in the case of individual pixels. The $N2O2$ metallicity indicator is calibrated using H II regions, thus it is not proven to be representative of the metallicity in the DIG. Nevertheless, Figure 2.31 allows to show chemical inhomogeneities on a small scale. The study of the global behaviour of the abundances in NGC 4449 is beyond the scope of this study and deserves to be compared to the trends obtained by Li et al. (2022) using *MUSE* data, for a sample of 219 local galaxies.

Figure 2.32 displays the location of the H II regions on the $\text{H}\alpha$ flux map, colour coded with their metallicity. It is important to note that the regions' integrated $[\text{O II}]\lambda 3727$ flux has been corrected for the local stellar absorption, compared to the other emission lines, which have been corrected using the global stellar absorption, as described in Section 2.6.7. The average $N2O2$ metallicity value for our emission regions is 8.27 ± 0.07 . This metallicity is in agreement, in general, with the low metallicities obtained with the direct method (see Section 2.4). A spatial gradient in the metallicity can be observed spreading from the bar of NGC 4449 and

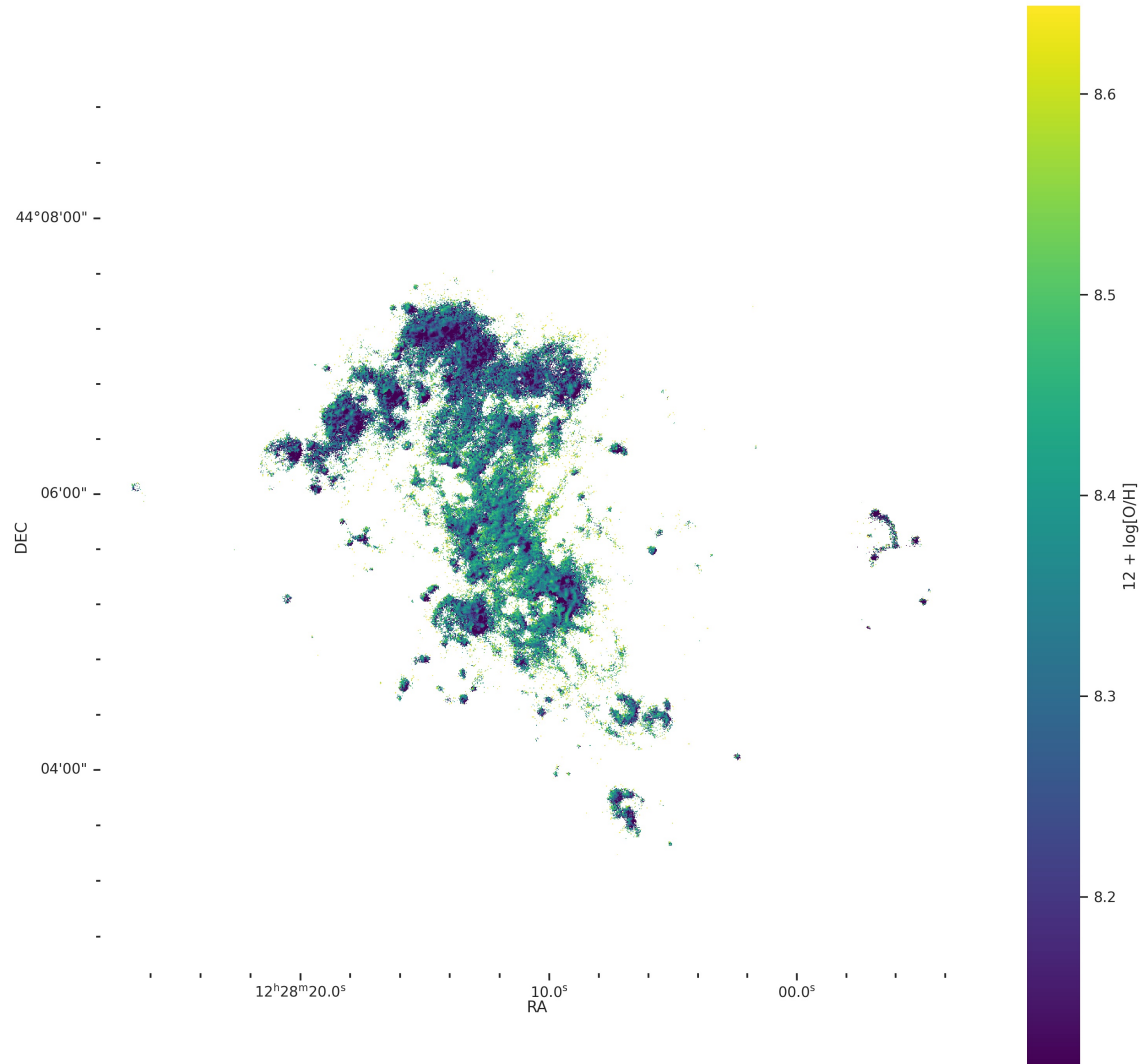


Figure 2.31 – Metallicity map of NGC 4449, using the Pilyugin & Grebel (2016) $N2O2$ metallicity indicator. The fluxes used are corrected for the global stellar absorption (except for the $[\text{O II}]\lambda 3727$ line) and the extinction. The pixels that are not corrected are not shown and the pixels with the S/N of a line measurement lower than 1 are also not shown.

diminishing towards the northern arm. This phenomenon is expected in spiral galaxies, but not as well defined in irregular galaxies. However, inhomogeneities in the chemical abundance's distribution of star forming galaxies are expected due to an inflow or outflow of gas (Ceverino et al. 2016; Cresci et al. 2010; Davé et al. 2011; Kewley et al. 2010; Kumari et al. 2017; Sánchez Almeida et al. 2013, 2014, 2015). As seen by Kumari et al. (2017), NGC 4449 also displays chemical inhomogeneities on a smaller scale. These inhomogeneities are best revealed here in Figure 2.31, where each individual pixel is considered.

Something not discussed by Kumari et al. (2017) nor Edmunds & Pagel (1984) is the impact of the bar on the chemical abundance's distribution of NGC 4449. In spiral galaxies, it is known that the presence of a bar impacts the kinematics of the gas (Martin & Roy 1994). For example, Elmegreen & Elmegreen (1980) suggested that a bar increases the gas compression, resulting in an enhanced star formation activity in Magellanic-type irregular galaxies. Figure 2.32 shows globally distinct metallicity values for the H II regions in the central bar compared to the ones in the northern arm. It is also possible to observe this difference in Figure 2.33, where the emission regions from the different morphological features fall in clusters of similar metallicities, with an average metallicity different from one another. The average metallicity value of the emission regions in the central bar is 8.32 ± 0.06 , and of 8.24 ± 0.06 in the northern arm. To statistically validate that the two populations have a different metallicity distribution, a Kolmogorov–Smirnov test is conducted. Using a significance level of 0.05, a clearly lower p-value of obtained 4.53×10^{-56} is obtained, which allows the rejection of the hypothesis that the two distributions are the same.

Kumari et al. (2017) studied the central H II region, using the *Gemini North Multi-Object Spectrograph*, allowing a spatial-scale of 5.5 pc px^{-1} in a FoV of $3''.5 \times 5''$, in order to study the existence of chemical inhomogeneities at this scale. Only one large emission region is located within this aperture, which they restrain to a $1''.2 \times 1''.2$ box. It corresponds to region 238 in our catalogue. Using the indicators $N2$ and $O2N2$ from Pettini & Pagel (2004), they obtain a metallicity of 8.39 ± 0.18 and 8.37 ± 0.14 , respectively. For this region (238), the metallicity values obtained in this study are 8.3 ± 0.2 and 8.2 ± 0.2 for the respective calibrators (and 8.35 ± 0.06 with the $N2O2$ calibrator from Pilyugin & Grebel 2016). Regardless of the indicator used, none of the metallicities measured in our study for region 238 compares to the metallicity value of 7.88 ± 0.14 obtained by Kumari et al. (2017), with the direct method. However, this value is also very different from the values they obtained using the strong lines methods, a well known effect.

Figure 2.33 shows the radial variation of our metallicity estimate in NGC 4449. The galactocentric-distance is computed at the photometric centre, assumed at RA 12h28m11.2s and DEC $+44^\circ 05\text{m}37.9\text{s}$, with a P.A. of 25° and an inclination of 43° , as used by Valdez-Gutiérrez et al. (2002). The different colours signify the morphological feature in the galaxy where the emission region is located. A linear regression (teal line) is fitted through the data,

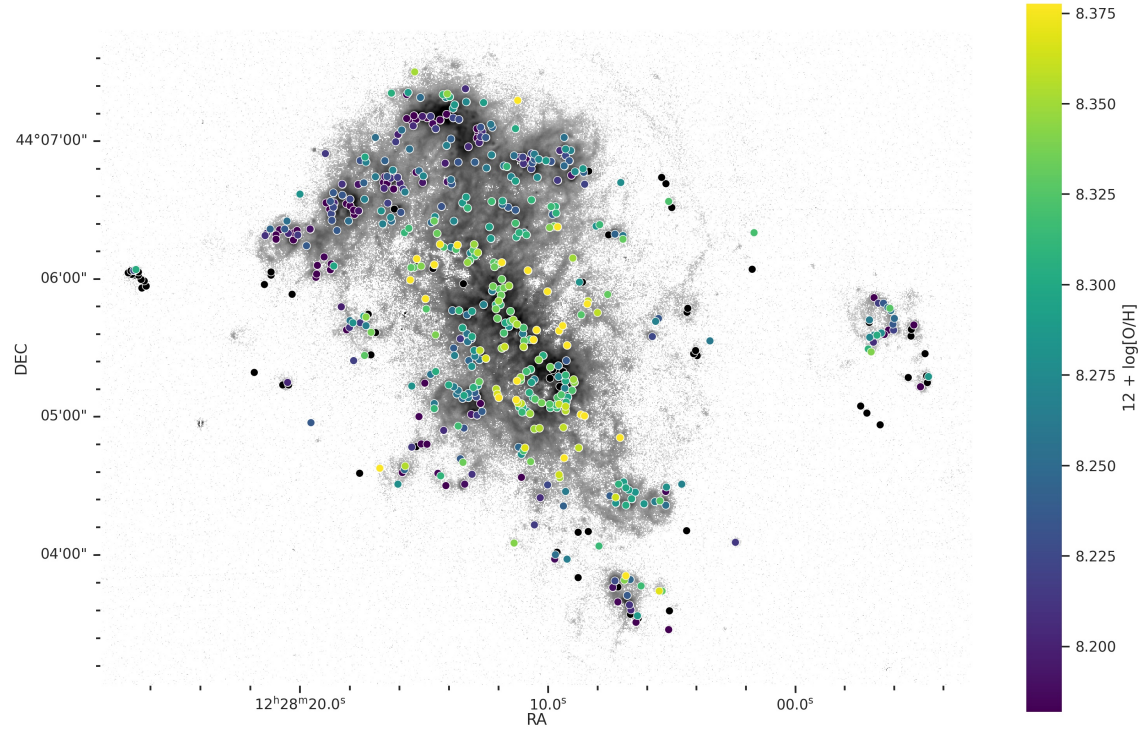


Figure 2.32 – Spatial distribution of the emission regions, colour coded by their metallicity value, using the Pilyugin & Grebel (2016) $N2O2$ metallicity indicator. The black regions are the regions that were cut from the study of the metallicity due to their poor measurements. The regions are superimposed on the log H α flux map, where the pixels with a H α or H β S/N lower than 1 are not shown.

resulting in a slope $\alpha = (-4.8 \pm 0.4) \times 10^{-5} \text{ pc}^{-1}$. Emission regions that are far away from the slope tend to have high uncertainties. Their relative weight on the relation is mitigated by propagating the uncertainties when fitting the slope parameters. The uncertainty on the fit corresponds to the confidence interval, estimated using a bootstrap method. The decreasing slope is visible, which is consistent with a higher metallicity in the centre of the galaxy, as shown in Figure 2.32.

NGC 4449’s irregular morphology makes it less probable to observe trends along the galactic radius. Nevertheless, a relatively well defined slope of $(-4.8 \pm 0.4) \times 10^{-5} \text{ pc}^{-1}$ with a central value of 8.32 is observed. It is typical for the centre of more massive galaxies to have a higher metallicity, as more generations of stars have formed there, compared to the outskirts. This is a pattern well known in spiral galaxies. However, Kumari et al. (2017) found the opposite trend, with the central part of NGC 4449 being the more metal-poor. Albeit, Kumari et al. (2017) use six data points to conclude this trend, from four other studies (Böker et al. 2001; Buckalew et al. 2005; Izotov et al. 2006; Martin 1997). Three of the six data points are located in the nucleus of the galaxy, resulting in a sampling of the galactocentric radius by four measurements. On the other hand, our study samples the galactocentric radius with 471

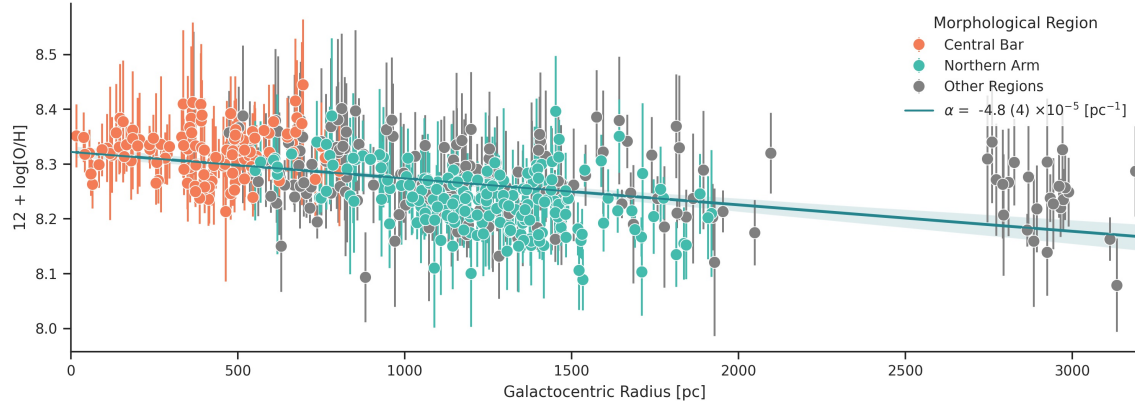


Figure 2.33 – Radial profile of the emission region’s metallicity in NGC 4449. The slope obtained from the linear fit (teal line) has a value of $(-4.8 \pm 0.4) \times 10^{-5} \text{ pc}^{-1}$. The photometric and dynamic centre is assumed to be at RA 12h28m11.2s and DEC $+44^{\circ}05\text{m}37.9\text{s}$, with a P.A. of 25° and an inclination of 43° (Valdez-Gutiérrez et al. 2002). The orange coloured data are regions located in the central bar of the galaxy and the teal coloured data are regions in the northern arm. The grey coloured data are the regions located elsewhere in the galaxy. The map showing the regions included in each morphological category is shown in Figure D.1.

data points, obtained with the same data and methodologies.

Not mentioned by Kumari et al. (2017) are the results obtained by Scowen (1992). Scowen (1992) produced a catalogue of 160 H II regions for NGC 4449 and calculated their metallicity using the correlation between the $[\text{O III}]/\text{H}\beta$ ratio and the derived oxygen abundance, as described by Edmunds & Pagel (1984). Scowen (1992) did not comment on the relationship of the metallicity as a function of the galactocentric radius, however a globally constant trend is observed in his figure. The amount of H II regions in their sample and the systematic metallicity calculation removes the uncertainties that are present in the results of Kumari et al. (2017). The differences in the slope between this study and the one of Scowen (1992) might be caused by the metallicity calibrator used, as described in more details below.

Sánchez Almeida et al. (2014) reported that some galaxies have lower metallicity inner regions and enhanced stellar formation activities, using long-slit spectra for galaxies at redshifts of the order of $\sim 1 \times 10^2$. Due to the proximity of NGC 4449, the gain in spatial resolution is incomparable, shedding doubt on the validity of the extrapolation of the conclusions made by Sánchez Almeida et al. (2014) for galaxies in the Local Universe. Kumari et al. (2017) suggest that the inverse metallicity gradient could be caused by the presence of an inflow or outflow of gas in the centre of NGC 4449. A potential inflow/outflow is discussed in more details in Section 2.7.10.

A major caveat related to this study of the metallicity is the indicator used. Different indicators actually yield different slopes, as it can be seen in Figure E.14. The slopes of the metallicity gradients of the emission regions for the calibrators from Denicoló et al. (2002), Dopita et al.

(2016), Kewley & Dopita (2002), Kobulnicky & Kewley (2004), Marino et al. (2013), Pettini & Pagel (2004), and Pilyugin & Grebel (2016) are compared in Figure E.14. The $R23$ calibrator from Kobulnicky & Kewley (2004) shows a positive slope, which would be in agreement with the conclusions from Kumari et al. (2017). The $O3N2$ calibrators from Marino et al. (2013) and Pettini & Pagel (2004) also show a slightly positive slope. However, all the other calibrators have negative slopes.

Furthermore, it should be noted that the $R23$ calibrator from Kobulnicky & Kewley (2004) shows a bimodal distribution in metallicity values for the H II regions. This is likely caused by the discontinuity in the calibrator that occurs at a metallicity of $12 + \log[\text{O}/\text{H}] = 8.4$. This value is very close to the average metallicity of NGC 4449, and it is likely that emission regions fall into both regimes, causing a very wide large range of metallicities for this calibrator. It could also induce artificial variations in the gradient when the values are around $12 + \log[\text{O}/\text{H}] = 8.4$. As a matter of fact, the average metallicity obtained using the $R23$ calibrator from Kobulnicky & Kewley (2004) is 8.83 ± 0.03 with a standard deviation of 0.75. Compared to the average metallicity obtained with the $N2O2$ calibrator from Pilyugin & Grebel (2016), the calibrator used in this study, the average metallicity is 8.27 ± 0.07 with a standard deviation of 0.06.

Also, the very high standard deviation of the $R23$ calibrator from Kobulnicky & Kewley (2004) would indicate very high variations and inhomogeneities in the chemical abundances throughout the galaxy, compared to the lower value from the $N2O2$ calibrator from Pilyugin & Grebel (2016). The high kinematics of the gas in NGC 4449 would suggest a higher degree of mixing from the gas, resulting in a more homogeneous ISM. However, the fact that NGC 4449 is considered to be in a post-starburst phase (Kumari et al. 2017; McQuinn et al. 2010) could indicate that a lot of chemicals are being introduced into the ISM already, through, for example, supernova explosions. However, as discussed further in Section 2.7.12 and 2.7.11, a few supernovae have been detected, in part using the *Chandra Telescope* (Summers et al. 2003), which could be related to the local increases in metallicity.

Further investigation is needed in order to confirm if the metallicity gradient in NGC 4449 has a negative, null, or positive slope, and to explain the underlying phenomenon causing the metallicity gradient in NGC 4449. A more robust metallicity indicator would be required. Optimally, obtaining data which include the $[\text{O III}]\lambda 4363$ auroral line over the whole galaxy would enable the use of the direct method to obtain the metallicity, which is considered as more robust (Kumari et al. 2017).

2.7.9 Kinematical Analysis

Figure 2.3 (top panel) shows the measured velocity of the ionized gas from the SN3 datacube in NGC 4449. The measured average heliocentric velocity of the galaxy, considering all the pix-

els, is 209 km s^{-1} . Valdez-Gutiérrez et al. (2002) adopted a systematic velocity of 217 km s^{-1} , whilst Bajaja et al. (1994) obtain a systematic velocity of 214 km s^{-1} . Globally, the north-east side (northern arm) is slightly redder (receding side), with a velocity near $\sim 225 \text{ km s}^{-1}$, whereas the south-western side of the central bar (approaching side) has a velocity around $\sim 190 \text{ km s}^{-1}$. In general, a global rotation is not well supported in irregular galaxies, but the presence of a bar in NGC 4449 and an arm-like structure in the north could be the result of a rotating disc. It is unlikely that NGC 4449 used to be a well defined spiral galaxy prior to its interactions (Hunter et al. 1999). None the less, the divergence in the polarization vectors observed by Chyží et al. (2000) reaches very low values in the east side of the junction between the bar and the northern arm, which is a characteristic of spiral galaxies. The southern part of the bar (approaching side) shows more perturbations in its gas with less H II regions, which could be due to the influence of previous interactions (Valdez-Gutiérrez et al. 2002).

Inspired by Valdez-Gutiérrez et al. (2002), a simple rotation curve is attempted to model the global motion of NGC 4449 along the major optical axis. However, the results were not conclusive. A more sophisticated model or a higher spectral resolution may be required in order to better measure the velocity (*i.e.* separate velocity components) and obtain results similar to Valdez-Gutiérrez et al. (2002), suggesting that solid body rotation takes place in the northeast part (northern arm) of NGC 4449.

Figure 2.34 shows the spatial distribution of the emission regions colour coded by their velocity (top panel) and velocity dispersion (bottom panel). The velocity gradient from the emission regions (Figure 2.34; top panel) is less obvious than the one seen for the individual pixels of the gas (Figure 2.3; top panel). The emission regions seem to be clustered in groups of similar velocities, whilst many pixels are dominated by the DIG. The spatial distribution of the velocity is similar to the one obtained by Hartmann et al. (1986), with a sample of 35 H II regions.

A very distinct velocity system west of the galaxy may be observed in Figure 2.34. Located more than 1 kpc to the west of the body of NGC 4449 lies a cluster of H II regions, which can be seen in Figure 2.2. These emission regions correspond to regions 196, 202, 211, 214, 218, 218, 222, 228, 229, 230, 237, 239, 243, 248, 251, 263, 267, 268, 274, 275, and 279 in our catalogue. This system is rarely discussed, as it is often not included in the field of view of the data and does not contain bright H II region as in the body of NGC 4449. However, it is discussed by Scowen (1992), who concluded that these regions have typical properties, compared to the regions in the body of NGC 4449. The morphology of this system is quite peculiar; a bow of gas links three bright H II regions, to the north, west, and south. The bow is centred on a faint H II region, which could be the cause of the gas arc surrounding it. It is suspected to be an old H II region, which would have expanded as an undisrupted shell, since it is isolated. It also appears to have condensed its gas to form new H II regions, which would be the young bright regions observed at the north, west, and south of the bow (Scowen 1992).

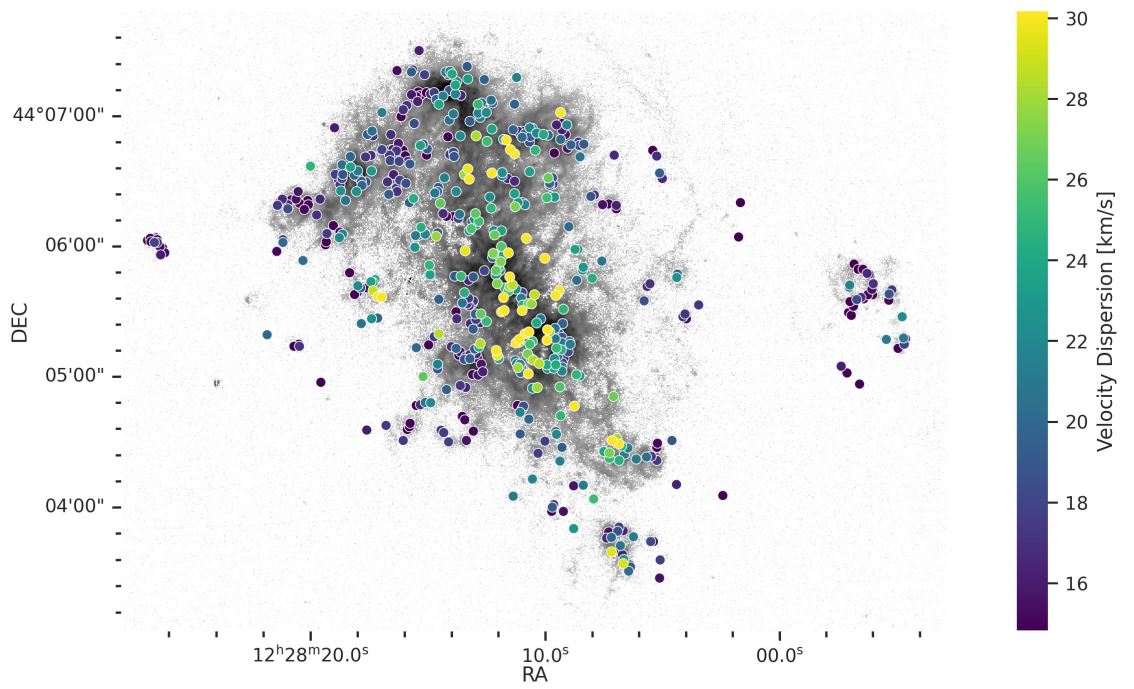
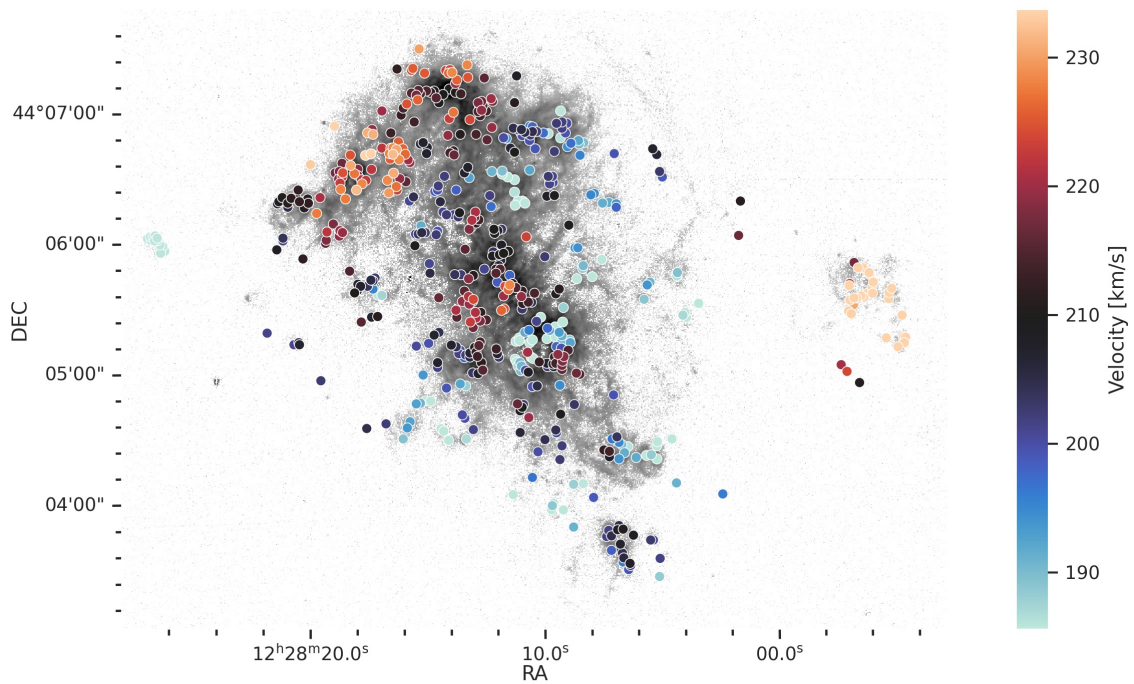


Figure 2.34 – Spatial distribution of the emission regions, colour coded with their velocity (top panel) and velocity dispersion (bottom panel). The OH sky lines have been used for the calibration and the heliocentric correction has been applied. The regions are superimposed on the log H α flux map, where the pixels with a H α or H β S/N lower than 1 are not shown.

Not discussed by Scowen (1992), the kinematics of this cluster is quite different from the rest of the body of the galaxy. The detected emission regions in the cluster have an average velocity of $(237 \pm 2) \text{ km s}^{-1}$, which is considerably higher than the average velocity in the body of the galaxy (as seen in Figure 2.34). The average velocity dispersion is $(15 \pm 1) \text{ km s}^{-1}$, which is lower than the average in the body of the galaxy, confirming that this cluster is isolated and unperturbed, compared to the chaotic kinematics in the body of NGC 4449. As concluded by Scowen (1992), the origin of this cluster is unclear.

As observed in Figure 2.34 (bottom panel), the emission region's velocity dispersion follows the dispersion seen from the individual pixels (Figure 2.3; bottom panel). The average velocity of the emission regions is $(207.1 \pm 0.8) \text{ km s}^{-1}$ and the average velocity dispersion is $(20.4 \pm 0.7) \text{ km s}^{-1}$. The average velocity of the emission regions located in the central bar is $(205 \pm 1) \text{ km s}^{-1}$, compared to $(212 \pm 1) \text{ km s}^{-1}$ for the regions in the northern arm. The regions included in each morphological regions is shown in Figure D.1 in Appendix D. The average velocity dispersion of the emission regions located in the central bar is $(24.1 \pm 0.7) \text{ km s}^{-1}$, compared to $(19.5 \pm 0.5) \text{ km s}^{-1}$ for the regions in the northern arm. The chaotic dynamics observed in the bar, especially in the south part, is consistent with a higher velocity dispersion than in the northern arm region. These values may be overestimated due to the crowding of the regions, as explained in Section 2.6.3.

Figure 2.3 (bottom panel) shows the measured velocity dispersion in NGC 4449. The regions with the highest velocity dispersion correspond to regions of DIG, where shocks or superposing structures may be located. Regions of strong stellar formation seem to have lower velocity dispersion. The gas flow mentioned by Summers et al. (2003) and Kumari et al. (2017) spatially coincides with the ionized gas showing the highest velocity dispersion, which would be consistent with their theory, further discussed in Section 2.7.10.

2.7.10 Inflow/Outflow

The inclination of NGC 4449 (43° ; Valdez-Gutiérrez et al. 2002) would allow for the observation of a potential inflow/outflow perpendicular to the disc of the galaxy. In which case, superimposed on the line of sight, multiple emission lines with different velocities would be observed in that region. In fact, owing to the high spectral resolution of the data used in this study, some double components in the emission lines are resolved.

While the study conducted by Kumari et al. (2017) for the central H II region in NGC 4449 allowed the separation of multiple spectral components in the H α emission line, broadened emission lines have been observed in that region with our data, but with a lower variety of double components compared to Kumari et al. (2017). An attempt to study them has been made, using the tool developed by Rhea et al. (2021) for this purpose. However, this tool is built for interacting galaxies, with considerably higher velocity differences in both of their

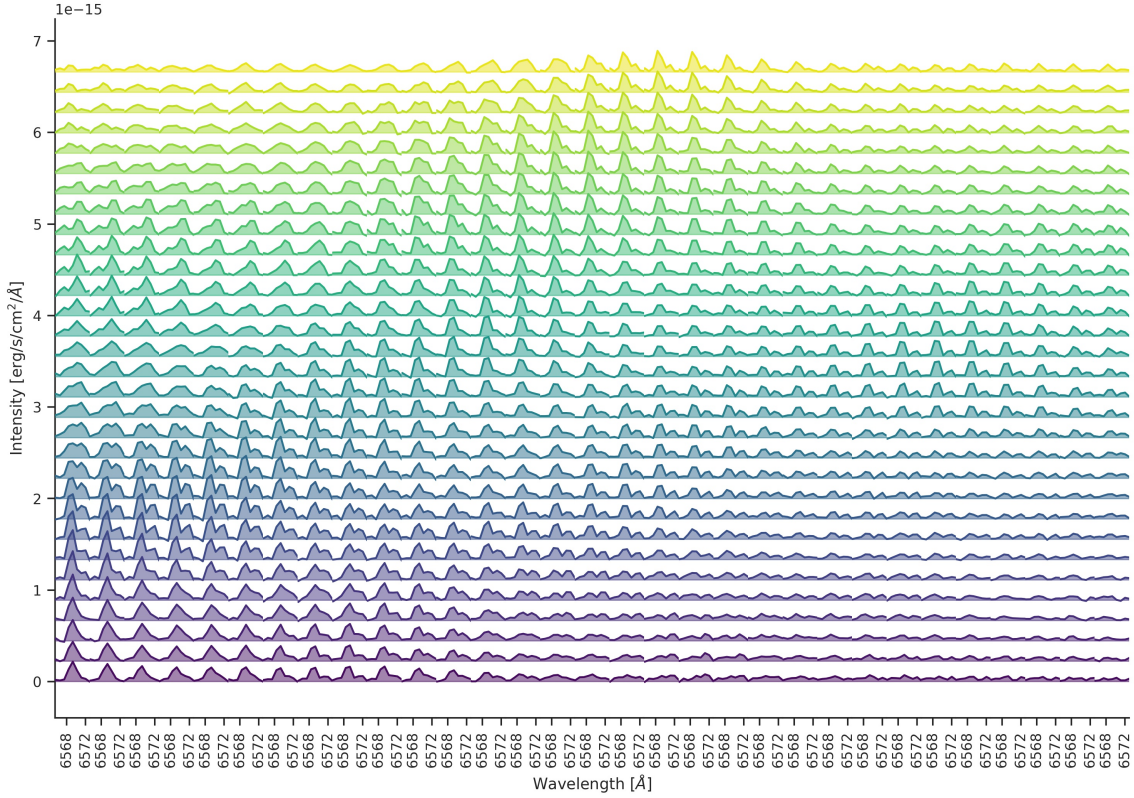


Figure 2.35 – Spectra of the H α line for each pixel from the region of the potential inflow/outflow, centred at RA 12h28m09.8s and DEC +44°05m49.2s in a \sim 180 pc \times 180 pc aperture. The intensity of the emission line is artificially scaled in order to display multiple spectra on the y axis.

components. A high spectral resolution would be required to better study the kinematics inside an individual H II region.

Figure 2.35 shows a mosaic of the H α line from each pixel located in the area of the potential gas flow, centred at RA 12h28m09.8s and DEC +44°05m49.2s. Figure 2.35 spatially covers a square of \sim 180 pc \times 180 pc. The baseline of the H α line is shifted in order to represent the spatial variation on the y axis, creating a spatial grid. The colours are only intended to help distinguish the spectra. Broadened emission lines and even double components are visible in many pixels.

Integrating in a circular aperture at the base of the suggested gas flow, centred at RA 12h28m09.8s and DEC +44°05m49.2s with a radius of \sim 90 pc, results in a spectrum showing two clear components in its H α emission line, as displayed in Figure 2.36. The left panel of Figure 2.36 shows the location of the aperture (teal circle) on the H α flux map and the right panel shows the integrated spectrum from this region (teal line) and the resulting ORCS fit done with two velocity components (blue line). The measured velocities of the components are (196 ± 1) km s $^{-1}$ and (302 ± 1) km s $^{-1}$, with a velocity dispersion of (30.0 ± 0.7) km s $^{-1}$ and

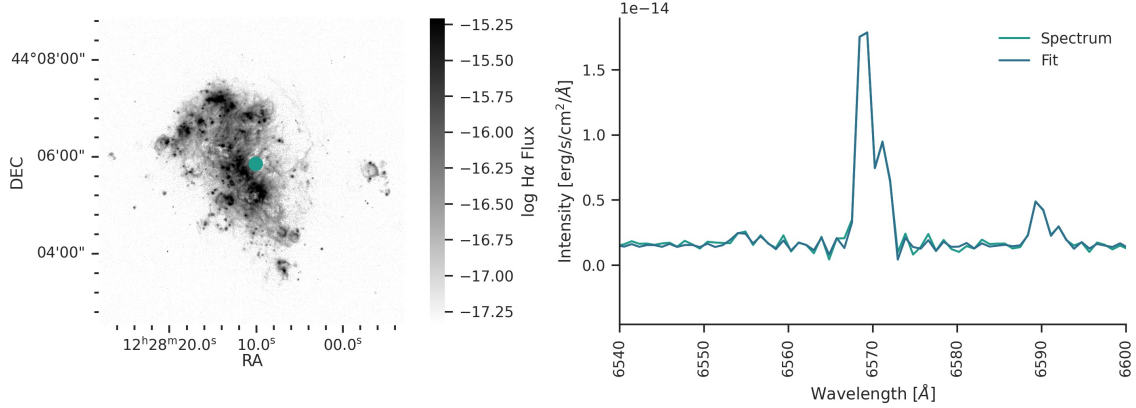


Figure 2.36 – Location (left panel, marked by a teal circle) and integrated spectrum (right panel) at the base of the potential inflow/outflow. The aperture is centred at RA 12h28m09.8s and DEC +44°05m49.2s with a radius of ~ 90 pc. The integrated spectrum correspond to the teal curve, and the blue curve corresponds to the resulting ORCS fit, using two sincgauss models.

(24 ± 2) km s $^{-1}$, respectively. The kinematical study done by Valdez-Gutiérrez et al. (2002), using the Fabry-Perot *PUMA* instrument, in this region (*i.e.* their region V76) also reveals two components with velocities of 199 km s $^{-1}$ and 288 km s $^{-1}$, and with a velocity dispersion of 26.4 km s $^{-1}$ and 22.1 km s $^{-1}$, respectively. These double components could be signatures as an outflow, it could also be two DIG filaments superimposed, or even an inflow.

Region 283, located slightly west from the base of the potential inflow/outflow, is the only emission region detected nearby. Two velocity components may still be observed in it, but are less prominent compared to the base (the region studied in Figure 2.36), as it is located further west. The spectrum of this region and its background, as well as its spatial location are displayed in Figure 2.37. Two different velocity components are clearly present in the region's spectrum, as well as the background's spectrum, for the H α line and the [N II] $\lambda 6583$. Valdez-Gutiérrez et al. (2002) does not detect any H II regions located near region 283, but it coincides spatially with the punctual X-ray emission source 11 detected by Summers et al. (2003), which is classified as an X-ray binary system.

Multiple suggestions have been made regarding the origin of this potential outflow. It is not believed that the outflow is related to an AGN, as no mention of the presence of one have been documented. No broad nor strong peculiar emission region in the centre of the galaxy is observed in our data, which reinforces the belief of the absence of an AGN. However, gas outflows and superwinds in the late-type galaxies in the Local Universe have been documented in the past related to active star formation (*e.g.* Kuchinski et al. 2000; Weaver 2001), thus it could be a possibility for NGC 4449 (Summers et al. 2003). This outflow is believed to be caused by stellar winds and supernova explosions causing pressure on the minor axis (Summers et al. 2003).

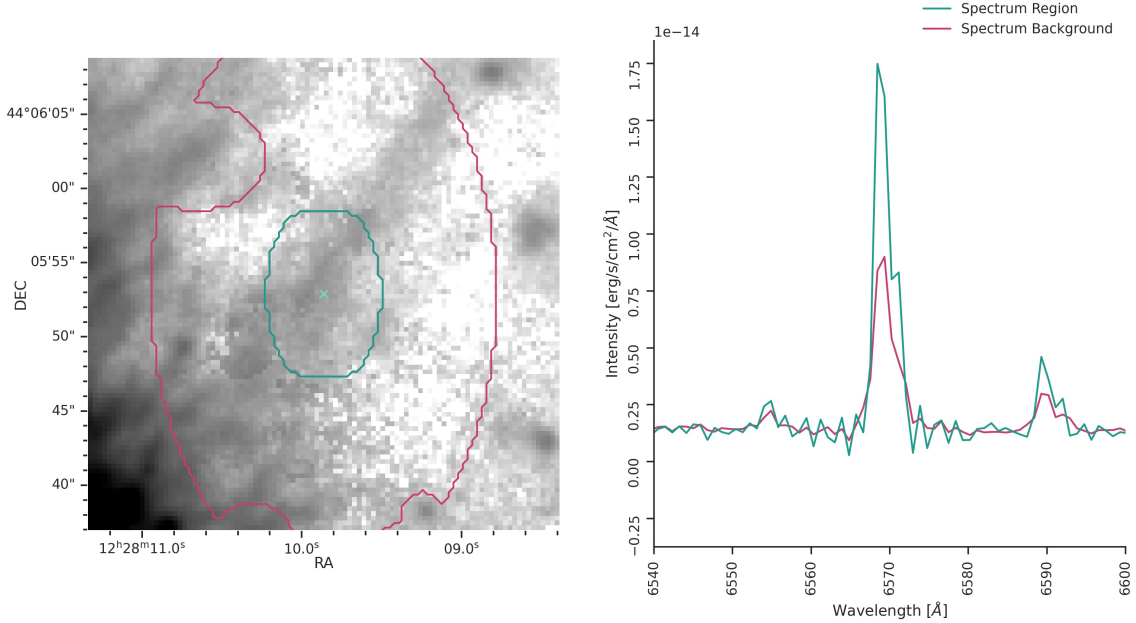


Figure 2.37 – Spatial location (left panel) and spectrum (right panel) of region 283 nearby the potential inflow/outflow, centred at RA 12h28m10.5s and DEC +44°06m00.4s. Its emission peak is marked by the teal cross on the log H α flux map (on the left panel), whilst the teal contour corresponds to the region’s domain, and the pink contour corresponds to its background domain. On the right panel, the teal curve corresponds to the spectrum associated with the emission regions, whilst the pink spectrum is the one associated with the background region. The spectrum is zoomed on the H α and [N II] lines, from the SN3 filter. The aperture size of the left panel is 597 pc × 597 pc.

Gas loss has been documented in dwarf galaxies (James et al. 2016; Meurer et al. 1992; Roy et al. 1991) caused by supernova explosions (Mac Low & Ferrara 1999), galactic winds originating from supernovae (Tremonti et al. 2004), or energy-driven outflows (Davé et al. 2013). These events carry energy and matter outside of the galaxy, into the intergalactic medium (Summers et al. 2003). The morphological link between the H α , H I and X-ray, along with the multiple velocity components, suggest that this type of outflow might be present in NGC 4449. The low angular velocity of the gas in the centre ($\sim 18 \text{ km s}^{-1}$; Hunter et al. 1998) could indicate a low escape velocity, however the large H I halo may prevent the hot ejecta from escaping the galaxy (Summers et al. 2003).

Kumari et al. (2017) suggest three mechanisms to explain the lower metallicity observed in their study at the centre of the galaxy. One of these mechanisms is a gas outflow of the newly enriched gas in the centre of the galaxy by supernovae-driven blowouts or galactic winds. Due to the low gravitational potential of NGC 4449, it is reasonable to believe in an exode of the newly formed high-metallicity gas (Kumari et al. 2017). However, as mentioned by Kumari et al. (2017), no supernovae remnants in the region of the nucleus of the galaxy have been detected by Summers et al. (2003) using the *Chandra Telescope*. The nearest documented

supernovae remnant lies about $1''$ north of the nucleus (Kumari et al. 2017) and is discussed in more details in Section 2.7.11.

Another mechanism proposed by Kumari et al. (2017) is an inflow, resulting in the accretion of metal-poor gas in the galaxy centre. This suggestion is also used by Sánchez Almeida et al. (2014, 2015) and Elmegreen et al. (2016) to explain their positive metallicity gradients. Accretion of gas has been suggested as an explanation of the starburst state of NGC 4449 and linked to past interactions by Karachentsev et al. (2007), Lelli et al. (2014b), and Martinez-Delgado et al. (2012). However, there is no strong reason for the new gas to be preferentially accreted in the centre of the galaxy, especially when considering the morphology of NGC 4449 and its low gravitational potential, due to its mass. On the other hand, Kumari et al. (2017) interpret the higher concentration of atomic gas in the galaxy centre, based on the H I map of Hunter et al. (1998), as indicating a possible source of the gas inflow in the centre of the galaxy. In addition, Kumari et al. (2017) also suggest that the inflow of low-metallicity gas could originate from the cosmic web and be primordial gas. This type of inflow would also cause chemical inhomogeneities (Ceverino et al. 2016) and Cresci et al. (2010) concluded that this was the cause of the positive metallicity gradients they observed in three rotationally-supported galaxies at a redshift $z \simeq 3$. Sánchez Almeida et al. (2015) also suggested that some localised starbursts in extremely metal-poor galaxies in the Local Universe are caused by the infall of primordial cosmic gas.

An alternative mechanism suggested by Kumari et al. (2017) is that the regions in the outskirts of the galaxy show a metallicity enhancement caused by accreted gas that has been pre-enriched by the past interacting galaxies. This alternate suggestion removes the need of an inflow/outflow to explain the inverse metallicity gradient (Kumari et al. 2017). However, this mechanism does not explain the presence of the multiple velocity components near the centre of the galaxy. Albeit, these multiple velocity components could be caused by superimposed DIG filaments, which would be inline with this suggested mechanism. Further studies of the global gas kinematics are required in order to confirm the presence of an outflow and the impact it would have on the galaxy.

The double components observed in Figure 2.35 are in agreement with the spectrum observed by Valdez-Gutiérrez et al. (2002) and consistent with the presence of an outflow, as suggested by Summers et al. (2003) and Kumari et al. (2017). However, the negative slope in the metallicity gradient, shown in Figure 2.33, is in disagreement with the positive slope obtained by Kumari et al. (2017) and constant gradient obtained by Scowen (1992), and inconsistent with the presence of an inflow of low-metallicity gas in the central region. In all cases, higher spectral resolution would be required in order to better resolve the multiple emission components on the line of sight to better understand the exact direction of the possible gas flow. The metallicity gradient should also be confirmed with the direct method.

2.7.11 Notable Objects

Summers et al. (2003) used X-ray data from the *Chandra Telescope* in the aim of studying the nature of point-like emission sources and the morphology of extended diffuse emission. They detect twenty-four point-like X-ray sources in NGC 4449. Seventeen of those sources are thought to be supernova remnants or X-ray binary systems, which would dynamically impact the ISM around them. These sources spatially correspond to nine of those detected in this study.

Reines et al. (2008) used radio data from the *Very Large Array*, in combination with ultraviolet, optical and infrared archived data from *Hubble Space Telescope*, and *Spitzer Space Telescope*, in order to study the embedded young massive clusters associated with the H II regions. Reines et al. (2008) detected 39 point-like radio sources in NGC 4449, out of which 37 spatially correspond to emission regions detected in this study. The correlation between the radio emission and the H II regions in NGC 4449 has previously been studied by Israel (1980), using the H II regions catalogue realised by Crillon & Monnet (1969). The presence of two sources without any matching optical counterparts is consistent with the findings from Reines et al. (2008), as no optical counterpart was found in *Hubble Space Telescope*'s data either. Thus all of the sources in Reines et al. (2008) are consistent with the findings in this study. Source 28 in Reines et al. (2008) does not have any optical counterpart. Source 6 in Reines et al. (2008) does not have any optical counterpart because it is thought to be a background AGN, which was not detected with *Chandra* by Summers et al. (2003).

Source 14 in Reines et al. (2008) and source 15 in Summers et al. (2003), correspond to region 467 in this catalogue, which is the young supernova remnant J1228+441 (studied lengthily, e.g. Balick & Heckman 1978; Bignell & Seaquist 1983; Blair et al. 1983, 1984; Patnaude & Fesen 2003; Seaquist & Bignell 1978) with an estimated age between 60–200 yr (Reines et al. 2008) and \sim 270 yr (Summers et al. 2003). The radio shows a spectrum with 2 components, a narrow-line ($<500 \text{ km s}^{-1}$) component and a broad-line ($\sim 4000 \text{ km s}^{-1}$) component (Seaquist & Bignell 1978). Seaquist & Bignell (1978) notes that the broad-line component is only observed in a few of the forbidden lines, especially [O I] and [O III]. Kirshner & Blair (1980) observed the broad-line components in the [O I] $\lambda\lambda 6300, 6363$, [O II] $\lambda\lambda 7320, 7330$, and [O III] $\lambda\lambda 4959, 5007$ and obtained a velocity dispersion of $\sim 3500 \text{ km s}^{-1}$.

The [O I] $\lambda\lambda 6300, 6363$ and [O II] $\lambda\lambda 7320, 7330$ emission lines is out of the spectral range covered by the data in this study, but the [O III] and the [O II] $\lambda\lambda 3726, 3729$ forbidden lines are observable. The spectrum centred on RA 12h28m10.9s and DEC +44°06m48.5s with an aperture of 18 pc, is shown in Figure 2.38. The spectrum is fitted with 2 sincgauss models. The [O III] line has a velocity dispersion for the narrow component of $(90 \pm 20) \text{ km s}^{-1}$ and for the broad component of $(2300 \pm 400) \text{ km s}^{-1}$. The [O II] $\lambda\lambda 3726, 3729$ line has a velocity dispersion, of $(135 \pm 9) \text{ km s}^{-1}$ and of $(1600 \pm 200) \text{ km s}^{-1}$, respectively. The measured velocity dispersion

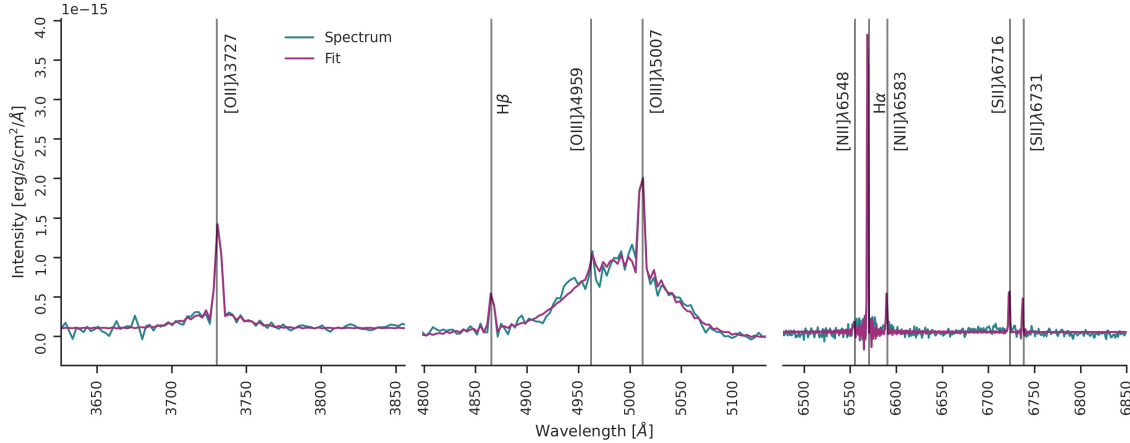


Figure 2.38 – Spectrum of the young supernova remnant J1228+441 in all three filters, centred at RA 12h28m10.9s and DEC +44°06m48.5s. The spectrum (teal curve) is integrated in an aperture with a radius of 18 pc. The fit (pink curve) is obtained with ORCS, using two sincgauss models. No background is subtracted. The different emisison lines are identified with the vertical grey lines.

Table 2.3 – Line ratios of region 467.

Line Ratio	Blair et al. (1983)	Scowen (1992)	This study
$\log [\text{O III}]/\text{H}\beta$	0.56	0.63	(0.5 ± 0.3)
$\log \text{H}\alpha/\text{H}\beta$	0.56	0.46	(0.45 ± 0.07)
$\log [\text{S II}]/\text{H}\alpha$	-0.51	-0.94	(-0.8 ± 0.3)

does not exactly match the ones obtained by Seaquist & Bignell (1978) and Kirshner & Blair (1980); nevertheless, this spectrum exhibits a peculiar dynamics.

The young supernova remnant J1228+441 is not directly located at the exact centroid of region 467. The narrow-line component is believed to be emitted from a superimposed H II region (Seaquist & Bignell 1978) which could explain the offset. Seaquist & Bignell (1978) notes an emission knot below the radio emission, which could correspond to the detected region. The measured radial velocities of $(190.4 \pm 0.3) \text{ km s}^{-1}$ from the H α line, suggests that the emission is correlated to NGC 4449, and not caused by another extragalactic object on the line of sight, as proposed by Seaquist & Bignell (1978).

Scowen (1992) and Blair et al. (1983) calculated the line ratios for the H II region (region 107 in the catalogue of Scowen 1992) associated with the young SNR. The values obtained by each study is presented in Table 2.3. All the line ratios obtained for region 467 fall in the range of the values obtained by Blair et al. (1983) and Scowen (1992). However, it is important to note that the region's domains in the study of Blair et al. (1983) and Scowen (1992) are not exactly defined as the one in this study, due to the different data resolution and detection method. Scowen (1992) has a larger box, with a size of $296 \text{ pc} \times 222 \text{ pc}$ (corrected for the

distance assumed in our study), compared to the region from this study (region 467), which is $(14.8 \pm 0.5) \text{ pc} \times (10.1 \pm 0.3) \text{ pc}$. Hence, the variations in the value of the line ratios may be caused by the fact that a wider area is considered by Scowen (1992).

Source 13 in Reines et al. (2008), corresponding to region 483 in our catalogue, is thought to be a supernova remnant partially embedded in a H II region, but was not detected by the *Chandra Telescope* in Summers et al. (2003).

2.7.12 Nature of the Emission Regions

The tool developed by Rhea et al. (in prep.) is used in order to gain more insight on the source of ionization of the emission regions detected. It uses line ratios and machine learning algorithms (see Rhea et al. (in prep.) for a more detailed description) to classify the most probable object type: either as an H II region, a planetary nebulae, or a supernova remnant.

Emission regions with a classification probability lower than 80 % and greater to 99 % are rejected from the sample as they are not considered reliable. Emission regions classified as a H II region with a $\text{H}\alpha$ S/N lower than 20 are rejected as well. Emission regions classified as a supernova remnant with a $[\text{S II}]\lambda 6716$ S/N and $[\text{S II}]\lambda 6548$ S/N lower than 3 are rejected. This leaves 380 emisssion regions in the sample used for Figures 2.39 and 2.40.

356 detections were classified as H II regions, which confirms that most of the emission regions detected are in fact consistent with the emission of standard H II regions. 19 are classified as possible planetary nebulae and 5 as possible supernova remnants. Their spatial distribution is shown in Figure 2.39, where the markers are colour coded by their predicted object type. The black markers correspond to the emission regions that have been rejected. Note that the classifier works very well for the identification of H II regions while some observational bias affect its ability to perform well for the planetary nebulae and the supernova remnants. For example, in the west arc located in the outskirt of the galaxy, a high concentration of planetary nebulae and supernova are detected, which are very unlikely to be real. This area is probably a shock emission driven filament, which is not well represented by the models used for this classification method. Also, the supernova remnants classified regions seem to fall into regions of high DIG and filaments in Figure 2.39, which are often associated with shocks.

The regions classified as supernova remnants do not coincide with the punctual objects detected by the *Chandra Telescope* classified as potential supernova remnants by Summers et al. (2003) using X-ray emission. Also, the very-well known young SNR observed by Balick & Heckman (1978), Bignell & Seaquist (1983), Blair et al. (1983, 1984), Lacey et al. (2007), Patnaude & Fesen (2003), Seaquist & Bignell (1978), and Summers et al. (2003) is not classified here as a supernova remnant, possibly due to its unusual line ratios as discussed more in Section 2.7.11.

Out of the 19 detections classified as planetary nebulae, 7 (with a classification probability greater than 75 %) of them coincide with punctual objects catalogued by Summers et al. (2003) using the *Chandra Telescope* and Reines et al. (2008) by using the *Very Large Array Telescope*. Regarding the X-ray sources, region 442 falls near the source 17 catalogued by Summers et al. (2003), which is classified as a potential supernova remnant or a X-ray binary. Region 283 falls on source 11 catalogued by Summers et al. (2003), which is classified as a X-ray binary. The probability that region 283 is a planetary nebula is 78.4 %. This region is located in a potential outflow of the galaxy (Summers et al. 2003). Thus, it is consistent with the hypothesis that the classification may not be accurate, but a strong indicator that it is atypical for an H II region. Kinematically, this region is also different from the standard H II regions, as it possesses two velocity components (discussed more in Section 2.7.11). Regarding the radio sources, region 339 falls near the source 24 catalogued by Reines et al. (2008) and region 461 falls on the source 8 catalogued by Reines et al. (2008), whose classification is uncertain. Region 249 coincides with the source 16 catalogued by Reines et al. (2008) and region 232 falls on the source 12 catalogued by Reines et al. (2008), whose type is classified as mixed. Region 173 falls near on the source 5 catalogued by Reines et al. (2008), which is classified as likely thermal.

Figure 2.40 shows the BPT diagrams, colour coded by the classified object type. The black curves are the same as in Figure 2.22. Most of the emission regions fall below the H II region line (Kewley et al. 2001), especially for the [O III] versus [N II] BPT diagram (left panel). As mentioned in Section 2.7.6, this confirms that most of the emission regions detected correspond to H II regions. It is also possible to see that the other types of objects fall into clusters near or above the H II region line in both BPT diagrams in Figure 2.40. Thus, the machine learning technique confirms the conclusions obtained by the classical approach. On the [O III] versus [S II] BPT diagram (right panel), the regions classified as planetary nebulae and supernova remnants fall outside of the H II region line (Kewley et al. 2001), which is consistent with their line ratios being atypical for H II regions. These same regions (planetary nebulae and supernova remnants) fall below the H II regions line on the [O III] versus [N II] BPT diagram (left panel) but above it in the [O III] versus [S II] BPT diagram (right panel). This is partly attributable by the fact that the [S II] emission is higher in DIG than H II regions.

These results suggest that the emission regions classified as planetary nebulae and supernova remnants might in fact be different objects than H II regions or object contaminated by the emission of multiple sources. More precise spectroscopic studies are required to confirm their existence, however they are beyond the scope of this study. It is most likely that these emission regions are not the predicted object type by the classification, as they have not yet been catalogued (*e.g.* by Summers et al. (2003) using the *Chandra Telescope* and Reines et al. (2008) by using the *Very Large Array Telescope*). In any case, these regions do not possess typical H II regions line ratios. Thus, they deserve to be studied more in depth in their own

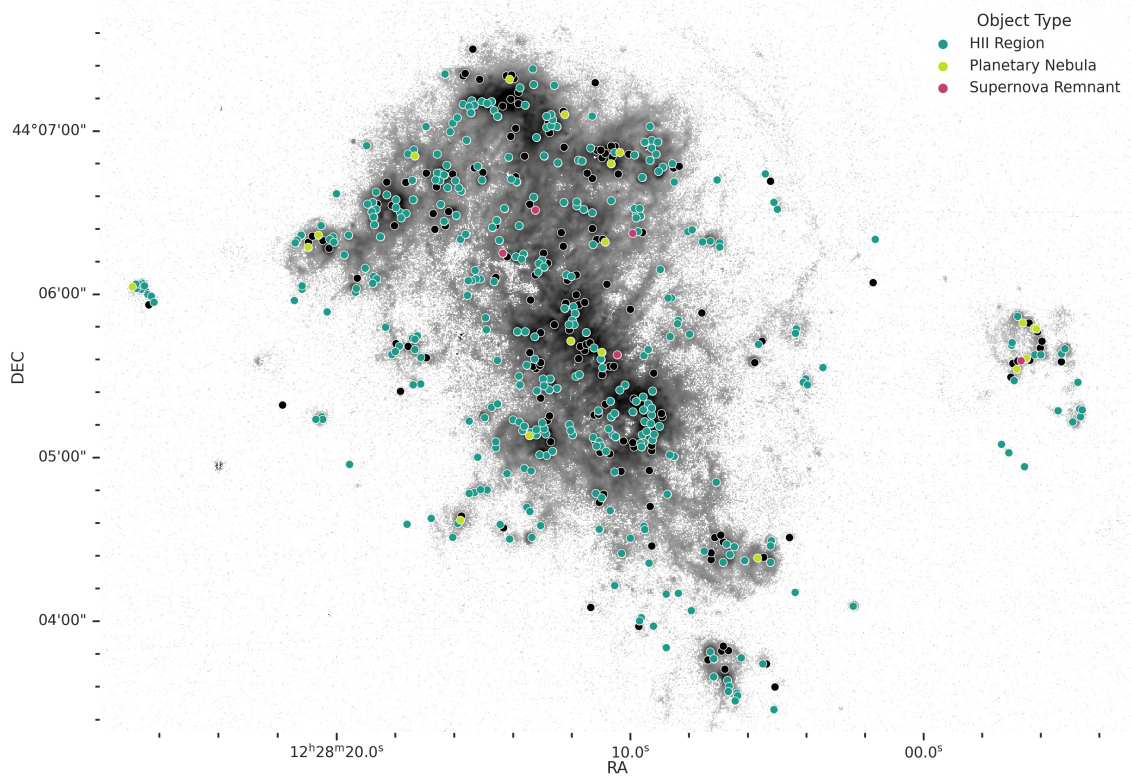


Figure 2.39 – Spatial distribution of the predicted object type for the emission regions classified by the algorithm described in Rhea et al. (in prep.). Each detection is colour coded by its predicted object type. The detections are spatially plotted over the log H α flux map, where the pixels with a H α or H β S/N lower than 1 are not shown. The black regions are the regions with a classification probability lower than 80 % and greater to 99 % or a S/N lower than 3, which were rejected from the sample.

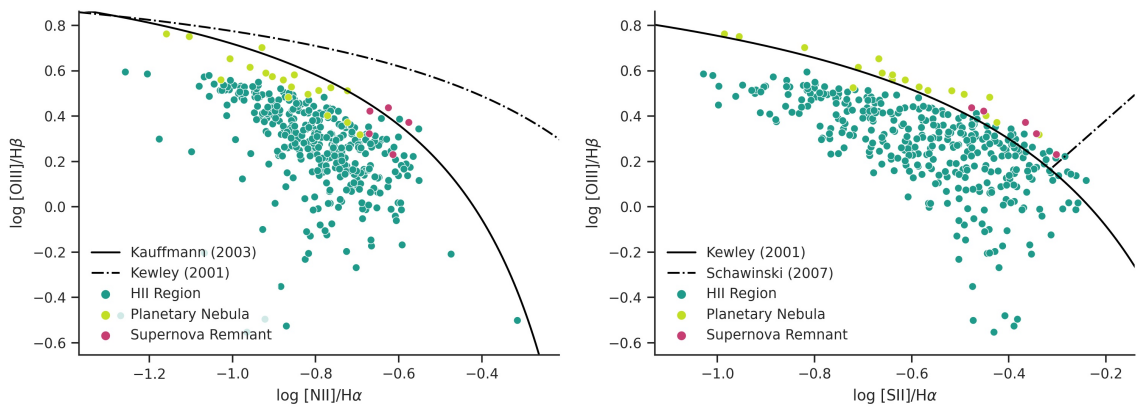


Figure 2.40 – BPT diagrams of the emission regions, colour coded with their predicted object type, classified by the algorithm described in Rhea et al. (in prep.). On the left panels, the Kauffmann et al. (2003) curve is plotted in solid black and the Kewley et al. (2001) curve in dashed black. On the right panels, the Schawinski et al. (2007) curve is plotted in dashed black.

right.

2.8 Conclusions

The H II regions of NGC 4449 have been the subject of many researches in order to better understand the star formation and evolution of irregular galaxies. A high detection level was used for the detection, as to avoid DIG regions that are ubiquitous in NGC 4449 and to focus on its H II regions. A catalogue of 535 emission regions is compiled, using the method developed for this purpose by Savard et al. (in prep.). This catalogue provides insight into the statistical behaviour of these regions.

The luminosity function is studied and its slope, $\alpha = -1.08 \pm 0.07$, is significantly shallower than the ones obtained in previous studies; -1.48 (Kennicutt et al. 1989), -1.9 (Fuentes-Masip et al. 2000a), -1.93 ± 0.02 (Valdez-Gutiérrez et al. 2002), -1.43 (Gutiérrez et al. 2011). However, the high spatial resolution of the data, the large field of view, and the improved methodology used allow for a better and different sampling of the faint end of the luminosity function by disentangling of the H II region complexes.

None the less, the total H α luminosity from the H II regions is in agreement with the value of Kennicutt et al. (1989), but not of Valdez-Gutiérrez et al. (2002); albeit considered relatively close, and Gutiérrez et al. (2011). However, the fraction of the H α luminosity from the H II regions measured in this study is in agreement with the values obtained by Kennicutt et al. (1989) and Gutiérrez et al. (2011), but not of Valdez-Gutiérrez et al. (2002), due to their assumed total H α luminosity of the galaxy.

The size function of the emission regions is also studied and the characteristic diameter, (48 ± 6) pc or $2''.6 \pm 0''.3$, is not in agreement with previous studies; $6''.2$ (Sabbadin & Bianchini 1979), $3''.2$ (van den Bergh 1981), $5''.5$ (Hodge 1983), $1''.6$ (Fuentes-Masip et al. 2000b), $1''.73 \pm 0''.10$ (Valdez-Gutiérrez et al. 2002), but the value falls between two groups of values. Once again, this discrepancy is explained by the higher spatial resolution of the data used in this study. No strong correlation between the H α luminosity, size, and velocity dispersion is observed for all the emission regions.

The proximity distance between the emission regions shows that the H II complexes are better resolved due to the higher spatial sampling, compared to the values obtained by Rousseau-Nepton et al. (2018) for NGC 628 at ~ 9 Mpc using SITELLE data and by Hunter et al. (1982) for NGC 4449.

The line ratios of the ionized gas, for each pixels of the entire galaxy and for the integrated emission regions are computed and the variations within the galaxy are studied. BPT diagrams for the regions confirm that most of the detected emission regions are H II regions. The properties of the background emission (DIG) are similar to the H II regions, suggesting a

common origin (*i.e.* photons escaping the H II regions).

The location of the emission regions is compared with the LEGUS stellar clusters' positions from the catalogue of Adamo et al. (2017). 40 % of the clusters coincide with an emission region. These associations are studied in relation with the age and mass of the stellar clusters and their position in the galaxy's central bar and northern arm, showing different stellar cluster populations. This could be caused by different star formation histories in the galactic features.

The low metallicity of the H II regions (on average 8.27 ± 0.07), obtained using the *N2O2* indicator from Pilyugin & Grebel (2016), is in agreement with most past studies. Our systematic study of our large sample of emission regions results in a clear metallicity gradient with a negative slope of $(-4.8 \pm 0.4) \times 10^{-5} \text{ pc}^{-1}$ throughout the galaxy, with the centre of the galaxy at 8.32. This result is the opposite of the trend obtained by Kumari et al. (2017), using the direct method and sampling only four locations in the galaxy with data from multiple studies. It is also in contradiction with the constant metallicity observed throughout the galaxy by Scowen (1992).

The global ionized gas and H II regions kinematics are also studied, indicating they coincide quite well with each other. Multiple velocity components near the centre of the galaxy also supports the potential inflow/outflow suggested by Summers et al. (2003) and Kumari et al. (2017).

The chemical profiles of the detected emission regions are classified using a machine learning tool developed by Rhea et al. (in prep.). This corroborates the results from the BPT diagrams, indicating that most of the detected emission regions are H II regions. A few of them are classified as planetary nebulae and supernova remnants, but do not correspond to documented objects. Yet, they do not possess the classical chemical ratios of H II regions and should be investigated further.

Throughout this study, the comparison between the properties of the emission regions' population (located in the central bar and the northern arm) is conducted, with the aim of gaining insight on NGC 4449's star formation history. Globally, the emission regions in the central bar are more luminous than in the northern arm. However, they do not possess statistically different sizes. In spite of that fact, they do have statistically different proximity distances between the H II regions on both galactic structures. Chemically, these populations also differ. In the BPT diagrams, the regions located in the central bar lie closer to the limit of the H II regions' regime and in a more compact cluster, globally showing a less diverse chemical profiles. The LEGUS star clusters show a statistically younger age distribution when associated to an emission region located in the northern arm, compared to the ones in the central bar. The average velocity dispersion also varies between the two populations. These differences might indicate that two episodes or modes of stellar formation are taking place in NGC 4449.

Different mechanisms, such as a gas flow, may be present, causing local differences in the initial mass function or in the temporal-scales of the stellar formation processes.

Further investigation is required in order to study the DIG emission in NGC 4449. An improved method could allow to detect odd-shaped regions, such as rings and filaments, resulting in a better understanding of their global properties. This more sophisticated detection method could remove the need to assume that the spatial morphology of the H II regions are represented by a 2D Gaussian profile. This would allow for a greater diversity in the emission region's morphology. It could also lead to a better distinction of the nature of the emission source, allowing to better classify them. A higher spectral resolution could help resolve the multiple velocity components in order to understand more the potential outflow phenomenon observed in the centre of the galaxy. It might also allow to better model the potential rotation curve of the disc of the galaxy. Observations with the C2 filter, to cover the $[\text{O II}]\lambda 4363$ line, should be attempted in order to use the more accurate direct method to measure the metallicity systematically over the whole galaxy. With all the information in hands, detailed simulations may be the next step to understand NGC 4449's formation.

The systematic methodology developed to detect and study the emission regions will be applied to the other galaxies in the SIGNALS sample. Similar work has already been done for other galaxies by Rousseau-Nepton et al. (2018) on NGC 628, by Savard et al. (in prep.) on NGC 7479, and by Massé et al. (in prep.) on NGC 1637. These studies and future studies on galaxies of diverse morphological types will enable the analysis of the differences in the emission regions population. Thus, a better understanding of the stellar formation processes will be acquired for galaxies with different properties and environments.

Acknowledgements

This work is based on observations obtained with SITELLE, a joint project of Université Laval, ABB, Université de Montréal, and the Canada-France-Hawaii Telescope which is operated by the National Research Council of Canada (NSERC), the Institut National des Sciences de l'Univers of the Centre National de la Recherche Scientifique of France, and the University of Hawaii. The authors wish to recognize and acknowledge the very significant cultural role that the summit of Mauna Kea has always had within the indigenous Hawaiian community. We are most grateful to have the opportunity to conduct observations from this mountain. J. Giroux and E. Massé are grateful for the Hubert Reeves fellowship. J. Giroux, E. Massé, G. Savard, and S. Vicens are grateful for a CRAQ/FRQNT fellowship. C. Robert and L. Drissen are grateful to NSERC and FRQNT for financial support.

References

- Adamo, A. et al. (2017). *ApJ* 841, p. 131.
- Anderson, L. D. et al. (2014). *ApJS* 212, p. 1.
- Annibali, F. et al. (2008). *AJ* 135, pp. 1900–1916.
- Annibali, F. et al. (2011). *AJ* 142, p. 129.
- Annibali, F. et al. (2012). *ApJ* 745, p. L1.
- Annibali, F. et al. (2017). *ApJ* 843, p. 20.
- Arora, R., Krumholz, M. R., and Federrath, C. (2021). *MNRAS* 508.3, pp. 3290–3303.
- Arsenault, R. and Roy, J.-R. (1988). *A&A* 201, pp. 199–207.
- Arsenault, R., Roy, J.-R., and Boulesteix, J. (1990). *A&A* 234, p. 23.
- Bajaja, E., Huchtmeyer, W. K., and Klein, U. (1994). *A&A* 285, pp. 385–388.
- Baldwin, J. A., Phillips, M. M., and Terlevich, R. (1981). *PASP* 93, pp. 5–19.
- Balick, B. and Heckman, T. (1978). *ApJ* 226, pp. L7–L10.
- Berg, D. A. et al. (2012). *ApJ* 754, p. 98.
- van den Bergh, S. (1981). *AJ* 86, pp. 1464–1467.
- Bignell, R. C. and Seaquist, E. R. (1983). *ApJ* 270, pp. 140–143.
- Blair, W. P., Kirshner, R. P., and Winkler Jr., P. F. (1983). *ApJ* 272, pp. 84–91.
- Blair, W. P. et al. (1984). *ApJ* 279, pp. 708–713.
- Böker, T. et al. (2001). *AJ* 121, pp. 1473–1481.
- Brown, A. G. A. et al. (2021). *A&A* 649, A1.
- Buckalew, B. A. and Kobulnicky, H. A. (2006). *AJ* 132, pp. 1061–1073.
- Buckalew, B. A., Kobulnicky, H. A., and Dufour, R. J. (2005). *ApJS* 157, pp. 30–58.
- Calzetti, D. et al. (2015). *AJ* 149.2, p. 51.
- Calzetti, D. et al. (2018). *ApJ* 852, p. 106.
- Capuzzo Dolcetta, R., Di Matteo, P., and Miocchi, P. (2005). *AJ* 129, pp. 1906–1921.
- Cardelli, J. A., Clayton, G. C., and Mathis, J. S. (1989). *ApJ* 345, p. 245.
- Ceverino, D. et al. (2016). *MNRAS* 457, pp. 2605–2612.
- Chávez, R. et al. (2014). *MNRAS* 442.4, pp. 3565–3597.
- Chyží, K. T. et al. (2000). *A&A* 355, pp. 128–137.
- Cignoni, M. et al. (2018). *ApJ* 856.1, p. 62.
- Cignoni, M. et al. (2019). *ApJ* 887, p. 112.
- Cook, D. O. et al. (2014). *MNRAS* 445, pp. 899–912.
- Cresci, G. et al. (2010). *Nature* 467, pp. 811–813.
- Crillon, R. and Monnet, G. (1969). *A&A* 1, p. 449.
- Davé, R., Finlator, K., and Oppenheimer, B. D. (2011). *MNRAS* 416, pp. 1354–1376.
- Davé, R. et al. (2013). *MNRAS* 434, pp. 2645–2663.
- Denicoló, G., Terlevich, R., and Terlevich, E. (2002). *MNRAS* 330, pp. 69–74.
- Dopita, M. A. et al. (2016). *Ap&SS* 361, p. 61.
- Drissen, L. et al. (2019). *MNRAS* 485, pp. 3930–3946.

- Dyson, J. E. (1979). *A&A* 73.1-2, pp. 132–136.
- Edmunds, M. G. and Pagel, B. E. J. (1984). *MNRAS* 211, pp. 507–519.
- Elmegreen, D. M. and Elmegreen, B. G. (1980). *AJ* 85, pp. 1325–1327.
- Elmegreen, D. M. et al. (2016). *ApJ* 825, p. 145.
- Elwert, T. and Dettmar, R. -. (2005). « Photoionization Models of the DIG in Galactic Halos ». *Extra-Planar Gas*. Vol. 331, p. 203.
- Engelbracht, C. W. et al. (2008). *ApJ* 678, pp. 804–827.
- Espinosa-Ponce, C. et al. (2020). *MNRAS* 494.2, pp. 1622–1646.
- Feinstein, C. (1997). *ApJS* 112, pp. 29–47.
- Fisher, J. R. and Tully, R. B. (1981). *ApJS* 47, pp. 139–200.
- Fuentes-Masip, O., Castaneda, H. O., and Munoz-Tunon, C. (1995). « New Methods to Measure HII Regions Diameters ». *IAU Colloq. 149: Tridimensional Optical Spectroscopic Methods in Astrophysics*. Vol. 71. ASP Conference Series. Marseille, France: Astronomical Society of the Pacific, p. 143.
- Fuentes-Masip, O., Castañeda, H. O., and Muñoz-Tuñón, C. (2000a). *AJ* 119.5, p. 2166.
- Fuentes-Masip, O. et al. (2000b). *AJ* 120.2, p. 752.
- Gallagher, J. S. and Hunter, D. A. (1983). *ApJ* 274, pp. 141–151.
- González Delgado, R. M. and Pérez, E. (1997). *ApJS* 108, pp. 199–228.
- Gutiérrez, L. and Beckman, J. E. (2010). *ApJ* 710, pp. L44–L48.
- Gutiérrez, L., Beckman, J. E., and Buenrostro, V. (2011). *AJ* 141.4, p. 113.
- Haffner, L. M., Reynolds, R. J., and Tufte, S. L. (1999). *ApJ* 523, pp. 223–233.
- Hakobyan, A. A. et al. (2007). *Astrophysics* 50, pp. 426–439.
- Harris, C. R. et al. (2020). *Nature* 585.7825, pp. 357–362.
- Hartmann, L. W., Geller, M. J., and Huchra, J. P. (1986). *AJ* 92, pp. 1278–1290.
- Hill, R. S. et al. (1998). *ApJ* 507, pp. 179–198.
- Hippelein, H. H. (1986). *A&A* 160, p. 374.
- Hodge, P. W. (1974). *PASP* 86, p. 845.
- Hodge, P. W. (1976). *ApJ* 205, pp. 728–744.
- Hodge, P. W. (1983). *AJ* 88, pp. 1323–1329.
- Hodge, P. W. and Kennicutt Jr., R. C. (1983). *AJ* 88, pp. 296–328.
- Hodge, P., Kennicutt, R. C., and Strobel, N. (1994a). *PASP* 106, p. 765.
- Hodge, P., Lee, M. G., and Kennicutt Jr., R. C. (1989a). *PASP* 101, p. 32.
- Hodge, P. and Lee, M. G. (1990). *PASP* 102, p. 26.
- Hodge, P., Lee, M. G., and Kennicutt Robert C., J. (1989b). *PASP* 101, p. 640.
- Hodge, P., Strobel, N. V., and Kennicutt, R. C. (1994b). *PASP* 106, p. 309.
- Hodge, P. W. (1967). *AJ* 72, p. 129.
- Hodge, P. W. (1969a). *ApJ* 156, p. 847.
- Hodge, P. W. (1969b). *ApJS* 18, p. 73.
- Hodge, P. W. (1987). *PASP* 99, pp. 915–920.

- Huchtmeier, W. K., Seiradakis, J. H., and Materne, J. (1981). *A&A* 102, pp. 134–141.
- Hunter, D. A. (1982). *ApJ* 260, pp. 81–103.
- Hunter, D. A., Gallagher, J. S., and Rautenkranz, D. (1982). *ApJS* 49, pp. 53–88.
- Hunter, D. A. and Gallagher, J. S. (1986). *PASP* 98.599, pp. 5–28.
- Hunter, D. A. and Gallagher III, J. S. (1997). *ApJ* 475, pp. 65–82.
- Hunter, D. A., Woerden, H. van, and Gallagher, J. S. (1999). *AJ* 118, pp. 2184–2210.
- Hunter, D. A. et al. (1998). *ApJ* 495, pp. L47–L50.
- Israel, F. P. (1980). *A&A* 90, pp. 246–268.
- Izotov, Y. I. et al. (2006). *A&A* 448.3, pp. 955–970.
- James, B. L. et al. (2016). *ApJ* 816, p. 40.
- Karachentsev, I. D., Karachentseva, V. E., and Huchtmeier, W. K. (2007). *Astronomy Letters* 33, pp. 512–519.
- Karczewski, O. L. et al. (2013). *MNRAS* 431, pp. 2493–2512.
- Kauffmann, G. et al. (2003). *MNRAS* 346.4, pp. 1055–1077.
- Kennicutt, J. (1998). *ARA&A* 36.1, pp. 189–231.
- Kennicutt, R. C. and Hodge, P. W. (1980). *ApJ* 241, pp. 573–586.
- Kennicutt Jr., R. C. (1979). *ApJ* 228, pp. 394–404.
- Kennicutt Jr., R. C. (1984). *ApJ* 287, pp. 116–130.
- Kennicutt Jr., R. C. (1988). *ApJ* 334, p. 144.
- Kennicutt Jr., R. C., Edgar, B. K., and Hodge, P. W. (1989). *ApJ* 337, p. 761.
- Kewley, L. J. and Dopita, M. A. (2002). *ApJS* 142, pp. 35–52.
- Kewley, L. J. et al. (2001). *ApJ* 556.1, p. 121.
- Kewley, L. J. et al. (2010). *ApJ* 721, pp. L48–L52.
- Kirshner, R. P. and Blair, W. P. (1980). *ApJ* 236, pp. 135–142.
- Knapen, J. H. et al. (1993). *AJ* 106, p. 56.
- Kobulnicky, H. A., Kennicutt Jr., R. C., and Pizagno, J. L. (1999). *ApJ* 514, pp. 544–557.
- Kobulnicky, H. A. and Kewley, L. J. (2004). *ApJ* 617, pp. 240–261.
- Kreckel, K. et al. (2016). *ApJ* 827, p. 103.
- Kuchinski, L. E. et al. (2000). *ApJS* 131, pp. 441–463.
- Kumari, N., James, B. L., and Irwin, M. J. (2017). *MNRAS* 470.4, pp. 4618–4637.
- Kunth, D. and Östlin, G. (2000). *A&ARv* 10.1-2, pp. 1–79.
- Lacey, C. K., Goss, W. M., and Mizouni, L. K. (2007). *AJ* 133, pp. 2156–2162.
- Larson, R. B. (1983). *Highlights of Astronomy* 6, pp. 191–198.
- Lee, J. C. et al. (2009). *ApJ* 706, pp. 599–613.
- Lee, J. C. et al. (2011). *ApJS* 192, p. 6.
- Leitherer, C., Robert, C., and Drissen, L. (1992). *ApJ* 401, p. 596.
- Lelli, F., Verheijen, M., and Fraternali, F. (2014a). *A&A* 566, A71.
- Lelli, F., Verheijen, M., and Fraternali, F. (2014b). *MNRAS* 445, pp. 1694–1712.
- Lequeux, J. et al. (1979). *A&A* 80, p. 155.

- Levesque, E. M., Kewley, L. J., and Larson, K. L. (2010). *AJ* 139, pp. 712–727.
- Li, Z. et al. (2022).
- Luridiana, V., Morisset, C., and Shaw, R. A. (2015). *A&A* 573, A42.
- Mac Low, M.-M. and Ferrara, A. (1999). *ApJ* 513, pp. 142–155.
- MacKenty, J. W. et al. (2000). *AJ* 120, pp. 3007–3026.
- Malumuth, E. M., Williams, T. B., and Schommer, R. A. (1986). *AJ* 91, pp. 1295–1300.
- Marble, A. R. et al. (2010). *ApJ* 715, pp. 506–540.
- Marino, R. A. et al. (2013). *A&A* 559, A114.
- Martin, C. L. (1997). *ApJ* 491, pp. 561–583.
- Martin, P. and Roy, J.-R. (1994). *ApJ* 424, p. 599.
- Martin, T., Drissen, L., and Joncas, G. (2015). « ORBS, ORCS, OACS, a Software Suite for Data Reduction and Analysis of the Hyperspectral Imagers SITELLE and SpiOmm ». *Astronomical Data Analysis Software an Systems XXIV (ADASS XXIV)*. Vol. 495, p. 327.
- Martin, T., Drissen, L., and Prunet, S. (2021). *MNRAS* 505, pp. 5514–5529.
- Martin, T. B., Drissen, L., and Melchior, A.-L. (2018). *MNRAS* 473, pp. 4130–4149.
- Martin, T. B., Prunet, S., and Drissen, L. (2016). *MNRAS* 463, pp. 4223–4238.
- Martinez-Delgado, D. et al. (2012). *ApJ* 748.2, p. L24.
- Massé, E., Robert, C., and Drissen, L. (in prep.).
- McCall, M. L., Rybski, P. M., and Shields, G. A. (1985). *ApJS* 57, pp. 1–62.
- McQuinn, K. B. W. et al. (2010). *ApJ* 721, pp. 297–317.
- Melnick, J. (1977). *ApJ* 213, pp. 15–17.
- Melnick, J. (1979). *ApJ* 228, pp. 112–117.
- Melnick, J., Terlevich, R., and Moles, M. (1988). *MNRAS* 235, pp. 297–313.
- Melnick, J. et al. (1987). *MNRAS* 226, pp. 849–866.
- Menon, S. H. et al. (2021). *MNRAS* 507, pp. 5542–5566.
- Meurer, G. R. et al. (1992). *AJ* 103, p. 60.
- Miller, B. W. and Hodge, P. (1994). *ApJ* 427, p. 656.
- Munoz-Tunon, C. (1994). « Supersonic Motions in Giant HII Regions ». *Violent Star Formation: From 30 Doradus to QSOs*. Cambridge: Cambridge University Press, pp. 25–38.
- Munoz-Tunon, C., Fuentes-Masip, O., and Castañeda, H. (1998). *Publ. Astron. Soc. Australia* 15, pp. 103–5.
- Odenkirchen, M. et al. (2003). *AJ* 126, pp. 2385–2407.
- Osterbrock, D. E. (1989). *Astrophysics of gaseous nebulae and active galactic nuclei*. University Science Books.
- Patnaude, D. J. and Fesen, R. A. (2003). *ApJ* 587, pp. 221–226.
- Peñarrubia, J. et al. (2009). *ApJ* 698, pp. 222–232.
- Pettini, M. and Pagel, B. E. J. (2004). *MNRAS* 348, pp. L59–L63.
- Pilyugin, L. S. and Grebel, E. K. (2016). *MNRAS* 457, pp. 3678–3692.
- Rand, R. J. (1992). *AJ* 103, p. 815.

- Reines, A. E., Johnson, K. E., and Goss, W. M. (2008). *AJ* 135, pp. 2222–2239.
- Rhea, C. L. et al. (2021). *ApJ* 923.2, p. 169.
- Rhea, C. L. et al. (in prep.).
- Rich, R. M. et al. (2012). *Nature* 482.7384, pp. 192–194.
- Rousseau-Nepton, L. et al. (2018). *MNRAS* 477, pp. 4152–4186.
- Rousseau-Nepton, L. et al. (2019). *MNRAS* 489, pp. 5530–5546.
- Roy, J.-R., Arsenault, R., and Joncas, G. (1986). *ApJ* 300, p. 624.
- Roy, J.-R. et al. (1991). *ApJ* 367, p. 141.
- Rozas, M., Beckman, J. E., and Knapen, J. H. (1996). *A&A* 307, pp. 735–744.
- Rozas, M., Zurita, A., and Beckman, J. E. (2000). *A&A* 354, pp. 823–835.
- Rozas, M. et al. (1998). *A&A* 338, pp. 15–26.
- Rozas, M. et al. (1999). *A&AS* 135, pp. 145–158.
- Sabalisk, N. S. P. et al. (1995). *ApJ* 444, p. 200.
- Sabbadin, F. and Bianchini, A. (1979). *PASP* 91, pp. 280–288.
- Sabbadin, F., Ortolani, S., and Bianchini, A. (1984). *A&A* 131, pp. 1–8.
- Sacchi, E. et al. (2018). *ApJ* 857.1, p. 63.
- Sánchez Almeida, J. et al. (2013). *ApJ* 767, p. 74.
- Sánchez Almeida, J. et al. (2014). *ApJ* 783, p. 45.
- Sánchez Almeida, J. et al. (2015). *ApJ* 810, p. L15.
- Sandage, A. and Tammann, G. A. (1974). *ApJ* 190, pp. 525–538.
- Santoro, F. et al. (2022). *A&A* 658, A188.
- Savard, G. et al. (in prep.).
- Schawinski, K. et al. (2007). *MNRAS* 382.4, pp. 1415–1431.
- Schneider, S. E. et al. (1992). *ApJS* 81, p. 5.
- Scowen, P. A. (1992). Thesis. Rice University.
- Sequoia, E. R. and Bignell, R. C. (1978). *ApJ* 226, pp. L5–L6.
- Skillman, E. D. and Balick, B. (1984). *ApJ* 280, pp. 580–591.
- Skillman, E. D., Kennicutt, R. C., and Hodge, P. W. (1989). *ApJ* 347, p. 875.
- Smith, M. G. and Weedman, D. W. (1970). *ApJ* 161, p. 33.
- Smith, M. G. and Weedman, D. W. (1971). *ApJ* 169, p. 271.
- Sokal, K. R. et al. (2015). *AJ* 149, p. 115.
- Stetson, P. B. (1987). *PASP* 99, p. 191.
- Strobel, N. V., Hodge, P., and Kennicutt Jr., R. C. (1991). *ApJ* 383, p. 148.
- Strömgren, B. (1939). *ApJ* 89, p. 526.
- Summers, L. K. et al. (2003). *MNRAS* 342.3, pp. 690–708.
- Tenorio-Tagle, G., Muñoz-Tunon, C., and Cox, D. P. (1993). *ApJ* 418, p. 767.
- Terlevich, R. and Melnick, J. (1981). *MNRAS* 195, pp. 839–851.
- Theis, C. and Kohle, S. (2001). *A&A* 370, pp. 365–383.
- Theis, C. (1999). *Reviews in Modern Astronomy* 12, p. 309.

- Thilker, D. A. et al. (2002). *AJ* 124, pp. 3118–3134.
- Thronson Jr., H. A. et al. (1987). *ApJ* 317, p. 180.
- Toloba, E. et al. (2016). *ApJ* 824, p. 35.
- Tremonti, C. A. et al. (2004). *ApJ* 613, pp. 898–913.
- Valdez-Gutiérrez, M. et al. (2002). *AJ* 124, pp. 3157–3178.
- de Vaucouleurs, G. (1975). *Nearby Groups of Galaxies*. Vol. 9. Stars and Stellar Systems. Chicago, IL, USA: University of Chicago Press.
- de Vaucouleurs, G. et al. (1991). *Third Reference Catalogue of Bright Galaxies*. New York, NY, USA: Springer.
- Virtanen, P. et al. (2020). *Nature Methods* 17.3, pp. 261–272.
- Walt, S. v. d. et al. (2014). *PeerJ* 2, e453.
- Weaver, K. A. (2001). « X-Ray Properties of the Central kpc of AGN and Starbursts: The Latest News from Chandra ». *The Central Kiloparsec of Starbursts and AGN: The La Palma Connection*. Vol. 249, p. 389.
- Whitmore, B. C. et al. (2020). *ApJ* 889, p. 154.
- van Woerden, H., Bosma, A., and Mebold, U. (1975). « Distribution and Motions of Neutral Hydrogen in the Giant Irregular Galaxy NGC 4449 ». *La Dynamique des galaxies spirales*. Vol. 241, p. 483.
- Youngblood, A. J. and Hunter, D. A. (1999). *ApJ* 519, pp. 55–68.
- Zamora-Avilés, M. et al. (2019). *MNRAS* 487, pp. 2200–2214.
- Zaragoza-Cardiel, J. et al. (2015). *MNRAS* 451.2, pp. 1307–1330.
- Zurita, A. et al. (2004). *A&A* 413, pp. 73–89.

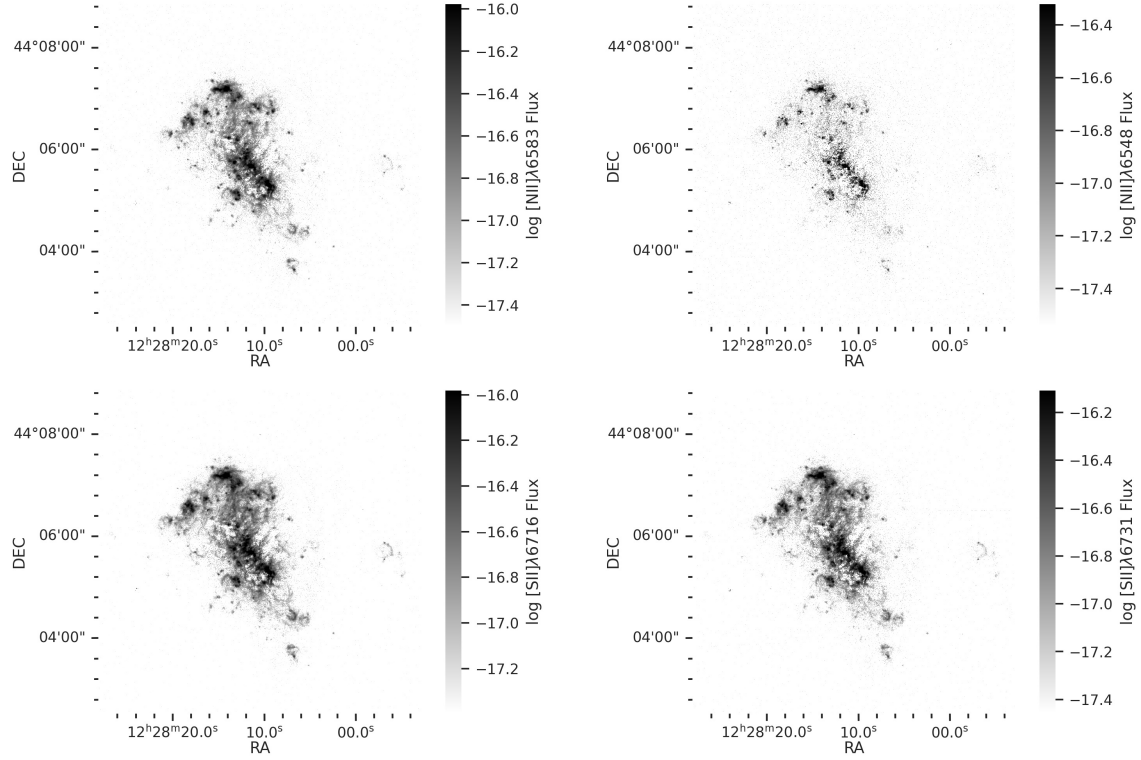


Figure A.1 – Flux maps obtained by fitting the lines in the SN3 datacube (excluding the H α flux map, which is presented in Figure 2.2). All the maps are in log-scale. Corrections for the stellar absorption and extinction are not applied. The pixels with a emission line S/N lower than 1 or with a H α and H β S/N lower than 1 are not shown.

Appendix A Emission Line Maps

The maps obtained by fitting the emission lines in the three datacubes, as described in Section 2.5.3, are shown here. The flux maps are presented in Figure A.1 for the lines in SN3 filter and in Figure A.2 for the lines in the SN1 and SN2 filters. The global stellar absorption and extinction corrections are not applied to these figures.

Appendix B Calibration Data

The calibration data mentionned in Section 2.5.4 and Section 2.5.5 are presented below. The SN3 sky spectrum subtracted from each spectrum from the cubes is shown in Figure B.1. The SN3 OH sky lines velocity map is presented in Figure B.2.

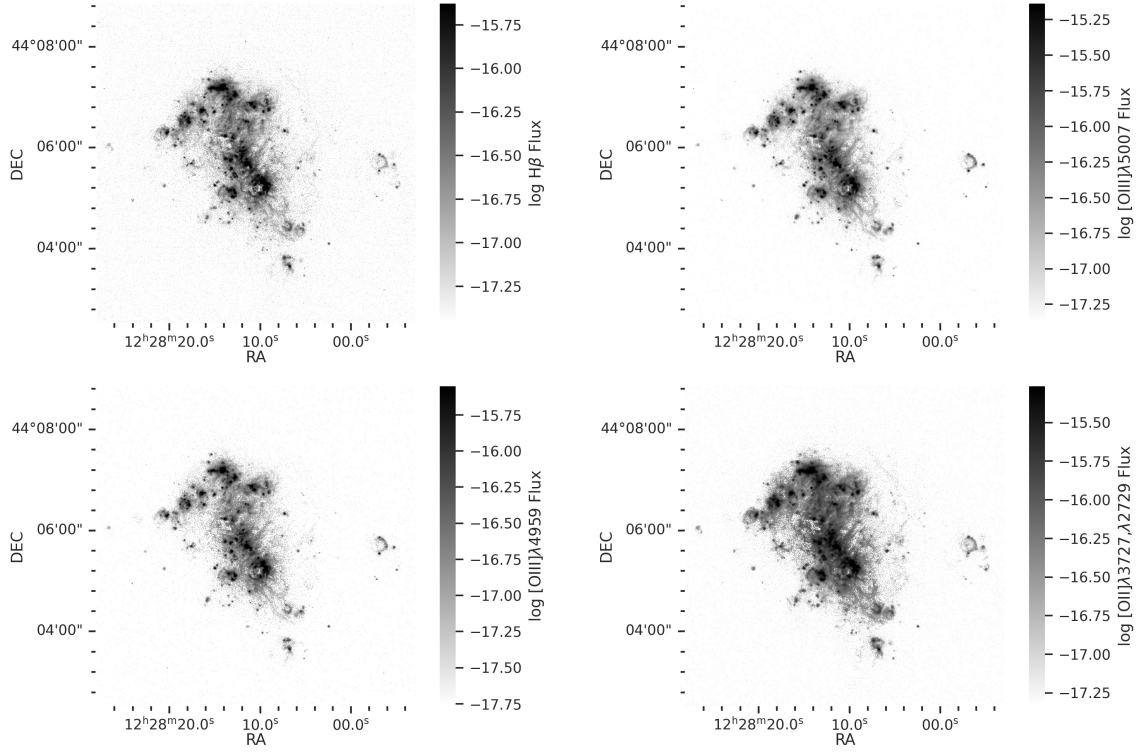


Figure A.2 – Flux maps obtained by fitting the lines in the SN1 and SN2 datacubes. All the maps are in log-scale. Corrections for the stellar absorption and extinction are not applied. The pixels with a emission line S/N lower than 1 or with a $\text{H}\alpha$ and $\text{H}\beta$ S/N lower than 1 are not shown.

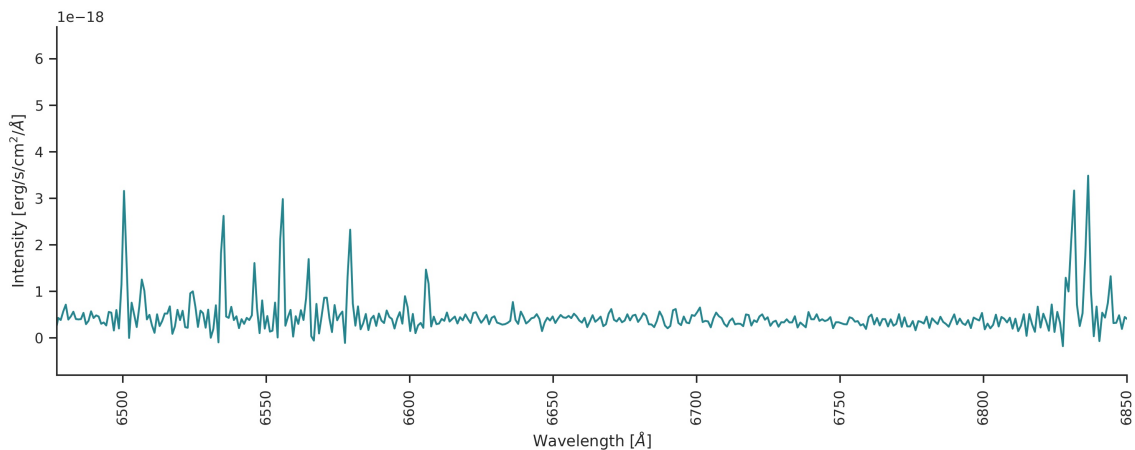


Figure B.1 – Median sky spectrum in the SN3 filter. The circular aperture used to obtain the sky spectrum uses a ~ 150 pc radius and is centred at RA 12h28m34.7s and DEC $+44^\circ 05\text{m}46.5\text{s}$. Multiple OH sky lines are present.

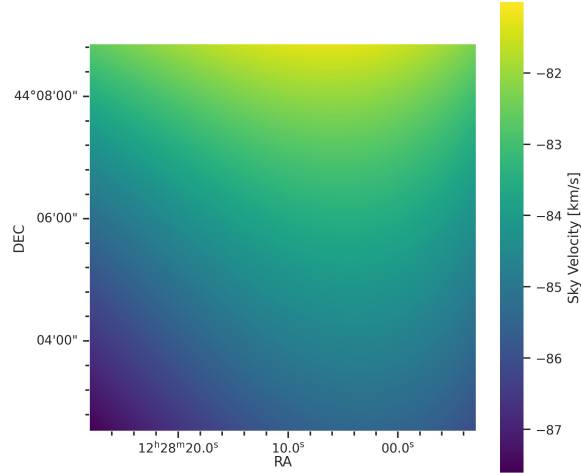


Figure B.2 – Sky velocity map, obtained to refine the wavelength calibration, as described in Section 2.5.5.

Appendix C Detection Parameters

The amplitude map of the H α line, used for the peak detection in Section 2.6.1, is shown in Figure C.1. The effect of the selected detection parameters (Section 2.6.1) used to create the catalogue used in this study is explored. The effect of the `Laplacian sigma` value and of the `detection box size` are displayed in Figure C.2 and in Figure C.3, respectively. The effect of the `noise sigma` value, of the `local background box` size, and of the `scaling factor` value are displayed in Figure C.4, in Figure C.5, and in Figure C.6, respectively. The convergence curve of the luminosity detection limit, described in Section 2.6.5, is presented in Figure C.7.

Appendix D Morphology

The location of the emission regions associated to each morphological features of NGC 4449 are shown in Figure D.1. The location in NGC 4449 of the areas used as examples throughout this study is shown in Figure D.2. Examples for different measured eccentricities of H II regions are shown in Figure D.3, as described in Section 2.7.2. The spatial location of GEHRs are shown in Figure D.4, as described in Section 2.7.3.

Appendix E Line Ratio Maps

The line ratio maps, for different emission lines, are presented Figures E.1 to E.11. The equivalent width maps for the H α and H β lines are shown in Figures E.12 and E.13. The global stellar absorption (Section 2.6.7), except for the [O II] $\lambda 3727$ line, and extinction corrections (Section 2.6.8) are applied to these figures. The pixels with a H α and H β S/N lower than 3 are not corrected for extinction, and thus not shown. Also, only the pixels with a S/N superior to

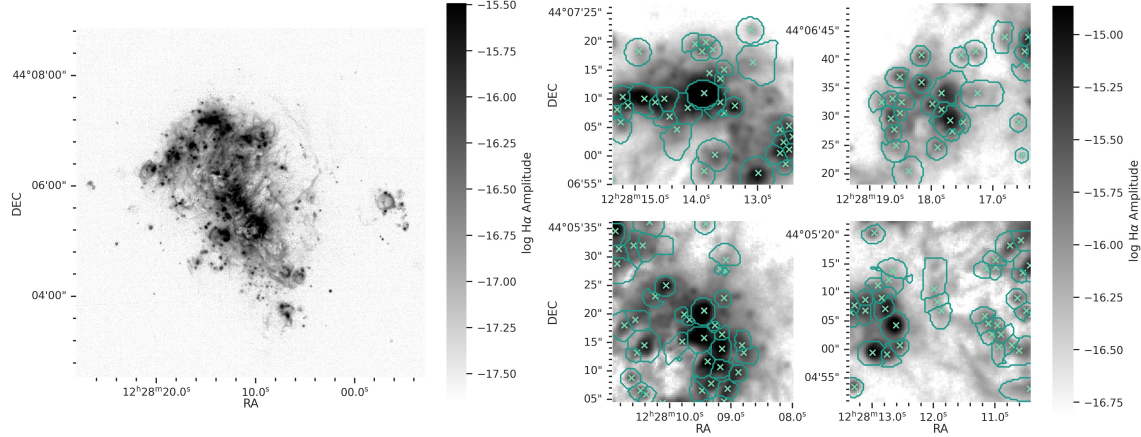


Figure C.1 – H α amplitude map in log-scale. Corrections for the global stellar absorption and extinction are not applied. The pixels with a H α S/N lower than 1 are not shown. On the left panel, the entire galaxy is shown. On the right panel, four regions are shown as examples, which are centred the same regions as Figure 2.4 and shown on Figure D.2. The teal cross indicate the centroid of the regions. The teal contours represent the intersection of the zone of influence and the 2D Gaussian profile for each region. Each panel shows an aperture of 597 pc \times 597 pc.

3 for the concerned maps are shown. The radial profiles of the different metallicity calibrators is presented in Figure E.14, as described in Section 2.7.8.

Appendix F Catalogue

The physical parameters of the 535 emission regions detected are presented in the tables below. The morphology parameters are presented in Table F.1, the raw flux values without corrections are in Table F.2, the flux values corrected for the local background (including the local stellar absorption and the diffuse emission), by subtracting the background spectrum (Section 2.6.7) are in Table F.3, the flux values corrected for the local background diffuse emission (Section 2.6.3), for the global stellar absorption (Section 2.6.7), and for the extinction (Section 2.6.8) are given in Table F.4, and the kinematical and chemical (extinction and metallicity) properties are displayed in Table F.5. The catalogue presented here is split for convenience, but are all included in the same file digitally. A map of the emission domains may be obtained on request.

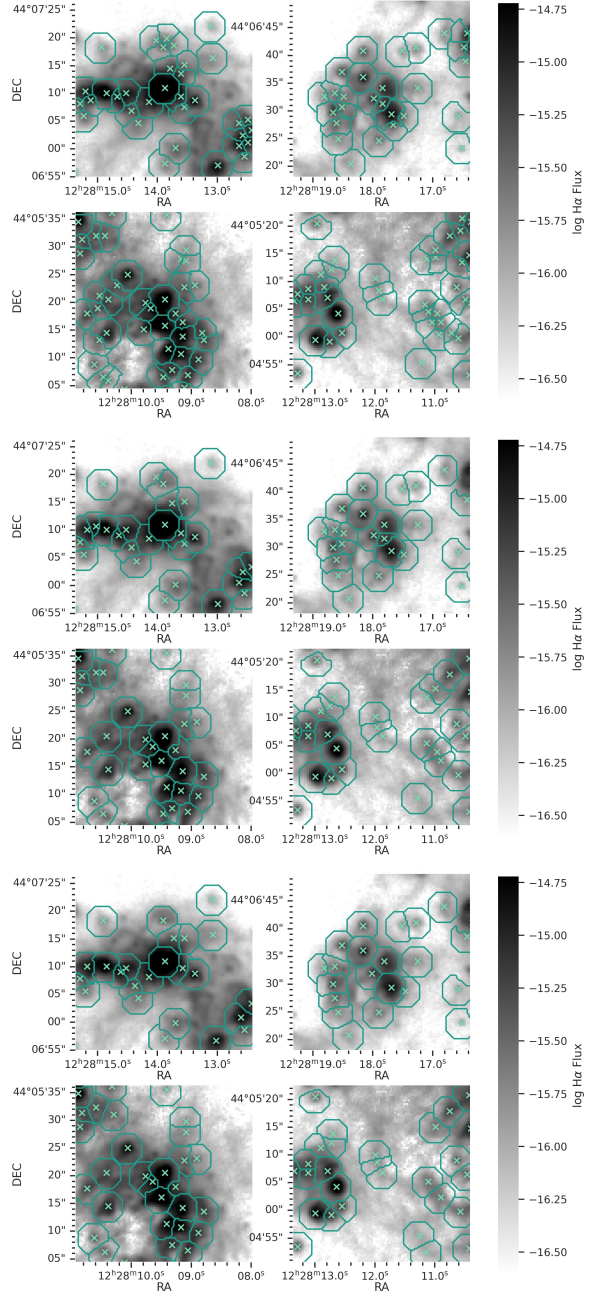


Figure C.2 – Different Laplacian sigma values for the detection algorithm, described in Section 2.6.1. A Laplacian sigma value of 1 (top panel), 1.5 (middle panel), and 2 (bottom panel) are compared. This study uses a Laplacian sigma value of 1.5. The peak detection is done using a detection box size of $5\text{ px} \times 5\text{ px}$, a noise sigma of 3, a local background box of $40\text{ px} \times 40\text{ px}$, and a scaling factor of 1.6 (as described in Section 2.6.1). The teal cross indicate the centroid of the detected regions. The blue contours represent the zone of influence of each detected region. Each panel shows four regions as examples, with their locations indicated on Figure D.2. The background image corresponds to the log H α flux map. The aperture size is $597\text{ pc} \times 597\text{ pc}$.

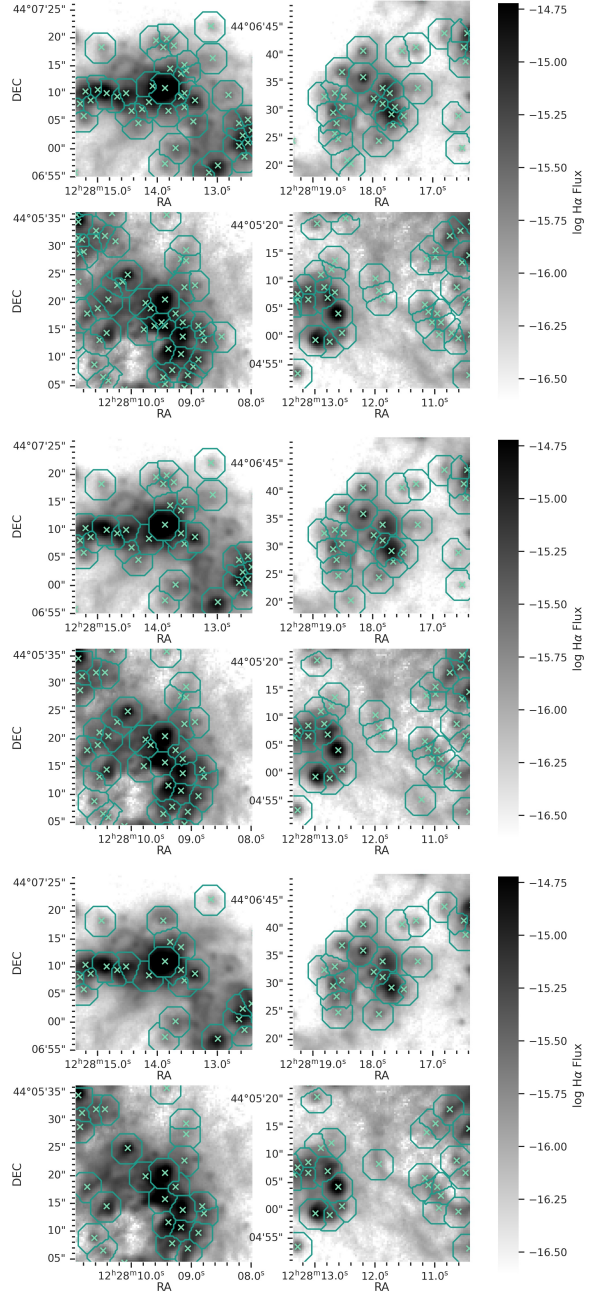


Figure C.3 – Different detection box sizes for the detection algorithm, described in Section 2.6.1. A detection box size of $3\text{ px} \times 3\text{ px}$ (top panel), $5\text{ px} \times 5\text{ px}$ (middle panel), and $7\text{ px} \times 7\text{ px}$ (bottom panel) are compared. This study uses a detection box size of $5\text{ px} \times 5\text{ px}$. The peak detection is done with a Laplacian sigma of 1.5, a noise sigma of 3, a local background box of $40\text{ px} \times 40\text{ px}$, and a scaling factor of 1.6 (as described in Section 2.6.1). The teal cross indicate the centroid of the detected regions. The blue contours represent the zone of influence of each detected region. Each panel shows four regions as examples, with their locations indicated on Figure D.2. The background image corresponds to the log H α flux map. The aperture size is $597\text{ pc} \times 597\text{ pc}$.

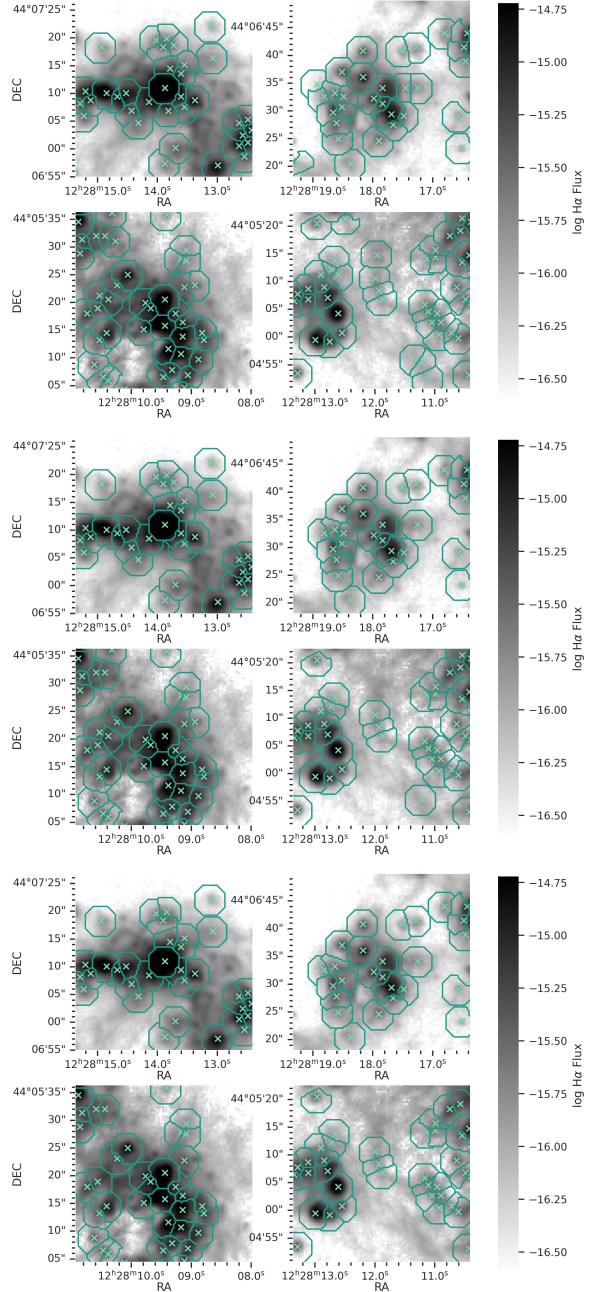


Figure C.4 – Different **noise sigma** values for the detection algorithm, described in Section 2.6.1. A **noise sigma** value of 2 (top panel), 3 (middle panel), and 4 (bottom panel) are compared. This study uses a detection **noise sigma** value of 3. The peak detection is done with a Laplacian **sigma** of 1.5, a detection **box size** of $5\text{ px} \times 5\text{ px}$, a **local background box** of $40\text{ px} \times 40\text{ px}$, and a **scaling factor** of 1.6 (as described in Section 2.6.1). The teal cross indicate the centroid of the detected regions. The blue contours represent the zone of influence of each detected region. Each panel shows four regions as examples, with their locations indicated on Figure D.2. The background image corresponds to the log H α flux map. The aperture size is $597\text{ pc} \times 597\text{ pc}$.

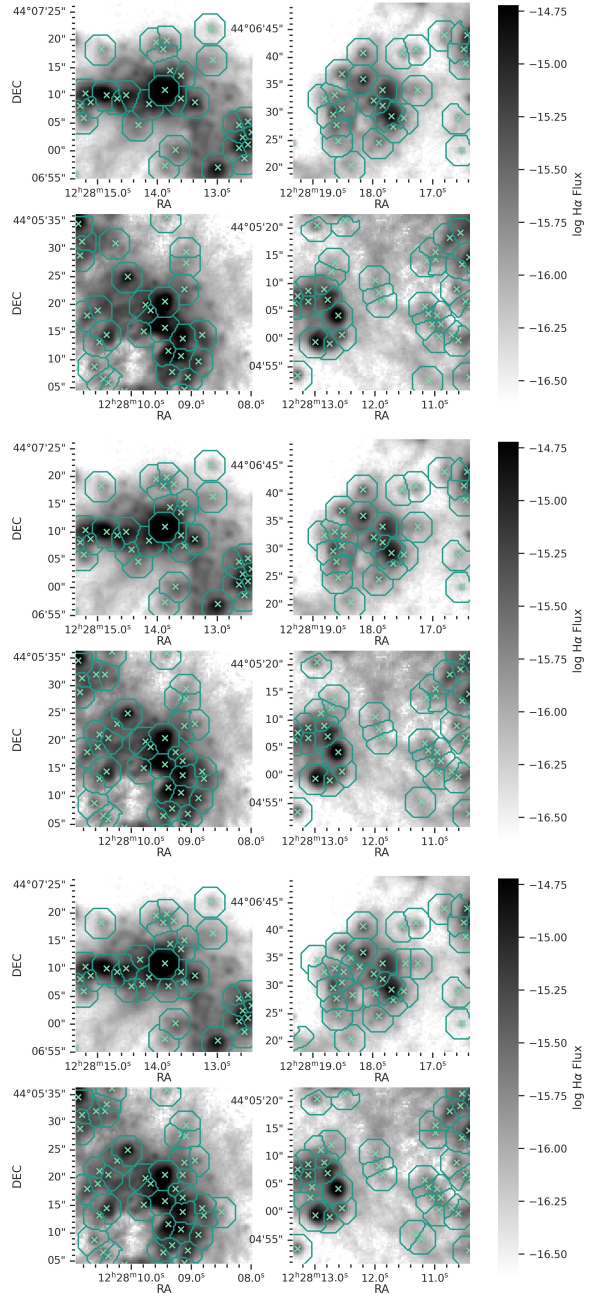


Figure C.5 – Different **local background box** sizes for the detection algorithm, described in Section 2.6.1. A **local background box** size of $30\text{ px} \times 30\text{ px}$ (top panel), $40\text{ px} \times 40\text{ px}$ (middle panel), and $50\text{ px} \times 50\text{ px}$ (bottom panel) are compared. This study uses a **local background box** size of $40\text{ px} \times 40\text{ px}$. The peak detection is done with a **Laplacian sigma** of 1.5, a **detection box size** of $5\text{ px} \times 5\text{ px}$, a **noise sigma** of 3, and a **scaling factor** of 1.6 (as described in Section 2.6.1). The teal cross indicate the centroid of the detected regions. The blue contours represent the zone of influence of each detected region. Each panel shows four regions as examples, with their locations indicated on Figure D.2. The background image corresponds to the log H α flux map. The aperture size is $597\text{ pc} \times 597\text{ pc}$.

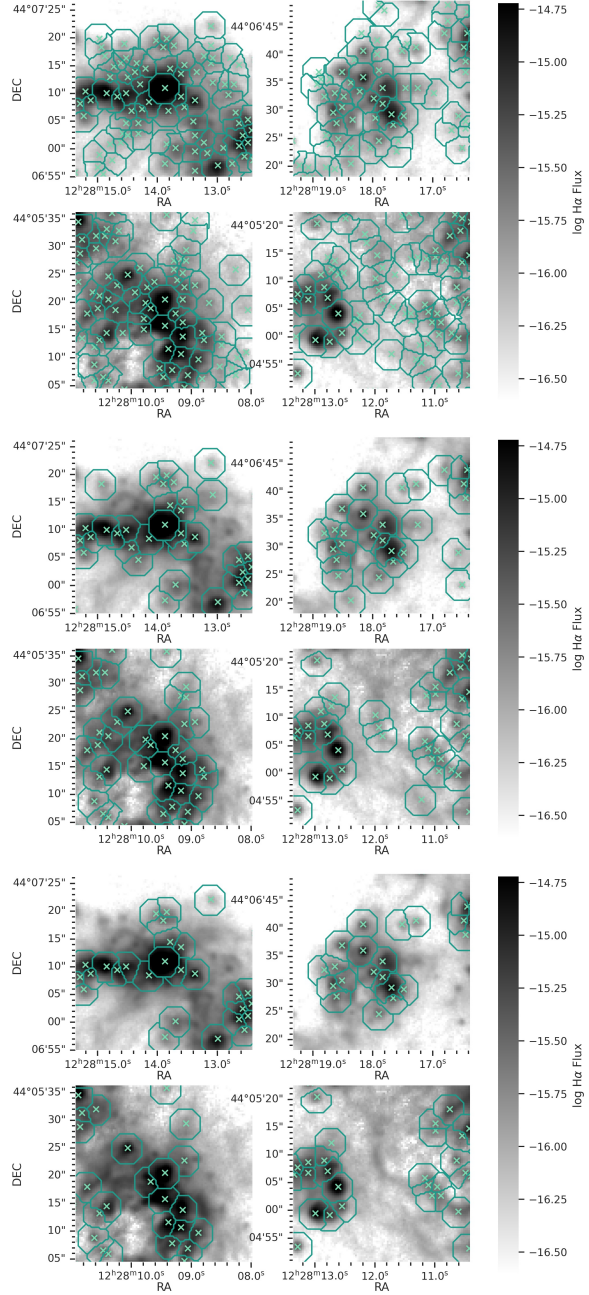


Figure C.6 – Different **scaling factor** values for the detection algorithm, described in Section 2.6.1. A **scaling factor** value of 1 (top panel), 1.6 (middle panel), and 2 (bottom panel) are compared. This study uses a **scaling factor** value of 1.6. The peak detection is done with a **Laplacian sigma** of 1.5, a **detection box size** of $5\text{ px} \times 5\text{ px}$, a **noise sigma** of 3, and a **local background box** of $40\text{ px} \times 40\text{ px}$ (as described in Section 2.6.1). The teal cross indicate the centroid of the detected regions. The blue contours represent the zone of influence of each detected region. Each panel shows four regions as examples, with their locations indicated on Figure D.2. The background image corresponds to the log H α flux map. The aperture size is $597\text{ pc} \times 597\text{ pc}$.

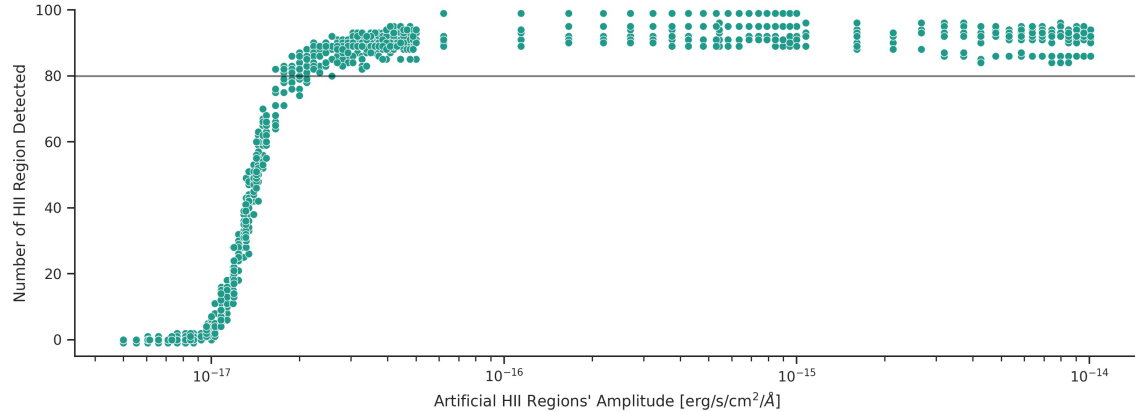


Figure C.7 – Convergence curve of the number of detections of the artificial H II regions in order to compute the level of completeness. Each data point represents the number of detected artificial H II regions for a given centroid amplitude. The grey horizontal line corresponds to the 80 % threshold used to determine the completeness luminosity, as described in Section 2.6.5.

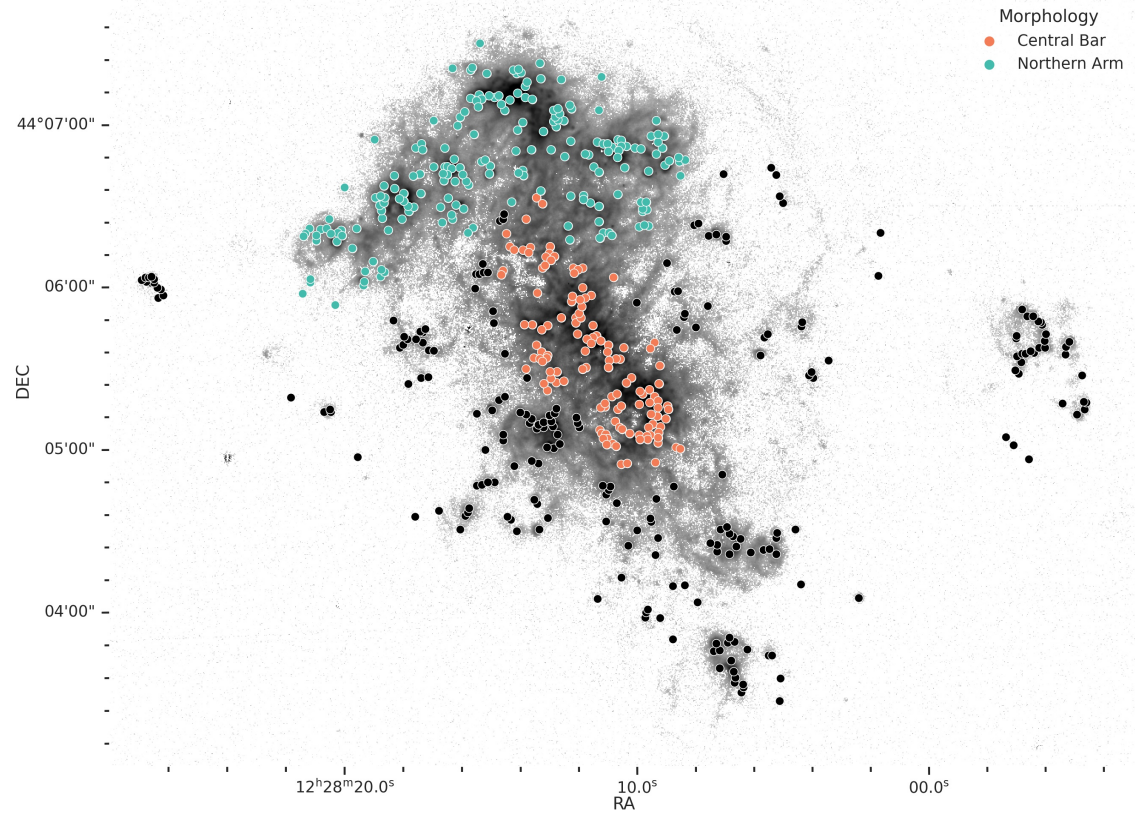


Figure D.1 – Location of the emission regions detected in the different morphological features of NGC 4449. The emission regions located in the central bar are coloured in orange, whilst the H II regions located in the northern arm are coloured in teal. The emission regions located in other morphological features are coloured in black. These categories are used to study the difference in the populations based on their spatial distribution. The emission regions are spatially plotted over the log H α flux map, where the pixels with a H α or H β S/N lower than 1 are not shown.

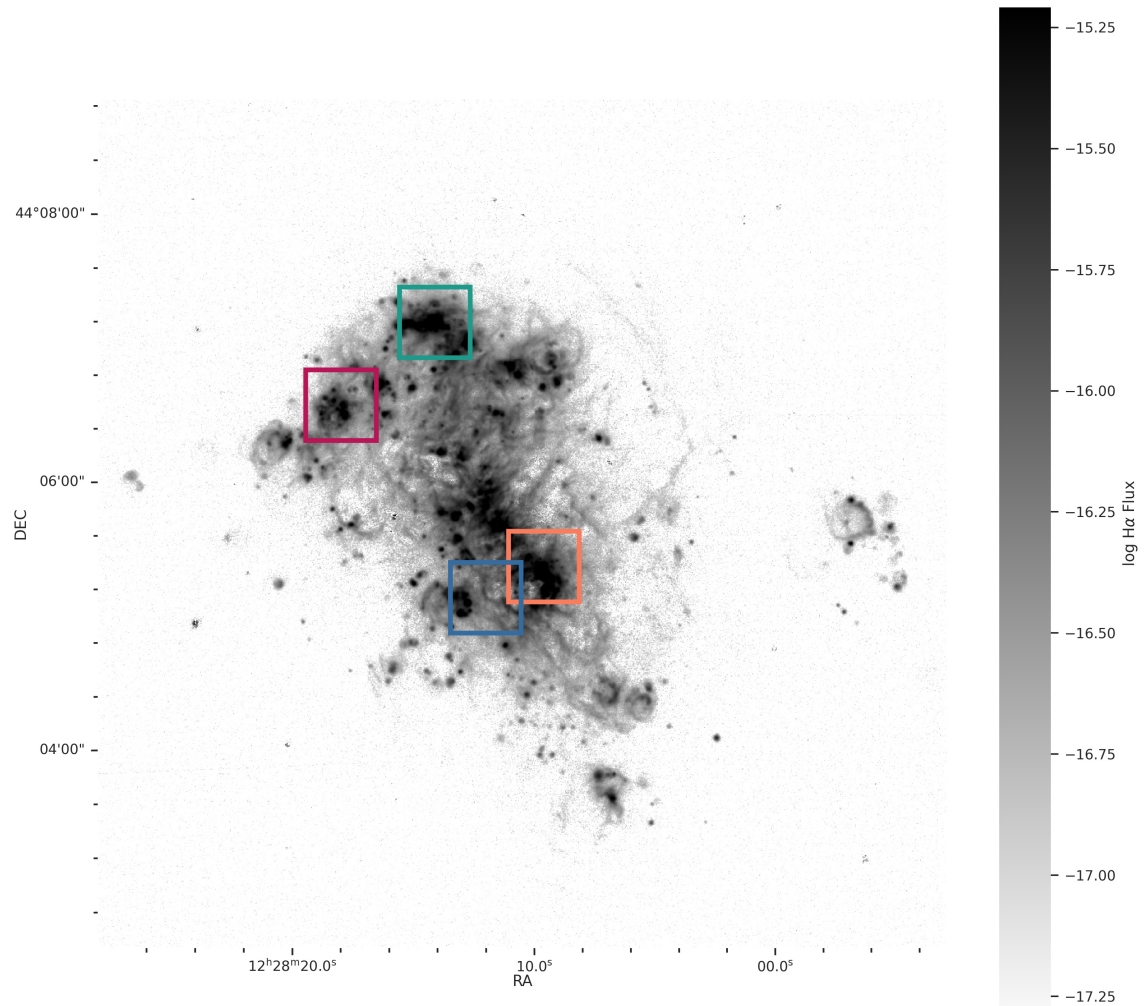


Figure D.2 – Location of the four detections used as examples. The boxes are centred on regions 527 (teal box), 420 (pink box), 175 (orange box), and 123 (blue box), with the length of the sides of boxes of 596.8 pc. The background image corresponds to the log H α flux map.

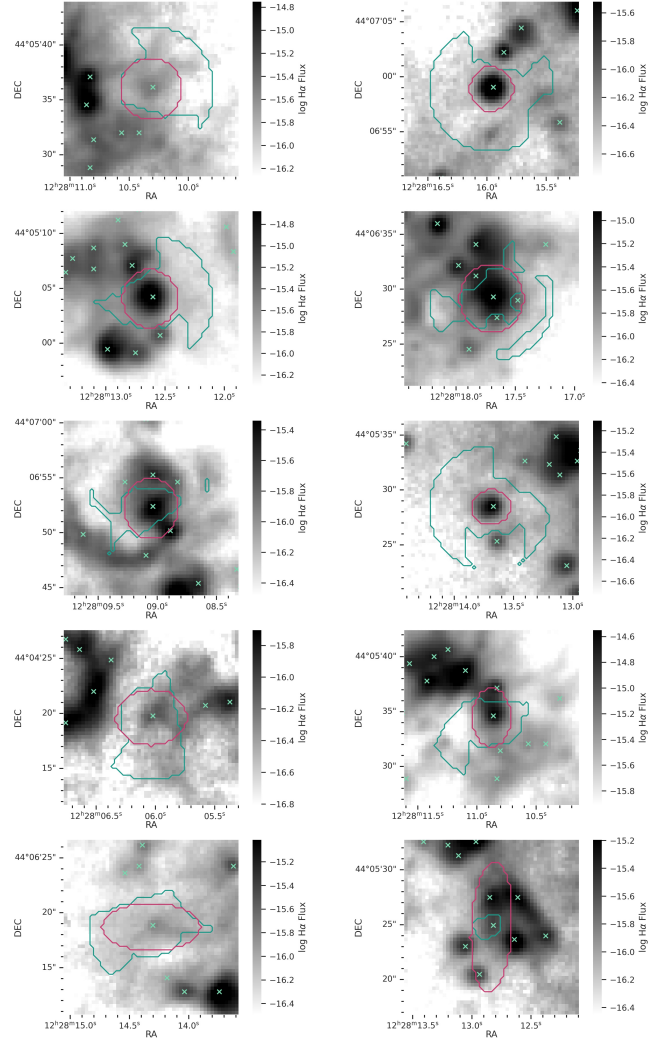


Figure D.3 – Examples of detected emission regions superimposed with the log H α flux map with varying eccentricities. The centroids of the region and its surrounding regions are shown in teal crosses. The teal contour corresponds to the zone of influence of the region in the centre of the area, with an aperture size of ~ 150 pc \times ~ 150 pc. The pink contour corresponds to the 3σ on the major and minor axis of the 2D Gaussian profile (as described in Section 2.6.2). The regions have varying measured eccentricities. The top left panel shows an example of a region with $E \leq 0.1$ (region 227) and the top right panel shows an example of a region with $E \in [0.1, 0.2]$ (region 497). The left panel of the second row shows an example of a region with $E \in [0.2, 0.3]$ (region 114) and the right panel of the second row shows an example of a region with $E \in [0.3, 0.4]$ (region 396). The left panel of the third row shows an example of a region with $E \in [0.4, 0.5]$ (region 485) and the right panel of the third row shows an example of a region with $E \in [0.5, 0.6]$ (region 197). The left panel of the fourth row shows an example of a region with $E \in [0.6, 0.7]$ (region 38) and the right panel of the fourth row shows an example of a region with $E \in [0.7, 0.8]$ (region 220). The bottom left panel shows an example of a region with $E \in [0.8, 0.9]$ (region 358) and the bottom right panel shows an example of a region with $E \geq 0.9$ (region 182).

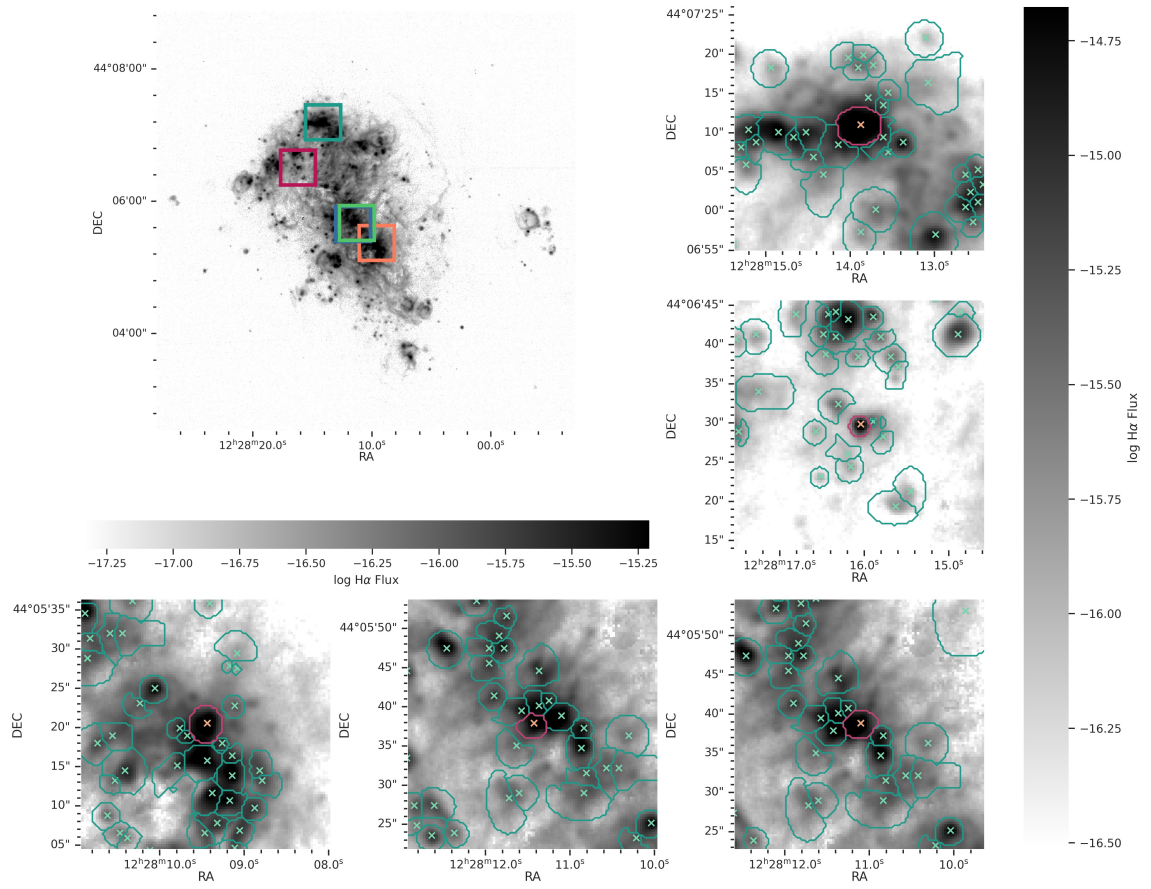


Figure D.4 – Spatial location of the detected GEHRs in Section 2.7.3. The left top panel shows the locations on the galaxy of the five detected GEHRs on the log H α flux map. The boxes are centred on the GEHRs, where the size of the box corresponds to the aperture size of the zoomed regions on the right and bottom panels. The right and bottom panels show the GEHRs and their neighbours. The top right panel is region 527, centred on RA 12h28m03.4s and DEC +44°05m15.5s and corresponds to the teal box on the full size map (top left panel). The middle right panel is region 399, centred on RA 12h28m07.3s and DEC +44°04m52.9s and corresponds to the pink box on the full size map (top left panel). The bottom left panel is region 175, centred on RA 12h28m13.6s and DEC +44°06m05.5s and corresponds to the orange box on the full size map (top left panel). The bottom middle panel is region 234, centred on RA 12h28m11.9s and DEC +44°05m43.7s and corresponds to the blue box on the full size map (top left panel). The bottom right panel is region 238, centred on RA 12h28m11.9s and DEC +44°05m47.2s and corresponds to the green box on the full size map (top left panel). The cross indicate the centroid of the regions. The contours represent the intersection of the zone of influence and the 2D Gaussian profile for each region. The pink cross and contour indicate the GEHR, whilst the teal crosses and blue contours indicate their neighbouring detected emission regions. Each panel shows an aperture of 597 pc \times 597 pc. Region 234 and 238 are superimposed on the left panel.

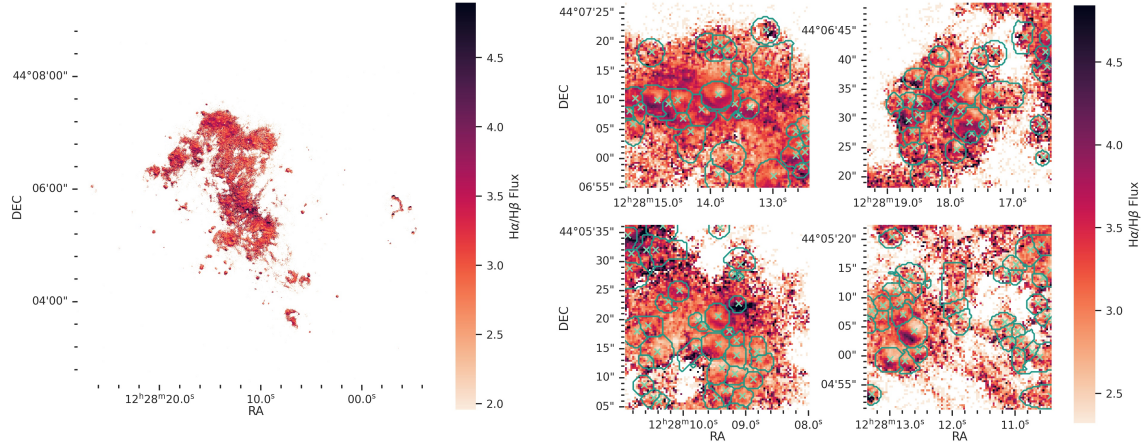


Figure E.1 – Map of the $\text{H}\alpha/\text{H}\beta$ line ratio. The line maps are corrected for the global stellar absorption and extinction. Only the pixels corrected for the extinction and with a S/N superior to 3 are shown. On the left panel, the entire galaxy is shown. On the right panel, four regions are shown as examples, with their locations indicated on Figure D.2. The teal cross indicate the centroid of the regions. The teal contours represent the intersection of the zone of influence and the 2D Gaussian profile for each region. Each panel shows an aperture of $597 \text{ pc} \times 597 \text{ pc}$.

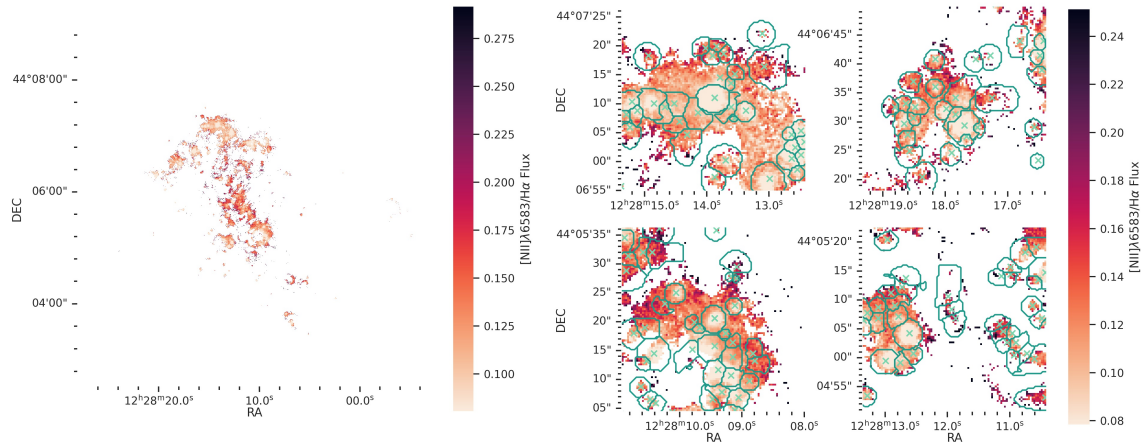


Figure E.2 – Map of the $[\text{N II}]\lambda 6583/\text{H}\alpha$ line ratio. See information in the description of Figure E.1.

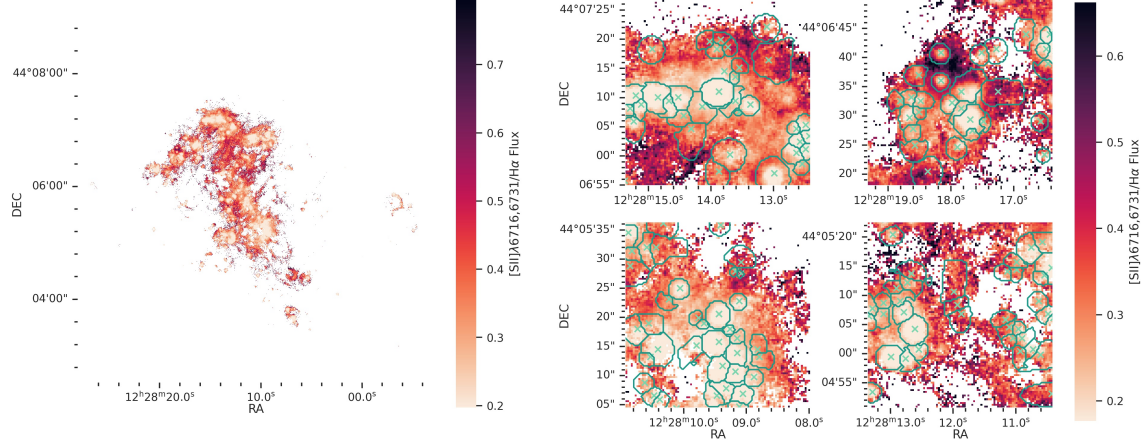


Figure E.3 – Map of the $[\text{S II}]\lambda\lambda 6716,6731/\text{H}\alpha$ line ratio. See information in the description of Figure E.1.

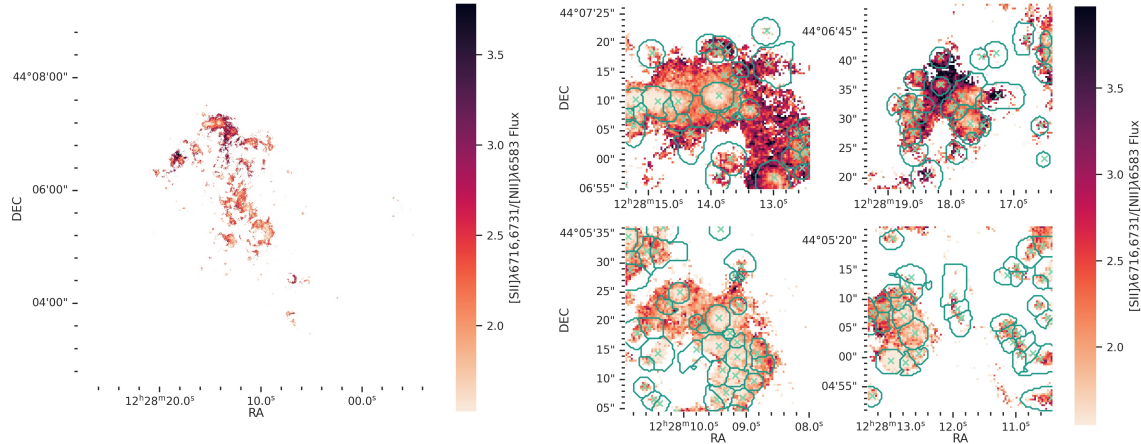


Figure E.4 – Map of the $[\text{S II}]\lambda\lambda 6716,6731/[\text{N II}]\lambda 6583$ line ratio. See information in the description of Figure E.1.

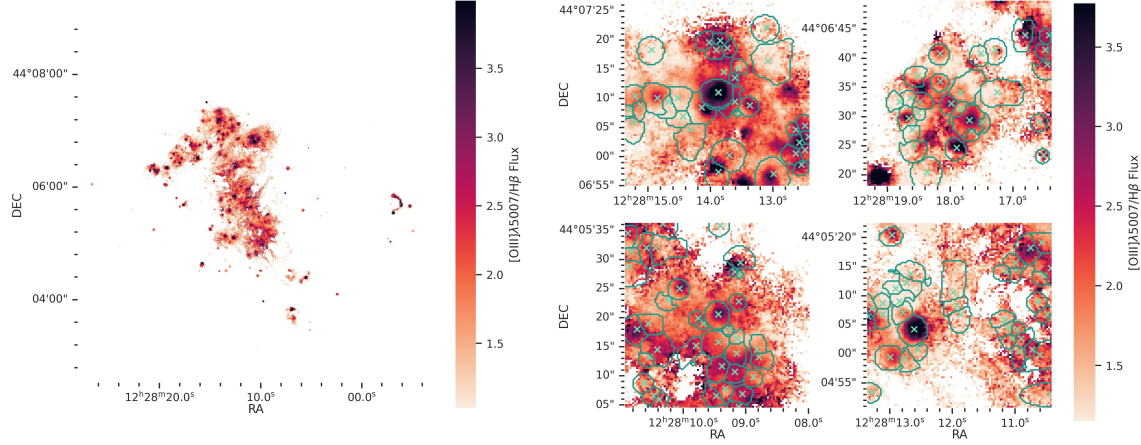


Figure E.5 – Map of the $[\text{O III}]\lambda 5007/\text{H}\beta$ line ratio. See information in the description of Figure E.1.

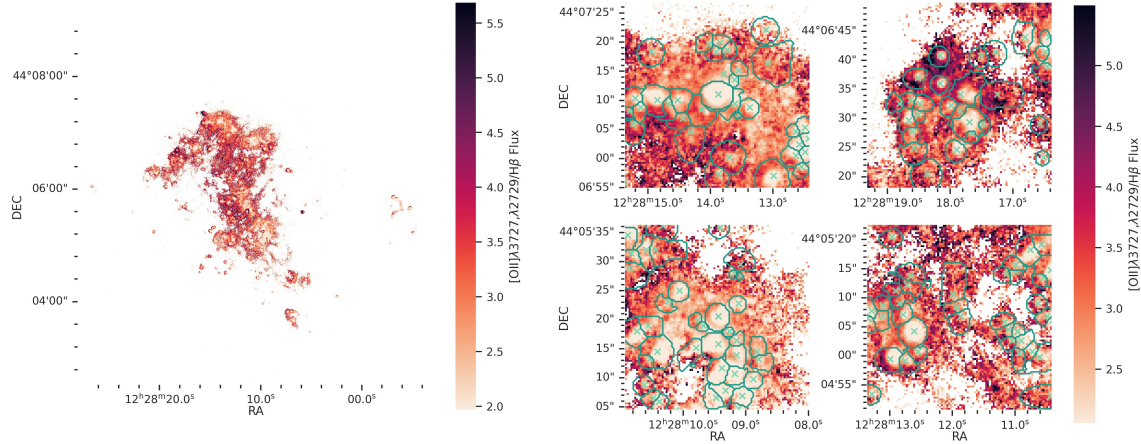


Figure E.6 – Map of the $[\text{O II}]\lambda\lambda 3726,3729/\text{H}\beta$ line ratio. The $[\text{O II}]\lambda\lambda 3726,3729$ map is not corrected for the global stellar absorption, but is corrected for the extinction. See other information in the description of Figure E.1.

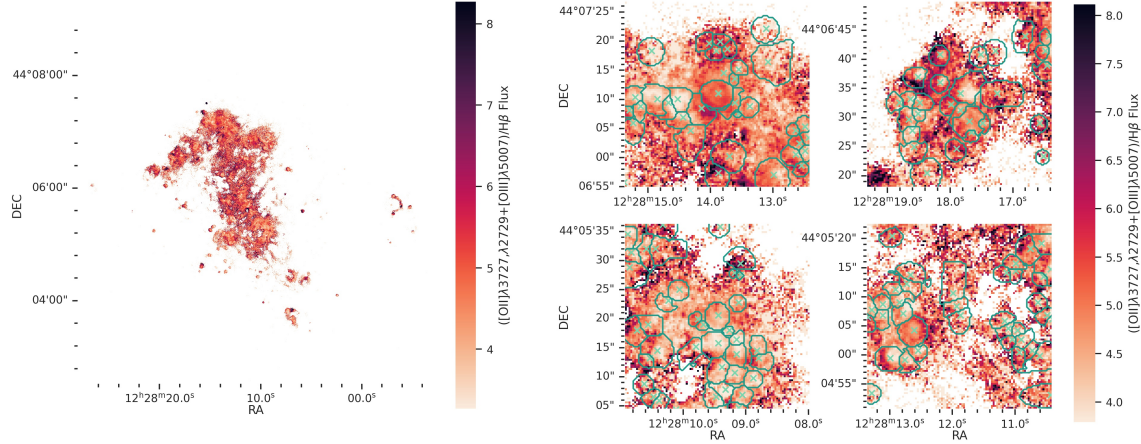


Figure E.7 – Map of the $(\text{[O II]}\lambda\lambda 3726,3729 + \text{[O III]}\lambda 5007)/\text{H}\beta$ line ratio. The $\text{[O II]}\lambda\lambda 3726,3729$ map is not corrected for the global stellar absorption, but is corrected for the extinction. See other information in the description of Figure E.1.

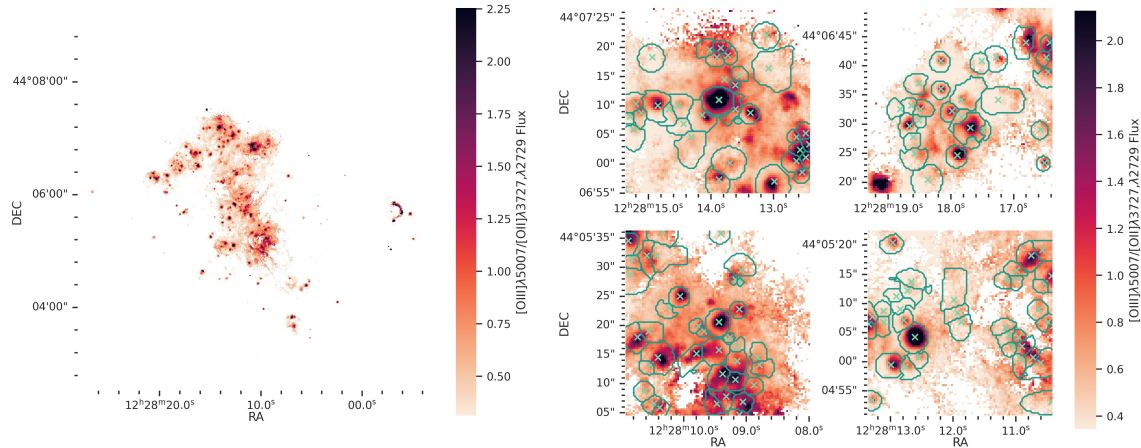


Figure E.8 – Map of the $\text{[O III]}\lambda 5007/\text{[O II]}\lambda\lambda 3726,3729$ line ratio. The $\text{[O II]}\lambda\lambda 3726,3729$ map is not corrected for the global stellar absorption, but is corrected for the extinction. See other information in the description of Figure E.1.

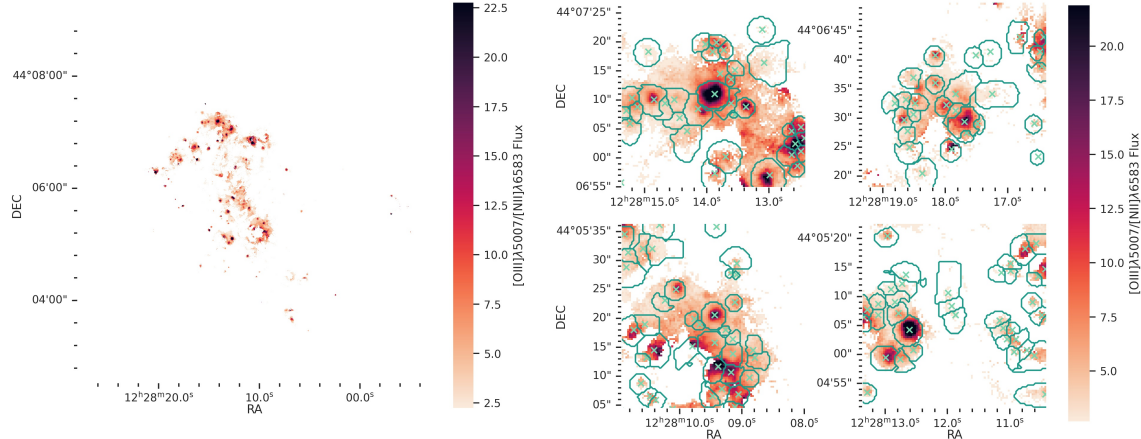


Figure E.9 – Map of the $[\text{O III}]\lambda 5007/\text{[N II}]\lambda 6583$ line ratio. See information in the description of Figure E.1.

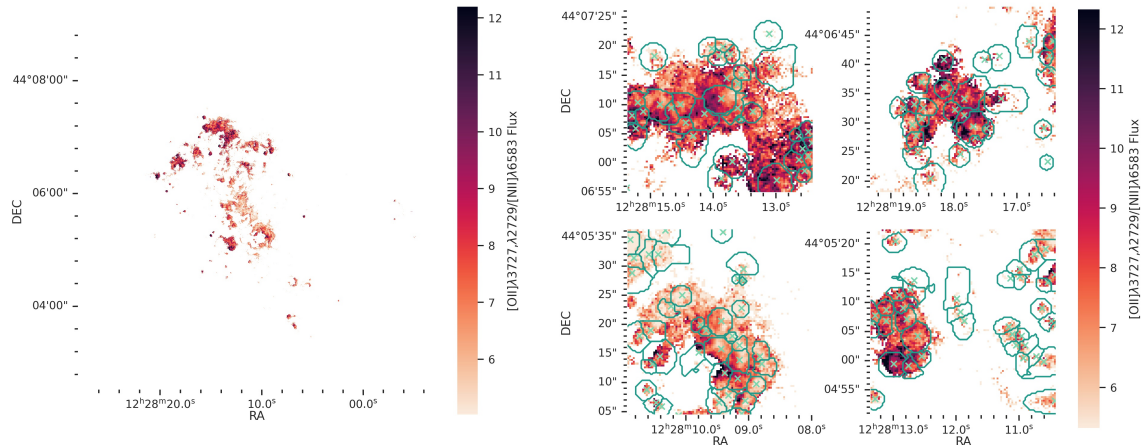


Figure E.10 – Map of the $[\text{O II}]\lambda\lambda 3726,3729/\text{[N II}]\lambda 6583$ line ratio. The $[\text{O II}]\lambda\lambda 3726,3729$ map is not corrected for the global stellar absorption, but is corrected for the extinction. See other information in the description of Figure E.1.

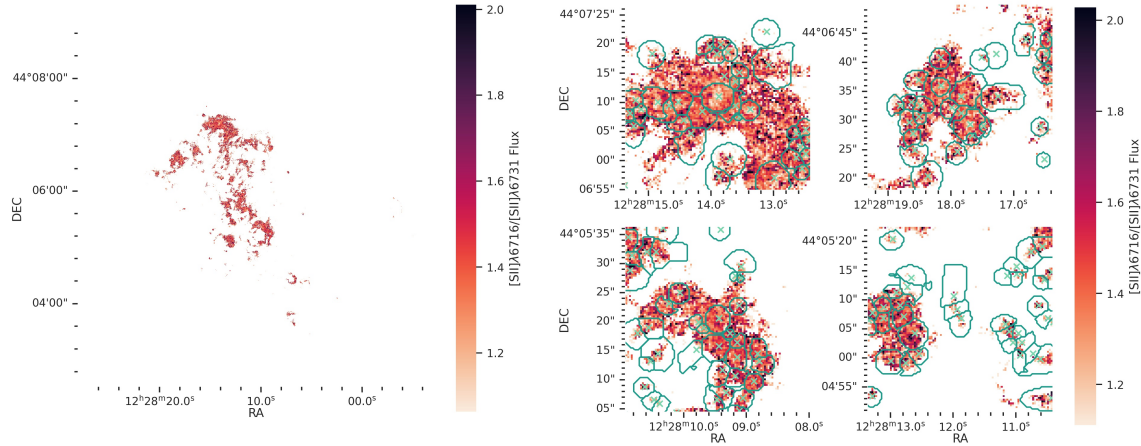


Figure E.11 – Map of the $[S\text{ II}]\lambda 6716/[S\text{ II}]\lambda 6731$ line ratio. See information in the description of Figure E.1.

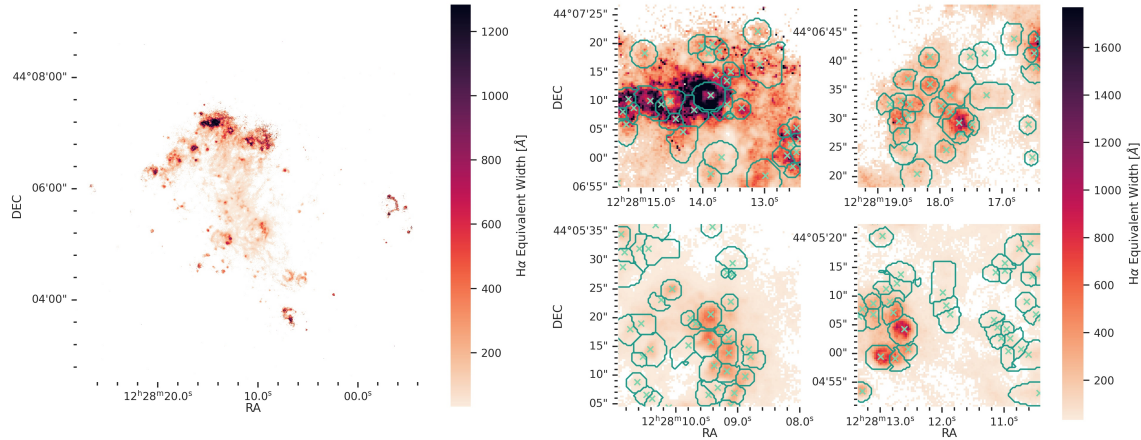


Figure E.12 – Map of the $H\alpha$ equivalent width. See information in the description of Figure E.1.

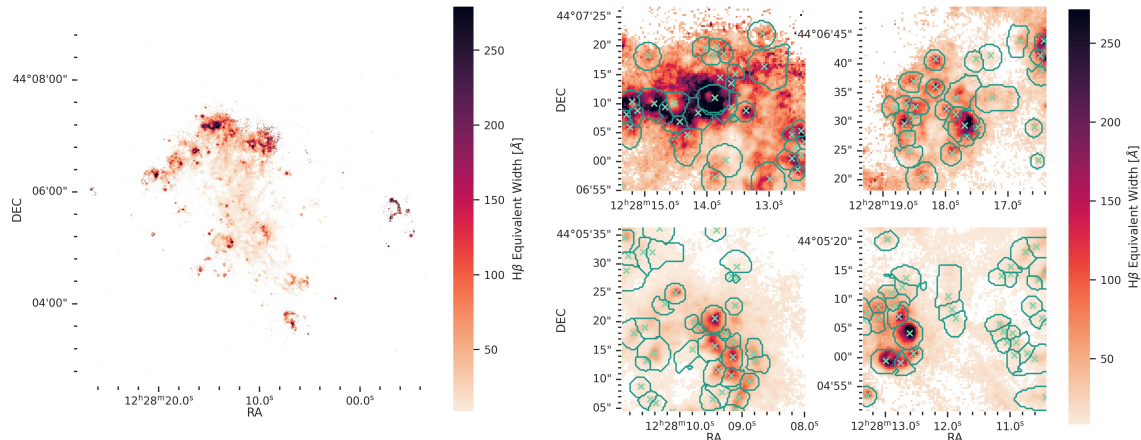


Figure E.13 – Map of the $H\beta$ equivalent width. See information in the description of Figure E.1.

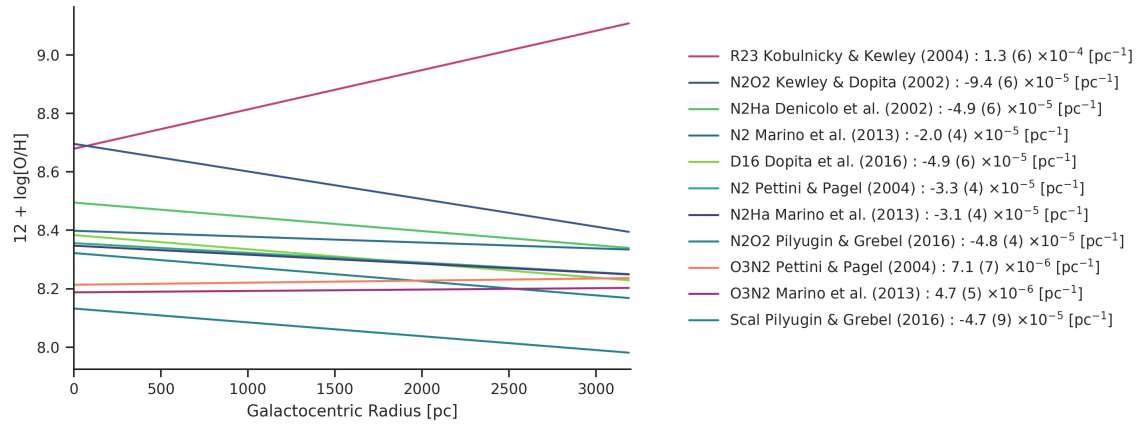


Figure E.14 – Radial profile of the H II region’s metallicity in NGC 4449 using different indicators. The slopes obtained from the linear fit have a value of $(1.4 \pm 0.6) \times 10^{-4} \text{ pc}^{-1}$ for the *R23* calibrator from Kobulnicky & Kewley (2004), $(-9.6 \pm 0.6) \times 10^{-5} \text{ pc}^{-1}$ for the *N2O2* calibrator from Kewley & Dopita (2002), $(-4.9 \pm 0.6) \times 10^{-5} \text{ pc}^{-1}$ for the *N2H}\alpha* calibrator from Denicoló et al. (2002), $(-2.1 \pm 0.4) \times 10^{-5} \text{ pc}^{-1}$ for the *N2* calibrator from Marino et al. (2013), $(-5.1 \pm 0.6) \times 10^{-5} \text{ pc}^{-1}$ for the *D16* calibrator from Dopita et al. (2016), $(-3.1 \pm 0.4) \times 10^{-5} \text{ pc}^{-1}$ for the *N2H}\alpha* calibrator from Marino et al. (2013), $(-4.8 \pm 0.4) \times 10^{-5} \text{ pc}^{-1}$ for the *N2O2* calibrator from Pilyugin & Grebel (2016), $(-3.4 \pm 0.4) \times 10^{-5} \text{ pc}^{-1}$ for the *N2* calibrator from Pettini & Pagel (2004), $(5.5 \pm 0.7) \times 10^{-6} \text{ pc}^{-1}$ for the *O3N2* calibrator from Pettini & Pagel (2004), $(3.6 \pm 0.5) \times 10^{-6} \text{ pc}^{-1}$ for the *O3N2* calibrator from Marino et al. (2013), and $(-4.4 \pm 0.9) \times 10^{-5} \text{ pc}^{-1}$ for the *Scal* calibrator from Pilyugin & Grebel (2016). The galaxy centre is assumed to be at RA 12h28m11.2s and DEC +44°05m37.9s, with a P.A. of 25° and an inclination of 43° (Valdez-Gutiérrez et al. 2002).

Table F.1

Morphological parameters of the emission regions in the catalogue from this study. The RA and DEC column correspond to the position of the centroid of the region. The columns with σ_x and σ_y correspond to the standard deviation of the 2D Gaussian spatial profile (described in Section 2.6.2). The radius corresponds to the geometrical mean of $3\sigma_x$ and $3\sigma_y$ (as defined in Section 2.7.2). The E value corresponds to the eccentricity of the region (described in Section 2.7.2). The angle corresponds to the spatial inclination of the region, obtained from the 2D Gaussian fit (described in Section 2.6.2). The first (1NN), second (2NN), and third (3NN) nearest neighbour corresponds to the proximity distance between the centroids of the regions (described in Section 2.7.4).

ID	RA	DEC	σ_x [px]	σ_y [px]	Radius [pc]	E	Angle [°]	1NN [pc]	2NN [pc]	3NN [pc]
0	44.127428	187.134852	1.82 ± 0.06	1.13 ± 0.03	17.1 ± 0.4	0.79 ± 0.02	-17 ± 3	1880	2021	2063
2	44.115184	187.100827	1.872 ± 0.009	1.687 ± 0.007	21.21 ± 0.07	0.43 ± 0.01	0 ± 2	157	269	275
3	44.111214	187.099652	3.3 ± 0.3	2.4 ± 0.1	33 ± 2	0.69 ± 0.07	0 ± 8	40	55	81
4	44.111459	187.098915	2.6 ± 0.2	1.9 ± 0.1	27 ± 1	0.67 ± 0.07	1 ± 4	19	40	71
6	44.111385	187.098551	3.0 ± 0.4	1.6 ± 0.1	27 ± 2	0.84 ± 0.05	0 ± 8	19	55	61
7	44.110502	187.098318	1.4 ± 0.2	2.9 ± 0.4	24 ± 2	0.9 ± 0.4	-1 ± 8	36	61	71
8	44.11524	187.097609	1.55 ± 0.03	1.53 ± 0.04	18.4 ± 0.3	0.2 ± 0.2	0 ± 4	157	170	180
9	44.110584	187.097584	1.90 ± 0.06	2.06 ± 0.06	23.6 ± 0.5	0.4 ± 0.1	0 ± 8	36	43	72
10	44.110406	187.096732	3.00 ± 0.02	3.01 ± 0.02	35.9 ± 0.2	0.1 ± 0.1	0 ± 2	43	78	78
11	44.108993	187.096262	2.2 ± 0.2	3.2 ± 0.2	31 ± 2	0.7 ± 0.2	0 ± 9	35	94	98
13	44.110133	187.095146	9.1 ± 0.7	3.04 ± 0.09	63 ± 2	0.943 ± 0.009	0 ± 2	60	80	94
14	44.114008	187.094356	5.3 ± 0.3	4.2 ± 0.3	56 ± 3	0.61 ± 0.09	0 ± 5	24	155	180
15	44.114358	187.094351	3.0 ± 0.2	2.4 ± 0.2	32 ± 2	0.6 ± 0.1	1 ± 9	24	170	178
16	44.108362	187.093824	2.1 ± 0.2	1.9 ± 0.2	24 ± 1	0.5 ± 0.2	0 ± 5	42	57	113
17	44.108979	187.093694	1.5 ± 0.3	1.3 ± 0.3	17 ± 2	0.5 ± 0.4	0 ± 10	42	53	76
18	44.1118	187.093533	1.86 ± 0.05	1.87 ± 0.04	22.2 ± 0.4	0.1 ± 0.3	0 ± 4	104	137	145
19	44.108621	187.09272	3.78 ± 0.03	3.73 ± 0.03	44.8 ± 0.3	0.16 ± 0.07	0 ± 3	53	57	78

Morphological parameters of the emission regions in the catalogue from this study. The RA and DEC column correspond to the position of the centroid of the region. The columns with σ_x and σ_y correspond to the standard deviation of the 2D Gaussian spatial profile (described in Section 2.6.2). The radius corresponds to the geometrical mean of $3\sigma_x$ and $3\sigma_y$ (as defined in Section 2.7.2). The E value corresponds to the eccentricity of the region (described in Section 2.7.2). The angle corresponds to the spatial inclination of the region, obtained from the 2D Gaussian fit (described in Section 2.6.2). The first (1NN), second (2NN), and third (3NN) nearest neighbour corresponds to the proximity distance between the centroids of the regions (described in Section 2.7.4).

ID	RA	DEC	σ_x [px]	σ_y [px]	Radius [pc]	E	Angle [°]	1NN [pc]	2NN [pc]	3NN [pc]
20	44.109767	187.092583	2.00 ± 0.04	2.97 ± 0.07	29.1 ± 0.5	0.74 ± 0.07	0 ± 3	38	48	76
21	44.110474	187.092477	1.80 ± 0.02	1.71 ± 0.02	21.0 ± 0.2	0.30 ± 0.05	2 ± 3	48	48	104
22	44.104119	187.092183	2.1 ± 0.1	2.3 ± 0.1	26 ± 1	0.5 ± 0.2	0 ± 10	174	243	262
23	44.10994	187.091845	2.0 ± 0.2	1.5 ± 0.1	21 ± 1	0.7 ± 0.1	0 ± 8	38	48	99
24	44.101277	187.089143	2.41 ± 0.04	2.42 ± 0.04	28.8 ± 0.3	0.1 ± 0.2	0 ± 3	36	61	102
25	44.102783	187.089141	2.06 ± 0.03	1.75 ± 0.02	22.7 ± 0.2	0.53 ± 0.03	0 ± 3	102	102	103
26	44.101362	187.088406	2.2 ± 0.1	1.84 ± 0.06	24.2 ± 0.7	0.57 ± 0.07	0 ± 9	25	36	103
27	44.101535	187.087953	1.80 ± 0.05	1.84 ± 0.06	21.7 ± 0.5	0.2 ± 0.2	0 ± 4	25	61	102
28	44.10665	187.086879	2.35 ± 0.08	1.94 ± 0.05	25.5 ± 0.6	0.57 ± 0.05	0 ± 5	150	208	284
29	44.096318	187.086506	3.8 ± 0.1	3.3 ± 0.1	42 ± 1	0.48 ± 0.07	0 ± 9	224	353	359
30	44.123219	187.086013	1.935 ± 0.008	1.908 ± 0.009	22.94 ± 0.07	0.16 ± 0.04	0 ± 3	413	649	650
31	44.104068	187.084564	2.07 ± 0.03	2.00 ± 0.03	24.3 ± 0.3	0.27 ± 0.08	2 ± 3	84	208	238
32	44.105311	187.084434	2.15 ± 0.06	2.27 ± 0.07	26.4 ± 0.6	0.3 ± 0.1	0 ± 6	84	150	286
33	44.1117275	187.084143	2.11 ± 0.05	2.29 ± 0.05	26.2 ± 0.4	0.38 ± 0.09	-2 ± 6	270	328	353
34	44.098771	187.083415	2.19 ± 0.04	3.33 ± 0.08	32.3 ± 0.5	0.75 ± 0.06	0 ± 2	224	228	285
35	44.102285	187.080181	2.7 ± 0.1	2.5 ± 0.1	31 ± 1	0.4 ± 0.1	0 ± 10	121	202	216
36	44.109879	187.079956	2.33 ± 0.05	4.7 ± 0.2	39.6 ± 0.8	0.9 ± 0.1	-16 ± 2	71	86	106
37	44.114732	187.079887	5.15 ± 0.09	2.03 ± 0.03	38.6 ± 0.5	0.919 ± 0.004	-4 ± 1	60	94	113
38	44.112084	187.079679	2.67 ± 0.06	3.36 ± 0.08	35.8 ± 0.6	0.61 ± 0.07	-1 ± 3	91	110	119
39	44.10864	187.079606	3.0 ± 0.1	2.7 ± 0.1	33.8 ± 0.9	0.4 ± 0.1	0 ± 10	48	76	86

Morphological parameters of the emission regions in the catalogue from this study. The RA and DEC column correspond to the position of the centroid of the region. The columns with σ_x and σ_y correspond to the standard deviation of the 2D Gaussian spatial profile (described in Section 2.6.2). The radius corresponds to the geometrical mean of $3\sigma_x$ and $3\sigma_y$ (as defined in Section 2.7.2). The E value corresponds to the eccentricity of the region (described in Section 2.7.2). The angle corresponds to the spatial inclination of the region, obtained from the 2D Gaussian fit (described in Section 2.6.2). The first (1NN), second (2NN), and third (3NN) nearest neighbour corresponds to the proximity distance between the centroids of the regions (described in Section 2.7.4).

ID	RA	DEC	σ_x [px]	σ_y [px]	Radius [pc]	E	Angle [°]	1NN [pc]	2NN [pc]	3NN [pc]
40	44.113405	187.079291	1.79 ± 0.09	2.5 ± 0.1	25.3 ± 0.9	0.7 ± 0.1	-2 ± 2	42	91	94
41	44.114019	187.079116	2.66 ± 0.06	5.5 ± 0.2	46 ± 1	0.9 ± 0.1	-1 ± 2	42	60	91
42	44.110575	187.078848	7.8 ± 0.1	2.81 ± 0.02	56.0 ± 0.5	0.933 ± 0.003	14.1 ± 0.6	62	71	76
43	44.099456	187.078825	2.16 ± 0.02	2.31 ± 0.02	26.6 ± 0.1	0.36 ± 0.03	24 ± 3	122	202	215
44	44.108634	187.078623	2.9 ± 0.1	2.79 ± 0.09	33.9 ± 0.8	0.3 ± 0.2	0 ± 9	48	49	106
45	44.107927	187.078388	2.12 ± 0.05	2.58 ± 0.08	28.0 ± 0.5	0.57 ± 0.08	0 ± 7	49	76	120
46	44.111013	187.077773	2.2 ± 0.1	2.8 ± 0.1	29 ± 1	0.6 ± 0.2	0 ± 2	57	62	85
47	44.102536	187.077724	2.60 ± 0.05	2.76 ± 0.05	32.0 ± 0.4	0.33 ± 0.08	0 ± 7	121	123	147
48	44.114719	187.077556	2.67 ± 0.03	2.61 ± 0.02	31.5 ± 0.2	0.21 ± 0.06	0 ± 4	36	91	113
49	44.110217	187.077375	5.3 ± 0.2	4.64 ± 0.08	59 ± 1	0.50 ± 0.06	0 ± 10	30	57	76
50	44.109862	187.07701	2.2 ± 0.1	3.1 ± 0.4	32 ± 2	0.7 ± 0.3	0 ± 10	30	51	67
51	44.114803	187.076817	1.9 ± 0.1	2.4 ± 0.1	26 ± 1	0.6 ± 0.2	0 ± 5	36	125	128
52	44.087961	187.076919	2.55 ± 0.04	2.96 ± 0.04	32.8 ± 0.3	0.50 ± 0.04	0 ± 4	91	120	155
53	44.10034	187.076648	2.35 ± 0.02	2.56 ± 0.02	29.2 ± 0.2	0.40 ± 0.03	0 ± 3	117	122	126
54	44.08213	187.076738	2.53 ± 0.04	2.28 ± 0.04	28.7 ± 0.3	0.43 ± 0.04	0 ± 4	102	131	161
55	44.090245	187.076648	4.25 ± 0.07	5.15 ± 0.08	55.8 ± 0.6	0.56 ± 0.05	0 ± 3	101	155	180
56	44.108976	187.076404	2.88 ± 0.09	3.02 ± 0.09	35.2 ± 0.8	0.3 ± 0.2	-3 ± 9	45	67	96
57	44.116654	187.0763	2.50 ± 0.07	2.36 ± 0.05	29.0 ± 0.5	0.3 ± 0.1	0 ± 7	128	144	217
58	44.109591	187.076031	1.6 ± 0.1	1.6 ± 0.1	19 ± 1	0.2 ± 0.8	0 ± 10	45	51	78
59	44.097147	187.075341	1.45 ± 0.03	1.52 ± 0.03	17.7 ± 0.2	0.3 ± 0.1	-44 ± 5	149	189	219

Morphological parameters of the emission regions in the catalogue from this study. The RA and DEC column correspond to the position of the centroid of the region. The columns with σ_x and σ_y correspond to the standard deviation of the 2D Gaussian spatial profile (described in Section 2.6.2). The radius corresponds to the geometrical mean of $3\sigma_x$ and $3\sigma_y$ (as defined in Section 2.7.2). The E value corresponds to the eccentricity of the region (described in Section 2.7.2). The angle corresponds to the spatial inclination of the region, obtained from the 2D Gaussian fit (described in Section 2.6.2). The first (1NN), second (2NN), and third (3NN) nearest neighbour corresponds to the proximity distance between the centroids of the regions (described in Section 2.7.4).

ID	RA	DEC	σ_x [px]	σ_y [px]	Radius [pc]	E	Angle [°]	1NN [pc]	2NN [pc]	3NN [pc]
60	44.101815	187.0754	2.9 ± 0.2	2.8 ± 0.1	34 ± 1	0.3 ± 0.3	0 ± 10	25	117	123
61	44.087318	187.07528	1.94 ± 0.07	1.60 ± 0.07	21.1 ± 0.6	0.57 ± 0.07	0 ± 6	31	91	209
62	44.101724	187.07491	1.72 ± 0.09	2.1 ± 0.1	22.6 ± 0.9	0.6 ± 0.2	0 ± 8	25	126	143
63	44.091128	187.074971	1.66 ± 0.02	1.74 ± 0.01	20.3 ± 0.1	0.30 ± 0.05	10 ± 2	101	123	160
64	44.077436	187.074931	1.51 ± 0.04	1.43 ± 0.03	17.5 ± 0.3	0.3 ± 0.1	-2 ± 5	172	330	353
65	44.086977	187.074857	2.32 ± 0.04	2.29 ± 0.04	27.5 ± 0.3	0.2 ± 0.1	0 ± 4	31	120	220
66	44.082646	187.074772	3.12 ± 0.03	2.75 ± 0.03	35.0 ± 0.2	0.47 ± 0.02	-1 ± 3	30	59	102
67	44.082904	187.074279	3.1 ± 0.2	2.23 ± 0.07	31 ± 1	0.69 ± 0.05	1 ± 5	30	30	131
68	44.079907	187.074073	1.94 ± 0.04	2.21 ± 0.06	24.7 ± 0.4	0.48 ± 0.08	0 ± 4	172	188	199
69	44.082991	187.073666	2.1 ± 0.1	2.2 ± 0.1	26 ± 1	0.3 ± 0.3	0 ± 10	30	59	161
70	44.090015	187.072969	1.89 ± 0.04	1.80 ± 0.05	22.0 ± 0.4	0.3 ± 0.1	3 ± 4	37	123	180
71	44.098249	187.072744	1.48 ± 0.03	1.77 ± 0.03	19.4 ± 0.2	0.55 ± 0.05	7 ± 3	97	107	123
72	44.089693	187.072361	2.95 ± 0.03	2.64 ± 0.02	33.3 ± 0.2	0.44 ± 0.02	-1 ± 3	37	160	212
73	44.102326	187.072077	3.0 ± 0.2	2.7 ± 0.1	34 ± 1	0.4 ± 0.1	0 ± 7	143	146	165
74	44.097109	187.071531	2.7 ± 0.2	3.2 ± 0.2	35 ± 2	0.5 ± 0.2	0 ± 10	35	61	64
75	44.097371	187.070914	1.4 ± 0.1	1.3 ± 0.1	16 ± 1	0.3 ± 0.4	0 ± 20	27	35	50
76	44.097545	187.07042	2.7 ± 0.2	1.9 ± 0.1	27 ± 1	0.72 ± 0.07	0 ± 10	27	53	61
77	44.104083	187.070328	18.6 ± 0.7	4.5 ± 0.1	110 ± 3	0.970 ± 0.003	-31 ± 1	146	209	267
78	44.083765	187.07047	3.1 ± 0.1	1.83 ± 0.08	28.5 ± 0.9	0.81 ± 0.03	0 ± 4	36	83	128
79	44.096765	187.070306	1.979 ± 0.006	1.971 ± 0.006	23.58 ± 0.05	0.09 ± 0.04	-7 ± 3	50	53	64

Morphological parameters of the emission regions in the catalogue from this study. The RA and DEC column correspond to the position of the centroid of the region. The columns with σ_x and σ_y correspond to the standard deviation of the 2D Gaussian spatial profile (described in Section 2.6.2). The radius corresponds to the geometrical mean of $3\sigma_x$ and $3\sigma_y$ (as defined in Section 2.7.2). The E value corresponds to the eccentricity of the region (described in Section 2.7.2). The angle corresponds to the spatial inclination of the region, obtained from the 2D Gaussian fit (described in Section 2.6.2). The first (1NN), second (2NN), and third (3NN) nearest neighbour corresponds to the proximity distance between the centroids of the regions (described in Section 2.7.4).

ID	RA	DEC	σ_x [px]	σ_y [px]	Radius [pc]	E	Angle [$^{\circ}$]	1NN [pc]	2NN [pc]	3NN [pc]
80	44.084294	187.070341	3.7 ± 0.1	3.2 ± 0.1	41 ± 1	0.46 ± 0.09	-1 ± 8	36	47	91
81	44.085614	187.069957	2.77 ± 0.05	2.24 ± 0.04	29.8 ± 0.4	0.59 ± 0.03	0 ± 2	47	91	128
82	44.084921	187.069922	2.65 ± 0.05	2.50 ± 0.05	30.7 ± 0.4	0.33 ± 0.07	3 ± 3	47	47	83
83	44.109109	187.068544	6.7 ± 0.4	5.2 ± 0.3	70 ± 3	0.63 ± 0.07	0 ± 10	343	350	365
84	44.087631	187.067599	2.78 ± 0.05	2.16 ± 0.03	29.2 ± 0.3	0.63 ± 0.02	-1 ± 3	125	168	178
85	44.098673	187.067209	2.14 ± 0.05	5.4 ± 0.2	40.6 ± 0.8	0.9 ± 0.1	-1 ± 1	42	131	155
86	44.090099	187.067184	1.75 ± 0.02	1.81 ± 0.01	21.2 ± 0.1	0.27 ± 0.05	0 ± 7	51	128	151
87	44.099293	187.067078	2.13 ± 0.07	3.3 ± 0.2	32 ± 1	0.8 ± 0.1	0 ± 9	42	143	170
88	44.102206	187.066915	2.05 ± 0.08	1.81 ± 0.06	23.0 ± 0.6	0.47 ± 0.08	0 ± 10	138	170	174
89	44.089393	187.066841	1.70 ± 0.08	2.6 ± 0.1	25.0 ± 0.9	0.8 ± 0.1	0 ± 6	51	125	144
90	44.14061	187.06583	3.0 ± 0.2	2.3 ± 0.1	32 ± 1	0.64 ± 0.08	0 ± 9	146	222	452
91	44.071495	187.066486	1.81 ± 0.02	1.66 ± 0.02	20.7 ± 0.2	0.41 ± 0.03	0 ± 3	364	382	390
92	44.084613	187.065306	3.1 ± 0.1	3.45 ± 0.09	39 ± 1	0.4 ± 0.1	0 ± 8	141	165	226
93	44.104759	187.064913	4.0 ± 0.1	4.4 ± 0.1	50 ± 1	0.4 ± 0.1	-1 ± 8	31	161	173
94	44.091677	187.064968	2.22 ± 0.04	3.40 ± 0.06	32.8 ± 0.4	0.76 ± 0.05	0 ± 3	48	51	100
95	44.090971	187.064855	2.32 ± 0.03	2.66 ± 0.03	29.7 ± 0.2	0.49 ± 0.04	-2 ± 7	48	92	117
96	44.104318	187.06471	2.48 ± 0.07	27 ± 3	98 ± 5	1 ± 1	16 ± 1	31	129	142
97	44.098128	187.064623	2.53 ± 0.05	10.7 ± 0.4	62 ± 1	1.0 ± 0.2	-7 ± 1	29	67	80
98	44.139003	187.063865	1.59 ± 0.01	1.51 ± 0.01	18.49 ± 0.09	0.33 ± 0.03	5 ± 2	77	146	449
99	44.097154	187.064403	3.3 ± 0.2	1.30 ± 0.09	25 ± 1	0.92 ± 0.02	0 ± 4	42	42	48

Morphological parameters of the emission regions in the catalogue from this study. The RA and DEC column correspond to the position of the centroid of the region. The columns with σ_x and σ_y correspond to the standard deviation of the 2D Gaussian spatial profile (described in Section 2.6.2). The radius corresponds to the geometrical mean of $3\sigma_x$ and $3\sigma_y$ (as defined in Section 2.7.2). The E value corresponds to the eccentricity of the region (described in Section 2.7.2). The angle corresponds to the spatial inclination of the region, obtained from the 2D Gaussian fit (described in Section 2.6.2). The first (1NN), second (2NN), and third (3NN) nearest neighbour corresponds to the proximity distance between the centroids of the regions (described in Section 2.7.4).

ID	RA	DEC	σ_x [px]	σ_y [px]	Radius [pc]	E	Angle [°]	1NN [pc]	2NN [pc]	3NN [pc]
100	44.092276	187.064345	1.89 ± 0.01	1.93 ± 0.01	22.8 ± 0.1	0.20 ± 0.05	4 ± 6	51	67	92
101	44.097772	187.064285	1.91 ± 0.04	21.0 ± 0.8	76 ± 2	1.0 ± 0.5	37 ± 1	29	42	51
102	44.102456	187.064084	1.8 ± 0.1	2.5 ± 0.2	25 ± 1	0.7 ± 0.2	0 ± 9	36	72	75
103	44.0986458	187.063931	2.43 ± 0.04	1.76 ± 0.03	24.7 ± 0.3	0.69 ± 0.02	0 ± 2	42	141	195
104	44.100597	187.063619	2.77 ± 0.08	3.61 ± 0.08	37.7 ± 0.7	0.64 ± 0.08	0 ± 5	30	53	54
105	44.101393	187.063608	1.7 ± 0.1	2.0 ± 0.1	22.1 ± 0.9	0.5 ± 0.2	0 ± 10	25	35	54
106	44.096796	187.063548	1.87 ± 0.09	1.96 ± 0.08	22.8 ± 0.7	0.3 ± 0.2	0 ± 6	30	35	38
107	44.097238	187.063542	3.5 ± 0.1	2.62 ± 0.08	36.1 ± 0.9	0.66 ± 0.04	-1 ± 4	30	32	42
108	44.102455	187.063348	3.2 ± 0.2	1.42 ± 0.05	25 ± 1	0.90 ± 0.02	4 ± 4	36	36	57
109	44.138254	187.062676	1.39 ± 0.02	1.31 ± 0.02	16.1 ± 0.1	0.35 ± 0.04	-2 ± 3	77	222	451
110	44.101301	187.063117	2.0 ± 0.2	1.3 ± 6	60 ± 10	1 ± 3	0 ± 7	25	25	53
111	44.100504	187.063005	4.6 ± 0.1	4.02 ± 0.09	51.4 ± 0.9	0.49 ± 0.05	-1 ± 9	30	54	67
112	44.101655	187.062989	4.0 ± 0.2	1.26 ± 0.03	26.7 ± 0.8	0.949 ± 0.006	-1 ± 2	25	35	55
113	44.0986454	187.063077	5.4 ± 0.3	2.10 ± 0.08	40 ± 1	0.92 ± 0.01	1 ± 2	42	165	184
114	44.0992084	187.062996	2.74 ± 0.03	2.62 ± 0.02	32.0 ± 0.2	0.29 ± 0.05	0 ± 4	64	67	100
115	44.097057	187.06293	1.5 ± 0.1	1.6 ± 0.2	18 ± 1	0.4 ± 0.4	0 ± 9	30	32	35
116	44.096621	187.062813	5.1 ± 0.4	2.13 ± 0.05	39 ± 1	0.91 ± 0.01	-21 ± 2	27	30	38
117	44.09953	187.062776	2.35 ± 0.07	5.5 ± 0.4	43 ± 2	0.9 ± 0.2	11 ± 3	62	67	83
118	44.102516	187.062606	7.5 ± 0.9	1.75 ± 0.01	43 ± 3	0.973 ± 0.007	7 ± 1	36	42	61
119	44.096435	187.062324	1.81 ± 0.08	2.44 ± 0.09	25.0 ± 0.7	0.7 ± 0.1	0 ± 6	27	51	64

Morphological parameters of the emission regions in the catalogue from this study. The RA and DEC column correspond to the position of the centroid of the region. The columns with σ_x and σ_y correspond to the standard deviation of the 2D Gaussian spatial profile (described in Section 2.6.2). The radius corresponds to the geometrical mean of $3\sigma_x$ and $3\sigma_y$ (as defined in Section 2.7.2). The E value corresponds to the eccentricity of the region (described in Section 2.7.2). The angle corresponds to the spatial inclination of the region, obtained from the 2D Gaussian fit (described in Section 2.6.2). The first (1NN), second (2NN), and third (3NN) nearest neighbour corresponds to the proximity distance between the centroids of the regions (described in Section 2.7.4).

ID	RA	DEC	σ_x [px]	σ_y [px]	Radius [pc]	E	Angle [°]	1NN [pc]	2NN [pc]	3NN [pc]
120	44.09873	187.062169	1.55 ± 0.04	2.21 ± 0.08	22.1 ± 0.5	0.71 ± 0.09	4 ± 6	21	62	72
121	44.089893	187.062167	2.60 ± 0.08	2.69 ± 0.05	31.6 ± 0.6	0.3 ± 0.1	0 ± 10	27	48	60
122	44.090598	187.062035	2.39 ± 0.06	2.33 ± 0.05	28.2 ± 0.5	0.2 ± 0.1	0 ± 9	36	40	48
123	44.094309	187.061983	3.2 ± 0.2	2.0 ± 0.2	31 ± 2	0.78 ± 0.05	0 ± 8	32	74	145
124	44.098466	187.061928	1.72 ± 0.05	2.02 ± 0.06	22.2 ± 0.4	0.53 ± 0.09	0 ± 5	21	51	83
125	44.101471	187.061884	4.5 ± 0.2	2.02 ± 0.07	36 ± 1	0.89 ± 0.01	-1 ± 3	38	55	61
126	44.09157	187.061898	2.5 ± 0.1	1.86 ± 0.07	25.6 ± 0.7	0.65 ± 0.05	0 ± 8	38	64	66
127	44.102697	187.061777	6.8 ± 0.2	1.94 ± 0.02	43.4 ± 0.8	0.959 ± 0.003	27.0 ± 0.8	42	56	66
128	44.090066	187.061674	2.83 ± 0.07	2.85 ± 0.05	33.9 ± 0.5	0.1 ± 0.3	0 ± 5	27	40	40
129	44.101913	187.061396	2.65 ± 0.07	3.11 ± 0.07	34.3 ± 0.6	0.53 ± 0.08	1 ± 5	38	56	62
130	44.089182	187.061439	2.09 ± 0.05	2.47 ± 0.06	27.1 ± 0.4	0.53 ± 0.07	-1 ± 6	32	60	61
131	44.094123	187.061373	3.5 ± 0.2	2.28 ± 0.07	34 ± 1	0.75 ± 0.04	1 ± 4	32	42	159
132	44.090595	187.061299	2.02 ± 0.06	1.70 ± 0.04	22.1 ± 0.4	0.54 ± 0.05	1 ± 3	36	40	54
133	44.091389	187.061158	37 ± 3	3.9 ± 0.2	143 ± 7	0.995 ± 0.001	-18 ± 5	38	43	54
134	44.098018	187.061072	1.86 ± 0.02	1.80 ± 0.01	21.9 ± 0.1	0.25 ± 0.04	0 ± 3	51	72	85
135	44.089355	187.060823	3.06 ± 0.09	2.06 ± 0.05	30.0 ± 0.6	0.74 ± 0.02	-1 ± 4	32	47	63
136	44.103232	187.06063	1.63 ± 0.03	1.89 ± 0.03	21.0 ± 0.2	0.51 ± 0.05	0 ± 20	62	66	68
137	44.093982	187.060526	55 ± 8	2.10 ± 0.07	128 ± 9	0.9993 ± 0.0002	4.7 ± 0.9	42	74	152
138	44.102348	187.060274	1.89 ± 0.06	2.77 ± 0.09	27.3 ± 0.6	0.73 ± 0.09	-1 ± 5	44	60	62
139	44.091207	187.060306	1.6 ± 0.2	2.3 ± 0.3	23 ± 2	0.7 ± 0.4	0 ± 20	40	43	63

Morphological parameters of the emission regions in the catalogue from this study. The RA and DEC column correspond to the position of the centroid of the region. The columns with σ_x and σ_y correspond to the standard deviation of the 2D Gaussian spatial profile (described in Section 2.6.2). The radius corresponds to the geometrical mean of $3\sigma_x$ and $3\sigma_y$ (as defined in Section 2.7.2). The E value corresponds to the eccentricity of the region (described in Section 2.7.2). The angle corresponds to the spatial inclination of the region, obtained from the 2D Gaussian fit (described in Section 2.6.2). The first (1NN), second (2NN), and third (3NN) nearest neighbour corresponds to the proximity distance between the centroids of the regions (described in Section 2.7.4).

ID	RA	DEC	σ_x [px]	σ_y [px]	Radius [pc]	E	Angle [°]	1NN [pc]	2NN [pc]	3NN [pc]
140	44.088821	187.060216	2.8 ± 0.1	2.5 ± 0.1	31 ± 1	0.4 ± 0.1	0 ± 8	44	47	64
141	44.145479	187.059353	2.10 ± 0.02	2.26 ± 0.02	26.0 ± 0.2	0.37 ± 0.04	0 ± 5	65	102	106
142	44.083704	187.060164	1.88 ± 0.06	1.50 ± 0.05	20.0 ± 0.5	0.60 ± 0.05	0 ± 5	110	182	230
143	44.101723	187.059991	3.03 ± 0.03	2.29 ± 0.04	31.5 ± 0.3	0.65 ± 0.02	36 ± 3	44	66	69
144	44.091738	187.059949	9.7 ± 0.8	16 ± 1	148 ± 9	0.8 ± 0.2	0 ± 9	33	40	63
145	44.068006	187.060114	2.4 ± 0.1	3.0 ± 0.1	32 ± 1	0.6 ± 0.1	0 ± 10	45	48	254
146	44.068708	187.060106	3.38 ± 0.08	3.16 ± 0.06	39.0 ± 0.6	0.36 ± 0.07	0 ± 3	19	48	298
147	44.088201	187.059916	2.67 ± 0.03	2.24 ± 0.02	29.2 ± 0.2	0.54 ± 0.02	2 ± 3	44	90	99
148	44.085284	187.059665	1.903 ± 0.003	1.852 ± 0.002	22.41 ± 0.02	0.232 ± 0.008	0 ± 10	86	110	131
149	44.068619	187.059739	2.20 ± 0.06	2.19 ± 0.04	26.2 ± 0.4	0.1 ± 0.3	0 ± 4	19	45	287
150	44.098273	187.059347	1.68 ± 0.05	1.86 ± 0.06	21.1 ± 0.4	0.4 ± 0.1	0 ± 9	34	85	91
151	44.10349	187.05927	3.76 ± 0.08	2.70 ± 0.04	38.0 ± 0.5	0.70 ± 0.02	-6 ± 3	25	68	73
152	44.146262	187.058601	2.4 ± 0.1	2.3 ± 0.1	27.8 ± 0.9	0.2 ± 0.3	0 ± 7	49	54	65
153	44.091908	187.059314	2.4 ± 0.1	2.9 ± 0.1	31 ± 1	0.5 ± 0.2	0 ± 10	33	67	96
154	44.096504	187.059127	1.6 ± 0.1	2.2 ± 0.2	23 ± 1	0.7 ± 0.2	1 ± 9	30	42	110
155	44.102425	187.059041	3.02 ± 0.05	1.95 ± 0.04	29.0 ± 0.4	0.76 ± 0.01	0 ± 3	48	60	66
156	44.096945	187.058997	2.3 ± 0.3	1.34 ± 0.08	21 ± 1	0.81 ± 0.05	0 ± 9	24	30	86
157	44.098624	187.058885	3.44 ± 0.04	3.12 ± 0.06	39.1 ± 0.4	0.42 ± 0.04	0 ± 10	34	89	93
158	44.103397	187.058781	3.53 ± 0.09	1.99 ± 0.03	31.7 ± 0.5	0.83 ± 0.01	0 ± 1	25	67	75
159	44.10049	187.0586	1.57 ± 0.06	96 ± 4	147 ± 4	1 ± 3	-40 ± 2	74	76	91

Morphological parameters of the emission regions in the catalogue from this study. The RA and DEC column correspond to the position of the centroid of the region. The columns with σ_x and σ_y correspond to the standard deviation of the 2D Gaussian spatial profile (described in Section 2.6.2). The radius corresponds to the geometrical mean of $3\sigma_x$ and $3\sigma_y$ (as defined in Section 2.7.2). The E value corresponds to the eccentricity of the region (described in Section 2.7.2). The angle corresponds to the spatial inclination of the region, obtained from the 2D Gaussian fit (described in Section 2.6.2). The first (1NN), second (2NN), and third (3NN) nearest neighbour corresponds to the proximity distance between the centroids of the regions (described in Section 2.7.4).

ID	RA	DEC	σ_x [px]	σ_y [px]	Radius [pc]	E	Angle [°]	1NN [pc]	2NN [pc]	3NN [pc]
160	44.096942	187.058505	1.9	± 0.1	2.2	± 0.1	24	± 1	0.5	± 0.2
161	44.143984	187.057781	5.2	± 0.3	5.6	± 0.3	65	± 2	0.4	± 0.2
162	44.101566	187.058321	28.8	± 0.5	20.8	± 0.2	293	± 3	0.69	± 0.02
163	44.146432	187.057615	2.62	± 0.06	1.93	± 0.04	26.8	± 0.4	0.68	± 0.03
164	44.14617	187.057496	1.54	± 0.06	1.50	± 0.07	18.1	± 0.6	0.2	± 0.3
165	44.10242	187.058057	2.7	± 0.3	1.6	± 0.1	24	± 2	0.82	± 0.06
166	44.085981	187.058166	2.38	± 0.02	2.22	± 0.02	27.4	± 0.2	0.36	± 0.03
167	44.06456	187.058091	1.65	± 0.05	1.29	± 0.04	17.5	± 0.4	0.62	± 0.04
168	44.086596	187.057669	1.85	± 0.09	3.0	± 0.1	27.9	± 0.9	0.8	± 0.1
169	44.097643	187.057511	2.69	± 0.04	2.55	± 0.03	31.3	± 0.3	0.33	± 0.05
170	44.102063	187.057447	0.95	± 0.09	1.05	± 0.08	12.0	± 0.8	0.4	± 0.3
171	44.098167	187.057135	1.8	± 0.1	8.7	± 0.4	47	± 2	1.0	± 0.4
172	44.100824	187.057096	0.9	± 0.2	1.1	± 0.5	12	± 3	1	± 1
173	44.100556	187.056731	1.43	± 0.04	1.63	± 0.04	18.2	± 0.3	0.48	± 0.09
174	44.090986	187.056743	1.87	± 0.02	2.22	± 0.03	24.3	± 0.2	0.54	± 0.03
175	44.101526	187.056471	2.54	± 0.05	2.19	± 0.04	28.1	± 0.4	0.51	± 0.04
176	44.076606	187.055962	2.43	± 0.08	1.93	± 0.05	25.9	± 0.5	0.61	± 0.04
177	44.090618	187.055763	2.06	± 0.02	2.07	± 0.02	24.7	± 0.2	0.1	± 0.1
178	44.102494	187.055596	1.54	± 0.06	1.64	± 0.06	19.0	± 0.5	0.3	± 0.2
179	44.099134	187.055522	1.88	± 0.09	2.1	± 0.1	23.5	± 0.8	0.4	± 0.2

Morphological parameters of the emission regions in the catalogue from this study. The RA and DEC column correspond to the position of the centroid of the region. The columns with σ_x and σ_y correspond to the standard deviation of the 2D Gaussian spatial profile (described in Section 2.6.2). The radius corresponds to the geometrical mean of $3\sigma_x$ and $3\sigma_y$ (as defined in Section 2.7.2). The E value corresponds to the eccentricity of the region (described in Section 2.7.2). The angle corresponds to the spatial inclination of the region, obtained from the 2D Gaussian fit (described in Section 2.6.2). The first (1NN), second (2NN), and third (3NN) nearest neighbour corresponds to the proximity distance between the centroids of the regions (described in Section 2.7.4).

ID	RA	DEC	σ_x [px]	σ_y [px]	Radius [pc]	E	Angle [°]	1NN [pc]	2NN [pc]	3NN [pc]
180	44.091895	187.055582	1.75 ± 0.01	1.88 ± 0.01	21.6 ± 0.1	0.37 ± 0.03	16 ± 6	46	54	76
181	44.092678	187.055368	1.87 ± 0.04	2.07 ± 0.04	23.5 ± 0.3	0.43 ± 0.08	0 ± 6	54	81	91
182	44.091349	187.05502	6.3 ± 0.5	1.96 ± 0.05	42 ± 2	0.950 ± 0.008	3 ± 2	46	48	61
183	44.077927	187.05073	1.46 ± 0.06	1.58 ± 0.07	18.2 ± 0.5	0.4 ± 0.2	0 ± 7	53	99	198
184	44.088876	187.054931	1.50 ± 0.01	1.48 ± 0.01	17.8 ± 0.1	0.14 ± 0.08	0 ± 2	61	124	145
185	44.09966	187.054778	1.83 ± 0.02	1.99 ± 0.03	22.8 ± 0.2	0.39 ± 0.05	0 ± 6	51	113	137
186	44.11839	187.054495	1.0 ± 0.2	1.1 ± 0.2	12 ± 2	0.4 ± 0.9	0 ± 20	35	43	161
187	44.078702	187.054944	1.77 ± 0.04	2.14 ± 0.06	23.2 ± 0.4	0.56 ± 0.08	4 ± 5	53	150	185
188	44.117946	187.054133	2.9 ± 0.3	1.9 ± 0.1	28 ± 2	0.76 ± 0.07	-1 ± 7	30	35	171
189	44.145971	187.053685	2.38 ± 0.08	2.7 ± 0.1	30.0 ± 0.8	0.4 ± 0.1	0 ± 7	184	185	193
190	44.139497	187.053546	2.13 ± 0.08	1.78 ± 0.09	23.3 ± 0.8	0.55 ± 0.08	0 ± 7	34	81	120
191	44.091257	187.054038	1.84 ± 0.06	2.11 ± 0.07	23.5 ± 0.5	0.5 ± 0.1	0 ± 9	48	48	86
192	44.091962	187.054026	2.42 ± 0.04	3.01 ± 0.08	32.2 ± 0.5	0.59 ± 0.06	0 ± 2	48	64	76
193	44.118208	187.053637	2.72 ± 0.05	2.74 ± 0.05	32.6 ± 0.4	0.1 ± 0.2	0 ± 4	30	43	142
196	44.139145	187.05306	1.6 ± 0.1	2.4 ± 0.2	23 ± 1	0.7 ± 0.2	0 ± 7	34	70	96
197	44.088758	187.053678	1.64 ± 0.02	1.90 ± 0.01	21.1 ± 0.2	0.51 ± 0.03	0 ± 6	61	94	120
198	44.094615	187.05362	4.7 ± 0.1	2.83 ± 0.08	43.4 ± 0.8	0.80 ± 0.02	-2 ± 3	27	127	156
199	44.094965	187.053368	2.4 ± 0.1	2.7 ± 0.1	31 ± 1	0.4 ± 0.2	0 ± 10	27	114	155
200	44.097266	187.053333	3.53 ± 0.07	4.9 ± 0.1	49.7 ± 0.8	0.69 ± 0.07	-2 ± 4	48	80	101
201	44.102566	187.053008	3.1 ± 0.1	2.95 ± 0.07	36.0 ± 0.8	0.3 ± 0.1	-1 ± 6	35	36	126

Morphological parameters of the emission regions in the catalogue from this study. The RA and DEC column correspond to the position of the centroid of the region. The columns with σ_x and σ_y correspond to the standard deviation of the 2D Gaussian spatial profile (described in Section 2.6.2). The radius corresponds to the geometrical mean of $3\sigma_x$ and $3\sigma_y$ (as defined in Section 2.7.2). The E value corresponds to the eccentricity of the region (described in Section 2.7.2). The angle corresponds to the spatial inclination of the region, obtained from the 2D Gaussian fit (described in Section 2.6.2). The first (1NN), second (2NN), and third (3NN) nearest neighbour corresponds to the proximity distance between the centroids of the regions (described in Section 2.7.4).

ID	RA	DEC	σ_x [px]	σ_y [px]	Radius [pc]	E	Angle [°]	1NN [pc]	2NN [pc]	3NN [pc]
202	44.139762	187.051906	1.467 ± 0.009	1.51 ± 0.01	17.77 ± 0.08	0.24	± 0.04	-6 ± 9	50	58
203	44.090452	187.052572	1.9 ± 0.1	1.33 ± 0.06	19.0 ± 0.7	0.72	± 0.05	0 ± 7	25	38
204	44.097345	187.052349	2.49 ± 0.09	2.60 ± 0.08	30.3 ± 0.7	0.3	± 0.2	0 ± 2	48	49
205	44.119953	187.05199	1.88 ± 0.02	1.59 ± 0.01	20.6 ± 0.1	0.53	± 0.02	0 ± 2	142	161
206	44.090185	187.052208	1.0 ± 0.2	1.1 ± 0.4	13 ± 2	0	± 1	0 ± 4	25	42
207	44.098051	187.052092	6.9 ± 0.2	5.2 ± 0.3	72 ± 2	0.65	± 0.05	-2 ± 6	29	49
208	44.098473	187.052117	3.5 ± 0.1	110 ± 10	229 ± 20	1	± 4	21 ± 2	29	77
209	44.089566	187.052094	1.40 ± 0.06	1.97 ± 0.09	19.8 ± 0.6	0.7	± 0.1	0 ± 6	42	68
210	44.090891	187.052075	1.68 ± 0.08	2.4 ± 0.1	24.1 ± 0.9	0.7	± 0.1	0 ± 7	19	38
211	44.139311	187.051085	2.1 ± 0.1	20 ± 2	77 ± 4	1	± 1	-1 ± 2	40	50
212	44.090977	187.051705	2.21 ± 0.06	2.81 ± 0.06	29.7 ± 0.5	0.62	± 0.07	0 ± 6	19	48
213	44.112941	187.051364	2.79 ± 0.02	2.49 ± 0.02	31.4 ± 0.2	0.45	± 0.02	11 ± 3	128	157
214	44.144256	187.050759	1.19 ± 0.04	1.45 ± 0.05	15.7 ± 0.4	0.6	± 0.1	20 ± 4	54	93
215	44.086541	187.051482	1.78 ± 0.02	1.91 ± 0.02	22.0 ± 0.1	0.37	± 0.04	-6 ± 2	184	207
216	44.139832	187.05071	1.8 ± 0.1	2.1 ± 0.2	24 ± 1	0.5	± 0.2	0 ± 10	24	40
217	44.140181	187.050706	2.6 ± 0.1	4.0 ± 0.3	39 ± 2	0.8	± 0.2	1 ± 8	24	60
218	44.141057	187.050567	1.5 ± 0.1	1.66 ± 0.09	19.0 ± 0.8	0.4	± 0.2	0 ± 10	27	51
219	44.090355	187.051223	1.66 ± 0.08	29 ± 3	82 ± 5	1	± 2	26 ± 6	48	49
220	44.097162	187.05112	2.82 ± 0.04	1.83 ± 0.04	27.1 ± 0.4	0.76	± 0.02	0 ± 3	48	61
221	44.094861	187.051032	2.8 ± 0.1	2.7 ± 0.1	32 ± 1	0.3	± 0.2	0 ± 10	68	85

Morphological parameters of the emission regions in the catalogue from this study. The RA and DEC column correspond to the position of the centroid of the region. The columns with σ_x and σ_y correspond to the standard deviation of the 2D Gaussian spatial profile (described in Section 2.6.2). The radius corresponds to the geometrical mean of $3\sigma_x$ and $3\sigma_y$ (as defined in Section 2.7.2). The E value corresponds to the eccentricity of the region (described in Section 2.7.2). The angle corresponds to the spatial inclination of the region, obtained from the 2D Gaussian fit (described in Section 2.6.2). The first (1NN), second (2NN), and third (3NN) nearest neighbour corresponds to the proximity distance between the centroids of the regions (described in Section 2.7.4).

ID	RA	DEC	σ_x [px]	σ_y [px]	Radius [pc]	E	Angle [°]	1NN [pc]	2NN [pc]	3NN [pc]
222	44.140707	187.050327	1.9 ± 0.1	3.4 ± 0.3	30 ± 2	0.8 ± 0.3	-1 ± 6	27	40	62
223	44.078695	187.051149	2.6 ± 0.1	5.7 ± 0.5	46 ± 2	0.9 ± 0.2	2 ± 3	36	68	119
224	44.079225	187.051165	4.1 ± 0.2	9.5 ± 0.6	74 ± 3	0.9 ± 0.2	13 ± 3	36	95	148
225	44.10158	187.050563	1.78 ± 0.05	1.80 ± 0.05	21.4 ± 0.5	0.1 ± 0.3	0 ± 5	51	136	157
226	44.075717	187.050779	1.59 ± 0.07	1.83 ± 0.08	20.4 ± 0.6	0.5 ± 0.1	-6 ± 7	31	78	81
227	44.098836	187.050448	2.91 ± 0.06	2.91 ± 0.07	34.7 ± 0.6	0 ± 1	0 ± 7	83	94	109
228	44.141577	187.049822	3.0 ± 0.1	4.3 ± 0.3	43 ± 2	0.7 ± 0.2	0 ± 8	42	51	60
229	44.142189	187.049811	4.69 ± 0.08	5.8 ± 0.1	62.1 ± 0.8	0.58 ± 0.05	0 ± 3	42	48	85
230	44.144289	187.049645	1.9 ± 0.2	2.0 ± 0.3	23 ± 2	0.3 ± 0.6	-23 ± 3	42	54	144
231	44.089819	187.050246	1.48 ± 0.06	2.20 ± 0.08	21.5 ± 0.6	0.7 ± 0.1	0 ± 4	60	91	98
232	44.097244	187.050135	1.43 ± 0.03	1.44 ± 0.02	17.1 ± 0.2	0.1 ± 0.4	0 ± 6	48	61	106
233	44.07607	187.050368	1.53 ± 0.01	1.43 ± 0.01	17.7 ± 0.1	0.37 ± 0.03	-1 ± 5	31	47	56
234	44.095474	187.049917	1.87 ± 0.06	2.23 ± 0.07	24.3 ± 0.6	0.5 ± 0.1	0 ± 10	42	43	65
235	44.078072	187.05005	2.5 ± 0.1	2.0 ± 0.1	26 ± 1	0.6 ± 0.1	0 ± 9	53	68	72
236	44.102016	187.049694	1.67 ± 0.09	1.51 ± 0.08	18.9 ± 0.7	0.4 ± 0.1	0 ± 9	51	165	177
237	44.144624	187.048908	2.37 ± 0.02	2.00 ± 0.01	26.0 ± 0.1	0.54 ± 0.01	2 ± 2	42	93	169
238	44.096445	187.049532	1.88 ± 0.07	2.63 ± 0.07	26.6 ± 0.6	0.70 ± 0.09	-1 ± 6	47	59	61
239	44.142098	187.048828	4.13 ± 0.06	3.40 ± 0.05	44.7 ± 0.4	0.57 ± 0.02	-1 ± 5	48	49	60
240	44.076481	187.049584	2.5 ± 0.1	2.8 ± 0.2	32 ± 2	0.5 ± 0.2	0 ± 7	30	47	60
241	44.077363	187.049568	1.77 ± 0.01	2.61 ± 0.02	25.7 ± 0.2	0.74 ± 0.02	0 ± 1	53	60	61

Morphological parameters of the emission regions in the catalogue from this study. The RA and DEC column correspond to the position of the centroid of the region. The columns with σ_x and σ_y correspond to the standard deviation of the 2D Gaussian spatial profile (described in Section 2.6.2). The radius corresponds to the geometrical mean of $3\sigma_x$ and $3\sigma_y$ (as defined in Section 2.7.2). The E value corresponds to the eccentricity of the region (described in Section 2.7.2). The angle corresponds to the spatial inclination of the region, obtained from the 2D Gaussian fit (described in Section 2.6.2). The first (1NN), second (2NN), and third (3NN) nearest neighbour corresponds to the proximity distance between the centroids of the regions (described in Section 2.7.4).

ID	RA	DEC	σ_x [px]	σ_y [px]	Radius [pc]	E	Angle [$^{\circ}$]	1NN [pc]	2NN [pc]	3NN [pc]
242	44.095029	187.049304	1.91 \pm 0.07	4.7 \pm 0.3	36 \pm 1	0.9 \pm 0.2	1 \pm 4	42	43	70
243	44.139204	187.048501	1.7 \pm 0.1	1.9 \pm 0.1	21 \pm 1	0.4 \pm 0.2	0 \pm 9	18	115	125
244	44.095647	187.049053	2.15 \pm 0.04	3.8 \pm 0.3	34 \pm 1	0.8 \pm 0.1	-1 \pm 4	27	43	43
245	44.113324	187.048783	1.87 \pm 0.06	1.69 \pm 0.07	21.2 \pm 0.6	0.4 \pm 0.1	0 \pm 9	34	128	268
246	44.076125	187.049219	3.0 \pm 0.2	2.24 \pm 0.09	31 \pm 1	0.67 \pm 0.05	0 \pm 3	30	56	81
247	44.095998	187.040488	1.2 \pm 0.1	1.3 \pm 0.2	15 \pm 1	0.4 \pm 0.5	0 \pm 60	27	47	65
248	44.139258	187.048134	2.00 \pm 0.06	2.09 \pm 0.06	24.4 \pm 0.5	0.3 \pm 0.2	7 \pm 8	18	131	140
249	44.094052	187.048584	1.88 \pm 0.01	1.83 \pm 0.02	22.1 \pm 0.1	0.23 \pm 0.05	0 \pm 9	75	79	110
250	44.113673	187.048285	3.36 \pm 0.03	3.17 \pm 0.03	38.9 \pm 0.3	0.34 \pm 0.04	0 \pm 3	34	157	239
251	44.142262	187.047837	4.6 \pm 0.2	3.93 \pm 0.09	51 \pm 1	0.51 \pm 0.06	0 \pm 2	49	72	91
252	44.078062	187.048576	2.0 \pm 0.1	1.6 \pm 0.1	21.5 \pm 0.9	0.61 \pm 0.08	0 \pm 8	19	30	68
253	44.077799	187.048459	2.44 \pm 0.08	2.9 \pm 0.1	31.6 \pm 0.8	0.5 \pm 0.1	-1 \pm 4	19	40	61
254	44.090344	187.048031	3.08 \pm 0.04	2.24 \pm 0.03	31.4 \pm 0.3	0.69 \pm 0.01	1 \pm 2	50	74	113
255	44.104257	187.047806	1.67 \pm 0.04	1.90 \pm 0.04	21.3 \pm 0.3	0.48 \pm 0.08	24 \pm 4	103	126	136
256	44.07832	187.04808	2.0 \pm 0.1	4.3 \pm 0.4	35 \pm 2	0.9 \pm 0.3	-1 \pm 5	30	40	97
257	44.106246	187.047416	4.9 \pm 0.1	3.0 \pm 0.1	46 \pm 1	0.78 \pm 0.02	0 \pm 3	110	123	136
258	44.117109	187.047122	2.5 \pm 0.3	1.28 \pm 0.09	21 \pm 1	0.85 \pm 0.04	-3 \pm 5	30	239	268
259	44.09095	187.047429	1.92 \pm 0.05	2.16 \pm 0.05	24.3 \pm 0.4	0.46 \pm 0.08	0 \pm 10	50	107	110
260	44.095636	187.047329	3.88 \pm 0.09	2.84 \pm 0.05	39.7 \pm 0.6	0.68 \pm 0.02	0 \pm 2	75	84	99
261	44.088563	187.047316	2.46 \pm 0.03	3.42 \pm 0.04	34.6 \pm 0.3	0.69 \pm 0.03	0 \pm 2	54	125	161

Morphological parameters of the emission regions in the catalogue from this study. The RA and DEC column correspond to the position of the centroid of the region. The columns with σ_x and σ_y correspond to the standard deviation of the 2D Gaussian spatial profile (described in Section 2.6.2). The radius corresponds to the geometrical mean of $3\sigma_x$ and $3\sigma_y$ (as defined in Section 2.7.2). The E value corresponds to the eccentricity of the region (described in Section 2.7.2). The angle corresponds to the spatial inclination of the region, obtained from the 2D Gaussian fit (described in Section 2.6.2). The first (1NN), second (2NN), and third (3NN) nearest neighbour corresponds to the proximity distance between the centroids of the regions (described in Section 2.7.4).

ID	RA	DEC	σ_x [px]	σ_y [px]	Radius [pc]	E	Angle [°]	1NN [pc]	2NN [pc]	3NN [pc]
262	44.089369	187.047325	2.43 ± 0.08	21 ± 2	84 ± 5	1.0 ± 0.9	-16 ± 2	54	74	107
263	44.141826	187.046497	22 ± 5	2.58 ± 0.08	90 ± 10	0.993 ± 0.003	-3 ± 2	20	34	72
264	44.085381	187.047117	2.28 ± 0.05	1.78 ± 0.04	24.0 ± 0.4	0.62 ± 0.03	0 ± 4	84	215	226
265	44.093865	187.046988	3.25 ± 0.08	2.37 ± 0.05	33.1 ± 0.5	0.68 ± 0.02	0 ± 4	36	51	69
266	44.117194	187.046506	2.26 ± 0.07	2.23 ± 0.06	26.8 ± 0.5	0.1 ± 0.3	0 ± 6	30	253	284
267	44.141714	187.046125	1.83 ± 0.06	1.7 ± 0.1	21.0 ± 0.7	0.4 ± 0.1	6 ± 5	18	20	67
268	44.141467	187.046006	3.7 ± 0.1	3.3 ± 0.1	41.7 ± 0.9	0.43 ± 0.08	0 ± 10	18	34	51
269	44.075048	187.046902	1.540 ± 0.003	1.545 ± 0.005	18.41 ± 0.03	0.08 ± 0.05	0.6 ± 0.8	134	163	182
270	44.092357	187.046272	2.52 ± 0.02	2.41 ± 0.03	29.4 ± 0.2	0.29 ± 0.05	0 ± 3	102	108	110
271	44.093861	187.046249	1.44 ± 0.09	12 ± 7	50 ± 10	1 ± 5	0 ± 3	36	36	37
272	44.09439	187.046242	1.78 ± 0.02	1.71 ± 0.02	20.8 ± 0.1	0.29 ± 0.04	0 ± 9	33	36	51
273	44.104999	187.045956	2.7 ± 0.2	1.9 ± 0.1	27 ± 1	0.71 ± 0.06	0 ± 8	24	103	110
274	44.140324	187.045285	1.55 ± 0.09	2.9 ± 0.3	25 ± 1	0.8 ± 0.2	0 ± 6	42	58	85
275	44.140938	187.045276	3.57 ± 0.04	3.87 ± 0.06	44.3 ± 0.4	0.39 ± 0.05	0 ± 3	42	51	67
276	44.094192	187.045629	9.1 ± 0.9	2.69 ± 0.08	59 ± 3	0.96 ± 0.01	-9 ± 3	33	37	51
277	44.105075	187.045462	3.3 ± 0.2	2.42 ± 0.09	34 ± 1	0.68 ± 0.07	7 ± 4	24	123	126
278	44.085282	187.045397	2.26 ± 0.06	1.68 ± 0.04	23.3 ± 0.4	0.67 ± 0.03	-2 ± 3	84	199	241
279	44.139792	187.044358	1.94 ± 0.02	1.97 ± 0.01	23.3 ± 0.1	0.18 ± 0.06	1 ± 8	58	90	139
280	44.094469	187.044642	1.76 ± 0.09	1.38 ± 0.07	18.6 ± 0.7	0.62 ± 0.07	0 ± 10	49	51	64
281	44.107464	187.044318	2.64 ± 0.05	2.69 ± 0.05	31.8 ± 0.4	0.2 ± 0.1	0 ± 4	170	171	184

Morphological parameters of the emission regions in the catalogue from this study. The RA and DEC column correspond to the position of the centroid of the region. The columns with σ_x and σ_y correspond to the standard deviation of the 2D Gaussian spatial profile (described in Section 2.6.2). The radius corresponds to the geometrical mean of $3\sigma_x$ and $3\sigma_y$ (as defined in Section 2.7.2). The E value corresponds to the eccentricity of the region (described in Section 2.7.2). The angle corresponds to the spatial inclination of the region, obtained from the 2D Gaussian fit (described in Section 2.6.2). The first (1NN), second (2NN), and third (3NN) nearest neighbour corresponds to the proximity distance between the centroids of the regions (described in Section 2.7.4).

ID	RA	DEC	σ_x [px]	σ_y [px]	Radius [pc]	E	Angle [°]	1NN [pc]	2NN [pc]	3NN [pc]
282	44.069056	187.044812	1.56 ± 0.03	1.54 ± 0.03	18.5 ± 0.3	0.2 ± 0.2	6 ± 4	234	239	241
283	44.100123	187.043937	6.8 ± 0.2	4.1 ± 0.2	63 ± 2	0.80 ± 0.03	-1 ± 2	237	274	297
284	44.093403	187.04392	1.97 ± 0.02	2.07 ± 0.02	24.1 ± 0.2	0.30 ± 0.05	0 ± 2	36	61	80
285	44.094286	187.04366	2.17 ± 0.06	2.8 ± 0.1	29.2 ± 0.7	0.6 ± 0.1	0 ± 6	38	49	59
286	44.050885	187.044055	2.5 ± 0.1	2.1 ± 0.1	27 ± 1	0.5 ± 0.1	0 ± 7	40	62	72
287	44.094817	187.043406	2.78 ± 0.03	5.5 ± 0.1	46.7 ± 0.7	0.86 ± 0.07	-3 ± 1	38	45	64
288	44.093488	187.043181	2.7 ± 0.2	1.7 ± 0.3	26 ± 3	0.8 ± 0.1	0 ± 8	36	59	90
289	44.051406	187.043682	2.1 ± 0.2	1.9 ± 0.2	24 ± 1	0.5 ± 0.2	0 ± 10	40	45	68
290	44.095432	187.04303	3.04 ± 0.06	3.32 ± 0.08	37.9 ± 0.6	0.40 ± 0.09	0 ± 4	45	80	83
291	44.065697	187.043238	2.17 ± 0.08	2.10 ± 0.06	25.5 ± 0.6	0.2 ± 0.2	-2 ± 5	94	115	241
292	44.089866	187.04276	2.32 ± 0.09	7.4 ± 0.4	49 ± 2	0.9 ± 0.2	2 ± 2	177	199	224
293	44.104003	187.042285	3.43 ± 0.05	2.56 ± 0.05	35.4 ± 0.4	0.67 ± 0.02	2 ± 2	24	170	190
294	44.104357	187.042271	1.67 ± 0.07	1.55 ± 0.09	19.2 ± 0.7	0.4 ± 0.2	0 ± 9	24	162	184
295	44.051138	187.042833	2.1 ± 0.1	2.4 ± 0.1	26 ± 1	0.5 ± 0.2	1 ± 8	27	45	62
296	44.083407	187.042233	4.1 ± 0.2	2.6 ± 0.1	39 ± 1	0.76 ± 0.04	0 ± 6	102	106	128
297	44.050787	187.042591	1.4 ± 0.1	3.3 ± 0.5	26 ± 2	0.9 ± 0.5	6 ± 6	27	43	60
298	44.09454	187.041933	2.34 ± 0.04	2.72 ± 0.07	30.2 ± 0.5	0.51 ± 0.07	-1 ± 8	74	80	85
299	44.071936	187.041971	1.77 ± 0.03	1.74 ± 0.02	20.9 ± 0.2	0.2 ± 0.1	-2 ± 4	27	99	135
300	44.050083	187.041867	1.8 ± 0.1	1.9 ± 0.1	22.3 ± 0.9	0.3 ± 0.3	0 ± 10	24	30	34
301	44.050433	187.041862	1.3 ± 0.2	2.3 ± 0.2	21 ± 2	0.8 ± 0.3	0 ± 10	24	24	43

Morphological parameters of the emission regions in the catalogue from this study. The RA and DEC column correspond to the position of the centroid of the region. The columns with σ_x and σ_y correspond to the standard deviation of the 2D Gaussian spatial profile (described in Section 2.6.2). The radius corresponds to the geometrical mean of $3\sigma_x$ and $3\sigma_y$ (as defined in Section 2.7.2). The E value corresponds to the eccentricity of the region (described in Section 2.7.2). The angle corresponds to the spatial inclination of the region, obtained from the 2D Gaussian fit (described in Section 2.6.2). The first (1NN), second (2NN), and third (3NN) nearest neighbour corresponds to the proximity distance between the centroids of the regions (described in Section 2.7.4).

ID	RA	DEC	σ_x [px]	σ_y [px]	Radius [pc]	E	Angle [$^{\circ}$]	1NN [pc]	2NN [pc]	3NN [pc]
302	44.066477	187.041631	1.6	± 0.1	3.2	± 0.2	27	± 1	0.9	± 0.2
303	44.049646	187.04175	1.9	± 0.1	2.6	± 0.3	26	± 1	0.7	± 0.2
304	44.072021	187.041426	2.86	± 0.02	3.50	± 0.03	37.7	± 0.2	0.58	± 0.03
305	44.049208	187.041513	2.0	± 0.2	2.0	± 0.2	24	± 2	0	± 1
306	44.05043	187.041373	1.4	± 0.2	1.1	± 0.1	14	± 1	0.6	± 0.2
307	44.066474	187.041144	2.5	± 0.1	3.0	± 0.1	33	± 1	0.5	± 0.1
308	44.049555	187.041141	1.3	± 0.1	1.3	± 0.1	16	± 1	0	± 1
309	44.049905	187.041137	1.5	± 0.1	1.7	± 0.1	19.4	± 0.9	0.4	± 0.2
310	44.097711	187.040406	3.8	± 0.1	4.9	± 0.1	52	± 1	0.64	± 0.08
311	44.073692	187.040669	4.8	± 0.3	2.04	± 0.08	37	± 1	0.91	± 0.01
312	44.050166	187.040975	1.6	± 0.1	1.49	± 0.09	18.4	± 0.8	0.4	± 0.2
313	44.124997	187.039735	2.70	± 0.07	2.99	± 0.06	33.9	± 0.6	0.43	± 0.09
314	44.086131	187.040222	1.9	± 0.1	1.9	± 0.1	23	± 1	0.2	± 0.6
315	44.083483	187.040141	2.5	± 0.1	1.64	± 0.08	24.0	± 0.9	0.75	± 0.04
316	44.083828	187.040136	3.03	± 0.09	2.42	± 0.09	32.4	± 0.8	0.60	± 0.05
317	44.093645	187.039858	3.8	± 0.3	2.1	± 0.2	34	± 2	0.82	± 0.04
318	44.074095	187.040022	2.3	± 0.1	1.38	± 0.07	21.4	± 0.8	0.81	± 0.03
319	44.084274	187.039883	1.0	± 0.1	20	± 20	60	± 20	0	± 20
320	44.084719	187.039876	1.8	± 0.1	3.3	± 0.4	29	± 2	0.8	± 0.3
321	44.0721	187.039953	2.17	± 0.08	1.93	± 0.07	24.4	± 0.6	0.46	± 0.08

Morphological parameters of the emission regions in the catalogue from this study. The RA and DEC column correspond to the position of the centroid of the region. The columns with σ_x and σ_y correspond to the standard deviation of the 2D Gaussian spatial profile (described in Section 2.6.2). The radius corresponds to the geometrical mean of $3\sigma_x$ and $3\sigma_y$ (as defined in Section 2.7.2). The E value corresponds to the eccentricity of the region (described in Section 2.7.2). The angle corresponds to the spatial inclination of the region, obtained from the 2D Gaussian fit (described in Section 2.6.2). The first (1NN), second (2NN), and third (3NN) nearest neighbour corresponds to the proximity distance between the centroids of the regions (described in Section 2.7.4).

ID	RA	DEC	σ_x [px]	σ_y [px]	Radius [pc]	E	Angle [°]	1NN [pc]	2NN [pc]	3NN [pc]
322	44.086305	187.039604	1.83 ± 0.09	1.73 ± 0.07	21.3 ± 0.7	0.3 ± 0.2	0 ± 10	32	108	138
323	44.073773	187.039682	1.58 ± 0.02	1.46 ± 0.02	18.1 ± 0.2	0.37 ± 0.04	0 ± 8	27	48	82
324	44.094047	187.039357	2.19 ± 0.02	2.20 ± 0.02	26.2 ± 0.2	0.1 ± 0.1	2 ± 5	34	35	36
325	44.090368	187.03917	1.93 ± 0.04	2.50 ± 0.05	26.2 ± 0.4	0.64 ± 0.05	0 ± 4	25	80	81
326	44.09355	187.03912	1.34 ± 0.06	1.85 ± 0.08	18.8 ± 0.5	0.7 ± 0.1	0 ± 6	35	36	66
327	44.094523	187.039104	2.54 ± 0.09	2.23 ± 0.08	28.4 ± 0.7	0.48 ± 0.08	-1 ± 6	34	66	70
328	44.090629	187.039388	4.8 ± 0.2	9.6 ± 0.7	81 ± 4	0.9 ± 0.2	1 ± 4	25	55	60
329	44.084176	187.038653	6.5 ± 0.4	3.1 ± 0.2	53 ± 2	0.88 ± 0.02	-1 ± 4	60	70	76
330	44.103181	187.038226	1.81 ± 0.04	2.19 ± 0.05	23.8 ± 0.4	0.56 ± 0.07	0 ± 4	205	212	286
332	44.072908	187.038515	1.98 ± 0.02	2.06 ± 0.02	24.1 ± 0.2	0.27 ± 0.05	2 ± 4	82	89	109
333	44.091245	187.038049	2.15 ± 0.06	1.71 ± 0.05	22.9 ± 0.5	0.60 ± 0.04	0 ± 7	36	43	49
334	44.090711	187.037565	1.62 ± 0.05	2.23 ± 0.09	22.7 ± 0.6	0.7 ± 0.1	-1 ± 7	33	43	60
335	44.091595	187.037476	1.4 ± 0.1	5.1 ± 0.5	32 ± 2	1.0 ± 0.5	-1 ± 3	36	42	60
336	44.09105	187.037071	4.4 ± 0.1	1.50 ± 0.03	30.6 ± 0.6	0.939 ± 0.005	9 ± 1	33	42	48
337	44.088939	187.03698	1.69 ± 0.05	2.16 ± 0.09	22.8 ± 0.6	0.6 ± 0.1	0 ± 6	38	44	103
338	44.087435	187.036636	1.87 ± 0.02	2.69 ± 0.04	26.7 ± 0.2	0.72 ± 0.03	0 ± 2	38	62	103
339	44.088347	187.036623	2.07 ± 0.03	2.19 ± 0.02	25.4 ± 0.2	0.34 ± 0.05	0 ± 8	44	55	62
340	44.070758	187.036662	2.37 ± 0.06	2.27 ± 0.05	27.7 ± 0.5	0.3 ± 0.1	0 ± 8	114	118	140
341	44.08911	187.03624	2.23 ± 0.09	1.47 ± 0.08	21.6 ± 0.7	0.75 ± 0.04	1 ± 7	38	55	115
342	44.086991	187.036156	1.9 ± 0.1	2.9 ± 0.2	28 ± 1	0.8 ± 0.2	0 ± 7	38	93	94

Morphological parameters of the emission regions in the catalogue from this study. The RA and DEC column correspond to the position of the centroid of the region. The columns with σ_x and σ_y correspond to the standard deviation of the 2D Gaussian spatial profile (described in Section 2.6.2). The radius corresponds to the geometrical mean of $3\sigma_x$ and $3\sigma_y$ (as defined in Section 2.7.2). The E value corresponds to the eccentricity of the region (described in Section 2.7.2). The angle corresponds to the spatial inclination of the region, obtained from the 2D Gaussian fit (described in Section 2.6.2). The first (1NN), second (2NN), and third (3NN) nearest neighbour corresponds to the proximity distance between the centroids of the regions (described in Section 2.7.4).

ID	RA	DEC	σ_x [px]	σ_y [px]	Radius [pc]	E	Angle [°]	1NN [pc]	2NN [pc]	3NN [pc]
343	44.091143	187.036082	2.7 ± 0.1	2.66 ± 0.07	32.0 ± 0.9	0.2 ± 0.3	-1 ± 8	48	74	78
344	44.069167	187.035709	3.73 ± 0.03	3.71 ± 0.02	44.4 ± 0.2	0.12 ± 0.09	0 ± 3	54	60	68
345	44.067055	187.035617	2.62 ± 0.03	2.00 ± 0.02	27.3 ± 0.2	0.65 ± 0.02	-2 ± 2	36	83	91
346	44.109259	187.034927	2.3 ± 0.1	1.88 ± 0.07	24.6 ± 0.7	0.55 ± 0.07	-2 ± 8	30	78	125
347	44.093166	187.035064	1.88 ± 0.09	1.50 ± 0.07	20.0 ± 0.7	0.61 ± 0.07	1 ± 7	96	145	158
348	44.096263	187.034769	1.46 ± 0.05	1.76 ± 0.06	19.1 ± 0.5	0.6 ± 0.1	0 ± 8	43	75	85
349	44.065732	187.035026	1.8 ± 0.1	1.68 ± 0.09	20.8 ± 0.8	0.4 ± 0.2	0 ± 10	21	68	90
350	44.109256	187.034314	2.62 ± 0.09	2.20 ± 0.07	28.6 ± 0.6	0.54 ± 0.06	0 ± 8	30	67	120
351	44.06705	187.034884	4.3 ± 0.9	1.7 ± 0.2	32 ± 4	0.92 ± 0.04	2 ± 8	36	51	68
352	44.069689	187.034868	10.1 ± 0.9	1.59 ± 0.04	48 ± 2	0.988 ± 0.002	31 ± 2	35	38	54
353	44.097497	187.034379	2.04 ± 0.07	3.5 ± 0.1	31.8 ± 0.8	0.8 ± 0.1	-1 ± 3	25	62	85
354	44.107487	187.034218	1.81 ± 0.07	1.38 ± 0.08	18.9 ± 0.7	0.65 ± 0.06	0 ± 8	54	110	120
355	44.108281	187.034081	1.798 ± 0.007	1.749 ± 0.009	21.17 ± 0.07	0.23 ± 0.03	0 ± 10	54	67	78
356	44.065906	187.034657	1.94 ± 0.08	2.05 ± 0.09	23.8 ± 0.7	0.3 ± 0.2	0 ± 7	21	47	78
357	44.068545	187.034613	2.5 ± 0.2	2.6 ± 0.2	30 ± 2	0.3 ± 0.3	0 ± 4	47	48	68
358	44.086624	187.034314	2.24 ± 0.08	4.7 ± 0.2	39 ± 1	0.9 ± 0.1	0 ± 3	93	101	104
359	44.069248	187.034479	1.63 ± 0.07	1.48 ± 0.06	18.5 ± 0.5	0.4 ± 0.1	0 ± 6	30	35	48
360	44.08265	187.034256	2.34 ± 0.04	3.56 ± 0.06	34.4 ± 0.4	0.76 ± 0.05	-1 ± 2	51	144	169
361	44.096611	187.034025	2.40 ± 0.09	2.6 ± 0.1	29.6 ± 0.8	0.4 ± 0.2	0 ± 9	42	43	62
362	44.09723	187.034015	1.4 ± 0.3	2.7 ± 0.8	24 ± 4	0.9 ± 0.8	0 ± 20	25	42	75

Morphological parameters of the emission regions in the catalogue from this study. The RA and DEC column correspond to the position of the centroid of the region. The columns with σ_x and σ_y correspond to the standard deviation of the 2D Gaussian spatial profile (described in Section 2.6.2). The radius corresponds to the geometrical mean of $3\sigma_x$ and $3\sigma_y$ (as defined in Section 2.7.2). The E value corresponds to the eccentricity of the region (described in Section 2.7.2). The angle corresponds to the spatial inclination of the region, obtained from the 2D Gaussian fit (described in Section 2.6.2). The first (1NN), second (2NN), and third (3NN) nearest neighbour corresponds to the proximity distance between the centroids of the regions (described in Section 2.7.4).

ID	RA	DEC	σ_x [px]	σ_y [px]	Radius [pc]	E	Angle [°]	1NN [pc]	2NN [pc]	3NN [pc]
363	44.12519	187.03357	1.279 ± 0.008	1.266 ± 0.007	15.19 ± 0.06	0.14 ± 0.06	17 ± 1	299	710	748
364	44.069596	187.034104	2.27 ± 0.05	1.70 ± 0.03	23.4 ± 0.3	0.66 ± 0.02	0 ± 4	30	38	75
365	44.074442	187.034025	3.7 ± 0.1	2.73 ± 0.09	38.0 ± 0.9	0.67 ± 0.04	-1 ± 5	93	123	145
366	44.067485	187.034017	2.4 ± 0.1	3.4 ± 0.3	34 ± 2	0.7 ± 0.2	0 ± 9	42	51	78
367	44.066341	187.033913	2.4 ± 0.1	2.23 ± 0.09	27.5 ± 0.8	0.3 ± 0.1	0 ± 6	47	68	68
368	44.0681	187.033886	2.37 ± 0.04	2.91 ± 0.05	31.3 ± 0.4	0.58 ± 0.05	0 ± 3	42	47	68
369	44.071181	187.033833	3.83 ± 0.09	2.65 ± 0.06	38.1 ± 0.6	0.72 ± 0.02	-1 ± 5	108	113	135
370	44.083174	187.033512	3.4 ± 0.1	2.22 ± 0.08	32.7 ± 0.9	0.75 ± 0.03	3 ± 3	51	147	155
371	44.100319	187.033103	4.5 ± 0.2	2.27 ± 0.08	38 ± 1	0.86 ± 0.02	0 ± 3	38	66	110
372	44.092978	187.033103	3.65 ± 0.07	2.27 ± 0.04	34.3 ± 0.4	0.78 ± 0.01	20 ± 2	96	190	210
373	44.101291	187.032964	2.0 ± 0.1	2.8 ± 0.3	28 ± 2	0.7 ± 0.2	0 ± 10	30	66	110
374	44.100847	187.032848	2.1 ± 0.1	5.2 ± 0.7	40 ± 3	0.9 ± 0.4	0 ± 5	30	38	96
375	44.105974	187.032765	2.61 ± 0.08	3.0 ± 0.1	33.3 ± 0.8	0.5 ± 0.1	-1 ± 8	32	124	169
376	44.106415	187.032511	1.73 ± 0.04	2.17 ± 0.06	23.1 ± 0.4	0.60 ± 0.08	-1 ± 4	32	110	147
377	44.079992	187.032827	1.34 ± 0.05	1.19 ± 0.04	15.1 ± 0.4	0.46 ± 0.09	0 ± 8	75	85	108
378	44.096159	187.032431	7.0 ± 0.3	3.1 ± 0.1	55 ± 2	0.90 ± 0.01	-1 ± 2	83	106	107
379	44.085906	187.032481	2.6 ± 0.1	2.0 ± 0.1	26.9 ± 0.9	0.63 ± 0.07	0 ± 7	27	56	101
380	44.068366	187.032533	5.2 ± 0.3	1.80 ± 0.07	37 ± 1	0.938 ± 0.009	-18 ± 2	68	94	102
381	44.075842	187.032405	2.05 ± 0.05	1.98 ± 0.04	24.0 ± 0.4	0.3 ± 0.1	0 ± 20	72	99	117
382	44.081048	187.032318	2.02 ± 0.04	1.78 ± 0.04	22.6 ± 0.4	0.47 ± 0.05	0 ± 3	31	75	102

Morphological parameters of the emission regions in the catalogue from this study. The RA and DEC column correspond to the position of the centroid of the region. The columns with σ_x and σ_y correspond to the standard deviation of the 2D Gaussian spatial profile (described in Section 2.6.2). The radius corresponds to the geometrical mean of $3\sigma_x$ and $3\sigma_y$ (as defined in Section 2.7.2). The E value corresponds to the eccentricity of the region (described in Section 2.7.2). The angle corresponds to the spatial inclination of the region, obtained from the 2D Gaussian fit (described in Section 2.6.2). The first (1NN), second (2NN), and third (3NN) nearest neighbour corresponds to the proximity distance between the centroids of the regions (described in Section 2.7.4).

ID	RA	DEC	σ_x [px]	σ_y [px]	Radius [pc]	E	Angle [$^{\circ}$]	1NN [pc]	2NN [pc]	3NN [pc]
383	44.086258	187.03223	2.24 ± 0.08	1.95 ± 0.07	25.0 ± 0.6	0.49 ± 0.08	0 ± 8	27	36	104
384	44.088644	187.03219	1.80 ± 0.04	1.94 ± 0.05	22.3 ± 0.4	0.38 ± 0.09	0 ± 7	156	157	159
385	44.073814	187.032316	2.81 ± 0.08	2.42 ± 0.06	31.1 ± 0.6	0.51 ± 0.06	-1 ± 4	54	91	93
386	44.080952	187.031705	5.6 ± 0.4	2.9 ± 0.1	48 ± 2	0.86 ± 0.03	0 ± 5	31	75	85
387	44.086342	187.031492	2.01 ± 0.05	2.09 ± 0.06	24.5 ± 0.4	0.3 ± 0.1	0 ± 4	36	56	99
388	44.076541	187.031288	1.68 ± 0.08	1.8 ± 0.1	20.8 ± 0.8	0.4 ± 0.2	0 ± 10	36	46	72
389	44.100658	187.030881	1.3 ± 0.1	2.4 ± 0.2	21 ± 1	0.8 ± 0.3	-1 ± 6	18	32	66
390	44.07372	187.031215	2.7 ± 0.1	1.59 ± 0.06	24.7 ± 0.8	0.81 ± 0.03	0 ± 3	38	54	57
391	44.101098	187.030628	1.84 ± 0.05	1.67 ± 0.05	20.9 ± 0.4	0.43 ± 0.08	0 ± 5	30	32	54
392	44.082186	187.030824	2.19 ± 0.06	1.60 ± 0.05	22.3 ± 0.5	0.69 ± 0.03	0 ± 4	43	60	94
393	44.100656	187.030512	1.1 ± 0.2	1.2 ± 0.2	14 ± 1	0.4 ± 0.5	0 ± 10	18	30	48
394	44.077046	187.030665	1.91 ± 0.09	1.57 ± 0.05	20.7 ± 0.6	0.57 ± 0.07	0 ± 4	41	46	82
395	44.079802	187.030619	1.69 ± 0.06	1.51 ± 0.05	19.1 ± 0.5	0.44 ± 0.09	0 ± 8	83	94	108
396	44.076449	187.030554	3.31 ± 0.03	3.04 ± 0.03	37.8 ± 0.3	0.40 ± 0.03	-1 ± 6	36	41	46
397	44.096145	187.030218	2.50 ± 0.04	2.30 ± 0.04	28.7 ± 0.3	0.39 ± 0.05	0 ± 3	64	107	118
398	44.073539	187.03048	2.78 ± 0.08	1.69 ± 0.05	25.9 ± 0.5	0.80 ± 0.02	0 ± 3	35	38	61
399	44.081388	187.030279	1.40 ± 0.01	1.37 ± 0.01	16.5 ± 0.1	0.21 ± 0.06	20 ± 10	31	60	72
401	44.090307	187.029949	7.6 ± 0.2	4.4 ± 0.1	69 ± 1	0.81 ± 0.02	-1 ± 3	59	90	156
402	44.073977	187.030105	1.4 ± 0.1	1.53 ± 0.09	17 ± 1	0.4 ± 0.3	0 ± 5	35	36	53
403	44.095258	187.029744	3.14 ± 0.04	3.75 ± 0.08	41.0 ± 0.5	0.55 ± 0.05	0 ± 5	54	64	70

Morphological parameters of the emission regions in the catalogue from this study. The RA and DEC column correspond to the position of the centroid of the region. The columns with σ_x and σ_y correspond to the standard deviation of the 2D Gaussian spatial profile (described in Section 2.6.2). The radius corresponds to the geometrical mean of $3\sigma_x$ and $3\sigma_y$ (as defined in Section 2.7.2). The E value corresponds to the eccentricity of the region (described in Section 2.7.2). The angle corresponds to the spatial inclination of the region, obtained from the 2D Gaussian fit (described in Section 2.6.2). The first (1NN), second (2NN), and third (3NN) nearest neighbour corresponds to the proximity distance between the centroids of the regions (described in Section 2.7.4).

ID	RA	DEC	σ_x [px]	σ_y [px]	Radius [pc]	E	Angle [$^{\circ}$]	1NN [pc]	2NN [pc]	3NN [pc]
404	44.115139	187.029415	2.19 ± 0.08	1.83 ± 0.07	23.9 ± 0.6	0.55 ± 0.07	0 ± 5	53	201	259
405	44.087126	187.029757	1.59 ± 0.05	1.76 ± 0.05	20.0 ± 0.4	0.4 ± 0.1	0 ± 5	99	133	156
406	44.100473	187.029547	2.3 ± 0.2	2.2 ± 0.1	27 ± 1	0.3 ± 0.2	3 ± 7	36	48	66
407	44.101011	187.029522	2.72 ± 0.04	3.04 ± 0.04	34.3 ± 0.3	0.45 ± 0.05	44 ± 5	36	54	54
408	44.076004	187.029829	11.0 ± 0.4	6.3 ± 0.2	99 ± 2	0.82 ± 0.02	2 ± 5	34	46	54
409	44.094544	187.029259	2.89 ± 0.06	1.86 ± 0.03	27.7 ± 0.4	0.77 ± 0.01	-1 ± 2	27	54	92
410	44.075561	187.02949	1.92 ± 0.04	1.99 ± 0.04	23.3 ± 0.4	0.3 ± 0.1	0 ± 10	34	48	79
411	44.073091	187.029384	2.29 ± 0.08	2.09 ± 0.05	26.2 ± 0.5	0.41 ± 0.09	0 ± 6	38	61	66
412	44.074061	187.029368	1.8 ± 0.1	2.7 ± 0.2	26 ± 1	0.7 ± 0.2	0 ± 10	32	36	65
413	44.080588	187.029393	2.24 ± 0.03	2.50 ± 0.05	28.2 ± 0.3	0.44 ± 0.06	12 ± 3	72	83	92
414	44.089685	187.029098	2.5 ± 0.2	2.0 ± 0.2	27 ± 1	0.6 ± 0.1	0 ± 10	56	59	166
415	44.073619	187.02913	1.55 ± 0.03	1.86 ± 0.05	20.3 ± 0.3	0.56 ± 0.07	0 ± 5	32	38	53
416	44.093218	187.028792	3.8 ± 0.1	6.7 ± 0.3	60 ± 2	0.8 ± 0.1	0 ± 3	90	92	145
417	44.114778	187.028436	1.58 ± 0.06	2.5 ± 0.1	23.8 ± 0.7	0.8 ± 0.1	0 ± 4	53	149	206
418	44.094543	187.028703	1.44 ± 0.04	1.99 ± 0.05	20.2 ± 0.4	0.69 ± 0.07	4 ± 3	27	70	90
419	44.098078	187.028464	2.1 ± 0.1	2.3 ± 0.2	26 ± 1	0.5 ± 0.2	0 ± 20	156	170	191
420	44.075996	187.02871	6.7 ± 0.1	5.27 ± 0.08	71 ± 1	0.62 ± 0.03	-5 ± 3	48	54	72
421	44.077754	187.028687	2.34 ± 0.06	10.6 ± 0.6	59 ± 2	1.0 ± 0.3	-1 ± 1	107	119	126
422	44.090117	187.028107	8.1 ± 0.3	4.17 ± 0.08	69 ± 1	0.86 ± 0.01	0 ± 2	56	90	160
423	44.075052	187.028034	1.65 ± 0.01	1.64 ± 0.02	19.6 ± 0.2	0.1 ± 0.1	0 ± 10	72	76	79

Morphological parameters of the emission regions in the catalogue from this study. The RA and DEC column correspond to the position of the centroid of the region. The columns with σ_x and σ_y correspond to the standard deviation of the 2D Gaussian spatial profile (described in Section 2.6.2). The radius corresponds to the geometrical mean of $3\sigma_x$ and $3\sigma_y$ (as defined in Section 2.7.2). The E value corresponds to the eccentricity of the region (described in Section 2.7.2). The angle corresponds to the spatial inclination of the region, obtained from the 2D Gaussian fit (described in Section 2.6.2). The first (1NN), second (2NN), and third (3NN) nearest neighbour corresponds to the proximity distance between the centroids of the regions (described in Section 2.7.4).

ID	RA	DEC	σ_x [px]	σ_y [px]	Radius [pc]	E	Angle [°]	1NN [pc]	2NN [pc]	3NN [pc]
424	44.069911	187.027968	3.8 ± 0.1	3.7 ± 0.1	45 ± 1	0.2 ± 0.2	-1 ± 5	226	245	258
425	44.073961	187.02765	1.87 ± 0.02	2.42 ± 0.04	25.4 ± 0.3	0.64 ± 0.04	0 ± 3	76	76	84
426	44.082669	187.027374	4.9 ± 0.3	1.41 ± 0.05	31 ± 1	0.959 ± 0.006	7 ± 2	28	82	97
427	44.081279	187.026908	1.31 ± 0.05	1.7 ± 0.1	17.8 ± 0.6	0.6 ± 0.1	0 ± 9	72	72	78
428	44.082431	187.026893	2.03 ± 0.04	2.12 ± 0.04	24.8 ± 0.3	0.3 ± 0.1	0 ± 4	28	54	78
429	44.08013	187.026805	2.7 ± 0.1	2.5 ± 0.1	31 ± 1	0.4 ± 0.2	0 ± 10	48	48	78
430	44.075012	187.026181	1.94 ± 0.02	1.79 ± 0.02	22.3 ± 0.2	0.38 ± 0.03	0 ± 6	90	101	132
431	44.076965	187.026203	1.90 ± 0.05	1.90 ± 0.05	22.7 ± 0.4	0.1 ± 0.4	13 ± 6	49	132	132
432	44.088338	187.025925	1.7 ± 0.1	1.8 ± 0.1	21 ± 1	0.1 ± 0.7	0 ± 20	36	40	160
433	44.104532	187.025695	1.67 ± 0.03	1.48 ± 0.03	18.8 ± 0.2	0.47 ± 0.04	5 ± 5	98	115	128
434	44.080477	187.02594	2.01 ± 0.07	3.1 ± 0.1	29.9 ± 0.8	0.8 ± 0.1	1 ± 4	30	48	51
435	44.082064	187.025912	1.91 ± 0.03	2.12 ± 0.04	24.0 ± 0.3	0.44 ± 0.06	0 ± 6	52	54	72
436	44.114394	187.02541	1.23 ± 0.01	1.34 ± 0.01	15.4 ± 0.1	0.40 ± 0.04	13 ± 2	61	149	201
437	44.077655	187.025916	2.35 ± 0.05	2.25 ± 0.06	27.4 ± 0.5	0.3 ± 0.1	0 ± 8	49	108	135
438	44.080036	187.025825	1.6 ± 0.1	1.7 ± 0.1	19 ± 1	0.3 ± 0.3	0 ± 20	30	48	49
439	44.084802	187.025741	3.00 ± 0.02	3.11 ± 0.02	36.4 ± 0.1	0.27 ± 0.03	-1 ± 2	54	100	100
440	44.108928	187.02533	1.65 ± 0.07	1.88 ± 0.08	21.0 ± 0.6	0.5 ± 0.1	0 ± 5	281	297	316
441	44.087806	187.025566	2.77 ± 0.03	2.28 ± 0.03	30.0 ± 0.3	0.57 ± 0.02	0 ± 3	35	40	154
442	44.096112	187.025299	2.87 ± 0.07	2.47 ± 0.07	31.8 ± 0.6	0.51 ± 0.05	0 ± 4	51	139	158
443	44.101224	187.025087	2.88 ± 0.03	2.55 ± 0.02	32.4 ± 0.2	0.47 ± 0.02	4 ± 4	122	131	161

Morphological parameters of the emission regions in the catalogue from this study. The RA and DEC column correspond to the position of the centroid of the region. The columns with σ_x and σ_y correspond to the standard deviation of the 2D Gaussian spatial profile (described in Section 2.6.2). The radius corresponds to the geometrical mean of $3\sigma_x$ and $3\sigma_y$ (as defined in Section 2.7.2). The E value corresponds to the eccentricity of the region (described in Section 2.7.2). The angle corresponds to the spatial inclination of the region, obtained from the 2D Gaussian fit (described in Section 2.6.2). The first (1NN), second (2NN), and third (3NN) nearest neighbour corresponds to the proximity distance between the centroids of the regions (described in Section 2.7.4).

ID	RA	DEC	σ_x [px]	σ_y [px]	Radius [pc]	E	Angle [°]	1NN [pc]	2NN [pc]	3NN [pc]
444	44.088245	187.02519	3.4 ± 0.8	1.78 ± 0.09	29 ± 3	0.85 ± 0.08	0 ± 2	35	36	143
445	44.080914	187.025072	2.75 ± 0.01	2.38 ± 0.03	30.6 ± 0.2	0.50 ± 0.02	0 ± 4	33	49	51
446	44.081757	187.02493	1.61 ± 0.03	1.78 ± 0.03	20.2 ± 0.2	0.43 ± 0.06	0 ± 10	52	57	71
447	44.098757	187.024639	30 ± 10	2.9 ± 0.1	110 ± 30	0.994 ± 0.006	-35 ± 2	87	126	150
448	44.113867	187.024388	2.05 ± 0.03	1.73 ± 0.03	22.5 ± 0.3	0.54 ± 0.03	0 ± 3	61	206	259
449	44.079059	187.024861	3.54 ± 0.09	2.07 ± 0.06	32.3 ± 0.6	0.81 ± 0.02	0 ± 2	78	81	96
450	44.080206	187.02484	1.77 ± 0.04	1.50 ± 0.04	19.4 ± 0.3	0.53 ± 0.05	0 ± 10	18	49	49
451	44.095576	187.02457	2.30 ± 0.03	3.34 ± 0.04	33.1 ± 0.3	0.73 ± 0.04	0 ± 2	51	91	108
452	44.080474	187.024798	2.51 ± 0.04	4.8 ± 0.7	42 ± 3	0.9 ± 0.3	-9 ± 4	18	33	55
453	44.084885	187.024634	1.7 ± 0.1	2.0 ± 0.1	22.4 ± 0.9	0.5 ± 0.2	0 ± 10	54	55	67
454	44.102909	187.024199	4.22 ± 0.05	2.86 ± 0.04	41.5 ± 0.4	0.73 ± 0.01	-1 ± 2	42	98	104
455	44.083998	187.024024	1.43 ± 0.05	1.35 ± 0.06	16.6 ± 0.5	0.3 ± 0.2	-4 ± 6	26	67	100
456	44.10441	187.023682	1.79 ± 0.07	2.14 ± 0.09	23.4 ± 0.7	0.6 ± 0.1	0 ± 7	30	42	72
457	44.103348	187.023577	2.55 ± 0.07	2.10 ± 0.06	27.6 ± 0.6	0.57 ± 0.05	0 ± 7	42	70	72
458	44.084349	187.023782	2.25 ± 0.03	1.81 ± 0.02	24.1 ± 0.2	0.59 ± 0.02	-1 ± 2	26	55	100
459	44.105005	187.023426	2.0 ± 0.1	3.0 ± 0.2	30 ± 1	0.7 ± 0.2	8 ± 5	42	50	112
460	44.081168	187.023717	2.9 ± 0.1	1.90 ± 0.07	28.1 ± 0.8	0.76 ± 0.03	0 ± 6	68	70	71
461	44.098018	187.023174	2.13 ± 0.01	2.16 ± 0.01	25.6 ± 0.1	0.15 ± 0.06	0 ± 20	48	76	82
462	44.104317	187.023068	2.0 ± 0.1	3.3 ± 0.2	31 ± 1	0.8 ± 0.2	0 ± 6	30	50	70
463	44.092561	187.023146	1.36 ± 0.05	1.72 ± 0.07	18.2 ± 0.5	0.6 ± 0.1	0 ± 6	107	115	144

Morphological parameters of the emission regions in the catalogue from this study. The RA and DEC column correspond to the position of the centroid of the region. The columns with σ_x and σ_y correspond to the standard deviation of the 2D Gaussian spatial profile (described in Section 2.6.2). The radius corresponds to the geometrical mean of $3\sigma_x$ and $3\sigma_y$ (as defined in Section 2.7.2). The E value corresponds to the eccentricity of the region (described in Section 2.7.2). The angle corresponds to the spatial inclination of the region, obtained from the 2D Gaussian fit (described in Section 2.6.2). The first (1NN), second (2NN), and third (3NN) nearest neighbour corresponds to the proximity distance between the centroids of the regions (described in Section 2.7.4).

ID	RA	DEC	σ_x [px]	σ_y [px]	Radius [pc]	E	Angle [°]	1NN [pc]	2NN [pc]	3NN [pc]
464	44.095034	187.022858	1.95 ± 0.06	2.02 ± 0.06	23.7 ± 0.5	0.3 ± 0.2	0 ± 6	25	91	108
465	44.09468	187.02274	1.50 ± 0.06	2.06 ± 0.09	21.0 ± 0.6	0.7 ± 0.1	0 ± 6	25	108	118
466	44.102011	187.022624	2.25 ± 0.05	3.6 ± 5	107 ± 8	1 ± 2	-11.1 ± 0.8	60	85	98
467	44.097064	187.02233	2.48 ± 0.08	1.70 ± 0.05	24.5 ± 0.5	0.73 ± 0.03	0 ± 4	38	54	64
468	44.087522	187.022427	1.755 ± 0.006	1.970 ± 0.006	22.20 ± 0.05	0.45 ± 0.01	12 ± 2	108	143	146
469	44.098124	187.022189	4.7 ± 0.4	5.0 ± 0.3	58 ± 3	0.3 ± 0.3	0 ± 20	35	48	53
470	44.077895	187.022425	2.79 ± 0.04	2.51 ± 0.04	31.6 ± 0.4	0.43 ± 0.04	0 ± 4	43	49	142
471	44.089109	187.022224	2.59 ± 0.07	3.15 ± 0.07	34.1 ± 0.6	0.57 ± 0.07	0 ± 6	108	137	152
472	44.091142	187.022188	3.20 ± 0.07	2.35 ± 0.05	32.7 ± 0.5	0.68 ± 0.02	-1 ± 4	107	137	138
473	44.100419	187.021904	3.7 ± 0.1	3.6 ± 0.1	43 ± 1	0.3 ± 0.2	0 ± 1	42	103	113
474	44.07719	187.022177	2.09 ± 0.06	3.8 ± 0.1	33.5 ± 0.7	0.83 ± 0.09	-18 ± 3	49	49	182
475	44.080189	187.022137	1.54 ± 0.03	1.41 ± 0.03	17.6 ± 0.3	0.41 ± 0.06	0 ± 4	102	131	131
476	44.099801	187.021791	3.23 ± 0.06	3.15 ± 0.08	38.0 ± 0.6	0.2 ± 0.1	-1 ± 7	42	61	96
477	44.102628	187.021744	1.96 ± 0.03	2.00 ± 0.03	23.6 ± 0.3	0.2 ± 0.1	0 ± 3	51	60	84
478	44.097413	187.02171	2.66 ± 0.04	1.99 ± 0.03	27.5 ± 0.3	0.66 ± 0.02	0 ± 4	38	38	53
479	44.098384	187.021569	4.3 ± 0.4	1.82 ± 0.07	34 ± 2	0.91 ± 0.02	-6 ± 3	35	36	42
480	44.098915	187.02156	2.28 ± 0.06	2.00 ± 0.06	25.5 ± 0.5	0.48 ± 0.07	0 ± 7	36	55	61
481	44.077775	187.021563	37 ± 3	2.6 ± 0.2	118 ± 6	0.9975 ± 0.0005	-6 ± 3	43	49	166
482	44.096523	187.021253	1.78 ± 0.05	2.72 ± 0.08	26.3 ± 0.5	0.76 ± 0.08	20 ± 4	30	43	64
483	44.096966	187.021226	1.93 ± 0.06	25 ± 6	80 ± 10	1 ± 3	17 ± 3	30	38	54

Morphological parameters of the emission regions in the catalogue from this study. The RA and DEC column correspond to the position of the centroid of the region. The columns with σ_x and σ_y correspond to the standard deviation of the 2D Gaussian spatial profile (described in Section 2.6.2). The radius corresponds to the geometrical mean of $3\sigma_x$ and $3\sigma_y$ (as defined in Section 2.7.2). The E value corresponds to the eccentricity of the region (described in Section 2.7.2). The angle corresponds to the spatial inclination of the region, obtained from the 2D Gaussian fit (described in Section 2.6.2). The first (1NN), second (2NN), and third (3NN) nearest neighbour corresponds to the proximity distance between the centroids of the regions (described in Section 2.7.4).

ID	RA	DEC	σ_x [px]	σ_y [px]	Radius [pc]	E	Angle [°]	1NN [pc]	2NN [pc]	3NN [pc]
484	44.095906	187.020998	2.62 ± 0.07	3.73 ± 0.09	37.3 ± 0.7	0.71 ± 0.07	-1 ± 5	43	72	102
485	44.102181	187.020891	2.89 ± 0.04	2.60 ± 0.03	32.7 ± 0.3	0.44 ± 0.04	0 ± 6	51	54	59
486	44.093165	187.020924	3.2 ± 0.2	2.1 ± 0.1	31 ± 1	0.75 ± 0.04	0.1 ± 0.7	115	135	144
487	44.098378	187.020709	1.99 ± 0.06	1.75 ± 0.06	22.3 ± 0.5	0.47 ± 0.07	0 ± 7	24	42	55
488	44.072953	187.021064	2.14 ± 0.02	2.30 ± 0.02	26.5 ± 0.2	0.37 ± 0.03	3 ± 2	286	292	327
489	44.098035	187.020626	1.63 ± 0.04	10.4 ± 0.8	49 ± 2	1.0 ± 0.5	-12 ± 1	24	52	67
490	44.101467	187.020042	2.1 ± 0.2	2.4 ± 0.2	27 ± 1	0.5 ± 0.2	0 ± 10	49	64	90
491	44.102792	187.020019	2.0 ± 0.2	2.5 ± 0.3	27 ± 2	0.6 ± 0.3	0 ± 10	43	59	84
492	44.083177	187.020118	1.56 ± 0.09	1.6 ± 0.1	19.0 ± 0.8	0.3 ± 0.3	0 ± 10	129	153	169
493	44.102172	187.019784	3.09 ± 0.05	4.09 ± 0.08	42.5 ± 0.5	0.66 ± 0.05	0 ± 3	43	49	54
494	44.090336	187.019582	3.47 ± 0.03	3.25 ± 0.03	40.1 ± 0.3	0.35 ± 0.03	22 ± 5	95	100	130
495	44.087676	187.019425	3.25 ± 0.07	2.31 ± 0.05	32.7 ± 0.5	0.70 ± 0.02	0 ± 3	65	146	164
496	44.091649	187.01886	1.93 ± 0.08	1.58 ± 0.03	20.8 ± 0.5	0.58 ± 0.05	0 ± 7	40	49	67
497	44.081485	187.018919	2.107 ± 0.009	2.075 ± 0.007	24.96 ± 0.07	0.17 ± 0.03	0 ± 3	63	109	129
498	44.088199	187.01831	3.0 ± 0.1	3.27 ± 0.08	37.6 ± 0.8	0.4 ± 0.1	0 ± 9	65	141	151
499	44.091378	187.018127	2.01 ± 0.06	2.52 ± 0.09	26.8 ± 0.6	0.6 ± 0.1	0 ± 8	32	33	40
500	44.079016	187.018229	1.72 ± 0.06	1.95 ± 0.08	21.9 ± 0.6	0.5 ± 0.1	0 ± 7	171	182	186
501	44.09243	187.017984	2.9 ± 0.1	2.45 ± 0.09	31.8 ± 0.8	0.53 ± 0.07	1 ± 9	42	56	64
502	44.101981	187.017818	2.00 ± 0.08	3.8 ± 0.2	33 ± 1	0.8 ± 0.1	0 ± 4	96	113	120
503	44.091819	187.017874	1.81 ± 0.04	2.10 ± 0.06	23.3 ± 0.4	0.50 ± 0.08	0 ± 6	26	32	42

Morphological parameters of the emission regions in the catalogue from this study. The RA and DEC column correspond to the position of the centroid of the region. The columns with σ_x and σ_y correspond to the standard deviation of the 2D Gaussian spatial profile (described in Section 2.6.2). The radius corresponds to the geometrical mean of $3\sigma_x$ and $3\sigma_y$ (as defined in Section 2.7.2). The E value corresponds to the eccentricity of the region (described in Section 2.7.2). The angle corresponds to the spatial inclination of the region, obtained from the 2D Gaussian fit (described in Section 2.6.2). The first (1NN), second (2NN), and third (3NN) nearest neighbour corresponds to the proximity distance between the centroids of the regions (described in Section 2.7.4).

ID	RA	DEC	σ_x [px]	σ_y [px]	Radius [pc]	E	Angle [°]	1NN [pc]	2NN [pc]	3NN [pc]
504	44.081745	187.017679	1.38 ± 0.03	1.46 ± 0.03	16.9 ± 0.2	0.32 ± 0.09	0 ± 7	48	63	145
505	44.091551	187.017488	2.5 ± 0.1	1.93 ± 0.09	26.2 ± 0.9	0.64 ± 0.06	22 ± 9	26	33	38
506	44.091989	187.01701	2.6 ± 0.1	1.65 ± 0.03	24.6 ± 0.6	0.77 ± 0.02	0 ± 3	38	38	43
507	44.082202	187.016913	2.64 ± 0.08	2.22 ± 0.07	28.8 ± 0.6	0.54 ± 0.06	9 ± 7	48	101	102
508	44.086332	187.016623	5.5 ± 0.2	2.79 ± 0.07	47 ± 1	0.86 ± 0.02	0 ± 3	48	80	110
509	44.091367	187.01653	1.6 ± 0.1	1.6 ± 0.1	19 ± 1	0.2 ± 0.4	0 ± 10	32	48	48
510	44.096045	187.016432	1.67 ± 0.03	1.70 ± 0.03	20.1 ± 0.2	0.2 ± 0.1	0 ± 5	191	206	222
511	44.091807	187.016276	2.2 ± 0.1	1.56 ± 0.04	22.0 ± 0.6	0.70 ± 0.04	0 ± 9	32	38	61
512	44.093221	187.016251	2.04 ± 0.09	2.2 ± 0.1	25.2 ± 0.8	0.4 ± 0.2	0 ± 10	27	91	95
513	44.083596	187.016179	3.69 ± 0.07	2.22 ± 0.03	34.2 ± 0.4	0.80 ± 0.01	-2 ± 2	43	59	80
514	44.093041	187.015763	2.3 ± 0.2	1.79 ± 0.08	24 ± 1	0.63 ± 0.08	0 ± 8	27	87	93
515	44.085973	187.015768	1.79 ± 0.05	3.8 ± 0.4	31 ± 2	0.9 ± 0.3	0 ± 3	48	62	67
517	44.08341	187.015324	1.30 ± 0.09	3.5 ± 0.6	25 ± 3	0.9 ± 0.6	0 ± 5	38	43	45
518	44.08685	187.015138	3.40 ± 0.07	3.7 ± 0.1	42.3 ± 0.9	0.4 ± 0.1	-1 ± 3	67	72	80
519	44.083937	187.015068	2.7 ± 0.5	1.15 ± 0.07	21 ± 2	0.91 ± 0.04	0 ± 5	35	38	57
520	44.089148	187.014984	1.81 ± 0.01	1.86 ± 0.01	21.8 ± 0.1	0.23 ± 0.05	0 ± 20	43	49	102
521	44.08279	187.014968	2.24 ± 0.04	3.3 ± 0.1	32.6 ± 0.6	0.74 ± 0.08	-1 ± 4	45	64	78
522	44.08526	187.014148	3.45 ± 0.04	4.3 ± 0.3	46 ± 1	0.6 ± 0.1	0 ± 6	32	39	67
523	44.088442	187.01474	4.1 ± 0.4	3.2 ± 0.1	43 ± 2	0.6 ± 0.1	-2 ± 5	38	49	61
524	44.084707	187.014563	2.71 ± 0.05	4.19 ± 0.07	40.2 ± 0.5	0.76 ± 0.05	17 ± 2	39	57	67

Morphological parameters of the emission regions in the catalogue from this study. The RA and DEC column correspond to the position of the centroid of the region. The columns with σ_x and σ_y correspond to the standard deviation of the 2D Gaussian spatial profile (described in Section 2.6.2). The radius corresponds to the geometrical mean of $3\sigma_x$ and $3\sigma_y$ (as defined in Section 2.7.2). The E value corresponds to the eccentricity of the region (described in Section 2.7.2). The angle corresponds to the spatial inclination of the region, obtained from the 2D Gaussian fit (described in Section 2.6.2). The first (1NN), second (2NN), and third (3NN) nearest neighbour corresponds to the proximity distance between the centroids of the regions (described in Section 2.7.4).

ID	RA	DEC	σ_x [px]	σ_y [px]	Radius [pc]	E	Angle [°]	1NN [pc]	2NN [pc]	3NN [pc]
525	44.0857	187.014543	2.3	± 0.1	3.5	± 0.2	34	± 1	0.7	± 0.2
526	44.083669	187.014461	2.04	± 0.05	4.6	± 0.2	36.5	± 0.8	0.9	± 0.1
527	44.087643	187.014147	2.52	± 0.05	3.18	± 0.05	33.8	± 0.4	0.61	± 0.05
528	44.088429	187.013143	1.1	± 0.6	0.9	± 0.6	12	± 5	1	± 1
530	44.088601	187.012527	1.8	± 0.1	1.8	± 0.1	22	± 1	0.2	± 0.4
531	44.092132	187.012098	1.82	± 0.07	1.57	± 0.06	20.2	± 0.5	0.50	± 0.08
532	44.090009	187.012024	4.4	± 0.1	12.1	± 0.7	87	± 3	0.9	± 0.2
533	44.096281	187.011651	1.9	± 0.1	2.0	± 0.1	23	± 1	0.3	± 0.3
534	44.084443	187.011375	2.47	± 0.09	2.4	± 0.1	29.1	± 0.8	0.2	± 0.3
535	44.087533	187.011318	1.61	± 0.08	1.98	± 0.07	21.3	± 0.7	0.6	± 0.1
536	44.087978	187.011187	2.26	± 0.07	2.12	± 0.07	26.1	± 0.6	0.3	± 0.1
537	44.082763	187.010916	2.31	± 0.04	2.00	± 0.03	25.7	± 0.3	0.50	± 0.04
538	44.087177	187.010836	2.18	± 0.06	2.31	± 0.06	26.7	± 0.5	0.3	± 0.1
539	44.087705	187.010107	1.5	± 0.1	2.5	± 0.2	23	± 1	0.8	± 0.2
540	44.080908	187.010704	2.61	± 0.04	2.70	± 0.05	31.7	± 0.4	0.3	± 0.1
541	44.082937	187.01056	2.17	± 0.02	2.47	± 0.02	27.6	± 0.2	0.48	± 0.03
542	44.089907	187.00998	2.39	± 0.03	2.48	± 0.04	29.0	± 0.3	0.27	± 0.08
543	44.083714	187.007073	1.59	± 0.01	1.61	± 0.01	19.09	± 0.09	0.14	± 0.07

Table F.2

Uncorrected flux values of the emission regions in the catalogue from this study. The measured fluxes of the nine emission lines for the detected emission regions are presented. These fluxes are not corrected for the local background diffuse emission (described in Section 2.6.3), the global stellar absorption (described in Section 2.6.7), nor the extinction (described in Section 2.6.8). These fluxes are obtained directly from the fit of the integrated region's spectrum and the uncertainties correspond to the fitting uncertainties from ORCS. All flux values are scaled by 1×10^{-15} .

ID	$H\alpha$ [erg s $^{-1}$ cm $^{-2}$]	[N II] $\lambda 6583$ [erg s $^{-1}$ cm $^{-2}$]	[N II] $\lambda 6548$ [erg s $^{-1}$ cm $^{-2}$]	[S II] $\lambda 6731$ [erg s $^{-1}$ cm $^{-2}$]	[S II] $\lambda 6716$ [erg s $^{-1}$ cm $^{-2}$]	$H\beta$ [erg s $^{-1}$ cm $^{-2}$]	[O III] $\lambda 5007$ [erg s $^{-1}$ cm $^{-2}$]	[O III] $\lambda 4959$ [erg s $^{-1}$ cm $^{-2}$]	[O III] $\lambda 3727$ [erg s $^{-1}$ cm $^{-2}$]
0	0.47 ± 0.09	-0.03 ± 0.06	0.02 ± 0.06	0.06 ± 0.06	0.02 ± 0.06	0.15 ± 0.06	0.78 ± 0.08	0.29 ± 0.06	-0.05 ± 0.08
2	3.1 ± 0.1	0.32 ± 0.07	0.08 ± 0.07	0.27 ± 0.07	0.41 ± 0.07	0.9 ± 0.1	1.4 ± 0.1	0.48 ± 0.09	2.7 ± 0.3
3	2.1 ± 0.1	0.22 ± 0.09	0.11 ± 0.09	0.3 ± 0.1	0.5 ± 0.1	0.6 ± 0.1	0.9 ± 0.2	0.3 ± 0.1	2.8 ± 0.4
4	1.19 ± 0.08	0.22 ± 0.06	0.04 ± 0.06	0.17 ± 0.06	0.28 ± 0.06	0.41 ± 0.06	0.33 ± 0.07	0.08 ± 0.07	1.5 ± 0.2
6	1.56 ± 0.08	0.26 ± 0.06	0.06 ± 0.06	0.25 ± 0.06	0.37 ± 0.06	0.55 ± 0.07	0.42 ± 0.07	0.14 ± 0.07	1.8 ± 0.3
7	2.5 ± 0.1	0.38 ± 0.07	0.13 ± 0.07	0.28 ± 0.07	0.45 ± 0.07	0.78 ± 0.08	1.06 ± 0.08	0.39 ± 0.08	2.9 ± 0.3
8	0.81 ± 0.08	0.10 ± 0.06	0.03 ± 0.06	0.11 ± 0.06	0.16 ± 0.06	0.29 ± 0.08	1.0 ± 0.1	0.38 ± 0.08	1.0 ± 0.2
9	4.7 ± 0.1	0.54 ± 0.07	0.18 ± 0.07	0.56 ± 0.07	0.62 ± 0.07	1.4 ± 0.1	1.8 ± 0.1	0.7 ± 0.1	4.4 ± 0.3
10	50.0 ± 0.6	4.3 ± 0.4	1.3 ± 0.4	2.8 ± 0.5	3.9 ± 0.5	15 ± 1	33 ± 1	11 ± 1	36 ± 2
11	4.4 ± 0.2	0.5 ± 0.1	0.1 ± 0.1	0.6 ± 0.1	0.7 ± 0.1	1.4 ± 0.2	2.2 ± 0.2	0.8 ± 0.1	4.4 ± 0.4
13	9.7 ± 0.2	1.2 ± 0.1	0.3 ± 0.1	1.2 ± 0.1	1.8 ± 0.1	3.0 ± 0.3	5.7 ± 0.4	1.8 ± 0.3	9.4 ± 0.6
14	2.7 ± 0.2	0.5 ± 0.1	0.2 ± 0.1	0.5 ± 0.1	0.7 ± 0.1	1.0 ± 0.2	0.5 ± 0.2	0.2 ± 0.2	2.8 ± 0.5
15	1.7 ± 0.1	0.3 ± 0.1	0.2 ± 0.1	0.2 ± 0.1	0.3 ± 0.1	0.6 ± 0.1	0.4 ± 0.1	0.1 ± 0.1	2.2 ± 0.3
16	2.67 ± 0.09	0.34 ± 0.06	0.11 ± 0.06	0.28 ± 0.06	0.42 ± 0.06	0.72 ± 0.08	0.55 ± 0.08	0.21 ± 0.08	2.5 ± 0.3
17	2.46 ± 0.08	0.36 ± 0.06	0.10 ± 0.06	0.32 ± 0.06	0.48 ± 0.06	0.75 ± 0.09	0.81 ± 0.09	0.26 ± 0.07	2.2 ± 0.2
18	2.9 ± 0.1	0.47 ± 0.08	0.20 ± 0.08	0.45 ± 0.08	0.60 ± 0.08	0.8 ± 0.1	1.2 ± 0.1	0.4 ± 0.1	2.5 ± 0.3
19	33.8 ± 0.4	4.0 ± 0.3	1.2 ± 0.3	3.3 ± 0.3	4.3 ± 0.3	10.7 ± 0.7	13.4 ± 0.8	4.5 ± 0.6	32 ± 2
20	7.0 ± 0.1	0.8 ± 0.1	0.3 ± 0.1	1.0 ± 0.1	1.3 ± 0.1	2.3 ± 0.3	10.5 ± 0.5	3.6 ± 0.4	5.5 ± 0.4
21	7.9 ± 0.2	0.8 ± 0.1	0.3 ± 0.1	0.9 ± 0.1	1.2 ± 0.1	2.3 ± 0.2	5.8 ± 0.3	1.9 ± 0.2	6.0 ± 0.4
22	1.1 ± 0.1	0.16 ± 0.09	0.06 ± 0.09	0.2 ± 0.1	0.3 ± 0.1	0.2 ± 0.1	0.0 ± 0.1	0.0 ± 0.1	1.3 ± 0.4

Uncorrected flux values of the emission regions in the catalogue from this study. The measured fluxes of the nine emission lines for the detected emission regions are presented. These fluxes are not corrected for the local background diffuse emission (described in Section 2.6.3), the global stellar absorption (described in Section 2.6.7), nor the extinction (described in Section 2.6.8). These fluxes are obtained directly from the fit of the integrated region's spectrum and the uncertainties correspond to the fitting uncertainties from ORCS.

All flux values are scaled by 1×10^{-15} .

ID	$H\alpha$ [erg s ⁻¹ cm ⁻²]	[N II] $\lambda 6583$ [erg s ⁻¹ cm ⁻²]	[N II] $\lambda 6548$ [erg s ⁻¹ cm ⁻²]	[S II] $\lambda 6731$ [erg s ⁻¹ cm ⁻²]	[S II] $\lambda 6716$ [erg s ⁻¹ cm ⁻²]	$H\beta$ [erg s ⁻¹ cm ⁻²]	[O III] $\lambda 5007$ [erg s ⁻¹ cm ⁻²]	[O III] $\lambda 4959$ [erg s ⁻¹ cm ⁻²]	[O II] $\lambda 3727$ [erg s ⁻¹ cm ⁻²]
23	2.1 ± 0.1	0.35 ± 0.07	0.12 ± 0.07	0.46 ± 0.07	0.66 ± 0.07	0.70 ± 0.09	2.5 ± 0.1	0.8 ± 0.1	3.0 ± 0.3
24	3.7 ± 0.1	0.32 ± 0.09	0.16 ± 0.09	0.4 ± 0.1	0.5 ± 0.1	1.2 ± 0.2	3.7 ± 0.3	1.3 ± 0.2	4.2 ± 0.4
25	2.8 ± 0.1	0.3 ± 0.1	0.14 ± 0.09	0.2 ± 0.1	0.4 ± 0.1	0.9 ± 0.3	0.7 ± 0.3	0.2 ± 0.2	3.1 ± 0.5
26	1.26 ± 0.07	0.16 ± 0.05	0.06 ± 0.05	0.18 ± 0.05	0.26 ± 0.05	0.3 ± 0.1	0.3 ± 0.1	0.03 ± 0.09	1.1 ± 0.2
27	1.16 ± 0.09	0.16 ± 0.06	0.00 ± 0.06	0.19 ± 0.06	0.20 ± 0.06	0.4 ± 0.1	0.21 ± 0.09	0.08 ± 0.08	1.2 ± 0.3
28	2.1 ± 0.1	0.3 ± 0.1	0.2 ± 0.1	0.4 ± 0.1	0.7 ± 0.1	0.6 ± 0.2	0.5 ± 0.2	0.2 ± 0.1	2.4 ± 0.3
29	3.5 ± 0.2	0.6 ± 0.2	0.2 ± 0.2	0.4 ± 0.2	1.1 ± 0.2	1.1 ± 0.3	4.5 ± 0.4	1.5 ± 0.3	5.1 ± 0.6
30	8.5 ± 0.2	0.6 ± 0.1	0.3 ± 0.1	0.6 ± 0.1	0.8 ± 0.1	2.7 ± 0.2	6.5 ± 0.3	2.2 ± 0.2	6.1 ± 0.4
31	2.9 ± 0.1	0.32 ± 0.09	0.03 ± 0.08	0.47 ± 0.09	0.57 ± 0.09	0.9 ± 0.2	0.5 ± 0.1	0.2 ± 0.1	3.0 ± 0.4
32	1.6 ± 0.1	0.3 ± 0.1	0.1 ± 0.1	0.3 ± 0.1	0.5 ± 0.1	0.5 ± 0.2	0.3 ± 0.2	0.1 ± 0.1	2.0 ± 0.3
33	1.3 ± 0.1	0.23 ± 0.08	0.05 ± 0.08	0.21 ± 0.09	0.22 ± 0.09	0.4 ± 0.1	0.3 ± 0.1	0.0 ± 0.1	1.7 ± 0.4
34	3.9 ± 0.2	0.6 ± 0.1	0.2 ± 0.1	0.7 ± 0.1	0.8 ± 0.1	1.0 ± 0.2	0.5 ± 0.2	0.1 ± 0.2	3.1 ± 0.6
35	3.5 ± 0.2	0.6 ± 0.1	0.1 ± 0.1	0.7 ± 0.1	0.8 ± 0.1	1.0 ± 0.3	1.0 ± 0.3	0.3 ± 0.2	4.5 ± 0.5
36	18.3 ± 0.3	2.6 ± 0.2	0.9 ± 0.2	3.1 ± 0.2	4.3 ± 0.2	6.2 ± 0.6	8.5 ± 0.7	3.0 ± 0.5	20 ± 1
37	14.6 ± 0.3	2.0 ± 0.2	0.6 ± 0.2	1.7 ± 0.2	2.6 ± 0.2	4.7 ± 0.4	4.8 ± 0.4	1.7 ± 0.3	15.9 ± 0.8
38	10.2 ± 0.2	1.6 ± 0.2	0.3 ± 0.2	2.0 ± 0.2	2.9 ± 0.2	3.2 ± 0.4	3.4 ± 0.4	1.2 ± 0.3	10.5 ± 0.8
39	8.5 ± 0.2	1.3 ± 0.2	0.4 ± 0.2	1.4 ± 0.2	2.1 ± 0.2	2.6 ± 0.4	3.8 ± 0.4	1.4 ± 0.3	10.1 ± 0.7
40	6.0 ± 0.1	0.9 ± 0.1	0.3 ± 0.1	1.0 ± 0.1	1.3 ± 0.1	1.7 ± 0.1	3.2 ± 0.2	1.2 ± 0.1	6.4 ± 0.4
41	12.0 ± 0.2	1.6 ± 0.1	0.5 ± 0.1	1.4 ± 0.2	1.8 ± 0.2	3.9 ± 0.4	12.1 ± 0.6	4.1 ± 0.5	10.9 ± 0.6
42	22.9 ± 0.4	3.3 ± 0.2	0.8 ± 0.2	3.5 ± 0.3	5.3 ± 0.3	7.7 ± 0.6	9.7 ± 0.7	3.2 ± 0.6	24 ± 1
43	12.5 ± 0.2	1.2 ± 0.1	0.4 ± 0.1	1.0 ± 0.2	1.5 ± 0.2	3.4 ± 0.4	6.6 ± 0.5	2.2 ± 0.4	8.9 ± 0.7
44	8.8 ± 0.3	1.5 ± 0.2	0.3 ± 0.2	1.5 ± 0.2	2.2 ± 0.2	2.8 ± 0.9	4 ± 1	1.5 ± 0.8	11 ± 1
45	6.0 ± 0.2	0.8 ± 0.1	0.2 ± 0.1	1.0 ± 0.1	1.5 ± 0.1	1.8 ± 0.4	2.5 ± 0.4	0.8 ± 0.3	7.5 ± 0.6
46	1.2 ± 0.1	0.17 ± 0.07	0.05 ± 0.07	0.19 ± 0.07	0.29 ± 0.07	0.4 ± 0.1	0.4 ± 0.1	0.1 ± 0.1	1.2 ± 0.3

Uncorrected flux values of the emission regions in the catalogue from this study. The measured fluxes of the nine emission lines for the detected emission regions are presented. These fluxes are not corrected for the local background diffuse emission (described in Section 2.6.3), the global stellar absorption (described in Section 2.6.7), nor the extinction (described in Section 2.6.8). These fluxes are obtained directly from the fit of the integrated region's spectrum and the uncertainties correspond to the fitting uncertainties from ORCS.

All flux values are scaled by 1×10^{-15} .

ID	H α [erg s $^{-1}$ cm $^{-2}$]	[N II] λ 6583 [erg s $^{-1}$ cm $^{-2}$]	[N II] λ 6548 [erg s $^{-1}$ cm $^{-2}$]	[S II] λ 6731 [erg s $^{-1}$ cm $^{-2}$]	[S II] λ 6716 [erg s $^{-1}$ cm $^{-2}$]	H β [erg s $^{-1}$ cm $^{-2}$]	[O III] λ 5007 [erg s $^{-1}$ cm $^{-2}$]	[O III] λ 4959 [erg s $^{-1}$ cm $^{-2}$]	[O II] λ 3727 [erg s $^{-1}$ cm $^{-2}$]
47	4.2 ± 0.2	0.6 ± 0.1	0.2 ± 0.1	0.6 ± 0.1	1.0 ± 0.1	1.4 ± 0.3	1.0 ± 0.3	0.2 ± 0.3	5.4 ± 0.6
48	12.8 ± 0.2	1.4 ± 0.1	0.4 ± 0.1	1.0 ± 0.1	1.5 ± 0.1	3.4 ± 0.3	5.4 ± 0.4	1.9 ± 0.3	9.0 ± 0.6
49	12.3 ± 0.3	1.9 ± 0.2	0.5 ± 0.2	2.2 ± 0.2	3.1 ± 0.2	4.2 ± 0.5	4.4 ± 0.5	1.5 ± 0.4	15.0 ± 0.9
50	5.3 ± 0.2	0.9 ± 0.1	0.2 ± 0.1	1.0 ± 0.1	1.4 ± 0.1	1.7 ± 0.3	2.4 ± 0.3	0.8 ± 0.2	7.2 ± 0.5
51	2.41 ± 0.09	0.31 ± 0.06	0.08 ± 0.06	0.25 ± 0.07	0.32 ± 0.07	0.8 ± 0.1	1.0 ± 0.1	0.3 ± 0.1	2.5 ± 0.3
52	4.1 ± 0.2	0.5 ± 0.1	0.1 ± 0.1	0.6 ± 0.1	0.6 ± 0.1	1.3 ± 0.2	2.2 ± 0.2	0.7 ± 0.2	5.1 ± 0.4
53	8.9 ± 0.2	1.1 ± 0.2	0.3 ± 0.1	1.1 ± 0.2	1.4 ± 0.2	2.4 ± 0.4	4.8 ± 0.5	1.6 ± 0.4	8.1 ± 0.5
54	3.9 ± 0.1	0.49 ± 0.09	0.30 ± 0.09	0.5 ± 0.1	0.6 ± 0.1	1.3 ± 0.2	1.3 ± 0.2	0.5 ± 0.2	4.4 ± 0.4
55	14.9 ± 0.3	1.6 ± 0.2	0.6 ± 0.2	1.5 ± 0.2	2.2 ± 0.2	4.6 ± 0.4	6.0 ± 0.5	1.9 ± 0.4	14.8 ± 0.9
56	12.1 ± 0.4	1.8 ± 0.3	0.6 ± 0.3	2.4 ± 0.3	3.1 ± 0.3	3.7 ± 0.8	7 ± 1	2.3 ± 0.8	15 ± 1
57	2.0 ± 0.2	0.3 ± 0.1	0.1 ± 0.1	0.4 ± 0.1	0.4 ± 0.1	0.6 ± 0.2	0.4 ± 0.2	0.2 ± 0.2	2.0 ± 0.4
58	4.3 ± 0.1	0.7 ± 0.1	0.2 ± 0.1	1.0 ± 0.1	1.5 ± 0.1	1.4 ± 0.2	1.8 ± 0.2	0.6 ± 0.2	5.9 ± 0.3
59	2.5 ± 0.1	0.20 ± 0.07	0.07 ± 0.07	0.31 ± 0.07	0.32 ± 0.07	0.6 ± 0.1	1.4 ± 0.2	0.5 ± 0.1	1.7 ± 0.3
60	4.0 ± 0.2	0.7 ± 0.1	0.1 ± 0.1	0.8 ± 0.1	1.1 ± 0.1	1.5 ± 0.3	1.6 ± 0.3	0.6 ± 0.3	5.2 ± 0.5
61	1.51 ± 0.08	0.20 ± 0.06	0.12 ± 0.05	0.19 ± 0.06	0.30 ± 0.06	0.6 ± 0.1	0.3 ± 0.1	0.08 ± 0.09	1.6 ± 0.2
62	2.5 ± 0.1	0.41 ± 0.09	0.11 ± 0.09	0.39 ± 0.09	0.66 ± 0.09	0.9 ± 0.2	0.8 ± 0.2	0.3 ± 0.2	3.0 ± 0.3
63	7.3 ± 0.1	0.6 ± 0.1	0.3 ± 0.1	0.5 ± 0.1	0.7 ± 0.1	2.1 ± 0.2	3.5 ± 0.2	1.2 ± 0.2	5.2 ± 0.5
64	0.56 ± 0.08	0.04 ± 0.05	0.03 ± 0.05	0.05 ± 0.06	0.06 ± 0.06	0.11 ± 0.07	0.2 ± 0.1	0.06 ± 0.07	0.6 ± 0.2
65	3.3 ± 0.1	0.35 ± 0.09	0.16 ± 0.09	0.4 ± 0.1	0.6 ± 0.1	1.1 ± 0.2	0.6 ± 0.2	0.2 ± 0.1	4.0 ± 0.4
66	10.0 ± 0.2	1.0 ± 0.1	0.3 ± 0.1	0.7 ± 0.1	1.2 ± 0.1	3.1 ± 0.3	6.2 ± 0.4	2.1 ± 0.3	10.6 ± 0.6
67	6.1 ± 0.1	0.68 ± 0.08	0.18 ± 0.08	0.54 ± 0.09	0.87 ± 0.09	2.1 ± 0.2	5.9 ± 0.3	2.0 ± 0.2	6.5 ± 0.4
68	1.6 ± 0.1	0.30 ± 0.08	0.09 ± 0.07	0.16 ± 0.08	0.32 ± 0.08	0.6 ± 0.1	0.4 ± 0.1	0.1 ± 0.1	1.7 ± 0.2
69	2.8 ± 0.1	0.36 ± 0.07	0.11 ± 0.07	0.34 ± 0.07	0.53 ± 0.07	1.1 ± 0.2	4.5 ± 0.2	1.5 ± 0.2	3.0 ± 0.3
70	2.14 ± 0.08	0.25 ± 0.06	0.18 ± 0.06	0.21 ± 0.06	0.38 ± 0.06	0.7 ± 0.1	0.8 ± 0.1	0.29 ± 0.09	2.4 ± 0.3

Uncorrected flux values of the emission regions in the catalogue from this study. The measured fluxes of the nine emission lines for the detected emission regions are presented. These fluxes are not corrected for the local background diffuse emission (described in Section 2.6.3), the global stellar absorption (described in Section 2.6.7), nor the extinction (described in Section 2.6.8). These fluxes are obtained directly from the fit of the integrated region's spectrum and the uncertainties correspond to the fitting uncertainties from ORCS.

All flux values are scaled by 1×10^{-15} .

ID	H α [erg s $^{-1}$ cm $^{-2}$]	[N II] λ 6583 [erg s $^{-1}$ cm $^{-2}$]	[N II] λ 6548 [erg s $^{-1}$ cm $^{-2}$]	[S II] λ 6731 [erg s $^{-1}$ cm $^{-2}$]	[S II] λ 6716 [erg s $^{-1}$ cm $^{-2}$]	H β [erg s $^{-1}$ cm $^{-2}$]	[O III] λ 5007 [erg s $^{-1}$ cm $^{-2}$]	[O III] λ 4959 [erg s $^{-1}$ cm $^{-2}$]	[O II] λ 3727 [erg s $^{-1}$ cm $^{-2}$]
71	4.2 ± 0.1	0.8 ± 0.1	0.1 ± 0.1	0.7 ± 0.1	0.8 ± 0.1	1.3 ± 0.3	1.1 ± 0.3	0.3 ± 0.2	4.0 ± 0.3
72	8.6 ± 0.2	1.1 ± 0.1	0.3 ± 0.1	0.9 ± 0.1	1.4 ± 0.1	2.9 ± 0.3	2.3 ± 0.3	0.8 ± 0.2	10.3 ± 0.7
73	8.8 ± 0.4	1.5 ± 0.3	0.5 ± 0.3	1.4 ± 0.3	2.2 ± 0.3	2.9 ± 0.8	5 ± 1	1.8 ± 0.8	12 ± 1
74	2.1 ± 0.2	0.3 ± 0.1	0.1 ± 0.1	0.3 ± 0.1	0.5 ± 0.1	0.6 ± 0.4	1.2 ± 0.4	0.4 ± 0.3	2.0 ± 0.5
75	2.56 ± 0.08	0.33 ± 0.06	0.15 ± 0.05	0.35 ± 0.06	0.51 ± 0.06	0.8 ± 0.1	1.4 ± 0.2	0.5 ± 0.1	2.4 ± 0.2
76	7.0 ± 0.2	1.0 ± 0.1	0.4 ± 0.1	1.1 ± 0.1	1.6 ± 0.1	2.2 ± 0.3	4.0 ± 0.4	1.5 ± 0.3	7.6 ± 0.7
77	32 ± 1	5.1 ± 0.8	1.7 ± 0.7	5.2 ± 0.8	7.3 ± 0.8	10 ± 3	16 ± 3	6 ± 2	39 ± 3
78	2.1 ± 0.1	0.30 ± 0.08	0.08 ± 0.07	0.33 ± 0.08	0.45 ± 0.08	0.8 ± 0.2	0.4 ± 0.2	0.0 ± 0.1	2.8 ± 0.3
79	32.0 ± 0.4	2.7 ± 0.3	0.9 ± 0.3	2.0 ± 0.3	2.8 ± 0.3	9.6 ± 0.9	25 ± 1	8 ± 1	20 ± 1
80	3.3 ± 0.1	0.45 ± 0.09	0.06 ± 0.09	0.48 ± 0.09	0.72 ± 0.09	1.1 ± 0.2	0.6 ± 0.1	0.1 ± 0.1	3.9 ± 0.4
81	5.1 ± 0.2	0.7 ± 0.1	0.2 ± 0.1	0.8 ± 0.1	1.2 ± 0.1	1.7 ± 0.2	1.1 ± 0.2	0.3 ± 0.1	6.3 ± 0.4
82	8.0 ± 0.2	0.9 ± 0.1	0.3 ± 0.1	1.0 ± 0.1	1.6 ± 0.1	2.6 ± 0.2	1.8 ± 0.2	0.7 ± 0.2	9.9 ± 0.5
83	16.1 ± 0.9	3.0 ± 0.6	0.9 ± 0.6	3.2 ± 0.6	4.3 ± 0.6	5 ± 2	6 ± 2	2 ± 2	22 ± 2
84	7.4 ± 0.2	0.8 ± 0.1	0.1 ± 0.1	0.6 ± 0.1	1.1 ± 0.1	2.6 ± 0.3	4.5 ± 0.3	1.6 ± 0.2	7.6 ± 0.6
85	26.6 ± 0.7	4.1 ± 0.5	1.4 ± 0.5	3.9 ± 0.5	5.7 ± 0.5	9 ± 1	15 ± 2	5 ± 1	29 ± 2
86	12.5 ± 0.2	1.4 ± 0.1	0.4 ± 0.1	1.0 ± 0.1	1.6 ± 0.1	3.7 ± 0.3	5.4 ± 0.4	1.8 ± 0.3	10.1 ± 0.6
87	20.9 ± 0.4	3.1 ± 0.3	1.0 ± 0.3	3.0 ± 0.3	4.5 ± 0.3	6.7 ± 0.9	12 ± 1	4.4 ± 0.8	21 ± 1
88	6.9 ± 0.3	0.8 ± 0.2	0.2 ± 0.2	0.6 ± 0.2	1.0 ± 0.2	2.5 ± 0.6	6.5 ± 0.8	2.4 ± 0.6	6.7 ± 0.7
89	4.6 ± 0.1	0.63 ± 0.08	0.28 ± 0.08	0.60 ± 0.09	0.77 ± 0.09	1.6 ± 0.2	1.9 ± 0.2	0.6 ± 0.2	5.2 ± 0.4
90	0.8 ± 0.1	0.2 ± 0.1	0.1 ± 0.1	0.1 ± 0.1	0.2 ± 0.1	0.4 ± 0.1	0.0 ± 0.1	0.1 ± 0.1	1.3 ± 0.4
91	1.27 ± 0.09	0.18 ± 0.06	0.06 ± 0.06	0.17 ± 0.06	0.21 ± 0.06	0.4 ± 0.1	0.4 ± 0.1	0.06 ± 0.08	1.2 ± 0.2
92	2.9 ± 0.2	0.3 ± 0.2	0.1 ± 0.2	0.5 ± 0.2	0.7 ± 0.2	0.9 ± 0.3	0.9 ± 0.3	0.3 ± 0.2	3.9 ± 0.5
93	14.4 ± 0.6	2.8 ± 0.4	1.1 ± 0.4	2.3 ± 0.4	3.3 ± 0.4	5 ± 1	8 ± 2	3 ± 1	21 ± 2
94	31.4 ± 0.4	3.2 ± 0.3	1.0 ± 0.3	2.1 ± 0.3	2.9 ± 0.3	10.1 ± 0.7	17.2 ± 0.8	6.0 ± 0.6	28 ± 1

Uncorrected flux values of the emission regions in the catalogue from this study. The measured fluxes of the nine emission lines for the detected emission regions are presented. These fluxes are not corrected for the local background diffuse emission (described in Section 2.6.3), the global stellar absorption (described in Section 2.6.7), nor the extinction (described in Section 2.6.8). These fluxes are obtained directly from the fit of the integrated region's spectrum and the uncertainties correspond to the fitting uncertainties from ORCS.

All flux values are scaled by 1×10^{-15} .

ID	H α [erg s $^{-1}$ cm $^{-2}$]	[N II] λ 6583 [erg s $^{-1}$ cm $^{-2}$]	[N II] λ 6548 [erg s $^{-1}$ cm $^{-2}$]	[S II] λ 6731 [erg s $^{-1}$ cm $^{-2}$]	[S II] λ 6716 [erg s $^{-1}$ cm $^{-2}$]	H β [erg s $^{-1}$ cm $^{-2}$]	[O III] λ 5007 [erg s $^{-1}$ cm $^{-2}$]	[O III] λ 4959 [erg s $^{-1}$ cm $^{-2}$]	[O II] λ 3727 [erg s $^{-1}$ cm $^{-2}$]
95	108 ± 1	8.0 ± 0.9	2.5 ± 0.8	4.3 ± 0.9	6.3 ± 0.9	36 ± 2	75 ± 3	26 ± 2	81 ± 3
96	11.4 ± 0.4	1.8 ± 0.3	0.7 ± 0.3	1.4 ± 0.3	2.1 ± 0.3	4 ± 1	7 ± 1	2 ± 1	14 ± 1
97	43.0 ± 0.9	5.8 ± 0.6	1.6 ± 0.6	5.1 ± 0.6	7.0 ± 0.6	14 ± 2	31 ± 3	11 ± 2	38 ± 3
98	2.74 ± 0.09	0.13 ± 0.06	0.03 ± 0.06	0.11 ± 0.06	0.15 ± 0.06	1.0 ± 0.1	2.8 ± 0.2	1.0 ± 0.1	1.7 ± 0.2
99	8.4 ± 0.2	1.1 ± 0.2	0.2 ± 0.2	1.0 ± 0.2	1.6 ± 0.2	2.7 ± 0.6	5.6 ± 0.7	1.9 ± 0.6	9.4 ± 0.8
100	21.0 ± 0.3	2.2 ± 0.2	0.8 ± 0.2	1.7 ± 0.2	2.3 ± 0.2	6.7 ± 0.5	10.5 ± 0.6	3.6 ± 0.4	19.5 ± 0.9
101	7.5 ± 0.2	0.6 ± 0.1	0.3 ± 0.1	0.5 ± 0.1	0.8 ± 0.1	2.6 ± 0.5	6.2 ± 0.6	2.2 ± 0.5	6.1 ± 0.6
102	12.9 ± 0.3	2.0 ± 0.2	0.6 ± 0.2	1.9 ± 0.2	2.7 ± 0.2	4.0 ± 0.6	8.2 ± 0.8	2.7 ± 0.6	12.8 ± 0.9
103	7.2 ± 0.2	0.9 ± 0.1	0.3 ± 0.1	0.8 ± 0.1	1.1 ± 0.1	2.5 ± 0.3	3.2 ± 0.4	1.0 ± 0.3	6.8 ± 0.5
104	57.6 ± 0.8	5.8 ± 0.5	1.8 ± 0.5	5.1 ± 0.6	7.0 ± 0.6	19 ± 2	53 ± 3	18 ± 2	40 ± 2
105	15.4 ± 0.3	1.8 ± 0.2	0.4 ± 0.2	1.6 ± 0.2	2.1 ± 0.2	4.8 ± 0.6	11.4 ± 0.8	4.0 ± 0.6	11.0 ± 0.8
106	8.0 ± 0.3	1.0 ± 0.2	0.3 ± 0.2	0.9 ± 0.2	1.4 ± 0.2	2.7 ± 0.4	5.2 ± 0.5	1.9 ± 0.4	8.5 ± 0.6
107	10.3 ± 0.3	0.9 ± 0.2	0.3 ± 0.2	0.8 ± 0.2	1.3 ± 0.2	3.6 ± 0.7	8.3 ± 0.9	2.9 ± 0.7	8.4 ± 0.7
108	12.0 ± 0.2	1.6 ± 0.2	0.6 ± 0.1	1.4 ± 0.2	2.0 ± 0.2	4.0 ± 0.5	8.5 ± 0.7	2.9 ± 0.5	10.3 ± 0.6
109	1.10 ± 0.07	0.06 ± 0.05	0.00 ± 0.05	0.08 ± 0.05	0.08 ± 0.05	0.29 ± 0.07	0.9 ± 0.1	0.31 ± 0.07	0.9 ± 0.2
110	13.7 ± 0.2	1.4 ± 0.1	0.4 ± 0.1	1.1 ± 0.1	1.6 ± 0.1	4.6 ± 0.5	10.4 ± 0.7	3.6 ± 0.5	9.4 ± 0.6
111	65.4 ± 0.9	6.9 ± 0.6	2.1 ± 0.6	5.7 ± 0.6	8.2 ± 0.6	22 ± 3	55 ± 4	19 ± 3	49 ± 3
112	17.0 ± 0.3	1.9 ± 0.2	0.6 ± 0.2	1.3 ± 0.2	2.3 ± 0.2	5.7 ± 0.6	12.2 ± 0.8	4.5 ± 0.6	11.2 ± 0.8
113	17.0 ± 0.3	2.1 ± 0.2	0.7 ± 0.2	2.6 ± 0.2	3.8 ± 0.2	6.0 ± 0.6	6.6 ± 0.6	2.3 ± 0.5	19 ± 1
114	1.52 ± 2	9 ± 1	3 ± 1	7 ± 1	10 ± 1	49 ± 5	169 ± 7	58 ± 5	72 ± 3
115	8.3 ± 0.3	0.9 ± 0.2	0.4 ± 0.2	0.8 ± 0.2	1.1 ± 0.2	3.1 ± 0.5	6.3 ± 0.6	2.0 ± 0.5	8.4 ± 0.6
116	11.1 ± 0.3	1.7 ± 0.2	0.5 ± 0.2	1.4 ± 0.2	2.1 ± 0.2	3.8 ± 0.5	6.3 ± 0.6	2.2 ± 0.4	11.2 ± 0.7
117	25.1 ± 0.6	3.2 ± 0.4	1.0 ± 0.4	2.8 ± 0.4	4.0 ± 0.4	8 ± 2	17 ± 2	6 ± 2	23 ± 2
118	24.0 ± 0.4	2.6 ± 0.2	0.7 ± 0.2	2.0 ± 0.3	3.2 ± 0.3	7.7 ± 0.9	18 ± 1	6.5 ± 0.9	18 ± 1

Uncorrected flux values of the emission regions in the catalogue from this study. The measured fluxes of the nine emission lines for the detected emission regions are presented. These fluxes are not corrected for the local background diffuse emission (described in Section 2.6.3), the global stellar absorption (described in Section 2.6.7), nor the extinction (described in Section 2.6.8). These fluxes are obtained directly from the fit of the integrated region's spectrum and the uncertainties correspond to the fitting uncertainties from ORCS.

All flux values are scaled by 1×10^{-15} .

ID	$\text{H}\alpha$ [$\text{erg s}^{-1} \text{cm}^{-2}$]	$[\text{N II}]\lambda 6583$ [$\text{erg s}^{-1} \text{cm}^{-2}$]	$[\text{N II}]\lambda 6548$ [$\text{erg s}^{-1} \text{cm}^{-2}$]	$[\text{S II}]\lambda 6731$ [$\text{erg s}^{-1} \text{cm}^{-2}$]	$[\text{S II}]\lambda 6716$ [$\text{erg s}^{-1} \text{cm}^{-2}$]	$\text{H}\beta$ [$\text{erg s}^{-1} \text{cm}^{-2}$]	$[\text{O III}]\lambda 5007$ [$\text{erg s}^{-1} \text{cm}^{-2}$]	$[\text{O III}]\lambda 4959$ [$\text{erg s}^{-1} \text{cm}^{-2}$]	$[\text{O II}]\lambda 3727$ [$\text{erg s}^{-1} \text{cm}^{-2}$]
119	11.4 ± 0.3	1.7 ± 0.2	0.7 ± 0.2	1.5 ± 0.2	2.2 ± 0.2	4.2 ± 0.7	6.9 ± 0.9	2.2 ± 0.7	14 ± 1
120	8.9 ± 0.4	0.9 ± 0.3	0.3 ± 0.3	0.7 ± 0.3	0.8 ± 0.3	3.0 ± 0.8	7 ± 1	2.5 ± 0.7	8 ± 1
121	37.0 ± 0.5	3.0 ± 0.3	1.1 ± 0.3	3.0 ± 0.3	4.3 ± 0.3	12 ± 1	36 ± 2	13 ± 2	29 ± 2
122	38.9 ± 0.5	4.3 ± 0.3	1.6 ± 0.3	4.0 ± 0.3	5.7 ± 0.3	12.6 ± 0.9	21 ± 1	7.3 ± 0.8	35 ± 2
123	9.8 ± 0.3	1.5 ± 0.2	0.6 ± 0.2	1.4 ± 0.2	2.1 ± 0.2	3.4 ± 0.7	5.0 ± 0.9	1.9 ± 0.7	12 ± 1
124	10.9 ± 0.4	1.1 ± 0.3	0.3 ± 0.3	0.8 ± 0.3	1.3 ± 0.3	3.8 ± 0.8	8 ± 1	2.7 ± 0.8	11 ± 1
125	40.7 ± 0.7	4.0 ± 0.4	1.4 ± 0.4	2.8 ± 0.5	4.1 ± 0.5	12 ± 2	30 ± 3	11 ± 2	25 ± 2
126	68.4 ± 0.8	7.4 ± 0.5	2.3 ± 0.5	5.1 ± 0.5	7.3 ± 0.5	21 ± 1	33 ± 2	12 ± 1	57 ± 2
127	51.0 ± 0.8	4.4 ± 0.5	1.4 ± 0.5	3.1 ± 0.5	4.5 ± 0.5	17 ± 2	44 ± 2	16 ± 2	32 ± 2
128	22.4 ± 0.3	2.3 ± 0.2	0.8 ± 0.2	2.1 ± 0.2	3.1 ± 0.2	8.0 ± 0.7	15.8 ± 0.9	5.6 ± 0.7	19 ± 1
129	51 ± 1	4.9 ± 0.7	1.6 ± 0.6	3.1 ± 0.7	4.5 ± 0.7	16 ± 3	35 ± 4	13 ± 3	32 ± 3
130	22.1 ± 0.3	2.1 ± 0.2	0.7 ± 0.2	1.9 ± 0.2	2.6 ± 0.2	7.2 ± 0.7	14.3 ± 0.8	5.1 ± 0.6	18 ± 1
131	6.3 ± 0.3	0.9 ± 0.2	0.4 ± 0.2	0.9 ± 0.2	1.4 ± 0.2	2.0 ± 0.5	3.0 ± 0.6	1.1 ± 0.5	6.5 ± 0.6
132	26.7 ± 0.3	3.4 ± 0.2	1.1 ± 0.2	3.0 ± 0.2	4.3 ± 0.2	8.8 ± 0.5	11.1 ± 0.6	3.9 ± 0.5	29 ± 1
133	18.9 ± 0.3	2.4 ± 0.2	0.7 ± 0.2	1.8 ± 0.2	2.7 ± 0.2	6.1 ± 0.5	6.5 ± 0.5	2.3 ± 0.4	20 ± 1
134	15.2 ± 0.5	1.8 ± 0.3	0.6 ± 0.3	1.6 ± 0.3	2.3 ± 0.3	5 ± 1	9 ± 1	3 ± 1	16 ± 1
135	16.9 ± 0.2	2.1 ± 0.2	0.7 ± 0.2	1.8 ± 0.2	2.7 ± 0.2	5.6 ± 0.5	6.4 ± 0.5	2.2 ± 0.4	18.1 ± 0.9
136	58.1 ± 0.8	6.8 ± 0.5	2.0 ± 0.5	5.0 ± 0.6	7.3 ± 0.6	19 ± 1	39 ± 2	14 ± 1	44 ± 2
137	14.7 ± 0.9	2.2 ± 0.6	0.7 ± 0.5	2.1 ± 0.6	3.2 ± 0.6	5 ± 2	7 ± 2	2 ± 1	17 ± 2
138	11.7 ± 2	9 ± 1	3 ± 1	5 ± 1	8 ± 1	40 ± 3	103 ± 5	37 ± 4	71 ± 3
139	10.0 ± 0.2	1.5 ± 0.1	0.5 ± 0.1	1.4 ± 0.1	1.9 ± 0.1	3.6 ± 0.3	3.4 ± 0.3	1.0 ± 0.3	13.5 ± 0.7
140	4.7 ± 0.1	0.68 ± 0.09	0.10 ± 0.09	0.60 ± 0.09	0.83 ± 0.09	1.5 ± 0.2	1.7 ± 0.3	0.6 ± 0.2	5.4 ± 0.4
141	8.3 ± 0.1	0.6 ± 0.1	0.3 ± 0.1	0.6 ± 0.1	0.8 ± 0.1	2.6 ± 0.2	3.4 ± 0.2	1.2 ± 0.2	6.6 ± 0.5
142	1.9 ± 0.1	0.30 ± 0.09	0.08 ± 0.08	0.20 ± 0.09	0.32 ± 0.09	0.6 ± 0.1	0.6 ± 0.1	0.2 ± 0.1	2.1 ± 0.3

Uncorrected flux values of the emission regions in the catalogue from this study. The measured fluxes of the nine emission lines for the detected emission regions are presented. These fluxes are not corrected for the local background diffuse emission (described in Section 2.6.3), the global stellar absorption (described in Section 2.6.7), nor the extinction (described in Section 2.6.8). These fluxes are obtained directly from the fit of the integrated region's spectrum and the uncertainties correspond to the fitting uncertainties from ORCS.

All flux values are scaled by 1×10^{-15} .

ID	$H\alpha$ [erg s ⁻¹ cm ⁻²]	[N II] λ 6583 [erg s ⁻¹ cm ⁻²]	[N II] λ 6548 [erg s ⁻¹ cm ⁻²]	[S II] λ 6731 [erg s ⁻¹ cm ⁻²]	[S III] λ 6716 [erg s ⁻¹ cm ⁻²]	$H\beta$ [erg s ⁻¹ cm ⁻²]	[O III] λ 5007 [erg s ⁻¹ cm ⁻²]	[O III] λ 4959 [erg s ⁻¹ cm ⁻²]	[O II] λ 3727 [erg s ⁻¹ cm ⁻²]
143	131 ± 2	8 ± 1	2 ± 1	5 ± 1	7 ± 1	45 ± 5	115 ± 6	41 ± 5	79 ± 4
144	4.3 ± 0.2	0.5 ± 0.1	0.2 ± 0.1	0.4 ± 0.1	0.7 ± 0.2	1.5 ± 0.4	1.9 ± 0.5	0.6 ± 0.4	5.0 ± 0.6
145	1.7 ± 0.1	0.2 ± 0.1	0.02 ± 0.09	0.1 ± 0.1	0.3 ± 0.1	0.58 ± 0.09	0.7 ± 0.1	0.20 ± 0.09	2.0 ± 0.3
146	4.3 ± 0.2	0.4 ± 0.1	0.0 ± 0.1	0.2 ± 0.1	0.5 ± 0.1	1.4 ± 0.2	2.1 ± 0.2	0.7 ± 0.2	4.3 ± 0.4
147	18.0 ± 0.3	2.2 ± 0.2	0.8 ± 0.2	1.9 ± 0.2	2.9 ± 0.2	6.3 ± 0.7	4.9 ± 0.6	1.7 ± 0.5	18.1 ± 0.9
148	33.1 ± 0.4	2.0 ± 0.3	0.9 ± 0.3	1.3 ± 0.3	1.9 ± 0.3	11 ± 1	32 ± 1	11 ± 1	22 ± 1
149	3.2 ± 0.1	0.32 ± 0.07	0.13 ± 0.07	0.24 ± 0.07	0.27 ± 0.07	1.0 ± 0.1	1.5 ± 0.1	0.5 ± 0.1	3.5 ± 0.3
150	14.7 ± 0.5	1.6 ± 0.3	0.5 ± 0.3	1.3 ± 0.4	1.8 ± 0.4	5.1 ± 0.7	9.8 ± 0.9	3.6 ± 0.7	15 ± 1
151	34.6 ± 0.5	4.7 ± 0.4	1.5 ± 0.3	4.0 ± 0.4	5.7 ± 0.4	11 ± 1	24 ± 1	9 ± 1	31 ± 1
152	1.49 ± 0.09	0.09 ± 0.06	0.05 ± 0.06	0.26 ± 0.06	0.29 ± 0.06	0.41 ± 0.07	0.15 ± 0.07	0.11 ± 0.07	1.2 ± 0.3
153	11.6 ± 0.4	1.8 ± 0.3	0.5 ± 0.3	1.8 ± 0.3	2.7 ± 0.3	4.1 ± 0.7	5.2 ± 0.8	1.6 ± 0.6	16 ± 1
154	5.9 ± 0.4	0.8 ± 0.2	0.4 ± 0.2	0.8 ± 0.2	1.0 ± 0.2	2.1 ± 0.6	4.2 ± 0.8	1.4 ± 0.6	7.0 ± 0.7
155	168 ± 2	18 ± 1	6 ± 1	12 ± 1	17 ± 1	56 ± 4	119 ± 6	42 ± 4	131 ± 5
156	8.8 ± 0.3	1.1 ± 0.2	0.4 ± 0.2	1.1 ± 0.2	1.6 ± 0.2	2.9 ± 0.5	5.8 ± 0.6	1.9 ± 0.5	9.7 ± 0.8
157	83 ± 2	6 ± 1	2 ± 1	4 ± 1	6 ± 1	29 ± 4	72 ± 5	25 ± 4	60 ± 4
158	39.4 ± 0.5	5.5 ± 0.3	1.8 ± 0.3	4.5 ± 0.3	6.5 ± 0.4	13 ± 1	23 ± 1	8 ± 1	36 ± 2
159	47 ± 3	3 ± 2	1 ± 2	2 ± 2	3 ± 2	16 ± 4	37 ± 5	13 ± 4	31 ± 4
160	13.7 ± 0.5	1.6 ± 0.3	0.6 ± 0.3	1.5 ± 0.3	2.2 ± 0.3	5.0 ± 0.8	10 ± 1	3.5 ± 0.7	15 ± 1
161	2.5 ± 0.3	0.5 ± 0.2	0.4 ± 0.2	0.3 ± 0.2	0.8 ± 0.2	0.8 ± 0.4	0.6 ± 0.3	0.0 ± 0.3	3.8 ± 0.9
162	276 ± 3	25 ± 2	8 ± 2	16 ± 2	24 ± 2	89 ± 7	183 ± 9	65 ± 7	182 ± 8
163	1.59 ± 0.09	0.15 ± 0.06	0.06 ± 0.06	0.20 ± 0.07	0.31 ± 0.07	0.6 ± 0.1	0.25 ± 0.08	0.02 ± 0.07	1.0 ± 0.2
164	0.97 ± 0.08	0.09 ± 0.05	0.04 ± 0.05	0.12 ± 0.05	0.17 ± 0.05	0.25 ± 0.06	0.21 ± 0.06	0.07 ± 0.06	0.6 ± 0.1
165	43.0 ± 0.5	5.5 ± 0.3	1.8 ± 0.3	3.9 ± 0.3	5.7 ± 0.3	13.5 ± 0.9	21 ± 1	7.1 ± 0.8	34 ± 1
166	14.4 ± 0.3	1.5 ± 0.2	0.6 ± 0.2	1.5 ± 0.2	2.2 ± 0.2	4.9 ± 0.5	8.3 ± 0.7	2.8 ± 0.5	15.2 ± 0.8

Uncorrected flux values of the emission regions in the catalogue from this study. The measured fluxes of the nine emission lines for the detected emission regions are presented. These fluxes are not corrected for the local background diffuse emission (described in Section 2.6.3), the global stellar absorption (described in Section 2.6.7), nor the extinction (described in Section 2.6.8). These fluxes are obtained directly from the fit of the integrated region's spectrum and the uncertainties correspond to the fitting uncertainties from ORCS.

All flux values are scaled by 1×10^{-15} .

ID	$H\alpha$ [erg s ⁻¹ cm ⁻²]	[N II] $\lambda 6583$ [erg s ⁻¹ cm ⁻²]	[N II] $\lambda 6548$ [erg s ⁻¹ cm ⁻²]	[S II] $\lambda 6731$ [erg s ⁻¹ cm ⁻²]	[S II] $\lambda 6716$ [erg s ⁻¹ cm ⁻²]	$H\beta$ [erg s ⁻¹ cm ⁻²]	[O III] $\lambda 5007$ [erg s ⁻¹ cm ⁻²]	[O III] $\lambda 4959$ [erg s ⁻¹ cm ⁻²]	[O II] $\lambda 3727$ [erg s ⁻¹ cm ⁻²]
167	0.51 ± 0.08	-0.01 ± 0.05	0.06 ± 0.05	0.05 ± 0.05	0.03 ± 0.05	0.09 ± 0.06	0.18 ± 0.08	0.06 ± 0.06	0.2 ± 0.1
168	3.8 ± 0.2	0.5 ± 0.1	0.1 ± 0.1	0.8 ± 0.2	1.2 ± 0.2	1.2 ± 0.4	1.3 ± 0.4	0.4 ± 0.3	5.2 ± 0.5
169	42 ± 1	4.2 ± 0.7	1.5 ± 0.7	3.5 ± 0.8	4.8 ± 0.8	14 ± 2	38 ± 3	13 ± 2	34 ± 2
170	34.3 ± 0.4	4.1 ± 0.3	1.3 ± 0.3	2.6 ± 0.3	4.0 ± 0.3	9.9 ± 0.6	18.2 ± 0.7	6.2 ± 0.6	24.7 ± 0.9
171	51.7 ± 0.9	6.8 ± 0.5	2.1 ± 0.5	5.9 ± 0.6	8.0 ± 0.6	16 ± 2	30 ± 2	10 ± 2	44 ± 2
172	55.6 ± 0.6	5.8 ± 0.4	1.8 ± 0.4	4.9 ± 0.4	6.5 ± 0.4	18 ± 1	39 ± 2	13 ± 1	43 ± 2
173	37.4 ± 0.7	5.0 ± 0.5	1.3 ± 0.5	4.8 ± 0.5	6.2 ± 0.5	14 ± 1	31 ± 2	10 ± 1	38 ± 2
174	11.4 ± 0.3	1.5 ± 0.2	0.4 ± 0.2	1.4 ± 0.2	1.9 ± 0.2	3.4 ± 0.6	7.5 ± 0.7	2.5 ± 0.5	11.9 ± 0.8
175	277 ± 3	23 ± 2	7 ± 2	16 ± 2	22 ± 2	85 ± 7	220 ± 10	75 ± 7	159 ± 7
176	2.1 ± 0.1	0.31 ± 0.09	0.10 ± 0.09	0.2 ± 0.1	0.4 ± 0.1	0.6 ± 0.1	0.4 ± 0.1	0.1 ± 0.1	2.3 ± 0.3
177	16.8 ± 0.3	1.9 ± 0.2	0.7 ± 0.2	1.7 ± 0.2	2.3 ± 0.2	5.0 ± 0.6	8.0 ± 0.7	2.6 ± 0.6	16.0 ± 0.8
178	23.7 ± 0.3	2.5 ± 0.2	0.7 ± 0.2	2.0 ± 0.2	2.8 ± 0.2	5.7 ± 0.7	13.5 ± 0.9	4.5 ± 0.6	13.0 ± 0.8
179	23.1 ± 0.5	3.3 ± 0.3	1.1 ± 0.3	2.8 ± 0.3	3.8 ± 0.3	7 ± 1	12 ± 1	3.9 ± 0.9	19 ± 1
180	34.5 ± 0.5	4.1 ± 0.3	1.4 ± 0.3	3.2 ± 0.4	4.6 ± 0.4	11 ± 1	12 ± 1	3.9 ± 0.8	31 ± 1
181	22.1 ± 0.5	3.2 ± 0.3	1.1 ± 0.3	3.2 ± 0.3	4.7 ± 0.3	8 ± 1	8 ± 1	2.7 ± 0.9	24 ± 1
182	9.9 ± 0.2	1.4 ± 0.1	0.4 ± 0.1	1.3 ± 0.1	1.9 ± 0.1	2.9 ± 0.3	2.6 ± 0.3	0.9 ± 0.3	9.5 ± 0.6
183	1.8 ± 0.1	0.33 ± 0.08	0.13 ± 0.08	0.29 ± 0.08	0.47 ± 0.08	0.6 ± 0.2	0.4 ± 0.1	0.1 ± 0.1	2.3 ± 0.3
184	5.9 ± 0.2	0.7 ± 0.1	0.3 ± 0.1	0.6 ± 0.1	0.8 ± 0.1	1.6 ± 0.2	2.4 ± 0.3	0.7 ± 0.2	4.9 ± 0.4
185	87 ± 1	8.9 ± 0.7	3.0 ± 0.7	6.3 ± 0.7	9.0 ± 0.7	26 ± 2	62 ± 3	21 ± 2	51 ± 2
186	2.7 ± 0.1	0.26 ± 0.08	0.04 ± 0.08	0.37 ± 0.09	0.48 ± 0.09	0.8 ± 0.2	0.8 ± 0.2	0.2 ± 0.2	3.3 ± 0.3
187	2.4 ± 0.1	0.3 ± 0.1	0.1 ± 0.1	0.5 ± 0.1	0.6 ± 0.1	0.6 ± 0.2	0.8 ± 0.2	0.3 ± 0.2	2.9 ± 0.4
188	1.1 ± 0.1	0.17 ± 0.08	0.02 ± 0.08	0.10 ± 0.08	0.24 ± 0.08	0.2 ± 0.2	0.5 ± 0.2	0.2 ± 0.2	1.5 ± 0.4
189	1.5 ± 0.2	0.2 ± 0.1	0.1 ± 0.1	0.2 ± 0.1	0.3 ± 0.1	0.5 ± 0.2	0.0 ± 0.1	0.0 ± 0.1	1.6 ± 0.4
190	1.06 ± 0.09	0.18 ± 0.06	0.07 ± 0.06	0.17 ± 0.06	0.19 ± 0.06	0.4 ± 0.1	0.3 ± 0.1	0.06 ± 0.08	1.3 ± 0.3

Uncorrected flux values of the emission regions in the catalogue from this study. The measured fluxes of the nine emission lines for the detected emission regions are presented. These fluxes are not corrected for the local background diffuse emission (described in Section 2.6.3), the global stellar absorption (described in Section 2.6.7), nor the extinction (described in Section 2.6.8). These fluxes are obtained directly from the fit of the integrated region's spectrum and the uncertainties correspond to the fitting uncertainties from ORCS.

All flux values are scaled by 1×10^{-15} .

ID	$H\alpha$ [erg s ⁻¹ cm ⁻²]	[N II] $\lambda 6583$ [erg s ⁻¹ cm ⁻²]	[N II] $\lambda 6548$ [erg s ⁻¹ cm ⁻²]	[S II] $\lambda 6731$ [erg s ⁻¹ cm ⁻²]	[S III] $\lambda 6716$ [erg s ⁻¹ cm ⁻²]	$H\beta$ [erg s ⁻¹ cm ⁻²]	[O III] $\lambda 5007$ [erg s ⁻¹ cm ⁻²]	[O III] $\lambda 4959$ [erg s ⁻¹ cm ⁻²]	[O II] $\lambda 3727$ [erg s ⁻¹ cm ⁻²]
191	25.3 ± 0.4	3.6 ± 0.3	1.1 ± 0.3	3.0 ± 0.3	4.4 ± 0.3	7.9 ± 0.7	8.7 ± 0.8	2.9 ± 0.6	26 ± 1
192	41.0 ± 0.9	6.3 ± 0.6	1.9 ± 0.6	5.7 ± 0.6	7.8 ± 0.6	14 ± 2	20 ± 2	7 ± 2	44 ± 2
193	3.6 ± 0.2	0.4 ± 0.1	0.1 ± 0.1	0.2 ± 0.1	0.5 ± 0.1	1.2 ± 0.3	1.6 ± 0.4	0.5 ± 0.3	4.3 ± 0.6
196	1.16 ± 0.07	0.13 ± 0.05	0.13 ± 0.05	0.10 ± 0.05	0.22 ± 0.05	0.4 ± 0.1	0.24 ± 0.09	0.07 ± 0.08	1.3 ± 0.2
197	20.1 ± 0.3	1.7 ± 0.2	0.6 ± 0.2	1.3 ± 0.2	1.8 ± 0.2	5.9 ± 0.6	16.3 ± 0.8	5.4 ± 0.6	12.5 ± 0.7
198	46 ± 2	7 ± 1	2 ± 1	7 ± 1	11 ± 1	14 ± 3	20 ± 3	7 ± 3	55 ± 4
199	23 ± 1	3.7 ± 0.6	1.1 ± 0.6	3.4 ± 0.6	4.7 ± 0.6	7 ± 2	11 ± 2	4 ± 1	27 ± 2
200	85 ± 3	13 ± 2	5 ± 2	12 ± 2	17 ± 2	25 ± 6	45 ± 7	16 ± 5	92 ± 7
201	18.0 ± 0.6	3.1 ± 0.4	1.0 ± 0.4	2.8 ± 0.4	4.2 ± 0.4	5 ± 2	11 ± 2	4 ± 2	21 ± 2
202	13.3 ± 0.2	0.7 ± 0.1	0.3 ± 0.1	0.6 ± 0.1	0.8 ± 0.1	3.9 ± 0.5	17.2 ± 0.7	6.0 ± 0.5	5.6 ± 0.3
203	13.8 ± 0.2	1.8 ± 0.2	0.7 ± 0.2	1.5 ± 0.2	2.0 ± 0.2	3.9 ± 0.4	8.1 ± 0.5	2.9 ± 0.4	14.1 ± 0.6
204	34.2 ± 0.7	4.6 ± 0.5	1.6 ± 0.5	3.9 ± 0.5	5.4 ± 0.5	10 ± 2	17 ± 2	6 ± 2	27 ± 2
205	2.1 ± 0.1	0.24 ± 0.08	0.16 ± 0.08	0.18 ± 0.08	0.33 ± 0.08	0.6 ± 0.2	0.8 ± 0.2	0.2 ± 0.1	2.2 ± 0.3
206	9.3 ± 0.2	1.1 ± 0.1	0.4 ± 0.1	0.9 ± 0.1	1.4 ± 0.1	2.9 ± 0.3	6.3 ± 0.4	2.2 ± 0.3	9.2 ± 0.5
207	38.3 ± 0.9	5.0 ± 0.6	1.4 ± 0.6	3.9 ± 0.6	5.8 ± 0.6	10 ± 2	22 ± 3	8 ± 2	27 ± 3
208	51 ± 2	8 ± 1	3 ± 1	7 ± 1	9 ± 1	14 ± 4	26 ± 5	9 ± 4	47 ± 5
209	6.3 ± 0.2	0.9 ± 0.1	0.2 ± 0.1	0.9 ± 0.1	1.2 ± 0.1	1.7 ± 0.3	2.6 ± 0.4	0.8 ± 0.3	7.3 ± 0.6
210	31.9 ± 0.4	2.9 ± 0.3	0.9 ± 0.3	2.3 ± 0.3	3.3 ± 0.3	9.7 ± 0.9	28 ± 1	10 ± 1	23 ± 1
211	2.2 ± 0.1	0.28 ± 0.09	0.19 ± 0.09	0.2 ± 0.1	0.5 ± 0.1	0.7 ± 0.1	1.2 ± 0.2	0.4 ± 0.1	2.7 ± 0.3
212	43.2 ± 0.6	3.7 ± 0.4	1.4 ± 0.4	2.9 ± 0.4	4.3 ± 0.4	14 ± 1	46 ± 2	16 ± 2	29 ± 1
213	13.6 ± 0.3	1.9 ± 0.2	0.6 ± 0.2	1.6 ± 0.2	2.3 ± 0.2	4.2 ± 0.5	8.0 ± 0.6	2.7 ± 0.5	20.0 ± 0.9
214	0.91 ± 0.07	0.03 ± 0.05	0.09 ± 0.05	0.13 ± 0.05	0.19 ± 0.05	0.3 ± 0.1	0.07 ± 0.09	0.01 ± 0.08	0.7 ± 0.2
215	6.6 ± 0.2	0.9 ± 0.2	0.4 ± 0.2	0.9 ± 0.2	1.2 ± 0.2	2.2 ± 0.5	3.2 ± 0.6	1.2 ± 0.5	8.8 ± 0.7
216	1.03 ± 0.06	0.10 ± 0.04	0.07 ± 0.04	0.13 ± 0.05	0.21 ± 0.05	0.37 ± 0.06	0.76 ± 0.07	0.24 ± 0.06	1.3 ± 0.2

Uncorrected flux values of the emission regions in the catalogue from this study. The measured fluxes of the nine emission lines for the detected emission regions are presented. These fluxes are not corrected for the local background diffuse emission (described in Section 2.6.3), the global stellar absorption (described in Section 2.6.7), nor the extinction (described in Section 2.6.8). These fluxes are obtained directly from the fit of the integrated region's spectrum and the uncertainties correspond to the fitting uncertainties from ORCS.

All flux values are scaled by 1×10^{-15} .

ID	$H\alpha$ [erg s ⁻¹ cm ⁻²]	[N II] $\lambda 6583$ [erg s ⁻¹ cm ⁻²]	[N II] $\lambda 6548$ [erg s ⁻¹ cm ⁻²]	[S II] $\lambda 6731$ [erg s ⁻¹ cm ⁻²]	[S III] $\lambda 6716$ [erg s ⁻¹ cm ⁻²]	$H\beta$ [erg s ⁻¹ cm ⁻²]	[O III] $\lambda 5007$ [erg s ⁻¹ cm ⁻²]	[O III] $\lambda 4959$ [erg s ⁻¹ cm ⁻²]	[O II] $\lambda 3727$ [erg s ⁻¹ cm ⁻²]
217	1.75 ± 0.08	0.23 ± 0.06	0.16 ± 0.06	0.26 ± 0.06	0.37 ± 0.06	0.52 ± 0.09	1.1 ± 0.1	0.32 ± 0.09	1.9 ± 0.2
218	1.67 ± 0.08	0.16 ± 0.05	0.08 ± 0.05	0.30 ± 0.05	0.31 ± 0.05	0.49 ± 0.06	0.96 ± 0.06	0.33 ± 0.06	1.6 ± 0.3
219	19.5 ± 0.4	2.2 ± 0.3	0.7 ± 0.2	1.9 ± 0.3	2.7 ± 0.3	6.3 ± 0.7	14 ± 1	4.9 ± 0.7	20 ± 1
220	114 ± 2	12 ± 1	4 ± 1	8 ± 1	11 ± 1	29 ± 4	71 ± 5	24 ± 4	66 ± 4
221	17 ± 1	2.2 ± 0.7	0.7 ± 0.6	2.0 ± 0.7	2.9 ± 0.7	5 ± 2	10 ± 3	3 ± 2	15 ± 2
222	1.90 ± 0.09	0.23 ± 0.06	0.11 ± 0.06	0.25 ± 0.06	0.43 ± 0.06	0.6 ± 0.1	1.2 ± 0.1	0.4 ± 0.1	2.0 ± 0.3
223	4.0 ± 0.2	0.7 ± 0.1	0.3 ± 0.1	0.8 ± 0.2	1.1 ± 0.2	1.1 ± 0.4	1.2 ± 0.4	0.4 ± 0.3	5.4 ± 0.6
224	9.5 ± 0.6	2.1 ± 0.4	0.6 ± 0.4	2.5 ± 0.5	3.0 ± 0.5	3 ± 1	3 ± 1	1 ± 1	16 ± 2
225	6.1 ± 0.4	0.9 ± 0.3	0.4 ± 0.3	0.8 ± 0.3	1.1 ± 0.3	1.9 ± 0.9	3 ± 1	1.0 ± 0.8	7.6 ± 0.9
226	1.17 ± 0.06	0.13 ± 0.04	0.06 ± 0.04	0.12 ± 0.04	0.22 ± 0.04	0.34 ± 0.06	0.32 ± 0.06	0.13 ± 0.05	1.2 ± 0.1
227	42 ± 1	7.1 ± 0.8	2.5 ± 0.8	5.6 ± 0.8	8.0 ± 0.8	11 ± 3	23 ± 4	8 ± 3	37 ± 4
228	3.0 ± 0.1	0.16 ± 0.08	0.12 ± 0.08	0.40 ± 0.08	0.56 ± 0.08	1.0 ± 0.1	1.9 ± 0.2	0.6 ± 0.1	2.6 ± 0.3
229	5.1 ± 0.2	0.5 ± 0.1	0.3 ± 0.1	0.6 ± 0.1	1.1 ± 0.1	1.5 ± 0.1	1.4 ± 0.2	0.5 ± 0.2	4.4 ± 0.5
230	1.01 ± 0.07	0.11 ± 0.04	0.03 ± 0.04	0.14 ± 0.05	0.20 ± 0.05	0.30 ± 0.05	0.36 ± 0.05	0.17 ± 0.05	1.1 ± 0.2
231	11.3 ± 0.3	1.8 ± 0.2	0.5 ± 0.2	1.6 ± 0.2	2.2 ± 0.2	3.3 ± 0.6	4.2 ± 0.7	1.5 ± 0.6	13.4 ± 0.9
232	69.1 ± 0.8	6.1 ± 0.5	2.2 ± 0.5	4.4 ± 0.6	6.7 ± 0.6	20 ± 2	77 ± 4	26 ± 3	36 ± 2
233	7.0 ± 0.1	0.62 ± 0.09	0.21 ± 0.09	0.44 ± 0.09	0.57 ± 0.09	2.0 ± 0.2	4.1 ± 0.2	1.3 ± 0.2	4.7 ± 0.3
234	147 ± 3	16 ± 2	5 ± 2	13 ± 2	17 ± 2	40 ± 4	112 ± 6	38 ± 5	96 ± 5
235	4.8 ± 0.2	0.6 ± 0.1	0.1 ± 0.1	0.6 ± 0.1	0.8 ± 0.1	1.6 ± 0.2	1.9 ± 0.3	0.7 ± 0.2	5.6 ± 0.6
236	3.0 ± 0.3	0.4 ± 0.2	0.3 ± 0.2	0.3 ± 0.2	0.6 ± 0.2	0.9 ± 0.4	1.8 ± 0.5	0.6 ± 0.4	3.8 ± 0.5
237	10.3 ± 0.2	0.6 ± 0.1	0.3 ± 0.1	0.6 ± 0.1	0.8 ± 0.1	3.2 ± 0.3	9.2 ± 0.4	3.1 ± 0.3	7.1 ± 0.4
238	247 ± 5	33 ± 3	10 ± 3	22 ± 3	28 ± 3	70 ± 10	140 ± 10	50 ± 10	180 ± 10
239	6.1 ± 0.2	0.4 ± 0.1	0.3 ± 0.1	0.7 ± 0.1	1.0 ± 0.1	1.9 ± 0.3	8.0 ± 0.4	2.7 ± 0.3	4.3 ± 0.4
240	1.08 ± 0.06	0.13 ± 0.04	0.07 ± 0.04	0.12 ± 0.04	0.16 ± 0.04	0.35 ± 0.07	0.38 ± 0.07	0.17 ± 0.06	1.1 ± 0.2

Uncorrected flux values of the emission regions in the catalogue from this study. The measured fluxes of the nine emission lines for the detected emission regions are presented. These fluxes are not corrected for the local background diffuse emission (described in Section 2.6.3), the global stellar absorption (described in Section 2.6.7), nor the extinction (described in Section 2.6.8). These fluxes are obtained directly from the fit of the integrated region's spectrum and the uncertainties correspond to the fitting uncertainties from ORCS.

All flux values are scaled by 1×10^{-15} .

ID	$\text{H}\alpha$ [$\text{erg s}^{-1} \text{cm}^{-2}$]	$[\text{N II}]\lambda 6583$ [$\text{erg s}^{-1} \text{cm}^{-2}$]	$[\text{N II}]\lambda 6548$ [$\text{erg s}^{-1} \text{cm}^{-2}$]	$[\text{S II}]\lambda 6731$ [$\text{erg s}^{-1} \text{cm}^{-2}$]	$[\text{S II}]\lambda 6716$ [$\text{erg s}^{-1} \text{cm}^{-2}$]	$\text{H}\beta$ [$\text{erg s}^{-1} \text{cm}^{-2}$]	$[\text{O III}]\lambda 5007$ [$\text{erg s}^{-1} \text{cm}^{-2}$]	$[\text{O III}]\lambda 4959$ [$\text{erg s}^{-1} \text{cm}^{-2}$]	$[\text{O II}]\lambda 3727$ [$\text{erg s}^{-1} \text{cm}^{-2}$]
241	22.5 ± 0.3	1.7 ± 0.2	0.7 ± 0.2	1.4 ± 0.2	2.2 ± 0.2	7.3 ± 0.7	21 ± 1	7.3 ± 0.7	17.9 ± 0.9
242	88 ± 1	10.9 ± 0.9	3.5 ± 0.9	9.2 ± 0.9	13.1 ± 0.9	24 ± 3	58 ± 4	20 ± 3	64 ± 3
243	1.50 ± 0.09	0.21 ± 0.06	0.05 ± 0.06	0.23 ± 0.07	0.36 ± 0.07	0.40 ± 0.07	0.68 ± 0.07	0.22 ± 0.07	1.5 ± 0.2
244	81 ± 1	9.0 ± 0.8	3.0 ± 0.8	6.9 ± 0.9	9.4 ± 0.9	25 ± 3	62 ± 4	22 ± 3	53 ± 3
245	1.7 ± 0.1	0.18 ± 0.07	0.07 ± 0.07	0.25 ± 0.07	0.35 ± 0.07	0.5 ± 0.2	0.3 ± 0.2	0.1 ± 0.1	1.5 ± 0.3
246	0.49 ± 0.09	0.07 ± 0.06	0.03 ± 0.06	0.05 ± 0.06	0.06 ± 0.06	0.2 ± 0.1	0.2 ± 0.1	0.0 ± 0.1	0.5 ± 0.2
247	48.9 ± 0.6	6.0 ± 0.4	1.9 ± 0.4	4.2 ± 0.4	6.2 ± 0.4	15 ± 1	40 ± 2	14 ± 1	35 ± 2
248	1.9 ± 0.1	0.21 ± 0.08	0.14 ± 0.07	0.32 ± 0.08	0.39 ± 0.08	0.65 ± 0.09	0.75 ± 0.09	0.20 ± 0.09	1.9 ± 0.3
249	49.5 ± 0.8	6.8 ± 0.5	2.3 ± 0.5	6.3 ± 0.5	8.6 ± 0.5	13 ± 2	35 ± 3	12 ± 2	37 ± 2
250	5.9 ± 0.2	0.8 ± 0.1	0.3 ± 0.1	0.7 ± 0.2	1.1 ± 0.2	1.8 ± 0.4	1.0 ± 0.3	0.3 ± 0.3	5.7 ± 0.6
251	4.3 ± 0.2	0.4 ± 0.1	0.1 ± 0.1	0.7 ± 0.1	0.9 ± 0.1	1.3 ± 0.2	4.4 ± 0.2	1.4 ± 0.2	3.4 ± 0.5
252	2.8 ± 0.1	0.23 ± 0.08	0.13 ± 0.08	0.24 ± 0.08	0.31 ± 0.08	0.9 ± 0.2	1.5 ± 0.3	0.6 ± 0.2	2.3 ± 0.3
253	2.4 ± 0.1	0.25 ± 0.09	0.15 ± 0.09	0.2 ± 0.1	0.3 ± 0.1	0.8 ± 0.2	1.5 ± 0.2	0.6 ± 0.2	2.8 ± 0.3
254	200 ± 3	23 ± 2	8 ± 2	16 ± 2	21 ± 2	58 ± 4	103 ± 5	36 ± 4	160 ± 6
255	5.3 ± 0.2	0.8 ± 0.1	0.2 ± 0.1	0.9 ± 0.1	1.2 ± 0.1	1.8 ± 0.4	2.0 ± 0.5	0.7 ± 0.4	6.9 ± 0.5
256	2.5 ± 0.2	0.3 ± 0.1	0.1 ± 0.1	0.3 ± 0.1	0.4 ± 0.1	0.8 ± 0.4	1.2 ± 0.5	0.4 ± 0.4	3.5 ± 0.6
257	14.2 ± 0.5	2.6 ± 0.4	0.7 ± 0.4	3.0 ± 0.4	4.3 ± 0.4	4 ± 1	5 ± 1	1 ± 1	20 ± 1
258	2.8 ± 0.1	0.49 ± 0.08	0.17 ± 0.08	0.46 ± 0.09	0.72 ± 0.09	0.8 ± 0.2	0.9 ± 0.2	0.3 ± 0.1	3.3 ± 0.3
259	28.2 ± 0.5	2.7 ± 0.3	1.0 ± 0.3	2.0 ± 0.3	2.9 ± 0.3	9 ± 1	20 ± 1	7 ± 1	22 ± 1
260	88 ± 3	10 ± 2	3 ± 2	7 ± 2	10 ± 2	27 ± 4	62 ± 5	21 ± 4	61 ± 4
261	81 ± 1	8.0 ± 0.8	2.7 ± 0.8	6.1 ± 0.9	8.8 ± 0.9	25 ± 3	64 ± 4	22 ± 3	68 ± 3
262	24.5 ± 0.7	3.7 ± 0.4	1.2 ± 0.4	3.4 ± 0.5	4.7 ± 0.5	7 ± 1	8 ± 1	3 ± 1	25 ± 2
263	3.6 ± 0.1	0.35 ± 0.08	0.20 ± 0.08	0.47 ± 0.08	0.64 ± 0.08	1.0 ± 0.1	3.6 ± 0.2	1.1 ± 0.1	3.0 ± 0.3
264	6.7 ± 0.3	1.2 ± 0.2	0.5 ± 0.2	1.3 ± 0.2	1.7 ± 0.2	1.8 ± 0.6	2.1 ± 0.7	0.6 ± 0.6	9.0 ± 0.8

Uncorrected flux values of the emission regions in the catalogue from this study. The measured fluxes of the nine emission lines for the detected emission regions are presented. These fluxes are not corrected for the local background diffuse emission (described in Section 2.6.3), the global stellar absorption (described in Section 2.6.7), nor the extinction (described in Section 2.6.8). These fluxes are obtained directly from the fit of the integrated region's spectrum and the uncertainties correspond to the fitting uncertainties from ORCS.

All flux values are scaled by 1×10^{-15} .

ID	H α [erg s $^{-1}$ cm $^{-2}$]	[N II] λ 6583 [erg s $^{-1}$ cm $^{-2}$]	[N II] λ 6548 [erg s $^{-1}$ cm $^{-2}$]	[S II] λ 6731 [erg s $^{-1}$ cm $^{-2}$]	[S II] λ 6716 [erg s $^{-1}$ cm $^{-2}$]	H β [erg s $^{-1}$ cm $^{-2}$]	[O III] λ 5007 [erg s $^{-1}$ cm $^{-2}$]	[O III] λ 4959 [erg s $^{-1}$ cm $^{-2}$]	[O II] λ 3727 [erg s $^{-1}$ cm $^{-2}$]
265	57 ± 1	7.7 ± 0.7	2.6 ± 0.7	7.2 ± 0.7	10.2 ± 0.8	18 ± 2	39 ± 3	13 ± 2	49 ± 3
266	3.2 ± 0.1	0.3 ± 0.1	0.1 ± 0.1	0.4 ± 0.1	0.5 ± 0.1	1.0 ± 0.2	2.1 ± 0.2	0.7 ± 0.2	3.7 ± 0.5
267	1.09 ± 0.06	0.09 ± 0.04	0.07 ± 0.04	0.16 ± 0.04	0.24 ± 0.04	0.43 ± 0.05	1.00 ± 0.07	0.25 ± 0.05	1.0 ± 0.2
268	3.1 ± 0.1	0.23 ± 0.07	0.17 ± 0.07	0.31 ± 0.07	0.44 ± 0.07	0.9 ± 0.1	2.5 ± 0.2	0.9 ± 0.1	2.2 ± 0.3
269	6.7 ± 0.1	0.53 ± 0.09	0.23 ± 0.09	0.47 ± 0.09	0.58 ± 0.09	2.1 ± 0.2	5.0 ± 0.3	1.7 ± 0.2	5.3 ± 0.4
270	129 ± 2	10 ± 1	3 ± 1	7 ± 1	9 ± 1	39 ± 5	139 ± 8	48 ± 6	72 ± 5
271	25.5 ± 0.7	3.7 ± 0.5	1.4 ± 0.4	3.3 ± 0.5	4.6 ± 0.5	7 ± 2	9 ± 2	3 ± 1	22 ± 2
272	55.4 ± 0.7	6.6 ± 0.5	2.2 ± 0.5	5.0 ± 0.5	7.0 ± 0.5	17 ± 2	33 ± 2	11 ± 1	39 ± 2
273	3.4 ± 0.2	0.6 ± 0.1	0.2 ± 0.1	0.6 ± 0.1	0.9 ± 0.1	1.1 ± 0.3	1.3 ± 0.4	0.4 ± 0.3	5.0 ± 0.4
274	2.21 ± 0.08	0.14 ± 0.05	0.09 ± 0.05	0.22 ± 0.05	0.26 ± 0.05	0.7 ± 0.1	2.2 ± 0.1	0.8 ± 0.1	1.3 ± 0.2
275	8.6 ± 0.2	0.6 ± 0.1	0.3 ± 0.1	0.9 ± 0.1	1.3 ± 0.1	2.7 ± 0.3	6.7 ± 0.4	2.3 ± 0.3	5.9 ± 0.6
276	53.5 ± 0.7	7.8 ± 0.5	2.8 ± 0.5	6.5 ± 0.5	9.4 ± 0.5	16 ± 2	24 ± 2	8 ± 1	43 ± 2
277	6.0 ± 0.3	1.1 ± 0.2	0.3 ± 0.2	1.2 ± 0.2	1.8 ± 0.2	1.9 ± 0.5	2.6 ± 0.5	0.8 ± 0.4	8.9 ± 0.7
278	9.9 ± 0.3	1.9 ± 0.2	0.7 ± 0.2	1.8 ± 0.2	2.7 ± 0.2	2.8 ± 0.7	3.2 ± 0.7	1.0 ± 0.6	12.2 ± 0.9
279	17.0 ± 0.2	1.2 ± 0.1	0.5 ± 0.1	0.9 ± 0.2	1.1 ± 0.2	4.6 ± 0.3	11.2 ± 0.5	4.0 ± 0.3	9.8 ± 0.5
280	31.5 ± 0.7	3.9 ± 0.5	1.4 ± 0.5	3.7 ± 0.5	5.2 ± 0.5	10 ± 1	15 ± 1	5.1 ± 0.9	23 ± 1
281	5.2 ± 0.2	0.9 ± 0.2	0.2 ± 0.2	0.9 ± 0.2	1.2 ± 0.2	1.5 ± 0.4	5.3 ± 0.6	1.9 ± 0.4	7.0 ± 0.6
282	1.3 ± 0.1	0.09 ± 0.07	0.07 ± 0.07	0.23 ± 0.07	0.32 ± 0.07	0.36 ± 0.08	0.10 ± 0.09	0.03 ± 0.09	1.3 ± 0.3
283	51 ± 4	9 ± 2	3 ± 2	9 ± 2	13 ± 2	15 ± 4	32 ± 5	11 ± 4	68 ± 4
284	52.6 ± 0.8	5.8 ± 0.5	1.6 ± 0.5	4.6 ± 0.5	6.4 ± 0.5	1.5 ± 2	34 ± 2	12 ± 2	40 ± 2
285	45.0 ± 0.7	5.9 ± 0.4	1.8 ± 0.4	4.8 ± 0.5	6.8 ± 0.5	14 ± 1	29 ± 2	10 ± 1	39 ± 2
286	0.9 ± 0.1	0.09 ± 0.07	0.03 ± 0.07	0.09 ± 0.07	0.16 ± 0.07	0.3 ± 0.1	0.12 ± 0.08	0.02 ± 0.07	1.2 ± 0.3
287	53.5 ± 0.8	7.4 ± 0.6	2.3 ± 0.5	6.4 ± 0.6	9.0 ± 0.6	17 ± 2	34 ± 2	12 ± 2	49 ± 2
288	26.8 ± 0.6	3.8 ± 0.4	1.2 ± 0.4	3.2 ± 0.4	4.5 ± 0.4	8 ± 2	17 ± 2	6 ± 2	27 ± 2

Uncorrected flux values of the emission regions in the catalogue from this study. The measured fluxes of the nine emission lines for the detected emission regions are presented. These fluxes are not corrected for the local background diffuse emission (described in Section 2.6.3), the global stellar absorption (described in Section 2.6.7), nor the extinction (described in Section 2.6.8). These fluxes are obtained directly from the fit of the integrated region's spectrum and the uncertainties correspond to the fitting uncertainties from ORCS.

All flux values are scaled by 1×10^{-15} .

ID	$H\alpha$ [erg s ⁻¹ cm ⁻²]	[N II] $\lambda 6583$ [erg s ⁻¹ cm ⁻²]	[N II] $\lambda 6548$ [erg s ⁻¹ cm ⁻²]	[S II] $\lambda 6731$ [erg s ⁻¹ cm ⁻²]	[S II] $\lambda 6716$ [erg s ⁻¹ cm ⁻²]	$H\beta$ [erg s ⁻¹ cm ⁻²]	[O III] $\lambda 5007$ [erg s ⁻¹ cm ⁻²]	[O III] $\lambda 4959$ [erg s ⁻¹ cm ⁻²]	[O II] $\lambda 3727$ [erg s ⁻¹ cm ⁻²]
289	0.77 ± 0.09	0.10 ± 0.06	0.01 ± 0.06	0.13 ± 0.07	0.17 ± 0.07	0.23 ± 0.07	0.07 ± 0.07	-0.01 ± 0.07	1.0 ± 0.3
290	44 ± 1	5.2 ± 0.6	1.8 ± 0.6	4.7 ± 0.6	6.9 ± 0.7	15 ± 2	37 ± 3	13 ± 2	39 ± 2
291	1.2 ± 0.1	0.11 ± 0.08	0.06 ± 0.08	0.17 ± 0.08	0.21 ± 0.08	0.3 ± 0.1	0.2 ± 0.1	0.1 ± 0.1	1.4 ± 0.4
292	13 ± 1	2.3 ± 0.9	0.8 ± 0.9	2.2 ± 0.9	3 ± 1	4 ± 4	6 ± 5	2 ± 4	16 ± 4
293	7.4 ± 0.3	1.1 ± 0.2	0.4 ± 0.2	1.3 ± 0.2	1.7 ± 0.2	2.2 ± 0.7	2.3 ± 0.7	0.8 ± 0.6	10.2 ± 0.8
294	2.1 ± 0.1	0.36 ± 0.07	0.10 ± 0.07	0.31 ± 0.08	0.53 ± 0.08	0.6 ± 0.1	0.6 ± 0.1	0.2 ± 0.1	2.5 ± 0.3
295	0.92 ± 0.09	0.12 ± 0.07	-0.02 ± 0.06	0.10 ± 0.07	0.23 ± 0.07	0.4 ± 0.1	0.10 ± 0.07	0.01 ± 0.07	1.0 ± 0.2
296	13.0 ± 0.5	2.7 ± 0.4	0.9 ± 0.3	3.0 ± 0.4	4.4 ± 0.4	4 ± 1	4 ± 1	1 ± 1	20 ± 2
297	0.51 ± 0.06	0.03 ± 0.04	-0.01 ± 0.04	0.10 ± 0.04	0.09 ± 0.04	0.19 ± 0.09	0.05 ± 0.07	0.00 ± 0.06	0.7 ± 0.2
298	68 ± 1	7.8 ± 0.9	2.5 ± 0.9	6.7 ± 0.9	9.4 ± 0.9	22 ± 3	52 ± 5	18 ± 3	55 ± 4
299	3.45 ± 0.08	0.27 ± 0.06	0.15 ± 0.06	0.27 ± 0.06	0.36 ± 0.06	0.9 ± 0.1	1.8 ± 0.1	0.6 ± 0.1	3.3 ± 0.3
300	1.56 ± 0.08	0.09 ± 0.05	0.04 ± 0.05	0.13 ± 0.06	0.22 ± 0.06	0.48 ± 0.08	0.55 ± 0.09	0.20 ± 0.07	1.7 ± 0.2
301	1.3 ± 0.3	0.11 ± 0.07	0.02 ± 0.04	0.17 ± 0.07	0.18 ± 0.08	0.4 ± 0.1	0.6 ± 0.2	0.19 ± 0.09	3.7 ± 0.9
302	1.3 ± 0.1	0.11 ± 0.07	0.02 ± 0.07	0.23 ± 0.08	0.28 ± 0.08	0.4 ± 0.1	0.4 ± 0.1	0.09 ± 0.09	1.8 ± 0.3
303	1.20 ± 0.07	0.13 ± 0.05	0.03 ± 0.05	0.12 ± 0.05	0.14 ± 0.05	0.35 ± 0.07	0.39 ± 0.08	0.15 ± 0.06	1.5 ± 0.2
304	23.9 ± 0.3	1.8 ± 0.2	0.7 ± 0.2	1.6 ± 0.2	2.3 ± 0.2	7.4 ± 0.6	17.0 ± 0.8	5.9 ± 0.6	20 ± 1
305	0.57 ± 0.07	0.05 ± 0.05	0.04 ± 0.05	-0.01 ± 0.05	0.13 ± 0.05	0.15 ± 0.06	0.36 ± 0.08	0.13 ± 0.06	0.7 ± 0.2
306	0.73 ± 0.05	0.06 ± 0.04	0.01 ± 0.04	0.05 ± 0.04	0.12 ± 0.04	0.26 ± 0.05	0.34 ± 0.05	0.13 ± 0.05	0.9 ± 0.1
307	3.2 ± 0.2	0.4 ± 0.1	0.1 ± 0.1	0.7 ± 0.1	0.7 ± 0.1	1.0 ± 0.2	1.1 ± 0.2	0.3 ± 0.1	4.4 ± 0.5
308	0.50 ± 0.05	0.04 ± 0.03	0.01 ± 0.03	0.07 ± 0.04	0.07 ± 0.04	0.16 ± 0.03	0.23 ± 0.04	0.09 ± 0.04	0.8 ± 0.1
309	1.08 ± 0.06	0.09 ± 0.04	0.08 ± 0.04	0.07 ± 0.04	0.08 ± 0.04	0.38 ± 0.06	0.66 ± 0.07	0.26 ± 0.06	1.1 ± 0.2
310	27 ± 1	4.7 ± 0.8	1.8 ± 0.8	4.4 ± 0.8	6.7 ± 0.9	9 ± 2	18 ± 3	6 ± 2	37 ± 3
311	5.3 ± 0.2	0.7 ± 0.1	0.2 ± 0.1	1.1 ± 0.1	1.6 ± 0.1	1.4 ± 0.2	0.8 ± 0.2	0.3 ± 0.2	5.4 ± 0.6
312	0.71 ± 0.05	0.08 ± 0.04	0.03 ± 0.04	0.10 ± 0.04	0.13 ± 0.04	0.28 ± 0.05	0.31 ± 0.06	0.16 ± 0.05	0.9 ± 0.1

Uncorrected flux values of the emission regions in the catalogue from this study. The measured fluxes of the nine emission lines for the detected emission regions are presented. These fluxes are not corrected for the local background diffuse emission (described in Section 2.6.3), the global stellar absorption (described in Section 2.6.7), nor the extinction (described in Section 2.6.8). These fluxes are obtained directly from the fit of the integrated region's spectrum and the uncertainties correspond to the fitting uncertainties from ORCS.

All flux values are scaled by 1×10^{-15} .

ID	H α [erg s $^{-1}$ cm $^{-2}$]	[N II] λ 6583 [erg s $^{-1}$ cm $^{-2}$]	[N II] λ 6548 [erg s $^{-1}$ cm $^{-2}$]	[S II] λ 6731 [erg s $^{-1}$ cm $^{-2}$]	[S II] λ 6716 [erg s $^{-1}$ cm $^{-2}$]	H β [erg s $^{-1}$ cm $^{-2}$]	[O III] λ 5007 [erg s $^{-1}$ cm $^{-2}$]	[O III] λ 4959 [erg s $^{-1}$ cm $^{-2}$]	[O II] λ 3727 [erg s $^{-1}$ cm $^{-2}$]
313	1.2 ± 0.1	0.2 ± 0.1	0.1 ± 0.1	0.1 ± 0.1	0.2 ± 0.1	0.3 ± 0.1	0.2 ± 0.1	0.0 ± 0.1	1.5 ± 0.4
314	5.6 ± 0.3	1.0 ± 0.2	0.3 ± 0.2	1.0 ± 0.2	1.4 ± 0.2	1.8 ± 0.5	2.3 ± 0.6	1.0 ± 0.5	7.9 ± 0.7
315	3.1 ± 0.1	0.5 ± 0.1	0.17 ± 0.09	0.6 ± 0.1	0.9 ± 0.1	0.9 ± 0.3	0.9 ± 0.3	0.3 ± 0.3	4.6 ± 0.4
316	8.1 ± 0.2	1.3 ± 0.2	0.4 ± 0.2	1.5 ± 0.2	2.0 ± 0.2	2.5 ± 0.6	2.2 ± 0.5	0.8 ± 0.5	10.4 ± 0.8
317	17.2 ± 0.5	2.5 ± 0.3	0.9 ± 0.3	2.4 ± 0.3	3.3 ± 0.3	5.1 ± 0.9	10 ± 1	3.3 ± 0.9	17 ± 1
318	2.3 ± 0.1	0.29 ± 0.07	0.12 ± 0.06	0.41 ± 0.07	0.53 ± 0.07	0.7 ± 0.3	0.5 ± 0.2	0.2 ± 0.2	2.6 ± 0.3
319	3.9 ± 0.1	0.73 ± 0.08	0.23 ± 0.08	0.72 ± 0.08	1.05 ± 0.08	1.1 ± 0.2	0.9 ± 0.2	0.3 ± 0.2	5.0 ± 0.3
320	5.7 ± 0.3	1.0 ± 0.2	0.3 ± 0.2	0.9 ± 0.2	1.4 ± 0.2	1.7 ± 0.6	1.6 ± 0.6	0.5 ± 0.5	8.1 ± 0.9
321	4.1 ± 0.1	0.40 ± 0.09	0.11 ± 0.08	0.47 ± 0.09	0.73 ± 0.09	1.2 ± 0.2	1.5 ± 0.2	0.5 ± 0.1	4.7 ± 0.4
322	5.2 ± 0.2	0.9 ± 0.1	0.3 ± 0.1	0.8 ± 0.1	1.2 ± 0.2	1.7 ± 0.5	4.4 ± 0.6	1.7 ± 0.5	7.3 ± 0.6
323	7.0 ± 0.1	0.69 ± 0.09	0.29 ± 0.09	0.8 ± 0.1	1.0 ± 0.1	2.0 ± 0.2	2.0 ± 0.2	0.7 ± 0.2	6.2 ± 0.4
324	28.6 ± 0.5	3.5 ± 0.4	1.1 ± 0.4	2.7 ± 0.4	3.8 ± 0.4	9 ± 1	17 ± 1	6.0 ± 0.9	24 ± 1
325	15.9 ± 0.4	2.6 ± 0.3	0.8 ± 0.3	2.3 ± 0.3	3.2 ± 0.3	4.7 ± 0.8	9 ± 1	3.3 ± 0.8	17 ± 1
326	9.0 ± 0.2	1.3 ± 0.2	0.4 ± 0.2	1.2 ± 0.2	1.6 ± 0.2	2.7 ± 0.5	5.1 ± 0.6	1.6 ± 0.4	10.1 ± 0.6
327	14.5 ± 0.3	2.2 ± 0.2	0.8 ± 0.2	2.1 ± 0.2	3.1 ± 0.2	4.9 ± 0.6	9.2 ± 0.7	3.4 ± 0.6	14.8 ± 0.9
328	17.3 ± 0.4	2.3 ± 0.2	0.8 ± 0.2	2.1 ± 0.3	3.0 ± 0.3	5.3 ± 0.8	9.1 ± 0.9	3.2 ± 0.7	15 ± 1
329	13.3 ± 0.6	2.7 ± 0.4	0.9 ± 0.4	2.7 ± 0.4	4.0 ± 0.4	4 ± 2	5 ± 2	1 ± 1	20 ± 2
330	6.2 ± 0.2	1.0 ± 0.1	0.4 ± 0.1	1.0 ± 0.1	1.4 ± 0.1	2.2 ± 0.3	2.9 ± 0.4	1.1 ± 0.3	8.0 ± 0.5
332	12.3 ± 0.2	1.1 ± 0.1	0.4 ± 0.1	1.1 ± 0.1	1.5 ± 0.1	3.8 ± 0.3	7.1 ± 0.4	2.4 ± 0.3	10.6 ± 0.6
333	34.1 ± 0.5	4.7 ± 0.3	1.6 ± 0.3	3.9 ± 0.3	5.3 ± 0.3	11 ± 1	16 ± 1	6 ± 1	31 ± 2
334	24.4 ± 0.4	2.6 ± 0.3	0.9 ± 0.3	1.9 ± 0.3	2.6 ± 0.3	7 ± 1	16 ± 1	6 ± 1	21 ± 1
335	17.5 ± 0.3	2.8 ± 0.2	0.9 ± 0.2	2.6 ± 0.2	3.9 ± 0.2	5.5 ± 0.8	9 ± 1	3.3 ± 0.7	19 ± 1
336	31.3 ± 0.5	3.8 ± 0.3	1.5 ± 0.3	3.1 ± 0.3	4.3 ± 0.3	10 ± 1	22 ± 1	8 ± 1	29 ± 2
337	21.1 ± 0.3	2.0 ± 0.2	0.8 ± 0.2	1.4 ± 0.2	1.9 ± 0.2	6.9 ± 0.8	17 ± 1	6.0 ± 0.8	15 ± 1

Uncorrected flux values of the emission regions in the catalogue from this study. The measured fluxes of the nine emission lines for the detected emission regions are presented. These fluxes are not corrected for the local background diffuse emission (described in Section 2.6.3), the global stellar absorption (described in Section 2.6.7), nor the extinction (described in Section 2.6.8). These fluxes are obtained directly from the fit of the integrated region's spectrum and the uncertainties correspond to the fitting uncertainties from ORCS.

All flux values are scaled by 1×10^{-15} .

ID	H α [erg s $^{-1}$ cm $^{-2}$]	[N II] λ 6583 [erg s $^{-1}$ cm $^{-2}$]	[N II] λ 6548 [erg s $^{-1}$ cm $^{-2}$]	[S II] λ 6731 [erg s $^{-1}$ cm $^{-2}$]	[S II] λ 6716 [erg s $^{-1}$ cm $^{-2}$]	H β [erg s $^{-1}$ cm $^{-2}$]	[O III] λ 5007 [erg s $^{-1}$ cm $^{-2}$]	[O III] λ 4959 [erg s $^{-1}$ cm $^{-2}$]	[O II] λ 3727 [erg s $^{-1}$ cm $^{-2}$]
338	13.2 ± 0.3	1.7 ± 0.2	0.7 ± 0.2	1.5 ± 0.2	2.0 ± 0.2	4.2 ± 0.6	9.2 ± 0.7	3.3 ± 0.6	13.4 ± 0.8
339	79 ± 1	7.1 ± 0.7	2.4 ± 0.6	4.7 ± 0.7	6.3 ± 0.7	26 ± 2	61 ± 3	21 ± 2	55 ± 3
340	8.6 ± 0.2	1.1 ± 0.1	0.4 ± 0.1	1.5 ± 0.1	2.1 ± 0.1	2.7 ± 0.2	3.4 ± 0.3	1.2 ± 0.2	9.8 ± 0.6
341	7.6 ± 0.2	0.9 ± 0.1	0.3 ± 0.1	0.6 ± 0.1	0.8 ± 0.1	2.6 ± 0.5	6.1 ± 0.6	2.2 ± 0.5	5.9 ± 0.7
342	2.8 ± 0.2	0.5 ± 0.1	0.2 ± 0.1	0.4 ± 0.1	0.7 ± 0.1	0.8 ± 0.4	1.5 ± 0.5	0.5 ± 0.4	4.0 ± 0.5
343	28.1 ± 0.6	3.7 ± 0.4	1.5 ± 0.4	3.5 ± 0.4	4.9 ± 0.4	10 ± 1	21 ± 2	7 ± 1	30 ± 2
344	78.6 ± 0.9	4.5 ± 0.6	1.7 ± 0.6	4.1 ± 0.6	6.0 ± 0.6	24 ± 2	76 ± 3	26 ± 2	53 ± 2
345	7.9 ± 0.2	0.6 ± 0.1	0.1 ± 0.1	0.7 ± 0.1	1.1 ± 0.1	2.7 ± 0.4	7.4 ± 0.5	2.6 ± 0.4	7.9 ± 0.6
346	2.9 ± 0.1	0.46 ± 0.07	0.16 ± 0.07	0.34 ± 0.08	0.49 ± 0.08	1.1 ± 0.2	1.1 ± 0.2	0.4 ± 0.1	3.5 ± 0.3
347	10.2 ± 0.2	1.6 ± 0.2	0.5 ± 0.2	1.5 ± 0.2	2.4 ± 0.2	3.1 ± 0.5	3.3 ± 0.5	1.1 ± 0.4	12.3 ± 0.8
348	7.2 ± 0.2	1.2 ± 0.1	0.3 ± 0.1	1.2 ± 0.1	1.7 ± 0.1	2.4 ± 0.3	2.5 ± 0.3	1.0 ± 0.3	9.5 ± 0.6
349	1.46 ± 0.08	0.17 ± 0.06	0.06 ± 0.06	0.22 ± 0.06	0.38 ± 0.06	0.54 ± 0.08	0.7 ± 0.1	0.25 ± 0.07	2.0 ± 0.2
350	3.6 ± 0.1	0.50 ± 0.08	0.17 ± 0.08	0.54 ± 0.08	0.74 ± 0.08	1.3 ± 0.1	1.2 ± 0.1	0.4 ± 0.1	4.5 ± 0.4
351	3.06 ± 0.09	0.31 ± 0.06	0.05 ± 0.06	0.32 ± 0.06	0.53 ± 0.06	0.97 ± 0.09	2.2 ± 0.1	0.81 ± 0.09	3.3 ± 0.3
352	18.6 ± 0.3	1.4 ± 0.2	0.5 ± 0.2	1.0 ± 0.2	1.5 ± 0.2	6.4 ± 0.5	15.7 ± 0.7	5.5 ± 0.5	13.9 ± 0.8
353	9.4 ± 0.2	1.5 ± 0.2	0.4 ± 0.2	1.7 ± 0.2	2.5 ± 0.2	3.1 ± 0.4	5.0 ± 0.5	1.7 ± 0.4	11.4 ± 0.6
354	1.38 ± 0.08	0.21 ± 0.05	0.07 ± 0.05	0.17 ± 0.05	0.25 ± 0.05	0.50 ± 0.08	0.56 ± 0.09	0.17 ± 0.07	2.0 ± 0.2
355	27.9 ± 0.3	2.2 ± 0.2	0.8 ± 0.2	1.4 ± 0.2	2.1 ± 0.2	9.4 ± 0.8	24 ± 1	8.5 ± 0.8	19.4 ± 0.9
356	2.08 ± 0.09	0.28 ± 0.06	0.09 ± 0.06	0.34 ± 0.06	0.51 ± 0.06	0.68 ± 0.09	1.0 ± 0.1	0.31 ± 0.08	2.8 ± 0.3
357	3.37 ± 0.09	0.34 ± 0.06	0.11 ± 0.06	0.34 ± 0.07	0.43 ± 0.07	1.1 ± 0.1	2.7 ± 0.2	0.9 ± 0.1	2.9 ± 0.4
358	21.5 ± 0.5	3.7 ± 0.4	1.1 ± 0.4	4.0 ± 0.4	5.9 ± 0.4	7 ± 1	9 ± 1	3 ± 1	28 ± 2
359	11.8 ± 0.2	1.0 ± 0.1	0.4 ± 0.1	0.9 ± 0.1	1.2 ± 0.1	3.7 ± 0.2	6.7 ± 0.3	2.3 ± 0.2	10.7 ± 0.5
360	12.8 ± 0.4	2.0 ± 0.2	0.7 ± 0.2	2.0 ± 0.3	2.8 ± 0.3	4 ± 1	1.8 ± 0.9	0.6 ± 0.8	15 ± 1
361	11.1 ± 0.2	1.5 ± 0.1	0.5 ± 0.1	1.6 ± 0.2	2.4 ± 0.2	3.7 ± 0.4	8.1 ± 0.5	2.8 ± 0.4	12.6 ± 0.6

Uncorrected flux values of the emission regions in the catalogue from this study. The measured fluxes of the nine emission lines for the detected emission regions are presented. These fluxes are not corrected for the local background diffuse emission (described in Section 2.6.3), the global stellar absorption (described in Section 2.6.7), nor the extinction (described in Section 2.6.8). These fluxes are obtained directly from the fit of the integrated region's spectrum and the uncertainties correspond to the fitting uncertainties from ORCS. All flux values are scaled by 1×10^{-15} .

ID	$H\alpha$ [erg s ⁻¹ cm ⁻²]	[N II] $\lambda 6583$ [erg s ⁻¹ cm ⁻²]	[N II] $\lambda 6548$ [erg s ⁻¹ cm ⁻²]	[S II] $\lambda 6731$ [erg s ⁻¹ cm ⁻²]	[S II] $\lambda 6716$ [erg s ⁻¹ cm ⁻²]	$H\beta$ [erg s ⁻¹ cm ⁻²]	[O III] $\lambda 5007$ [erg s ⁻¹ cm ⁻²]	[O III] $\lambda 4959$ [erg s ⁻¹ cm ⁻²]	[O II] $\lambda 3727$ [erg s ⁻¹ cm ⁻²]
362	5.4 ± 0.1	0.72 ± 0.09	0.17 ± 0.09	0.83 ± 0.09	1.18 ± 0.09	1.8 ± 0.2	3.8 ± 0.3	1.3 ± 0.2	5.8 ± 0.4
363	1.14 ± 0.06	0.11 ± 0.04	0.09 ± 0.04	0.08 ± 0.05	0.12 ± 0.05	0.40 ± 0.06	0.58 ± 0.07	0.21 ± 0.06	1.0 ± 0.2
364	6.5 ± 0.1	0.64 ± 0.07	0.21 ± 0.07	0.61 ± 0.07	0.79 ± 0.07	2.0 ± 0.1	2.5 ± 0.1	0.9 ± 0.1	5.7 ± 0.3
365	8.7 ± 0.2	1.2 ± 0.2	0.4 ± 0.2	1.5 ± 0.2	2.2 ± 0.2	2.7 ± 0.4	3.7 ± 0.4	1.2 ± 0.3	9.4 ± 0.8
366	4.8 ± 0.1	0.43 ± 0.08	0.17 ± 0.08	0.43 ± 0.09	0.76 ± 0.09	1.4 ± 0.2	3.5 ± 0.2	1.2 ± 0.2	5.1 ± 0.4
367	3.2 ± 0.1	0.40 ± 0.08	0.21 ± 0.08	0.52 ± 0.09	0.71 ± 0.09	1.1 ± 0.1	1.7 ± 0.1	0.6 ± 0.1	4.3 ± 0.3
368	11.0 ± 0.2	0.9 ± 0.1	0.4 ± 0.1	1.0 ± 0.1	1.5 ± 0.1	3.7 ± 0.4	10.4 ± 0.5	3.7 ± 0.4	9.8 ± 0.6
369	15.4 ± 0.3	1.7 ± 0.2	0.5 ± 0.2	1.7 ± 0.2	2.5 ± 0.2	4.8 ± 0.4	8.5 ± 0.5	2.8 ± 0.4	16.2 ± 0.9
370	8.4 ± 0.3	1.5 ± 0.2	0.5 ± 0.2	1.5 ± 0.2	2.3 ± 0.2	2.4 ± 0.7	1.7 ± 0.7	0.6 ± 0.6	11.2 ± 0.9
371	8.8 ± 0.3	1.5 ± 0.2	0.6 ± 0.2	1.8 ± 0.2	2.6 ± 0.2	3.0 ± 0.5	3.9 ± 0.5	1.4 ± 0.4	13.3 ± 0.9
372	39.1 ± 0.6	3.9 ± 0.4	1.4 ± 0.4	4.0 ± 0.4	5.9 ± 0.4	13 ± 2	43 ± 2	15 ± 2	36 ± 2
373	4.8 ± 0.2	0.9 ± 0.1	0.4 ± 0.1	1.2 ± 0.1	1.6 ± 0.1	1.7 ± 0.2	1.8 ± 0.2	0.6 ± 0.2	7.2 ± 0.5
374	5.8 ± 0.2	1.1 ± 0.1	0.3 ± 0.1	1.3 ± 0.1	1.8 ± 0.1	1.9 ± 0.2	2.0 ± 0.2	0.7 ± 0.2	8.1 ± 0.5
375	3.8 ± 0.2	0.5 ± 0.1	0.2 ± 0.1	0.7 ± 0.1	0.7 ± 0.1	1.5 ± 0.2	1.3 ± 0.2	0.4 ± 0.2	5.2 ± 0.5
376	2.4 ± 0.1	0.38 ± 0.08	0.16 ± 0.08	0.33 ± 0.08	0.45 ± 0.08	0.8 ± 0.1	0.8 ± 0.1	0.3 ± 0.1	3.0 ± 0.3
377	2.5 ± 0.1	0.26 ± 0.07	0.12 ± 0.07	0.32 ± 0.07	0.37 ± 0.07	0.7 ± 0.1	1.6 ± 0.2	0.5 ± 0.1	2.0 ± 0.3
378	35.0 ± 0.6	4.9 ± 0.4	1.5 ± 0.4	5.1 ± 0.4	7.0 ± 0.4	12 ± 1	21 ± 2	8 ± 1	41 ± 2
379	5.6 ± 0.2	0.7 ± 0.1	0.3 ± 0.1	1.1 ± 0.1	1.6 ± 0.1	1.7 ± 0.3	2.1 ± 0.4	0.7 ± 0.3	7.4 ± 0.6
380	3.1 ± 0.1	0.31 ± 0.09	0.20 ± 0.09	0.44 ± 0.09	0.56 ± 0.09	1.0 ± 0.1	1.8 ± 0.2	0.6 ± 0.1	3.8 ± 0.5
381	15.9 ± 0.2	1.4 ± 0.2	0.5 ± 0.2	1.8 ± 0.2	2.6 ± 0.2	5.0 ± 0.5	15.8 ± 0.8	5.4 ± 0.6	12.0 ± 0.7
382	6.6 ± 0.2	0.8 ± 0.1	0.3 ± 0.1	0.9 ± 0.1	1.3 ± 0.1	1.8 ± 0.3	1.7 ± 0.3	0.6 ± 0.3	6.4 ± 0.5
383	5.2 ± 0.1	0.9 ± 0.1	0.3 ± 0.1	0.8 ± 0.1	1.3 ± 0.1	1.5 ± 0.2	2.1 ± 0.3	0.8 ± 0.2	5.7 ± 0.5
384	14.4 ± 0.3	2.0 ± 0.2	0.6 ± 0.2	1.9 ± 0.2	2.7 ± 0.2	4.4 ± 0.6	5.7 ± 0.7	1.9 ± 0.5	15.1 ± 0.9
385	18.8 ± 0.3	2.2 ± 0.2	0.8 ± 0.2	2.4 ± 0.2	3.5 ± 0.2	5.6 ± 0.5	9.7 ± 0.7	3.1 ± 0.5	18.4 ± 0.9

Uncorrected flux values of the emission regions in the catalogue from this study. The measured fluxes of the nine emission lines for the detected emission regions are presented. These fluxes are not corrected for the local background diffuse emission (described in Section 2.6.3), the global stellar absorption (described in Section 2.6.7), nor the extinction (described in Section 2.6.8). These fluxes are obtained directly from the fit of the integrated region's spectrum and the uncertainties correspond to the fitting uncertainties from ORCS.

All flux values are scaled by 1×10^{-15} .

ID	$H\alpha$ [erg s ⁻¹ cm ⁻²]	[N II] λ 6583 [erg s ⁻¹ cm ⁻²]	[N II] λ 6548 [erg s ⁻¹ cm ⁻²]	[S II] λ 6731 [erg s ⁻¹ cm ⁻²]	[S II] λ 6716 [erg s ⁻¹ cm ⁻²]	$H\beta$ [erg s ⁻¹ cm ⁻²]	[O III] λ 5007 [erg s ⁻¹ cm ⁻²]	[O III] λ 4959 [erg s ⁻¹ cm ⁻²]	[O II] λ 3727 [erg s ⁻¹ cm ⁻²]
386	6.3 ± 0.2	0.7 ± 0.1	0.3 ± 0.1	0.7 ± 0.1	1.0 ± 0.1	1.8 ± 0.2	3.9 ± 0.3	1.3 ± 0.2	5.9 ± 0.4
387	8.4 ± 0.2	1.2 ± 0.1	0.5 ± 0.1	1.3 ± 0.1	2.0 ± 0.1	2.4 ± 0.4	2.7 ± 0.4	0.8 ± 0.4	9.3 ± 0.8
388	11.5 ± 0.2	1.0 ± 0.1	0.3 ± 0.1	1.0 ± 0.1	1.5 ± 0.1	3.0 ± 0.2	6.2 ± 0.3	2.2 ± 0.2	9.2 ± 0.5
389	3.28 ± 0.09	0.50 ± 0.06	0.16 ± 0.06	0.56 ± 0.07	0.76 ± 0.07	0.98 ± 0.09	1.3 ± 0.1	0.45 ± 0.08	4.3 ± 0.3
390	18.2 ± 0.2	2.0 ± 0.2	0.8 ± 0.2	2.0 ± 0.2	2.8 ± 0.2	5.5 ± 0.4	6.9 ± 0.4	2.5 ± 0.3	16.8 ± 0.8
391	6.2 ± 0.1	1.0 ± 0.1	0.3 ± 0.1	1.0 ± 0.1	1.5 ± 0.1	2.1 ± 0.2	2.3 ± 0.2	0.8 ± 0.1	7.5 ± 0.4
392	6.3 ± 0.1	0.79 ± 0.09	0.29 ± 0.09	0.83 ± 0.09	1.2 ± 0.1	1.6 ± 0.2	2.3 ± 0.2	0.8 ± 0.2	5.2 ± 0.4
393	4.1 ± 0.1	0.53 ± 0.08	0.21 ± 0.07	0.59 ± 0.08	0.89 ± 0.08	1.3 ± 0.1	1.7 ± 0.1	0.64 ± 0.09	5.1 ± 0.3
394	8.2 ± 0.1	0.87 ± 0.09	0.28 ± 0.09	0.96 ± 0.09	1.39 ± 0.09	2.5 ± 0.2	4.4 ± 0.2	1.6 ± 0.2	8.1 ± 0.4
395	5.5 ± 0.1	0.76 ± 0.09	0.30 ± 0.09	0.83 ± 0.09	1.19 ± 0.09	1.6 ± 0.2	3.2 ± 0.3	1.1 ± 0.2	6.1 ± 0.4
396	125 ± 1	9 ± 1	4 ± 1	8 ± 1	11 ± 1	37 ± 3	96 ± 4	33 ± 3	84 ± 4
397	35.3 ± 0.5	3.2 ± 0.3	1.1 ± 0.3	2.6 ± 0.3	3.9 ± 0.3	12 ± 1	23 ± 1	8 ± 1	30 ± 1
398	27.5 ± 0.3	2.5 ± 0.2	0.9 ± 0.2	2.4 ± 0.2	3.3 ± 0.2	7.3 ± 0.5	15.6 ± 0.7	5.3 ± 0.5	19.3 ± 0.9
399	55.6 ± 0.7	2.6 ± 0.5	1.2 ± 0.5	2.0 ± 0.5	2.3 ± 0.5	15 ± 3	89 ± 4	31 ± 3	15.0 ± 0.9
401	40.9 ± 0.8	6.4 ± 0.5	2.2 ± 0.5	7.6 ± 0.5	11.0 ± 0.6	13 ± 2	20 ± 2	7 ± 2	51 ± 3
402	9.2 ± 0.2	1.0 ± 0.1	0.4 ± 0.1	1.1 ± 0.1	1.5 ± 0.1	2.8 ± 0.2	3.8 ± 0.2	1.3 ± 0.2	8.0 ± 0.5
403	67.9 ± 0.9	7.7 ± 0.6	2.5 ± 0.6	6.0 ± 0.6	8.5 ± 0.6	22 ± 2	32 ± 2	11 ± 1	68 ± 3
404	1.4 ± 0.1	0.2 ± 0.1	0.06 ± 0.09	0.3 ± 0.1	0.4 ± 0.1	0.6 ± 0.1	0.4 ± 0.1	0.2 ± 0.1	1.9 ± 0.3
405	7.5 ± 0.2	1.0 ± 0.1	0.4 ± 0.1	1.1 ± 0.1	1.6 ± 0.1	2.0 ± 0.3	3.0 ± 0.3	1.0 ± 0.3	8.3 ± 0.5
406	5.0 ± 0.2	0.7 ± 0.1	0.3 ± 0.1	0.8 ± 0.1	1.1 ± 0.1	1.8 ± 0.2	2.2 ± 0.2	0.8 ± 0.2	7.2 ± 0.5
407	12.9 ± 0.2	1.9 ± 0.2	0.7 ± 0.2	1.8 ± 0.2	2.6 ± 0.2	4.7 ± 0.3	4.2 ± 0.3	1.5 ± 0.3	15.6 ± 0.8
408	34.1 ± 0.4	3.3 ± 0.3	1.1 ± 0.3	3.0 ± 0.3	4.2 ± 0.3	10.1 ± 0.7	18.4 ± 0.9	6.5 ± 0.7	32 ± 1
409	19.1 ± 0.3	2.5 ± 0.2	0.9 ± 0.2	2.3 ± 0.2	3.3 ± 0.2	5.9 ± 0.5	7.0 ± 0.5	2.3 ± 0.4	20 ± 1
410	27.7 ± 0.4	2.4 ± 0.3	0.8 ± 0.2	2.4 ± 0.3	3.3 ± 0.3	7.7 ± 0.7	20 ± 1	6.8 ± 0.7	22 ± 1

Uncorrected flux values of the emission regions in the catalogue from this study. The measured fluxes of the nine emission lines for the detected emission regions are presented. These fluxes are not corrected for the local background diffuse emission (described in Section 2.6.3), the global stellar absorption (described in Section 2.6.7), nor the extinction (described in Section 2.6.8). These fluxes are obtained directly from the fit of the integrated region's spectrum and the uncertainties correspond to the fitting uncertainties from ORCS.

All flux values are scaled by 1×10^{-15} .

ID	H α [erg s $^{-1}$ cm $^{-2}$]	[N II] λ 6583 [erg s $^{-1}$ cm $^{-2}$]	[N II] λ 6548 [erg s $^{-1}$ cm $^{-2}$]	[S II] λ 6731 [erg s $^{-1}$ cm $^{-2}$]	[S II] λ 6716 [erg s $^{-1}$ cm $^{-2}$]	H β [erg s $^{-1}$ cm $^{-2}$]	[O III] λ 5007 [erg s $^{-1}$ cm $^{-2}$]	[O III] λ 4959 [erg s $^{-1}$ cm $^{-2}$]	[O II] λ 3727 [erg s $^{-1}$ cm $^{-2}$]
411	9.1 ± 0.2	1.2 ± 0.1	0.4 ± 0.1	1.2 ± 0.1	1.7 ± 0.1	2.7 ± 0.3	3.1 ± 0.3	0.9 ± 0.2	10.4 ± 0.6
412	20.3 ± 0.3	2.2 ± 0.2	0.8 ± 0.2	2.4 ± 0.2	3.4 ± 0.2	5.7 ± 0.4	12.2 ± 0.5	4.2 ± 0.4	17.7 ± 0.8
413	17.7 ± 0.3	1.7 ± 0.2	0.7 ± 0.2	1.9 ± 0.2	2.6 ± 0.2	4.9 ± 0.4	10.5 ± 0.6	3.5 ± 0.4	13.9 ± 0.7
414	18.4 ± 0.3	2.4 ± 0.2	0.8 ± 0.2	2.7 ± 0.2	4.0 ± 0.2	6.0 ± 0.6	14.5 ± 0.8	5.1 ± 0.6	21 ± 1
415	11.6 ± 0.2	1.3 ± 0.1	0.5 ± 0.1	1.2 ± 0.1	1.8 ± 0.1	3.8 ± 0.3	5.4 ± 0.3	1.9 ± 0.2	12.3 ± 0.5
416	36 ± 1	5.4 ± 0.6	1.7 ± 0.6	6.0 ± 0.7	8.7 ± 0.7	11 ± 3	16 ± 3	5 ± 2	46 ± 4
417	1.3 ± 0.1	0.19 ± 0.08	0.12 ± 0.08	0.26 ± 0.09	0.39 ± 0.09	0.5 ± 0.1	0.4 ± 0.1	0.07 ± 0.09	2.0 ± 0.3
418	6.0 ± 0.1	0.83 ± 0.09	0.29 ± 0.09	0.9 ± 0.1	1.2 ± 0.1	2.0 ± 0.2	2.3 ± 0.2	0.7 ± 0.2	6.5 ± 0.4
419	9.6 ± 0.2	1.4 ± 0.2	0.5 ± 0.2	1.6 ± 0.2	2.2 ± 0.2	3.4 ± 0.4	5.0 ± 0.5	1.7 ± 0.4	12.7 ± 0.8
420	58.2 ± 0.9	5.7 ± 0.6	2.0 ± 0.6	5.3 ± 0.7	7.3 ± 0.7	19 ± 2	30 ± 2	10 ± 2	52 ± 3
421	28.3 ± 0.5	3.8 ± 0.3	1.6 ± 0.3	4.9 ± 0.3	7.2 ± 0.3	9.1 ± 0.9	13 ± 1	4.6 ± 0.8	37 ± 2
422	55 ± 1	7.7 ± 0.7	2.7 ± 0.7	9.7 ± 0.7	13.8 ± 0.7	18 ± 2	29 ± 2	10 ± 2	69 ± 3
423	41.6 ± 0.7	4.3 ± 0.4	1.7 ± 0.4	5.1 ± 0.5	6.9 ± 0.5	13.1 ± 0.9	26 ± 1	9.0 ± 0.9	38 ± 2
424	2.9 ± 0.3	0.4 ± 0.2	0.2 ± 0.2	0.5 ± 0.2	0.8 ± 0.2	0.9 ± 0.2	1.1 ± 0.2	0.2 ± 0.2	4.5 ± 0.6
425	21.2 ± 0.3	2.8 ± 0.2	0.9 ± 0.2	3.1 ± 0.2	4.2 ± 0.2	6.5 ± 0.4	10.5 ± 0.5	3.4 ± 0.4	23 ± 1
426	3.8 ± 0.1	0.42 ± 0.08	0.19 ± 0.08	0.37 ± 0.08	0.59 ± 0.08	1.2 ± 0.2	1.8 ± 0.2	0.6 ± 0.2	3.5 ± 0.4
427	6.5 ± 0.1	0.69 ± 0.09	0.21 ± 0.09	0.75 ± 0.09	1.10 ± 0.09	1.7 ± 0.2	2.4 ± 0.2	0.9 ± 0.2	5.6 ± 0.4
428	12.1 ± 0.2	1.4 ± 0.1	0.5 ± 0.1	1.2 ± 0.1	1.8 ± 0.1	3.4 ± 0.3	4.0 ± 0.4	1.4 ± 0.3	11.1 ± 0.6
429	13.6 ± 0.2	1.6 ± 0.1	0.5 ± 0.1	1.9 ± 0.1	2.7 ± 0.1	3.9 ± 0.3	7.9 ± 0.4	2.8 ± 0.3	13.1 ± 0.7
430	17.7 ± 0.3	2.0 ± 0.2	0.6 ± 0.2	2.5 ± 0.2	3.6 ± 0.2	6.0 ± 0.4	11.3 ± 0.5	3.7 ± 0.4	22 ± 1
431	6.8 ± 0.2	0.8 ± 0.1	0.3 ± 0.1	0.8 ± 0.1	1.1 ± 0.1	2.1 ± 0.3	2.7 ± 0.3	0.9 ± 0.3	8.5 ± 0.5
432	3.5 ± 0.1	0.43 ± 0.08	0.16 ± 0.08	0.54 ± 0.08	0.84 ± 0.08	1.0 ± 0.2	1.5 ± 0.2	0.5 ± 0.2	3.7 ± 0.3
433	2.6 ± 0.1	0.33 ± 0.07	0.11 ± 0.07	0.27 ± 0.07	0.41 ± 0.07	0.9 ± 0.1	1.0 ± 0.1	0.32 ± 0.08	3.0 ± 0.3
434	30.1 ± 0.4	2.5 ± 0.2	0.8 ± 0.2	2.0 ± 0.3	2.9 ± 0.3	8.2 ± 0.6	18.6 ± 0.8	6.5 ± 0.6	18.6 ± 0.9

Uncorrected flux values of the emission regions in the catalogue from this study. The measured fluxes of the nine emission lines for the detected emission regions are presented. These fluxes are not corrected for the local background diffuse emission (described in Section 2.6.3), the global stellar absorption (described in Section 2.6.7), nor the extinction (described in Section 2.6.8). These fluxes are obtained directly from the fit of the integrated region's spectrum and the uncertainties correspond to the fitting uncertainties from ORCS.

All flux values are scaled by 1×10^{-15} .

ID	H α [erg s $^{-1}$ cm $^{-2}$]	[N II] λ 6583 [erg s $^{-1}$ cm $^{-2}$]	[N II] λ 6548 [erg s $^{-1}$ cm $^{-2}$]	[S II] λ 6731 [erg s $^{-1}$ cm $^{-2}$]	[S II] λ 6716 [erg s $^{-1}$ cm $^{-2}$]	H β [erg s $^{-1}$ cm $^{-2}$]	[O III] λ 5007 [erg s $^{-1}$ cm $^{-2}$]	[O III] λ 4959 [erg s $^{-1}$ cm $^{-2}$]	[O II] λ 3727 [erg s $^{-1}$ cm $^{-2}$]
435	12.2 ± 0.2	1.4 ± 0.1	0.4 ± 0.1	1.1 ± 0.1	1.6 ± 0.1	3.4 ± 0.3	4.3 ± 0.3	1.4 ± 0.2	10.0 ± 0.5
436	1.02 ± 0.07	0.13 ± 0.05	0.02 ± 0.04	0.09 ± 0.05	0.30 ± 0.06	0.89 ± 0.08	0.30 ± 0.06	0.7 ± 0.1	
437	8.3 ± 0.3	0.9 ± 0.2	0.3 ± 0.2	0.8 ± 0.2	1.3 ± 0.2	2.5 ± 0.6	3.8 ± 0.7	1.4 ± 0.5	9.0 ± 0.7
438	19.3 ± 0.2	1.6 ± 0.2	0.5 ± 0.2	1.4 ± 0.2	1.9 ± 0.2	5.3 ± 0.4	13.0 ± 0.5	4.5 ± 0.4	12.5 ± 0.6
439	58.9 ± 0.7	4.6 ± 0.5	1.6 ± 0.5	3.5 ± 0.5	4.7 ± 0.5	19 ± 2	48 ± 2	16 ± 2	47 ± 2
440	1.2 ± 0.1	0.18 ± 0.07	0.07 ± 0.07	0.19 ± 0.07	0.21 ± 0.07	0.4 ± 0.1	0.5 ± 0.1	0.12 ± 0.09	2.1 ± 0.3
441	17.3 ± 0.4	1.9 ± 0.3	0.8 ± 0.3	2.1 ± 0.3	3.2 ± 0.3	4.4 ± 0.8	6.5 ± 0.9	2.1 ± 0.8	18 ± 1
442	12.3 ± 0.4	1.7 ± 0.3	0.5 ± 0.2	1.7 ± 0.3	2.3 ± 0.3	3.6 ± 0.6	7.3 ± 0.8	2.6 ± 0.6	12.9 ± 0.8
443	54.3 ± 0.7	4.8 ± 0.5	1.6 ± 0.5	3.6 ± 0.5	4.5 ± 0.5	18 ± 1	35 ± 2	12 ± 1	46 ± 2
444	14.2 ± 0.2	1.6 ± 0.2	0.4 ± 0.2	2.0 ± 0.2	3.0 ± 0.2	4.6 ± 0.5	9.7 ± 0.6	3.4 ± 0.5	14.6 ± 0.7
445	149 ± 2	11 ± 1	3 ± 1	8 ± 1	10 ± 1	45 ± 3	112 ± 5	39 ± 3	85 ± 4
446	25.9 ± 0.3	1.7 ± 0.2	0.6 ± 0.2	1.5 ± 0.2	1.8 ± 0.2	8.2 ± 0.8	27 ± 1	9.1 ± 0.8	14.9 ± 0.7
447	20.9 ± 0.4	2.6 ± 0.3	0.9 ± 0.2	2.6 ± 0.3	3.9 ± 0.3	6.9 ± 0.7	16.0 ± 0.9	5.6 ± 0.7	22 ± 1
448	1.5 ± 0.1	0.16 ± 0.07	0.05 ± 0.07	0.16 ± 0.07	0.21 ± 0.07	0.49 ± 0.09	0.7 ± 0.1	0.23 ± 0.08	2.0 ± 0.3
449	14.3 ± 0.3	1.5 ± 0.2	0.6 ± 0.2	1.7 ± 0.2	2.6 ± 0.2	4.2 ± 0.6	12.1 ± 0.8	4.0 ± 0.6	12.4 ± 0.8
450	28.9 ± 0.3	2.1 ± 0.2	0.8 ± 0.2	1.6 ± 0.2	2.4 ± 0.2	8.4 ± 0.6	21.7 ± 0.9	7.4 ± 0.7	17.8 ± 0.8
451	33.9 ± 0.5	4.3 ± 0.3	1.1 ± 0.3	4.0 ± 0.3	5.8 ± 0.3	11 ± 1	22 ± 1	7 ± 1	33 ± 1
452	33.1 ± 0.4	2.1 ± 0.3	0.8 ± 0.3	1.4 ± 0.3	1.9 ± 0.3	10.6 ± 0.9	27 ± 1	9.4 ± 0.9	17.1 ± 0.9
453	3.08 ± 0.09	0.43 ± 0.06	0.13 ± 0.06	0.38 ± 0.07	0.57 ± 0.07	1.0 ± 0.1	2.1 ± 0.2	0.7 ± 0.1	3.8 ± 0.3
454	81 ± 1	9.0 ± 0.7	2.5 ± 0.7	7.0 ± 0.7	9.7 ± 0.7	26 ± 2	36 ± 2	12 ± 1	83 ± 4
455	2.17 ± 0.08	0.20 ± 0.06	0.07 ± 0.06	0.23 ± 0.06	0.37 ± 0.06	0.6 ± 0.1	2.0 ± 0.2	0.6 ± 0.1	2.5 ± 0.3
456	3.2 ± 0.1	0.47 ± 0.07	0.08 ± 0.07	0.32 ± 0.08	0.46 ± 0.08	1.1 ± 0.1	1.2 ± 0.1	0.41 ± 0.08	4.0 ± 0.3
457	13.6 ± 0.2	2.1 ± 0.2	0.6 ± 0.1	1.7 ± 0.2	2.5 ± 0.2	4.5 ± 0.2	6.4 ± 0.3	2.2 ± 0.2	17.2 ± 0.8
458	10.6 ± 0.2	1.4 ± 0.1	0.5 ± 0.1	1.3 ± 0.1	1.7 ± 0.1	3.1 ± 0.3	4.8 ± 0.3	1.6 ± 0.2	10.8 ± 0.5

Uncorrected flux values of the emission regions in the catalogue from this study. The measured fluxes of the nine emission lines for the detected emission regions are presented. These fluxes are not corrected for the local background diffuse emission (described in Section 2.6.3), the global stellar absorption (described in Section 2.6.7), nor the extinction (described in Section 2.6.8). These fluxes are obtained directly from the fit of the integrated region's spectrum and the uncertainties correspond to the fitting uncertainties from ORCS.

All flux values are scaled by 1×10^{-15} .

ID	$H\alpha$ [erg s ⁻¹ cm ⁻²]	[N II] $\lambda 6583$ [erg s ⁻¹ cm ⁻²]	[N II] $\lambda 6548$ [erg s ⁻¹ cm ⁻²]	[S II] $\lambda 6731$ [erg s ⁻¹ cm ⁻²]	[S II] $\lambda 6716$ [erg s ⁻¹ cm ⁻²]	$H\beta$ [erg s ⁻¹ cm ⁻²]	[O III] $\lambda 5007$ [erg s ⁻¹ cm ⁻²]	[O III] $\lambda 4959$ [erg s ⁻¹ cm ⁻²]	[O II] $\lambda 3727$ [erg s ⁻¹ cm ⁻²]
459	2.7 ± 0.1	0.43 ± 0.09	0.05 ± 0.09	0.2 ± 0.1	0.4 ± 0.1	1.02 ± 0.07	1.12 ± 0.08	0.36 ± 0.08	3.7 ± 0.3
460	11.7 ± 0.2	1.3 ± 0.1	0.4 ± 0.1	1.1 ± 0.1	1.6 ± 0.1	4.0 ± 0.3	6.0 ± 0.3	2.0 ± 0.3	11.1 ± 0.7
461	117 ± 1	6.9 ± 0.9	2.3 ± 0.9	6 ± 1	8 ± 1	39 ± 5	165 ± 7	57 ± 5	54 ± 3
462	5.6 ± 0.1	0.7 ± 0.1	0.3 ± 0.1	0.6 ± 0.1	0.7 ± 0.1	2.0 ± 0.1	2.8 ± 0.2	1.0 ± 0.1	6.5 ± 0.4
463	8.0 ± 0.2	1.0 ± 0.1	0.3 ± 0.1	1.3 ± 0.1	1.9 ± 0.1	2.6 ± 0.2	4.1 ± 0.3	1.3 ± 0.2	9.0 ± 0.5
464	13.8 ± 0.2	1.9 ± 0.2	0.6 ± 0.1	1.8 ± 0.2	2.7 ± 0.2	4.5 ± 0.3	7.7 ± 0.4	2.7 ± 0.3	13.4 ± 0.7
465	10.9 ± 0.2	1.4 ± 0.1	0.3 ± 0.1	1.5 ± 0.1	2.1 ± 0.1	3.5 ± 0.3	6.0 ± 0.4	2.1 ± 0.3	11.4 ± 0.6
466	21.3 ± 0.3	2.2 ± 0.2	0.7 ± 0.2	2.1 ± 0.2	2.9 ± 0.2	7.1 ± 0.4	11.7 ± 0.5	4.0 ± 0.4	18.4 ± 0.9
467	41.4 ± 0.5	3.5 ± 0.3	1.1 ± 0.3	2.8 ± 0.3	3.8 ± 0.3	12 ± 1	32 ± 2	12 ± 1	25 ± 1
468	34.9 ± 0.5	2.5 ± 0.3	0.9 ± 0.3	2.1 ± 0.3	2.8 ± 0.3	11.6 ± 0.9	32 ± 1	10.9 ± 0.9	28 ± 1
469	8.8 ± 0.1	0.7 ± 0.1	0.2 ± 0.1	0.6 ± 0.1	0.9 ± 0.1	2.9 ± 0.3	8.3 ± 0.4	2.9 ± 0.3	6.5 ± 0.3
470	22.1 ± 0.3	2.2 ± 0.2	0.9 ± 0.2	2.4 ± 0.2	3.5 ± 0.2	7.2 ± 0.6	17.8 ± 0.9	6.3 ± 0.6	20 ± 1
471	40.8 ± 0.7	4.1 ± 0.5	1.3 ± 0.5	4.5 ± 0.5	6.3 ± 0.5	14 ± 1	31 ± 2	11 ± 1	42 ± 2
472	31.6 ± 0.5	4.2 ± 0.3	1.3 ± 0.3	5.6 ± 0.3	8.0 ± 0.3	10.1 ± 0.9	12 ± 1	4.4 ± 0.8	38 ± 2
473	20.7 ± 0.3	2.1 ± 0.2	0.4 ± 0.2	1.9 ± 0.2	2.8 ± 0.2	7.1 ± 0.5	13.9 ± 0.6	4.9 ± 0.5	18.1 ± 0.9
474	12.3 ± 0.2	1.5 ± 0.2	0.6 ± 0.2	1.6 ± 0.2	2.4 ± 0.2	3.8 ± 0.3	4.8 ± 0.3	1.7 ± 0.3	13.5 ± 0.8
475	6.0 ± 0.1	0.76 ± 0.09	0.31 ± 0.09	0.83 ± 0.09	1.2 ± 0.1	2.0 ± 0.2	2.3 ± 0.2	0.8 ± 0.2	7.5 ± 0.5
476	20.8 ± 0.4	2.2 ± 0.2	0.7 ± 0.2	2.2 ± 0.2	3.1 ± 0.2	7.1 ± 0.6	20.1 ± 0.8	7.1 ± 0.6	17.5 ± 0.9
477	21.0 ± 0.3	2.1 ± 0.2	0.7 ± 0.2	1.7 ± 0.2	2.4 ± 0.2	6.8 ± 0.4	11.1 ± 0.5	4.0 ± 0.4	17.5 ± 0.9
478	71.1 ± 0.9	3.6 ± 0.6	1.3 ± 0.6	3.3 ± 0.6	4.3 ± 0.6	21 ± 2	76 ± 3	26 ± 2	28 ± 1
479	13.4 ± 0.2	1.2 ± 0.1	0.4 ± 0.1	1.0 ± 0.1	1.5 ± 0.1	4.5 ± 0.3	10.7 ± 0.4	3.8 ± 0.3	10.3 ± 0.6
480	18.2 ± 0.3	1.6 ± 0.2	0.6 ± 0.2	1.7 ± 0.2	2.3 ± 0.2	6.2 ± 0.5	18.3 ± 0.7	6.4 ± 0.5	13.9 ± 0.7
481	8.1 ± 0.2	1.0 ± 0.1	0.4 ± 0.1	1.0 ± 0.1	1.4 ± 0.1	2.7 ± 0.3	4.7 ± 0.4	1.7 ± 0.3	8.4 ± 0.7
482	48.1 ± 0.6	4.1 ± 0.4	1.2 ± 0.4	3.7 ± 0.4	5.3 ± 0.4	14 ± 1	36 ± 2	13 ± 1	31 ± 1

Uncorrected flux values of the emission regions in the catalogue from this study. The measured fluxes of the nine emission lines for the detected emission regions are presented. These fluxes are not corrected for the local background diffuse emission (described in Section 2.6.3), the global stellar absorption (described in Section 2.6.7), nor the extinction (described in Section 2.6.8). These fluxes are obtained directly from the fit of the integrated region's spectrum and the uncertainties correspond to the fitting uncertainties from ORCS.

All flux values are scaled by 1×10^{-15} .

ID	$H\alpha$ [erg s ⁻¹ cm ⁻²]	[N II] $\lambda 6583$ [erg s ⁻¹ cm ⁻²]	[N II] $\lambda 6548$ [erg s ⁻¹ cm ⁻²]	[S II] $\lambda 6731$ [erg s ⁻¹ cm ⁻²]	[S II] $\lambda 6716$ [erg s ⁻¹ cm ⁻²]	$H\beta$ [erg s ⁻¹ cm ⁻²]	[O III] $\lambda 5007$ [erg s ⁻¹ cm ⁻²]	[O III] $\lambda 4959$ [erg s ⁻¹ cm ⁻²]	[O II] $\lambda 3727$ [erg s ⁻¹ cm ⁻²]
483	20.4 ± 0.3	1.5 ± 0.2	0.5 ± 0.2	1.3 ± 0.2	1.7 ± 0.2	5.7 ± 0.5	17.1 ± 0.7	5.9 ± 0.5	10.0 ± 0.6
484	19.6 ± 0.3	2.2 ± 0.2	0.8 ± 0.2	2.3 ± 0.2	3.4 ± 0.2	5.9 ± 0.4	9.6 ± 0.5	3.3 ± 0.4	16.3 ± 0.9
485	33.2 ± 0.5	2.4 ± 0.4	0.9 ± 0.4	2.0 ± 0.4	3.0 ± 0.4	10 ± 1	23 ± 2	9 ± 1	22 ± 3
486	30.1 ± 0.4	3.9 ± 0.3	1.4 ± 0.3	4.8 ± 0.3	7.0 ± 0.3	9.4 ± 0.7	17.9 ± 0.9	6.3 ± 0.7	33 ± 1
487	15.8 ± 0.3	1.4 ± 0.2	0.4 ± 0.2	1.4 ± 0.2	1.8 ± 0.2	5.3 ± 0.4	14.5 ± 0.5	5.0 ± 0.4	11.4 ± 0.6
488	5.0 ± 0.1	0.6 ± 0.1	0.3 ± 0.1	0.6 ± 0.1	0.8 ± 0.1	1.7 ± 0.1	1.4 ± 0.1	0.4 ± 0.1	6.3 ± 0.3
489	13.1 ± 0.2	1.1 ± 0.1	0.3 ± 0.1	1.0 ± 0.1	1.5 ± 0.1	4.3 ± 0.3	12.6 ± 0.5	4.5 ± 0.3	9.1 ± 0.5
490	2.3 ± 0.1	0.19 ± 0.08	0.07 ± 0.07	0.22 ± 0.08	0.26 ± 0.08	0.8 ± 0.2	1.6 ± 0.2	0.5 ± 0.2	2.1 ± 0.4
491	5.7 ± 0.2	0.6 ± 0.1	0.2 ± 0.1	0.5 ± 0.1	0.8 ± 0.1	2.1 ± 0.2	3.7 ± 0.2	1.3 ± 0.1	4.8 ± 0.4
492	4.1 ± 0.1	0.49 ± 0.08	0.18 ± 0.08	0.64 ± 0.08	0.86 ± 0.08	1.3 ± 0.2	1.7 ± 0.2	0.6 ± 0.1	4.8 ± 0.4
493	22.1 ± 0.4	2.0 ± 0.2	0.8 ± 0.2	1.7 ± 0.3	2.3 ± 0.3	7.7 ± 0.6	16.3 ± 0.7	5.9 ± 0.6	16.8 ± 0.9
494	138 ± 2	11 ± 1	4 ± 1	12 ± 2	16 ± 2	43 ± 3	101 ± 4	36 ± 3	107 ± 5
495	16.9 ± 0.3	1.9 ± 0.2	0.7 ± 0.2	2.2 ± 0.2	3.2 ± 0.2	5.8 ± 0.5	15.0 ± 0.7	5.2 ± 0.6	20 ± 1
496	19.1 ± 0.2	1.7 ± 0.2	0.7 ± 0.2	2.1 ± 0.2	2.9 ± 0.2	5.5 ± 0.4	14.3 ± 0.6	5.0 ± 0.4	14.7 ± 0.7
497	19.1 ± 0.3	1.8 ± 0.2	0.8 ± 0.2	1.4 ± 0.2	2.0 ± 0.2	6.0 ± 0.4	10.1 ± 0.5	3.6 ± 0.4	18.1 ± 0.8
498	42 ± 1	4.3 ± 0.7	1.6 ± 0.7	4.4 ± 0.7	5.8 ± 0.7	14 ± 2	26 ± 2	9 ± 2	45 ± 2
499	76.6 ± 0.9	5.4 ± 0.6	2.0 ± 0.6	5.5 ± 0.6	8.0 ± 0.6	23 ± 2	58 ± 2	20 ± 2	50 ± 2
500	3.0 ± 0.1	0.28 ± 0.09	0.24 ± 0.09	0.5 ± 0.1	0.7 ± 0.1	1.0 ± 0.2	0.8 ± 0.2	0.3 ± 0.1	3.6 ± 0.4
501	28.1 ± 0.4	2.9 ± 0.3	1.0 ± 0.3	3.2 ± 0.3	4.5 ± 0.3	8.6 ± 0.5	15.6 ± 0.7	5.4 ± 0.5	22.4 ± 0.8
502	11.8 ± 0.3	1.5 ± 0.2	0.4 ± 0.2	1.6 ± 0.2	2.5 ± 0.2	4.0 ± 0.2	5.9 ± 0.3	2.2 ± 0.2	12.2 ± 0.7
503	47.1 ± 0.6	3.2 ± 0.4	1.2 ± 0.4	3.2 ± 0.5	4.2 ± 0.5	14 ± 1	35 ± 1	12 ± 1	26 ± 1
504	6.8 ± 0.1	0.75 ± 0.09	0.25 ± 0.09	0.76 ± 0.09	0.94 ± 0.09	2.0 ± 0.2	2.7 ± 0.2	1.0 ± 0.1	6.4 ± 0.3
505	41.8 ± 0.5	2.3 ± 0.3	0.9 ± 0.3	2.2 ± 0.3	3.1 ± 0.3	13 ± 1	44 ± 2	15 ± 1	24 ± 1
506	40.9 ± 0.5	2.8 ± 0.3	1.0 ± 0.3	2.8 ± 0.3	3.9 ± 0.3	12.5 ± 0.9	33 ± 1	11 ± 1	24 ± 1

Uncorrected flux values of the emission regions in the catalogue from this study. The measured fluxes of the nine emission lines for the detected emission regions are presented. These fluxes are not corrected for the local background diffuse emission (described in Section 2.6.3), the global stellar absorption (described in Section 2.6.7), nor the extinction (described in Section 2.6.8). These fluxes are obtained directly from the fit of the integrated region's spectrum and the uncertainties correspond to the fitting uncertainties from ORCS.

All flux values are scaled by 1×10^{-15} .

ID	H α [erg s $^{-1}$ cm $^{-2}$]	[N II] λ 6583 [erg s $^{-1}$ cm $^{-2}$]	[N II] λ 6548 [erg s $^{-1}$ cm $^{-2}$]	[S II] λ 6731 [erg s $^{-1}$ cm $^{-2}$]	[S II] λ 6716 [erg s $^{-1}$ cm $^{-2}$]	H β [erg s $^{-1}$ cm $^{-2}$]	[O III] λ 5007 [erg s $^{-1}$ cm $^{-2}$]	[O III] λ 4959 [erg s $^{-1}$ cm $^{-2}$]	[O II] λ 3727 [erg s $^{-1}$ cm $^{-2}$]
507	10.0 ± 0.2	1.1 ± 0.1	0.5 ± 0.1	1.3 ± 0.1	1.9 ± 0.1	3.2 ± 0.3	2.1 ± 0.3	0.6 ± 0.3	9.1 ± 0.6
508	34.3 ± 0.5	4.0 ± 0.3	1.5 ± 0.3	4.5 ± 0.3	6.4 ± 0.3	10.5 ± 0.6	16.9 ± 0.8	5.9 ± 0.6	35 ± 2
509	24.8 ± 0.3	2.1 ± 0.2	0.6 ± 0.2	2.3 ± 0.2	3.3 ± 0.2	7.8 ± 0.5	17.7 ± 0.7	6.1 ± 0.5	19.9 ± 0.8
510	3.1 ± 0.1	0.37 ± 0.07	0.27 ± 0.07	0.39 ± 0.08	0.61 ± 0.08	1.0 ± 0.1	1.6 ± 0.1	0.5 ± 0.1	3.3 ± 0.3
511	28.8 ± 0.3	2.4 ± 0.2	0.8 ± 0.2	2.6 ± 0.2	3.7 ± 0.2	9.5 ± 0.6	22.8 ± 0.8	7.8 ± 0.6	21 ± 1
512	1.6 ± 0.1	0.15 ± 0.07	0.07 ± 0.07	0.19 ± 0.07	0.27 ± 0.07	0.6 ± 0.1	1.5 ± 0.2	0.5 ± 0.1	1.5 ± 0.3
513	19.4 ± 0.3	2.2 ± 0.2	0.8 ± 0.2	2.0 ± 0.2	2.9 ± 0.2	6.1 ± 0.4	8.5 ± 0.4	2.9 ± 0.3	22 ± 1
514	6.2 ± 0.1	0.7 ± 0.1	0.27 ± 0.09	0.9 ± 0.1	1.2 ± 0.1	2.1 ± 0.2	5.7 ± 0.3	1.9 ± 0.2	6.5 ± 0.4
515	33.8 ± 0.4	3.8 ± 0.3	1.4 ± 0.3	3.6 ± 0.3	5.1 ± 0.3	9.8 ± 0.5	12.6 ± 0.6	4.5 ± 0.4	32 ± 2
517	17.6 ± 0.2	1.7 ± 0.2	0.7 ± 0.2	1.3 ± 0.2	1.8 ± 0.2	5.1 ± 0.3	8.4 ± 0.4	3.0 ± 0.3	17.3 ± 0.8
518	134 ± 2	13 ± 1	5 ± 1	12 ± 1	17 ± 1	39 ± 3	92 ± 4	32 ± 3	121 ± 6
519	36.0 ± 0.5	2.9 ± 0.3	1.2 ± 0.3	1.9 ± 0.4	2.7 ± 0.4	10.1 ± 0.6	18.9 ± 0.8	6.7 ± 0.6	26 ± 1
520	64.5 ± 0.7	4.8 ± 0.5	1.9 ± 0.5	4.3 ± 0.5	5.8 ± 0.5	20 ± 2	51 ± 2	18 ± 2	40 ± 2
521	25.6 ± 0.4	2.0 ± 0.2	0.9 ± 0.2	1.7 ± 0.3	2.5 ± 0.3	7.6 ± 0.6	18.4 ± 0.8	6.5 ± 0.6	22 ± 1
522	62.3 ± 0.8	5.9 ± 0.5	2.2 ± 0.5	4.6 ± 0.5	6.3 ± 0.5	17.5 ± 0.9	23 ± 1	7.9 ± 0.8	49 ± 2
523	65.8 ± 0.8	6.4 ± 0.5	2.0 ± 0.5	5.6 ± 0.5	7.9 ± 0.5	19 ± 1	48 ± 2	17 ± 1	49 ± 2
524	194 ± 2	16 ± 2	6 ± 2	10 ± 2	14 ± 2	56 ± 3	111 ± 4	39 ± 3	127 ± 6
525	101 ± 1	9.9 ± 0.8	3.8 ± 0.8	7.7 ± 0.8	10.9 ± 0.8	31 ± 2	43 ± 2	15 ± 1	82 ± 4
526	77 ± 1	6.6 ± 0.7	2.6 ± 0.7	4.4 ± 0.7	6.0 ± 0.7	22 ± 1	40 ± 2	14 ± 1	57 ± 3
527	845 ± 9	47 ± 6	18 ± 6	36 ± 7	48 ± 7	260 ± 20	940 ± 40	330 ± 30	420 ± 20
528	23 ± 2	2.1 ± 0.3	0.7 ± 0.2	2.2 ± 0.2	3.1 ± 0.3	8.4 ± 0.9	21 ± 2	7.5 ± 0.8	21 ± 2
530	13.6 ± 0.2	1.7 ± 0.1	0.6 ± 0.1	1.9 ± 0.1	2.7 ± 0.1	4.2 ± 0.3	8.3 ± 0.4	2.8 ± 0.3	11.5 ± 0.7
531	4.0 ± 0.1	0.56 ± 0.08	0.23 ± 0.08	0.65 ± 0.08	1.00 ± 0.08	1.4 ± 0.1	1.1 ± 0.1	0.5 ± 0.1	4.1 ± 0.3
532	33.1 ± 0.5	4.5 ± 0.3	1.6 ± 0.3	5.4 ± 0.3	7.5 ± 0.3	10.8 ± 0.6	14.5 ± 0.7	5.2 ± 0.5	35 ± 2

Uncorrected flux values of the emission regions in the catalogue from this study. The measured fluxes of the nine emission lines for the detected emission regions are presented. These fluxes are not corrected for the local background diffuse emission (described in Section 2.6.3), the global stellar absorption (described in Section 2.6.7), nor the extinction (described in Section 2.6.8). These fluxes are obtained directly from the fit of the integrated region's spectrum and the uncertainties correspond to the fitting uncertainties from ORCS. All flux values are scaled by 1×10^{-15} .

ID	$H\alpha$ [$\text{erg s}^{-1} \text{cm}^{-2}$]	[N II] $\lambda 6583$ [$\text{erg s}^{-1} \text{cm}^{-2}$]	[N II] $\lambda 6548$ [$\text{erg s}^{-1} \text{cm}^{-2}$]	[S II] $\lambda 6731$ [$\text{erg s}^{-1} \text{cm}^{-2}$]	[S II] $\lambda 6716$ [$\text{erg s}^{-1} \text{cm}^{-2}$]	$H\beta$ [$\text{erg s}^{-1} \text{cm}^{-2}$]	[O III] $\lambda 5007$ [$\text{erg s}^{-1} \text{cm}^{-2}$]	[O III] $\lambda 4959$ [$\text{erg s}^{-1} \text{cm}^{-2}$]	[O II] $\lambda 3727$ [$\text{erg s}^{-1} \text{cm}^{-2}$]
533	2.3 ± 0.1	0.41 ± 0.09	0.16 ± 0.09	0.39 ± 0.09	0.7 ± 0.1	0.9 ± 0.1	1.5 ± 0.2	0.5 ± 0.1	3.3 ± 0.4
534	12.0 ± 0.2	1.5 ± 0.2	0.7 ± 0.2	1.5 ± 0.2	2.1 ± 0.2	3.7 ± 0.3	4.0 ± 0.3	1.4 ± 0.2	11.6 ± 0.6
535	15.0 ± 0.2	1.7 ± 0.1	0.7 ± 0.1	1.7 ± 0.2	2.4 ± 0.2	4.5 ± 0.4	11.3 ± 0.5	3.9 ± 0.4	13.6 ± 0.7
536	8.4 ± 0.2	1.0 ± 0.1	0.4 ± 0.1	1.4 ± 0.1	1.8 ± 0.1	2.7 ± 0.2	7.3 ± 0.3	2.4 ± 0.2	8.0 ± 0.5
537	11.0 ± 0.2	1.6 ± 0.1	0.6 ± 0.1	1.3 ± 0.1	1.9 ± 0.1	3.1 ± 0.2	6.0 ± 0.3	2.1 ± 0.2	17.0 ± 0.8
538	10.2 ± 0.2	1.3 ± 0.1	0.5 ± 0.1	1.5 ± 0.1	2.2 ± 0.1	3.1 ± 0.3	8.0 ± 0.4	2.6 ± 0.3	9.1 ± 0.4
539	8.7 ± 0.1	1.1 ± 0.1	0.4 ± 0.1	1.3 ± 0.1	1.9 ± 0.1	2.8 ± 0.3	8.6 ± 0.4	3.0 ± 0.3	7.5 ± 0.4
540	5.4 ± 0.2	0.8 ± 0.1	0.4 ± 0.1	0.8 ± 0.1	1.1 ± 0.1	1.9 ± 0.2	1.6 ± 0.2	0.6 ± 0.1	7.3 ± 0.5
541	12.0 ± 0.2	1.8 ± 0.1	0.8 ± 0.1	1.3 ± 0.1	2.1 ± 0.1	3.9 ± 0.2	7.1 ± 0.3	2.4 ± 0.2	16.8 ± 0.7
542	7.5 ± 0.2	0.8 ± 0.1	0.4 ± 0.1	0.9 ± 0.1	1.3 ± 0.1	2.1 ± 0.2	3.2 ± 0.2	1.1 ± 0.2	6.0 ± 0.4
543	3.4 ± 0.1	0.35 ± 0.07	0.17 ± 0.07	0.41 ± 0.07	0.57 ± 0.07	1.1 ± 0.2	7.7 ± 0.4	2.5 ± 0.3	2.4 ± 0.3

Table F.3

Corrected flux values with the local background of the emission regions in the catalogue from this study. The measured fluxes of the nine emission lines for the detected emission regions are presented. These fluxes are corrected for the local background, which includes the local emission and the stellar population (described in Section 2.6.7), and the extinction (described in Section 2.6.8). These flux are obtained by subtracting the background spectrum, instead of the background flux measured for each line (methodology used in this study), as discussed in Section 2.6.7. The uncertainties correspond to the propagated uncertainties (described in Section 2.6.4). All flux values are scaled by 1×10^{-15} .

ID	H α	[N II] $\lambda 6583$	[N II] $\lambda 6548$	[S II] $\lambda 6731$	[S II] $\lambda 6716$	H β	[O III] $\lambda 5007$	[O III] $\lambda 4959$	[O II] $\lambda 3727$
	[erg s $^{-1}$ cm $^{-2}$]								
0	0.48 ± 0.05	-0.02 ± 0.03	-0.01 ± 0.03	0.06 ± 0.03	0.02 ± 0.03	0.13 ± 0.03	0.76 ± 0.05	0.32 ± 0.03	-0.09 ± 0.08
2	2.83 ± 0.05	0.28 ± 0.03	0.06 ± 0.03	0.23 ± 0.04	0.35 ± 0.04	0.87 ± 0.05	1.38 ± 0.06	0.47 ± 0.05	2.3 ± 0.1
3	1.33 ± 0.06	0.05 ± 0.04	0.01 ± 0.04	0.15 ± 0.04	0.31 ± 0.04	0.34 ± 0.06	0.50 ± 0.07	0.19 ± 0.06	1.6 ± 0.2
4	0.78 ± 0.04	0.14 ± 0.03	-0.01 ± 0.02	0.10 ± 0.03	0.17 ± 0.03	0.25 ± 0.03	0.11 ± 0.03	0.04 ± 0.03	0.9 ± 0.1
6	1.11 ± 0.04	0.16 ± 0.03	0.01 ± 0.03	0.16 ± 0.03	0.25 ± 0.03	0.36 ± 0.03	0.17 ± 0.03	0.07 ± 0.03	1.2 ± 0.1
7	1.19 ± 0.04	0.15 ± 0.03	0.04 ± 0.03	0.11 ± 0.03	0.18 ± 0.03	0.36 ± 0.03	0.52 ± 0.03	0.21 ± 0.03	1.2 ± 0.1
8	0.61 ± 0.04	0.04 ± 0.03	0.02 ± 0.03	0.07 ± 0.03	0.12 ± 0.03	0.26 ± 0.04	0.94 ± 0.06	0.35 ± 0.04	0.7 ± 0.1
9	3.39 ± 0.05	0.35 ± 0.03	0.09 ± 0.03	0.38 ± 0.03	0.37 ± 0.03	0.97 ± 0.05	1.28 ± 0.05	0.52 ± 0.04	2.7 ± 0.1
10	48.8 ± 0.3	3.9 ± 0.2	1.2 ± 0.2	2.4 ± 0.2	3.4 ± 0.2	14.9 ± 0.5	32.3 ± 0.7	11.1 ± 0.5	33.2 ± 0.7
11	2.83 ± 0.07	0.18 ± 0.05	0.01 ± 0.05	0.27 ± 0.05	0.27 ± 0.05	0.78 ± 0.06	1.52 ± 0.08	0.62 ± 0.06	2.2 ± 0.2
13	8.60 ± 0.09	0.96 ± 0.06	0.18 ± 0.06	0.94 ± 0.06	1.44 ± 0.06	2.5 ± 0.1	5.1 ± 0.2	1.7 ± 0.1	7.6 ± 0.2
14	1.55 ± 0.08	0.22 ± 0.05	0.09 ± 0.05	0.23 ± 0.06	0.20 ± 0.06	0.55 ± 0.06	-0.10 ± 0.06	0.09 ± 0.06	0.9 ± 0.2
15	1.05 ± 0.06	0.13 ± 0.04	0.13 ± 0.04	0.08 ± 0.04	0.18 ± 0.04	0.37 ± 0.06	0.11 ± 0.04	0.11 ± 0.04	1.2 ± 0.2
16	2.27 ± 0.05	0.27 ± 0.03	0.10 ± 0.03	0.14 ± 0.03	0.27 ± 0.03	0.54 ± 0.04	0.16 ± 0.04	0.13 ± 0.04	1.8 ± 0.1
17	0.91 ± 0.04	0.14 ± 0.03	0.01 ± 0.02	0.07 ± 0.03	0.11 ± 0.03	0.25 ± 0.05	0.16 ± 0.04	0.05 ± 0.04	0.4 ± 0.1
18	1.92 ± 0.06	0.29 ± 0.04	0.12 ± 0.04	0.20 ± 0.04	0.28 ± 0.04	0.47 ± 0.05	0.79 ± 0.07	0.25 ± 0.05	1.2 ± 0.1
19	31.3 ± 0.2	3.4 ± 0.1	1.0 ± 0.1	2.7 ± 0.1	3.5 ± 0.1	9.8 ± 0.3	12.3 ± 0.4	4.3 ± 0.3	28.5 ± 0.7
20	5.53 ± 0.07	0.59 ± 0.04	0.17 ± 0.04	0.65 ± 0.05	0.94 ± 0.05	1.8 ± 0.2	9.9 ± 0.2	3.4 ± 0.2	3.6 ± 0.2
21	6.54 ± 0.07	0.59 ± 0.05	0.20 ± 0.05	0.60 ± 0.05	0.84 ± 0.05	1.88 ± 0.09	5.2 ± 0.1	1.74 ± 0.09	4.3 ± 0.2

Corrected flux values with the local background of the emission regions in the catalogue from this study. The measured fluxes of the nine emission lines for the detected emission regions are presented. These fluxes are corrected for the local background, which includes the local emission and the stellar population (described in Section 2.6.7), and the extinction (described in Section 2.6.8). These flux are obtained by subtracting the background spectrum, instead of the background flux measured for each line (methodology used in this study), as discussed in Section 2.6.7. The uncertainties correspond to the propagated uncertainties (described in Section 2.6.4). All flux values are scaled by 1×10^{-15} .

ID	$H\alpha$ [erg s ⁻¹ cm ⁻²]	[N II] $\lambda 6583$ [erg s ⁻¹ cm ⁻²]	[N II] $\lambda 6548$ [erg s ⁻¹ cm ⁻²]	[S II] $\lambda 6731$ [erg s ⁻¹ cm ⁻²]	[S II] $\lambda 6716$ [erg s ⁻¹ cm ⁻²]	$H\beta$ [erg s ⁻¹ cm ⁻²]	[O III] $\lambda 5007$ [erg s ⁻¹ cm ⁻²]	[O III] $\lambda 4959$ [erg s ⁻¹ cm ⁻²]	[O II] $\lambda 3727$ [erg s ⁻¹ cm ⁻²]
22	0.57 ± 0.07	0.05 ± 0.05	0.07 ± 0.05	0.11 ± 0.05	0.08 ± 0.05	0.10 ± 0.05	0.01 ± 0.05	-0.04 ± 0.05	0.5 ± 0.2
23	0.80 ± 0.03	0.13 ± 0.02	0.04 ± 0.02	0.12 ± 0.02	0.22 ± 0.03	0.26 ± 0.04	1.57 ± 0.06	0.52 ± 0.04	1.1 ± 0.1
24	3.47 ± 0.07	0.28 ± 0.05	0.19 ± 0.05	0.32 ± 0.05	0.44 ± 0.05	1.19 ± 0.09	3.8 ± 0.1	1.26 ± 0.09	3.8 ± 0.2
25	2.21 ± 0.07	0.20 ± 0.05	0.13 ± 0.04	0.09 ± 0.05	0.28 ± 0.05	0.75 ± 0.09	0.52 ± 0.08	0.18 ± 0.07	2.1 ± 0.2
26	1.01 ± 0.04	0.14 ± 0.02	0.05 ± 0.02	0.14 ± 0.03	0.21 ± 0.03	0.29 ± 0.05	0.18 ± 0.04	0.00 ± 0.03	0.7 ± 0.1
27	0.75 ± 0.04	0.11 ± 0.03	0.01 ± 0.03	0.13 ± 0.03	0.12 ± 0.03	0.28 ± 0.03	0.05 ± 0.03	0.05 ± 0.03	0.7 ± 0.1
28	1.30 ± 0.07	0.20 ± 0.05	0.13 ± 0.05	0.25 ± 0.05	0.38 ± 0.05	0.4 ± 0.1	0.3 ± 0.1	0.13 ± 0.09	1.1 ± 0.1
29	2.1 ± 0.1	0.34 ± 0.07	0.14 ± 0.07	0.14 ± 0.07	0.60 ± 0.08	0.6 ± 0.1	3.9 ± 0.2	1.4 ± 0.1	2.6 ± 0.3
30	8.33 ± 0.08	0.61 ± 0.05	0.28 ± 0.05	0.59 ± 0.06	0.79 ± 0.06	2.7 ± 0.1	6.4 ± 0.2	2.2 ± 0.1	5.7 ± 0.2
31	2.17 ± 0.06	0.21 ± 0.04	0.02 ± 0.04	0.30 ± 0.04	0.33 ± 0.04	0.59 ± 0.09	0.21 ± 0.07	0.12 ± 0.06	1.8 ± 0.2
32	0.75 ± 0.06	0.06 ± 0.04	0.05 ± 0.04	0.17 ± 0.05	0.21 ± 0.05	0.13 ± 0.05	0.03 ± 0.05	0.04 ± 0.05	0.7 ± 0.1
33	1.06 ± 0.06	0.15 ± 0.04	0.03 ± 0.04	0.13 ± 0.04	0.10 ± 0.04	0.29 ± 0.05	0.17 ± 0.05	-0.01 ± 0.05	1.1 ± 0.2
34	2.7 ± 0.1	0.35 ± 0.07	0.17 ± 0.07	0.37 ± 0.07	0.36 ± 0.07	0.62 ± 0.07	0.02 ± 0.07	-0.12 ± 0.07	1.2 ± 0.2
35	1.54 ± 0.08	0.20 ± 0.05	-0.02 ± 0.05	0.23 ± 0.06	0.19 ± 0.06	0.41 ± 0.09	0.42 ± 0.09	0.08 ± 0.07	1.4 ± 0.2
36	14.2 ± 0.2	1.9 ± 0.1	0.6 ± 0.1	2.3 ± 0.1	3.1 ± 0.1	4.8 ± 0.2	7.2 ± 0.2	2.5 ± 0.2	15.2 ± 0.5
37	12.8 ± 0.1	1.57 ± 0.08	0.57 ± 0.08	1.18 ± 0.08	1.95 ± 0.08	4.1 ± 0.2	4.2 ± 0.2	1.6 ± 0.1	13.0 ± 0.3
38	4.4 ± 0.1	0.54 ± 0.07	0.00 ± 0.07	0.81 ± 0.08	1.17 ± 0.08	1.3 ± 0.1	1.6 ± 0.1	0.5 ± 0.1	3.0 ± 0.3
39	4.7 ± 0.1	0.61 ± 0.07	0.09 ± 0.06	0.69 ± 0.07	1.06 ± 0.07	1.36 ± 0.09	2.5 ± 0.1	0.93 ± 0.09	5.1 ± 0.3
40	2.48 ± 0.07	0.33 ± 0.05	0.04 ± 0.05	0.35 ± 0.05	0.41 ± 0.05	0.67 ± 0.04	1.89 ± 0.06	0.71 ± 0.05	2.3 ± 0.2
41	9.8 ± 0.1	1.16 ± 0.07	0.39 ± 0.06	0.99 ± 0.07	1.21 ± 0.07	3.1 ± 0.2	11.5 ± 0.3	3.9 ± 0.2	7.9 ± 0.3
42	20.0 ± 0.2	2.7 ± 0.1	0.7 ± 0.1	2.8 ± 0.1	4.3 ± 0.1	6.7 ± 0.2	8.8 ± 0.3	3.0 ± 0.2	19.8 ± 0.5
43	10.0 ± 0.1	0.74 ± 0.07	0.27 ± 0.06	0.55 ± 0.07	0.74 ± 0.07	2.7 ± 0.1	5.8 ± 0.2	1.9 ± 0.1	5.2 ± 0.3

Corrected flux values with the local background of the emission regions in the catalogue from this study. The measured fluxes of the nine emission lines for the detected emission regions are presented. These fluxes are corrected for the local background, which includes the local emission and the stellar population (described in Section 2.6.7), and the extinction (described in Section 2.6.8). These flux are obtained by subtracting the background spectrum, instead of the background flux measured for each line (methodology used in this study), as discussed in Section 2.6.7. The uncertainties correspond to the propagated uncertainties (described in Section 2.6.4). All flux values are scaled by 1×10^{-15} .

ID	$H\alpha$ [erg s ⁻¹ cm ⁻²]	[N II] $\lambda 6583$ [erg s ⁻¹ cm ⁻²]	[N II] $\lambda 6548$ [erg s ⁻¹ cm ⁻²]	[S II] $\lambda 6731$ [erg s ⁻¹ cm ⁻²]	[S II] $\lambda 6716$ [erg s ⁻¹ cm ⁻²]	$H\beta$ [erg s ⁻¹ cm ⁻²]	[O III] $\lambda 5007$ [erg s ⁻¹ cm ⁻²]	[O III] $\lambda 4959$ [erg s ⁻¹ cm ⁻²]	[O II] $\lambda 3727$ [erg s ⁻¹ cm ⁻²]
44	5.6 ± 0.1	0.90 ± 0.07	0.13 ± 0.07	0.94 ± 0.08	1.42 ± 0.08	1.9 ± 0.2	3.1 ± 0.2	1.2 ± 0.2	7.1 ± 0.4
45	2.74 ± 0.07	0.31 ± 0.05	0.09 ± 0.05	0.40 ± 0.05	0.64 ± 0.05	0.85 ± 0.08	1.3 ± 0.1	0.43 ± 0.07	3.0 ± 0.2
46	4.49 ± 0.07	0.63 ± 0.05	0.15 ± 0.05	0.52 ± 0.05	0.91 ± 0.05	1.42 ± 0.08	1.45 ± 0.08	0.49 ± 0.06	4.2 ± 0.2
47	1.58 ± 0.05	0.05 ± 0.05	-0.01 ± 0.05	-0.03 ± 0.06	0.13 ± 0.06	0.6 ± 0.1	0.16 ± 0.07	-0.19 ± 0.07	1.5 ± 0.2
48	11.2 ± 0.1	1.04 ± 0.07	0.30 ± 0.06	0.55 ± 0.07	0.94 ± 0.07	2.8 ± 0.1	4.8 ± 0.2	1.7 ± 0.1	6.3 ± 0.3
49	10.1 ± 0.1	1.38 ± 0.08	0.40 ± 0.08	1.67 ± 0.08	2.38 ± 0.08	3.4 ± 0.1	3.7 ± 0.1	1.3 ± 0.1	11.6 ± 0.4
50	4.27 ± 0.09	0.71 ± 0.06	0.18 ± 0.06	0.67 ± 0.06	1.04 ± 0.06	1.34 ± 0.07	1.99 ± 0.09	0.65 ± 0.07	5.5 ± 0.2
51	1.66 ± 0.04	0.18 ± 0.03	0.05 ± 0.03	0.08 ± 0.03	0.13 ± 0.03	0.56 ± 0.04	0.71 ± 0.05	0.25 ± 0.04	1.3 ± 0.1
52	3.03 ± 0.08	0.21 ± 0.06	0.08 ± 0.06	0.41 ± 0.06	0.30 ± 0.06	0.87 ± 0.08	1.7 ± 0.1	0.62 ± 0.08	3.1 ± 0.2
53	5.67 ± 0.09	0.51 ± 0.06	0.09 ± 0.06	0.51 ± 0.07	0.46 ± 0.07	1.4 ± 0.1	3.6 ± 0.1	1.3 ± 0.1	3.4 ± 0.2
54	2.79 ± 0.07	0.32 ± 0.04	0.25 ± 0.04	0.28 ± 0.05	0.34 ± 0.05	0.93 ± 0.08	0.91 ± 0.08	0.44 ± 0.07	2.7 ± 0.2
55	12.6 ± 0.1	1.1 ± 0.1	0.4 ± 0.1	1.0 ± 0.1	1.4 ± 0.1	3.6 ± 0.2	4.7 ± 0.2	1.8 ± 0.1	10.0 ± 0.4
56	6.8 ± 0.2	0.9 ± 0.1	0.2 ± 0.1	1.2 ± 0.1	1.5 ± 0.1	2.1 ± 0.2	5.0 ± 0.2	1.7 ± 0.2	7.3 ± 0.4
57	1.52 ± 0.07	0.24 ± 0.05	0.09 ± 0.05	0.20 ± 0.05	0.24 ± 0.05	0.6 ± 0.1	0.07 ± 0.08	0.06 ± 0.08	1.0 ± 0.2
58	2.20 ± 0.07	0.34 ± 0.04	0.07 ± 0.04	0.45 ± 0.05	0.65 ± 0.05	0.65 ± 0.05	1.01 ± 0.06	0.36 ± 0.05	2.5 ± 0.2
59	1.57 ± 0.05	0.06 ± 0.03	0.04 ± 0.03	0.12 ± 0.03	0.05 ± 0.03	0.34 ± 0.05	1.11 ± 0.06	0.42 ± 0.05	0.4 ± 0.2
60	1.27 ± 0.07	0.19 ± 0.05	-0.03 ± 0.05	0.23 ± 0.05	0.26 ± 0.05	0.7 ± 0.1	0.27 ± 0.09	0.04 ± 0.08	1.0 ± 0.2
61	1.12 ± 0.04	0.12 ± 0.03	0.09 ± 0.03	0.09 ± 0.03	0.19 ± 0.03	0.40 ± 0.06	0.05 ± 0.04	0.03 ± 0.04	1.0 ± 0.1
62	1.05 ± 0.06	0.11 ± 0.04	0.01 ± 0.04	0.10 ± 0.04	0.17 ± 0.04	0.41 ± 0.08	0.19 ± 0.07	0.10 ± 0.06	0.7 ± 0.1
63	6.33 ± 0.07	0.45 ± 0.05	0.21 ± 0.05	0.32 ± 0.05	0.43 ± 0.05	1.81 ± 0.08	3.1 ± 0.1	1.14 ± 0.07	3.7 ± 0.3
64	0.43 ± 0.03	0.02 ± 0.02	0.04 ± 0.02	0.05 ± 0.02	0.04 ± 0.02	0.08 ± 0.04	0.18 ± 0.05	0.04 ± 0.03	0.4 ± 0.1
65	2.59 ± 0.06	0.24 ± 0.04	0.11 ± 0.04	0.26 ± 0.04	0.40 ± 0.04	0.83 ± 0.08	0.29 ± 0.06	0.12 ± 0.06	2.7 ± 0.2

Corrected flux values with the local background of the emission regions in the catalogue from this study. The measured fluxes of the nine emission lines for the detected emission regions are presented. These fluxes are corrected for the local background, which includes the local emission and the stellar population (described in Section 2.6.7), and the extinction (described in Section 2.6.8). These flux are obtained by subtracting the background spectrum, instead of the background flux measured for each line (methodology used in this study), as discussed in Section 2.6.7. The uncertainties correspond to the propagated uncertainties (described in Section 2.6.4). All flux values are scaled by 1×10^{-15} .

ID	$H\alpha$ [erg s ⁻¹ cm ⁻²]	[N II] $\lambda 6583$ [erg s ⁻¹ cm ⁻²]	[N II] $\lambda 6548$ [erg s ⁻¹ cm ⁻²]	[S II] $\lambda 6731$ [erg s ⁻¹ cm ⁻²]	[S II] $\lambda 6716$ [erg s ⁻¹ cm ⁻²]	$H\beta$ [erg s ⁻¹ cm ⁻²]	[O III] $\lambda 5007$ [erg s ⁻¹ cm ⁻²]	[O III] $\lambda 4959$ [erg s ⁻¹ cm ⁻²]	[O II] $\lambda 3727$ [erg s ⁻¹ cm ⁻²]
66	8.37 ± 0.08	0.79 ± 0.06	0.22 ± 0.06	0.50 ± 0.06	0.83 ± 0.06	2.5 ± 0.1	5.6 ± 0.2	1.9 ± 0.1	8.0 ± 0.3
67	5.06 ± 0.06	0.52 ± 0.04	0.16 ± 0.04	0.39 ± 0.04	0.65 ± 0.04	1.72 ± 0.09	5.4 ± 0.1	1.85 ± 0.09	5.0 ± 0.2
68	0.99 ± 0.05	0.21 ± 0.04	0.03 ± 0.04	0.05 ± 0.04	0.20 ± 0.04	0.41 ± 0.07	0.19 ± 0.05	0.12 ± 0.05	0.7 ± 0.1
69	1.77 ± 0.05	0.18 ± 0.03	0.10 ± 0.03	0.17 ± 0.03	0.27 ± 0.03	0.70 ± 0.07	4.0 ± 0.1	1.34 ± 0.07	1.4 ± 0.2
70	1.43 ± 0.04	0.17 ± 0.03	0.15 ± 0.03	0.10 ± 0.03	0.19 ± 0.03	0.47 ± 0.04	0.50 ± 0.05	0.22 ± 0.04	1.2 ± 0.1
71	2.27 ± 0.06	0.37 ± 0.04	0.04 ± 0.04	0.24 ± 0.04	0.27 ± 0.04	0.8 ± 0.1	0.04 ± 0.07	-0.05 ± 0.07	1.4 ± 0.2
72	7.01 ± 0.09	0.88 ± 0.06	0.24 ± 0.06	0.61 ± 0.06	0.99 ± 0.06	2.3 ± 0.1	1.54 ± 0.09	0.58 ± 0.08	7.5 ± 0.3
73	1.92 ± 0.06	0.22 ± 0.07	0.18 ± 0.06	0.12 ± 0.07	0.42 ± 0.07	0.6 ± 0.1	1.3 ± 0.2	0.4 ± 0.1	1.8 ± 0.4
74	1.79 ± 0.07	0.01 ± 0.05	0.02 ± 0.05	0.09 ± 0.05	0.16 ± 0.05	0.38 ± 0.08	1.1 ± 0.1	0.31 ± 0.08	0.7 ± 0.2
75	0.93 ± 0.03	0.08 ± 0.02	0.07 ± 0.02	0.06 ± 0.02	0.11 ± 0.02	0.22 ± 0.05	0.50 ± 0.06	0.11 ± 0.04	0.5 ± 0.1
76	1.39 ± 0.04	0.17 ± 0.04	0.12 ± 0.04	0.09 ± 0.04	0.20 ± 0.04	0.45 ± 0.06	0.77 ± 0.08	0.40 ± 0.06	0.6 ± 0.2
77	11.0 ± 0.5	0.9 ± 0.3	0.0 ± 0.3	0.8 ± 0.3	1.3 ± 0.3	4.1 ± 0.3	8.3 ± 0.4	2.9 ± 0.3	9.9 ± 0.7
78	1.07 ± 0.03	0.12 ± 0.03	0.04 ± 0.03	0.12 ± 0.03	0.17 ± 0.03	0.33 ± 0.07	-0.11 ± 0.06	-0.01 ± 0.05	1.0 ± 0.1
79	27.1 ± 0.2	2.0 ± 0.1	0.7 ± 0.1	1.3 ± 0.1	1.7 ± 0.1	8.0 ± 0.4	21.7 ± 0.5	7.5 ± 0.4	13.5 ± 0.4
80	2.51 ± 0.06	0.31 ± 0.04	0.02 ± 0.04	0.32 ± 0.04	0.48 ± 0.04	0.73 ± 0.06	0.12 ± 0.05	-0.02 ± 0.05	2.4 ± 0.2
81	3.65 ± 0.07	0.44 ± 0.05	0.12 ± 0.05	0.58 ± 0.05	0.83 ± 0.05	1.06 ± 0.08	0.40 ± 0.06	0.07 ± 0.05	3.6 ± 0.2
82	6.87 ± 0.08	0.74 ± 0.05	0.26 ± 0.05	0.85 ± 0.06	1.29 ± 0.06	2.13 ± 0.09	1.34 ± 0.08	0.60 ± 0.07	7.8 ± 0.2
83	12.2 ± 0.2	1.9 ± 0.2	0.4 ± 0.2	2.1 ± 0.2	2.6 ± 0.2	4.1 ± 0.3	3.4 ± 0.3	1.5 ± 0.2	12.1 ± 0.5
84	5.39 ± 0.08	0.42 ± 0.06	0.02 ± 0.06	0.28 ± 0.06	0.50 ± 0.06	1.68 ± 0.09	3.5 ± 0.1	1.24 ± 0.09	4.3 ± 0.2
85	13.5 ± 0.2	2.2 ± 0.2	0.8 ± 0.2	2.1 ± 0.2	3.1 ± 0.2	3.8 ± 0.2	4.8 ± 0.2	1.6 ± 0.2	11.9 ± 0.4
86	10.21 ± 0.09	1.06 ± 0.06	0.35 ± 0.06	0.66 ± 0.06	1.06 ± 0.06	2.8 ± 0.1	4.2 ± 0.1	1.5 ± 0.1	6.8 ± 0.2
87	6.5 ± 0.1	1.05 ± 0.08	0.35 ± 0.08	0.97 ± 0.08	1.53 ± 0.09	1.8 ± 0.1	2.0 ± 0.1	0.8 ± 0.1	4.4 ± 0.3

Corrected flux values with the local background of the emission regions in the catalogue from this study. The measured fluxes of the nine emission lines for the detected emission regions are presented. These fluxes are corrected for the local background, which includes the local emission and the stellar population (described in Section 2.6.7), and the extinction (described in Section 2.6.8). These flux are obtained by subtracting the background spectrum, instead of the background flux measured for each line (methodology used in this study), as discussed in Section 2.6.7. The uncertainties correspond to the propagated uncertainties (described in Section 2.6.4). All flux values are scaled by 1×10^{-15} .

ID	$H\alpha$ [erg s ⁻¹ cm ⁻²]	[N II] $\lambda 6583$ [erg s ⁻¹ cm ⁻²]	[N II] $\lambda 6548$ [erg s ⁻¹ cm ⁻²]	[S II] $\lambda 6731$ [erg s ⁻¹ cm ⁻²]	[S II] $\lambda 6716$ [erg s ⁻¹ cm ⁻²]	$H\beta$ [erg s ⁻¹ cm ⁻²]	[O III] $\lambda 5007$ [erg s ⁻¹ cm ⁻²]	[O III] $\lambda 4959$ [erg s ⁻¹ cm ⁻²]	[O II] $\lambda 3727$ [erg s ⁻¹ cm ⁻²]
88	3.42 ± 0.06	0.28 ± 0.06	0.12 ± 0.06	0.25 ± 0.06	0.58 ± 0.06	1.1 ± 0.1	3.5 ± 0.2	1.3 ± 0.1	1.5 ± 0.2
89	2.20 ± 0.05	0.28 ± 0.04	0.19 ± 0.04	0.27 ± 0.04	0.29 ± 0.04	0.74 ± 0.07	0.65 ± 0.06	0.21 ± 0.05	1.9 ± 0.2
90	0.55 ± 0.04	0.15 ± 0.04	0.08 ± 0.04	0.02 ± 0.04	0.12 ± 0.04	0.32 ± 0.05	-0.08 ± 0.05	0.11 ± 0.05	0.8 ± 0.2
91	1.16 ± 0.04	0.16 ± 0.03	0.05 ± 0.03	0.12 ± 0.03	0.18 ± 0.03	0.30 ± 0.03	0.30 ± 0.04	0.08 ± 0.04	0.9 ± 0.1
92	1.29 ± 0.09	0.01 ± 0.06	-0.04 ± 0.06	0.07 ± 0.06	0.21 ± 0.06	0.4 ± 0.1	0.06 ± 0.08	0.07 ± 0.08	0.6 ± 0.2
93	4.3 ± 0.1	0.7 ± 0.1	0.4 ± 0.1	0.6 ± 0.1	0.7 ± 0.1	1.6 ± 0.2	2.0 ± 0.2	0.6 ± 0.2	4.8 ± 0.4
94	26.8 ± 0.2	2.5 ± 0.1	0.7 ± 0.1	1.5 ± 0.1	2.0 ± 0.1	8.4 ± 0.3	15.0 ± 0.3	5.2 ± 0.2	22.2 ± 0.5
95	98.5 ± 0.6	6.6 ± 0.4	2.1 ± 0.4	3.2 ± 0.4	4.7 ± 0.4	32 ± 1	71 ± 1	24 ± 1	69 ± 1
96	8.2 ± 0.1	1.15 ± 0.09	0.44 ± 0.09	0.72 ± 0.09	1.2 ± 0.1	2.5 ± 0.2	4.9 ± 0.3	1.7 ± 0.2	7.6 ± 0.4
97	28.8 ± 0.3	3.5 ± 0.2	0.9 ± 0.2	3.0 ± 0.2	4.0 ± 0.2	8.9 ± 0.4	22.0 ± 0.6	7.6 ± 0.4	19.6 ± 0.7
98	2.62 ± 0.04	0.11 ± 0.03	0.03 ± 0.03	0.09 ± 0.03	0.11 ± 0.03	0.94 ± 0.06	2.70 ± 0.08	1.00 ± 0.06	1.5 ± 0.1
99	4.40 ± 0.09	0.56 ± 0.06	0.07 ± 0.06	0.48 ± 0.06	0.78 ± 0.06	1.25 ± 0.09	2.7 ± 0.1	0.92 ± 0.09	3.2 ± 0.2
100	15.7 ± 0.1	1.50 ± 0.08	0.61 ± 0.08	0.98 ± 0.09	1.35 ± 0.08	5.0 ± 0.2	8.2 ± 0.2	2.6 ± 0.1	13.2 ± 0.3
101	5.68 ± 0.07	0.32 ± 0.05	0.18 ± 0.05	0.18 ± 0.05	0.39 ± 0.05	1.9 ± 0.1	5.1 ± 0.2	1.8 ± 0.1	3.0 ± 0.2
102	7.1 ± 0.1	1.04 ± 0.07	0.35 ± 0.07	1.05 ± 0.07	1.58 ± 0.07	2.0 ± 0.1	3.5 ± 0.1	1.1 ± 0.1	6.1 ± 0.3
103	4.89 ± 0.08	0.52 ± 0.05	0.17 ± 0.05	0.41 ± 0.06	0.58 ± 0.06	1.65 ± 0.09	2.2 ± 0.1	0.65 ± 0.07	3.4 ± 0.2
104	39.7 ± 0.3	3.6 ± 0.2	1.2 ± 0.2	3.3 ± 0.2	4.5 ± 0.2	12.1 ± 0.6	37.0 ± 0.8	12.6 ± 0.6	21.2 ± 0.6
105	7.3 ± 0.1	0.59 ± 0.07	0.13 ± 0.07	0.59 ± 0.07	0.86 ± 0.07	2.0 ± 0.1	4.7 ± 0.2	1.6 ± 0.1	3.2 ± 0.3
106	4.2 ± 0.1	0.41 ± 0.06	0.15 ± 0.06	0.37 ± 0.07	0.56 ± 0.07	1.36 ± 0.08	2.6 ± 0.1	1.06 ± 0.08	3.2 ± 0.2
107	5.93 ± 0.08	0.36 ± 0.05	0.15 ± 0.05	0.28 ± 0.06	0.52 ± 0.06	1.9 ± 0.1	4.9 ± 0.2	1.7 ± 0.1	1.6 ± 0.2
108	9.17 ± 0.09	1.10 ± 0.06	0.44 ± 0.06	0.90 ± 0.06	1.46 ± 0.06	3.0 ± 0.1	6.1 ± 0.2	2.0 ± 0.1	6.9 ± 0.2
109	0.97 ± 0.04	0.03 ± 0.02	-0.02 ± 0.02	0.09 ± 0.03	0.06 ± 0.02	0.27 ± 0.03	0.83 ± 0.05	0.29 ± 0.04	0.63 ± 0.09

Corrected flux values with the local background of the emission regions in the catalogue from this study. The measured fluxes of the nine emission lines for the detected emission regions are presented. These fluxes are corrected for the local background, which includes the local emission and the stellar population (described in Section 2.6.7), and the extinction (described in Section 2.6.8). These flux are obtained by subtracting the background spectrum, instead of the background flux measured for each line (methodology used in this study), as discussed in Section 2.6.7. The uncertainties correspond to the propagated uncertainties (described in Section 2.6.4). All flux values are scaled by 1×10^{-15} .

ID	$H\alpha$ [erg s ⁻¹ cm ⁻²]	[N II] $\lambda 6583$ [erg s ⁻¹ cm ⁻²]	[N II] $\lambda 6548$ [erg s ⁻¹ cm ⁻²]	[S II] $\lambda 6731$ [erg s ⁻¹ cm ⁻²]	[S II] $\lambda 6716$ [erg s ⁻¹ cm ⁻²]	$H\beta$ [erg s ⁻¹ cm ⁻²]	[O III] $\lambda 5007$ [erg s ⁻¹ cm ⁻²]	[O III] $\lambda 4959$ [erg s ⁻¹ cm ⁻²]	[O II] $\lambda 3727$ [erg s ⁻¹ cm ⁻²]
110	12.27 ± 0.09	1.12 ± 0.06	0.30 ± 0.06	0.86 ± 0.06	1.27 ± 0.06	4.0 ± 0.2	9.3 ± 0.2	3.3 ± 0.2	6.9 ± 0.3
111	49.8 ± 0.3	4.8 ± 0.2	1.4 ± 0.2	4.0 ± 0.2	5.9 ± 0.2	15.7 ± 0.6	40.0 ± 0.9	13.6 ± 0.6	30 ± 1
112	11.5 ± 0.1	1.21 ± 0.07	0.47 ± 0.07	0.78 ± 0.08	1.54 ± 0.08	3.8 ± 0.2	7.2 ± 0.2	2.7 ± 0.1	6.1 ± 0.3
113	8.1 ± 0.1	0.77 ± 0.07	0.21 ± 0.07	0.91 ± 0.07	1.55 ± 0.07	2.7 ± 0.1	2.5 ± 0.1	0.8 ± 0.1	7.3 ± 0.3
114	142.1 ± 0.8	7.6 ± 0.6	2.6 ± 0.5	5.1 ± 0.6	7.8 ± 0.6	45 ± 2	164 ± 3	57 ± 2	57 ± 1
115	4.63 ± 0.08	0.39 ± 0.06	0.20 ± 0.06	0.38 ± 0.06	0.49 ± 0.06	1.9 ± 0.1	3.6 ± 0.1	1.23 ± 0.09	2.7 ± 0.2
116	7.68 ± 0.09	1.17 ± 0.06	0.37 ± 0.06	0.92 ± 0.06	1.40 ± 0.06	2.38 ± 0.09	3.6 ± 0.1	1.32 ± 0.09	5.7 ± 0.2
117	16.1 ± 0.2	1.7 ± 0.1	0.5 ± 0.1	1.6 ± 0.1	2.4 ± 0.1	4.2 ± 0.3	9.6 ± 0.4	3.2 ± 0.3	10.5 ± 0.6
118	19.2 ± 0.2	1.9 ± 0.1	0.5 ± 0.1	1.5 ± 0.1	2.4 ± 0.1	5.7 ± 0.2	13.7 ± 0.3	4.9 ± 0.2	11.3 ± 0.4
119	7.0 ± 0.1	1.03 ± 0.07	0.47 ± 0.07	0.92 ± 0.08	1.33 ± 0.08	2.4 ± 0.1	3.0 ± 0.2	0.9 ± 0.1	5.5 ± 0.3
120	4.98 ± 0.09	0.43 ± 0.06	0.15 ± 0.06	0.38 ± 0.06	0.32 ± 0.06	1.5 ± 0.1	3.6 ± 0.2	1.3 ± 0.1	1.6 ± 0.3
121	25.1 ± 0.2	1.7 ± 0.1	0.6 ± 0.1	1.6 ± 0.1	2.5 ± 0.1	7.7 ± 0.5	28.9 ± 0.7	10.4 ± 0.5	16.3 ± 0.6
122	25.2 ± 0.2	2.6 ± 0.1	1.0 ± 0.1	2.4 ± 0.1	3.4 ± 0.1	7.9 ± 0.3	13.0 ± 0.3	4.6 ± 0.3	20.5 ± 0.5
123	3.40 ± 0.07	0.52 ± 0.07	0.28 ± 0.07	0.42 ± 0.07	0.70 ± 0.07	1.0 ± 0.1	0.8 ± 0.1	0.4 ± 0.1	2.5 ± 0.3
124	7.6 ± 0.1	0.70 ± 0.07	0.25 ± 0.06	0.57 ± 0.07	0.90 ± 0.07	2.4 ± 0.1	4.7 ± 0.2	1.5 ± 0.1	5.1 ± 0.3
125	28.0 ± 0.2	2.5 ± 0.1	0.8 ± 0.1	1.7 ± 0.1	2.6 ± 0.1	7.9 ± 0.4	17.1 ± 0.5	6.3 ± 0.4	12.8 ± 0.9
126	50.7 ± 0.3	5.1 ± 0.2	1.7 ± 0.2	3.2 ± 0.2	4.6 ± 0.2	15.3 ± 0.5	24.1 ± 0.6	8.5 ± 0.5	38.0 ± 0.8
127	44.0 ± 0.3	3.5 ± 0.2	1.2 ± 0.2	2.4 ± 0.2	3.5 ± 0.2	14.3 ± 0.6	38.4 ± 0.8	13.8 ± 0.6	23.5 ± 0.6
128	22.1 ± 0.2	2.2 ± 0.1	0.7 ± 0.1	2.0 ± 0.1	2.9 ± 0.1	7.9 ± 0.3	16.4 ± 0.4	5.9 ± 0.3	17.7 ± 0.4
129	45.0 ± 0.3	3.9 ± 0.2	1.3 ± 0.2	2.3 ± 0.2	3.5 ± 0.2	13.5 ± 0.7	28.5 ± 0.9	10.4 ± 0.7	22 ± 1
130	13.6 ± 0.1	1.08 ± 0.08	0.40 ± 0.08	0.84 ± 0.08	1.23 ± 0.08	4.3 ± 0.2	9.5 ± 0.2	3.5 ± 0.2	8.5 ± 0.3
131	3.80 ± 0.09	0.54 ± 0.06	0.30 ± 0.06	0.51 ± 0.07	0.84 ± 0.07	1.0 ± 0.1	1.5 ± 0.1	0.51 ± 0.09	2.4 ± 0.3

Corrected flux values with the local background of the emission regions in the catalogue from this study. The measured fluxes of the nine emission lines for the detected emission regions are presented. These fluxes are corrected for the local background, which includes the local emission and the stellar population (described in Section 2.6.7), and the extinction (described in Section 2.6.8). These flux are obtained by subtracting the background spectrum, instead of the background flux measured for each line (methodology used in this study), as discussed in Section 2.6.7. The uncertainties correspond to the propagated uncertainties (described in Section 2.6.4). All flux values are scaled by 1×10^{-15} .

ID	$H\alpha$ [erg s ⁻¹ cm ⁻²]	[N II] $\lambda 6583$ [erg s ⁻¹ cm ⁻²]	[N II] $\lambda 6548$ [erg s ⁻¹ cm ⁻²]	[S II] $\lambda 6731$ [erg s ⁻¹ cm ⁻²]	[S II] $\lambda 6716$ [erg s ⁻¹ cm ⁻²]	$H\beta$ [erg s ⁻¹ cm ⁻²]	[O III] $\lambda 5007$ [erg s ⁻¹ cm ⁻²]	[O III] $\lambda 4959$ [erg s ⁻¹ cm ⁻²]	[O II] $\lambda 3727$ [erg s ⁻¹ cm ⁻²]
132	17.9 ± 0.1	2.20 ± 0.09	0.67 ± 0.08	1.81 ± 0.09	2.62 ± 0.09	6.2 ± 0.2	7.8 ± 0.2	2.7 ± 0.1	17.5 ± 0.5
133	19.7 ± 0.1	2.47 ± 0.09	0.72 ± 0.09	1.85 ± 0.09	2.70 ± 0.09	6.3 ± 0.2	6.5 ± 0.2	2.3 ± 0.2	20.4 ± 0.5
134	9.3 ± 0.1	0.84 ± 0.09	0.35 ± 0.08	0.92 ± 0.09	1.37 ± 0.09	2.7 ± 0.1	4.2 ± 0.2	1.6 ± 0.1	6.5 ± 0.5
135	12.3 ± 0.1	1.46 ± 0.07	0.51 ± 0.07	1.16 ± 0.08	1.81 ± 0.08	4.0 ± 0.1	3.7 ± 0.1	1.3 ± 0.1	11.3 ± 0.4
136	35.4 ± 0.2	4.0 ± 0.2	1.3 ± 0.2	2.8 ± 0.2	4.1 ± 0.2	11.4 ± 0.4	22.3 ± 0.5	8.1 ± 0.4	22.2 ± 0.5
137	26.9 ± 0.4	3.9 ± 0.3	1.1 ± 0.2	3.2 ± 0.3	5.2 ± 0.3	9.0 ± 0.5	13.3 ± 0.6	4.6 ± 0.5	31 ± 1
138	95.6 ± 0.7	6.0 ± 0.4	2.0 ± 0.4	3.4 ± 0.5	5.3 ± 0.5	32 ± 1	85 ± 2	30 ± 1	48 ± 1
139	6.07 ± 0.08	0.87 ± 0.06	0.20 ± 0.05	0.66 ± 0.06	1.00 ± 0.06	2.18 ± 0.08	1.39 ± 0.07	0.31 ± 0.06	7.0 ± 0.2
140	3.16 ± 0.06	0.40 ± 0.04	0.03 ± 0.04	0.31 ± 0.04	0.47 ± 0.04	0.95 ± 0.07	0.77 ± 0.07	0.24 ± 0.06	2.6 ± 0.1
141	8.00 ± 0.07	0.57 ± 0.05	0.27 ± 0.05	0.54 ± 0.05	0.73 ± 0.05	2.5 ± 0.1	3.4 ± 0.1	1.17 ± 0.09	6.2 ± 0.2
142	1.15 ± 0.06	0.16 ± 0.04	0.05 ± 0.04	0.11 ± 0.04	0.15 ± 0.04	0.33 ± 0.07	0.16 ± 0.06	0.10 ± 0.06	0.7 ± 0.1
143	119.5 ± 0.7	6.0 ± 0.5	1.5 ± 0.5	3.7 ± 0.5	5.4 ± 0.5	38 ± 2	102 ± 2	36 ± 2	57 ± 1
144	8.1 ± 0.1	0.97 ± 0.07	0.27 ± 0.07	0.81 ± 0.07	1.25 ± 0.07	2.6 ± 0.1	3.0 ± 0.1	0.9 ± 0.1	8.2 ± 0.3
145	1.47 ± 0.07	0.19 ± 0.05	0.00 ± 0.05	0.08 ± 0.05	0.18 ± 0.05	0.50 ± 0.04	0.57 ± 0.04	0.18 ± 0.04	1.4 ± 0.1
146	4.01 ± 0.09	0.39 ± 0.06	-0.03 ± 0.06	0.20 ± 0.06	0.38 ± 0.06	1.29 ± 0.07	1.96 ± 0.08	0.75 ± 0.07	3.5 ± 0.2
147	13.5 ± 0.1	1.47 ± 0.09	0.55 ± 0.09	1.06 ± 0.09	1.69 ± 0.09	4.6 ± 0.1	2.4 ± 0.1	0.8 ± 0.1	10.7 ± 0.3
148	31.1 ± 0.2	1.8 ± 0.1	0.8 ± 0.1	1.0 ± 0.1	1.6 ± 0.1	10.6 ± 0.5	30.8 ± 0.7	10.8 ± 0.5	19.2 ± 0.5
149	2.69 ± 0.05	0.23 ± 0.03	0.12 ± 0.03	0.21 ± 0.04	0.20 ± 0.04	0.90 ± 0.05	1.42 ± 0.06	0.53 ± 0.05	2.6 ± 0.1
150	10.7 ± 0.1	1.21 ± 0.08	0.38 ± 0.08	0.87 ± 0.09	1.19 ± 0.09	3.0 ± 0.1	5.9 ± 0.2	2.2 ± 0.1	7.4 ± 0.3
151	26.6 ± 0.2	3.6 ± 0.1	1.1 ± 0.1	3.0 ± 0.1	4.1 ± 0.1	8.7 ± 0.3	18.7 ± 0.5	6.7 ± 0.3	22.8 ± 0.5
152	1.22 ± 0.04	0.08 ± 0.03	0.00 ± 0.03	0.20 ± 0.03	0.20 ± 0.03	0.33 ± 0.04	0.13 ± 0.03	0.11 ± 0.03	0.9 ± 0.1
153	3.5 ± 0.1	0.35 ± 0.08	0.02 ± 0.08	0.19 ± 0.09	0.47 ± 0.09	1.0 ± 0.1	0.9 ± 0.1	0.09 ± 0.09	1.8 ± 0.3

Corrected flux values with the local background of the emission regions in the catalogue from this study. The measured fluxes of the nine emission lines for the detected emission regions are presented. These fluxes are corrected for the local background, which includes the local emission and the stellar population (described in Section 2.6.7), and the extinction (described in Section 2.6.8). These flux are obtained by subtracting the background spectrum, instead of the background flux measured for each line (methodology used in this study), as discussed in Section 2.6.7. The uncertainties correspond to the propagated uncertainties (described in Section 2.6.4). All flux values are scaled by 1×10^{-15} .

ID	$H\alpha$ [erg s ⁻¹ cm ⁻²]	[N II] $\lambda 6583$ [erg s ⁻¹ cm ⁻²]	[N II] $\lambda 6548$ [erg s ⁻¹ cm ⁻²]	[S II] $\lambda 6731$ [erg s ⁻¹ cm ⁻²]	[S II] $\lambda 6716$ [erg s ⁻¹ cm ⁻²]	$H\beta$ [erg s ⁻¹ cm ⁻²]	[O III] $\lambda 5007$ [erg s ⁻¹ cm ⁻²]	[O III] $\lambda 4959$ [erg s ⁻¹ cm ⁻²]	[O II] $\lambda 3727$ [erg s ⁻¹ cm ⁻²]
154	3.8 ± 0.1	0.5 ± 0.1	0.22 ± 0.09	0.5 ± 0.1	0.5 ± 0.1	0.94 ± 0.09	1.7 ± 0.1	0.64 ± 0.09	2.1 ± 0.2
155	136.7 ± 0.8	14.1 ± 0.5	5.0 ± 0.5	9.0 ± 0.5	12.8 ± 0.5	46 ± 2	99 ± 2	35 ± 2	100 ± 2
156	5.3 ± 0.1	0.65 ± 0.08	0.27 ± 0.07	0.71 ± 0.08	0.96 ± 0.08	1.30 ± 0.08	2.4 ± 0.1	0.76 ± 0.08	3.1 ± 0.3
157	70.8 ± 0.5	3.9 ± 0.4	1.1 ± 0.4	2.1 ± 0.4	3.5 ± 0.4	21.2 ± 0.9	58 ± 1	19.8 ± 0.9	31.5 ± 0.9
158	25.4 ± 0.2	3.7 ± 0.1	1.2 ± 0.1	2.9 ± 0.1	4.1 ± 0.1	8.8 ± 0.3	15.4 ± 0.4	5.5 ± 0.3	23.1 ± 0.5
159	54 ± 1	2.9 ± 0.9	0.7 ± 0.9	1 ± 1	2 ± 1	18 ± 1	44 ± 2	16 ± 1	36 ± 2
160	8.2 ± 0.2	0.8 ± 0.1	0.4 ± 0.1	0.8 ± 0.1	1.2 ± 0.1	2.7 ± 0.1	5.3 ± 0.2	1.9 ± 0.1	5.4 ± 0.3
161	1.7 ± 0.1	0.40 ± 0.08	0.05 ± 0.08	0.09 ± 0.09	0.51 ± 0.09	0.6 ± 0.1	0.4 ± 0.1	0.0 ± 0.1	2.9 ± 0.5
162	272 ± 1	24.3 ± 0.8	8.0 ± 0.8	15.9 ± 0.9	23.2 ± 0.9	87 ± 3	182 ± 4	64 ± 3	175 ± 4
163	1.38 ± 0.05	0.12 ± 0.03	0.03 ± 0.03	0.16 ± 0.03	0.24 ± 0.03	0.50 ± 0.06	0.21 ± 0.04	0.01 ± 0.04	0.8 ± 0.1
164	0.65 ± 0.04	0.05 ± 0.03	0.02 ± 0.03	0.08 ± 0.03	0.08 ± 0.03	0.16 ± 0.03	0.19 ± 0.03	0.06 ± 0.03	0.33 ± 0.08
165	22.4 ± 0.2	2.9 ± 0.1	1.0 ± 0.1	1.9 ± 0.1	2.8 ± 0.1	7.6 ± 0.2	9.3 ± 0.3	3.2 ± 0.2	16.2 ± 0.4
166	12.5 ± 0.1	1.20 ± 0.08	0.52 ± 0.08	1.06 ± 0.09	1.68 ± 0.09	4.2 ± 0.2	7.5 ± 0.2	2.4 ± 0.2	11.4 ± 0.3
167	0.42 ± 0.04	-0.01 ± 0.03	0.04 ± 0.03	0.02 ± 0.03	0.01 ± 0.03	0.04 ± 0.03	0.11 ± 0.04	0.04 ± 0.03	0.15 ± 0.05
168	1.75 ± 0.08	0.19 ± 0.05	0.01 ± 0.05	0.35 ± 0.06	0.48 ± 0.06	0.6 ± 0.1	0.42 ± 0.09	0.10 ± 0.08	1.6 ± 0.2
169	24.4 ± 0.2	1.3 ± 0.2	0.5 ± 0.2	1.1 ± 0.2	1.3 ± 0.2	7.0 ± 0.4	26.4 ± 0.5	8.7 ± 0.4	8.7 ± 0.5
170	11.2 ± 0.1	1.29 ± 0.07	0.44 ± 0.06	0.67 ± 0.07	1.11 ± 0.07	3.6 ± 0.1	5.6 ± 0.1	1.9 ± 0.1	6.6 ± 0.2
171	42.0 ± 0.3	4.6 ± 0.2	1.4 ± 0.2	3.9 ± 0.2	5.2 ± 0.2	12.4 ± 0.4	24.4 ± 0.5	8.2 ± 0.4	29.0 ± 0.6
172	20.4 ± 0.2	2.3 ± 0.1	0.6 ± 0.1	2.1 ± 0.1	2.5 ± 0.1	6.4 ± 0.3	14.8 ± 0.4	5.1 ± 0.3	13.8 ± 0.4
173	16.7 ± 0.3	2.4 ± 0.2	0.4 ± 0.2	2.8 ± 0.2	3.4 ± 0.2	6.4 ± 0.3	17.5 ± 0.4	5.8 ± 0.3	19.7 ± 0.5
174	7.88 ± 0.09	0.85 ± 0.06	0.26 ± 0.06	0.63 ± 0.07	0.89 ± 0.07	2.1 ± 0.1	5.7 ± 0.2	1.9 ± 0.1	5.2 ± 0.3
175	235 ± 1	17.8 ± 0.8	5.8 ± 0.8	11.5 ± 0.9	16.2 ± 0.9	74 ± 3	200 ± 4	67 ± 3	124 ± 3

Corrected flux values with the local background of the emission regions in the catalogue from this study. The measured fluxes of the nine emission lines for the detected emission regions are presented. These fluxes are corrected for the local background, which includes the local emission and the stellar population (described in Section 2.6.7), and the extinction (described in Section 2.6.8). These flux are obtained by subtracting the background spectrum, instead of the background flux measured for each line (methodology used in this study), as discussed in Section 2.6.7. The uncertainties correspond to the propagated uncertainties (described in Section 2.6.4). All flux values are scaled by 1×10^{-15} .

ID	$H\alpha$ [erg s ⁻¹ cm ⁻²]	[N II] $\lambda 6583$ [erg s ⁻¹ cm ⁻²]	[N II] $\lambda 6548$ [erg s ⁻¹ cm ⁻²]	[S II] $\lambda 6731$ [erg s ⁻¹ cm ⁻²]	[S II] $\lambda 6716$ [erg s ⁻¹ cm ⁻²]	$H\beta$ [erg s ⁻¹ cm ⁻²]	[O III] $\lambda 5007$ [erg s ⁻¹ cm ⁻²]	[O III] $\lambda 4959$ [erg s ⁻¹ cm ⁻²]	[O II] $\lambda 3727$ [erg s ⁻¹ cm ⁻²]
176	1.26 ± 0.06	0.19 ± 0.04	0.02 ± 0.04	-0.01 ± 0.04	0.15 ± 0.04	0.35 ± 0.06	0.05 ± 0.06	0.8 ± 0.2	
177	12.1 ± 0.1	1.17 ± 0.08	0.47 ± 0.08	0.89 ± 0.08	1.24 ± 0.08	3.4 ± 0.1	5.8 ± 0.2	1.8 ± 0.1	8.9 ± 0.3
178	10.3 ± 0.1	0.76 ± 0.07	0.19 ± 0.07	0.44 ± 0.07	0.68 ± 0.07	1.9 ± 0.1	6.2 ± 0.2	1.9 ± 0.1	1.4 ± 0.3
179	8.5 ± 0.1	1.34 ± 0.08	0.51 ± 0.08	1.11 ± 0.08	1.37 ± 0.08	2.5 ± 0.2	3.8 ± 0.2	1.1 ± 0.1	4.3 ± 0.3
180	28.1 ± 0.2	3.0 ± 0.1	1.1 ± 0.1	2.1 ± 0.1	3.0 ± 0.1	8.6 ± 0.3	9.2 ± 0.3	3.0 ± 0.2	21.0 ± 0.5
181	11.5 ± 0.1	1.4 ± 0.1	0.45 ± 0.09	1.4 ± 0.1	1.9 ± 0.1	4.6 ± 0.3	3.4 ± 0.3	1.0 ± 0.2	8.5 ± 0.3
182	7.05 ± 0.07	0.94 ± 0.05	0.27 ± 0.05	0.83 ± 0.05	1.17 ± 0.05	1.95 ± 0.09	1.08 ± 0.08	0.32 ± 0.07	4.4 ± 0.2
183	1.25 ± 0.06	0.23 ± 0.04	0.07 ± 0.04	0.15 ± 0.04	0.25 ± 0.04	0.37 ± 0.06	0.20 ± 0.05	0.06 ± 0.04	1.3 ± 0.1
184	4.19 ± 0.06	0.47 ± 0.04	0.18 ± 0.04	0.35 ± 0.04	0.43 ± 0.04	1.12 ± 0.07	1.43 ± 0.08	0.39 ± 0.06	2.3 ± 0.2
185	58.0 ± 0.4	4.7 ± 0.3	1.7 ± 0.3	3.0 ± 0.3	4.3 ± 0.3	16.8 ± 0.7	46.9 ± 0.9	15.2 ± 0.7	23.4 ± 0.6
186	0.29 ± 0.02	0.01 ± 0.02	0.02 ± 0.02	0.02 ± 0.02	0.05 ± 0.02	0.19 ± 0.04	0.13 ± 0.04	0.01 ± 0.03	0.20 ± 0.06
187	1.73 ± 0.06	0.16 ± 0.04	0.03 ± 0.04	0.25 ± 0.05	0.27 ± 0.05	0.42 ± 0.05	0.47 ± 0.06	0.24 ± 0.06	1.3 ± 0.2
188	0.54 ± 0.03	0.04 ± 0.03	0.03 ± 0.03	0.02 ± 0.03	0.08 ± 0.03	0.09 ± 0.04	0.25 ± 0.04	0.05 ± 0.04	0.4 ± 0.1
189	1.12 ± 0.08	0.16 ± 0.05	0.04 ± 0.05	0.10 ± 0.06	0.17 ± 0.06	0.36 ± 0.09	-0.04 ± 0.06	-0.02 ± 0.06	1.2 ± 0.2
190	0.78 ± 0.04	0.11 ± 0.03	-0.02 ± 0.03	0.11 ± 0.03	0.09 ± 0.03	0.28 ± 0.07	0.12 ± 0.05	-0.04 ± 0.05	0.9 ± 0.2
191	19.0 ± 0.1	2.5 ± 0.1	0.7 ± 0.1	2.0 ± 0.1	2.8 ± 0.1	5.7 ± 0.2	5.1 ± 0.2	1.6 ± 0.2	14.9 ± 0.5
192	28.0 ± 0.3	3.9 ± 0.2	1.2 ± 0.2	3.3 ± 0.2	4.4 ± 0.2	9.7 ± 0.3	13.3 ± 0.4	4.3 ± 0.3	23.7 ± 0.8
193	2.65 ± 0.08	0.15 ± 0.05	0.05 ± 0.05	0.08 ± 0.06	0.23 ± 0.06	1.0 ± 0.1	1.3 ± 0.1	0.42 ± 0.08	2.3 ± 0.2
196	0.82 ± 0.04	0.07 ± 0.02	0.05 ± 0.02	0.06 ± 0.03	0.13 ± 0.03	0.23 ± 0.05	0.03 ± 0.04	-0.03 ± 0.04	0.8 ± 0.1
197	16.6 ± 0.1	1.13 ± 0.09	0.45 ± 0.09	0.8 ± 0.1	1.1 ± 0.1	4.8 ± 0.2	14.7 ± 0.3	4.9 ± 0.2	7.5 ± 0.3
198	17.7 ± 0.2	2.6 ± 0.2	0.9 ± 0.2	2.7 ± 0.2	4.1 ± 0.2	5.2 ± 0.3	5.7 ± 0.3	1.9 ± 0.2	14.4 ± 0.6
199	10.2 ± 0.2	1.3 ± 0.1	0.4 ± 0.1	1.4 ± 0.1	1.7 ± 0.1	3.8 ± 0.2	5.6 ± 0.2	1.7 ± 0.2	8.8 ± 0.4

Corrected flux values with the local background of the emission regions in the catalogue from this study. The measured fluxes of the nine emission lines for the detected emission regions are presented. These fluxes are corrected for the local background, which includes the local emission and the stellar population (described in Section 2.6.7), and the extinction (described in Section 2.6.8). These flux are obtained by subtracting the background spectrum, instead of the background flux measured for each line (methodology used in this study), as discussed in Section 2.6.7. The uncertainties correspond to the propagated uncertainties (described in Section 2.6.4). All flux values are scaled by 1×10^{-15} .

ID	$H\alpha$ [$\text{erg s}^{-1} \text{cm}^{-2}$]	$[\text{N II}] \lambda 6583$ [$\text{erg s}^{-1} \text{cm}^{-2}$]	$[\text{N II}] \lambda 6548$ [$\text{erg s}^{-1} \text{cm}^{-2}$]	$[\text{S II}] \lambda 6731$ [$\text{erg s}^{-1} \text{cm}^{-2}$]	$[\text{S II}] \lambda 6716$ [$\text{erg s}^{-1} \text{cm}^{-2}$]	$\text{H}\beta$ [$\text{erg s}^{-1} \text{cm}^{-2}$]	$[\text{O III}] \lambda 5007$ [$\text{erg s}^{-1} \text{cm}^{-2}$]	$[\text{O III}] \lambda 4959$ [$\text{erg s}^{-1} \text{cm}^{-2}$]	$[\text{O II}] \lambda 3727$ [$\text{erg s}^{-1} \text{cm}^{-2}$]
200	33.3 ± 0.7	4.0 ± 0.5	1.8 ± 0.4	4.2 ± 0.5	6.2 ± 0.5	9.0 ± 0.6	14.9 ± 0.7	5.4 ± 0.5	28 ± 1
201	5.1 ± 0.2	0.8 ± 0.1	0.3 ± 0.1	0.7 ± 0.1	1.1 ± 0.1	0.6 ± 0.2	4.0 ± 0.2	1.1 ± 0.2	4.6 ± 0.4
202	12.50 ± 0.09	0.56 ± 0.06	0.20 ± 0.06	0.52 ± 0.07	0.60 ± 0.07	3.6 ± 0.2	16.9 ± 0.3	5.9 ± 0.2	4.8 ± 0.2
203	9.14 ± 0.09	1.02 ± 0.06	0.41 ± 0.06	0.76 ± 0.06	1.03 ± 0.06	2.6 ± 0.1	6.0 ± 0.2	2.1 ± 0.1	7.8 ± 0.2
204	21.3 ± 0.2	2.6 ± 0.1	1.0 ± 0.1	2.2 ± 0.1	3.1 ± 0.1	5.4 ± 0.2	9.3 ± 0.3	3.1 ± 0.2	10.8 ± 0.5
205	1.84 ± 0.05	0.18 ± 0.04	0.15 ± 0.04	0.12 ± 0.04	0.26 ± 0.04	0.63 ± 0.07	0.75 ± 0.08	0.15 ± 0.06	1.7 ± 0.1
206	6.15 ± 0.07	0.59 ± 0.05	0.19 ± 0.05	0.45 ± 0.05	0.75 ± 0.05	2.1 ± 0.1	4.6 ± 0.1	1.6 ± 0.1	5.1 ± 0.2
207	28.8 ± 0.2	3.3 ± 0.1	0.9 ± 0.1	2.5 ± 0.2	3.9 ± 0.2	6.4 ± 0.3	14.8 ± 0.5	5.1 ± 0.3	12.4 ± 0.7
208	46.0 ± 0.4	6.9 ± 0.3	2.5 ± 0.3	5.6 ± 0.3	7.7 ± 0.3	13 ± 1	24 ± 1	9 ± 1	38 ± 2
209	2.46 ± 0.07	0.22 ± 0.05	-0.03 ± 0.05	0.18 ± 0.05	0.20 ± 0.05	0.59 ± 0.09	0.40 ± 0.08	0.03 ± 0.07	1.8 ± 0.2
210	25.3 ± 0.2	1.9 ± 0.1	0.6 ± 0.1	1.3 ± 0.1	1.9 ± 0.1	7.3 ± 0.4	24.3 ± 0.5	8.4 ± 0.4	12.7 ± 0.3
211	1.89 ± 0.06	0.19 ± 0.04	0.13 ± 0.04	0.17 ± 0.05	0.33 ± 0.05	0.55 ± 0.07	1.17 ± 0.09	0.41 ± 0.07	2.0 ± 0.2
212	32.6 ± 0.2	2.1 ± 0.1	0.9 ± 0.1	1.3 ± 0.1	2.0 ± 0.1	10.7 ± 0.5	39.4 ± 0.8	13.5 ± 0.5	13.1 ± 0.4
213	12.0 ± 0.1	1.55 ± 0.08	0.53 ± 0.08	1.28 ± 0.09	1.88 ± 0.09	3.8 ± 0.1	7.5 ± 0.2	2.5 ± 0.1	17.0 ± 0.4
214	0.45 ± 0.03	0.01 ± 0.02	0.05 ± 0.02	0.05 ± 0.02	0.09 ± 0.02	0.16 ± 0.07	-0.08 ± 0.06	-0.08 ± 0.06	0.3 ± 0.1
215	4.27 ± 0.09	0.39 ± 0.06	0.21 ± 0.06	0.29 ± 0.06	0.46 ± 0.06	1.59 ± 0.08	2.18 ± 0.09	0.92 ± 0.07	4.2 ± 0.3
216	0.55 ± 0.03	0.04 ± 0.02	0.02 ± 0.02	0.05 ± 0.02	0.07 ± 0.02	0.20 ± 0.03	0.52 ± 0.04	0.12 ± 0.03	0.60 ± 0.09
217	1.23 ± 0.04	0.15 ± 0.03	0.09 ± 0.03	0.18 ± 0.03	0.22 ± 0.03	0.34 ± 0.04	0.83 ± 0.05	0.24 ± 0.04	1.2 ± 0.1
218	0.93 ± 0.03	0.06 ± 0.02	0.02 ± 0.02	0.15 ± 0.02	0.11 ± 0.02	0.22 ± 0.02	0.55 ± 0.02	0.19 ± 0.02	0.7 ± 0.1
219	20.9 ± 0.2	2.2 ± 0.1	0.7 ± 0.1	2.0 ± 0.1	2.8 ± 0.1	6.7 ± 0.2	14.7 ± 0.3	5.0 ± 0.2	19.7 ± 0.4
220	88.6 ± 0.7	7.8 ± 0.5	2.8 ± 0.5	5.3 ± 0.5	7.5 ± 0.5	21.4 ± 0.9	54 ± 1	18.6 ± 0.9	37.2 ± 0.9
221	17.5 ± 0.3	1.4 ± 0.2	0.3 ± 0.2	0.7 ± 0.2	1.4 ± 0.2	2.9 ± 0.3	8.0 ± 0.4	2.7 ± 0.3	6.2 ± 0.6

Corrected flux values with the local background of the emission regions in the catalogue from this study. The measured fluxes of the nine emission lines for the detected emission regions are presented. These fluxes are corrected for the local background, which includes the local emission and the stellar population (described in Section 2.6.7), and the extinction (described in Section 2.6.8). These flux are obtained by subtracting the background spectrum, instead of the background flux measured for each line (methodology used in this study), as discussed in Section 2.6.7. The uncertainties correspond to the propagated uncertainties (described in Section 2.6.4). All flux values are scaled by 1×10^{-15} .

ID	$H\alpha$ [erg s $^{-1}$ cm $^{-2}$]	[N II] $\lambda 6583$ [erg s $^{-1}$ cm $^{-2}$]	[N II] $\lambda 6548$ [erg s $^{-1}$ cm $^{-2}$]	[S II] $\lambda 6731$ [erg s $^{-1}$ cm $^{-2}$]	[S II] $\lambda 6716$ [erg s $^{-1}$ cm $^{-2}$]	$H\beta$ [erg s $^{-1}$ cm $^{-2}$]	[O III] $\lambda 5007$ [erg s $^{-1}$ cm $^{-2}$]	[O III] $\lambda 4959$ [erg s $^{-1}$ cm $^{-2}$]	[O II] $\lambda 3727$ [erg s $^{-1}$ cm $^{-2}$]
222	1.13 ± 0.04	0.11 ± 0.03	0.04 ± 0.03	0.14 ± 0.03	0.22 ± 0.03	0.40 ± 0.05	0.86 ± 0.06	0.26 ± 0.04	1.1 ± 0.2
223	2.39 ± 0.08	0.38 ± 0.06	0.15 ± 0.05	0.45 ± 0.06	0.63 ± 0.06	0.62 ± 0.09	0.60 ± 0.09	0.16 ± 0.07	2.4 ± 0.3
224	4.4 ± 0.1	0.8 ± 0.1	0.2 ± 0.1	1.1 ± 0.1	1.2 ± 0.1	1.4 ± 0.2	1.4 ± 0.2	0.4 ± 0.2	5.9 ± 0.5
225	3.1 ± 0.1	0.43 ± 0.08	0.14 ± 0.08	0.33 ± 0.08	0.47 ± 0.08	1.2 ± 0.1	1.1 ± 0.1	0.3 ± 0.1	2.8 ± 0.3
226	0.70 ± 0.03	0.06 ± 0.02	0.04 ± 0.02	0.04 ± 0.02	0.11 ± 0.02	0.17 ± 0.03	0.12 ± 0.02	0.06 ± 0.02	0.52 ± 0.06
227	20.9 ± 0.3	3.4 ± 0.2	1.2 ± 0.2	2.4 ± 0.2	3.5 ± 0.2	4.0 ± 0.3	9.5 ± 0.4	3.0 ± 0.3	9.8 ± 0.5
228	2.14 ± 0.06	0.06 ± 0.04	0.02 ± 0.04	0.28 ± 0.04	0.33 ± 0.04	0.69 ± 0.05	1.54 ± 0.07	0.45 ± 0.05	1.5 ± 0.2
229	3.90 ± 0.08	0.36 ± 0.05	0.16 ± 0.05	0.31 ± 0.06	0.73 ± 0.06	1.0 ± 0.1	0.80 ± 0.09	0.28 ± 0.08	3.0 ± 0.3
230	0.55 ± 0.03	0.06 ± 0.02	-0.01 ± 0.02	0.06 ± 0.02	0.08 ± 0.02	0.17 ± 0.02	0.23 ± 0.02	0.11 ± 0.02	0.61 ± 0.08
231	4.5 ± 0.1	0.61 ± 0.07	0.14 ± 0.07	0.34 ± 0.07	0.30 ± 0.07	1.3 ± 0.1	0.8 ± 0.1	0.1 ± 0.1	4.0 ± 0.3
232	45.2 ± 0.3	2.9 ± 0.2	1.3 ± 0.2	2.0 ± 0.2	3.3 ± 0.2	13.3 ± 0.9	60 ± 1	20.9 ± 0.9	14.8 ± 0.6
233	5.97 ± 0.06	0.45 ± 0.04	0.19 ± 0.04	0.29 ± 0.05	0.35 ± 0.05	1.71 ± 0.08	3.7 ± 0.1	1.23 ± 0.08	3.2 ± 0.1
234	120 ± 1	12.3 ± 0.7	3.9 ± 0.7	9.9 ± 0.7	12.7 ± 0.7	31 ± 1	91 ± 2	31 ± 1	67 ± 2
235	2.62 ± 0.08	0.28 ± 0.05	0.08 ± 0.05	0.21 ± 0.05	0.25 ± 0.05	0.87 ± 0.07	1.03 ± 0.08	0.38 ± 0.06	2.2 ± 0.2
236	1.55 ± 0.08	0.10 ± 0.05	0.12 ± 0.05	0.10 ± 0.05	0.19 ± 0.05	0.49 ± 0.08	0.7 ± 0.1	0.30 ± 0.08	1.5 ± 0.4
237	9.42 ± 0.09	0.48 ± 0.06	0.25 ± 0.06	0.46 ± 0.06	0.54 ± 0.06	3.0 ± 0.1	9.0 ± 0.2	3.1 ± 0.1	6.1 ± 0.2
238	185 ± 1	24 ± 1	8 ± 1	16 ± 1	19 ± 1	50 ± 3	103 ± 4	37 ± 3	114 ± 4
239	4.81 ± 0.08	0.29 ± 0.05	0.10 ± 0.05	0.53 ± 0.05	0.70 ± 0.05	1.4 ± 0.1	7.6 ± 0.2	2.5 ± 0.1	2.9 ± 0.2
240	0.68 ± 0.03	0.07 ± 0.02	0.04 ± 0.02	0.04 ± 0.02	0.07 ± 0.02	0.20 ± 0.03	0.21 ± 0.03	0.12 ± 0.03	0.44 ± 0.08
241	20.6 ± 0.1	1.4 ± 0.1	0.7 ± 0.1	1.2 ± 0.1	1.7 ± 0.1	6.5 ± 0.3	20.7 ± 0.5	7.1 ± 0.3	14.6 ± 0.4
242	68.4 ± 0.4	7.8 ± 0.3	2.6 ± 0.3	6.5 ± 0.3	9.4 ± 0.3	18.1 ± 0.8	46 ± 1	15.7 ± 0.8	41 ± 1
243	0.69 ± 0.04	0.11 ± 0.03	0.01 ± 0.03	0.07 ± 0.03	0.14 ± 0.03	0.30 ± 0.03	0.30 ± 0.03	0.07 ± 0.03	0.6 ± 0.1

Corrected flux values with the local background of the emission regions in the catalogue from this study. The measured fluxes of the nine emission lines for the detected emission regions are presented. These fluxes are corrected for the local background, which includes the local emission and the stellar population (described in Section 2.6.7), and the extinction (described in Section 2.6.8). These flux are obtained by subtracting the background spectrum, instead of the background flux measured for each line (methodology used in this study), as discussed in Section 2.6.7. The uncertainties correspond to the propagated uncertainties (described in Section 2.6.4). All flux values are scaled by 1×10^{-15} .

ID	$H\alpha$ [erg s ⁻¹ cm ⁻²]	[N II] $\lambda 6583$ [erg s ⁻¹ cm ⁻²]	[N II] $\lambda 6548$ [erg s ⁻¹ cm ⁻²]	[S II] $\lambda 6731$ [erg s ⁻¹ cm ⁻²]	[S II] $\lambda 6716$ [erg s ⁻¹ cm ⁻²]	$H\beta$ [erg s ⁻¹ cm ⁻²]	[O III] $\lambda 5007$ [erg s ⁻¹ cm ⁻²]	[O III] $\lambda 4959$ [erg s ⁻¹ cm ⁻²]	[O II] $\lambda 3727$ [erg s ⁻¹ cm ⁻²]
244	76.7 ± 0.5	7.8 ± 0.3	2.5 ± 0.3	5.7 ± 0.3	7.9 ± 0.3	23 ± 1	63 ± 1	22 ± 1	44 ± 1
245	1.03 ± 0.04	0.05 ± 0.03	0.04 ± 0.03	0.10 ± 0.03	0.16 ± 0.03	0.27 ± 0.06	0.03 ± 0.04	0.07 ± 0.05	0.4 ± 0.1
246	1.16 ± 0.06	0.16 ± 0.04	0.07 ± 0.04	0.15 ± 0.04	0.10 ± 0.04	0.31 ± 0.08	0.26 ± 0.08	0.19 ± 0.07	0.7 ± 0.2
247	20.5 ± 0.2	2.9 ± 0.1	0.9 ± 0.1	2.0 ± 0.1	2.8 ± 0.1	6.8 ± 0.3	20.9 ± 0.4	7.2 ± 0.3	15.0 ± 0.4
248	0.89 ± 0.05	0.08 ± 0.03	0.05 ± 0.03	0.15 ± 0.03	0.18 ± 0.03	0.30 ± 0.03	0.16 ± 0.04	0.02 ± 0.04	0.8 ± 0.2
249	23.8 ± 0.2	2.9 ± 0.2	1.2 ± 0.1	2.4 ± 0.2	3.1 ± 0.2	6.1 ± 0.3	20.5 ± 0.5	6.9 ± 0.3	11.0 ± 0.4
250	4.17 ± 0.09	0.49 ± 0.06	0.19 ± 0.06	0.38 ± 0.07	0.59 ± 0.07	1.2 ± 0.1	0.17 ± 0.07	0.12 ± 0.07	2.8 ± 0.2
251	2.92 ± 0.07	0.27 ± 0.05	0.00 ± 0.05	0.47 ± 0.05	0.54 ± 0.05	0.88 ± 0.07	4.0 ± 0.1	1.28 ± 0.07	2.0 ± 0.2
252	2.07 ± 0.05	0.15 ± 0.03	0.13 ± 0.03	0.15 ± 0.03	0.17 ± 0.03	0.72 ± 0.06	1.19 ± 0.08	0.44 ± 0.06	1.1 ± 0.1
253	1.65 ± 0.06	0.10 ± 0.04	0.12 ± 0.04	0.05 ± 0.04	0.08 ± 0.04	0.54 ± 0.06	1.13 ± 0.08	0.48 ± 0.06	1.1 ± 0.1
254	171 ± 1	18.4 ± 0.7	6.2 ± 0.7	11.3 ± 0.8	15.1 ± 0.8	49 ± 2	88 ± 2	30 ± 1	122 ± 2
255	2.90 ± 0.07	0.34 ± 0.05	0.06 ± 0.05	0.45 ± 0.05	0.56 ± 0.05	1.0 ± 0.1	0.8 ± 0.1	0.26 ± 0.09	2.5 ± 0.2
256	1.22 ± 0.05	0.07 ± 0.05	0.12 ± 0.05	0.11 ± 0.05	0.03 ± 0.05	0.39 ± 0.09	0.7 ± 0.1	0.22 ± 0.09	0.7 ± 0.2
257	6.7 ± 0.2	1.2 ± 0.1	0.3 ± 0.1	1.4 ± 0.1	1.9 ± 0.1	1.9 ± 0.2	1.6 ± 0.2	0.2 ± 0.2	6.0 ± 0.4
258	0.63 ± 0.04	0.12 ± 0.03	0.07 ± 0.03	0.06 ± 0.03	0.16 ± 0.03	0.13 ± 0.04	0.17 ± 0.05	0.08 ± 0.04	0.5 ± 0.1
259	14.0 ± 0.1	0.5 ± 0.1	0.26 ± 0.09	0.0 ± 0.1	0.0 ± 0.1	4.4 ± 0.2	12.5 ± 0.3	4.3 ± 0.2	3.9 ± 0.3
260	49 ± 1	4.1 ± 0.8	1.2 ± 0.8	2.4 ± 0.8	3.6 ± 0.8	15.7 ± 0.7	40 ± 1	13.2 ± 0.7	21 ± 1
261	59.8 ± 0.4	4.4 ± 0.3	1.5 ± 0.3	2.8 ± 0.3	4.0 ± 0.3	19.2 ± 0.8	53 ± 1	18.5 ± 0.8	38.2 ± 0.9
262	30.5 ± 0.3	4.6 ± 0.2	1.5 ± 0.2	4.3 ± 0.2	5.8 ± 0.2	9.1 ± 0.3	9.9 ± 0.3	3.2 ± 0.3	30.4 ± 0.7
263	3.45 ± 0.06	0.32 ± 0.04	0.14 ± 0.04	0.43 ± 0.04	0.57 ± 0.04	1.00 ± 0.06	3.67 ± 0.09	1.13 ± 0.07	2.7 ± 0.2
264	3.21 ± 0.09	0.46 ± 0.06	0.17 ± 0.06	0.45 ± 0.06	0.47 ± 0.06	0.86 ± 0.06	0.65 ± 0.07	0.06 ± 0.07	2.5 ± 0.2
265	25.8 ± 0.2	2.9 ± 0.1	1.2 ± 0.1	2.8 ± 0.2	3.9 ± 0.2	8.3 ± 0.4	20.7 ± 0.5	7.2 ± 0.4	17.5 ± 0.6

Corrected flux values with the local background of the emission regions in the catalogue from this study. The measured fluxes of the nine emission lines for the detected emission regions are presented. These fluxes are corrected for the local background, which includes the local emission and the stellar population (described in Section 2.6.7), and the extinction (described in Section 2.6.8). These flux are obtained by subtracting the background spectrum, instead of the background flux measured for each line (methodology used in this study), as discussed in Section 2.6.7. The uncertainties correspond to the propagated uncertainties (described in Section 2.6.4). All flux values are scaled by 1×10^{-15} .

ID	$H\alpha$ [erg s ⁻¹ cm ⁻²]	[N II] $\lambda 6583$ [erg s ⁻¹ cm ⁻²]	[N II] $\lambda 6548$ [erg s ⁻¹ cm ⁻²]	[S II] $\lambda 6731$ [erg s ⁻¹ cm ⁻²]	[S II] $\lambda 6716$ [erg s ⁻¹ cm ⁻²]	$H\beta$ [erg s ⁻¹ cm ⁻²]	[O III] $\lambda 5007$ [erg s ⁻¹ cm ⁻²]	[O III] $\lambda 4959$ [erg s ⁻¹ cm ⁻²]	[O II] $\lambda 3727$ [erg s ⁻¹ cm ⁻²]
266	1.57 ± 0.06	0.07 ± 0.04	0.00 ± 0.04	0.10 ± 0.04	0.07 ± 0.04	0.47 ± 0.05	1.41 ± 0.07	0.53 ± 0.06	1.4 ± 0.2
267	0.82 ± 0.03	0.08 ± 0.02	0.02 ± 0.02	0.12 ± 0.02	0.15 ± 0.02	0.33 ± 0.02	0.90 ± 0.03	0.23 ± 0.02	0.70 ± 0.08
268	2.44 ± 0.05	0.15 ± 0.03	0.10 ± 0.03	0.22 ± 0.03	0.28 ± 0.03	0.74 ± 0.06	2.33 ± 0.08	0.82 ± 0.06	1.5 ± 0.1
269	5.91 ± 0.06	0.41 ± 0.04	0.16 ± 0.04	0.33 ± 0.05	0.37 ± 0.04	1.81 ± 0.09	4.7 ± 0.1	1.57 ± 0.09	3.9 ± 0.2
270	92.1 ± 0.6	4.3 ± 0.4	1.6 ± 0.4	2.4 ± 0.4	2.9 ± 0.4	28 ± 2	118 ± 2	40 ± 2	33 ± 1
271	30.4 ± 0.3	4.3 ± 0.2	1.5 ± 0.2	4.1 ± 0.2	5.6 ± 0.2	7.6 ± 0.4	9.9 ± 0.4	3.1 ± 0.3	23.5 ± 0.7
272	32.0 ± 0.2	3.1 ± 0.1	1.3 ± 0.1	2.0 ± 0.1	2.9 ± 0.1	9.5 ± 0.3	19.5 ± 0.4	6.4 ± 0.3	17.7 ± 0.6
273	1.40 ± 0.06	0.29 ± 0.05	0.09 ± 0.04	0.24 ± 0.05	0.31 ± 0.05	0.43 ± 0.06	0.46 ± 0.06	0.06 ± 0.06	1.5 ± 0.2
274	1.57 ± 0.03	0.06 ± 0.02	0.05 ± 0.02	0.13 ± 0.02	0.13 ± 0.02	0.47 ± 0.04	1.77 ± 0.06	0.65 ± 0.04	0.63 ± 0.09
275	7.30 ± 0.09	0.48 ± 0.06	0.17 ± 0.06	0.68 ± 0.06	0.95 ± 0.06	2.3 ± 0.1	6.2 ± 0.2	2.1 ± 0.1	4.4 ± 0.3
276	43.1 ± 0.2	6.1 ± 0.2	2.2 ± 0.2	5.0 ± 0.2	7.1 ± 0.2	12.9 ± 0.4	17.3 ± 0.4	6.0 ± 0.3	29.7 ± 0.7
277	1.99 ± 0.08	0.32 ± 0.05	0.09 ± 0.05	0.37 ± 0.06	0.41 ± 0.06	0.6 ± 0.1	0.7 ± 0.1	0.24 ± 0.09	1.6 ± 0.2
278	4.3 ± 0.1	0.73 ± 0.07	0.25 ± 0.07	0.58 ± 0.07	0.93 ± 0.07	1.4 ± 0.1	1.2 ± 0.1	0.5 ± 0.1	3.3 ± 0.2
279	16.0 ± 0.1	1.09 ± 0.07	0.45 ± 0.07	0.79 ± 0.08	0.95 ± 0.08	4.3 ± 0.2	10.6 ± 0.2	3.7 ± 0.2	8.6 ± 0.3
280	13.2 ± 0.3	1.1 ± 0.2	0.7 ± 0.2	1.1 ± 0.2	1.6 ± 0.2	4.5 ± 0.2	4.7 ± 0.2	1.6 ± 0.2	5.7 ± 0.3
281	3.02 ± 0.09	0.47 ± 0.06	0.15 ± 0.06	0.44 ± 0.07	0.54 ± 0.07	0.9 ± 0.1	4.4 ± 0.2	1.5 ± 0.1	3.1 ± 0.3
282	0.87 ± 0.05	0.05 ± 0.03	0.02 ± 0.03	0.11 ± 0.03	0.16 ± 0.03	0.24 ± 0.04	-0.02 ± 0.04	-0.02 ± 0.04	0.6 ± 0.1
283	17.2 ± 0.7	2.7 ± 0.5	1.0 ± 0.5	2.8 ± 0.5	4.2 ± 0.5	5.9 ± 0.4	12.0 ± 0.5	4.4 ± 0.4	21.9 ± 0.8
284	27.6 ± 0.2	2.3 ± 0.1	0.6 ± 0.1	1.4 ± 0.1	2.0 ± 0.1	8.4 ± 0.3	19.2 ± 0.4	6.5 ± 0.3	17.4 ± 0.6
285	23.4 ± 0.2	2.9 ± 0.1	1.0 ± 0.1	2.0 ± 0.1	3.0 ± 0.1	7.6 ± 0.3	15.7 ± 0.3	5.5 ± 0.3	18.3 ± 0.7
286	0.65 ± 0.05	0.04 ± 0.04	0.04 ± 0.04	0.13 ± 0.04	0.13 ± 0.03	0.23 ± 0.03	0.09 ± 0.04	0.04 ± 0.03	0.9 ± 0.2
287	38.6 ± 0.3	5.2 ± 0.2	1.5 ± 0.2	4.4 ± 0.2	6.2 ± 0.2	12.6 ± 0.4	23.6 ± 0.5	8.1 ± 0.4	31.9 ± 0.8

Corrected flux values with the local background of the emission regions in the catalogue from this study. The measured fluxes of the nine emission lines for the detected emission regions are presented. These fluxes are corrected for the local background, which includes the local emission and the stellar population (described in Section 2.6.7), and the extinction (described in Section 2.6.8). These flux are obtained by subtracting the background spectrum, instead of the background flux measured for each line (methodology used in this study), as discussed in Section 2.6.7. The uncertainties correspond to the propagated uncertainties (described in Section 2.6.4). All flux values are scaled by 1×10^{-15} .

ID	$H\alpha$ [erg s $^{-1}$ cm $^{-2}$]	[N II] $\lambda 6583$ [erg s $^{-1}$ cm $^{-2}$]	[N II] $\lambda 6548$ [erg s $^{-1}$ cm $^{-2}$]	[S II] $\lambda 6731$ [erg s $^{-1}$ cm $^{-2}$]	[S II] $\lambda 6716$ [erg s $^{-1}$ cm $^{-2}$]	$H\beta$ [erg s $^{-1}$ cm $^{-2}$]	[O III] $\lambda 5007$ [erg s $^{-1}$ cm $^{-2}$]	[O III] $\lambda 4959$ [erg s $^{-1}$ cm $^{-2}$]	[O II] $\lambda 3727$ [erg s $^{-1}$ cm $^{-2}$]
288	11.7 ± 0.2	1.5 ± 0.1	0.5 ± 0.1	1.2 ± 0.1	1.7 ± 0.1	4.4 ± 0.3	9.1 ± 0.4	2.9 ± 0.3	13.5 ± 0.6
289	0.62 ± 0.04	0.98 ± 0.03	0.03 ± 0.03	0.09 ± 0.03	0.14 ± 0.03	0.16 ± 0.03	0.03 ± 0.04	-0.03 ± 0.04	0.7 ± 0.1
290	26.9 ± 0.3	2.7 ± 0.2	0.9 ± 0.2	2.4 ± 0.2	3.8 ± 0.2	9.8 ± 0.4	23.7 ± 0.5	8.0 ± 0.4	19.1 ± 0.5
291	0.87 ± 0.05	0.07 ± 0.04	0.02 ± 0.04	0.09 ± 0.04	0.11 ± 0.04	0.22 ± 0.08	-0.04 ± 0.06	-0.04 ± 0.06	0.7 ± 0.2
292	10.5 ± 0.3	1.9 ± 0.2	0.6 ± 0.2	1.6 ± 0.2	2.2 ± 0.2	2.4 ± 0.4	5.1 ± 0.5	1.3 ± 0.4	9.5 ± 0.8
293	4.7 ± 0.1	0.60 ± 0.07	0.14 ± 0.07	0.72 ± 0.08	0.96 ± 0.08	1.1 ± 0.1	0.5 ± 0.1	0.2 ± 0.1	4.0 ± 0.3
294	1.17 ± 0.05	0.21 ± 0.03	0.05 ± 0.03	0.12 ± 0.04	0.24 ± 0.04	0.29 ± 0.04	0.17 ± 0.04	0.10 ± 0.04	0.8 ± 0.1
295	0.74 ± 0.04	0.11 ± 0.03	-0.01 ± 0.03	0.06 ± 0.03	0.18 ± 0.03	0.28 ± 0.05	0.06 ± 0.03	0.01 ± 0.03	0.7 ± 0.1
296	4.5 ± 0.1	0.75 ± 0.09	0.21 ± 0.09	0.89 ± 0.09	1.32 ± 0.09	1.7 ± 0.2	1.3 ± 0.2	0.4 ± 0.1	4.2 ± 0.3
297	0.47 ± 0.03	0.03 ± 0.02	0.00 ± 0.02	0.09 ± 0.02	0.08 ± 0.02	0.18 ± 0.08	-0.05 ± 0.05	0.07 ± 0.06	0.59 ± 0.09
298	42.9 ± 0.4	4.2 ± 0.2	1.4 ± 0.2	3.3 ± 0.3	4.3 ± 0.3	13.8 ± 0.8	35 ± 1	11.9 ± 0.8	29 ± 1
299	2.78 ± 0.04	0.19 ± 0.03	0.11 ± 0.03	0.13 ± 0.03	0.18 ± 0.03	0.69 ± 0.04	1.54 ± 0.06	0.50 ± 0.04	2.2 ± 0.1
300	1.17 ± 0.04	0.05 ± 0.03	0.03 ± 0.03	0.06 ± 0.03	0.13 ± 0.03	0.36 ± 0.04	0.55 ± 0.04	0.19 ± 0.03	1.06 ± 0.09
301	0.55 ± 0.03	0.04 ± 0.02	0.01 ± 0.02	0.06 ± 0.02	0.07 ± 0.02	0.12 ± 0.02	0.25 ± 0.02	0.06 ± 0.02	0.8 ± 0.1
302	0.77 ± 0.05	0.05 ± 0.03	0.03 ± 0.03	0.12 ± 0.03	0.14 ± 0.03	0.20 ± 0.04	0.20 ± 0.04	0.04 ± 0.04	0.9 ± 0.2
303	1.01 ± 0.04	0.10 ± 0.02	0.02 ± 0.02	0.10 ± 0.03	0.09 ± 0.03	0.28 ± 0.04	0.37 ± 0.04	0.16 ± 0.03	1.2 ± 0.1
304	21.1 ± 0.1	1.3 ± 0.1	0.5 ± 0.1	0.9 ± 0.1	1.4 ± 0.1	6.5 ± 0.3	16.1 ± 0.3	5.5 ± 0.3	14.9 ± 0.4
305	0.37 ± 0.03	0.02 ± 0.02	0.05 ± 0.02	-0.03 ± 0.02	0.07 ± 0.02	0.05 ± 0.03	0.37 ± 0.05	0.14 ± 0.04	0.37 ± 0.08
306	0.45 ± 0.02	0.02 ± 0.02	-0.01 ± 0.02	0.01 ± 0.02	0.05 ± 0.02	0.17 ± 0.03	0.28 ± 0.03	0.10 ± 0.02	0.41 ± 0.05
307	1.37 ± 0.06	0.10 ± 0.04	0.00 ± 0.04	0.16 ± 0.04	0.19 ± 0.04	0.46 ± 0.08	0.43 ± 0.08	0.02 ± 0.06	1.2 ± 0.1
308	0.38 ± 0.02	0.02 ± 0.02	0.03 ± 0.02	0.04 ± 0.02	0.03 ± 0.02	0.11 ± 0.02	0.20 ± 0.02	0.08 ± 0.02	0.49 ± 0.05
309	0.92 ± 0.03	0.05 ± 0.02	0.07 ± 0.02	0.05 ± 0.02	0.03 ± 0.02	0.31 ± 0.03	0.64 ± 0.03	0.24 ± 0.03	0.80 ± 0.07

Corrected flux values with the local background of the emission regions in the catalogue from this study. The measured fluxes of the nine emission lines for the detected emission regions are presented. These fluxes are corrected for the local background, which includes the local emission and the stellar population (described in Section 2.6.7), and the extinction (described in Section 2.6.8). These flux are obtained by subtracting the background spectrum, instead of the background flux measured for each line (methodology used in this study), as discussed in Section 2.6.7. The uncertainties correspond to the propagated uncertainties (described in Section 2.6.4). All flux values are scaled by 1×10^{-15} .

ID	$H\alpha$ [$\text{erg s}^{-1} \text{cm}^{-2}$]	$[\text{N II}]\lambda 6583$ [$\text{erg s}^{-1} \text{cm}^{-2}$]	$[\text{N II}]\lambda 6548$ [$\text{erg s}^{-1} \text{cm}^{-2}$]	$[\text{S II}]\lambda 6731$ [$\text{erg s}^{-1} \text{cm}^{-2}$]	$[\text{S II}]\lambda 6716$ [$\text{erg s}^{-1} \text{cm}^{-2}$]	$\text{H}\beta$ [$\text{erg s}^{-1} \text{cm}^{-2}$]	$[\text{O III}]\lambda 5007$ [$\text{erg s}^{-1} \text{cm}^{-2}$]	$[\text{O III}]\lambda 4959$ [$\text{erg s}^{-1} \text{cm}^{-2}$]	$[\text{O II}]\lambda 3727$ [$\text{erg s}^{-1} \text{cm}^{-2}$]
310	11.8 ± 0.2	1.8 ± 0.2	0.6 ± 0.2	1.5 ± 0.2	2.8 ± 0.2	4.0 ± 0.3	9.2 ± 0.4	3.1 ± 0.3	11.6 ± 0.6
311	2.48 ± 0.08	0.25 ± 0.05	0.04 ± 0.05	0.43 ± 0.05	0.68 ± 0.06	0.6 ± 0.1	-0.03 ± 0.07	-0.06 ± 0.07	1.3 ± 0.2
312	0.50 ± 0.03	0.04 ± 0.02	0.03 ± 0.02	0.07 ± 0.02	0.08 ± 0.02	0.22 ± 0.02	0.31 ± 0.03	0.13 ± 0.02	0.57 ± 0.07
313	1.03 ± 0.04	0.17 ± 0.04	0.03 ± 0.04	0.07 ± 0.05	0.06 ± 0.05	0.3 ± 0.1	0.08 ± 0.07	0.04 ± 0.07	0.9 ± 0.2
314	2.3 ± 0.1	0.34 ± 0.07	0.11 ± 0.07	0.39 ± 0.07	0.51 ± 0.08	0.78 ± 0.08	0.74 ± 0.08	0.43 ± 0.08	2.3 ± 0.2
315	1.38 ± 0.06	0.17 ± 0.04	0.00 ± 0.04	0.17 ± 0.04	0.31 ± 0.04	0.6 ± 0.1	0.29 ± 0.08	0.13 ± 0.08	1.6 ± 0.2
316	4.88 ± 0.09	0.67 ± 0.06	0.15 ± 0.06	0.74 ± 0.06	0.94 ± 0.06	1.8 ± 0.1	1.0 ± 0.1	0.32 ± 0.09	4.5 ± 0.3
317	9.4 ± 0.1	1.10 ± 0.09	0.43 ± 0.09	1.1 ± 0.1	1.4 ± 0.1	2.8 ± 0.2	5.5 ± 0.2	1.8 ± 0.1	7.0 ± 0.3
318	1.22 ± 0.04	0.14 ± 0.03	0.07 ± 0.03	0.19 ± 0.03	0.21 ± 0.03	0.37 ± 0.09	0.30 ± 0.09	0.07 ± 0.07	1.2 ± 0.2
319	1.65 ± 0.04	0.27 ± 0.03	0.09 ± 0.03	0.28 ± 0.03	0.42 ± 0.03	0.53 ± 0.06	0.16 ± 0.05	0.06 ± 0.04	1.63 ± 0.09
320	2.62 ± 0.09	0.32 ± 0.06	0.07 ± 0.06	0.26 ± 0.06	0.43 ± 0.06	0.9 ± 0.1	0.11 ± 0.09	-0.08 ± 0.09	2.2 ± 0.3
321	1.35 ± 0.06	0.03 ± 0.04	-0.04 ± 0.04	-0.06 ± 0.04	0.01 ± 0.04	0.39 ± 0.07	0.63 ± 0.08	0.21 ± 0.06	1.0 ± 0.2
322	1.75 ± 0.05	0.28 ± 0.05	0.10 ± 0.05	0.18 ± 0.05	0.35 ± 0.05	0.67 ± 0.08	2.6 ± 0.1	0.94 ± 0.09	1.0 ± 0.2
323	5.03 ± 0.06	0.45 ± 0.04	0.18 ± 0.04	0.40 ± 0.04	0.52 ± 0.04	1.40 ± 0.07	1.61 ± 0.07	0.46 ± 0.05	3.7 ± 0.2
324	19.5 ± 0.2	2.0 ± 0.1	0.7 ± 0.1	1.4 ± 0.1	2.0 ± 0.1	6.6 ± 0.2	11.9 ± 0.3	4.1 ± 0.2	12.1 ± 0.4
325	8.8 ± 0.1	1.33 ± 0.08	0.36 ± 0.07	1.26 ± 0.08	1.68 ± 0.08	2.4 ± 0.1	4.8 ± 0.2	1.6 ± 0.1	6.8 ± 0.3
326	4.18 ± 0.07	0.51 ± 0.05	0.15 ± 0.05	0.46 ± 0.05	0.64 ± 0.05	1.31 ± 0.09	2.2 ± 0.1	0.66 ± 0.08	3.7 ± 0.2
327	6.12 ± 0.09	0.79 ± 0.06	0.38 ± 0.06	0.70 ± 0.06	1.08 ± 0.06	2.1 ± 0.1	4.1 ± 0.1	1.6 ± 0.1	3.5 ± 0.2
328	14.8 ± 0.1	1.77 ± 0.09	0.57 ± 0.08	1.50 ± 0.09	2.20 ± 0.09	4.5 ± 0.2	7.7 ± 0.2	2.6 ± 0.1	10.1 ± 0.3
329	5.6 ± 0.2	1.1 ± 0.1	0.3 ± 0.1	0.9 ± 0.1	1.5 ± 0.1	1.6 ± 0.2	2.1 ± 0.2	0.4 ± 0.2	4.8 ± 0.4
330	4.02 ± 0.07	0.60 ± 0.05	0.21 ± 0.05	0.65 ± 0.05	0.81 ± 0.05	1.27 ± 0.08	1.34 ± 0.08	0.56 ± 0.07	3.8 ± 0.2
332	8.62 ± 0.09	0.60 ± 0.06	0.22 ± 0.06	0.48 ± 0.06	0.57 ± 0.06	2.6 ± 0.1	6.0 ± 0.1	1.9 ± 0.1	5.9 ± 0.2

Corrected flux values with the local background of the emission regions in the catalogue from this study. The measured fluxes of the nine emission lines for the detected emission regions are presented. These fluxes are corrected for the local background, which includes the local emission and the stellar population (described in Section 2.6.7), and the extinction (described in Section 2.6.8). These flux are obtained by subtracting the background spectrum, instead of the background flux measured for each line (methodology used in this study), as discussed in Section 2.6.7. The uncertainties correspond to the propagated uncertainties (described in Section 2.6.4). All flux values are scaled by 1×10^{-15} .

ID	$H\alpha$ [$\text{erg s}^{-1} \text{cm}^{-2}$]	$[\text{N II}] \lambda 6583$ [$\text{erg s}^{-1} \text{cm}^{-2}$]	$[\text{N II}] \lambda 6548$ [$\text{erg s}^{-1} \text{cm}^{-2}$]	$[\text{S II}] \lambda 6731$ [$\text{erg s}^{-1} \text{cm}^{-2}$]	$[\text{S II}] \lambda 6716$ [$\text{erg s}^{-1} \text{cm}^{-2}$]	$\text{H}\beta$ [$\text{erg s}^{-1} \text{cm}^{-2}$]	$[\text{O III}] \lambda 5007$ [$\text{erg s}^{-1} \text{cm}^{-2}$]	$[\text{O III}] \lambda 4959$ [$\text{erg s}^{-1} \text{cm}^{-2}$]	$[\text{O II}] \lambda 3727$ [$\text{erg s}^{-1} \text{cm}^{-2}$]
333	23.4 ± 0.2	3.0 ± 0.1	1.0 ± 0.1	2.3 ± 0.1	3.2 ± 0.1	7.2 ± 0.2	10.0 ± 0.3	3.6 ± 0.2	18.2 ± 0.5
334	17.2 ± 0.1	1.55 ± 0.09	0.57 ± 0.09	1.1 ± 0.1	1.5 ± 0.1	5.0 ± 0.2	11.0 ± 0.3	3.9 ± 0.2	11.8 ± 0.5
335	12.0 ± 0.1	1.79 ± 0.08	0.54 ± 0.08	1.69 ± 0.08	2.63 ± 0.08	3.8 ± 0.2	6.5 ± 0.2	2.3 ± 0.2	10.8 ± 0.4
336	24.4 ± 0.2	2.7 ± 0.1	1.1 ± 0.1	2.2 ± 0.1	3.0 ± 0.1	8.2 ± 0.3	17.0 ± 0.4	5.8 ± 0.3	19.5 ± 0.6
337	15.5 ± 0.1	1.26 ± 0.08	0.46 ± 0.08	0.81 ± 0.09	1.08 ± 0.09	5.0 ± 0.2	12.6 ± 0.3	4.5 ± 0.2	6.5 ± 0.4
338	9.6 ± 0.1	1.04 ± 0.07	0.46 ± 0.07	0.86 ± 0.08	1.18 ± 0.08	3.1 ± 0.2	7.3 ± 0.2	2.6 ± 0.2	7.1 ± 0.2
339	72.4 ± 0.4	6.2 ± 0.3	2.0 ± 0.3	3.8 ± 0.3	5.1 ± 0.3	23.3 ± 0.9	56 ± 1	19.7 ± 0.9	44 ± 1
340	3.34 ± 0.09	0.40 ± 0.06	0.09 ± 0.06	0.64 ± 0.06	0.84 ± 0.06	1.02 ± 0.09	1.1 ± 0.1	0.22 ± 0.08	3.1 ± 0.2
341	4.14 ± 0.07	0.36 ± 0.04	0.16 ± 0.04	0.21 ± 0.05	0.27 ± 0.05	1.57 ± 0.09	4.1 ± 0.1	1.51 ± 0.09	0.9 ± 0.2
342	2.18 ± 0.05	0.44 ± 0.05	0.16 ± 0.05	0.33 ± 0.05	0.59 ± 0.05	0.6 ± 0.1	1.4 ± 0.1	0.3 ± 0.1	2.0 ± 0.2
343	16.9 ± 0.2	1.9 ± 0.1	0.9 ± 0.1	1.8 ± 0.1	2.4 ± 0.1	6.2 ± 0.3	14.3 ± 0.4	4.7 ± 0.3	15.4 ± 0.5
344	70.3 ± 0.4	3.6 ± 0.3	1.2 ± 0.3	2.9 ± 0.3	4.3 ± 0.3	21 ± 1	72 ± 1	25 ± 1	42.1 ± 0.9
345	5.14 ± 0.07	0.19 ± 0.05	0.01 ± 0.05	0.29 ± 0.05	0.42 ± 0.05	1.7 ± 0.1	6.3 ± 0.2	2.2 ± 0.1	4.5 ± 0.3
346	2.02 ± 0.05	0.24 ± 0.03	0.10 ± 0.03	0.16 ± 0.03	0.27 ± 0.03	0.74 ± 0.07	0.57 ± 0.07	0.29 ± 0.06	1.8 ± 0.2
347	2.85 ± 0.08	0.45 ± 0.05	0.11 ± 0.05	0.38 ± 0.05	0.63 ± 0.06	0.9 ± 0.1	-0.06 ± 0.07	-0.29 ± 0.08	2.4 ± 0.2
348	3.32 ± 0.08	0.49 ± 0.06	0.06 ± 0.05	0.43 ± 0.06	0.60 ± 0.06	1.0 ± 0.1	0.59 ± 0.09	0.25 ± 0.08	3.3 ± 0.2
349	0.86 ± 0.04	0.07 ± 0.03	0.04 ± 0.03	0.11 ± 0.03	0.19 ± 0.03	0.33 ± 0.04	0.41 ± 0.05	0.13 ± 0.04	1.1 ± 0.1
350	2.58 ± 0.05	0.26 ± 0.04	0.10 ± 0.04	0.31 ± 0.04	0.47 ± 0.04	0.97 ± 0.06	0.68 ± 0.05	0.19 ± 0.04	2.7 ± 0.2
351	2.24 ± 0.04	0.20 ± 0.03	0.01 ± 0.03	0.17 ± 0.03	0.33 ± 0.03	0.70 ± 0.04	1.95 ± 0.06	0.70 ± 0.04	2.2 ± 0.1
352	22.9 ± 0.2	1.8 ± 0.1	0.6 ± 0.1	1.2 ± 0.1	1.9 ± 0.1	7.5 ± 0.3	17.9 ± 0.4	6.2 ± 0.3	17.4 ± 0.4
353	4.20 ± 0.08	0.57 ± 0.06	0.15 ± 0.06	0.79 ± 0.06	1.17 ± 0.06	1.15 ± 0.07	2.08 ± 0.07	0.67 ± 0.07	3.2 ± 0.2
354	0.57 ± 0.03	0.07 ± 0.02	0.00 ± 0.02	0.05 ± 0.02	0.07 ± 0.02	0.20 ± 0.04	0.14 ± 0.04	0.01 ± 0.03	0.65 ± 0.09

Corrected flux values with the local background of the emission regions in the catalogue from this study. The measured fluxes of the nine emission lines for the detected emission regions are presented. These fluxes are corrected for the local background, which includes the local emission and the stellar population (described in Section 2.6.7), and the extinction (described in Section 2.6.8). These flux are obtained by subtracting the background spectrum, instead of the background flux measured for each line (methodology used in this study), as discussed in Section 2.6.7. The uncertainties correspond to the propagated uncertainties (described in Section 2.6.4). All flux values are scaled by 1×10^{-15} .

ID	$H\alpha$ [erg s $^{-1}$ cm $^{-2}$]	[N II] $\lambda 6583$ [erg s $^{-1}$ cm $^{-2}$]	[N II] $\lambda 6548$ [erg s $^{-1}$ cm $^{-2}$]	[S II] $\lambda 6731$ [erg s $^{-1}$ cm $^{-2}$]	[S II] $\lambda 6716$ [erg s $^{-1}$ cm $^{-2}$]	$H\beta$ [erg s $^{-1}$ cm $^{-2}$]	[O III] $\lambda 5007$ [erg s $^{-1}$ cm $^{-2}$]	[O III] $\lambda 4959$ [erg s $^{-1}$ cm $^{-2}$]	[O II] $\lambda 3727$ [erg s $^{-1}$ cm $^{-2}$]
355	26.3 ± 0.2	1.9 ± 0.1	0.7 ± 0.1	1.1 ± 0.1	1.8 ± 0.1	8.8 ± 0.4	23.1 ± 0.5	8.2 ± 0.4	16.9 ± 0.4
356	1.46 ± 0.04	0.17 ± 0.03	0.05 ± 0.03	0.19 ± 0.03	0.30 ± 0.03	0.48 ± 0.04	0.68 ± 0.05	0.19 ± 0.04	1.9 ± 0.1
357	3.61 ± 0.05	0.27 ± 0.03	0.09 ± 0.03	0.29 ± 0.04	0.32 ± 0.04	1.12 ± 0.07	3.7 ± 0.1	1.21 ± 0.07	2.2 ± 0.2
358	8.3 ± 0.2	1.2 ± 0.1	0.3 ± 0.1	1.4 ± 0.1	2.3 ± 0.1	2.5 ± 0.2	2.5 ± 0.2	0.8 ± 0.2	7.1 ± 0.5
359	8.80 ± 0.07	0.68 ± 0.05	0.27 ± 0.05	0.61 ± 0.05	0.73 ± 0.05	2.76 ± 0.09	5.5 ± 0.1	1.82 ± 0.09	7.3 ± 0.2
360	7.4 ± 0.1	0.94 ± 0.08	0.38 ± 0.08	0.90 ± 0.09	1.16 ± 0.09	2.4 ± 0.2	-0.1 ± 0.1	-0.2 ± 0.1	5.7 ± 0.4
361	4.92 ± 0.08	0.51 ± 0.05	0.14 ± 0.05	0.54 ± 0.06	0.88 ± 0.06	1.61 ± 0.09	5.0 ± 0.1	1.66 ± 0.09	3.9 ± 0.2
362	2.91 ± 0.06	0.33 ± 0.04	0.06 ± 0.04	0.40 ± 0.04	0.59 ± 0.04	0.84 ± 0.06	2.55 ± 0.09	0.84 ± 0.07	2.2 ± 0.1
363	1.03 ± 0.03	0.10 ± 0.02	0.06 ± 0.02	0.08 ± 0.02	0.09 ± 0.02	0.38 ± 0.03	0.56 ± 0.04	0.22 ± 0.03	0.77 ± 0.09
364	4.76 ± 0.05	0.41 ± 0.03	0.14 ± 0.03	0.39 ± 0.03	0.44 ± 0.03	1.45 ± 0.06	1.80 ± 0.06	0.67 ± 0.05	3.5 ± 0.1
365	7.0 ± 0.1	0.89 ± 0.07	0.13 ± 0.07	1.10 ± 0.07	1.70 ± 0.07	2.2 ± 0.2	3.9 ± 0.2	1.0 ± 0.1	6.4 ± 0.3
366	4.16 ± 0.06	0.27 ± 0.04	0.11 ± 0.04	0.27 ± 0.04	0.53 ± 0.04	1.19 ± 0.07	3.51 ± 0.09	1.19 ± 0.07	3.9 ± 0.2
367	1.99 ± 0.05	0.16 ± 0.04	0.10 ± 0.04	0.25 ± 0.04	0.32 ± 0.04	0.67 ± 0.06	1.13 ± 0.07	0.38 ± 0.06	2.2 ± 0.1
368	8.56 ± 0.08	0.53 ± 0.06	0.27 ± 0.05	0.67 ± 0.06	0.93 ± 0.06	2.8 ± 0.1	9.3 ± 0.2	3.2 ± 0.2	6.3 ± 0.2
369	11.3 ± 0.1	1.08 ± 0.08	0.24 ± 0.08	0.99 ± 0.08	1.37 ± 0.08	3.2 ± 0.1	6.3 ± 0.2	2.1 ± 0.1	9.7 ± 0.3
370	4.3 ± 0.1	0.64 ± 0.07	0.18 ± 0.07	0.55 ± 0.07	0.92 ± 0.07	1.19 ± 0.09	0.2 ± 0.1	0.1 ± 0.1	4.2 ± 0.3
371	4.6 ± 0.1	0.76 ± 0.07	0.27 ± 0.07	0.87 ± 0.07	1.34 ± 0.07	1.1 ± 0.1	1.4 ± 0.1	0.5 ± 0.1	4.8 ± 0.3
372	21.7 ± 0.2	1.6 ± 0.1	0.5 ± 0.1	1.4 ± 0.1	2.2 ± 0.1	7.3 ± 0.4	31.4 ± 0.6	10.6 ± 0.5	12.6 ± 0.6
373	2.06 ± 0.07	0.37 ± 0.05	0.17 ± 0.05	0.50 ± 0.05	0.70 ± 0.05	0.62 ± 0.06	0.54 ± 0.06	0.12 ± 0.06	2.3 ± 0.2
374	3.43 ± 0.06	0.68 ± 0.04	0.12 ± 0.04	0.76 ± 0.05	1.11 ± 0.05	1.00 ± 0.07	0.91 ± 0.06	0.24 ± 0.05	4.0 ± 0.2
375	1.80 ± 0.07	0.17 ± 0.05	0.06 ± 0.05	0.24 ± 0.05	0.15 ± 0.05	0.7 ± 0.1	0.30 ± 0.07	0.07 ± 0.07	1.4 ± 0.2
376	1.29 ± 0.05	0.20 ± 0.04	0.07 ± 0.04	0.12 ± 0.04	0.15 ± 0.04	0.45 ± 0.07	0.27 ± 0.06	0.13 ± 0.05	1.0 ± 0.1

Corrected flux values with the local background of the emission regions in the catalogue from this study. The measured fluxes of the nine emission lines for the detected emission regions are presented. These fluxes are corrected for the local background, which includes the local emission and the stellar population (described in Section 2.6.7), and the extinction (described in Section 2.6.8). These flux are obtained by subtracting the background spectrum, instead of the background flux measured for each line (methodology used in this study), as discussed in Section 2.6.7. The uncertainties correspond to the propagated uncertainties (described in Section 2.6.4). All flux values are scaled by 1×10^{-15} .

ID	$H\alpha$ [erg s $^{-1}$ cm $^{-2}$]	[N II] $\lambda 6583$ [erg s $^{-1}$ cm $^{-2}$]	[N II] $\lambda 6548$ [erg s $^{-1}$ cm $^{-2}$]	[S II] $\lambda 6731$ [erg s $^{-1}$ cm $^{-2}$]	[S II] $\lambda 6716$ [erg s $^{-1}$ cm $^{-2}$]	$H\beta$ [erg s $^{-1}$ cm $^{-2}$]	[O III] $\lambda 5007$ [erg s $^{-1}$ cm $^{-2}$]	[O III] $\lambda 4959$ [erg s $^{-1}$ cm $^{-2}$]	[O II] $\lambda 3727$ [erg s $^{-1}$ cm $^{-2}$]
377	1.01 ± 0.05	0.01 ± 0.03	0.02 ± 0.03	0.01 ± 0.03	-0.06 ± 0.03	0.26 ± 0.05	1.04 ± 0.07	0.30 ± 0.05	0.1 ± 0.1
378	18.5 ± 0.2	2.1 ± 0.1	0.7 ± 0.1	2.2 ± 0.1	2.8 ± 0.1	6.2 ± 0.3	12.4 ± 0.4	4.5 ± 0.3	16.6 ± 0.6
379	1.79 ± 0.05	0.16 ± 0.05	0.08 ± 0.05	0.32 ± 0.05	0.50 ± 0.05	0.52 ± 0.08	0.73 ± 0.09	0.15 ± 0.07	1.9 ± 0.2
380	3.07 ± 0.08	0.21 ± 0.05	0.15 ± 0.05	0.33 ± 0.05	0.38 ± 0.05	0.93 ± 0.08	1.8 ± 0.1	0.57 ± 0.08	3.1 ± 0.2
381	8.75 ± 0.09	0.59 ± 0.06	0.20 ± 0.06	0.74 ± 0.06	1.10 ± 0.06	2.8 ± 0.2	12.3 ± 0.3	4.2 ± 0.2	4.4 ± 0.2
382	3.01 ± 0.06	0.30 ± 0.04	0.13 ± 0.04	0.24 ± 0.05	0.29 ± 0.04	0.9 ± 0.1	0.4 ± 0.1	-0.06 ± 0.09	1.6 ± 0.2
383	2.36 ± 0.05	0.41 ± 0.04	0.14 ± 0.04	0.29 ± 0.04	0.50 ± 0.04	0.64 ± 0.06	1.04 ± 0.07	0.40 ± 0.05	1.7 ± 0.2
384	7.15 ± 0.08	0.74 ± 0.06	0.22 ± 0.06	0.63 ± 0.06	1.04 ± 0.06	1.9 ± 0.1	2.3 ± 0.1	0.7 ± 0.1	5.6 ± 0.3
385	6.9 ± 0.1	0.69 ± 0.08	0.21 ± 0.08	0.78 ± 0.08	0.96 ± 0.08	2.1 ± 0.1	4.4 ± 0.2	1.3 ± 0.1	5.9 ± 0.3
386	3.39 ± 0.06	0.30 ± 0.04	0.13 ± 0.04	0.17 ± 0.04	0.23 ± 0.04	0.92 ± 0.07	2.7 ± 0.1	0.85 ± 0.07	1.8 ± 0.2
387	3.74 ± 0.07	0.52 ± 0.05	0.23 ± 0.05	0.46 ± 0.05	0.77 ± 0.05	0.9 ± 0.1	0.8 ± 0.1	0.14 ± 0.08	3.0 ± 0.3
388	8.12 ± 0.07	0.64 ± 0.05	0.21 ± 0.05	0.53 ± 0.05	0.84 ± 0.05	2.05 ± 0.09	4.6 ± 0.1	1.61 ± 0.09	5.6 ± 0.2
389	1.56 ± 0.04	0.22 ± 0.02	0.05 ± 0.02	0.22 ± 0.03	0.28 ± 0.03	0.36 ± 0.03	0.57 ± 0.03	0.18 ± 0.03	1.4 ± 0.1
390	11.85 ± 0.09	1.23 ± 0.06	0.51 ± 0.06	1.06 ± 0.07	1.50 ± 0.07	3.5 ± 0.1	4.0 ± 0.1	1.55 ± 0.09	9.2 ± 0.3
391	3.10 ± 0.06	0.50 ± 0.04	0.13 ± 0.04	0.34 ± 0.04	0.56 ± 0.04	1.05 ± 0.05	1.07 ± 0.05	0.39 ± 0.04	2.7 ± 0.2
392	3.22 ± 0.05	0.33 ± 0.04	0.11 ± 0.04	0.24 ± 0.04	0.38 ± 0.04	0.70 ± 0.06	1.24 ± 0.07	0.37 ± 0.05	1.3 ± 0.2
393	1.53 ± 0.04	0.19 ± 0.03	0.06 ± 0.03	0.15 ± 0.03	0.23 ± 0.03	0.44 ± 0.04	0.55 ± 0.04	0.25 ± 0.03	1.5 ± 0.1
394	4.85 ± 0.05	0.44 ± 0.04	0.14 ± 0.04	0.45 ± 0.04	0.64 ± 0.04	1.43 ± 0.06	2.84 ± 0.08	1.06 ± 0.06	4.1 ± 0.1
395	2.40 ± 0.06	0.29 ± 0.04	0.11 ± 0.04	0.24 ± 0.04	0.42 ± 0.04	0.69 ± 0.06	1.48 ± 0.08	0.43 ± 0.06	2.2 ± 0.1
396	111.4 ± 0.6	7.3 ± 0.4	2.9 ± 0.4	6.1 ± 0.4	8.1 ± 0.4	32 ± 1	89 ± 2	31 ± 1	68 ± 1
397	23.6 ± 0.2	1.6 ± 0.1	0.6 ± 0.1	1.1 ± 0.1	1.6 ± 0.1	7.8 ± 0.3	17.5 ± 0.4	5.8 ± 0.3	15.0 ± 0.4
398	21.9 ± 0.1	1.74 ± 0.09	0.60 ± 0.09	1.5 ± 0.1	2.1 ± 0.1	5.6 ± 0.2	13.3 ± 0.3	4.4 ± 0.2	12.7 ± 0.3

Corrected flux values with the local background of the emission regions in the catalogue from this study. The measured fluxes of the nine emission lines for the detected emission regions are presented. These fluxes are corrected for the local background, which includes the local emission and the stellar population (described in Section 2.6.7), and the extinction (described in Section 2.6.8). These flux are obtained by subtracting the background spectrum, instead of the background flux measured for each line (methodology used in this study), as discussed in Section 2.6.7. The uncertainties correspond to the propagated uncertainties (described in Section 2.6.4). All flux values are scaled by 1×10^{-15} .

ID	H α	[N II] $\lambda 6583$ [erg s $^{-1}$ cm $^{-2}$]	[N II] $\lambda 6548$ [erg s $^{-1}$ cm $^{-2}$]	[S II] $\lambda 6731$ [erg s $^{-1}$ cm $^{-2}$]	[S II] $\lambda 6716$ [erg s $^{-1}$ cm $^{-2}$]	H β [erg s $^{-1}$ cm $^{-2}$]	[O III] $\lambda 5007$ [erg s $^{-1}$ cm $^{-2}$]	[O III] $\lambda 4959$ [erg s $^{-1}$ cm $^{-2}$]	[O II] $\lambda 3727$ [erg s $^{-1}$ cm $^{-2}$]
	[erg s $^{-1}$ cm $^{-2}$]	[erg s $^{-1}$ cm $^{-2}$]	[erg s $^{-1}$ cm $^{-2}$]	[erg s $^{-1}$ cm $^{-2}$]	[erg s $^{-1}$ cm $^{-2}$]	[erg s $^{-1}$ cm $^{-2}$]	[erg s $^{-1}$ cm $^{-2}$]	[erg s $^{-1}$ cm $^{-2}$]	[erg s $^{-1}$ cm $^{-2}$]
399	51.1 ± 0.3	2.1 ± 0.2	1.0 ± 0.2	1.5 ± 0.2	1.5 ± 0.2	14 ± 1	86 ± 2	30 ± 1	10.8 ± 0.4
401	11.4 ± 0.2	1.9 ± 0.2	0.8 ± 0.2	2.3 ± 0.2	3.5 ± 0.2	3.2 ± 0.2	4.9 ± 0.2	1.6 ± 0.2	10.9 ± 0.7
402	3.16 ± 0.06	0.40 ± 0.04	0.13 ± 0.04	0.31 ± 0.04	0.42 ± 0.04	0.81 ± 0.07	0.23 ± 0.05	0.12 ± 0.05	1.9 ± 0.2
403	54.8 ± 0.4	5.8 ± 0.3	1.9 ± 0.3	4.0 ± 0.3	5.5 ± 0.3	17.0 ± 0.5	24.7 ± 0.5	8.1 ± 0.4	49 ± 1
404	0.93 ± 0.06	0.17 ± 0.04	-0.01 ± 0.04	0.17 ± 0.04	0.26 ± 0.04	0.37 ± 0.06	0.10 ± 0.05	0.11 ± 0.05	0.7 ± 0.1
405	2.54 ± 0.07	0.26 ± 0.05	0.07 ± 0.05	0.19 ± 0.05	0.35 ± 0.05	0.47 ± 0.05	0.65 ± 0.06	0.11 ± 0.06	1.7 ± 0.2
406	1.82 ± 0.06	0.26 ± 0.04	0.12 ± 0.04	0.18 ± 0.04	0.25 ± 0.04	0.61 ± 0.06	0.78 ± 0.07	0.32 ± 0.06	2.0 ± 0.1
407	8.38 ± 0.09	1.20 ± 0.06	0.37 ± 0.06	0.96 ± 0.07	1.47 ± 0.07	3.0 ± 0.1	1.95 ± 0.09	0.73 ± 0.08	8.0 ± 0.3
408	32.3 ± 0.2	3.1 ± 0.1	0.9 ± 0.1	2.6 ± 0.1	3.7 ± 0.1	9.6 ± 0.3	17.7 ± 0.4	6.1 ± 0.3	29.1 ± 0.6
409	13.8 ± 0.1	1.66 ± 0.07	0.59 ± 0.07	1.41 ± 0.08	2.05 ± 0.08	4.0 ± 0.1	4.1 ± 0.1	1.1 ± 0.1	12.4 ± 0.3
410	15.0 ± 0.1	0.98 ± 0.08	0.35 ± 0.08	0.82 ± 0.09	1.02 ± 0.09	3.6 ± 0.2	13.2 ± 0.3	4.4 ± 0.2	8.7 ± 0.3
411	5.92 ± 0.06	0.65 ± 0.04	0.18 ± 0.04	0.66 ± 0.05	0.89 ± 0.05	1.7 ± 0.1	1.8 ± 0.1	0.4 ± 0.1	6.1 ± 0.2
412	10.43 ± 0.09	0.94 ± 0.06	0.37 ± 0.06	1.02 ± 0.06	1.40 ± 0.06	2.5 ± 0.1	5.7 ± 0.1	2.0 ± 0.1	5.9 ± 0.2
413	10.9 ± 0.1	0.86 ± 0.07	0.37 ± 0.07	0.77 ± 0.07	1.13 ± 0.07	2.9 ± 0.1	7.1 ± 0.2	2.3 ± 0.1	5.9 ± 0.2
414	7.8 ± 0.1	0.67 ± 0.08	0.23 ± 0.08	0.75 ± 0.09	1.16 ± 0.09	2.6 ± 0.1	8.7 ± 0.2	3.0 ± 0.2	7.2 ± 0.3
415	6.90 ± 0.06	0.65 ± 0.04	0.27 ± 0.04	0.43 ± 0.04	0.74 ± 0.04	2.46 ± 0.09	3.1 ± 0.1	1.12 ± 0.08	6.1 ± 0.1
416	8.0 ± 0.2	0.9 ± 0.2	0.2 ± 0.2	1.2 ± 0.2	1.6 ± 0.2	1.1 ± 0.3	-0.3 ± 0.3	-0.6 ± 0.3	5.1 ± 0.8
417	0.95 ± 0.05	0.16 ± 0.04	0.07 ± 0.04	0.19 ± 0.04	0.27 ± 0.04	0.30 ± 0.06	0.20 ± 0.05	-0.03 ± 0.05	1.1 ± 0.1
418	2.94 ± 0.05	0.33 ± 0.04	0.14 ± 0.03	0.29 ± 0.04	0.35 ± 0.04	0.96 ± 0.06	0.95 ± 0.06	0.21 ± 0.05	2.4 ± 0.2
419	3.47 ± 0.08	0.43 ± 0.06	0.18 ± 0.05	0.50 ± 0.06	0.66 ± 0.06	1.09 ± 0.09	1.6 ± 0.1	0.48 ± 0.08	3.7 ± 0.2
420	74.3 ± 0.5	7.5 ± 0.3	2.4 ± 0.3	7.3 ± 0.3	10.0 ± 0.3	24.1 ± 0.7	36.5 ± 0.8	12.4 ± 0.6	70 ± 1
421	16.3 ± 0.2	1.9 ± 0.1	0.9 ± 0.1	2.7 ± 0.1	4.1 ± 0.1	5.5 ± 0.2	7.1 ± 0.2	2.5 ± 0.2	21.0 ± 0.5

Corrected flux values with the local background of the emission regions in the catalogue from this study. The measured fluxes of the nine emission lines for the detected emission regions are presented. These fluxes are corrected for the local background, which includes the local emission and the stellar population (described in Section 2.6.7), and the extinction (described in Section 2.6.8). These flux are obtained by subtracting the background spectrum, instead of the background flux measured for each line (methodology used in this study), as discussed in Section 2.6.7. The uncertainties correspond to the propagated uncertainties (described in Section 2.6.4). All flux values are scaled by 1×10^{-15} .

ID	$H\alpha$ [erg s ⁻¹ cm ⁻²]	[N II] $\lambda 6583$ [erg s ⁻¹ cm ⁻²]	[N II] $\lambda 6548$ [erg s ⁻¹ cm ⁻²]	[S II] $\lambda 6731$ [erg s ⁻¹ cm ⁻²]	[S II] $\lambda 6716$ [erg s ⁻¹ cm ⁻²]	$H\beta$ [erg s ⁻¹ cm ⁻²]	[O III] $\lambda 5007$ [erg s ⁻¹ cm ⁻²]	[O III] $\lambda 4959$ [erg s ⁻¹ cm ⁻²]	[O II] $\lambda 3727$ [erg s ⁻¹ cm ⁻²]
422	15.3 ± 0.3	1.8 ± 0.2	0.8 ± 0.2	2.8 ± 0.2	3.8 ± 0.2	5.1 ± 0.3	8.0 ± 0.3	2.6 ± 0.2	16.2 ± 0.7
423	28.2 ± 0.3	2.4 ± 0.2	1.1 ± 0.2	2.6 ± 0.2	3.1 ± 0.2	8.8 ± 0.3	20.3 ± 0.4	6.8 ± 0.3	19.8 ± 0.6
424	1.5 ± 0.1	0.22 ± 0.08	0.06 ± 0.08	0.11 ± 0.09	0.27 ± 0.09	0.5 ± 0.1	0.2 ± 0.1	0.0 ± 0.1	1.6 ± 0.2
425	16.8 ± 0.1	2.08 ± 0.08	0.63 ± 0.08	2.24 ± 0.08	3.03 ± 0.08	5.2 ± 0.2	8.9 ± 0.2	2.8 ± 0.2	16.9 ± 0.4
426	3.00 ± 0.05	0.22 ± 0.04	0.13 ± 0.04	0.14 ± 0.04	0.24 ± 0.04	0.98 ± 0.09	1.6 ± 0.1	0.51 ± 0.08	1.8 ± 0.2
427	3.99 ± 0.06	0.31 ± 0.04	0.05 ± 0.04	0.36 ± 0.04	0.48 ± 0.04	0.99 ± 0.07	1.25 ± 0.08	0.42 ± 0.06	2.8 ± 0.2
428	9.22 ± 0.08	0.99 ± 0.06	0.33 ± 0.06	0.75 ± 0.06	1.08 ± 0.06	2.6 ± 0.1	2.6 ± 0.1	0.84 ± 0.09	6.7 ± 0.3
429	7.63 ± 0.08	0.70 ± 0.05	0.14 ± 0.05	0.84 ± 0.05	1.26 ± 0.05	2.01 ± 0.09	4.9 ± 0.1	1.60 ± 0.09	5.5 ± 0.2
430	13.0 ± 0.1	1.27 ± 0.08	0.32 ± 0.08	1.53 ± 0.09	2.29 ± 0.09	4.5 ± 0.1	8.8 ± 0.2	2.7 ± 0.1	15.1 ± 0.3
431	3.04 ± 0.05	0.21 ± 0.05	0.06 ± 0.05	0.17 ± 0.05	0.14 ± 0.05	0.80 ± 0.09	0.73 ± 0.09	0.15 ± 0.07	2.4 ± 0.2
432	2.21 ± 0.05	0.25 ± 0.04	0.11 ± 0.03	0.29 ± 0.04	0.46 ± 0.04	0.46 ± 0.06	0.62 ± 0.07	0.28 ± 0.05	1.5 ± 0.1
433	1.37 ± 0.04	0.13 ± 0.03	0.07 ± 0.03	0.09 ± 0.03	0.17 ± 0.03	0.36 ± 0.04	0.42 ± 0.05	0.12 ± 0.04	1.2 ± 0.1
434	24.5 ± 0.1	1.8 ± 0.1	0.5 ± 0.1	1.2 ± 0.1	1.8 ± 0.1	6.5 ± 0.2	15.8 ± 0.3	5.3 ± 0.2	12.5 ± 0.4
435	9.23 ± 0.08	1.00 ± 0.05	0.17 ± 0.05	0.70 ± 0.06	0.97 ± 0.05	2.52 ± 0.08	2.78 ± 0.08	0.82 ± 0.07	5.8 ± 0.2
436	0.80 ± 0.03	0.09 ± 0.02	0.01 ± 0.02	0.06 ± 0.02	0.03 ± 0.02	0.23 ± 0.03	0.80 ± 0.04	0.26 ± 0.03	0.30 ± 0.09
437	4.51 ± 0.06	0.33 ± 0.06	0.17 ± 0.06	0.19 ± 0.06	0.33 ± 0.06	1.2 ± 0.1	1.8 ± 0.1	0.7 ± 0.1	2.6 ± 0.3
438	12.82 ± 0.09	0.93 ± 0.06	0.27 ± 0.06	0.71 ± 0.06	0.90 ± 0.06	3.5 ± 0.1	8.4 ± 0.2	3.0 ± 0.1	6.9 ± 0.3
439	51.0 ± 0.3	3.6 ± 0.2	1.1 ± 0.2	2.2 ± 0.2	2.9 ± 0.2	16.0 ± 0.7	44.6 ± 0.9	14.9 ± 0.7	34.9 ± 0.8
440	0.62 ± 0.04	0.07 ± 0.03	0.06 ± 0.03	0.07 ± 0.03	0.07 ± 0.03	0.17 ± 0.05	0.16 ± 0.05	0.03 ± 0.04	0.6 ± 0.1
441	8.9 ± 0.1	0.78 ± 0.08	0.36 ± 0.08	0.66 ± 0.08	1.17 ± 0.08	1.6 ± 0.1	1.9 ± 0.1	0.5 ± 0.1	6.1 ± 0.4
442	4.4 ± 0.1	0.6 ± 0.1	0.1 ± 0.1	0.4 ± 0.1	0.6 ± 0.1	0.84 ± 0.09	2.9 ± 0.1	0.78 ± 0.09	3.1 ± 0.3
443	44.8 ± 0.3	3.7 ± 0.2	1.2 ± 0.2	2.3 ± 0.2	2.8 ± 0.2	14.4 ± 0.5	28.7 ± 0.6	10.0 ± 0.4	32.8 ± 0.7

Corrected flux values with the local background of the emission regions in the catalogue from this study. The measured fluxes of the nine emission lines for the detected emission regions are presented. These fluxes are corrected for the local background, which includes the local emission and the stellar population (described in Section 2.6.7), and the extinction (described in Section 2.6.8). These flux are obtained by subtracting the background spectrum, instead of the background flux measured for each line (methodology used in this study), as discussed in Section 2.6.7. The uncertainties correspond to the propagated uncertainties (described in Section 2.6.4). All flux values are scaled by 1×10^{-15} .

ID	$H\alpha$ [erg s ⁻¹ cm ⁻²]	[N II] $\lambda 6583$ [erg s ⁻¹ cm ⁻²]	[N II] $\lambda 6548$ [erg s ⁻¹ cm ⁻²]	[S II] $\lambda 6731$ [erg s ⁻¹ cm ⁻²]	[S II] $\lambda 6716$ [erg s ⁻¹ cm ⁻²]	$H\beta$ [erg s ⁻¹ cm ⁻²]	[O III] $\lambda 5007$ [erg s ⁻¹ cm ⁻²]	[O III] $\lambda 4959$ [erg s ⁻¹ cm ⁻²]	[O II] $\lambda 3727$ [erg s ⁻¹ cm ⁻²]
444	5.13 ± 0.07	0.45 ± 0.05	0.07 ± 0.05	0.52 ± 0.05	0.85 ± 0.05	1.5 ± 0.1	5.0 ± 0.2	1.7 ± 0.1	2.8 ± 0.2
445	135.3 ± 0.7	9.3 ± 0.5	2.6 ± 0.5	5.9 ± 0.5	7.8 ± 0.5	41 ± 2	105 ± 2	36 ± 2	70 ± 2
446	24.1 ± 0.1	1.5 ± 0.1	0.4 ± 0.1	1.1 ± 0.1	1.3 ± 0.1	7.4 ± 0.3	25.9 ± 0.5	8.5 ± 0.4	11.6 ± 0.3
447	17.8 ± 0.2	1.8 ± 0.1	0.5 ± 0.1	1.7 ± 0.1	2.7 ± 0.1	5.6 ± 0.3	15.4 ± 0.4	5.1 ± 0.3	15.8 ± 0.5
448	1.13 ± 0.05	0.10 ± 0.03	0.01 ± 0.03	0.13 ± 0.03	0.14 ± 0.03	0.37 ± 0.04	0.58 ± 0.05	0.17 ± 0.04	1.2 ± 0.2
449	6.26 ± 0.09	0.42 ± 0.06	0.15 ± 0.06	0.43 ± 0.06	0.68 ± 0.06	1.5 ± 0.2	8.1 ± 0.2	2.5 ± 0.2	1.9 ± 0.3
450	20.5 ± 0.1	1.24 ± 0.08	0.47 ± 0.08	0.70 ± 0.09	1.07 ± 0.09	5.9 ± 0.3	15.9 ± 0.3	5.3 ± 0.3	9.9 ± 0.3
451	18.2 ± 0.2	2.0 ± 0.1	0.3 ± 0.1	1.5 ± 0.1	2.3 ± 0.1	5.3 ± 0.2	12.8 ± 0.3	3.9 ± 0.2	14.1 ± 0.5
452	37.4 ± 0.2	2.4 ± 0.1	0.9 ± 0.1	1.6 ± 0.1	2.2 ± 0.1	11.9 ± 0.4	30.5 ± 0.6	10.4 ± 0.4	19.6 ± 0.5
453	2.02 ± 0.04	0.27 ± 0.03	0.05 ± 0.03	0.18 ± 0.03	0.27 ± 0.03	0.61 ± 0.05	1.55 ± 0.06	0.54 ± 0.05	1.9 ± 0.1
454	73.0 ± 0.4	8.0 ± 0.3	2.1 ± 0.3	5.9 ± 0.3	8.0 ± 0.3	22.7 ± 0.6	31.6 ± 0.7	10.6 ± 0.6	71 ± 2
455	0.90 ± 0.04	0.01 ± 0.03	-0.01 ± 0.03	0.03 ± 0.03	0.07 ± 0.03	0.22 ± 0.04	1.32 ± 0.06	0.37 ± 0.04	0.56 ± 0.09
456	1.52 ± 0.04	0.17 ± 0.03	0.03 ± 0.03	0.07 ± 0.03	0.14 ± 0.03	0.47 ± 0.05	0.24 ± 0.04	0.09 ± 0.04	1.4 ± 0.1
457	8.56 ± 0.08	1.48 ± 0.05	0.41 ± 0.05	1.10 ± 0.06	1.61 ± 0.06	2.73 ± 0.08	4.0 ± 0.1	1.30 ± 0.07	11.1 ± 0.3
458	6.69 ± 0.08	0.86 ± 0.05	0.25 ± 0.05	0.60 ± 0.06	0.79 ± 0.06	1.82 ± 0.08	2.88 ± 0.09	0.89 ± 0.07	5.0 ± 0.2
459	1.24 ± 0.06	0.11 ± 0.04	0.00 ± 0.04	0.00 ± 0.04	0.05 ± 0.04	0.36 ± 0.05	0.27 ± 0.05	0.03 ± 0.04	1.1 ± 0.1
460	8.05 ± 0.07	0.75 ± 0.05	0.25 ± 0.05	0.51 ± 0.05	0.72 ± 0.05	2.72 ± 0.09	4.4 ± 0.1	1.30 ± 0.08	5.9 ± 0.2
461	102.6 ± 0.6	5.5 ± 0.4	1.8 ± 0.4	4.1 ± 0.4	5.6 ± 0.4	33 ± 2	151 ± 3	52 ± 2	41 ± 1
462	2.83 ± 0.05	0.28 ± 0.03	0.12 ± 0.03	0.18 ± 0.04	0.20 ± 0.04	0.93 ± 0.05	1.35 ± 0.06	0.39 ± 0.04	2.6 ± 0.2
463	2.04 ± 0.05	0.21 ± 0.04	0.06 ± 0.04	0.31 ± 0.04	0.39 ± 0.04	0.63 ± 0.07	1.07 ± 0.08	0.22 ± 0.06	1.5 ± 0.1
464	4.07 ± 0.08	0.57 ± 0.05	0.17 ± 0.05	0.49 ± 0.06	0.67 ± 0.06	1.24 ± 0.08	2.3 ± 0.1	0.73 ± 0.07	3.0 ± 0.2
465	4.09 ± 0.07	0.48 ± 0.05	0.05 ± 0.05	0.46 ± 0.05	0.62 ± 0.05	1.12 ± 0.08	1.83 ± 0.09	0.61 ± 0.07	3.4 ± 0.2

Corrected flux values with the local background of the emission regions in the catalogue from this study. The measured fluxes of the nine emission lines for the detected emission regions are presented. These fluxes are corrected for the local background, which includes the local emission and the stellar population (described in Section 2.6.7), and the extinction (described in Section 2.6.8). These flux are obtained by subtracting the background spectrum, instead of the background flux measured for each line (methodology used in this study), as discussed in Section 2.6.7. The uncertainties correspond to the propagated uncertainties (described in Section 2.6.4). All flux values are scaled by 1×10^{-15} .

ID	$H\alpha$ [erg s ⁻¹ cm ⁻²]	[N II] $\lambda 6583$ [erg s ⁻¹ cm ⁻²]	[N II] $\lambda 6548$ [erg s ⁻¹ cm ⁻²]	[S II] $\lambda 6731$ [erg s ⁻¹ cm ⁻²]	[S II] $\lambda 6716$ [erg s ⁻¹ cm ⁻²]	$H\beta$ [erg s ⁻¹ cm ⁻²]	[O III] $\lambda 5007$ [erg s ⁻¹ cm ⁻²]	[O III] $\lambda 4959$ [erg s ⁻¹ cm ⁻²]	[O II] $\lambda 3727$ [erg s ⁻¹ cm ⁻²]
466	19.8 ± 0.1	1.9 ± 0.1	0.6 ± 0.1	1.7 ± 0.1	2.4 ± 0.1	6.5 ± 0.2	11.0 ± 0.2	3.6 ± 0.2	15.6 ± 0.4
467	29.8 ± 0.2	2.3 ± 0.1	0.7 ± 0.1	1.6 ± 0.1	2.2 ± 0.1	7.8 ± 0.4	22.1 ± 0.6	7.8 ± 0.4	13.9 ± 0.4
468	29.9 ± 0.2	1.9 ± 0.1	0.7 ± 0.1	1.3 ± 0.1	1.8 ± 0.1	9.9 ± 0.4	29.0 ± 0.5	9.8 ± 0.4	21.0 ± 0.5
469	7.05 ± 0.06	0.51 ± 0.04	0.14 ± 0.04	0.38 ± 0.04	0.60 ± 0.04	2.3 ± 0.1	7.2 ± 0.2	2.5 ± 0.1	4.5 ± 0.1
470	14.6 ± 0.1	1.15 ± 0.09	0.43 ± 0.08	1.10 ± 0.09	1.59 ± 0.09	4.6 ± 0.2	14.5 ± 0.3	5.0 ± 0.2	9.4 ± 0.3
471	21.3 ± 0.2	1.7 ± 0.1	0.7 ± 0.1	1.6 ± 0.1	2.1 ± 0.1	7.1 ± 0.3	22.7 ± 0.4	7.6 ± 0.3	17.5 ± 0.5
472	6.0 ± 0.1	0.49 ± 0.09	0.10 ± 0.09	1.04 ± 0.09	1.50 ± 0.09	2.1 ± 0.2	1.4 ± 0.2	0.4 ± 0.1	5.5 ± 0.5
473	8.5 ± 0.1	0.65 ± 0.07	0.07 ± 0.07	0.45 ± 0.07	0.69 ± 0.07	3.0 ± 0.1	6.2 ± 0.1	2.2 ± 0.1	4.9 ± 0.3
474	8.17 ± 0.09	0.84 ± 0.06	0.30 ± 0.06	0.76 ± 0.06	1.23 ± 0.06	2.40 ± 0.08	2.94 ± 0.08	1.04 ± 0.08	7.0 ± 0.3
475	1.98 ± 0.05	0.13 ± 0.04	0.08 ± 0.04	0.13 ± 0.04	0.19 ± 0.04	0.73 ± 0.06	0.66 ± 0.06	0.14 ± 0.05	2.0 ± 0.2
476	9.5 ± 0.1	0.77 ± 0.08	0.24 ± 0.08	0.78 ± 0.08	1.01 ± 0.08	3.2 ± 0.2	12.9 ± 0.3	4.5 ± 0.2	5.7 ± 0.3
477	13.50 ± 0.09	1.34 ± 0.06	0.47 ± 0.06	0.97 ± 0.07	1.31 ± 0.07	4.3 ± 0.1	7.3 ± 0.2	2.6 ± 0.1	9.4 ± 0.3
478	60.6 ± 0.4	2.5 ± 0.3	0.8 ± 0.3	2.0 ± 0.3	2.7 ± 0.3	17.2 ± 0.9	68 ± 1	23 ± 1	17.8 ± 0.6
479	10.00 ± 0.08	0.77 ± 0.06	0.21 ± 0.06	0.56 ± 0.06	0.87 ± 0.06	3.4 ± 0.1	8.8 ± 0.2	3.0 ± 0.1	6.9 ± 0.2
480	8.8 ± 0.1	0.58 ± 0.07	0.22 ± 0.07	0.59 ± 0.07	0.78 ± 0.07	3.1 ± 0.1	11.2 ± 0.2	3.6 ± 0.2	5.2 ± 0.2
481	12.0 ± 0.1	1.49 ± 0.08	0.47 ± 0.07	1.36 ± 0.08	1.84 ± 0.08	3.8 ± 0.1	6.8 ± 0.2	2.3 ± 0.1	12.0 ± 0.3
482	35.1 ± 0.2	2.7 ± 0.2	0.8 ± 0.1	2.1 ± 0.2	3.1 ± 0.2	9.4 ± 0.4	28.5 ± 0.6	9.9 ± 0.4	18.0 ± 0.5
483	23.6 ± 0.1	1.8 ± 0.1	0.5 ± 0.1	1.4 ± 0.1	2.0 ± 0.1	6.5 ± 0.3	20.6 ± 0.4	7.0 ± 0.3	11.0 ± 0.3
484	11.4 ± 0.1	1.23 ± 0.07	0.43 ± 0.07	1.14 ± 0.07	1.77 ± 0.07	3.1 ± 0.1	5.0 ± 0.1	1.7 ± 0.1	7.3 ± 0.3
485	25.5 ± 0.2	1.6 ± 0.1	0.6 ± 0.1	1.2 ± 0.1	1.8 ± 0.1	7.7 ± 0.5	19.0 ± 0.7	7.0 ± 0.5	13 ± 2
486	6.1 ± 0.1	0.77 ± 0.07	0.31 ± 0.07	0.95 ± 0.07	1.35 ± 0.07	1.4 ± 0.1	4.9 ± 0.2	1.6 ± 0.1	4.0 ± 0.4
487	8.04 ± 0.09	0.53 ± 0.06	0.13 ± 0.06	0.40 ± 0.06	0.47 ± 0.06	2.8 ± 0.1	9.2 ± 0.2	3.0 ± 0.1	4.3 ± 0.2

Corrected flux values with the local background of the emission regions in the catalogue from this study. The measured fluxes of the nine emission lines for the detected emission regions are presented. These fluxes are corrected for the local background, which includes the local emission and the stellar population (described in Section 2.6.7), and the extinction (described in Section 2.6.8). These flux are obtained by subtracting the background spectrum, instead of the background flux measured for each line (methodology used in this study), as discussed in Section 2.6.7. The uncertainties correspond to the propagated uncertainties (described in Section 2.6.4). All flux values are scaled by 1×10^{-15} .

ID	$H\alpha$ [erg s $^{-1}$ cm $^{-2}$]	[N II] $\lambda 6583$ [erg s $^{-1}$ cm $^{-2}$]	[N II] $\lambda 6548$ [erg s $^{-1}$ cm $^{-2}$]	[S II] $\lambda 6731$ [erg s $^{-1}$ cm $^{-2}$]	[S II] $\lambda 6716$ [erg s $^{-1}$ cm $^{-2}$]	$H\beta$ [erg s $^{-1}$ cm $^{-2}$]	[O III] $\lambda 5007$ [erg s $^{-1}$ cm $^{-2}$]	[O III] $\lambda 4959$ [erg s $^{-1}$ cm $^{-2}$]	[O II] $\lambda 3727$ [erg s $^{-1}$ cm $^{-2}$]
488	3.96 ± 0.06	0.48 ± 0.04	0.16 ± 0.04	0.36 ± 0.04	0.50 ± 0.04	1.34 ± 0.07	0.87 ± 0.06	0.20 ± 0.06	4.3 ± 0.2
489	8.13 ± 0.07	0.50 ± 0.05	0.09 ± 0.05	0.35 ± 0.05	0.53 ± 0.05	2.7 ± 0.1	9.5 ± 0.2	3.3 ± 0.1	4.0 ± 0.2
490	2.46 ± 0.04	0.17 ± 0.04	0.05 ± 0.04	0.20 ± 0.04	0.15 ± 0.04	0.72 ± 0.06	1.85 ± 0.07	0.57 ± 0.06	1.7 ± 0.2
491	3.99 ± 0.06	0.40 ± 0.04	0.11 ± 0.04	0.34 ± 0.04	0.50 ± 0.04	1.48 ± 0.06	2.57 ± 0.07	0.97 ± 0.06	3.1 ± 0.2
492	1.21 ± 0.04	0.09 ± 0.03	0.02 ± 0.03	0.12 ± 0.03	0.15 ± 0.03	0.43 ± 0.06	0.49 ± 0.06	0.17 ± 0.05	0.9 ± 0.1
493	16.2 ± 0.1	1.32 ± 0.08	0.54 ± 0.08	1.09 ± 0.08	1.35 ± 0.08	5.5 ± 0.2	13.0 ± 0.3	4.7 ± 0.2	9.7 ± 0.4
494	98.7 ± 0.6	7.2 ± 0.4	2.8 ± 0.4	6.7 ± 0.5	9.1 ± 0.5	30 ± 1	74 ± 1	26 ± 1	65 ± 2
495	5.43 ± 0.06	0.56 ± 0.06	0.23 ± 0.06	0.63 ± 0.07	0.94 ± 0.07	1.5 ± 0.1	7.9 ± 0.2	2.6 ± 0.1	3.7 ± 0.3
496	11.37 ± 0.09	0.84 ± 0.06	0.37 ± 0.06	1.03 ± 0.06	1.44 ± 0.06	3.1 ± 0.1	10.8 ± 0.2	3.6 ± 0.2	7.0 ± 0.2
497	14.8 ± 0.1	1.25 ± 0.08	0.54 ± 0.08	0.68 ± 0.08	0.97 ± 0.08	4.7 ± 0.1	8.7 ± 0.2	3.0 ± 0.1	12.0 ± 0.3
498	11.5 ± 0.2	1.1 ± 0.2	0.6 ± 0.2	0.7 ± 0.2	0.7 ± 0.2	0.7 ± 0.3	-1.4 ± 0.3	-1.0 ± 0.3	6.4 ± 0.8
499	49.6 ± 0.3	2.9 ± 0.2	1.1 ± 0.2	2.5 ± 0.2	3.7 ± 0.2	14.1 ± 0.6	40.9 ± 0.9	14.2 ± 0.6	24.9 ± 0.6
500	1.19 ± 0.05	0.06 ± 0.04	0.12 ± 0.04	0.19 ± 0.04	0.19 ± 0.04	0.48 ± 0.09	0.06 ± 0.06	0.12 ± 0.06	0.9 ± 0.2
501	19.0 ± 0.1	1.75 ± 0.09	0.59 ± 0.09	1.7 ± 0.1	2.5 ± 0.1	5.7 ± 0.2	11.4 ± 0.2	3.8 ± 0.2	12.2 ± 0.2
502	5.3 ± 0.1	0.53 ± 0.08	0.09 ± 0.08	0.64 ± 0.09	1.00 ± 0.09	1.64 ± 0.08	2.6 ± 0.1	1.06 ± 0.08	4.1 ± 0.2
503	35.5 ± 0.3	2.2 ± 0.2	0.8 ± 0.2	1.9 ± 0.2	2.4 ± 0.2	10.5 ± 0.4	27.9 ± 0.6	9.5 ± 0.4	15.9 ± 0.5
504	4.35 ± 0.06	0.42 ± 0.04	0.11 ± 0.04	0.35 ± 0.04	0.36 ± 0.04	1.28 ± 0.06	1.84 ± 0.07	0.70 ± 0.05	3.1 ± 0.1
505	31.4 ± 0.2	1.3 ± 0.1	0.5 ± 0.1	1.0 ± 0.1	1.4 ± 0.1	10.3 ± 0.6	38.1 ± 0.8	13.1 ± 0.6	14.6 ± 0.5
506	31.9 ± 0.2	1.8 ± 0.1	0.6 ± 0.1	1.6 ± 0.1	2.2 ± 0.1	9.9 ± 0.4	28.2 ± 0.5	9.6 ± 0.4	15.7 ± 0.3
507	5.70 ± 0.08	0.55 ± 0.05	0.24 ± 0.05	0.61 ± 0.05	0.88 ± 0.05	2.0 ± 0.1	0.54 ± 0.07	0.03 ± 0.07	3.5 ± 0.2
508	17.8 ± 0.2	1.8 ± 0.1	0.6 ± 0.1	1.8 ± 0.1	2.6 ± 0.1	5.2 ± 0.2	9.1 ± 0.2	3.0 ± 0.2	15.4 ± 0.5
509	9.44 ± 0.08	0.50 ± 0.06	0.11 ± 0.05	0.31 ± 0.06	0.55 ± 0.06	3.2 ± 0.1	9.6 ± 0.2	3.3 ± 0.1	5.9 ± 0.2

Corrected flux values with the local background of the emission regions in the catalogue from this study. The measured fluxes of the nine emission lines for the detected emission regions are presented. These fluxes are corrected for the local background, which includes the local emission and the stellar population (described in Section 2.6.7), and the extinction (described in Section 2.6.8). These flux are obtained by subtracting the background spectrum, instead of the background flux measured for each line (methodology used in this study), as discussed in Section 2.6.7. The uncertainties correspond to the propagated uncertainties (described in Section 2.6.4). All flux values are scaled by 1×10^{-15} .

ID	$H\alpha$ [erg s ⁻¹ cm ⁻²]	[N II] $\lambda 6583$ [erg s ⁻¹ cm ⁻²]	[N II] $\lambda 6548$ [erg s ⁻¹ cm ⁻²]	[S II] $\lambda 6731$ [erg s ⁻¹ cm ⁻²]	[S II] $\lambda 6716$ [erg s ⁻¹ cm ⁻²]	$H\beta$ [erg s ⁻¹ cm ⁻²]	[O III] $\lambda 5007$ [erg s ⁻¹ cm ⁻²]	[O III] $\lambda 4959$ [erg s ⁻¹ cm ⁻²]	[O II] $\lambda 3727$ [erg s ⁻¹ cm ⁻²]
510	1.64 ± 0.05	0.19 ± 0.03	0.18 ± 0.03	0.08 ± 0.03	0.18 ± 0.03	0.44 ± 0.05	0.97 ± 0.07	0.31 ± 0.05	1.2 ± 0.2
511	15.8 ± 0.1	1.01 ± 0.07	0.32 ± 0.07	0.97 ± 0.08	1.24 ± 0.08	5.7 ± 0.2	15.7 ± 0.3	5.2 ± 0.2	10.2 ± 0.3
512	4.14 ± 0.06	0.36 ± 0.04	0.17 ± 0.04	0.36 ± 0.04	0.66 ± 0.05	1.27 ± 0.08	4.2 ± 0.1	1.43 ± 0.08	3.3 ± 0.2
513	11.34 ± 0.09	1.15 ± 0.06	0.38 ± 0.06	0.73 ± 0.07	1.06 ± 0.07	3.4 ± 0.1	5.2 ± 0.1	1.6 ± 0.1	11.3 ± 0.3
514	2.75 ± 0.05	0.24 ± 0.04	0.08 ± 0.04	0.28 ± 0.04	0.39 ± 0.04	0.86 ± 0.06	3.54 ± 0.09	1.22 ± 0.07	1.9 ± 0.1
515	21.2 ± 0.1	2.30 ± 0.09	0.91 ± 0.09	2.0 ± 0.1	2.7 ± 0.1	5.9 ± 0.2	6.3 ± 0.2	2.2 ± 0.1	17.5 ± 0.5
517	15.09 ± 0.09	1.44 ± 0.06	0.54 ± 0.06	0.95 ± 0.07	1.37 ± 0.07	4.2 ± 0.1	7.5 ± 0.2	2.5 ± 0.1	14.0 ± 0.4
518	106.6 ± 0.6	10.2 ± 0.4	3.3 ± 0.4	8.8 ± 0.4	12.7 ± 0.4	30 ± 1	76 ± 1	26 ± 1	93 ± 2
519	32.3 ± 0.2	2.5 ± 0.1	0.9 ± 0.1	1.4 ± 0.1	2.0 ± 0.1	9.0 ± 0.3	17.6 ± 0.3	6.1 ± 0.3	21.5 ± 0.5
520	46.9 ± 0.3	3.1 ± 0.2	1.1 ± 0.2	2.2 ± 0.2	2.9 ± 0.2	14.5 ± 0.6	39.9 ± 0.8	13.8 ± 0.6	24.2 ± 0.6
521	22.8 ± 0.1	1.6 ± 0.1	0.6 ± 0.1	1.1 ± 0.1	1.8 ± 0.1	6.5 ± 0.2	17.1 ± 0.3	5.8 ± 0.2	18.1 ± 0.4
522	54.6 ± 0.3	5.0 ± 0.2	1.8 ± 0.2	3.6 ± 0.2	4.8 ± 0.2	15.0 ± 0.4	19.4 ± 0.4	6.5 ± 0.3	39.7 ± 0.9
523	47.9 ± 0.3	4.5 ± 0.2	1.3 ± 0.2	3.5 ± 0.2	4.9 ± 0.2	13.9 ± 0.5	37.2 ± 0.5	12.8 ± 0.5	31.9 ± 0.8
524	174 ± 1	13.7 ± 0.7	5.0 ± 0.7	7.9 ± 0.7	10.6 ± 0.7	50 ± 1	103 ± 2	35 ± 1	104 ± 2
525	75.5 ± 0.4	7.0 ± 0.3	2.6 ± 0.3	4.8 ± 0.3	6.9 ± 0.3	23.4 ± 0.6	32.1 ± 0.6	10.9 ± 0.5	58 ± 1
526	70.9 ± 0.4	6.0 ± 0.3	2.1 ± 0.3	3.6 ± 0.3	4.9 ± 0.3	20.0 ± 0.6	37.1 ± 0.7	12.8 ± 0.5	50 ± 1
527	786 ± 4	42 ± 3	15 ± 3	30 ± 3	39 ± 3	240 ± 10	900 ± 20	310 ± 10	362 ± 8
528	7.85 ± 0.08	0.70 ± 0.05	0.28 ± 0.05	0.65 ± 0.05	0.88 ± 0.05	2.6 ± 0.1	7.8 ± 0.2	2.7 ± 0.1	4.1 ± 0.2
530	3.64 ± 0.05	0.40 ± 0.04	0.20 ± 0.04	0.60 ± 0.04	0.76 ± 0.04	1.00 ± 0.08	0.89 ± 0.08	0.18 ± 0.06	1.3 ± 0.2
531	2.24 ± 0.05	0.30 ± 0.03	0.10 ± 0.03	0.29 ± 0.03	0.52 ± 0.03	0.80 ± 0.07	0.18 ± 0.05	0.19 ± 0.05	1.5 ± 0.1
532	30.6 ± 0.2	3.7 ± 0.1	1.0 ± 0.1	4.6 ± 0.1	6.4 ± 0.1	10.0 ± 0.2	13.1 ± 0.3	4.4 ± 0.2	29.7 ± 0.6
533	0.71 ± 0.04	0.18 ± 0.03	-0.02 ± 0.03	0.10 ± 0.03	0.19 ± 0.03	0.31 ± 0.05	0.80 ± 0.07	0.25 ± 0.05	0.9 ± 0.1

Corrected flux values with the local background of the emission regions in the catalogue from this study. The measured fluxes of the nine emission lines for the detected emission regions are presented. These fluxes are corrected for the local background, which includes the local emission and the stellar population (described in Section 2.6.7), and the extinction (described in Section 2.6.8). These flux are obtained by subtracting the background spectrum, instead of the background flux measured for each line (methodology used in this study), as discussed in Section 2.6.7. The uncertainties correspond to the propagated uncertainties (described in Section 2.6.4). All flux values are scaled by 1×10^{-15} .

ID	$H\alpha$ [$\text{erg s}^{-1} \text{cm}^{-2}$]	$[\text{N II}]\lambda 6583$ [$\text{erg s}^{-1} \text{cm}^{-2}$]	$[\text{N II}]\lambda 6548$ [$\text{erg s}^{-1} \text{cm}^{-2}$]	$[\text{S II}]\lambda 6731$ [$\text{erg s}^{-1} \text{cm}^{-2}$]	$[\text{S II}]\lambda 6716$ [$\text{erg s}^{-1} \text{cm}^{-2}$]	$\text{H}\beta$ [$\text{erg s}^{-1} \text{cm}^{-2}$]	$[\text{O III}]\lambda 5007$ [$\text{erg s}^{-1} \text{cm}^{-2}$]	$[\text{O III}]\lambda 4959$ [$\text{erg s}^{-1} \text{cm}^{-2}$]	$[\text{O II}]\lambda 3727$ [$\text{erg s}^{-1} \text{cm}^{-2}$]
534	4.87 ± 0.08	0.49 ± 0.06	0.17 ± 0.06	0.32 ± 0.06	0.59 ± 0.06	1.6 ± 0.1	0.7 ± 0.1	-0.1 ± 0.1	2.7 ± 0.2
535	6.61 ± 0.08	0.75 ± 0.06	0.32 ± 0.05	0.58 ± 0.06	0.77 ± 0.06	2.0 ± 0.1	6.1 ± 0.1	2.1 ± 0.1	4.7 ± 0.2
536	4.27 ± 0.07	0.51 ± 0.05	0.14 ± 0.05	0.64 ± 0.05	0.71 ± 0.05	1.40 ± 0.07	4.9 ± 0.1	1.48 ± 0.07	3.4 ± 0.2
537	8.71 ± 0.07	1.23 ± 0.05	0.41 ± 0.05	0.90 ± 0.05	1.30 ± 0.05	2.30 ± 0.08	4.9 ± 0.1	1.66 ± 0.08	13.2 ± 0.3
538	4.95 ± 0.07	0.67 ± 0.05	0.18 ± 0.05	0.64 ± 0.05	1.09 ± 0.05	1.44 ± 0.09	4.8 ± 0.1	1.41 ± 0.09	3.8 ± 0.2
539	4.96 ± 0.06	0.68 ± 0.04	0.18 ± 0.04	0.66 ± 0.04	1.03 ± 0.04	1.63 ± 0.09	6.2 ± 0.1	2.0 ± 0.1	3.6 ± 0.1
540	3.44 ± 0.07	0.53 ± 0.05	0.12 ± 0.05	0.46 ± 0.05	0.57 ± 0.05	1.3 ± 0.1	0.61 ± 0.08	0.29 ± 0.07	4.0 ± 0.2
541	9.67 ± 0.08	1.46 ± 0.05	0.51 ± 0.05	0.90 ± 0.06	1.50 ± 0.06	3.2 ± 0.1	6.0 ± 0.1	1.98 ± 0.09	13.0 ± 0.3
542	4.68 ± 0.08	0.44 ± 0.05	0.06 ± 0.05	0.37 ± 0.05	0.68 ± 0.05	1.01 ± 0.09	1.5 ± 0.1	0.48 ± 0.08	2.5 ± 0.2
543	2.7 ± 0.2	0.32 ± 0.05	0.21 ± 0.06	0.39 ± 0.07	0.54 ± 0.07	1.0 ± 0.4	7.2 ± 0.6	2.1 ± 0.8	2.3 ± 0.5

Table F.4

Corrected flux values of the emission regions in the catalogue from this study. The measured fluxes of the nine emission lines for the detected emission regions are presented. These fluxes are corrected for the local background emission (described in Section 2.6.3), the global stellar absorption (described in Section 2.6.7), and the extinction (described in Section 2.6.8). The $[\text{O II}]\lambda 3727$ is listed here, but comes from Table F.3. The uncertainties correspond to the propagated uncertainties (described in Section 2.6.4). All flux values are scaled by 1×10^{-15} .

ID	$\text{H}\alpha$ [$\text{erg s}^{-1} \text{cm}^{-2}$]	$[\text{N II}]\lambda 6583$ [$\text{erg s}^{-1} \text{cm}^{-2}$]	$[\text{N II}]\lambda 6548$ [$\text{erg s}^{-1} \text{cm}^{-2}$]	$[\text{S II}]\lambda 6731$ [$\text{erg s}^{-1} \text{cm}^{-2}$]	$[\text{S II}]\lambda 6716$ [$\text{erg s}^{-1} \text{cm}^{-2}$]	$\text{H}\beta$ [$\text{erg s}^{-1} \text{cm}^{-2}$]	$[\text{O III}]\lambda 5007$ [$\text{erg s}^{-1} \text{cm}^{-2}$]	$[\text{O III}]\lambda 4959$ [$\text{erg s}^{-1} \text{cm}^{-2}$]	$[\text{O II}]\lambda 3727$ [$\text{erg s}^{-1} \text{cm}^{-2}$]	
215	0	0.7 ± 0.2	-0.05 ± 0.03	0.02 ± 0.05	0.09 ± 0.06	0.03 ± 0.05	0.2 ± 0.1	1.3 ± 0.4	0.5 ± 0.2	-0.09 ± 0.06
	2	4.6 ± 0.3	0.48 ± 0.08	0.12 ± 0.06	0.41 ± 0.08	0.61 ± 0.09	1.6 ± 0.2	2.5 ± 0.3	0.9 ± 0.1	5.8 ± 0.6
	3	3.1 ± 0.7	0.3 ± 0.1	0.14 ± 0.08	0.4 ± 0.1	0.8 ± 0.2	1.1 ± 0.3	1.6 ± 0.4	0.5 ± 0.2	5 ± 1
	4	1.4 ± 0.2	0.26 ± 0.06	0.04 ± 0.04	0.21 ± 0.05	0.34 ± 0.07	0.49 ± 0.09	0.39 ± 0.08	0.11 ± 0.05	2.0 ± 0.4
	6	1.6 ± 0.4	0.27 ± 0.08	0.06 ± 0.04	0.26 ± 0.08	0.4 ± 0.1	0.6 ± 0.1	0.5 ± 0.2	0.15 ± 0.06	2.0 ± 0.6
	7	3 ± 1	0.4 ± 0.2	0.14 ± 0.08	0.3 ± 0.1	0.5 ± 0.2	0.9 ± 0.4	1.3 ± 0.5	0.5 ± 0.2	4 ± 2
	8	0.7 ± 0.1	0.08 ± 0.04	0.03 ± 0.03	0.09 ± 0.04	0.14 ± 0.05	0.26 ± 0.07	0.9 ± 0.2	0.33 ± 0.08	0.8 ± 0.2
	9	6.5 ± 0.6	0.7 ± 0.1	0.25 ± 0.06	0.8 ± 0.1	0.8 ± 0.1	2.3 ± 0.3	3.0 ± 0.3	1.1 ± 0.2	9 ± 1
	10	71 ± 3	6.3 ± 0.5	1.9 ± 0.4	4.1 ± 0.5	5.7 ± 0.5	25 ± 2	52 ± 3	18 ± 2	69 ± 4
	11	6 ± 2	0.7 ± 0.2	0.2 ± 0.1	0.8 ± 0.2	1.0 ± 0.3	2.2 ± 0.6	3.7 ± 0.9	1.4 ± 0.4	9 ± 2
	13	13.7 ± 0.9	1.7 ± 0.2	0.4 ± 0.1	1.7 ± 0.2	2.6 ± 0.2	4.9 ± 0.5	9.1 ± 0.8	3.0 ± 0.4	18 ± 1
	14	2.7 ± 0.6	0.5 ± 0.1	0.2 ± 0.1	0.5 ± 0.1	0.7 ± 0.2	1.0 ± 0.3	0.4 ± 0.2	0.2 ± 0.1	2.8 ± 0.7
	15	1.7 ± 0.4	0.3 ± 0.1	0.17 ± 0.08	0.21 ± 0.09	0.4 ± 0.1	0.6 ± 0.2	0.4 ± 0.1	0.12 ± 0.07	2.4 ± 0.7
	16	7 ± 2	1.0 ± 0.3	0.3 ± 0.1	0.8 ± 0.2	1.2 ± 0.3	2.5 ± 0.6	1.9 ± 0.5	0.8 ± 0.2	12 ± 3
	17	3 ± 2	0.5 ± 0.3	0.1 ± 0.1	0.4 ± 0.3	0.6 ± 0.4	1.2 ± 0.7	1.2 ± 0.8	0.4 ± 0.3	4 ± 2
	18	5.9 ± 0.7	1.0 ± 0.2	0.4 ± 0.1	0.9 ± 0.2	1.2 ± 0.2	2.1 ± 0.4	3.2 ± 0.5	1.0 ± 0.2	9 ± 2
	19	44 ± 2	5.1 ± 0.4	1.6 ± 0.2	4.3 ± 0.3	5.6 ± 0.4	15 ± 1	19 ± 1	6.7 ± 0.7	52 ± 3
	20	8.0 ± 0.9	1.0 ± 0.1	0.30 ± 0.08	1.1 ± 0.2	1.5 ± 0.2	2.9 ± 0.5	13 ± 1	4.5 ± 0.6	7 ± 1
	21	12.3 ± 0.8	1.3 ± 0.1	0.5 ± 0.1	1.4 ± 0.2	1.9 ± 0.2	4.3 ± 0.4	10.7 ± 0.9	3.5 ± 0.4	14 ± 1
	22	3 ± 1	0.5 ± 0.3	0.2 ± 0.2	0.7 ± 0.3	0.7 ± 0.3	1.2 ± 0.5	1.1 ± 0.5	0.1 ± 0.3	10 ± 4

Corrected flux values of the emission regions in the catalogue from this study. The measured fluxes of the nine emission lines for the detected emission regions are presented. These fluxes are corrected for the local background emission (described in Section 2.6.3), the global stellar absorption (described in Section 2.6.7), and the extinction (described in Section 2.6.8). The [O II] λ 3727 is listed here, but comes from Table F.3. The uncertainties correspond to the propagated uncertainties (described in Section 2.6.4). All flux values are scaled by 1×10^{-15} .

ID	$H\alpha$ [erg s $^{-1}$ cm $^{-2}$]	[N II] λ 6583 [erg s $^{-1}$ cm $^{-2}$]	[N II] λ 6548 [erg s $^{-1}$ cm $^{-2}$]	[S II] λ 6731 [erg s $^{-1}$ cm $^{-2}$]	[S II] λ 6716 [erg s $^{-1}$ cm $^{-2}$]	$H\beta$ [erg s $^{-1}$ cm $^{-2}$]	[O III] λ 5007 [erg s $^{-1}$ cm $^{-2}$]	[O III] λ 4959 [erg s $^{-1}$ cm $^{-2}$]	[O II] λ 3727 [erg s $^{-1}$ cm $^{-2}$]
23	1.5 ± 0.4	0.25 ± 0.07	0.10 ± 0.05	0.27 ± 0.08	0.4 ± 0.1	0.5 ± 0.1	2.2 ± 0.5	0.7 ± 0.2	2.3 ± 0.6
24	5.2 ± 0.5	0.5 ± 0.1	0.23 ± 0.08	0.5 ± 0.1	0.8 ± 0.1	1.8 ± 0.3	5.3 ± 0.6	1.7 ± 0.3	7.2 ± 0.9
25	2.4 ± 0.5	0.26 ± 0.09	0.13 ± 0.06	0.21 ± 0.08	0.4 ± 0.1	0.9 ± 0.3	0.7 ± 0.3	0.2 ± 0.2	2.3 ± 0.6
26	1.7 ± 0.3	0.21 ± 0.07	0.08 ± 0.05	0.24 ± 0.07	0.35 ± 0.09	0.6 ± 0.2	0.4 ± 0.2	0.05 ± 0.08	1.8 ± 0.5
27	1.2 ± 0.3	0.17 ± 0.06	0.02 ± 0.04	0.21 ± 0.07	0.22 ± 0.07	0.4 ± 0.1	0.2 ± 0.1	0.10 ± 0.07	1.4 ± 0.4
28	3.0 ± 0.7	0.5 ± 0.2	0.3 ± 0.1	0.6 ± 0.2	1.0 ± 0.3	1.1 ± 0.3	0.8 ± 0.3	0.3 ± 0.2	5 ± 1
29	5 ± 1	0.9 ± 0.3	0.3 ± 0.2	0.6 ± 0.2	1.5 ± 0.4	1.8 ± 0.5	7 ± 1	2.6 ± 0.6	10 ± 2
30	10.9 ± 0.6	0.8 ± 0.1	0.37 ± 0.09	0.7 ± 0.1	1.0 ± 0.1	3.9 ± 0.4	9.1 ± 0.7	3.2 ± 0.3	9.7 ± 0.8
31	4.2 ± 0.5	0.5 ± 0.1	0.04 ± 0.06	0.7 ± 0.1	0.8 ± 0.2	1.5 ± 0.3	0.8 ± 0.2	0.3 ± 0.1	5.8 ± 0.9
32	2.2 ± 0.5	0.3 ± 0.1	0.11 ± 0.09	0.5 ± 0.2	0.7 ± 0.2	0.8 ± 0.3	0.6 ± 0.2	0.2 ± 0.1	4 ± 1
33	2.4 ± 0.5	0.4 ± 0.1	0.09 ± 0.09	0.4 ± 0.1	0.4 ± 0.1	0.8 ± 0.3	0.6 ± 0.2	0.0 ± 0.1	5 ± 1
34	7 ± 1	1.0 ± 0.3	0.4 ± 0.2	1.3 ± 0.3	1.5 ± 0.4	2.6 ± 0.8	1.2 ± 0.5	0.2 ± 0.3	10 ± 3
35	4 ± 1	0.6 ± 0.2	0.2 ± 0.1	0.8 ± 0.2	1.0 ± 0.3	1.4 ± 0.5	1.4 ± 0.5	0.4 ± 0.2	6 ± 2
36	20 ± 2	2.9 ± 0.3	1.0 ± 0.2	3.5 ± 0.3	4.9 ± 0.4	7.3 ± 0.8	10 ± 1	3.5 ± 0.5	24 ± 2
37	18 ± 1	2.4 ± 0.2	0.8 ± 0.1	2.1 ± 0.2	3.2 ± 0.3	6.3 ± 0.6	6.3 ± 0.6	2.3 ± 0.3	23 ± 2
38	12 ± 1	1.9 ± 0.3	0.4 ± 0.1	2.4 ± 0.3	3.4 ± 0.4	4.2 ± 0.6	4.5 ± 0.8	1.6 ± 0.4	14 ± 2
39	10 ± 1	1.5 ± 0.3	0.5 ± 0.1	1.7 ± 0.3	2.5 ± 0.4	3.6 ± 0.7	5.1 ± 0.8	1.9 ± 0.4	14 ± 2
40	8 ± 1	1.2 ± 0.2	0.3 ± 0.1	1.3 ± 0.2	1.7 ± 0.3	2.8 ± 0.5	4.7 ± 0.8	1.8 ± 0.3	12 ± 2
41	14 ± 1	1.9 ± 0.2	0.6 ± 0.1	1.7 ± 0.2	2.2 ± 0.2	5.1 ± 0.6	16 ± 1	5.5 ± 0.7	16 ± 2
42	24 ± 1	3.5 ± 0.3	0.9 ± 0.2	3.7 ± 0.3	5.5 ± 0.4	8.4 ± 0.8	10.6 ± 0.9	3.6 ± 0.5	26 ± 2
43	20 ± 2	1.9 ± 0.3	0.7 ± 0.2	1.7 ± 0.2	2.4 ± 0.3	7 ± 1	13 ± 2	4.5 ± 0.8	22 ± 2
44	7 ± 2	1.2 ± 0.3	0.3 ± 0.2	1.3 ± 0.4	1.9 ± 0.5	3 ± 1	4 ± 1	1.3 ± 0.7	8 ± 2
45	6 ± 1	0.8 ± 0.2	0.2 ± 0.1	1.0 ± 0.2	1.5 ± 0.3	2.1 ± 0.5	2.7 ± 0.7	0.9 ± 0.4	8 ± 1
46	8 ± 1	1.3 ± 0.2	0.3 ± 0.1	1.3 ± 0.2	2.0 ± 0.3	2.9 ± 0.4	2.7 ± 0.4	0.9 ± 0.2	10 ± 1

Corrected flux values of the emission regions in the catalogue from this study. The measured fluxes of the nine emission lines for the detected emission regions are presented. These fluxes are corrected for the local background emission (described in Section 2.6.3), the global stellar absorption (described in Section 2.6.7), and the extinction (described in Section 2.6.8). The [O II] λ 3727 is listed here, but comes from Table F.3. The uncertainties correspond to the propagated uncertainties (described in Section 2.6.4). All flux values are scaled by 1×10^{-15} .

ID	$H\alpha$ [erg s $^{-1}$ cm $^{-2}$]	[N II] λ 6583 [erg s $^{-1}$ cm $^{-2}$]	[N II] λ 6548 [erg s $^{-1}$ cm $^{-2}$]	[S II] λ 6731 [erg s $^{-1}$ cm $^{-2}$]	[S II] λ 6716 [erg s $^{-1}$ cm $^{-2}$]	$H\beta$ [erg s $^{-1}$ cm $^{-2}$]	[O III] λ 5007 [erg s $^{-1}$ cm $^{-2}$]	[O III] λ 4959 [erg s $^{-1}$ cm $^{-2}$]	[O II] λ 3727 [erg s $^{-1}$ cm $^{-2}$]
47	4.5 ± 0.8	0.6 ± 0.2	0.2 ± 0.1	0.7 ± 0.2	1.1 ± 0.2	1.6 ± 0.4	1.2 ± 0.4	0.2 ± 0.2	5 ± 1
48	25 ± 2	2.6 ± 0.3	0.7 ± 0.2	1.8 ± 0.2	2.8 ± 0.3	8.7 ± 0.9	13 ± 1	4.7 ± 0.7	31 ± 3
49	14 ± 1	2.1 ± 0.3	0.7 ± 0.2	2.5 ± 0.3	3.6 ± 0.4	5.0 ± 0.7	5.3 ± 0.8	1.9 ± 0.4	1.8 ± 2
50	7.1 ± 0.9	1.2 ± 0.2	0.4 ± 0.1	1.3 ± 0.2	1.9 ± 0.3	2.5 ± 0.4	3.4 ± 0.5	1.1 ± 0.3	10 ± 1
51	2.3 ± 0.5	0.29 ± 0.08	0.08 ± 0.04	0.23 ± 0.08	0.30 ± 0.09	0.8 ± 0.2	1.0 ± 0.2	0.3 ± 0.1	2.3 ± 0.6
52	5.6 ± 0.5	0.6 ± 0.1	0.16 ± 0.09	0.8 ± 0.1	0.8 ± 0.1	2.0 ± 0.3	3.2 ± 0.4	1.0 ± 0.2	9 ± 1
53	15 ± 2	1.8 ± 0.3	0.5 ± 0.2	2.0 ± 0.3	2.4 ± 0.4	5 ± 1	10 ± 2	3.5 ± 0.8	20 ± 3
54	4.4 ± 0.4	0.54 ± 0.09	0.33 ± 0.08	0.53 ± 0.09	0.6 ± 0.1	1.6 ± 0.2	1.5 ± 0.2	0.6 ± 0.1	5.6 ± 0.7
55	21 ± 1	2.2 ± 0.3	0.8 ± 0.2	2.2 ± 0.3	3.0 ± 0.3	7.4 ± 0.7	9.3 ± 0.8	3.3 ± 0.5	27 ± 2
56	12 ± 2	1.8 ± 0.4	0.5 ± 0.2	2.3 ± 0.5	3.0 ± 0.6	4 ± 1	8 ± 2	2.6 ± 0.9	15 ± 3
57	3.3 ± 0.7	0.5 ± 0.2	0.2 ± 0.1	0.6 ± 0.2	0.7 ± 0.2	1.2 ± 0.4	0.7 ± 0.3	0.3 ± 0.2	5 ± 1
58	3.6 ± 0.9	0.6 ± 0.2	0.15 ± 0.07	0.8 ± 0.2	1.2 ± 0.3	1.3 ± 0.4	1.7 ± 0.5	0.6 ± 0.2	5 ± 1
59	5 ± 1	0.4 ± 0.1	0.2 ± 0.1	0.6 ± 0.2	0.7 ± 0.2	1.8 ± 0.6	4 ± 1	1.5 ± 0.5	6 ± 2
60	3.1 ± 0.7	0.5 ± 0.1	0.09 ± 0.06	0.7 ± 0.2	0.9 ± 0.2	1.1 ± 0.3	1.2 ± 0.4	0.4 ± 0.2	2.9 ± 0.7
61	1.4 ± 0.2	0.17 ± 0.04	0.10 ± 0.04	0.17 ± 0.04	0.28 ± 0.06	0.5 ± 0.1	0.22 ± 0.07	0.07 ± 0.04	1.3 ± 0.3
62	2.3 ± 0.7	0.4 ± 0.1	0.13 ± 0.07	0.4 ± 0.1	0.6 ± 0.2	0.8 ± 0.3	0.8 ± 0.3	0.3 ± 0.2	2.3 ± 0.7
63	10.9 ± 0.7	0.9 ± 0.1	0.40 ± 0.09	0.8 ± 0.1	1.1 ± 0.1	3.9 ± 0.4	6.0 ± 0.5	2.1 ± 0.3	11 ± 1
64	2 ± 1	0.2 ± 0.2	0.1 ± 0.2	0.2 ± 0.2	0.2 ± 0.2	0.9 ± 0.6	2 ± 1	0.4 ± 0.4	9 ± 5
65	3.3 ± 0.4	0.36 ± 0.08	0.15 ± 0.06	0.42 ± 0.08	0.6 ± 0.1	1.2 ± 0.2	0.7 ± 0.1	0.22 ± 0.09	4.0 ± 0.5
66	13.6 ± 0.8	1.4 ± 0.2	0.4 ± 0.1	1.0 ± 0.1	1.6 ± 0.2	4.8 ± 0.5	9.6 ± 0.7	3.3 ± 0.4	1.9 ± 1
67	6.3 ± 0.5	0.69 ± 0.09	0.20 ± 0.05	0.55 ± 0.08	0.9 ± 0.1	2.2 ± 0.2	6.4 ± 0.5	2.2 ± 0.2	7.1 ± 0.7
68	1.3 ± 0.2	0.26 ± 0.07	0.07 ± 0.04	0.13 ± 0.05	0.29 ± 0.07	0.5 ± 0.1	0.27 ± 0.08	0.13 ± 0.06	1.2 ± 0.3
69	2.1 ± 0.3	0.24 ± 0.06	0.09 ± 0.04	0.24 ± 0.06	0.38 ± 0.08	0.7 ± 0.1	3.2 ± 0.5	1.1 ± 0.2	1.7 ± 0.3
70	2.1 ± 0.2	0.25 ± 0.05	0.19 ± 0.04	0.21 ± 0.05	0.37 ± 0.06	0.7 ± 0.1	0.8 ± 0.1	0.31 ± 0.07	2.3 ± 0.3

Corrected flux values of the emission regions in the catalogue from this study. The measured fluxes of the nine emission lines for the detected emission regions are presented. These fluxes are corrected for the local background emission (described in Section 2.6.3), the global stellar absorption (described in Section 2.6.7), and the extinction (described in Section 2.6.8). The [O II] λ 3727 is listed here, but comes from Table F.3. The uncertainties correspond to the propagated uncertainties (described in Section 2.6.4). All flux values are scaled by 1×10^{-15} .

ID	$H\alpha$ [erg s $^{-1}$ cm $^{-2}$]	[N II] λ 6583 [erg s $^{-1}$ cm $^{-2}$]	[N II] λ 6548 [erg s $^{-1}$ cm $^{-2}$]	[S II] λ 6731 [erg s $^{-1}$ cm $^{-2}$]	[S II] λ 6716 [erg s $^{-1}$ cm $^{-2}$]	$H\beta$ [erg s $^{-1}$ cm $^{-2}$]	[O III] λ 5007 [erg s $^{-1}$ cm $^{-2}$]	[O III] λ 4959 [erg s $^{-1}$ cm $^{-2}$]	[O II] λ 3727 [erg s $^{-1}$ cm $^{-2}$]
71	4.8 ± 0.9	0.9 ± 0.2	0.16 ± 0.08	0.8 ± 0.2	1.0 ± 0.2	1.7 ± 0.5	1.5 ± 0.4	0.5 ± 0.3	5 ± 1
72	8.6 ± 0.5	1.1 ± 0.1	0.35 ± 0.08	0.9 ± 0.1	1.4 ± 0.1	3.0 ± 0.3	2.3 ± 0.3	0.8 ± 0.2	10.2 ± 0.9
73	7 ± 2	1.1 ± 0.5	0.5 ± 0.3	1.0 ± 0.5	1.7 ± 0.7	2 ± 1	4 ± 2	1.4 ± 0.8	7 ± 3
74	6 ± 1	0.8 ± 0.3	0.3 ± 0.1	1.0 ± 0.3	1.4 ± 0.4	2.2 ± 0.8	4 ± 1	1.3 ± 0.6	8 ± 2
75	3 ± 1	0.4 ± 0.2	0.18 ± 0.08	0.4 ± 0.2	0.6 ± 0.2	1.1 ± 0.4	1.9 ± 0.7	0.6 ± 0.3	3 ± 1
76	5 ± 2	0.8 ± 0.3	0.3 ± 0.1	0.7 ± 0.3	1.2 ± 0.4	1.8 ± 0.7	3 ± 1	1.2 ± 0.5	5 ± 2
77	32 ± 6	5 ± 1	1.8 ± 0.7	5 ± 1	7 ± 2	11 ± 3	17 ± 5	6 ± 2	35 ± 7
78	1.9 ± 0.4	0.28 ± 0.08	0.08 ± 0.05	0.30 ± 0.08	0.4 ± 0.1	0.7 ± 0.2	0.4 ± 0.1	0.07 ± 0.07	2.6 ± 0.6
79	45 ± 3	3.7 ± 0.4	1.4 ± 0.3	2.9 ± 0.4	3.9 ± 0.4	16 ± 2	39 ± 3	14 ± 2	37 ± 3
80	4.0 ± 0.4	0.55 ± 0.09	0.07 ± 0.06	0.6 ± 0.1	0.9 ± 0.1	1.4 ± 0.2	0.7 ± 0.1	0.16 ± 0.08	5.6 ± 0.7
81	6.0 ± 0.5	0.8 ± 0.1	0.22 ± 0.07	1.0 ± 0.1	1.4 ± 0.2	2.1 ± 0.2	1.3 ± 0.2	0.4 ± 0.1	8.4 ± 0.8
82	9.6 ± 0.6	1.1 ± 0.1	0.41 ± 0.09	1.2 ± 0.1	1.9 ± 0.2	3.4 ± 0.3	2.4 ± 0.2	1.0 ± 0.2	14 ± 1
83	21 ± 5	4 ± 1	1.2 ± 0.6	4 ± 1	6 ± 2	7 ± 3	8 ± 3	3 ± 2	23 ± 6
84	8.1 ± 0.6	0.8 ± 0.1	0.17 ± 0.07	0.8 ± 0.1	1.2 ± 0.1	2.9 ± 0.3	4.8 ± 0.5	1.8 ± 0.2	8.5 ± 0.8
85	29 ± 4	4.6 ± 0.8	1.6 ± 0.4	4.5 ± 0.8	6 ± 1	10 ± 2	17 ± 3	6 ± 2	33 ± 5
86	19 ± 1	2.1 ± 0.2	0.7 ± 0.1	1.5 ± 0.2	2.3 ± 0.2	6.6 ± 0.7	9.3 ± 0.9	3.2 ± 0.5	21 ± 2
87	19 ± 3	2.9 ± 0.5	1.0 ± 0.3	2.7 ± 0.5	4.0 ± 0.7	7 ± 1	12 ± 2	4 ± 1	20 ± 3
88	6 ± 2	0.8 ± 0.2	0.2 ± 0.1	0.6 ± 0.2	1.0 ± 0.3	2.1 ± 0.7	5 ± 1	2.0 ± 0.6	5 ± 1
89	4.5 ± 0.9	0.6 ± 0.1	0.29 ± 0.08	0.6 ± 0.1	0.8 ± 0.2	1.6 ± 0.3	1.9 ± 0.4	0.6 ± 0.2	5 ± 1
90	0.27 ± 0.09	0.08 ± 0.04	0.05 ± 0.03	0.02 ± 0.03	0.07 ± 0.04	0.09 ± 0.04	0.01 ± 0.02	0.02 ± 0.02	0.19 ± 0.08
91	2.2 ± 0.4	0.3 ± 0.1	0.10 ± 0.07	0.28 ± 0.09	0.4 ± 0.1	0.8 ± 0.2	0.8 ± 0.2	0.1 ± 0.1	3.2 ± 0.8
92	4.1 ± 0.9	0.5 ± 0.2	0.2 ± 0.1	0.6 ± 0.2	1.0 ± 0.3	1.5 ± 0.4	1.5 ± 0.5	0.5 ± 0.3	6 ± 1
93	9 ± 2	1.8 ± 0.6	0.7 ± 0.3	1.5 ± 0.5	2.0 ± 0.6	3 ± 1	5 ± 2	2 ± 1	9 ± 3
94	38 ± 2	3.8 ± 0.3	1.2 ± 0.2	2.6 ± 0.3	3.6 ± 0.3	13 ± 1	22 ± 1	8.0 ± 0.7	41 ± 2

Corrected flux values of the emission regions in the catalogue from this study. The measured fluxes of the nine emission lines for the detected emission regions are presented. These fluxes are corrected for the local background emission (described in Section 2.6.3), the global stellar absorption (described in Section 2.6.7), and the extinction (described in Section 2.6.8). The [O II] λ 3727 is listed here, but comes from Table F.3. The uncertainties correspond to the propagated uncertainties (described in Section 2.6.4). All flux values are scaled by 1×10^{-15} .

ID	$H\alpha$ [erg s $^{-1}$ cm $^{-2}$]	[N II] λ 6583 [erg s $^{-1}$ cm $^{-2}$]	[N II] λ 6548 [erg s $^{-1}$ cm $^{-2}$]	[S II] λ 6731 [erg s $^{-1}$ cm $^{-2}$]	[S II] λ 6716 [erg s $^{-1}$ cm $^{-2}$]	$H\beta$ [erg s $^{-1}$ cm $^{-2}$]	[O III] λ 5007 [erg s $^{-1}$ cm $^{-2}$]	[O III] λ 4959 [erg s $^{-1}$ cm $^{-2}$]	[O II] λ 3727 [erg s $^{-1}$ cm $^{-2}$]
95	123 \pm 7	9.0 \pm 0.9	3.0 \pm 0.6	5.1 \pm 0.7	7.3 \pm 0.8	44 \pm 3	91 \pm 6	32 \pm 3	104 \pm 7
96	10 \pm 2	1.6 \pm 0.5	0.7 \pm 0.3	1.3 \pm 0.4	1.9 \pm 0.5	4 \pm 1	6 \pm 2	2 \pm 1	11 \pm 3
97	43 \pm 5	6 \pm 1	1.7 \pm 0.5	5.2 \pm 0.9	7 \pm 1	15 \pm 3	32 \pm 5	12 \pm 3	38 \pm 5
98	2.7 \pm 0.2	0.13 \pm 0.04	0.04 \pm 0.03	0.11 \pm 0.04	0.14 \pm 0.04	1.0 \pm 0.1	2.7 \pm 0.3	1.0 \pm 0.1	1.7 \pm 0.2
99	8 \pm 2	1.1 \pm 0.3	0.3 \pm 0.1	1.0 \pm 0.3	1.5 \pm 0.4	2.9 \pm 0.9	6 \pm 2	2.0 \pm 0.7	8 \pm 2
100	26 \pm 1	2.7 \pm 0.2	1.0 \pm 0.2	2.0 \pm 0.2	2.8 \pm 0.2	9.0 \pm 0.7	13.9 \pm 0.9	4.8 \pm 0.5	28 \pm 2
101	7.0 \pm 0.9	0.6 \pm 0.1	0.3 \pm 0.1	0.5 \pm 0.1	0.8 \pm 0.2	2.5 \pm 0.5	6 \pm 1	2.0 \pm 0.5	5.2 \pm 0.8
102	14 \pm 3	2.2 \pm 0.6	0.7 \pm 0.2	2.1 \pm 0.5	2.9 \pm 0.7	5 \pm 1	10 \pm 3	3 \pm 1	15 \pm 4
103	6.4 \pm 0.6	0.8 \pm 0.1	0.27 \pm 0.08	0.7 \pm 0.1	1.0 \pm 0.1	2.3 \pm 0.4	2.9 \pm 0.4	0.9 \pm 0.2	5.4 \pm 0.7
104	61 \pm 5	6.2 \pm 0.7	2.0 \pm 0.5	5.4 \pm 0.7	7.4 \pm 0.8	22 \pm 3	60 \pm 6	21 \pm 3	46 \pm 5
105	15 \pm 2	1.6 \pm 0.3	0.4 \pm 0.2	1.4 \pm 0.3	2.0 \pm 0.3	5 \pm 1	12 \pm 2	4.3 \pm 0.9	11 \pm 2
106	7 \pm 1	0.9 \pm 0.2	0.3 \pm 0.1	0.8 \pm 0.2	1.2 \pm 0.2	2.5 \pm 0.5	4.7 \pm 0.8	1.8 \pm 0.4	7 \pm 1
107	8 \pm 1	0.8 \pm 0.2	0.3 \pm 0.1	0.7 \pm 0.2	1.1 \pm 0.2	3.0 \pm 0.6	7 \pm 1	2.3 \pm 0.6	5.6 \pm 0.8
108	13 \pm 2	1.8 \pm 0.3	0.7 \pm 0.1	1.5 \pm 0.2	2.3 \pm 0.3	4.7 \pm 0.8	10 \pm 1	3.4 \pm 0.7	12 \pm 2
109	2.2 \pm 0.4	0.13 \pm 0.07	0.00 \pm 0.05	0.17 \pm 0.07	0.17 \pm 0.07	0.8 \pm 0.2	2.3 \pm 0.4	0.8 \pm 0.2	3.3 \pm 0.8
110	13.6 \pm 0.9	1.4 \pm 0.2	0.4 \pm 0.1	1.1 \pm 0.1	1.6 \pm 0.2	4.8 \pm 0.6	11 \pm 1	3.7 \pm 0.5	9.2 \pm 0.9
111	65 \pm 5	7.0 \pm 0.9	2.2 \pm 0.5	5.9 \pm 0.8	8 \pm 1	23 \pm 3	56 \pm 6	20 \pm 3	48 \pm 5
112	17 \pm 1	1.8 \pm 0.2	0.7 \pm 0.1	1.3 \pm 0.2	2.2 \pm 0.3	5.9 \pm 0.8	12 \pm 1	4.6 \pm 0.7	11 \pm 1
113	11 \pm 2	1.3 \pm 0.3	0.4 \pm 0.1	1.5 \pm 0.3	2.3 \pm 0.4	3.8 \pm 0.8	4.0 \pm 0.8	1.4 \pm 0.4	11 \pm 2
114	200 \pm 10	12 \pm 1	4.2 \pm 0.9	9 \pm 1	13 \pm 1	70 \pm 7	229 \pm 20	82 \pm 7	119 \pm 9
115	4.8 \pm 0.7	0.5 \pm 0.1	0.23 \pm 0.09	0.5 \pm 0.1	0.7 \pm 0.1	1.7 \pm 0.3	3.3 \pm 0.6	1.1 \pm 0.3	3.1 \pm 0.5
116	10 \pm 1	1.6 \pm 0.2	0.5 \pm 0.1	1.3 \pm 0.2	1.9 \pm 0.3	3.6 \pm 0.6	5.9 \pm 0.8	2.1 \pm 0.4	10 \pm 1
117	27 \pm 4	3.5 \pm 0.8	1.2 \pm 0.4	3.1 \pm 0.7	4.5 \pm 0.9	10 \pm 3	20 \pm 4	7 \pm 2	25 \pm 5
118	27 \pm 2	2.9 \pm 0.3	0.8 \pm 0.2	2.3 \pm 0.3	3.6 \pm 0.4	9 \pm 1	22 \pm 2	8 \pm 1	21 \pm 2

Corrected flux values of the emission regions in the catalogue from this study. The measured fluxes of the nine emission lines for the detected emission regions are presented. These fluxes are corrected for the local background emission (described in Section 2.6.3), the global stellar absorption (described in Section 2.6.7), and the extinction (described in Section 2.6.8). The [O II] λ 3727 is listed here, but comes from Table F.3. The uncertainties correspond to the propagated uncertainties (described in Section 2.6.4). All flux values are scaled by 1×10^{-15} .

ID	$H\alpha$ [erg s $^{-1}$ cm $^{-2}$]	[N II] λ 6583 [erg s $^{-1}$ cm $^{-2}$]	[N II] λ 6548 [erg s $^{-1}$ cm $^{-2}$]	[S II] λ 6731 [erg s $^{-1}$ cm $^{-2}$]	[S II] λ 6716 [erg s $^{-1}$ cm $^{-2}$]	$H\beta$ [erg s $^{-1}$ cm $^{-2}$]	[O III] λ 5007 [erg s $^{-1}$ cm $^{-2}$]	[O III] λ 4959 [erg s $^{-1}$ cm $^{-2}$]	[O II] λ 3727 [erg s $^{-1}$ cm $^{-2}$]
119	8 ± 1	1.1 ± 0.2	0.5 ± 0.1	1.0 ± 0.2	1.5 ± 0.3	2.7 ± 0.7	4.3 ± 0.9	1.4 ± 0.4	6 ± 1
120	8 ± 1	0.8 ± 0.3	0.3 ± 0.2	0.7 ± 0.2	0.7 ± 0.2	2.7 ± 0.8	6 ± 1	2.2 ± 0.7	5 ± 1
121	38 ± 4	3.1 ± 0.5	1.2 ± 0.3	3.1 ± 0.5	4.4 ± 0.6	14 ± 2	41 ± 5	15 ± 2	32 ± 4
122	41 ± 4	4.5 ± 0.5	1.7 ± 0.3	4.2 ± 0.5	6.0 ± 0.6	15 ± 2	24 ± 2	8 ± 1	43 ± 4
123	8 ± 3	1.3 ± 0.5	0.6 ± 0.3	1.3 ± 0.5	1.8 ± 0.7	3 ± 1	4 ± 2	1.6 ± 0.8	8 ± 3
124	9 ± 2	0.9 ± 0.3	0.3 ± 0.2	0.7 ± 0.2	1.1 ± 0.3	3.2 ± 0.9	6 ± 2	2.2 ± 0.7	7 ± 2
125	44 ± 6	4.3 ± 0.8	1.5 ± 0.4	3.2 ± 0.6	4.5 ± 0.8	15 ± 3	34 ± 6	13 ± 3	30 ± 5
126	92 ± 8	10 ± 1	3.2 ± 0.6	6.8 ± 0.8	10 ± 1	33 ± 3	51 ± 5	18 ± 2	100 ± 10
127	57 ± 4	4.9 ± 0.5	1.6 ± 0.4	3.6 ± 0.5	5.1 ± 0.6	20 ± 2	51 ± 4	18 ± 2	38 ± 3
128	26 ± 1	2.8 ± 0.2	0.9 ± 0.2	2.5 ± 0.2	3.7 ± 0.3	9.3 ± 0.8	18 ± 1	6.6 ± 0.7	21 ± 1
129	57 ± 6	5.4 ± 0.9	1.8 ± 0.6	3.6 ± 0.8	5.1 ± 0.9	20 ± 4	41 ± 6	15 ± 3	36 ± 5
130	22 ± 1	2.0 ± 0.2	0.7 ± 0.2	1.8 ± 0.2	2.6 ± 0.3	7.8 ± 0.8	15 ± 1	5.5 ± 0.7	19 ± 2
131	10 ± 2	1.5 ± 0.3	0.6 ± 0.2	1.4 ± 0.3	2.1 ± 0.4	3.4 ± 0.8	5 ± 1	1.8 ± 0.6	10 ± 2
132	27 ± 3	3.5 ± 0.4	1.1 ± 0.2	3.1 ± 0.4	4.4 ± 0.6	10 ± 1	12 ± 1	4.4 ± 0.6	32 ± 4
133	25 ± 1	3.2 ± 0.3	1.0 ± 0.2	2.5 ± 0.2	3.6 ± 0.3	8.7 ± 0.8	9.2 ± 0.8	3.3 ± 0.5	30 ± 2
134	13 ± 2	1.6 ± 0.4	0.6 ± 0.2	1.5 ± 0.4	2.1 ± 0.5	5 ± 1	8 ± 2	3 ± 1	12 ± 2
135	18 ± 1	2.3 ± 0.2	0.8 ± 0.1	2.0 ± 0.2	3.0 ± 0.3	6.5 ± 0.7	7.3 ± 0.7	2.6 ± 0.4	21 ± 2
136	52 ± 3	6.0 ± 0.5	2.0 ± 0.3	4.5 ± 0.5	6.5 ± 0.6	19 ± 2	36 ± 2	13 ± 1	42 ± 3
137	28 ± 5	4 ± 1	1.5 ± 0.6	4.0 ± 0.9	6 ± 1	10 ± 2	14 ± 3	5 ± 2	29 ± 5
138	115 ± 7	8 ± 1	2.6 ± 0.7	5.2 ± 0.8	7.8 ± 0.9	41 ± 4	103 ± 8	37 ± 4	71 ± 5
139	8 ± 2	1.2 ± 0.3	0.3 ± 0.1	1.1 ± 0.3	1.5 ± 0.4	2.7 ± 0.6	2.5 ± 0.7	0.8 ± 0.3	9 ± 2
140	5.0 ± 0.7	0.7 ± 0.1	0.13 ± 0.06	0.7 ± 0.1	1.0 ± 0.2	1.8 ± 0.3	1.9 ± 0.4	0.6 ± 0.2	5.4 ± 0.8
141	11.5 ± 0.7	0.8 ± 0.1	0.44 ± 0.09	0.9 ± 0.1	1.2 ± 0.1	4.1 ± 0.4	5.2 ± 0.4	1.8 ± 0.2	12 ± 1
142	2.3 ± 0.5	0.4 ± 0.1	0.10 ± 0.07	0.25 ± 0.09	0.4 ± 0.1	0.8 ± 0.2	0.8 ± 0.2	0.3 ± 0.1	3.0 ± 0.7

Corrected flux values of the emission regions in the catalogue from this study. The measured fluxes of the nine emission lines for the detected emission regions are presented. These fluxes are corrected for the local background emission (described in Section 2.6.3), the global stellar absorption (described in Section 2.6.7), and the extinction (described in Section 2.6.8). The [O II] λ 3727 is listed here, but comes from Table F.3. The uncertainties correspond to the propagated uncertainties (described in Section 2.6.4). All flux values are scaled by 1×10^{-15} .

ID	$H\alpha$ [erg s $^{-1}$ cm $^{-2}$]	[N II] λ 6583 [erg s $^{-1}$ cm $^{-2}$]	[N II] λ 6548 [erg s $^{-1}$ cm $^{-2}$]	[S II] λ 6731 [erg s $^{-1}$ cm $^{-2}$]	[S II] λ 6716 [erg s $^{-1}$ cm $^{-2}$]	$H\beta$ [erg s $^{-1}$ cm $^{-2}$]	[O III] λ 5007 [erg s $^{-1}$ cm $^{-2}$]	[O III] λ 4959 [erg s $^{-1}$ cm $^{-2}$]	[O II] λ 3727 [erg s $^{-1}$ cm $^{-2}$]
143	141 ± 9	9 ± 1	2.6 ± 0.7	6 ± 1	8 ± 1	50 ± 5	130 ± 10	45 ± 5	88 ± 7
144	11 ± 1	1.5 ± 0.2	0.5 ± 0.1	1.4 ± 0.2	2.0 ± 0.3	3.9 ± 0.7	4.9 ± 0.8	1.6 ± 0.4	13 ± 1
145	1.7 ± 0.3	0.23 ± 0.08	0.01 ± 0.05	0.12 ± 0.07	0.24 ± 0.08	0.6 ± 0.1	0.7 ± 0.1	0.19 ± 0.07	2.0 ± 0.4
146	5.4 ± 0.5	0.6 ± 0.1	-0.01 ± 0.08	0.3 ± 0.1	0.6 ± 0.1	1.9 ± 0.2	2.8 ± 0.3	1.0 ± 0.2	6.5 ± 0.8
147	16 ± 1	2.0 ± 0.3	0.7 ± 0.2	1.7 ± 0.2	2.6 ± 0.3	5.6 ± 0.8	4.3 ± 0.7	1.5 ± 0.4	14 ± 1
148	35 ± 2	2.2 ± 0.3	1.0 ± 0.2	1.4 ± 0.2	2.1 ± 0.3	13 ± 1	35 ± 2	12 ± 1	26 ± 2
149	3.3 ± 0.3	0.31 ± 0.06	0.15 ± 0.05	0.26 ± 0.06	0.29 ± 0.06	1.2 ± 0.1	1.8 ± 0.2	0.6 ± 0.1	4.0 ± 0.5
150	14 ± 2	1.6 ± 0.3	0.5 ± 0.2	1.2 ± 0.3	1.7 ± 0.3	4.9 ± 0.9	9 ± 1	3.4 ± 0.7	12 ± 2
151	38 ± 3	5.2 ± 0.5	1.7 ± 0.3	4.5 ± 0.5	6.3 ± 0.6	13 ± 2	27 ± 3	10 ± 1	36 ± 3
152	2.9 ± 0.4	0.18 ± 0.08	0.07 ± 0.07	0.5 ± 0.1	0.6 ± 0.1	1.0 ± 0.2	0.4 ± 0.1	0.3 ± 0.1	4 ± 1
153	8 ± 2	1.3 ± 0.4	0.4 ± 0.2	1.2 ± 0.4	1.9 ± 0.5	2.9 ± 0.9	4 ± 1	1.2 ± 0.5	9 ± 2
154	6 ± 2	0.9 ± 0.4	0.3 ± 0.2	0.8 ± 0.3	1.0 ± 0.4	2.0 ± 0.9	4 ± 1	1.4 ± 0.7	5 ± 2
155	189 ± 9	20 ± 2	7 ± 1	14 ± 1	20 ± 2	67 ± 5	141 ± 9	50 ± 4	160 ± 10
156	8 ± 3	1.0 ± 0.4	0.4 ± 0.2	1.0 ± 0.4	1.4 ± 0.5	3 ± 1	5 ± 2	1.8 ± 0.8	8 ± 3
157	85 ± 8	7 ± 1	2.1 ± 0.8	4 ± 1	6 ± 1	30 ± 4	71 ± 8	25 ± 4	57 ± 6
158	38 ± 3	5.4 ± 0.5	1.8 ± 0.3	4.4 ± 0.5	6.4 ± 0.6	14 ± 2	24 ± 2	8 ± 1	36 ± 3
159	60 ± 10	4 ± 2	1 ± 1	3 ± 1	4 ± 2	20 ± 5	50 ± 10	16 ± 5	39 ± 8
160	10 ± 1	1.3 ± 0.3	0.5 ± 0.2	1.1 ± 0.3	1.7 ± 0.3	3.5 ± 0.7	7 ± 1	2.4 ± 0.6	8 ± 1
161	2.6 ± 0.8	0.5 ± 0.2	0.3 ± 0.2	0.3 ± 0.2	0.8 ± 0.3	0.9 ± 0.4	0.6 ± 0.3	0.0 ± 0.1	4 ± 1
162	330 ± 20	30 ± 2	10 ± 2	20 ± 2	29 ± 2	120 ± 10	240 ± 20	84 ± 8	250 ± 20
163	1.6 ± 0.2	0.14 ± 0.05	0.06 ± 0.04	0.20 ± 0.05	0.33 ± 0.07	0.6 ± 0.1	0.23 ± 0.06	0.02 ± 0.04	1.0 ± 0.2
164	2.1 ± 0.4	0.18 ± 0.08	0.08 ± 0.07	0.25 ± 0.09	0.4 ± 0.1	0.7 ± 0.2	0.6 ± 0.2	0.2 ± 0.1	2.6 ± 0.7
165	47 ± 4	5.9 ± 0.6	2.0 ± 0.3	4.2 ± 0.5	6.0 ± 0.7	17 ± 2	25 ± 3	9 ± 1	44 ± 5
166	15 ± 1	1.6 ± 0.2	0.6 ± 0.1	1.6 ± 0.2	2.4 ± 0.3	5.3 ± 0.7	9 ± 1	3.0 ± 0.5	16 ± 2

Corrected flux values of the emission regions in the catalogue from this study. The measured fluxes of the nine emission lines for the detected emission regions are presented. These fluxes are corrected for the local background emission (described in Section 2.6.3), the global stellar absorption (described in Section 2.6.7), and the extinction (described in Section 2.6.8). The $[\text{O II}]\lambda 3727$ is listed here, but comes from Table F.3. The uncertainties correspond to the propagated uncertainties (described in Section 2.6.4). All flux values are scaled by 1×10^{-15} .

ID	$\text{H}\alpha$ [erg s $^{-1}$ cm $^{-2}$]	$[\text{N II}]\lambda 6583$ [erg s $^{-1}$ cm $^{-2}$]	$[\text{N II}]\lambda 6548$ [erg s $^{-1}$ cm $^{-2}$]	$[\text{S II}]\lambda 6731$ [erg s $^{-1}$ cm $^{-2}$]	$[\text{S II}]\lambda 6716$ [erg s $^{-1}$ cm $^{-2}$]	$\text{H}\beta$ [erg s $^{-1}$ cm $^{-2}$]	$[\text{O III}]\lambda 5007$ [erg s $^{-1}$ cm $^{-2}$]	$[\text{O III}]\lambda 4959$ [erg s $^{-1}$ cm $^{-2}$]	$[\text{O II}]\lambda 3727$ [erg s $^{-1}$ cm $^{-2}$]
167	5 ± 3	0.0 ± 0.2	0.5 ± 0.5	0.4 ± 0.4	0.2 ± 0.4	2 ± 2	4 ± 3	1 ± 1	20 ± 10
168	2.6 ± 0.7	0.4 ± 0.1	0.09 ± 0.08	0.6 ± 0.2	0.8 ± 0.2	0.9 ± 0.4	0.3 ± 0.2	2.7 ± 0.7	
169	46 ± 5	5.0 ± 0.9	1.8 ± 0.6	4.2 ± 0.9	6 ± 1	16 ± 3	42 ± 6	15 ± 3	39 ± 5
170	30 ± 20	4 ± 2	1.3 ± 0.8	2 ± 1	4 ± 2	12 ± 6	20 ± 10	7 ± 4	30 ± 20
171	68 ± 8	9 ± 1	2.8 ± 0.6	8 ± 1	10 ± 1	24 ± 4	44 ± 6	15 ± 3	67 ± 8
172	40 ± 50	5 ± 5	1 ± 2	4 ± 4	5 ± 6	20 ± 20	30 ± 40	10 ± 10	40 ± 40
173	33 ± 4	4.4 ± 0.7	1.2 ± 0.3	4.3 ± 0.6	5.6 ± 0.8	12 ± 2	26 ± 4	9 ± 1	30 ± 4
174	15 ± 2	2.0 ± 0.3	0.6 ± 0.2	1.8 ± 0.3	2.5 ± 0.4	5 ± 1	11 ± 2	3.6 ± 0.8	18 ± 2
175	390 ± 30	33 ± 3	11 ± 2	22 ± 3	32 ± 3	140 ± 10	350 ± 30	120 ± 10	300 ± 30
176	2.9 ± 0.5	0.4 ± 0.1	0.12 ± 0.08	0.3 ± 0.1	0.6 ± 0.1	1.0 ± 0.2	0.6 ± 0.2	0.2 ± 0.1	4.2 ± 0.9
177	23 ± 2	2.7 ± 0.4	0.9 ± 0.2	2.3 ± 0.3	3.2 ± 0.4	8 ± 1	12 ± 2	4.0 ± 0.8	27 ± 3
178	51 ± 6	5.4 ± 0.7	1.6 ± 0.4	4.3 ± 0.6	6.1 ± 0.8	18 ± 3	40 ± 5	13 ± 2	56 ± 7
179	40 ± 10	6 ± 1	1.8 ± 0.6	5 ± 1	7 ± 2	13 ± 4	21 ± 6	7 ± 2	40 ± 10
180	43 ± 3	5.1 ± 0.5	1.8 ± 0.3	4.0 ± 0.4	5.9 ± 0.5	15 ± 2	16 ± 2	5.5 ± 0.9	46 ± 3
181	14 ± 1	2.0 ± 0.3	0.7 ± 0.2	2.1 ± 0.3	3.0 ± 0.4	5.0 ± 0.8	4.8 ± 0.8	1.6 ± 0.5	11 ± 1
182	13 ± 1	1.9 ± 0.2	0.6 ± 0.1	1.8 ± 0.2	2.5 ± 0.3	4.8 ± 0.6	4.2 ± 0.6	1.4 ± 0.4	16 ± 2
183	1.9 ± 0.4	0.4 ± 0.1	0.13 ± 0.06	0.31 ± 0.09	0.5 ± 0.1	0.7 ± 0.2	0.5 ± 0.2	0.14 ± 0.09	2.7 ± 0.6
184	9 ± 1	1.2 ± 0.2	0.4 ± 0.1	1.0 ± 0.2	1.3 ± 0.2	3.3 ± 0.6	4.6 ± 0.8	1.4 ± 0.4	11 ± 2
185	120 ± 10	12 ± 1	4.3 ± 0.8	9 ± 1	12 ± 1	42 ± 5	101 ± 9	34 ± 4	95 ± 9
186	0.3 ± 0.3	0.03 ± 0.03	0.02 ± 0.02	0.04 ± 0.05	0.06 ± 0.06	0.1 ± 0.1	0.1 ± 0.1	0.03 ± 0.04	0.2 ± 0.2
187	3.6 ± 0.9	0.4 ± 0.2	0.2 ± 0.1	0.7 ± 0.2	0.8 ± 0.3	1.3 ± 0.6	1.6 ± 0.6	0.6 ± 0.4	6 ± 2
188	2 ± 1	0.3 ± 0.2	0.1 ± 0.1	0.3 ± 0.2	0.5 ± 0.3	0.8 ± 0.6	1.4 ± 0.8	0.4 ± 0.4	6 ± 3
189	1.6 ± 0.4	0.2 ± 0.1	0.10 ± 0.08	0.2 ± 0.1	0.3 ± 0.1	0.6 ± 0.2	-0.02 ± 0.07	-0.02 ± 0.06	1.7 ± 0.6
190	0.7 ± 0.2	0.11 ± 0.04	0.04 ± 0.03	0.12 ± 0.04	0.13 ± 0.04	0.27 ± 0.08	0.19 ± 0.06	0.05 ± 0.03	0.7 ± 0.2

Corrected flux values of the emission regions in the catalogue from this study. The measured fluxes of the nine emission lines for the detected emission regions are presented. These fluxes are corrected for the local background emission (described in Section 2.6.3), the global stellar absorption (described in Section 2.6.7), and the extinction (described in Section 2.6.8). The [O II] λ 3727 is listed here, but comes from Table F.3. The uncertainties correspond to the propagated uncertainties (described in Section 2.6.4). All flux values are scaled by 1×10^{-15} .

ID	$H\alpha$ [erg s $^{-1}$ cm $^{-2}$]	[N II] λ 6583 [erg s $^{-1}$ cm $^{-2}$]	[N II] λ 6548 [erg s $^{-1}$ cm $^{-2}$]	[S II] λ 6731 [erg s $^{-1}$ cm $^{-2}$]	[S II] λ 6716 [erg s $^{-1}$ cm $^{-2}$]	$H\beta$ [erg s $^{-1}$ cm $^{-2}$]	[O III] λ 5007 [erg s $^{-1}$ cm $^{-2}$]	[O III] λ 4959 [erg s $^{-1}$ cm $^{-2}$]	[O II] λ 3727 [erg s $^{-1}$ cm $^{-2}$]
191	31 ± 3	4.5 ± 0.5	1.4 ± 0.3	3.8 ± 0.5	5.4 ± 0.6	11 ± 1	12 ± 2	4.0 ± 0.8	37 ± 4
192	37 ± 3	5.7 ± 0.8	1.8 ± 0.4	5.3 ± 0.7	7.1 ± 0.9	13 ± 2	18 ± 2	6 ± 1	35 ± 4
193	2.9 ± 0.6	0.3 ± 0.1	0.08 ± 0.07	0.20 ± 0.09	0.4 ± 0.1	1.0 ± 0.4	1.4 ± 0.4	0.4 ± 0.2	2.8 ± 0.7
196	1.0 ± 0.2	0.11 ± 0.04	0.10 ± 0.04	0.09 ± 0.04	0.18 ± 0.06	0.3 ± 0.1	0.18 ± 0.07	0.04 ± 0.04	1.0 ± 0.3
197	30 ± 2	2.6 ± 0.3	0.9 ± 0.2	2.0 ± 0.3	2.8 ± 0.3	11 ± 1	28 ± 2	10 ± 1	27 ± 2
198	48 ± 8	8 ± 2	3 ± 1	8 ± 2	11 ± 2	17 ± 5	24 ± 6	8 ± 3	60 ± 10
199	23 ± 6	4 ± 1	1.3 ± 0.6	4 ± 1	5 ± 1	8 ± 3	12 ± 4	4 ± 2	25 ± 7
200	90 ± 20	13 ± 3	5 ± 2	13 ± 3	17 ± 4	30 ± 9	50 ± 10	18 ± 7	90 ± 20
201	18 ± 5	3 ± 1	1.2 ± 0.6	3 ± 1	4 ± 1	7 ± 3	15 ± 5	5 ± 3	25 ± 8
202	21 ± 2	1.0 ± 0.2	0.4 ± 0.1	1.0 ± 0.2	1.2 ± 0.2	7.4 ± 0.9	32 ± 3	11 ± 1	13 ± 1
203	19 ± 3	2.4 ± 0.4	0.9 ± 0.2	1.9 ± 0.4	2.6 ± 0.5	7 ± 1	14 ± 2	4.8 ± 0.9	26 ± 5
204	47 ± 6	6 ± 1	2.3 ± 0.6	6 ± 1	7 ± 1	17 ± 4	28 ± 5	10 ± 3	48 ± 7
205	2.8 ± 0.5	0.3 ± 0.1	0.20 ± 0.08	0.25 ± 0.09	0.5 ± 0.1	1.0 ± 0.3	1.2 ± 0.3	0.3 ± 0.2	3.6 ± 0.8
206	11 ± 9	1 ± 1	0.4 ± 0.4	1.0 ± 0.9	2 ± 1	4 ± 3	8 ± 6	3 ± 2	10 ± 10
207	65 ± 9	9 ± 2	2.7 ± 0.9	7 ± 1	10 ± 2	23 ± 6	47 ± 9	17 ± 5	70 ± 10
208	60 ± 10	10 ± 3	4 ± 2	9 ± 2	11 ± 3	22 ± 8	40 ± 10	13 ± 6	60 ± 10
209	10 ± 3	1.4 ± 0.4	0.3 ± 0.2	1.4 ± 0.4	1.8 ± 0.5	3 ± 1	5 ± 2	1.6 ± 0.7	16 ± 4
210	42 ± 4	3.7 ± 0.5	1.1 ± 0.3	2.9 ± 0.5	4.2 ± 0.6	15 ± 2	42 ± 5	15 ± 2	38 ± 5
211	3.2 ± 0.5	0.3 ± 0.1	0.3 ± 0.1	0.4 ± 0.1	0.7 ± 0.2	1.1 ± 0.3	2.0 ± 0.4	0.7 ± 0.2	5 ± 1
212	45 ± 3	3.9 ± 0.5	1.5 ± 0.3	3.0 ± 0.4	4.4 ± 0.5	16 ± 2	50 ± 4	17 ± 2	32 ± 3
213	17 ± 1	2.4 ± 0.3	0.8 ± 0.2	2.1 ± 0.3	3.0 ± 0.3	6.0 ± 0.8	11 ± 1	3.8 ± 0.6	30 ± 3
214	0.9 ± 0.2	0.03 ± 0.03	0.10 ± 0.04	0.14 ± 0.05	0.21 ± 0.07	0.3 ± 0.1	0.08 ± 0.06	0.00 ± 0.05	0.7 ± 0.3
215	6 ± 1	0.8 ± 0.2	0.4 ± 0.1	0.8 ± 0.2	1.1 ± 0.3	2.1 ± 0.6	2.9 ± 0.8	1.1 ± 0.4	7 ± 1
216	1.0 ± 0.2	0.10 ± 0.03	0.07 ± 0.03	0.12 ± 0.04	0.19 ± 0.05	0.35 ± 0.07	0.7 ± 0.1	0.21 ± 0.05	1.2 ± 0.2

Corrected flux values of the emission regions in the catalogue from this study. The measured fluxes of the nine emission lines for the detected emission regions are presented. These fluxes are corrected for the local background emission (described in Section 2.6.3), the global stellar absorption (described in Section 2.6.7), and the extinction (described in Section 2.6.8). The [O II] λ 3727 is listed here, but comes from Table F.3. The uncertainties correspond to the propagated uncertainties (described in Section 2.6.4). All flux values are scaled by 1×10^{-15} .

ID	$H\alpha$ [erg s $^{-1}$ cm $^{-2}$]	[N II] λ 6583 [erg s $^{-1}$ cm $^{-2}$]	[N II] λ 6548 [erg s $^{-1}$ cm $^{-2}$]	[S II] λ 6731 [erg s $^{-1}$ cm $^{-2}$]	[S II] λ 6716 [erg s $^{-1}$ cm $^{-2}$]	$H\beta$ [erg s $^{-1}$ cm $^{-2}$]	[O III] λ 5007 [erg s $^{-1}$ cm $^{-2}$]	[O III] λ 4959 [erg s $^{-1}$ cm $^{-2}$]	[O II] λ 3727 [erg s $^{-1}$ cm $^{-2}$]
217	2.6 ± 0.3	0.33 ± 0.08	0.22 ± 0.07	0.38 ± 0.08	0.5 ± 0.1	0.9 ± 0.2	1.9 ± 0.3	0.6 ± 0.1	4.0 ± 0.6
218	2.3 ± 0.5	0.20 ± 0.07	0.10 ± 0.05	0.4 ± 0.1	0.4 ± 0.1	0.8 ± 0.2	1.6 ± 0.3	0.6 ± 0.1	3.3 ± 0.8
219	28 ± 3	3.3 ± 0.4	1.1 ± 0.3	3.1 ± 0.4	4.3 ± 0.6	10 ± 1	20 ± 2	7 ± 1	33 ± 4
220	220 ± 20	22 ± 3	8 ± 2	16 ± 2	22 ± 3	80 ± 10	170 ± 20	60 ± 10	210 ± 20
221	50 ± 20	8 ± 3	2 ± 1	7 ± 2	10 ± 3	19 ± 7	30 ± 10	13 ± 5	60 ± 20
222	2.0 ± 0.3	0.23 ± 0.07	0.11 ± 0.05	0.27 ± 0.07	0.4 ± 0.1	0.7 ± 0.1	1.3 ± 0.3	0.5 ± 0.1	2.4 ± 0.5
223	5 ± 1	1.0 ± 0.3	0.4 ± 0.2	1.1 ± 0.4	1.5 ± 0.4	1.8 ± 0.7	1.9 ± 0.7	0.6 ± 0.4	8 ± 2
224	8 ± 3	1.9 ± 0.8	0.6 ± 0.4	2.2 ± 0.9	3 ± 1	3 ± 2	3 ± 2	1 ± 1	11 ± 4
225	6 ± 2	1.0 ± 0.4	0.5 ± 0.3	0.9 ± 0.4	1.2 ± 0.5	2 ± 1	3 ± 1	1.1 ± 0.7	6 ± 2
226	2.0 ± 0.3	0.23 ± 0.06	0.11 ± 0.05	0.19 ± 0.06	0.37 ± 0.09	0.7 ± 0.1	0.6 ± 0.1	0.26 ± 0.08	3.3 ± 0.6
227	60 ± 10	11 ± 3	4 ± 2	9 ± 3	12 ± 3	22 ± 8	40 ± 10	16 ± 7	80 ± 20
228	3.8 ± 0.3	0.21 ± 0.07	0.15 ± 0.06	0.51 ± 0.09	0.7 ± 0.1	1.3 ± 0.2	2.6 ± 0.3	0.8 ± 0.1	3.9 ± 0.5
229	8.7 ± 0.6	0.9 ± 0.2	0.6 ± 0.1	0.9 ± 0.2	1.9 ± 0.2	3.1 ± 0.3	2.7 ± 0.3	1.0 ± 0.2	11 ± 1
230	1.3 ± 0.6	0.14 ± 0.07	0.04 ± 0.06	0.2 ± 0.1	0.3 ± 0.1	0.5 ± 0.2	0.5 ± 0.3	0.2 ± 0.1	1.8 ± 0.9
231	15 ± 4	2.5 ± 0.7	0.7 ± 0.3	2.3 ± 0.7	3.0 ± 0.9	5 ± 2	7 ± 2	2.4 ± 0.9	21 ± 5
232	80 ± 10	7 ± 1	2.7 ± 0.6	4.9 ± 0.9	8 ± 1	29 ± 5	110 ± 10	38 ± 6	53 ± 8
233	11.0 ± 0.7	1.0 ± 0.1	0.35 ± 0.09	0.7 ± 0.1	0.9 ± 0.1	3.9 ± 0.4	7.7 ± 0.6	2.5 ± 0.3	11 ± 1
234	240 ± 20	26 ± 3	8 ± 2	21 ± 3	28 ± 3	80 ± 10	220 ± 20	80 ± 10	240 ± 20
235	4 ± 1	0.5 ± 0.2	0.11 ± 0.08	0.5 ± 0.2	0.6 ± 0.2	1.3 ± 0.4	1.6 ± 0.5	0.6 ± 0.2	4 ± 1
236	3 ± 1	0.5 ± 0.2	0.3 ± 0.2	0.4 ± 0.2	0.7 ± 0.3	1.1 ± 0.5	2.0 ± 0.8	0.7 ± 0.4	3 ± 1
237	13.5 ± 0.8	0.7 ± 0.1	0.4 ± 0.1	0.8 ± 0.1	1.0 ± 0.1	4.8 ± 0.4	13.3 ± 0.9	4.5 ± 0.4	11.8 ± 0.9
238	300 ± 40	40 ± 7	13 ± 4	27 ± 6	34 ± 6	100 ± 20	200 ± 40	70 ± 20	260 ± 40
239	8.6 ± 0.8	0.6 ± 0.1	0.4 ± 0.1	1.0 ± 0.2	1.5 ± 0.2	3.0 ± 0.4	13 ± 1	4.3 ± 0.5	8 ± 1
240	1.2 ± 0.3	0.16 ± 0.05	0.07 ± 0.04	0.12 ± 0.04	0.18 ± 0.05	0.4 ± 0.1	0.5 ± 0.1	0.22 ± 0.07	1.5 ± 0.4

Corrected flux values of the emission regions in the catalogue from this study. The measured fluxes of the nine emission lines for the detected emission regions are presented. These fluxes are corrected for the local background emission (described in Section 2.6.3), the global stellar absorption (described in Section 2.6.7), and the extinction (described in Section 2.6.8). The [O II] λ 3727 is listed here, but comes from Table F.3. The uncertainties correspond to the propagated uncertainties (described in Section 2.6.4). All flux values are scaled by 1×10^{-15} .

ID	$H\alpha$ [erg s $^{-1}$ cm $^{-2}$]	[N II] λ 6583 [erg s $^{-1}$ cm $^{-2}$]	[N II] λ 6548 [erg s $^{-1}$ cm $^{-2}$]	[S II] λ 6731 [erg s $^{-1}$ cm $^{-2}$]	[S II] λ 6716 [erg s $^{-1}$ cm $^{-2}$]	$H\beta$ [erg s $^{-1}$ cm $^{-2}$]	[O III] λ 5007 [erg s $^{-1}$ cm $^{-2}$]	[O III] λ 4959 [erg s $^{-1}$ cm $^{-2}$]	[O II] λ 3727 [erg s $^{-1}$ cm $^{-2}$]
241	28 ± 2	2.2 ± 0.2	0.9 ± 0.2	1.8 ± 0.2	2.6 ± 0.3	10 ± 1	28 ± 2	10 ± 1	26 ± 2
242	140 ± 10	18 ± 2	6 ± 1	15 ± 2	22 ± 2	51 ± 7	110 ± 10	39 ± 6	160 ± 20
243	2.6 ± 0.6	0.4 ± 0.1	0.10 ± 0.08	0.3 ± 0.1	0.6 ± 0.2	0.9 ± 0.3	1.7 ± 0.4	0.5 ± 0.2	5 ± 1
244	122 ± 8	14 ± 1	4.4 ± 0.9	10 ± 1	14 ± 1	43 ± 5	110 ± 10	38 ± 5	100 ± 8
245	1.8 ± 0.4	0.19 ± 0.07	0.09 ± 0.05	0.27 ± 0.09	0.4 ± 0.1	0.6 ± 0.2	0.4 ± 0.2	0.2 ± 0.1	1.6 ± 0.5
246	3.3 ± 0.6	0.5 ± 0.1	0.17 ± 0.08	0.5 ± 0.1	0.5 ± 0.1	1.2 ± 0.3	1.2 ± 0.3	0.5 ± 0.2	5 ± 1
247	45 ± 6	6.0 ± 0.8	1.9 ± 0.4	4.2 ± 0.6	5.9 ± 0.8	16 ± 2	42 ± 6	15 ± 2	41 ± 5
248	2.3 ± 0.4	0.26 ± 0.08	0.15 ± 0.07	0.4 ± 0.1	0.4 ± 0.1	0.8 ± 0.2	0.9 ± 0.2	0.24 ± 0.09	2.8 ± 0.6
249	81 ± 8	11 ± 2	4.0 ± 0.9	10 ± 1	14 ± 2	29 ± 5	70 ± 9	24 ± 4	90 ± 10
250	8 ± 1	1.1 ± 0.2	0.4 ± 0.2	1.0 ± 0.2	1.5 ± 0.3	2.9 ± 0.7	1.7 ± 0.5	0.6 ± 0.3	10 ± 2
251	6.1 ± 0.5	0.6 ± 0.1	0.22 ± 0.09	1.0 ± 0.1	1.3 ± 0.2	2.2 ± 0.3	7.0 ± 0.7	2.3 ± 0.3	6.5 ± 0.9
252	2.2 ± 0.5	0.20 ± 0.07	0.13 ± 0.05	0.20 ± 0.07	0.25 ± 0.08	0.8 ± 0.2	1.2 ± 0.4	0.5 ± 0.2	1.5 ± 0.4
253	2.5 ± 0.4	0.28 ± 0.09	0.17 ± 0.07	0.22 ± 0.08	0.31 ± 0.09	0.9 ± 0.2	1.6 ± 0.4	0.6 ± 0.2	2.8 ± 0.6
254	300 ± 10	35 ± 3	12 ± 2	24 ± 2	32 ± 3	108 ± 8	190 ± 10	65 ± 6	350 ± 20
255	4.0 ± 0.8	0.6 ± 0.2	0.15 ± 0.08	0.7 ± 0.2	0.9 ± 0.2	1.4 ± 0.4	1.5 ± 0.5	0.5 ± 0.2	4.0 ± 0.9
256	2.3 ± 0.8	0.3 ± 0.2	0.2 ± 0.1	0.3 ± 0.2	0.4 ± 0.2	0.8 ± 0.4	1.1 ± 0.5	0.4 ± 0.3	2 ± 1
257	12 ± 3	2.3 ± 0.6	0.7 ± 0.3	2.7 ± 0.7	3.8 ± 0.9	4 ± 1	5 ± 2	1.4 ± 0.9	15 ± 3
258	3 ± 1	0.5 ± 0.3	0.2 ± 0.1	0.4 ± 0.2	0.7 ± 0.4	1.0 ± 0.6	1.3 ± 0.7	0.4 ± 0.3	5 ± 3
259	31 ± 3	3.0 ± 0.5	1.1 ± 0.3	2.2 ± 0.4	3.2 ± 0.5	11 ± 2	23 ± 3	8 ± 1	25 ± 3
260	130 ± 10	15 ± 2	4 ± 1	11 ± 2	16 ± 2	44 ± 7	100 ± 10	33 ± 6	100 ± 10
261	96 ± 7	9 ± 1	3.2 ± 0.8	7 ± 1	10 ± 1	34 ± 4	83 ± 8	29 ± 4	93 ± 9
262	41 ± 5	7 ± 1	2.3 ± 0.6	6 ± 1	8 ± 1	15 ± 3	17 ± 3	6 ± 2	53 ± 7
263	5.8 ± 0.5	0.5 ± 0.1	0.33 ± 0.09	0.7 ± 0.1	1.0 ± 0.1	2.1 ± 0.3	7.1 ± 0.7	2.2 ± 0.3	7.3 ± 0.9
264	9 ± 2	1.6 ± 0.5	0.6 ± 0.3	1.7 ± 0.6	2.2 ± 0.7	3 ± 1	4 ± 2	1.0 ± 0.8	14 ± 4

Corrected flux values of the emission regions in the catalogue from this study. The measured fluxes of the nine emission lines for the detected emission regions are presented. These fluxes are corrected for the local background emission (described in Section 2.6.3), the global stellar absorption (described in Section 2.6.7), and the extinction (described in Section 2.6.8). The [O II] λ 3727 is listed here, but comes from Table F.3. The uncertainties correspond to the propagated uncertainties (described in Section 2.6.4). All flux values are scaled by 1×10^{-15} .

ID	$H\alpha$ [erg s $^{-1}$ cm $^{-2}$]	[N II] λ 6583 [erg s $^{-1}$ cm $^{-2}$]	[N II] λ 6548 [erg s $^{-1}$ cm $^{-2}$]	[S II] λ 6731 [erg s $^{-1}$ cm $^{-2}$]	[S II] λ 6716 [erg s $^{-1}$ cm $^{-2}$]	$H\beta$ [erg s $^{-1}$ cm $^{-2}$]	[O III] λ 5007 [erg s $^{-1}$ cm $^{-2}$]	[O III] λ 4959 [erg s $^{-1}$ cm $^{-2}$]	[O II] λ 3727 [erg s $^{-1}$ cm $^{-2}$]
265	66 ± 7	9 ± 1	3.1 ± 0.7	8 ± 1	12 ± 2	24 ± 4	50 ± 7	17 ± 3	66 ± 8
266	4.1 ± 0.5	0.4 ± 0.1	0.08 ± 0.07	0.5 ± 0.1	0.6 ± 0.1	1.5 ± 0.2	3.0 ± 0.4	1.0 ± 0.2	6.0 ± 0.9
267	0.8 ± 0.1	0.06 ± 0.02	0.04 ± 0.02	0.12 ± 0.02	0.17 ± 0.03	0.28 ± 0.04	0.66 ± 0.08	0.18 ± 0.03	0.54 ± 0.09
268	4.3 ± 0.4	0.33 ± 0.07	0.24 ± 0.06	0.43 ± 0.08	0.61 ± 0.09	1.5 ± 0.2	4.0 ± 0.4	1.4 ± 0.2	4.1 ± 0.6
269	9.2 ± 0.5	0.73 ± 0.09	0.32 ± 0.07	0.64 ± 0.09	0.8 ± 0.1	3.3 ± 0.3	7.7 ± 0.6	2.6 ± 0.3	9.4 ± 0.8
270	170 ± 10	13 ± 2	4 ± 1	9 ± 2	13 ± 2	59 ± 9	200 ± 20	70 ± 10	110 ± 10
271	56 ± 9	8 ± 2	2.9 ± 0.8	8 ± 1	11 ± 2	20 ± 5	28 ± 6	10 ± 3	70 ± 10
272	75 ± 5	9.0 ± 0.9	3.1 ± 0.5	6.9 ± 0.8	9.5 ± 0.9	26 ± 3	51 ± 5	17 ± 2	69 ± 6
273	2.7 ± 0.8	0.5 ± 0.2	0.17 ± 0.09	0.5 ± 0.2	0.8 ± 0.2	1.0 ± 0.4	1.1 ± 0.4	0.3 ± 0.2	3 ± 1
274	3.3 ± 0.5	0.20 ± 0.06	0.12 ± 0.05	0.32 ± 0.07	0.39 ± 0.08	1.2 ± 0.2	3.8 ± 0.6	1.4 ± 0.2	2.7 ± 0.6
275	11.0 ± 0.7	0.8 ± 0.1	0.4 ± 0.1	1.1 ± 0.1	1.7 ± 0.2	3.9 ± 0.4	9.4 ± 0.8	3.2 ± 0.4	9 ± 1
276	72 ± 4	10.6 ± 0.9	3.8 ± 0.6	8.9 ± 0.8	13 ± 1	26 ± 3	37 ± 4	13 ± 2	72 ± 6
277	4 ± 1	0.7 ± 0.3	0.2 ± 0.1	0.8 ± 0.3	1.1 ± 0.4	1.4 ± 0.6	1.8 ± 0.7	0.6 ± 0.4	5 ± 2
278	9 ± 2	1.8 ± 0.5	0.7 ± 0.3	1.7 ± 0.5	2.5 ± 0.6	3 ± 1	4 ± 1	1.3 ± 0.7	12 ± 3
279	31 ± 1	2.3 ± 0.2	1.0 ± 0.2	1.7 ± 0.2	2.1 ± 0.2	11.0 ± 0.8	26 ± 1	9.2 ± 0.7	31 ± 2
280	40 ± 10	5 ± 1	1.8 ± 0.7	5 ± 1	7 ± 2	15 ± 4	22 ± 6	8 ± 2	40 ± 10
281	7 ± 1	1.3 ± 0.3	0.3 ± 0.2	1.3 ± 0.3	1.8 ± 0.4	2.6 ± 0.8	8 ± 2	2.9 ± 0.9	12 ± 3
282	2.0 ± 0.3	0.14 ± 0.07	0.11 ± 0.07	0.3 ± 0.1	0.5 ± 0.1	0.7 ± 0.2	0.2 ± 0.1	0.04 ± 0.09	3.1 ± 0.8
283	40 ± 10	8 ± 3	4 ± 2	8 ± 3	11 ± 4	15 ± 6	29 ± 9	11 ± 5	60 ± 10
284	74 ± 5	8 ± 1	2.4 ± 0.6	6.5 ± 0.9	9 ± 1	26 ± 3	56 ± 6	19 ± 3	75 ± 7
285	52 ± 4	6.8 ± 0.7	2.2 ± 0.4	5.5 ± 0.6	7.9 ± 0.8	18 ± 2	36 ± 3	13 ± 2	50 ± 4
286	1.0 ± 0.3	0.10 ± 0.06	0.03 ± 0.05	0.11 ± 0.07	0.22 ± 0.09	0.4 ± 0.1	0.15 ± 0.08	0.05 ± 0.07	1.7 ± 0.6
287	59 ± 4	8.2 ± 0.8	2.6 ± 0.5	7.1 ± 0.8	10.0 ± 0.9	21 ± 2	40 ± 4	14 ± 2	58 ± 5
288	30 ± 10	4 ± 2	1.5 ± 0.7	4 ± 1	5 ± 2	11 ± 4	22 ± 8	8 ± 3	30 ± 10

Corrected flux values of the emission regions in the catalogue from this study. The measured fluxes of the nine emission lines for the detected emission regions are presented. These fluxes are corrected for the local background emission (described in Section 2.6.3), the global stellar absorption (described in Section 2.6.7), and the extinction (described in Section 2.6.8). The [O II] λ 3727 is listed here, but comes from Table F.3. The uncertainties correspond to the propagated uncertainties (described in Section 2.6.4). All flux values are scaled by 1×10^{-15} .

ID	$H\alpha$ [erg s $^{-1}$ cm $^{-2}$]	[N II] λ 6583 [erg s $^{-1}$ cm $^{-2}$]	[N II] λ 6548 [erg s $^{-1}$ cm $^{-2}$]	[S II] λ 6731 [erg s $^{-1}$ cm $^{-2}$]	[S II] λ 6716 [erg s $^{-1}$ cm $^{-2}$]	$H\beta$ [erg s $^{-1}$ cm $^{-2}$]	[O III] λ 5007 [erg s $^{-1}$ cm $^{-2}$]	[O III] λ 4959 [erg s $^{-1}$ cm $^{-2}$]	[O II] λ 3727 [erg s $^{-1}$ cm $^{-2}$]
289	1.2 ± 0.3	0.15 ± 0.08	0.02 ± 0.05	0.21 ± 0.09	0.3 ± 0.1	0.4 ± 0.1	0.13 ± 0.09	-0.01 ± 0.07	2.5 ± 0.7
290	45 ± 4	5.6 ± 0.8	2.0 ± 0.5	5.0 ± 0.8	7 ± 1	16 ± 2	37 ± 5	13 ± 2	37 ± 4
291	3.1 ± 0.7	0.3 ± 0.1	0.2 ± 0.1	0.4 ± 0.2	0.5 ± 0.2	1.1 ± 0.4	0.5 ± 0.3	0.1 ± 0.2	8 ± 2
292	40 ± 10	8 ± 3	3 ± 2	8 ± 3	11 ± 4	16 ± 8	30 ± 10	10 ± 6	60 ± 20
293	7 ± 2	1.1 ± 0.3	0.4 ± 0.2	1.3 ± 0.4	1.7 ± 0.4	2.6 ± 0.9	3 ± 1	1.0 ± 0.6	10 ± 2
294	2.5 ± 0.9	0.4 ± 0.2	0.12 ± 0.08	0.4 ± 0.2	0.6 ± 0.3	0.9 ± 0.4	0.9 ± 0.4	0.3 ± 0.2	3 ± 1
295	0.7 ± 0.1	0.10 ± 0.04	-0.03 ± 0.02	0.08 ± 0.04	0.19 ± 0.06	0.26 ± 0.07	0.07 ± 0.04	0.01 ± 0.03	0.7 ± 0.2
296	9 ± 3	1.9 ± 0.7	0.7 ± 0.3	2.1 ± 0.8	3 ± 1	3 ± 1	3 ± 1	1.1 ± 0.8	11 ± 4
297	0.9 ± 0.4	0.06 ± 0.05	-0.01 ± 0.03	0.18 ± 0.09	0.2 ± 0.1	0.3 ± 0.2	0.10 ± 0.09	0.00 ± 0.06	1.7 ± 0.8
298	70 ± 10	8 ± 2	2.9 ± 0.9	7 ± 1	10 ± 2	25 ± 5	60 ± 10	20 ± 5	60 ± 10
299	6.6 ± 0.5	0.52 ± 0.08	0.30 ± 0.07	0.49 ± 0.08	0.67 ± 0.09	2.4 ± 0.3	4.5 ± 0.4	1.5 ± 0.2	11 ± 1
300	1.8 ± 0.2	0.10 ± 0.04	0.04 ± 0.04	0.13 ± 0.05	0.23 ± 0.06	0.6 ± 0.1	0.8 ± 0.1	0.30 ± 0.08	2.4 ± 0.4
301	1.4 ± 0.3	0.13 ± 0.07	-0.01 ± 0.04	0.19 ± 0.07	0.20 ± 0.08	0.5 ± 0.1	0.7 ± 0.2	0.18 ± 0.09	3.9 ± 0.9
302	2.0 ± 0.5	0.16 ± 0.08	0.04 ± 0.07	0.4 ± 0.1	0.4 ± 0.1	0.7 ± 0.2	0.7 ± 0.2	0.2 ± 0.1	4 ± 1
303	1.9 ± 0.3	0.19 ± 0.06	0.04 ± 0.04	0.19 ± 0.07	0.22 ± 0.07	0.7 ± 0.2	0.7 ± 0.2	0.3 ± 0.1	3.6 ± 0.8
304	33 ± 2	2.4 ± 0.3	1.0 ± 0.2	2.2 ± 0.2	3.2 ± 0.3	11.6 ± 0.9	26 ± 2	9.0 ± 0.8	35 ± 2
305	1.0 ± 0.4	0.08 ± 0.07	0.09 ± 0.08	-0.02 ± 0.04	0.2 ± 0.1	0.4 ± 0.2	0.9 ± 0.4	0.3 ± 0.2	2 ± 1
306	0.6 ± 0.1	0.04 ± 0.02	0.00 ± 0.02	0.03 ± 0.02	0.08 ± 0.03	0.20 ± 0.06	0.28 ± 0.07	0.12 ± 0.04	0.6 ± 0.2
307	2.6 ± 0.5	0.26 ± 0.08	0.09 ± 0.06	0.5 ± 0.1	0.5 ± 0.1	0.9 ± 0.2	0.9 ± 0.2	0.19 ± 0.09	3.5 ± 0.7
308	0.6 ± 0.1	0.04 ± 0.03	0.04 ± 0.03	0.07 ± 0.04	0.08 ± 0.04	0.22 ± 0.07	0.34 ± 0.09	0.14 ± 0.05	1.2 ± 0.3
309	1.2 ± 0.1	0.08 ± 0.03	0.09 ± 0.03	0.08 ± 0.03	0.08 ± 0.03	0.43 ± 0.07	0.8 ± 0.1	0.30 ± 0.06	1.3 ± 0.2
310	30 ± 7	5 ± 1	2.2 ± 0.8	5 ± 1	8 ± 2	11 ± 3	20 ± 5	7 ± 2	33 ± 8
311	9 ± 2	1.0 ± 0.3	0.4 ± 0.1	1.7 ± 0.4	2.5 ± 0.5	3.0 ± 0.7	1.7 ± 0.5	0.6 ± 0.3	13 ± 3
312	0.42 ± 0.09	0.04 ± 0.02	0.03 ± 0.02	0.06 ± 0.02	0.08 ± 0.03	0.15 ± 0.04	0.19 ± 0.05	0.09 ± 0.03	0.4 ± 0.1

Corrected flux values of the emission regions in the catalogue from this study. The measured fluxes of the nine emission lines for the detected emission regions are presented. These fluxes are corrected for the local background emission (described in Section 2.6.3), the global stellar absorption (described in Section 2.6.7), and the extinction (described in Section 2.6.8). The [O II] λ 3727 is listed here, but comes from Table F.3. The uncertainties correspond to the propagated uncertainties (described in Section 2.6.4). All flux values are scaled by 1×10^{-15} .

ID	$H\alpha$ [erg s $^{-1}$ cm $^{-2}$]	[N II] λ 6583 [erg s $^{-1}$ cm $^{-2}$]	[N II] λ 6548 [erg s $^{-1}$ cm $^{-2}$]	[S II] λ 6731 [erg s $^{-1}$ cm $^{-2}$]	[S II] λ 6716 [erg s $^{-1}$ cm $^{-2}$]	$H\beta$ [erg s $^{-1}$ cm $^{-2}$]	[O III] λ 5007 [erg s $^{-1}$ cm $^{-2}$]	[O III] λ 4959 [erg s $^{-1}$ cm $^{-2}$]	[O II] λ 3727 [erg s $^{-1}$ cm $^{-2}$]
313	2.6 ± 0.7	0.5 ± 0.2	0.2 ± 0.1	0.2 ± 0.2	0.3 ± 0.2	0.9 ± 0.4	0.6 ± 0.3	0.0 ± 0.2	6 ± 2
314	5 ± 2	1.0 ± 0.4	0.3 ± 0.2	1.0 ± 0.4	1.4 ± 0.5	1.9 ± 0.9	2 ± 1	1.0 ± 0.6	7 ± 3
315	2.7 ± 0.8	0.5 ± 0.2	0.16 ± 0.08	0.5 ± 0.2	0.8 ± 0.3	1.0 ± 0.4	0.9 ± 0.4	0.4 ± 0.2	4 ± 1
316	8 ± 1	1.3 ± 0.3	0.4 ± 0.2	1.4 ± 0.3	1.9 ± 0.4	2.7 ± 0.7	2.3 ± 0.7	0.8 ± 0.4	9 ± 2
317	23 ± 5	3.3 ± 0.8	1.3 ± 0.4	3.2 ± 0.7	4 ± 1	8 ± 2	15 ± 3	5 ± 2	26 ± 5
318	1.9 ± 0.5	0.23 ± 0.08	0.11 ± 0.05	0.3 ± 0.1	0.4 ± 0.1	0.7 ± 0.3	0.5 ± 0.3	0.2 ± 0.2	1.8 ± 0.6
319	2 ± 1	0.4 ± 0.2	0.14 ± 0.08	0.4 ± 0.2	0.6 ± 0.3	0.8 ± 0.4	0.5 ± 0.3	0.2 ± 0.1	3 ± 1
320	6 ± 2	1.0 ± 0.4	0.3 ± 0.2	0.9 ± 0.3	1.4 ± 0.5	2.0 ± 0.8	1.8 ± 0.8	0.6 ± 0.4	7 ± 2
321	5.6 ± 0.6	0.6 ± 0.1	0.15 ± 0.07	0.6 ± 0.1	1.0 ± 0.2	2.0 ± 0.3	2.4 ± 0.4	0.9 ± 0.2	8 ± 1
322	4 ± 1	0.7 ± 0.2	0.2 ± 0.1	0.6 ± 0.2	0.9 ± 0.3	1.4 ± 0.5	3 ± 1	1.3 ± 0.5	4 ± 1
323	10.2 ± 0.9	1.0 ± 0.1	0.4 ± 0.1	1.1 ± 0.2	1.5 ± 0.2	3.6 ± 0.5	3.7 ± 0.5	1.2 ± 0.3	13 ± 1
324	28 ± 2	3.5 ± 0.4	1.1 ± 0.3	2.8 ± 0.4	3.8 ± 0.4	10 ± 1	18 ± 2	6 ± 1	24 ± 2
325	18 ± 2	2.9 ± 0.5	0.9 ± 0.3	2.7 ± 0.5	3.6 ± 0.6	6 ± 1	12 ± 2	4 ± 1	22 ± 3
326	8 ± 2	1.1 ± 0.3	0.4 ± 0.1	1.1 ± 0.3	1.4 ± 0.4	2.8 ± 0.8	5 ± 1	1.6 ± 0.5	9 ± 2
327	12 ± 2	1.8 ± 0.4	0.7 ± 0.2	1.8 ± 0.4	2.6 ± 0.5	4.2 ± 0.9	8 ± 1	2.8 ± 0.7	11 ± 2
328	25 ± 3	3.5 ± 0.5	1.2 ± 0.3	3.1 ± 0.5	4.5 ± 0.7	9 ± 2	15 ± 2	5 ± 1	26 ± 4
329	14 ± 4	3 ± 1	1.0 ± 0.5	3 ± 1	4 ± 1	5 ± 2	6 ± 3	2 ± 2	19 ± 6
330	5.3 ± 0.6	0.8 ± 0.1	0.30 ± 0.09	0.9 ± 0.2	1.2 ± 0.2	1.9 ± 0.4	2.5 ± 0.4	0.9 ± 0.2	5.8 ± 0.8
332	16.8 ± 0.9	1.5 ± 0.1	0.6 ± 0.1	1.5 ± 0.2	2.0 ± 0.2	6.0 ± 0.5	11.0 ± 0.7	3.7 ± 0.4	19 ± 1
333	38 ± 5	5.3 ± 0.8	1.8 ± 0.4	4.3 ± 0.7	5.9 ± 0.9	14 ± 2	21 ± 3	8 ± 2	40 ± 6
334	28 ± 4	2.9 ± 0.5	1.1 ± 0.3	2.2 ± 0.4	3.0 ± 0.5	10 ± 2	21 ± 3	7 ± 2	28 ± 4
335	18 ± 6	2.9 ± 0.9	1.0 ± 0.4	2.8 ± 0.9	4 ± 1	7 ± 2	11 ± 3	4 ± 1	20 ± 7
336	32 ± 2	3.9 ± 0.4	1.5 ± 0.3	3.2 ± 0.4	4.4 ± 0.4	11 ± 1	23 ± 2	8 ± 1	29 ± 3
337	20 ± 2	1.9 ± 0.3	0.7 ± 0.2	1.3 ± 0.3	1.8 ± 0.3	7 ± 1	17 ± 2	6 ± 1	14 ± 2

Corrected flux values of the emission regions in the catalogue from this study. The measured fluxes of the nine emission lines for the detected emission regions are presented. These fluxes are corrected for the local background emission (described in Section 2.6.3), the global stellar absorption (described in Section 2.6.7), and the extinction (described in Section 2.6.8). The $[\text{O II}]\lambda 3727$ is listed here, but comes from Table F.3. The uncertainties correspond to the propagated uncertainties (described in Section 2.6.4). All flux values are scaled by 1×10^{-15} .

ID	$\text{H}\alpha$ [erg s $^{-1}$ cm $^{-2}$]	$[\text{N II}]\lambda 6583$ [erg s $^{-1}$ cm $^{-2}$]	$[\text{N II}]\lambda 6548$ [erg s $^{-1}$ cm $^{-2}$]	$[\text{S II}]\lambda 6731$ [erg s $^{-1}$ cm $^{-2}$]	$[\text{S II}]\lambda 6716$ [erg s $^{-1}$ cm $^{-2}$]	$\text{H}\beta$ [erg s $^{-1}$ cm $^{-2}$]	$[\text{O III}]\lambda 5007$ [erg s $^{-1}$ cm $^{-2}$]	$[\text{O III}]\lambda 4959$ [erg s $^{-1}$ cm $^{-2}$]	$[\text{O II}]\lambda 3727$ [erg s $^{-1}$ cm $^{-2}$]
338	15 ± 1	2.0 ± 0.3	0.8 ± 0.2	1.7 ± 0.3	2.3 ± 0.3	5.4 ± 0.9	11 ± 1	4.1 ± 0.7	17 ± 2
339	93 ± 5	8.6 ± 0.8	2.8 ± 0.5	5.6 ± 0.7	7.5 ± 0.8	33 ± 3	77 ± 5	27 ± 3	75 ± 5
340	11 ± 1	1.4 ± 0.2	0.5 ± 0.1	1.9 ± 0.2	2.7 ± 0.3	3.8 ± 0.5	4.8 ± 0.6	1.6 ± 0.3	15 ± 2
341	7 ± 1	0.8 ± 0.2	0.3 ± 0.1	0.6 ± 0.2	0.8 ± 0.2	2.5 ± 0.6	6 ± 1	2.0 ± 0.5	5 ± 1
342	7 ± 2	1.3 ± 0.5	0.5 ± 0.2	1.2 ± 0.4	1.7 ± 0.6	2 ± 1	4 ± 2	1.4 ± 0.7	10 ± 4
343	27 ± 5	3.5 ± 0.7	1.4 ± 0.4	3.4 ± 0.7	4.7 ± 0.9	9 ± 2	20 ± 4	7 ± 2	26 ± 5
344	106 ± 6	6.1 ± 0.7	2.2 ± 0.5	5.3 ± 0.7	7.8 ± 0.8	38 ± 3	117 ± 8	40 ± 4	94 ± 6
345	7.9 ± 0.9	0.6 ± 0.1	0.12 ± 0.07	0.7 ± 0.1	1.1 ± 0.2	2.8 ± 0.4	7.5 ± 0.9	2.6 ± 0.4	8 ± 1
346	2.5 ± 0.3	0.38 ± 0.06	0.14 ± 0.04	0.29 ± 0.06	0.42 ± 0.07	0.9 ± 0.1	0.9 ± 0.1	0.35 ± 0.09	2.7 ± 0.4
347	11 ± 2	1.7 ± 0.4	0.5 ± 0.2	1.7 ± 0.4	2.6 ± 0.6	4 ± 1	4 ± 1	1.4 ± 0.6	14 ± 3
348	7 ± 1	1.2 ± 0.2	0.3 ± 0.1	1.2 ± 0.2	1.7 ± 0.3	2.5 ± 0.5	2.6 ± 0.6	1.0 ± 0.3	9 ± 2
349	1.5 ± 0.4	0.17 ± 0.06	0.06 ± 0.04	0.23 ± 0.07	0.4 ± 0.1	0.5 ± 0.1	0.7 ± 0.2	0.24 ± 0.07	2.0 ± 0.5
350	2.9 ± 0.3	0.37 ± 0.07	0.12 ± 0.04	0.42 ± 0.07	0.58 ± 0.09	1.0 ± 0.1	0.9 ± 0.1	0.27 ± 0.06	3.2 ± 0.4
351	4.3 ± 0.4	0.45 ± 0.07	0.08 ± 0.05	0.44 ± 0.07	0.7 ± 0.1	1.5 ± 0.2	3.5 ± 0.3	1.2 ± 0.2	6.0 ± 0.7
352	29 ± 1	2.4 ± 0.2	0.9 ± 0.2	1.8 ± 0.2	2.8 ± 0.2	10.3 ± 0.7	23 ± 1	8.1 ± 0.6	27 ± 2
353	11 ± 2	1.7 ± 0.3	0.5 ± 0.2	2.0 ± 0.4	2.9 ± 0.6	3.8 ± 0.8	6 ± 1	2.1 ± 0.5	14 ± 3
354	1.2 ± 0.4	0.19 ± 0.07	0.05 ± 0.04	0.16 ± 0.06	0.22 ± 0.08	0.4 ± 0.2	0.5 ± 0.2	0.13 ± 0.07	1.8 ± 0.6
355	30 ± 2	2.4 ± 0.2	0.8 ± 0.2	1.5 ± 0.2	2.3 ± 0.2	10.8 ± 0.9	27 ± 2	9.6 ± 0.9	23 ± 2
356	2.5 ± 0.3	0.33 ± 0.07	0.11 ± 0.05	0.40 ± 0.07	0.63 ± 0.09	0.9 ± 0.1	1.3 ± 0.2	0.40 ± 0.08	4.1 ± 0.6
357	7 ± 1	0.7 ± 0.1	0.22 ± 0.08	0.7 ± 0.1	0.9 ± 0.2	2.6 ± 0.5	7 ± 1	2.3 ± 0.4	8 ± 2
358	26 ± 5	4.7 ± 0.9	1.5 ± 0.4	5 ± 1	7 ± 1	9 ± 2	12 ± 3	4 ± 1	36 ± 7
359	14 ± 1	1.2 ± 0.1	0.44 ± 0.09	1.1 ± 0.1	1.4 ± 0.1	5.1 ± 0.4	9.2 ± 0.7	3.2 ± 0.3	17 ± 1
360	12 ± 2	1.8 ± 0.5	0.7 ± 0.3	1.9 ± 0.5	2.6 ± 0.6	4 ± 1	2.0 ± 0.9	0.7 ± 0.7	12 ± 3
361	10.5 ± 0.8	1.4 ± 0.2	0.4 ± 0.1	1.5 ± 0.2	2.3 ± 0.2	3.7 ± 0.4	7.9 ± 0.8	2.7 ± 0.4	12 ± 1

Corrected flux values of the emission regions in the catalogue from this study. The measured fluxes of the nine emission lines for the detected emission regions are presented. These fluxes are corrected for the local background emission (described in Section 2.6.3), the global stellar absorption (described in Section 2.6.7), and the extinction (described in Section 2.6.8). The $[\text{O II}]\lambda 3727$ is listed here, but comes from Table F.3. The uncertainties correspond to the propagated uncertainties (described in Section 2.6.4). All flux values are scaled by 1×10^{-15} .

ID	$\text{H}\alpha$ [erg s $^{-1}$ cm $^{-2}$]	$[\text{N II}]\lambda 6583$ [erg s $^{-1}$ cm $^{-2}$]	$[\text{N II}]\lambda 6548$ [erg s $^{-1}$ cm $^{-2}$]	$[\text{S II}]\lambda 6731$ [erg s $^{-1}$ cm $^{-2}$]	$[\text{S II}]\lambda 6716$ [erg s $^{-1}$ cm $^{-2}$]	$\text{H}\beta$ [erg s $^{-1}$ cm $^{-2}$]	$[\text{O III}]\lambda 5007$ [erg s $^{-1}$ cm $^{-2}$]	$[\text{O III}]\lambda 4959$ [erg s $^{-1}$ cm $^{-2}$]	$[\text{O II}]\lambda 3727$ [erg s $^{-1}$ cm $^{-2}$]
362	6 ± 2	0.9 ± 0.4	0.2 ± 0.1	1.0 ± 0.4	1.4 ± 0.6	2.3 ± 0.9	5 ± 2	1.7 ± 0.6	8 ± 3
363	1.2 ± 0.1	0.12 ± 0.03	0.10 ± 0.03	0.09 ± 0.03	0.12 ± 0.04	0.44 ± 0.07	0.6 ± 0.1	0.24 ± 0.05	1.2 ± 0.2
364	8.3 ± 0.4	0.81 ± 0.08	0.27 ± 0.06	0.76 ± 0.08	0.95 ± 0.08	2.9 ± 0.2	3.6 ± 0.2	1.3 ± 0.1	9.6 ± 0.6
365	26 ± 4	3.5 ± 0.5	1.2 ± 0.3	4.4 ± 0.6	6.5 ± 0.9	9 ± 1	12 ± 2	4.1 ± 0.7	37 ± 5
366	8.6 ± 0.9	0.8 ± 0.1	0.31 ± 0.09	0.8 ± 0.1	1.3 ± 0.2	3.1 ± 0.4	7.4 ± 0.8	2.5 ± 0.3	13 ± 2
367	3.0 ± 0.4	0.33 ± 0.08	0.19 ± 0.06	0.46 ± 0.09	0.6 ± 0.1	1.1 ± 0.2	1.7 ± 0.2	0.6 ± 0.1	4.1 ± 0.6
368	13 ± 1	1.1 ± 0.1	0.5 ± 0.1	1.2 ± 0.1	1.7 ± 0.2	4.5 ± 0.5	13 ± 1	4.4 ± 0.5	13 ± 1
369	26 ± 3	3.0 ± 0.4	0.9 ± 0.2	3.1 ± 0.4	4.5 ± 0.6	9 ± 1	16 ± 2	5.4 ± 0.9	37 ± 5
370	9 ± 2	1.6 ± 0.5	0.5 ± 0.2	1.6 ± 0.5	2.5 ± 0.7	3 ± 1	2 ± 1	0.8 ± 0.6	12 ± 3
371	10 ± 2	1.7 ± 0.3	0.6 ± 0.2	1.9 ± 0.4	2.8 ± 0.5	3.4 ± 0.7	4.2 ± 0.9	1.5 ± 0.4	13 ± 2
372	40 ± 3	4.2 ± 0.5	1.5 ± 0.3	4.3 ± 0.5	6.3 ± 0.7	14 ± 2	44 ± 4	15 ± 2	37 ± 4
373	4 ± 1	0.8 ± 0.3	0.4 ± 0.2	1.0 ± 0.4	1.4 ± 0.5	1.4 ± 0.6	1.5 ± 0.6	0.5 ± 0.2	5 ± 2
374	6.1 ± 0.8	1.2 ± 0.2	0.32 ± 0.09	1.4 ± 0.2	1.9 ± 0.3	2.1 ± 0.3	2.2 ± 0.4	0.7 ± 0.2	9 ± 1
375	3.0 ± 0.6	0.4 ± 0.1	0.15 ± 0.07	0.5 ± 0.1	0.6 ± 0.2	1.1 ± 0.3	1.0 ± 0.2	0.3 ± 0.1	3.4 ± 0.8
376	2.5 ± 0.4	0.40 ± 0.09	0.17 ± 0.06	0.35 ± 0.09	0.5 ± 0.1	0.9 ± 0.2	0.9 ± 0.2	0.3 ± 0.1	3.3 ± 0.6
377	4 ± 1	0.4 ± 0.1	0.21 ± 0.09	0.5 ± 0.2	0.6 ± 0.2	1.4 ± 0.4	3.0 ± 0.8	1.0 ± 0.3	5 ± 1
378	33 ± 3	4.7 ± 0.6	1.5 ± 0.3	4.9 ± 0.6	6.8 ± 0.8	12 ± 2	20 ± 3	7 ± 1	36 ± 4
379	6 ± 2	0.8 ± 0.3	0.3 ± 0.1	1.2 ± 0.4	1.8 ± 0.5	2.2 ± 0.7	2.7 ± 0.8	0.9 ± 0.4	9 ± 2
380	5.0 ± 0.8	0.6 ± 0.1	0.4 ± 0.1	0.7 ± 0.2	1.0 ± 0.2	1.8 ± 0.3	3.2 ± 0.5	1.1 ± 0.2	8 ± 1
381	22 ± 2	2.1 ± 0.2	0.8 ± 0.2	2.5 ± 0.3	3.7 ± 0.4	7.9 ± 0.9	24 ± 2	8.2 ± 0.9	22 ± 2
382	9 ± 2	1.2 ± 0.3	0.4 ± 0.1	1.3 ± 0.3	1.8 ± 0.4	3.3 ± 0.8	2.9 ± 0.7	1.0 ± 0.4	12 ± 2
383	7 ± 1	1.1 ± 0.2	0.4 ± 0.1	1.1 ± 0.2	1.7 ± 0.3	2.4 ± 0.5	3.3 ± 0.6	1.2 ± 0.3	9 ± 2
384	19 ± 4	2.6 ± 0.6	0.8 ± 0.2	2.5 ± 0.5	3.7 ± 0.8	7 ± 2	9 ± 2	3.0 ± 0.9	24 ± 5
385	23 ± 3	2.6 ± 0.4	1.0 ± 0.2	3.0 ± 0.4	4.2 ± 0.6	8 ± 1	13 ± 2	4.4 ± 0.8	29 ± 4

Corrected flux values of the emission regions in the catalogue from this study. The measured fluxes of the nine emission lines for the detected emission regions are presented. These fluxes are corrected for the local background emission (described in Section 2.6.3), the global stellar absorption (described in Section 2.6.7), and the extinction (described in Section 2.6.8). The [O II] λ 3727 is listed here, but comes from Table F.3. The uncertainties correspond to the propagated uncertainties (described in Section 2.6.4). All flux values are scaled by 1×10^{-15} .

ID	$H\alpha$ [erg s $^{-1}$ cm $^{-2}$]	[N II] λ 6583 [erg s $^{-1}$ cm $^{-2}$]	[N II] λ 6548 [erg s $^{-1}$ cm $^{-2}$]	[S II] λ 6731 [erg s $^{-1}$ cm $^{-2}$]	[S II] λ 6716 [erg s $^{-1}$ cm $^{-2}$]	$H\beta$ [erg s $^{-1}$ cm $^{-2}$]	[O III] λ 5007 [erg s $^{-1}$ cm $^{-2}$]	[O III] λ 4959 [erg s $^{-1}$ cm $^{-2}$]	[O II] λ 3727 [erg s $^{-1}$ cm $^{-2}$]
386	8.9 ± 0.8	1.1 ± 0.2	0.5 ± 0.1	1.0 ± 0.2	1.4 ± 0.2	3.2 ± 0.5	6.4 ± 0.8	2.2 ± 0.4	1.1 ± 1
387	12 ± 2	1.8 ± 0.4	0.8 ± 0.2	2.0 ± 0.4	3.0 ± 0.5	4 ± 1	5 ± 1	1.6 ± 0.6	1.8 ± 3
388	21 ± 3	2.0 ± 0.4	0.6 ± 0.2	1.8 ± 0.4	2.7 ± 0.5	8 ± 1	15 ± 2	5 ± 1	29 ± 5
389	4 ± 1	0.6 ± 0.2	0.19 ± 0.09	0.7 ± 0.2	0.9 ± 0.3	1.4 ± 0.5	1.8 ± 0.6	0.6 ± 0.2	7 ± 2
390	24 ± 2	2.6 ± 0.3	1.0 ± 0.2	2.5 ± 0.3	3.6 ± 0.3	8.3 ± 0.8	10 ± 1	3.8 ± 0.5	28 ± 3
391	5.7 ± 0.5	0.9 ± 0.1	0.28 ± 0.06	0.9 ± 0.1	1.3 ± 0.1	2.0 ± 0.2	2.1 ± 0.2	0.8 ± 0.1	6.9 ± 0.7
392	11 ± 1	1.5 ± 0.2	0.5 ± 0.1	1.4 ± 0.2	2.1 ± 0.3	4.0 ± 0.7	5.5 ± 0.8	2.0 ± 0.4	1.6 ± 2
393	4 ± 1	0.5 ± 0.2	0.18 ± 0.09	0.5 ± 0.2	0.7 ± 0.3	1.2 ± 0.5	1.5 ± 0.7	0.6 ± 0.3	5 ± 2
394	11 ± 1	1.1 ± 0.2	0.37 ± 0.09	1.2 ± 0.2	1.8 ± 0.2	3.8 ± 0.5	6.8 ± 0.8	2.5 ± 0.3	1.4 ± 2
395	8 ± 2	1.1 ± 0.3	0.5 ± 0.1	1.2 ± 0.3	1.7 ± 0.4	2.9 ± 0.7	6 ± 1	1.8 ± 0.5	1.2 ± 3
396	194 ± 9	14 ± 1	6 ± 1	12 ± 1	17 ± 1	69 ± 6	170 ± 10	61 ± 5	190 ± 10
397	37 ± 2	3.4 ± 0.3	1.1 ± 0.2	2.8 ± 0.3	4.1 ± 0.4	13 ± 1	26 ± 2	9 ± 1	33 ± 2
398	54 ± 4	4.9 ± 0.5	1.7 ± 0.3	4.5 ± 0.5	6.4 ± 0.6	19 ± 2	39 ± 3	13 ± 1	68 ± 6
399	100 ± 10	4.8 ± 0.9	2.2 ± 0.6	3.7 ± 0.8	4.2 ± 0.8	36 ± 7	210 ± 20	70 ± 10	48 ± 6
401	51 ± 5	8 ± 1	2.9 ± 0.6	9 ± 1	14 ± 2	18 ± 3	28 ± 4	10 ± 2	70 ± 8
402	15 ± 2	1.7 ± 0.2	0.6 ± 0.1	1.8 ± 0.2	2.4 ± 0.3	5.4 ± 0.7	7.3 ± 0.9	2.5 ± 0.4	1.8 ± 2
403	84 ± 4	9.7 ± 0.7	3.2 ± 0.5	7.7 ± 0.7	10.8 ± 0.8	30 ± 2	43 ± 3	15 ± 2	98 ± 6
404	1.0 ± 0.2	0.16 ± 0.06	0.04 ± 0.04	0.21 ± 0.06	0.32 ± 0.08	0.34 ± 0.09	0.21 ± 0.06	0.12 ± 0.05	1.0 ± 0.2
405	11 ± 2	1.5 ± 0.4	0.6 ± 0.2	1.6 ± 0.4	2.4 ± 0.6	4 ± 1	6 ± 1	1.8 ± 0.6	18 ± 4
406	3.8 ± 0.5	0.6 ± 0.1	0.23 ± 0.07	0.6 ± 0.1	0.8 ± 0.1	1.4 ± 0.2	1.7 ± 0.3	0.6 ± 0.2	4.7 ± 0.7
407	11.5 ± 0.5	1.7 ± 0.1	0.6 ± 0.1	1.6 ± 0.1	2.4 ± 0.2	4.1 ± 0.3	3.7 ± 0.3	1.3 ± 0.2	12.6 ± 0.8
408	50 ± 2	4.9 ± 0.4	1.5 ± 0.3	4.3 ± 0.4	6.1 ± 0.4	18 ± 1	31 ± 2	11 ± 1	64 ± 4
409	25 ± 2	3.3 ± 0.3	1.2 ± 0.2	3.1 ± 0.3	4.5 ± 0.4	9.0 ± 0.9	11 ± 1	3.5 ± 0.5	33 ± 3
410	51 ± 5	4.6 ± 0.6	1.5 ± 0.3	4.6 ± 0.6	6.2 ± 0.8	18 ± 2	44 ± 5	15 ± 2	66 ± 8

Corrected flux values of the emission regions in the catalogue from this study. The measured fluxes of the nine emission lines for the detected emission regions are presented. These fluxes are corrected for the local background emission (described in Section 2.6.3), the global stellar absorption (described in Section 2.6.7), and the extinction (described in Section 2.6.8). The [O II] λ 3727 is listed here, but comes from Table F.3. The uncertainties correspond to the propagated uncertainties (described in Section 2.6.4). All flux values are scaled by 1×10^{-15} .

ID	H α [erg s $^{-1}$ cm $^{-2}$]	[N II] λ 6583 [erg s $^{-1}$ cm $^{-2}$]	[N II] λ 6548 [erg s $^{-1}$ cm $^{-2}$]	[S II] λ 6731 [erg s $^{-1}$ cm $^{-2}$]	[S II] λ 6716 [erg s $^{-1}$ cm $^{-2}$]	H β [erg s $^{-1}$ cm $^{-2}$]	[O III] λ 5007 [erg s $^{-1}$ cm $^{-2}$]	[O III] λ 4959 [erg s $^{-1}$ cm $^{-2}$]	[O II] λ 3727 [erg s $^{-1}$ cm $^{-2}$]
411	11 ± 1	1.4 ± 0.2	0.5 ± 0.1	1.5 ± 0.2	2.1 ± 0.2	4.1 ± 0.5	4.4 ± 0.6	1.3 ± 0.3	1.8 ± 2
412	30 ± 7	3.2 ± 0.8	1.2 ± 0.3	3.5 ± 0.9	5 ± 1	11 ± 2	22 ± 5	7 ± 2	40 ± 10
413	30 ± 2	3.0 ± 0.3	1.3 ± 0.2	3.2 ± 0.4	4.5 ± 0.5	11 ± 1	22 ± 2	7.4 ± 0.9	38 ± 3
414	18 ± 5	2.3 ± 0.7	0.8 ± 0.3	2.7 ± 0.7	4 ± 1	6 ± 2	15 ± 4	5 ± 1	22 ± 6
415	13.2 ± 0.9	1.5 ± 0.1	0.59 ± 0.09	1.3 ± 0.1	2.0 ± 0.2	4.7 ± 0.4	6.6 ± 0.6	2.3 ± 0.3	16 ± 1
416	37 ± 7	6 ± 1	1.9 ± 0.7	6 ± 1	9 ± 2	13 ± 4	17 ± 5	6 ± 3	44 ± 9
417	1.2 ± 0.2	0.18 ± 0.06	0.12 ± 0.05	0.26 ± 0.08	0.38 ± 0.09	0.4 ± 0.1	0.4 ± 0.1	0.07 ± 0.05	1.7 ± 0.4
418	6.2 ± 0.5	0.9 ± 0.1	0.30 ± 0.07	0.9 ± 0.1	1.2 ± 0.1	2.2 ± 0.3	2.5 ± 0.3	0.8 ± 0.2	6.8 ± 0.7
419	8 ± 3	1.2 ± 0.4	0.4 ± 0.2	1.4 ± 0.4	1.9 ± 0.6	3 ± 1	4 ± 1	1.5 ± 0.5	10 ± 3
420	97 ± 5	10.4 ± 0.9	3.5 ± 0.6	10.4 ± 0.9	14 ± 1	34 ± 3	51 ± 4	18 ± 2	109 ± 7
421	31 ± 4	4.3 ± 0.6	1.8 ± 0.3	5.5 ± 0.7	8 ± 1	11 ± 2	15 ± 2	5 ± 1	45 ± 6
422	59 ± 5	8.5 ± 0.9	3.0 ± 0.6	10 ± 1	15 ± 1	21 ± 3	33 ± 4	11 ± 2	77 ± 7
423	54 ± 3	5.6 ± 0.5	2.1 ± 0.4	6.6 ± 0.6	8.9 ± 0.7	19 ± 2	38 ± 3	13 ± 1	62 ± 4
424	5 ± 1	0.7 ± 0.3	0.5 ± 0.2	0.8 ± 0.3	1.3 ± 0.4	1.7 ± 0.5	2.1 ± 0.5	0.5 ± 0.2	10 ± 2
425	30 ± 1	3.9 ± 0.3	1.2 ± 0.2	4.3 ± 0.3	5.9 ± 0.4	10.6 ± 0.8	17 ± 1	5.5 ± 0.5	42 ± 3
426	6.9 ± 0.8	0.8 ± 0.1	0.36 ± 0.08	0.7 ± 0.1	1.1 ± 0.2	2.4 ± 0.4	3.7 ± 0.5	1.2 ± 0.3	8 ± 1
427	14 ± 3	1.6 ± 0.3	0.4 ± 0.1	1.6 ± 0.3	2.4 ± 0.4	5 ± 1	7 ± 1	2.6 ± 0.6	21 ± 4
428	19 ± 1	2.3 ± 0.2	0.8 ± 0.2	1.9 ± 0.2	2.8 ± 0.3	6.8 ± 0.7	7.7 ± 0.8	2.6 ± 0.4	25 ± 2
429	19 ± 3	2.2 ± 0.4	0.6 ± 0.2	2.6 ± 0.5	3.7 ± 0.7	7 ± 1	14 ± 2	4.8 ± 0.9	27 ± 5
430	20 ± 1	2.3 ± 0.2	0.7 ± 0.1	2.8 ± 0.3	4.1 ± 0.4	7.0 ± 0.6	13 ± 1	4.2 ± 0.4	26 ± 2
431	8 ± 1	0.9 ± 0.2	0.3 ± 0.1	0.9 ± 0.2	1.3 ± 0.2	2.7 ± 0.5	3.5 ± 0.7	1.2 ± 0.3	11 ± 2
432	8 ± 2	1.0 ± 0.3	0.4 ± 0.1	1.3 ± 0.4	1.9 ± 0.5	2.8 ± 0.8	4 ± 1	1.5 ± 0.5	11 ± 3
433	3.1 ± 0.4	0.40 ± 0.08	0.13 ± 0.05	0.33 ± 0.07	0.49 ± 0.09	1.1 ± 0.2	1.3 ± 0.2	0.40 ± 0.09	4.2 ± 0.6
434	52 ± 4	4.3 ± 0.5	1.3 ± 0.3	3.3 ± 0.4	4.9 ± 0.5	19 ± 2	41 ± 3	14 ± 1	54 ± 5

Corrected flux values of the emission regions in the catalogue from this study. The measured fluxes of the nine emission lines for the detected emission regions are presented. These fluxes are corrected for the local background emission (described in Section 2.6.3), the global stellar absorption (described in Section 2.6.7), and the extinction (described in Section 2.6.8). The [O II] λ 3727 is listed here, but comes from Table F.3. The uncertainties correspond to the propagated uncertainties (described in Section 2.6.4). All flux values are scaled by 1×10^{-15} .

ID	$H\alpha$ [erg s $^{-1}$ cm $^{-2}$]	[N II] λ 6583 [erg s $^{-1}$ cm $^{-2}$]	[N II] λ 6548 [erg s $^{-1}$ cm $^{-2}$]	[S II] λ 6731 [erg s $^{-1}$ cm $^{-2}$]	[S II] λ 6716 [erg s $^{-1}$ cm $^{-2}$]	$H\beta$ [erg s $^{-1}$ cm $^{-2}$]	[O III] λ 5007 [erg s $^{-1}$ cm $^{-2}$]	[O III] λ 4959 [erg s $^{-1}$ cm $^{-2}$]	[O II] λ 3727 [erg s $^{-1}$ cm $^{-2}$]
435	20 ± 1	2.3 ± 0.2	0.6 ± 0.1	1.9 ± 0.2	2.7 ± 0.3	7.0 ± 0.7	8.6 ± 0.8	2.8 ± 0.4	25 ± 2
436	1.7 ± 0.2	0.20 ± 0.06	0.05 ± 0.04	0.15 ± 0.05	0.14 ± 0.05	0.6 ± 0.1	1.7 ± 0.3	0.6 ± 0.1	1.7 ± 0.4
437	10 ± 2	1.1 ± 0.3	0.4 ± 0.2	1.1 ± 0.3	1.6 ± 0.3	3.5 ± 0.9	5 ± 1	1.9 ± 0.7	11 ± 2
438	31 ± 4	2.6 ± 0.4	0.7 ± 0.2	2.2 ± 0.4	2.9 ± 0.5	11 ± 2	26 ± 4	9 ± 1	33 ± 5
439	74 ± 4	6.0 ± 0.6	1.9 ± 0.4	4.4 ± 0.5	6.0 ± 0.6	26 ± 2	66 ± 4	22 ± 2	72 ± 5
440	0.9 ± 0.2	0.13 ± 0.05	0.07 ± 0.04	0.13 ± 0.05	0.15 ± 0.06	0.3 ± 0.1	0.3 ± 0.1	0.07 ± 0.05	1.3 ± 0.3
441	26 ± 4	3.0 ± 0.6	1.2 ± 0.4	3.2 ± 0.6	4.8 ± 0.9	9 ± 2	13 ± 3	4 ± 2	40 ± 7
442	18 ± 3	2.6 ± 0.5	0.7 ± 0.3	2.4 ± 0.5	3.3 ± 0.6	6 ± 1	12 ± 2	4 ± 1	23 ± 4
443	63 ± 3	5.7 ± 0.5	1.8 ± 0.3	4.1 ± 0.4	5.2 ± 0.5	22 ± 2	43 ± 2	15 ± 1	60 ± 4
444	13 ± 3	1.5 ± 0.4	0.4 ± 0.2	1.9 ± 0.5	2.8 ± 0.8	5 ± 1	10 ± 3	4 ± 1	15 ± 4
445	209 ± 9	15 ± 1	4.4 ± 0.9	10 ± 1	14 ± 1	74 ± 5	180 ± 10	62 ± 5	160 ± 10
446	35 ± 2	2.5 ± 0.3	0.7 ± 0.2	2.0 ± 0.2	2.5 ± 0.3	13 ± 1	39 ± 2	13 ± 1	26 ± 2
447	27 ± 2	3.3 ± 0.3	1.1 ± 0.2	3.4 ± 0.4	5.1 ± 0.5	10 ± 1	22 ± 2	7.4 ± 0.9	32 ± 3
448	1.5 ± 0.2	0.15 ± 0.05	0.04 ± 0.04	0.17 ± 0.05	0.21 ± 0.06	0.5 ± 0.1	0.7 ± 0.1	0.24 ± 0.06	2.1 ± 0.4
449	20 ± 2	2.2 ± 0.3	0.8 ± 0.2	2.4 ± 0.4	3.5 ± 0.5	7 ± 1	19 ± 2	6 ± 1	22 ± 3
450	40 ± 3	2.9 ± 0.3	1.0 ± 0.2	2.0 ± 0.3	3.0 ± 0.3	14 ± 1	36 ± 3	12 ± 1	35 ± 3
451	40 ± 4	5.1 ± 0.6	1.3 ± 0.3	4.8 ± 0.6	6.8 ± 0.7	14 ± 2	28 ± 3	9 ± 1	45 ± 5
452	50 ± 4	3.5 ± 0.4	1.3 ± 0.3	2.5 ± 0.4	3.5 ± 0.4	18 ± 2	43 ± 3	15 ± 1	36 ± 3
453	4 ± 1	0.6 ± 0.2	0.16 ± 0.07	0.5 ± 0.1	0.7 ± 0.2	1.4 ± 0.4	3.0 ± 0.8	1.1 ± 0.3	6 ± 1
454	107 ± 4	12.0 ± 0.8	3.2 ± 0.5	9.2 ± 0.7	12.9 ± 0.8	38 ± 2	52 ± 3	18 ± 1	135 ± 7
455	2.9 ± 0.5	0.28 ± 0.07	0.09 ± 0.05	0.31 ± 0.08	0.5 ± 0.1	1.0 ± 0.2	3.0 ± 0.5	1.0 ± 0.2	4.2 ± 0.9
456	3.1 ± 0.2	0.45 ± 0.07	0.09 ± 0.04	0.28 ± 0.05	0.43 ± 0.06	1.1 ± 0.1	1.1 ± 0.1	0.40 ± 0.06	3.9 ± 0.4
457	15 ± 1	2.3 ± 0.3	0.6 ± 0.1	1.8 ± 0.2	2.7 ± 0.3	5.3 ± 0.6	7.4 ± 0.7	2.5 ± 0.3	21 ± 2
458	15.8 ± 0.9	2.1 ± 0.2	0.7 ± 0.1	1.8 ± 0.2	2.5 ± 0.2	5.6 ± 0.5	8.5 ± 0.7	2.8 ± 0.4	22 ± 2

Corrected flux values of the emission regions in the catalogue from this study. The measured fluxes of the nine emission lines for the detected emission regions are presented. These fluxes are corrected for the local background emission (described in Section 2.6.3), the global stellar absorption (described in Section 2.6.7), and the extinction (described in Section 2.6.8). The [O II] λ 3727 is listed here, but comes from Table F.3. The uncertainties correspond to the propagated uncertainties (described in Section 2.6.4). All flux values are scaled by 1×10^{-15} .

ID	$H\alpha$ [erg s $^{-1}$ cm $^{-2}$]	[N II] λ 6583 [erg s $^{-1}$ cm $^{-2}$]	[N II] λ 6548 [erg s $^{-1}$ cm $^{-2}$]	[S II] λ 6731 [erg s $^{-1}$ cm $^{-2}$]	[S II] λ 6716 [erg s $^{-1}$ cm $^{-2}$]	$H\beta$ [erg s $^{-1}$ cm $^{-2}$]	[O III] λ 5007 [erg s $^{-1}$ cm $^{-2}$]	[O III] λ 4959 [erg s $^{-1}$ cm $^{-2}$]	[O II] λ 3727 [erg s $^{-1}$ cm $^{-2}$]
459	2.5 ± 0.5	0.37 ± 0.09	0.04 ± 0.05	0.24 ± 0.07	0.36 ± 0.09	0.9 ± 0.2	1.0 ± 0.2	0.33 ± 0.08	3.1 ± 0.6
460	14 ± 1	1.6 ± 0.2	0.6 ± 0.1	1.4 ± 0.2	1.9 ± 0.2	4.8 ± 0.4	7.0 ± 0.6	2.3 ± 0.3	14 ± 1
461	137 ± 9	8 ± 1	2.6 ± 0.7	6.5 ± 0.9	9 ± 1	49 ± 6	200 ± 20	70 ± 7	72 ± 6
462	4.5 ± 0.7	0.6 ± 0.1	0.19 ± 0.06	0.4 ± 0.1	0.6 ± 0.1	1.6 ± 0.3	2.2 ± 0.4	0.7 ± 0.1	5.0 ± 0.8
463	9 ± 2	1.2 ± 0.4	0.4 ± 0.1	1.5 ± 0.5	2.2 ± 0.6	3.2 ± 0.9	5 ± 1	1.7 ± 0.5	11 ± 3
464	14 ± 2	1.9 ± 0.3	0.6 ± 0.1	2.0 ± 0.3	2.8 ± 0.4	5.0 ± 0.8	9 ± 1	2.9 ± 0.5	15 ± 2
465	13 ± 2	1.6 ± 0.2	0.4 ± 0.1	1.7 ± 0.3	2.5 ± 0.3	4.4 ± 0.6	7 ± 1	2.5 ± 0.4	15 ± 2
466	25 ± 1	2.6 ± 0.2	0.8 ± 0.2	2.4 ± 0.2	3.3 ± 0.2	8.7 ± 0.5	14.2 ± 0.8	4.8 ± 0.4	24 ± 1
467	68 ± 6	5.7 ± 0.7	1.7 ± 0.4	4.5 ± 0.6	6.1 ± 0.7	24 ± 3	62 ± 7	22 ± 3	63 ± 7
468	39 ± 2	2.9 ± 0.3	1.0 ± 0.2	2.3 ± 0.3	3.1 ± 0.3	14 ± 1	37 ± 2	13 ± 1	34 ± 2
469	10.1 ± 0.5	0.84 ± 0.09	0.25 ± 0.06	0.69 ± 0.09	1.1 ± 0.1	3.6 ± 0.3	10.0 ± 0.7	3.5 ± 0.3	8.4 ± 0.6
470	24 ± 2	2.3 ± 0.3	1.0 ± 0.2	2.5 ± 0.3	3.6 ± 0.4	8.4 ± 0.9	21 ± 2	7.3 ± 0.8	23 ± 2
471	49 ± 5	5.1 ± 0.7	1.7 ± 0.4	5.8 ± 0.8	8 ± 1	17 ± 2	38 ± 4	13 ± 2	55 ± 6
472	29 ± 5	3.7 ± 0.7	1.1 ± 0.3	5.0 ± 0.9	7 ± 1	10 ± 2	12 ± 2	4 ± 1	36 ± 6
473	22.0 ± 0.9	2.3 ± 0.2	0.4 ± 0.1	2.0 ± 0.2	3.0 ± 0.2	7.8 ± 0.5	15.1 ± 0.8	5.3 ± 0.4	20 ± 1
474	16 ± 2	2.0 ± 0.2	0.8 ± 0.2	2.1 ± 0.3	3.2 ± 0.4	5.8 ± 0.7	7.0 ± 0.8	2.5 ± 0.4	22 ± 2
475	5.8 ± 0.6	0.7 ± 0.1	0.30 ± 0.07	0.8 ± 0.1	1.1 ± 0.1	2.1 ± 0.3	2.3 ± 0.3	0.8 ± 0.2	7.7 ± 0.9
476	21 ± 1	2.2 ± 0.2	0.7 ± 0.2	2.3 ± 0.2	3.1 ± 0.3	7.6 ± 0.7	21 ± 1	7.5 ± 0.7	19 ± 1
477	25 ± 2	2.5 ± 0.3	0.8 ± 0.2	2.0 ± 0.2	2.8 ± 0.3	9.0 ± 0.8	15 ± 1	5.2 ± 0.5	25 ± 2
478	110 ± 10	5.5 ± 0.8	1.8 ± 0.6	4.8 ± 0.8	6.4 ± 0.9	38 ± 5	140 ± 10	47 ± 5	60 ± 7
479	15.1 ± 0.7	1.3 ± 0.1	0.38 ± 0.09	1.1 ± 0.1	1.7 ± 0.1	5.3 ± 0.4	12.7 ± 0.7	4.4 ± 0.3	12.9 ± 0.8
480	17 ± 2	1.6 ± 0.2	0.5 ± 0.1	1.6 ± 0.2	2.2 ± 0.3	6.2 ± 0.8	18 ± 2	6.1 ± 0.8	14 ± 2
481	16 ± 1	2.2 ± 0.3	0.9 ± 0.2	2.2 ± 0.3	2.9 ± 0.3	5.6 ± 0.7	9 ± 1	3.2 ± 0.5	20 ± 2
482	75 ± 4	6.4 ± 0.6	1.9 ± 0.4	5.4 ± 0.6	7.9 ± 0.7	27 ± 2	70 ± 5	25 ± 2	75 ± 5

Corrected flux values of the emission regions in the catalogue from this study. The measured fluxes of the nine emission lines for the detected emission regions are presented. These fluxes are corrected for the local background emission (described in Section 2.6.3), the global stellar absorption (described in Section 2.6.7), and the extinction (described in Section 2.6.8). The [O II] λ 3727 is listed here, but comes from Table F.3. The uncertainties correspond to the propagated uncertainties (described in Section 2.6.4). All flux values are scaled by 1×10^{-15} .

ID	$H\alpha$ [erg s $^{-1}$ cm $^{-2}$]	[N II] λ 6583 [erg s $^{-1}$ cm $^{-2}$]	[N II] λ 6548 [erg s $^{-1}$ cm $^{-2}$]	[S II] λ 6731 [erg s $^{-1}$ cm $^{-2}$]	[S II] λ 6716 [erg s $^{-1}$ cm $^{-2}$]	$H\beta$ [erg s $^{-1}$ cm $^{-2}$]	[O III] λ 5007 [erg s $^{-1}$ cm $^{-2}$]	[O III] λ 4959 [erg s $^{-1}$ cm $^{-2}$]	[O II] λ 3727 [erg s $^{-1}$ cm $^{-2}$]
483	43 ± 2	3.3 ± 0.3	1.1 ± 0.2	2.7 ± 0.3	3.8 ± 0.4	15 ± 1	45 ± 3	15 ± 1	36 ± 3
484	29 ± 3	3.4 ± 0.4	1.2 ± 0.2	3.6 ± 0.5	5.3 ± 0.7	10 ± 1	16 ± 2	5.7 ± 0.8	34 ± 4
485	41 ± 3	3.1 ± 0.4	1.1 ± 0.3	2.4 ± 0.4	3.7 ± 0.5	15 ± 2	31 ± 3	12 ± 2	32 ± 5
486	28 ± 6	3.7 ± 0.9	1.3 ± 0.4	5 ± 1	7 ± 1	10 ± 2	19 ± 4	6 ± 2	37 ± 8
487	14 ± 2	1.2 ± 0.2	0.3 ± 0.1	1.1 ± 0.2	1.5 ± 0.3	4.8 ± 0.8	13 ± 2	4.5 ± 0.8	10 ± 2
488	5.8 ± 0.3	0.73 ± 0.09	0.32 ± 0.07	0.67 ± 0.09	0.9 ± 0.1	2.1 ± 0.2	1.6 ± 0.1	0.41 ± 0.08	8.1 ± 0.6
489	13.7 ± 0.8	1.1 ± 0.1	0.26 ± 0.08	1.0 ± 0.1	1.4 ± 0.1	4.9 ± 0.4	14.3 ± 0.9	5.0 ± 0.4	10.5 ± 0.9
490	6 ± 2	0.6 ± 0.2	0.18 ± 0.09	0.6 ± 0.2	0.8 ± 0.2	2.3 ± 0.6	4 ± 1	1.5 ± 0.4	7 ± 2
491	7 ± 3	0.8 ± 0.3	0.2 ± 0.1	0.7 ± 0.3	1.0 ± 0.4	3 ± 1	4 ± 2	1.6 ± 0.6	7 ± 3
492	5 ± 2	0.6 ± 0.2	0.21 ± 0.09	0.7 ± 0.3	1.0 ± 0.4	1.6 ± 0.7	2.0 ± 0.8	0.7 ± 0.3	6 ± 2
493	23 ± 1	2.0 ± 0.2	0.8 ± 0.1	1.8 ± 0.2	2.4 ± 0.2	8.0 ± 0.6	17 ± 1	6.0 ± 0.5	17 ± 1
494	200 ± 10	17 ± 2	6 ± 1	17 ± 2	24 ± 2	70 ± 6	160 ± 10	56 ± 5	200 ± 10
495	18 ± 3	2.0 ± 0.3	0.7 ± 0.2	2.2 ± 0.4	3.3 ± 0.6	6 ± 1	16 ± 2	5.4 ± 0.9	20 ± 3
496	29 ± 2	2.6 ± 0.3	1.0 ± 0.2	3.0 ± 0.3	4.3 ± 0.4	10 ± 1	26 ± 2	9.0 ± 0.9	33 ± 3
497	24 ± 1	2.3 ± 0.2	1.0 ± 0.2	1.8 ± 0.2	2.5 ± 0.2	8.4 ± 0.6	13.7 ± 0.8	4.8 ± 0.4	27 ± 2
498	47 ± 6	4.9 ± 0.8	1.8 ± 0.5	5.1 ± 0.9	7 ± 1	17 ± 3	31 ± 4	10 ± 2	51 ± 7
499	104 ± 7	7.3 ± 0.8	2.6 ± 0.5	7.0 ± 0.8	10 ± 1	37 ± 3	93 ± 7	32 ± 3	94 ± 7
500	3.0 ± 0.9	0.3 ± 0.1	0.26 ± 0.09	0.5 ± 0.2	0.7 ± 0.2	1.1 ± 0.3	0.8 ± 0.3	0.3 ± 0.1	4 ± 1
501	38 ± 4	3.9 ± 0.5	1.3 ± 0.3	4.2 ± 0.6	5.9 ± 0.8	14 ± 2	24 ± 3	8 ± 1	40 ± 5
502	13 ± 3	1.7 ± 0.4	0.4 ± 0.2	1.8 ± 0.4	2.7 ± 0.6	5 ± 1	7 ± 2	2.6 ± 0.6	15 ± 3
503	65 ± 3	4.5 ± 0.5	1.6 ± 0.4	4.3 ± 0.5	5.7 ± 0.5	23 ± 2	56 ± 3	19 ± 2	49 ± 3
504	9 ± 1	1.0 ± 0.2	0.31 ± 0.08	1.0 ± 0.1	1.2 ± 0.2	3.2 ± 0.4	4.2 ± 0.5	1.5 ± 0.2	11 ± 2
505	49 ± 4	2.7 ± 0.4	1.0 ± 0.2	2.5 ± 0.3	3.6 ± 0.4	17 ± 2	55 ± 5	19 ± 2	32 ± 3
506	54 ± 3	3.7 ± 0.4	1.2 ± 0.3	3.6 ± 0.4	5.1 ± 0.4	19 ± 1	50 ± 3	17 ± 1	41 ± 3

Corrected flux values of the emission regions in the catalogue from this study. The measured fluxes of the nine emission lines for the detected emission regions are presented. These fluxes are corrected for the local background emission (described in Section 2.6.3), the global stellar absorption (described in Section 2.6.7), and the extinction (described in Section 2.6.8). The [O II] λ 3727 is listed here, but comes from Table F.3. The uncertainties correspond to the propagated uncertainties (described in Section 2.6.4). All flux values are scaled by 1×10^{-15} .

ID	$H\alpha$ [erg s $^{-1}$ cm $^{-2}$]	[N II] λ 6583 [erg s $^{-1}$ cm $^{-2}$]	[N II] λ 6548 [erg s $^{-1}$ cm $^{-2}$]	[S II] λ 6731 [erg s $^{-1}$ cm $^{-2}$]	[S II] λ 6716 [erg s $^{-1}$ cm $^{-2}$]	$H\beta$ [erg s $^{-1}$ cm $^{-2}$]	[O III] λ 5007 [erg s $^{-1}$ cm $^{-2}$]	[O III] λ 4959 [erg s $^{-1}$ cm $^{-2}$]	[O II] λ 3727 [erg s $^{-1}$ cm $^{-2}$]
507	11 ± 2	1.2 ± 0.2	0.6 ± 0.1	1.4 ± 0.2	2.1 ± 0.3	3.8 ± 0.7	2.5 ± 0.5	0.7 ± 0.3	11 ± 2
508	51 ± 4	6.1 ± 0.6	2.1 ± 0.3	6.6 ± 0.6	9.5 ± 0.8	18 ± 2	28 ± 2	10 ± 1	70 ± 6
509	22 ± 4	1.7 ± 0.4	0.5 ± 0.2	1.7 ± 0.4	2.6 ± 0.6	8 ± 2	19 ± 3	7 ± 1	21 ± 4
510	4.6 ± 0.6	0.6 ± 0.1	0.40 ± 0.09	0.6 ± 0.1	0.9 ± 0.2	1.6 ± 0.3	2.5 ± 0.4	0.8 ± 0.2	6 ± 1
511	27 ± 2	2.1 ± 0.2	0.7 ± 0.1	2.3 ± 0.2	3.1 ± 0.3	9.4 ± 0.7	23 ± 1	7.8 ± 0.6	21 ± 2
512	10 ± 2	1.0 ± 0.3	0.4 ± 0.1	1.2 ± 0.3	1.9 ± 0.5	3.4 ± 0.8	8 ± 2	2.8 ± 0.6	12 ± 3
513	24 ± 1	2.8 ± 0.2	1.0 ± 0.1	2.5 ± 0.2	3.6 ± 0.2	8.5 ± 0.5	11.6 ± 0.7	3.9 ± 0.3	33 ± 2
514	6 ± 1	0.7 ± 0.2	0.26 ± 0.09	0.9 ± 0.2	1.2 ± 0.3	2.3 ± 0.6	6 ± 1	2.1 ± 0.5	8 ± 2
515	52 ± 2	5.9 ± 0.4	2.1 ± 0.3	5.4 ± 0.4	7.7 ± 0.5	18 ± 1	23 ± 1	8.1 ± 0.7	75 ± 5
517	27 ± 5	2.7 ± 0.5	1.1 ± 0.2	1.9 ± 0.4	2.8 ± 0.6	10 ± 2	16 ± 3	5.6 ± 0.9	41 ± 8
518	223 ± 9	22 ± 2	7 ± 1	20 ± 2	29 ± 2	79 ± 5	180 ± 10	63 ± 5	310 ± 20
519	62 ± 8	5.3 ± 0.9	1.9 ± 0.4	3.4 ± 0.7	4.9 ± 0.9	22 ± 3	40 ± 5	14 ± 2	70 ± 10
520	88 ± 5	6.8 ± 0.6	2.4 ± 0.4	5.9 ± 0.6	8.0 ± 0.7	31 ± 2	78 ± 5	27 ± 2	72 ± 5
521	39 ± 2	3.3 ± 0.3	1.3 ± 0.2	2.7 ± 0.3	3.9 ± 0.3	14 ± 1	32 ± 2	11.2 ± 0.9	50 ± 3
522	107 ± 3	10.3 ± 0.7	3.6 ± 0.5	7.7 ± 0.6	10.6 ± 0.7	38 ± 2	48 ± 2	17 ± 1	135 ± 6
523	99 ± 4	9.8 ± 0.7	3.0 ± 0.5	8.4 ± 0.7	11.9 ± 0.8	35 ± 2	86 ± 4	30 ± 2	107 ± 6
524	300 ± 10	25 ± 2	9 ± 1	16 ± 2	22 ± 2	108 ± 6	210 ± 10	72 ± 5	300 ± 20
525	140 ± 10	14 ± 1	5.0 ± 0.7	10 ± 1	15 ± 1	49 ± 4	66 ± 5	23 ± 2	150 ± 10
526	125 ± 8	11 ± 1	3.9 ± 0.7	7.0 ± 0.8	10 ± 1	44 ± 3	78 ± 5	27 ± 2	140 ± 10
527	1150 ± 70	65 ± 7	23 ± 5	48 ± 7	64 ± 8	409 ± 40	1400 ± 100	500 ± 40	750 ± 60
528	24 ± 2	2.5 ± 0.3	0.8 ± 0.2	2.4 ± 0.2	3.2 ± 0.3	8.5 ± 0.9	22 ± 2	7.7 ± 0.8	21 ± 2
530	19 ± 4	2.3 ± 0.5	0.8 ± 0.2	2.7 ± 0.6	3.8 ± 0.9	7 ± 2	13 ± 3	4 ± 1	21 ± 5
531	4.8 ± 0.9	0.7 ± 0.1	0.28 ± 0.09	0.8 ± 0.2	1.2 ± 0.2	1.7 ± 0.4	1.5 ± 0.4	0.6 ± 0.2	5 ± 1
532	46 ± 2	6.2 ± 0.4	2.2 ± 0.3	7.5 ± 0.4	10.4 ± 0.5	16.3 ± 0.9	22 ± 1	7.7 ± 0.6	57 ± 3

Corrected flux values of the emission regions in the catalogue from this study. The measured fluxes of the nine emission lines for the detected emission regions are presented. These fluxes are corrected for the local background emission (described in Section 2.6.3), the global stellar absorption (described in Section 2.6.7), and the extinction (described in Section 2.6.8). The [O II] λ 3727 is listed here, but comes from Table F.3. The uncertainties correspond to the propagated uncertainties (described in Section 2.6.4). All flux values are scaled by 1×10^{-15} .

ID	$H\alpha$ [erg s $^{-1}$ cm $^{-2}$]	[N II] λ 6583 [erg s $^{-1}$ cm $^{-2}$]	[N II] λ 6548 [erg s $^{-1}$ cm $^{-2}$]	[S II] λ 6731 [erg s $^{-1}$ cm $^{-2}$]	[S II] λ 6716 [erg s $^{-1}$ cm $^{-2}$]	$H\beta$ [erg s $^{-1}$ cm $^{-2}$]	[O III] λ 5007 [erg s $^{-1}$ cm $^{-2}$]	[O III] λ 4959 [erg s $^{-1}$ cm $^{-2}$]	[O II] λ 3727 [erg s $^{-1}$ cm $^{-2}$]
533	1.5 ± 0.4	0.28 ± 0.08	0.09 ± 0.05	0.28 ± 0.08	0.5 ± 0.1	0.5 ± 0.1	1.0 ± 0.2	0.31 ± 0.09	1.8 ± 0.5
534	18 ± 3	2.2 ± 0.4	1.0 ± 0.2	2.2 ± 0.4	3.2 ± 0.7	6 ± 1	7 ± 1	2.2 ± 0.5	23 ± 4
535	19 ± 2	2.2 ± 0.3	0.9 ± 0.2	2.2 ± 0.3	3.0 ± 0.4	6.8 ± 0.8	17 ± 2	5.6 ± 0.7	23 ± 3
536	10.1 ± 0.6	1.3 ± 0.1	0.45 ± 0.08	1.6 ± 0.1	2.1 ± 0.2	3.6 ± 0.3	9.3 ± 0.6	3.1 ± 0.3	11.2 ± 0.8
537	18 ± 2	2.7 ± 0.3	1.0 ± 0.2	2.1 ± 0.2	3.0 ± 0.3	6.6 ± 0.6	13 ± 1	4.3 ± 0.4	47 ± 4
538	13 ± 1	1.8 ± 0.2	0.6 ± 0.1	1.9 ± 0.2	2.9 ± 0.3	4.7 ± 0.5	12 ± 1	3.9 ± 0.4	16 ± 2
539	9.0 ± 0.8	1.2 ± 0.1	0.38 ± 0.07	1.3 ± 0.1	1.9 ± 0.2	3.2 ± 0.4	9.8 ± 0.8	3.3 ± 0.4	8.7 ± 0.9
540	5.0 ± 0.4	0.8 ± 0.1	0.34 ± 0.08	0.8 ± 0.1	1.0 ± 0.1	1.8 ± 0.2	1.4 ± 0.2	0.6 ± 0.1	6.6 ± 0.7
541	13.4 ± 0.8	2.0 ± 0.2	0.8 ± 0.1	1.4 ± 0.1	2.3 ± 0.2	4.8 ± 0.3	8.6 ± 0.5	2.9 ± 0.2	22 ± 1
542	15 ± 1	1.6 ± 0.2	0.7 ± 0.2	1.8 ± 0.2	2.6 ± 0.3	5.3 ± 0.6	8.1 ± 0.8	2.8 ± 0.4	21 ± 2
543	4.4 ± 0.6	0.5 ± 0.1	0.21 ± 0.07	0.5 ± 0.1	0.8 ± 0.1	1.6 ± 0.4	11 ± 2	3.7 ± 0.6	4.1 ± 0.7

Table F.5

Kinematical and chemical parameters of the emission regions in the catalogue from this study. The velocity corresponds to the first moment of the sincgauss fit of the H α emission line, corrected for the sky velocity and heliocentric (described in Section 2.5.3 and obtained in the step described in Section 2.6.3). The velocity dispersion corresponds to the second moment of the sincgauss fit of the H α emission line (described in Section 2.5.3 and obtained in the step described in Section 2.6.3). The A_V value corresponds to the extinction computed with `pymeb` (described in Section 2.6.8). $12 + \log[\text{O}/\text{H}]$ is the metallicity computed with the *N2O2* indicator from Pilyugin & Grebel (2016), as described in Section 2.7.8.

ID	Velocity [km s $^{-1}$]	Velocity Dispersion [km s $^{-1}$]	A_V	$12 + \log[\text{O}/\text{H}]$
0	217 ± 3	29 ± 3	0.466	1 ± 1
2	188.4 ± 0.4	15.5 ± 0.7	0.536	8.18 ± 0.06
3	199.2 ± 0.7	20 ± 1	0.391	8.1 ± 0.1
4	202.5 ± 0.7	19 ± 1	0.222	8.27 ± 0.09
6	207.7 ± 0.6	19 ± 1	0.045	8.3 ± 0.1
7	196.1 ± 0.7	29.3 ± 0.8	0.444	8.3 ± 0.2
8	201 ± 1	18 ± 2	-0.163	8.3 ± 0.1
9	205.6 ± 0.3	22.8 ± 0.4	0.534	8.20 ± 0.05
10	204.1 ± 0.1	16.5 ± 0.2	0.411	8.21 ± 0.03
11	198.3 ± 0.5	29.5 ± 0.6	0.431	8.2 ± 0.1
13	207.2 ± 0.2	20.8 ± 0.4	0.432	8.24 ± 0.04
14	202.8 ± 0.8	18 ± 1	0.014	8.37 ± 0.09
15	200.7 ± 0.9	14 ± 2	0.111	8.3 ± 0.1
16	201.4 ± 0.3	16.7 ± 0.5	0.747	8.2 ± 0.1
17	204.9 ± 0.4	19.9 ± 0.6	0.414	8.3 ± 0.2
18	208.2 ± 0.4	21.3 ± 0.7	0.873	8.32 ± 0.07
19	201.6 ± 0.1	15.6 ± 0.3	0.317	8.23 ± 0.03

Kinematical and chemical parameters of the emission regions in the catalogue from this study. The velocity corresponds to the first moment of the sincgauss fit of the H α emission line, corrected for the sky velocity and heliocentric (described in Section 2.5.3 and obtained in the step described in Section 2.6.3). The velocity dispersion corresponds to the second moment of the sincgauss fit of the H α emission line (described in Section 2.5.3 and obtained in the step described in Section 2.6.3). The A_V value corresponds to the extinction computed with `pyngeb` (described in Section 2.6.8). $12 + \log[\text{O}/\text{H}]$ is the metallicity computed with the $N2O2$ indicator from Pilyugin & Grebel (2016), as described in Section 2.7.8.

ID	Velocity [km s $^{-1}$]	Velocity Dispersion [km s $^{-1}$]	A_V	$12 + \log[\text{O}/\text{H}]$
20	208.5 ± 0.2	18.9 ± 0.4	0.209	8.34 ± 0.05
21	211.1 ± 0.2	16.3 ± 0.4	0.566	8.25 ± 0.04
22	191 ± 1	23 ± 2	1.348	8.1 ± 0.2
23	204.7 ± 0.6	18 ± 1	0.185	8.4 ± 0.1
24	183.7 ± 0.4	14.4 ± 0.8	0.255	8.19 ± 0.07
25	185.5 ± 0.5	15 ± 1	-0.215	8.3 ± 0.1
26	188.8 ± 0.6	19 ± 1	0.373	8.3 ± 0.1
27	183.5 ± 0.8	17 ± 1	0.077	8.2 ± 0.1
28	198.8 ± 0.8	25 ± 1	0.424	8.3 ± 0.1
29	185.7 ± 0.8	21 ± 1	0.467	8.3 ± 0.1
30	196.1 ± 0.2	13.5 ± 0.4	0.329	8.21 ± 0.04
31	187.9 ± 0.4	15.7 ± 0.9	0.415	8.1 ± 0.1
32	182.2 ± 0.9	21 ± 1	0.299	8.2 ± 0.2
33	191.0 ± 0.9	16 ± 2	0.72	8.2 ± 0.2
34	196.9 ± 0.6	21.6 ± 0.9	0.783	8.2 ± 0.1
35	202.5 ± 0.6	21.7 ± 0.9	0.236	8.2 ± 0.1
36	193.9 ± 0.2	24.5 ± 0.3	0.054	8.30 ± 0.04
37	182.5 ± 0.2	17.4 ± 0.3	0.235	8.25 ± 0.04
38	191.7 ± 0.3	21.2 ± 0.4	0.229	8.29 ± 0.06
39	207.6 ± 0.4	24.9 ± 0.5	0.238	8.28 ± 0.07

Kinematical and chemical parameters of the emission regions in the catalogue from this study. The velocity corresponds to the first moment of the sincgauss fit of the H α emission line, corrected for the sky velocity and heliocentric (described in Section 2.5.3 and obtained in the step described in Section 2.6.3). The velocity dispersion corresponds to the second moment of the sincgauss fit of the H α emission line (described in Section 2.5.3 and obtained in the step described in Section 2.6.3). The A_V value corresponds to the extinction computed with `pyngeb` (described in Section 2.6.8). $12 + \log[\text{O}/\text{H}]$ is the metallicity computed with the $N2O2$ indicator from Pilyugin & Grebel (2016), as described in Section 2.7.8.

ID	Velocity [km s $^{-1}$]	Velocity Dispersion [km s $^{-1}$]	A_V	$12 + \log[\text{O}/\text{H}]$
40	184.4 ± 0.3	20.5 ± 0.5	0.506	8.27 ± 0.07
41	188.4 ± 0.2	17.8 ± 0.3	0.274	8.33 ± 0.04
42	191.6 ± 0.2	21.5 ± 0.3	0.045	8.30 ± 0.03
43	199.9 ± 0.2	17.7 ± 0.3	0.645	8.21 ± 0.05
44	213.7 ± 0.5	26.9 ± 0.6	-0.32	8.4 ± 0.1
45	212.3 ± 0.4	23.8 ± 0.6	0.121	8.24 ± 0.09
46	186.1 ± 0.3	21.5 ± 0.4	0.208	8.28 ± 0.06
47	202.0 ± 0.5	19.2 ± 0.8	-0.158	8.26 ± 0.09
48	173.5 ± 0.2	14.2 ± 0.4	0.858	8.18 ± 0.04
49	189.8 ± 0.3	24.9 ± 0.3	0.009	8.29 ± 0.05
50	195.1 ± 0.4	31.0 ± 0.5	0.149	8.30 ± 0.06
51	174.4 ± 0.4	15.1 ± 0.9	0.012	8.3 ± 0.1
52	181.1 ± 0.4	17.8 ± 0.8	0.351	8.13 ± 0.08
53	204.3 ± 0.3	17.8 ± 0.5	0.613	8.23 ± 0.06
54	189.4 ± 0.4	17.5 ± 0.7	0.185	8.28 ± 0.06
55	186.8 ± 0.2	15.6 ± 0.5	0.379	8.19 ± 0.04
56	196.6 ± 0.6	32.5 ± 0.6	0.058	8.31 ± 0.09
57	175.8 ± 0.8	19 ± 1	0.508	8.3 ± 0.1
58	203.6 ± 0.5	27.9 ± 0.6	0.076	8.3 ± 0.1
59	206.0 ± 0.5	19.1 ± 0.8	0.892	8.2 ± 0.1

Kinematical and chemical parameters of the emission regions in the catalogue from this study. The velocity corresponds to the first moment of the sincgauss fit of the H α emission line, corrected for the sky velocity and heliocentric (described in Section 2.5.3 and obtained in the step described in Section 2.6.3). The velocity dispersion corresponds to the second moment of the sincgauss fit of the H α emission line (described in Section 2.5.3 and obtained in the step described in Section 2.6.3). The A_V value corresponds to the extinction computed with `pyngeb` (described in Section 2.6.8). $12 + \log[\text{O}/\text{H}]$ is the metallicity computed with the $N2O2$ indicator from Pilyugin & Grebel (2016), as described in Section 2.7.8.

ID	Velocity [km s $^{-1}$]	Velocity Dispersion [km s $^{-1}$]	A_V	$12 + \log[\text{O}/\text{H}]$
60	200.4 ± 0.5	21.9 ± 0.7	-0.476	8.4 ± 0.1
61	185.4 ± 0.6	18 ± 1	-0.214	8.31 ± 0.08
62	204.3 ± 0.5	21.3 ± 0.8	-0.269	8.4 ± 0.1
63	201.4 ± 0.2	14.9 ± 0.4	0.484	8.21 ± 0.04
64	205 ± 2	16 ± 3	1.942	7.9 ± 0.4
65	180.8 ± 0.4	17.5 ± 0.8	-0.017	8.19 ± 0.07
66	193.7 ± 0.2	14.0 ± 0.4	0.412	8.16 ± 0.04
67	190.8 ± 0.2	14.8 ± 0.5	0.091	8.25 ± 0.04
68	202.2 ± 0.8	17 ± 1	-0.219	8.39 ± 0.09
69	192.4 ± 0.4	15.1 ± 0.8	-0.301	8.35 ± 0.07
70	199.7 ± 0.4	15.3 ± 0.8	0.003	8.33 ± 0.06
71	219.9 ± 0.4	19.9 ± 0.6	0.127	8.34 ± 0.08
72	200.2 ± 0.2	14.7 ± 0.5	-0.031	8.24 ± 0.04
73	209.6 ± 0.6	24.9 ± 0.8	-0.275	8.4 ± 0.1
74	208.9 ± 0.5	21.5 ± 0.8	0.247	8.3 ± 0.1
75	208.9 ± 0.4	18.6 ± 0.6	0.307	8.3 ± 0.1
76	203.0 ± 0.3	18.6 ± 0.6	0.006	8.4 ± 0.1
77	203.2 ± 0.7	38.4 ± 0.8	-0.099	8.36 ± 0.09
78	192.6 ± 0.6	14 ± 1	0.045	8.2 ± 0.1
79	216.1 ± 0.1	15.1 ± 0.3	0.43	8.25 ± 0.03

Kinematical and chemical parameters of the emission regions in the catalogue from this study. The velocity corresponds to the first moment of the sincgauss fit of the H α emission line, corrected for the sky velocity and heliocentric (described in Section 2.5.3 and obtained in the step described in Section 2.6.3). The velocity dispersion corresponds to the second moment of the sincgauss fit of the H α emission line (described in Section 2.5.3 and obtained in the step described in Section 2.6.3). The A_V value corresponds to the extinction computed with `pyngeb` (described in Section 2.6.8). $12 + \log[\text{O}/\text{H}]$ is the metallicity computed with the $N2O2$ indicator from Pilyugin & Grebel (2016), as described in Section 2.7.8.

ID	Velocity [km s $^{-1}$]	Velocity Dispersion [km s $^{-1}$]	A_V	$12 + \log[\text{O}/\text{H}]$
80	190.7 ± 0.4	16.9 ± 0.8	0.251	8.14 ± 0.07
81	178.9 ± 0.4	22.3 ± 0.5	0.265	8.18 ± 0.05
82	176.6 ± 0.3	20.8 ± 0.4	0.225	8.17 ± 0.04
83	199.5 ± 0.6	26.8 ± 0.8	-0.279	8.4 ± 0.1
84	199.3 ± 0.3	19.5 ± 0.4	-0.005	8.21 ± 0.05
85	199.7 ± 0.3	22.6 ± 0.5	0.071	8.35 ± 0.06
86	187.9 ± 0.2	16.7 ± 0.3	0.502	8.23 ± 0.04
87	205.0 ± 0.3	28.0 ± 0.4	0.114	8.36 ± 0.07
88	194.6 ± 0.5	26.0 ± 0.7	-0.391	8.36 ± 0.09
89	192.4 ± 0.3	17.4 ± 0.5	-0.053	8.32 ± 0.07
90	211 ± 2	10 ± 6	-1.289	8.6 ± 0.1
91	202.6 ± 0.7	11 ± 2	0.679	8.2 ± 0.1
92	193.6 ± 0.9	26 ± 1	0.159	8.2 ± 0.1
93	215.2 ± 0.6	23.0 ± 0.9	-0.442	8.4 ± 0.1
94	207.4 ± 0.1	15.9 ± 0.3	0.259	8.22 ± 0.03
95	203.2 ± 0.1	15.3 ± 0.3	0.188	8.19 ± 0.03
96	216.6 ± 0.6	24.8 ± 0.8	-0.092	8.4 ± 0.1
97	207.8 ± 0.4	33.0 ± 0.4	0.009	8.35 ± 0.05
98	223.8 ± 0.3	13.0 ± 0.8	-0.018	8.0 ± 0.1
99	189.9 ± 0.4	20.3 ± 0.6	-0.124	8.3 ± 0.1

Kinematical and chemical parameters of the emission regions in the catalogue from this study. The velocity corresponds to the first moment of the sincgauss fit of the H α emission line, corrected for the sky velocity and heliocentric (described in Section 2.5.3 and obtained in the step described in Section 2.6.3). The velocity dispersion corresponds to the second moment of the sincgauss fit of the H α emission line (described in Section 2.5.3 and obtained in the step described in Section 2.6.3). The A_V value corresponds to the extinction computed with `pyngeb` (described in Section 2.6.8). $12 + \log[\text{O}/\text{H}]$ is the metallicity computed with the $N2O2$ indicator from Pilyugin & Grebel (2016), as described in Section 2.7.8.

ID	Velocity [km s $^{-1}$]	Velocity Dispersion [km s $^{-1}$]	A_V	$12 + \log[\text{O}/\text{H}]$
100	215.4 ± 0.1	16.3 ± 0.3	0.257	8.24 ± 0.03
101	200.3 ± 0.3	19.7 ± 0.5	-0.159	8.29 ± 0.06
102	215.9 ± 0.3	21.9 ± 0.4	0.153	8.36 ± 0.09
103	201.8 ± 0.3	18.8 ± 0.5	-0.165	8.31 ± 0.05
104	202.3 ± 0.2	21.5 ± 0.3	0.166	8.31 ± 0.04
105	207.1 ± 0.3	23.9 ± 0.4	0.172	8.31 ± 0.06
106	187.2 ± 0.5	28.1 ± 0.6	-0.089	8.31 ± 0.07
107	190.4 ± 0.4	19.9 ± 0.6	-0.276	8.31 ± 0.06
108	217.2 ± 0.2	21.1 ± 0.3	0.018	8.36 ± 0.05
109	220.6 ± 0.7	16 ± 1	0.932	8.0 ± 0.3
110	208.0 ± 0.2	18.7 ± 0.3	-0.011	8.32 ± 0.03
111	206.8 ± 0.2	24.0 ± 0.3	-0.018	8.32 ± 0.04
112	213.8 ± 0.2	24.2 ± 0.3	0.02	8.36 ± 0.03
113	206.9 ± 0.3	21.7 ± 0.4	-0.158	8.26 ± 0.07
114	211.7 ± 0.1	15.8 ± 0.2	0.289	8.15 ± 0.08
115	190.3 ± 0.4	22.4 ± 0.6	-0.536	8.36 ± 0.06
116	180.4 ± 0.3	21.2 ± 0.4	-0.085	8.36 ± 0.05
117	212.8 ± 0.4	28.6 ± 0.5	0.026	8.34 ± 0.07
118	218.1 ± 0.2	18.1 ± 0.3	0.146	8.31 ± 0.04
119	171.0 ± 0.4	20.5 ± 0.6	-0.479	8.39 ± 0.07

Kinematical and chemical parameters of the emission regions in the catalogue from this study. The velocity corresponds to the first moment of the sincgauss fit of the H α emission line, corrected for the sky velocity and heliocentric (described in Section 2.5.3 and obtained in the step described in Section 2.6.3). The velocity dispersion corresponds to the second moment of the sincgauss fit of the H α emission line (described in Section 2.5.3 and obtained in the step described in Section 2.6.3). The A_V value corresponds to the extinction computed with `pyngeb` (described in Section 2.6.8). $12 + \log[\text{O}/\text{H}]$ is the metallicity computed with the $N2O2$ indicator from Pilyugin & Grebel (2016), as described in Section 2.7.8.

ID	Velocity [km s $^{-1}$]	Velocity Dispersion [km s $^{-1}$]	A_V	$12 + \log[\text{O}/\text{H}]$
120	185.2 ± 0.7	28.4 ± 0.8	-0.241	8.33 ± 0.09
121	197.4 ± 0.2	18.7 ± 0.3	0.156	8.25 ± 0.04
122	205.2 ± 0.1	19.6 ± 0.2	0.222	8.26 ± 0.04
123	203.1 ± 0.5	24.2 ± 0.6	-0.314	8.4 ± 0.1
124	184.0 ± 0.5	24.1 ± 0.7	-0.312	8.30 ± 0.09
125	213.3 ± 0.2	22.4 ± 0.3	0.191	8.32 ± 0.05
126	213.1 ± 0.1	15.4 ± 0.3	0.418	8.23 ± 0.04
127	218.6 ± 0.2	16.0 ± 0.3	0.115	8.30 ± 0.03
128	202.2 ± 0.1	16.9 ± 0.3	-0.066	8.30 ± 0.03
129	218.9 ± 0.2	20.3 ± 0.4	0.045	8.32 ± 0.05
130	201.5 ± 0.2	14.9 ± 0.3	0.127	8.26 ± 0.03
131	206.6 ± 0.5	29.8 ± 0.6	-0.008	8.37 ± 0.07
132	206.5 ± 0.1	17.1 ± 0.3	0.147	8.26 ± 0.05
133	212.3 ± 0.1	16.8 ± 0.3	0.188	8.24 ± 0.03
134	220.4 ± 0.5	27.0 ± 0.6	-0.209	8.30 ± 0.08
135	199.5 ± 0.2	16.0 ± 0.3	0.093	8.26 ± 0.03
136	214.7 ± 0.2	18.7 ± 0.3	0.159	8.32 ± 0.03
137	212.9 ± 0.8	42.9 ± 0.8	-0.139	8.36 ± 0.08
138	199.6 ± 0.2	24.6 ± 0.2	0.041	8.27 ± 0.03
139	210.3 ± 0.2	18.8 ± 0.4	-0.255	8.31 ± 0.09

Kinematical and chemical parameters of the emission regions in the catalogue from this study. The velocity corresponds to the first moment of the sincgauss fit of the H α emission line, corrected for the sky velocity and heliocentric (described in Section 2.5.3 and obtained in the step described in Section 2.6.3). The velocity dispersion corresponds to the second moment of the sincgauss fit of the H α emission line (described in Section 2.5.3 and obtained in the step described in Section 2.6.3). The A_V value corresponds to the extinction computed with `pyngeb` (described in Section 2.6.8). $12 + \log[\text{O}/\text{H}]$ is the metallicity computed with the $N2O2$ indicator from Pilyugin & Grebel (2016), as described in Section 2.7.8.

ID	Velocity [km s $^{-1}$]	Velocity Dispersion [km s $^{-1}$]	A_V	$12 + \log[\text{O}/\text{H}]$
140	204.2 ± 0.3	20.0 ± 0.5	-0.088	8.27 ± 0.06
141	259.3 ± 0.2	14.3 ± 0.4	0.398	8.16 ± 0.04
142	200.6 ± 0.7	20 ± 1	0.217	8.3 ± 0.1
143	197.7 ± 0.2	25.1 ± 0.2	0.022	8.03 ± 0.09
144	215.2 ± 0.3	24.3 ± 0.5	-0.06	8.28 ± 0.05
145	200.9 ± 0.9	14 ± 2	-0.022	8.2 ± 0.1
146	207.0 ± 0.5	17.3 ± 0.9	0.263	8.10 ± 0.09
147	207.1 ± 0.2	17.0 ± 0.4	-0.186	8.30 ± 0.04
148	199.5 ± 0.1	14.7 ± 0.3	0.105	8.09 ± 0.08
149	204.2 ± 0.4	13.3 ± 0.8	0.168	8.20 ± 0.06
150	172.4 ± 0.5	25.6 ± 0.6	-0.157	8.29 ± 0.06
151	192.3 ± 0.2	21.2 ± 0.3	0.081	8.34 ± 0.03
152	258.9 ± 0.6	18 ± 1	0.835	7.2 ± 0.2
153	213.8 ± 0.6	28.4 ± 0.7	-0.276	8.3 ± 0.1
154	158.7 ± 0.9	34.2 ± 0.9	-0.387	8.4 ± 0.1
155	190.6 ± 0.1	20.9 ± 0.2	0.14	8.30 ± 0.02
156	169.5 ± 0.5	27.7 ± 0.6	-0.026	8.3 ± 0.1
157	178.3 ± 0.3	25.3 ± 0.4	-0.157	8.27 ± 0.05
158	188.9 ± 0.2	19.8 ± 0.3	0.045	8.35 ± 0.03
159	177.2 ± 0.9	33.5 ± 0.9	-0.063	8.0 ± 0.2

Kinematical and chemical parameters of the emission regions in the catalogue from this study. The velocity corresponds to the first moment of the sincgauss fit of the H α emission line, corrected for the sky velocity and heliocentric (described in Section 2.5.3 and obtained in the step described in Section 2.6.3). The velocity dispersion corresponds to the second moment of the sincgauss fit of the H α emission line (described in Section 2.5.3 and obtained in the step described in Section 2.6.3). The A_V value corresponds to the extinction computed with `pyngeb` (described in Section 2.6.8). $12 + \log[\text{O}/\text{H}]$ is the metallicity computed with the $N2O2$ indicator from Pilyugin & Grebel (2016), as described in Section 2.7.8.

ID	Velocity [km s $^{-1}$]	Velocity Dispersion [km s $^{-1}$]	A_V	$12 + \log[\text{O}/\text{H}]$
160	167.1 ± 0.6	34.2 ± 0.7	-0.376	8.35 ± 0.06
161	239 ± 1	21 ± 2	-0.112	8.4 ± 0.2
162	185.7 ± 0.1	21.0 ± 0.2	0.228	8.27 ± 0.02
163	255.3 ± 0.6	17 ± 1	-0.058	8.29 ± 0.08
164	251.9 ± 0.9	21 ± 1	0.99	8.1 ± 0.1
165	191.2 ± 0.1	18.9 ± 0.2	0.295	8.31 ± 0.04
166	206.8 ± 0.2	17.7 ± 0.4	0.009	8.26 ± 0.04
167	201 ± 2	20 ± 3	2.96	7.9 ± 0.5
168	204.2 ± 0.9	28 ± 1	-0.353	8.3 ± 0.1
169	191.7 ± 0.5	33.9 ± 0.5	0.015	8.32 ± 0.05
170	193.3 ± 0.2	17.9 ± 0.3	0.519	8.3 ± 0.2
171	195.8 ± 0.3	34.6 ± 0.3	0.252	8.31 ± 0.05
172	192.0 ± 0.2	27.8 ± 0.2	0.144	8.3 ± 0.3
173	197.6 ± 0.3	30.1 ± 0.3	-0.175	8.33 ± 0.05
174	216.9 ± 0.3	19.5 ± 0.5	0.261	8.28 ± 0.06
175	177.3 ± 0.1	20.6 ± 0.2	0.415	8.26 ± 0.03
176	215.4 ± 0.7	21 ± 1	0.449	8.2 ± 0.1
177	222.7 ± 0.2	16.9 ± 0.4	0.353	8.25 ± 0.05
178	182.9 ± 0.2	19.6 ± 0.3	1.029	8.24 ± 0.05
179	201.3 ± 0.2	24.0 ± 0.3	0.251	8.34 ± 0.09

Kinematical and chemical parameters of the emission regions in the catalogue from this study. The velocity corresponds to the first moment of the sincgauss fit of the H α emission line, corrected for the sky velocity and heliocentric (described in Section 2.5.3 and obtained in the step described in Section 2.6.3). The velocity dispersion corresponds to the second moment of the sincgauss fit of the H α emission line (described in Section 2.5.3 and obtained in the step described in Section 2.6.3). The A_V value corresponds to the extinction computed with `pyngeb` (described in Section 2.6.8). $12 + \log[\text{O}/\text{H}]$ is the metallicity computed with the $N2O2$ indicator from Pilyugin & Grebel (2016), as described in Section 2.7.8.

ID	Velocity [km s $^{-1}$]	Velocity Dispersion [km s $^{-1}$]	A_V	$12 + \log[\text{O}/\text{H}]$
180	217.8 ± 0.2	16.3 ± 0.3	0.254	8.25 ± 0.03
181	214.6 ± 0.3	25.0 ± 0.4	-0.418	8.37 ± 0.05
182	220.9 ± 0.2	17.8 ± 0.4	0.362	8.27 ± 0.04
183	206.7 ± 0.8	23 ± 1	0.101	8.3 ± 0.1
184	215.0 ± 0.3	16.8 ± 0.6	0.581	8.27 ± 0.06
185	185.3 ± 0.2	20.8 ± 0.2	0.482	8.30 ± 0.03
186	183.2 ± 0.9	16 ± 2	-0.938	8.4 ± 0.3
187	211.5 ± 0.7	20 ± 1	0.551	8.2 ± 0.2
188	187 ± 1	17 ± 2	1.11	8.1 ± 0.3
189	262 ± 1	22 ± 2	0.018	—
190	233.4 ± 0.8	12 ± 2	-0.488	8.3 ± 0.1
191	221.1 ± 0.2	19.5 ± 0.3	0.254	8.28 ± 0.04
192	212.3 ± 0.3	26.6 ± 0.4	-0.157	8.36 ± 0.04
193	183.7 ± 0.6	17 ± 1	-0.273	8.2 ± 0.1
196	233.4 ± 0.6	6 ± 3	-0.156	8.3 ± 0.1
197	221.1 ± 0.2	14.8 ± 0.4	0.503	8.24 ± 0.04
198	226.2 ± 0.6	36.3 ± 0.7	0.073	8.34 ± 0.09
199	224.6 ± 0.8	39.0 ± 0.8	-0.104	8.4 ± 0.1
200	202.9 ± 0.7	35.8 ± 0.8	0.093	8.36 ± 0.09
201	188.0 ± 0.6	24.9 ± 0.8	0.253	8.4 ± 0.1

Kinematical and chemical parameters of the emission regions in the catalogue from this study. The velocity corresponds to the first moment of the sincgauss fit of the H α emission line, corrected for the sky velocity and heliocentric (described in Section 2.5.3 and obtained in the step described in Section 2.6.3). The velocity dispersion corresponds to the second moment of the sincgauss fit of the H α emission line (described in Section 2.5.3 and obtained in the step described in Section 2.6.3). The A_V value corresponds to the extinction computed with `pyngeb` (described in Section 2.6.8). $12 + \log[\text{O}/\text{H}]$ is the metallicity computed with the $N2O2$ indicator from Pilyugin & Grebel (2016), as described in Section 2.7.8.

ID	Velocity [km s $^{-1}$]	Velocity Dispersion [km s $^{-1}$]	A_V	$12 + \log[\text{O}/\text{H}]$
202	230.6 ± 0.1	12.3 ± 0.4	0.586	8.2 ± 0.1
203	220.0 ± 0.2	17.2 ± 0.4	0.552	8.26 ± 0.07
204	212.2 ± 0.3	24.1 ± 0.4	0.372	8.33 ± 0.06
205	172.6 ± 0.6	17 ± 1	0.305	8.3 ± 0.1
206	219.0 ± 0.2	17.3 ± 0.4	0.287	8.3 ± 0.3
207	213.6 ± 0.4	26.9 ± 0.4	0.587	8.32 ± 0.07
208	204.2 ± 0.5	27.8 ± 0.6	0.191	8.4 ± 0.1
209	219.6 ± 0.4	20.7 ± 0.6	0.541	8.2 ± 0.1
210	218.9 ± 0.1	16.4 ± 0.3	0.407	8.24 ± 0.05
211	239.2 ± 0.6	15 ± 1	0.45	8.3 ± 0.1
212	224.0 ± 0.2	17.1 ± 0.3	0.087	8.30 ± 0.03
213	188.8 ± 0.2	18.6 ± 0.4	0.292	8.22 ± 0.05
214	242.8 ± 0.8	15 ± 2	0.024	8.2 ± 0.1
215	216.2 ± 0.5	19.5 ± 0.8	-0.247	8.34 ± 0.09
216	241.5 ± 0.7	14 ± 1	0.002	8.3 ± 0.1
217	237.7 ± 0.5	18.4 ± 0.9	0.557	8.30 ± 0.08
218	236.1 ± 0.5	12 ± 1	0.647	8.2 ± 0.1
219	221.6 ± 0.2	17.6 ± 0.4	0.197	8.26 ± 0.05
220	219.4 ± 0.2	21.3 ± 0.3	0.803	8.26 ± 0.04
221	220.1 ± 0.7	38.9 ± 0.7	0.262	8.3 ± 0.1

Kinematical and chemical parameters of the emission regions in the catalogue from this study. The velocity corresponds to the first moment of the sincgauss fit of the H α emission line, corrected for the sky velocity and heliocentric (described in Section 2.5.3 and obtained in the step described in Section 2.6.3). The velocity dispersion corresponds to the second moment of the sincgauss fit of the H α emission line (described in Section 2.5.3 and obtained in the step described in Section 2.6.3). The A_V value corresponds to the extinction computed with `pyngeb` (described in Section 2.6.8). $12 + \log[\text{O}/\text{H}]$ is the metallicity computed with the $N2O2$ indicator from Pilyugin & Grebel (2016), as described in Section 2.7.8.

ID	Velocity [km s $^{-1}$]	Velocity Dispersion [km s $^{-1}$]	A_V	$12 + \log[\text{O}/\text{H}]$
222	236.6 ± 0.5	16.7 ± 0.9	0.151	8.28 ± 0.09
223	184.0 ± 0.8	30.3 ± 0.9	0.246	8.3 ± 0.1
224	187 ± 1	33 ± 1	-0.27	8.4 ± 0.2
225	208 ± 1	34 ± 1	-0.286	8.4 ± 0.1
226	210.4 ± 0.5	14 ± 1	0.779	8.2 ± 0.1
227	214.4 ± 0.6	28.8 ± 0.6	0.518	8.4 ± 0.1
228	235.4 ± 0.4	14.5 ± 0.9	0.289	8.14 ± 0.08
229	237.1 ± 0.3	13.1 ± 0.8	0.595	8.22 ± 0.05
230	246.1 ± 0.7	19 ± 1	0.362	8.1 ± 0.2
231	215.6 ± 0.4	24.3 ± 0.5	0.249	8.3 ± 0.1
232	212.0 ± 0.2	18.1 ± 0.3	0.42	8.32 ± 0.04
233	204.6 ± 0.2	12.5 ± 0.5	0.596	8.21 ± 0.04
234	226.3 ± 0.2	25.8 ± 0.3	0.641	8.28 ± 0.04
235	195.3 ± 0.6	28.9 ± 0.7	-0.101	8.3 ± 0.1
236	211 ± 1	34 ± 1	-0.215	8.4 ± 0.1
237	263.1 ± 0.2	17.3 ± 0.4	0.356	8.08 ± 0.09
238	214.9 ± 0.3	22.7 ± 0.4	0.402	8.35 ± 0.06
239	236.5 ± 0.3	15.3 ± 0.6	0.45	8.24 ± 0.06
240	207.2 ± 0.6	19 ± 1	0.191	8.3 ± 0.1
241	203.6 ± 0.1	15.4 ± 0.3	0.242	8.22 ± 0.03

Kinematical and chemical parameters of the emission regions in the catalogue from this study. The velocity corresponds to the first moment of the sincgauss fit of the H α emission line, corrected for the sky velocity and heliocentric (described in Section 2.5.3 and obtained in the step described in Section 2.6.3). The velocity dispersion corresponds to the second moment of the sincgauss fit of the H α emission line (described in Section 2.5.3 and obtained in the step described in Section 2.6.3). The A_V value corresponds to the extinction computed with `pyngeb` (described in Section 2.6.8). $12 + \log[\text{O}/\text{H}]$ is the metallicity computed with the $N2O2$ indicator from Pilyugin & Grebel (2016), as described in Section 2.7.8.

ID	Velocity [km s $^{-1}$]	Velocity Dispersion [km s $^{-1}$]	A_V	$12 + \log[\text{O}/\text{H}]$
242	224.5 ± 0.2	25.0 ± 0.3	0.595	8.30 ± 0.04
243	241.4 ± 0.8	19 ± 1	0.989	8.2 ± 0.1
244	228.4 ± 0.2	27.8 ± 0.3	0.354	8.32 ± 0.03
245	193.7 ± 0.6	16 ± 1	0.036	8.3 ± 0.1
246	206.5 ± 0.7	22 ± 1	0.403	8.3 ± 0.1
247	211.8 ± 0.2	28.6 ± 0.2	0.301	8.35 ± 0.05
248	223.0 ± 0.7	22 ± 1	0.301	8.3 ± 0.1
249	198.7 ± 0.3	27.2 ± 0.3	0.625	8.33 ± 0.05
250	190.7 ± 0.4	17.1 ± 0.7	0.342	8.24 ± 0.08
251	242.4 ± 0.4	17.2 ± 0.7	0.441	8.25 ± 0.06
252	204.0 ± 0.5	23.5 ± 0.7	-0.209	8.34 ± 0.09
253	205.3 ± 0.7	24 ± 1	-0.017	8.3 ± 0.1
254	218.7 ± 0.1	16.5 ± 0.3	0.568	8.25 ± 0.03
255	182.3 ± 0.5	20.5 ± 0.7	-0.393	8.33 ± 0.09
256	203 ± 1	23 ± 1	-0.381	8.4 ± 0.2
257	182.8 ± 0.6	24.5 ± 0.7	-0.143	8.4 ± 0.1
258	186.1 ± 0.8	23 ± 1	0.897	8.3 ± 0.2
259	211.2 ± 0.2	19.0 ± 0.4	0.102	8.29 ± 0.05
260	198.0 ± 0.4	34.2 ± 0.5	0.209	8.33 ± 0.05
261	204.0 ± 0.2	19.1 ± 0.3	0.28	8.25 ± 0.04

Kinematical and chemical parameters of the emission regions in the catalogue from this study. The velocity corresponds to the first moment of the sincgauss fit of the H α emission line, corrected for the sky velocity and heliocentric (described in Section 2.5.3 and obtained in the step described in Section 2.6.3). The velocity dispersion corresponds to the second moment of the sincgauss fit of the H α emission line (described in Section 2.5.3 and obtained in the step described in Section 2.6.3). The A_V value corresponds to the extinction computed with `pyngeb` (described in Section 2.6.8). $12 + \log[\text{O}/\text{H}]$ is the metallicity computed with the $N2O2$ indicator from Pilyugin & Grebel (2016), as described in Section 2.7.8.

ID	Velocity [km s $^{-1}$]	Velocity Dispersion [km s $^{-1}$]	A_V	$12 + \log[\text{O}/\text{H}]$
262	202.4 ± 0.3	25.2 ± 0.4	0.261	8.31 ± 0.06
263	236.5 ± 0.3	15.5 ± 0.7	0.625	8.26 ± 0.06
264	205.1 ± 0.6	23.5 ± 0.9	0.335	8.3 ± 0.1
265	215.1 ± 0.3	23.1 ± 0.4	0.238	8.34 ± 0.05
266	189.4 ± 0.5	19.8 ± 0.9	0.374	8.14 ± 0.09
267	238.1 ± 0.6	16 ± 1	-0.358	8.33 ± 0.07
268	234.6 ± 0.3	16.5 ± 0.7	0.445	8.26 ± 0.06
269	214.8 ± 0.2	14.1 ± 0.5	0.411	8.20 ± 0.04
270	201.1 ± 0.2	18.2 ± 0.3	0.324	8.27 ± 0.04
271	211.7 ± 0.3	26.4 ± 0.4	0.533	8.31 ± 0.07
272	215.0 ± 0.2	22.7 ± 0.2	0.4	8.31 ± 0.03
273	188.3 ± 0.7	22 ± 1	-0.269	8.4 ± 0.1
274	238.5 ± 0.4	14.7 ± 0.8	0.514	8.22 ± 0.08
275	237.9 ± 0.2	14.8 ± 0.5	0.315	8.24 ± 0.04
276	206.5 ± 0.2	25.6 ± 0.2	0.333	8.35 ± 0.03
277	190.2 ± 0.7	22.9 ± 0.9	-0.252	8.4 ± 0.1
278	200.9 ± 0.5	25.1 ± 0.7	0.166	8.4 ± 0.1
279	217.4 ± 0.1	14.3 ± 0.3	0.804	8.18 ± 0.03
280	205.9 ± 0.3	27.2 ± 0.4	0.223	8.33 ± 0.09
281	179.4 ± 0.5	21.0 ± 0.8	0.293	8.3 ± 0.1

Kinematical and chemical parameters of the emission regions in the catalogue from this study. The velocity corresponds to the first moment of the sincgauss fit of the H α emission line, corrected for the sky velocity and heliocentric (described in Section 2.5.3 and obtained in the step described in Section 2.6.3). The velocity dispersion corresponds to the second moment of the sincgauss fit of the H α emission line (described in Section 2.5.3 and obtained in the step described in Section 2.6.3). The A_V value corresponds to the extinction computed with `pyneb` (described in Section 2.6.8). $12 + \log[\text{O}/\text{H}]$ is the metallicity computed with the $N2O2$ indicator from Pilyugin & Grebel (2016), as described in Section 2.7.8.

ID	Velocity [km s $^{-1}$]	Velocity Dispersion [km s $^{-1}$]	A_V	$12 + \log[\text{O}/\text{H}]$
282	212.0 ± 0.9	20 ± 1	0.667	8.0 ± 0.2
283	203 ± 2	50 ± 2	-0.033	8.4 ± 0.1
284	208.1 ± 0.2	21.1 ± 0.3	0.459	8.27 ± 0.04
285	210.1 ± 0.2	21.9 ± 0.3	0.182	8.33 ± 0.03
286	174 ± 1	16 ± 3	0.183	8.0 ± 0.2
287	210.2 ± 0.2	23.7 ± 0.3	0.134	8.34 ± 0.03
288	203.7 ± 0.3	27.3 ± 0.4	0.087	8.3 ± 0.1
289	168 ± 1	15 ± 3	0.605	7.9 ± 0.2
290	209.3 ± 0.3	29.9 ± 0.4	-0.087	8.35 ± 0.04
291	208 ± 1	15 ± 2	1.144	8.0 ± 0.2
292	215.6 ± 0.8	29.7 ± 0.9	0.086	8.4 ± 0.2
293	194.0 ± 0.6	23.6 ± 0.8	-0.039	8.3 ± 0.1
294	194.3 ± 0.6	21.4 ± 0.9	0.268	8.3 ± 0.2
295	173 ± 1	15 ± 2	-0.329	8.1 ± 0.2
296	208.3 ± 0.6	22.8 ± 0.9	-0.323	8.4 ± 0.1
297	176 ± 1	16 ± 2	0.532	6.7 ± 0.7
298	207.6 ± 0.3	26.1 ± 0.4	0.047	8.33 ± 0.06
299	216.0 ± 0.3	14.2 ± 0.6	0.919	8.09 ± 0.06
300	180.6 ± 0.6	18 ± 1	0.367	7.7 ± 0.2
301	177.8 ± 0.9	16 ± 2	0.942	7.6 ± 0.3

Kinematical and chemical parameters of the emission regions in the catalogue from this study. The velocity corresponds to the first moment of the sincgauss fit of the H α emission line, corrected for the sky velocity and heliocentric (described in Section 2.5.3 and obtained in the step described in Section 2.6.3). The velocity dispersion corresponds to the second moment of the sincgauss fit of the H α emission line (described in Section 2.5.3 and obtained in the step described in Section 2.6.3). The A_V value corresponds to the extinction computed with `pyngeb` (described in Section 2.6.8). $12 + \log[\text{O}/\text{H}]$ is the metallicity computed with the $N2O2$ indicator from Pilyugin & Grebel (2016), as described in Section 2.7.8.

ID	Velocity [km s $^{-1}$]	Velocity Dispersion [km s $^{-1}$]	A_V	$12 + \log[\text{O}/\text{H}]$
302	202.1 ± 0.9	20 ± 1	0.558	7.9 ± 0.2
303	177.8 ± 0.7	15 ± 1	0.629	8.0 ± 0.1
304	218.0 ± 0.1	14.2 ± 0.3	0.403	8.16 ± 0.03
305	175 ± 1	12 ± 3	0.856	8.2 ± 0.3
306	181.7 ± 0.9	16 ± 2	0.012	7.7 ± 0.3
307	203.8 ± 0.6	17 ± 1	0.09	8.1 ± 0.1
308	178 ± 1	13 ± 2	0.439	8.0 ± 0.2
309	179.5 ± 0.5	12 ± 1	0.204	8.23 ± 0.08
310	223.4 ± 0.8	40.7 ± 0.8	-0.271	8.41 ± 0.09
311	219.2 ± 0.4	22.2 ± 0.5	0.671	8.2 ± 0.1
312	179.6 ± 0.8	11 ± 2	-0.467	8.3 ± 0.1
313	217 ± 1	13 ± 3	0.805	8.3 ± 0.2
314	202.5 ± 0.7	27.8 ± 0.9	-0.113	8.4 ± 0.2
315	201.1 ± 0.6	21.1 ± 0.9	-0.159	8.3 ± 0.1
316	203.2 ± 0.4	19.8 ± 0.6	-0.102	8.33 ± 0.08
317	207.8 ± 0.4	26.5 ± 0.5	0.224	8.33 ± 0.08
318	219.6 ± 0.5	21.6 ± 0.8	-0.144	8.3 ± 0.1
319	205.1 ± 0.5	17.6 ± 0.8	-0.102	8.3 ± 0.2
320	202.5 ± 0.6	21.8 ± 0.8	-0.207	8.3 ± 0.1
321	221.9 ± 0.3	17.6 ± 0.6	0.399	8.11 ± 0.07

Kinematical and chemical parameters of the emission regions in the catalogue from this study. The velocity corresponds to the first moment of the sincgauss fit of the H α emission line, corrected for the sky velocity and heliocentric (described in Section 2.5.3 and obtained in the step described in Section 2.6.3). The velocity dispersion corresponds to the second moment of the sincgauss fit of the H α emission line (described in Section 2.5.3 and obtained in the step described in Section 2.6.3). The A_V value corresponds to the extinction computed with `pyngeb` (described in Section 2.6.8). $12 + \log[\text{O}/\text{H}]$ is the metallicity computed with the $N2O2$ indicator from Pilyugin & Grebel (2016), as described in Section 2.7.8.

ID	Velocity [km s $^{-1}$]	Velocity Dispersion [km s $^{-1}$]	A_V	$12 + \log[\text{O}/\text{H}]$
322	199.5 ± 0.5	18.7 ± 0.9	-0.313	8.4 ± 0.1
323	219.6 ± 0.2	15.3 ± 0.4	0.529	8.17 ± 0.05
324	207.6 ± 0.2	20.4 ± 0.4	0.012	8.33 ± 0.04
325	218.0 ± 0.3	22.0 ± 0.5	0.226	8.35 ± 0.07
326	209.6 ± 0.4	22.4 ± 0.5	0.027	8.33 ± 0.09
327	203.5 ± 0.3	23.9 ± 0.4	-0.099	8.39 ± 0.06
328	210.3 ± 0.3	25.7 ± 0.3	0.214	8.32 ± 0.05
329	191.6 ± 0.6	24.4 ± 0.9	-0.116	8.4 ± 0.1
330	208.8 ± 0.4	20.1 ± 0.6	-0.223	8.35 ± 0.06
332	217.7 ± 0.2	14.5 ± 0.4	0.413	8.18 ± 0.03
333	211.4 ± 0.2	21.4 ± 0.3	0.213	8.32 ± 0.05
334	221.2 ± 0.2	20.1 ± 0.4	0.211	8.27 ± 0.06
335	213.7 ± 0.3	25.4 ± 0.4	0.066	8.4 ± 0.1
336	215.4 ± 0.2	21.7 ± 0.3	0.034	8.33 ± 0.03
337	203.1 ± 0.2	17.8 ± 0.4	0.02	8.32 ± 0.05
338	202.5 ± 0.2	15.3 ± 0.5	0.142	8.32 ± 0.05
339	201.1 ± 0.1	15.2 ± 0.3	0.206	8.27 ± 0.03
340	227.6 ± 0.2	17.0 ± 0.4	0.295	8.24 ± 0.05
341	208.8 ± 0.3	21.0 ± 0.5	-0.237	8.38 ± 0.07
342	201.1 ± 0.4	16.8 ± 0.8	0.065	8.4 ± 0.1

Kinematical and chemical parameters of the emission regions in the catalogue from this study. The velocity corresponds to the first moment of the sincgauss fit of the H α emission line, corrected for the sky velocity and heliocentric (described in Section 2.5.3 and obtained in the step described in Section 2.6.3). The velocity dispersion corresponds to the second moment of the sincgauss fit of the H α emission line (described in Section 2.5.3 and obtained in the step described in Section 2.6.3). The A_V value corresponds to the extinction computed with `pyneb` (described in Section 2.6.8). $12 + \log[\text{O}/\text{H}]$ is the metallicity computed with the $N2O2$ indicator from Pilyugin & Grebel (2016), as described in Section 2.7.8.

ID	Velocity [km s $^{-1}$]	Velocity Dispersion [km s $^{-1}$]	A_V	$12 + \log[\text{O}/\text{H}]$
343	220.7 ± 0.3	26.2 ± 0.4	-0.132	8.35 ± 0.07
344	211.1 ± 0.1	15.1 ± 0.3	0.428	8.10 ± 0.08
345	204.9 ± 0.2	18.5 ± 0.4	-0.016	8.16 ± 0.07
346	197.9 ± 0.4	12.9 ± 0.9	-0.127	8.33 ± 0.06
347	197.2 ± 0.3	24.9 ± 0.4	0.119	8.29 ± 0.09
348	183.7 ± 0.4	27.1 ± 0.5	-0.086	8.30 ± 0.07
349	206.7 ± 0.6	17 ± 1	-0.039	8.2 ± 0.1
350	193.9 ± 0.4	16.2 ± 0.7	-0.186	8.26 ± 0.06
351	211.0 ± 0.3	16.5 ± 0.6	0.379	8.15 ± 0.06
352	212.0 ± 0.1	15.0 ± 0.3	0.215	8.21 ± 0.03
353	183.8 ± 0.3	22.0 ± 0.4	0.07	8.31 ± 0.07
354	191.6 ± 0.6	15 ± 1	0.017	8.3 ± 0.2
355	191.6 ± 0.1	12.8 ± 0.3	0.127	8.25 ± 0.03
356	208.4 ± 0.4	15.4 ± 0.9	0.245	8.20 ± 0.08
357	212.2 ± 0.2	14.6 ± 0.5	0.375	8.20 ± 0.07
358	205.7 ± 0.4	26.4 ± 0.4	0.094	8.33 ± 0.08
359	210.4 ± 0.1	12.9 ± 0.4	0.383	8.17 ± 0.04
360	200.9 ± 0.4	19.5 ± 0.6	-0.141	8.31 ± 0.09
361	181.7 ± 0.3	22.4 ± 0.4	-0.016	8.31 ± 0.04
362	180.2 ± 0.3	20.1 ± 0.4	0.124	8.3 ± 0.1

Kinematical and chemical parameters of the emission regions in the catalogue from this study. The velocity corresponds to the first moment of the sincgauss fit of the H α emission line, corrected for the sky velocity and heliocentric (described in Section 2.5.3 and obtained in the step described in Section 2.6.3). The velocity dispersion corresponds to the second moment of the sincgauss fit of the H α emission line (described in Section 2.5.3 and obtained in the step described in Section 2.6.3). The A_V value corresponds to the extinction computed with `pyngeb` (described in Section 2.6.8). $12 + \log[\text{O}/\text{H}]$ is the metallicity computed with the $N2O2$ indicator from Pilyugin & Grebel (2016), as described in Section 2.7.8.

ID	Velocity [km s $^{-1}$]	Velocity Dispersion [km s $^{-1}$]	A_V	$12 + \log[\text{O}/\text{H}]$
363	211.0 ± 0.6	11 ± 2	0.105	8.32 ± 0.07
364	211.0 ± 0.2	14.3 ± 0.4	0.448	8.18 ± 0.03
365	227.5 ± 0.2	20.9 ± 0.3	0.394	8.24 ± 0.06
366	211.7 ± 0.2	14.3 ± 0.5	0.535	8.14 ± 0.06
367	210.5 ± 0.4	16.8 ± 0.8	0.09	8.25 ± 0.07
368	211.6 ± 0.2	15.6 ± 0.3	0.167	8.24 ± 0.04
369	220.8 ± 0.2	16.6 ± 0.3	0.446	8.19 ± 0.05
370	204.3 ± 0.5	24.5 ± 0.7	0.011	8.3 ± 0.1
371	207.7 ± 0.4	25.5 ± 0.5	-0.107	8.34 ± 0.07
372	201.8 ± 0.2	22.2 ± 0.3	-0.022	8.30 ± 0.04
373	208.6 ± 0.4	23.2 ± 0.6	-0.189	8.4 ± 0.1
374	202.3 ± 0.3	22.7 ± 0.5	0.034	8.34 ± 0.06
375	195.1 ± 0.5	19.0 ± 0.8	-0.264	8.28 ± 0.09
376	194.8 ± 0.5	16.8 ± 0.9	0.048	8.31 ± 0.08
377	229.7 ± 0.4	19.3 ± 0.7	0.461	8.3 ± 0.1
378	186.3 ± 0.2	23.7 ± 0.3	-0.109	8.32 ± 0.04
379	198.5 ± 0.4	21.1 ± 0.6	0.102	8.2 ± 0.1
380	212.2 ± 0.4	15.8 ± 0.8	0.283	8.25 ± 0.08
381	231.9 ± 0.2	22.6 ± 0.2	0.354	8.25 ± 0.04
382	223.3 ± 0.3	17.2 ± 0.5	0.376	8.25 ± 0.08

Kinematical and chemical parameters of the emission regions in the catalogue from this study. The velocity corresponds to the first moment of the sincgauss fit of the H α emission line, corrected for the sky velocity and heliocentric (described in Section 2.5.3 and obtained in the step described in Section 2.6.3). The velocity dispersion corresponds to the second moment of the sincgauss fit of the H α emission line (described in Section 2.5.3 and obtained in the step described in Section 2.6.3). The A_V value corresponds to the extinction computed with `pyngeb` (described in Section 2.6.8). $12 + \log[\text{O}/\text{H}]$ is the metallicity computed with the $N2O2$ indicator from Pilyugin & Grebel (2016), as described in Section 2.7.8.

ID	Velocity [km s $^{-1}$]	Velocity Dispersion [km s $^{-1}$]	A_V	$12 + \log[\text{O}/\text{H}]$
383	199.5 ± 0.3	19.3 ± 0.5	0.355	8.33 ± 0.07
384	198.3 ± 0.2	22.3 ± 0.3	0.27	8.27 ± 0.08
385	228.2 ± 0.2	22.6 ± 0.3	0.413	8.23 ± 0.05
386	227.1 ± 0.3	16.9 ± 0.5	0.449	8.27 ± 0.05
387	202.0 ± 0.3	19.0 ± 0.4	0.432	8.28 ± 0.08
388	228.4 ± 0.2	19.8 ± 0.3	0.839	8.14 ± 0.07
389	201.3 ± 0.4	19.6 ± 0.6	0.461	8.2 ± 0.1
390	222.8 ± 0.1	17.4 ± 0.3	0.412	8.23 ± 0.04
391	200.4 ± 0.3	17.3 ± 0.5	0.063	8.31 ± 0.04
392	215.8 ± 0.3	18.7 ± 0.4	0.886	8.23 ± 0.06
393	200.1 ± 0.3	20.1 ± 0.6	0.322	8.2 ± 0.2
394	222.5 ± 0.2	18.9 ± 0.3	0.472	8.19 ± 0.05
395	228.5 ± 0.3	17.0 ± 0.5	0.443	8.28 ± 0.09
396	221.3 ± 0.1	19.2 ± 0.2	0.58	8.18 ± 0.03
397	178.5 ± 0.1	16.8 ± 0.3	0.068	8.24 ± 0.03
398	219.0 ± 0.1	16.1 ± 0.3	0.885	8.17 ± 0.04
399	219.3 ± 0.1	18.1 ± 0.2	0.814	8.3 ± 0.2
401	192.5 ± 0.3	31.6 ± 0.3	0.158	8.31 ± 0.05
402	222.4 ± 0.2	18.7 ± 0.3	0.462	8.23 ± 0.05
403	181.0 ± 0.1	16.5 ± 0.3	0.206	8.24 ± 0.03

Kinematical and chemical parameters of the emission regions in the catalogue from this study. The velocity corresponds to the first moment of the sincgauss fit of the H α emission line, corrected for the sky velocity and heliocentric (described in Section 2.5.3 and obtained in the step described in Section 2.6.3). The velocity dispersion corresponds to the second moment of the sincgauss fit of the H α emission line (described in Section 2.5.3 and obtained in the step described in Section 2.6.3). The A_V value corresponds to the extinction computed with `pyngeb` (described in Section 2.6.8). $12 + \log[\text{O}/\text{H}]$ is the metallicity computed with the $N2O2$ indicator from Pilyugin & Grebel (2016), as described in Section 2.7.8.

ID	Velocity [km s $^{-1}$]	Velocity Dispersion [km s $^{-1}$]	A_V	$12 + \log[\text{O}/\text{H}]$
404	199 ± 1	17 ± 2	-0.434	8.3 ± 0.1
405	202.1 ± 0.3	21.5 ± 0.5	0.578	8.23 ± 0.09
406	202.8 ± 0.5	26.6 ± 0.6	-0.203	8.32 ± 0.06
407	201.3 ± 0.2	18.6 ± 0.4	-0.138	8.31 ± 0.03
408	220.7 ± 0.1	18.4 ± 0.2	0.498	8.17 ± 0.03
409	184.2 ± 0.2	21.3 ± 0.2	0.321	8.25 ± 0.03
410	227.1 ± 0.1	19.6 ± 0.2	0.698	8.16 ± 0.05
411	217.2 ± 0.2	17.9 ± 0.4	0.481	8.18 ± 0.05
412	224.6 ± 0.2	18.8 ± 0.3	0.692	8.20 ± 0.09
413	230.8 ± 0.2	16.2 ± 0.3	0.688	8.22 ± 0.04
414	207.0 ± 0.3	27.8 ± 0.3	0.094	8.3 ± 0.1
415	217.5 ± 0.2	17.4 ± 0.3	0.233	8.24 ± 0.03
416	190.8 ± 0.5	30.3 ± 0.5	-0.076	8.32 ± 0.09
417	203 ± 1	19 ± 2	-0.137	8.3 ± 0.1
418	189.6 ± 0.3	22.5 ± 0.4	0.044	8.30 ± 0.04
419	192.2 ± 0.3	23.8 ± 0.4	-0.146	8.3 ± 0.1
420	218.6 ± 0.2	21.4 ± 0.2	0.198	8.23 ± 0.03
421	222.0 ± 0.2	23.3 ± 0.3	0.124	8.27 ± 0.05
422	207.5 ± 0.3	29.8 ± 0.3	0.077	8.29 ± 0.04
423	230.7 ± 0.2	23.7 ± 0.3	0.329	8.23 ± 0.03

Kinematical and chemical parameters of the emission regions in the catalogue from this study. The velocity corresponds to the first moment of the sincgauss fit of the H α emission line, corrected for the sky velocity and heliocentric (described in Section 2.5.3 and obtained in the step described in Section 2.6.3). The velocity dispersion corresponds to the second moment of the sincgauss fit of the H α emission line (described in Section 2.5.3 and obtained in the step described in Section 2.6.3). The A_V value corresponds to the extinction computed with `pyngeb` (described in Section 2.6.8). $12 + \log[\text{O}/\text{H}]$ is the metallicity computed with the $N2O2$ indicator from Pilyugin & Grebel (2016), as described in Section 2.7.8.

ID	Velocity [km s $^{-1}$]	Velocity Dispersion [km s $^{-1}$]	A_V	$12 + \log[\text{O}/\text{H}]$
424	233 ± 1	25 ± 1	0.397	8.3 ± 0.1
425	216.8 ± 0.1	20.6 ± 0.2	0.407	8.24 ± 0.03
426	219.8 ± 0.3	19.0 ± 0.4	0.194	8.27 ± 0.06
427	228.7 ± 0.2	18.1 ± 0.3	0.81	8.15 ± 0.08
428	220.1 ± 0.2	17.1 ± 0.3	0.545	8.22 ± 0.04
429	225.8 ± 0.2	18.0 ± 0.3	0.573	8.20 ± 0.07
430	224.8 ± 0.2	19.8 ± 0.3	0.104	8.21 ± 0.04
431	234.3 ± 0.3	17.3 ± 0.6	0.145	8.19 ± 0.07
432	216.3 ± 0.3	18.9 ± 0.4	0.413	8.2 ± 0.1
433	195.5 ± 0.4	20.8 ± 0.7	0.199	8.22 ± 0.07
434	231.9 ± 0.1	17.1 ± 0.2	0.795	8.18 ± 0.04
435	226.5 ± 0.2	15.0 ± 0.3	0.605	8.20 ± 0.04
436	206.3 ± 0.7	17 ± 1	0.639	8.3 ± 0.1
437	237.2 ± 0.3	17.0 ± 0.6	0.089	8.24 ± 0.08
438	227.9 ± 0.1	17.6 ± 0.2	0.753	8.17 ± 0.06
439	206.9 ± 0.1	14.6 ± 0.3	0.287	8.19 ± 0.03
440	199 ± 1	17 ± 2	-0.201	8.3 ± 0.1
441	213.9 ± 0.3	16.9 ± 0.5	0.576	8.19 ± 0.08
442	209.6 ± 0.5	35.7 ± 0.5	0.329	8.29 ± 0.07
443	202.1 ± 0.1	14.9 ± 0.3	0.201	8.22 ± 0.03

Kinematical and chemical parameters of the emission regions in the catalogue from this study. The velocity corresponds to the first moment of the sincgauss fit of the H α emission line, corrected for the sky velocity and heliocentric (described in Section 2.5.3 and obtained in the step described in Section 2.6.3). The velocity dispersion corresponds to the second moment of the sincgauss fit of the H α emission line (described in Section 2.5.3 and obtained in the step described in Section 2.6.3). The A_V value corresponds to the extinction computed with `pyngeb` (described in Section 2.6.8). $12 + \log[\text{O}/\text{H}]$ is the metallicity computed with the $N2O2$ indicator from Pilyugin & Grebel (2016), as described in Section 2.7.8.

ID	Velocity [km s $^{-1}$]	Velocity Dispersion [km s $^{-1}$]	A_V	$12 + \log[\text{O}/\text{H}]$
444	212.4 ± 0.2	18.4 ± 0.4	0.104	8.3 ± 0.1
445	230.5 ± 0.1	17.3 ± 0.2	0.472	8.21 ± 0.03
446	226.1 ± 0.1	14.7 ± 0.3	0.339	8.22 ± 0.03
447	199.3 ± 0.2	25.0 ± 0.3	0.137	8.28 ± 0.04
448	207.1 ± 0.7	14 ± 2	0.023	8.1 ± 0.1
449	222.1 ± 0.2	18.0 ± 0.4	0.399	8.26 ± 0.05
450	226.9 ± 0.1	15.0 ± 0.3	0.614	8.19 ± 0.04
451	206.0 ± 0.3	35.8 ± 0.3	0.222	8.27 ± 0.04
452	228.5 ± 0.1	16.1 ± 0.2	0.292	8.24 ± 0.03
453	206.7 ± 0.3	19.4 ± 0.5	0.187	8.3 ± 0.1
454	194.4 ± 0.1	15.8 ± 0.3	0.315	8.19 ± 0.02
455	205.8 ± 0.5	23.6 ± 0.6	0.362	8.2 ± 0.1
456	190.2 ± 0.4	18.4 ± 0.7	0.059	8.24 ± 0.05
457	197.1 ± 0.2	19.7 ± 0.3	0.194	8.28 ± 0.04
458	207.0 ± 0.2	19.5 ± 0.3	0.504	8.25 ± 0.03
459	189.7 ± 0.6	19.4 ± 0.9	-0.171	8.24 ± 0.09
460	225.6 ± 0.2	16.1 ± 0.3	0.082	8.27 ± 0.03
461	199.6 ± 0.1	18.7 ± 0.2	0.209	8.2 ± 0.1
462	192.1 ± 0.3	17.6 ± 0.6	-0.054	8.29 ± 0.06
463	215.6 ± 0.3	25.4 ± 0.3	0.176	8.3 ± 0.1

Kinematical and chemical parameters of the emission regions in the catalogue from this study. The velocity corresponds to the first moment of the sincgauss fit of the H α emission line, corrected for the sky velocity and heliocentric (described in Section 2.5.3 and obtained in the step described in Section 2.6.3). The velocity dispersion corresponds to the second moment of the sincgauss fit of the H α emission line (described in Section 2.5.3 and obtained in the step described in Section 2.6.3). The A_V value corresponds to the extinction computed with `pyngeb` (described in Section 2.6.8). $12 + \log[\text{O}/\text{H}]$ is the metallicity computed with the $N2O2$ indicator from Pilyugin & Grebel (2016), as described in Section 2.7.8.

ID	Velocity [km s $^{-1}$]	Velocity Dispersion [km s $^{-1}$]	A_V	$12 + \log[\text{O}/\text{H}]$
464	194.5 ± 0.3	32.1 ± 0.3	0.172	8.31 ± 0.05
465	200.0 ± 0.2	23.2 ± 0.3	0.175	8.26 ± 0.05
466	186.4 ± 0.2	20.0 ± 0.3	0.191	8.25 ± 0.03
467	199.5 ± 0.1	20.2 ± 0.2	0.733	8.21 ± 0.04
468	219.1 ± 0.1	13.2 ± 0.3	0.151	8.20 ± 0.03
469	202.8 ± 0.2	19.4 ± 0.3	0.184	8.24 ± 0.03
470	231.2 ± 0.2	17.6 ± 0.3	0.175	8.27 ± 0.04
471	211.0 ± 0.2	22.3 ± 0.3	0.113	8.23 ± 0.05
472	214.0 ± 0.2	28.3 ± 0.3	0.108	8.24 ± 0.07
473	186.0 ± 0.2	20.0 ± 0.3	0.087	8.23 ± 0.03
474	231.0 ± 0.2	19.5 ± 0.3	0.343	8.23 ± 0.04
475	213.3 ± 0.2	16.9 ± 0.5	0.088	8.24 ± 0.05
476	197.2 ± 0.2	24.1 ± 0.3	0.087	8.29 ± 0.03
477	199.4 ± 0.2	15.8 ± 0.3	0.28	8.24 ± 0.03
478	205.2 ± 0.1	19.2 ± 0.2	0.567	8.1 ± 0.1
479	204.7 ± 0.2	18.5 ± 0.3	0.16	8.24 ± 0.03
480	202.2 ± 0.2	22.0 ± 0.3	0.085	8.27 ± 0.04
481	219.4 ± 0.2	20.5 ± 0.3	0.173	8.30 ± 0.04
482	202.2 ± 0.1	16.2 ± 0.3	0.716	8.20 ± 0.03
483	205.3 ± 0.1	15.4 ± 0.3	0.717	8.22 ± 0.03

Kinematical and chemical parameters of the emission regions in the catalogue from this study. The velocity corresponds to the first moment of the sincgauss fit of the H α emission line, corrected for the sky velocity and heliocentric (described in Section 2.5.3 and obtained in the step described in Section 2.6.3). The velocity dispersion corresponds to the second moment of the sincgauss fit of the H α emission line (described in Section 2.5.3 and obtained in the step described in Section 2.6.3). The A_V value corresponds to the extinction computed with `pyngeb` (described in Section 2.6.8). $12 + \log[\text{O}/\text{H}]$ is the metallicity computed with the $N2O2$ indicator from Pilyugin & Grebel (2016), as described in Section 2.7.8.

ID	Velocity [km s $^{-1}$]	Velocity Dispersion [km s $^{-1}$]	A_V	$12 + \log[\text{O}/\text{H}]$
484	204.7 ± 0.2	19.9 ± 0.2	0.443	8.25 ± 0.04
485	201.8 ± 0.2	16.2 ± 0.3	0.261	8.23 ± 0.05
486	219.6 ± 0.2	23.8 ± 0.3	0.298	8.27 ± 0.08
487	197.7 ± 0.2	21.8 ± 0.3	0.103	8.26 ± 0.06
488	240.8 ± 0.3	16.1 ± 0.6	0.147	8.22 ± 0.04
489	196.2 ± 0.2	21.9 ± 0.3	0.206	8.23 ± 0.03
490	202.6 ± 0.3	16.3 ± 0.5	0.02	8.2 ± 0.1
491	200.4 ± 0.3	21.8 ± 0.4	-0.051	8.3 ± 0.1
492	213.4 ± 0.3	18.5 ± 0.5	0.101	8.3 ± 0.1
493	201.9 ± 0.2	15.6 ± 0.3	0.019	8.28 ± 0.03
494	223.8 ± 0.2	19.4 ± 0.3	0.372	8.21 ± 0.03
495	222.9 ± 0.2	20.5 ± 0.3	-0.012	8.27 ± 0.06
496	213.9 ± 0.1	21.4 ± 0.2	0.628	8.20 ± 0.03
497	212.8 ± 0.2	14.8 ± 0.3	0.284	8.22 ± 0.03
498	227.1 ± 0.3	21.2 ± 0.4	-0.022	8.24 ± 0.06
499	214.3 ± 0.1	21.7 ± 0.2	0.524	8.18 ± 0.03
500	220.0 ± 0.5	21.5 ± 0.8	0.005	8.3 ± 0.1
501	213.7 ± 0.2	22.3 ± 0.2	0.432	8.24 ± 0.04
502	184.2 ± 0.4	30.6 ± 0.4	0.15	8.26 ± 0.08
503	219.1 ± 0.2	19.9 ± 0.2	0.473	8.21 ± 0.03

Kinematical and chemical parameters of the emission regions in the catalogue from this study. The velocity corresponds to the first moment of the sincgauss fit of the H α emission line, corrected for the sky velocity and heliocentric (described in Section 2.5.3 and obtained in the step described in Section 2.6.3). The velocity dispersion corresponds to the second moment of the sincgauss fit of the H α emission line (described in Section 2.5.3 and obtained in the step described in Section 2.6.3). The A_V value corresponds to the extinction computed with `pyneb` (described in Section 2.6.8). $12 + \log[\text{O}/\text{H}]$ is the metallicity computed with the $N2O2$ indicator from Pilyugin & Grebel (2016), as described in Section 2.7.8.

ID	Velocity [km s $^{-1}$]	Velocity Dispersion [km s $^{-1}$]	A_V	$12 + \log[\text{O}/\text{H}]$
504	214.2 ± 0.2	17.2 ± 0.4	0.453	8.20 ± 0.06
505	211.5 ± 0.1	21.7 ± 0.2	0.221	8.1 ± 0.1
506	214.8 ± 0.1	18.5 ± 0.2	0.422	8.21 ± 0.03
507	224.7 ± 0.2	17.1 ± 0.4	0.112	8.25 ± 0.06
508	209.0 ± 0.2	23.8 ± 0.2	0.414	8.22 ± 0.03
509	217.8 ± 0.2	25.1 ± 0.2	0.352	8.17 ± 0.08
510	210.8 ± 0.4	19.6 ± 0.6	0.413	8.30 ± 0.07
511	216.4 ± 0.1	21.0 ± 0.2	0.154	8.23 ± 0.03
512	217.7 ± 0.2	19.6 ± 0.3	0.27	8.25 ± 0.09
513	225.8 ± 0.1	16.4 ± 0.3	0.321	8.21 ± 0.03
514	220.1 ± 0.3	20.5 ± 0.4	0.161	8.26 ± 0.09
515	215.1 ± 0.1	19.8 ± 0.2	0.637	8.19 ± 0.03
517	217.4 ± 0.1	15.2 ± 0.3	0.664	8.15 ± 0.07
518	209.4 ± 0.1	21.3 ± 0.2	0.636	8.18 ± 0.03
519	215.1 ± 0.1	14.0 ± 0.3	0.685	8.16 ± 0.06
520	213.2 ± 0.1	16.7 ± 0.2	0.391	8.23 ± 0.03
521	215.2 ± 0.1	15.8 ± 0.3	0.528	8.16 ± 0.03
522	212.8 ± 0.1	16.6 ± 0.2	0.723	8.16 ± 0.02
523	210.2 ± 0.1	21.5 ± 0.2	0.552	8.22 ± 0.02
524	214.9 ± 0.1	14.3 ± 0.3	0.617	8.20 ± 0.02

Kinematical and chemical parameters of the emission regions in the catalogue from this study. The velocity corresponds to the first moment of the sincgauss fit of the H α emission line, corrected for the sky velocity and heliocentric (described in Section 2.5.3 and obtained in the step described in Section 2.6.3). The velocity dispersion corresponds to the second moment of the sincgauss fit of the H α emission line (described in Section 2.5.3 and obtained in the step described in Section 2.6.3). The A_V value corresponds to the extinction computed with `pyngeb` (described in Section 2.6.8). $12 + \log[\text{O}/\text{H}]$ is the metallicity computed with the $N2O2$ indicator from Pilyugin & Grebel (2016), as described in Section 2.7.8.

ID	Velocity [km s $^{-1}$]	Velocity Dispersion [km s $^{-1}$]	A_V	$12 + \log[\text{O}/\text{H}]$
525	210.8 ± 0.1	17.6 ± 0.2	0.41	8.22 ± 0.03
526	215.1 ± 0.1	13.2 ± 0.3	0.665	8.17 ± 0.03
527	208.7 ± 0.1	19.1 ± 0.2	0.428	8.15 ± 0.08
528	220.0 ± 0.2	23.9 ± 0.2	0.343	—
530	225.9 ± 0.1	22.5 ± 0.2	0.384	8.29 ± 0.08
531	215.6 ± 0.3	19.7 ± 0.5	0.129	8.29 ± 0.08
532	225.0 ± 0.2	23.3 ± 0.2	0.253	8.27 ± 0.02
533	208.1 ± 0.7	22. ± 1	-0.292	8.4 ± 0.1
534	225.3 ± 0.2	17.9 ± 0.3	0.403	8.25 ± 0.07
535	226.2 ± 0.2	19.1 ± 0.3	0.449	8.27 ± 0.04
536	228.3 ± 0.2	24.1 ± 0.3	0.237	8.31 ± 0.03
537	224.4 ± 0.2	19.6 ± 0.3	0.762	8.17 ± 0.05
538	223.5 ± 0.2	20.8 ± 0.3	0.446	8.31 ± 0.04
539	224.1 ± 0.2	21.3 ± 0.3	0.21	8.35 ± 0.04
540	212.4 ± 0.4	15.2 ± 0.7	-0.039	8.31 ± 0.05
541	225.5 ± 0.2	16.7 ± 0.3	0.223	8.29 ± 0.03
542	228.3 ± 0.3	19.1 ± 0.4	0.83	8.21 ± 0.05
543	230.0 ± 0.3	16.2 ± 0.6	0.361	8.35 ± 0.07

Conclusion

Les régions d'émission de NGC 4449 sont étudiées systématiquement dans ce mémoire. Un catalogue détaillé liste les propriétés morphologiques, cinématiques, et chimiques de ces régions d'émission. À travers l'étude de ces régions d'émission, les endroits de formation stellaire récente et passée dans la galaxie peuvent être mieux compris et des scénarios de l'évolution de la galaxie, qui impliquent des mécanismes globaux et locaux sont discutés. Ultimement, les processus régulant la formation stellaire dans les galaxies irrégulières naines peuvent être mieux compris grâce aux études systématiques des régions H II.

Concrètement, un catalogue de 535 régions d'émission de la galaxie NGC 4449 est produit. Pour le réaliser, une suite d'outils numériques développés pour ce but est utilisée. Les régions d'émission sont détectées en utilisant les minima locaux du laplacien de l'amplitude de la raie H α . Un seuil de tolérance est ensuite appliqué pour retirer les détections qui sont considérées trop semblables au bruit. Subséquemment, les régions détectées sont modélisées avec une gaussienne 2D pour obtenir des paramètres morphologiques. Les spectres contenus dans la région sont combinés et le flux pour toutes les raies d'émission est mesuré. Les propriétés cinématiques sont aussi extraites de ces spectres. Les paramètres peuvent alors être traités pour être interprétés comme des paramètres physiques.

Une fonction de luminosité est réalisée, résultant en une pente $\alpha = -1.08 \pm 0.07$. Cette valeur ne tombe pas dans l'intervalle typique pour les galaxies irrégulières (entre -1.9 et -1.6) selon Kennicutt et al. (1989). De plus, cette valeur n'est pas en accord avec les pentes obtenues dans le passé par Kennicutt et al. (1989), $\alpha = -1.48$; Valdez-Gutiérrez et al. (2002), $\alpha = -1.93 \pm 0.02$; Fuentes-Masip et al. (2000a), $\alpha = -1.9$; et Gutiérrez et al. (2011), $\alpha = -1.43$. Il est difficile de réconcilier ces différences de pente sur le plan de la résolution spatiale variable entre les études. Une explication possible peut venir de la méthode de détection et de la sélection des régions étudiées. Cependant, une partie de cette différence peut être associée à la meilleure résolution spatiale des données utilisées. Ainsi, les complexes de régions H II sont mieux résolus et peuvent être séparés. Alors, à la place d'avoir une région d'émission très brillante, il est possible de la séparer en plusieurs régions moins brillantes. Ceci diminue le module de la pente de la fonction de luminosité, donc cet effet est attendu et cohérent avec une amélioration de la résolution spatiale. De plus, la luminosité totale de NGC 4449 provenant

des régions H II est de $(50 \pm 5)\%$, ce qui est similaire aux valeurs obtenues par Kennicutt et al. (1989) : 48 %, Valdez-Gutiérrez et al. (2002) : 38 % et Gutiérrez et al. (2011) : 46 %.

Une fonction de taille est produite, résultant en une pente de $(-0.042 \pm 0.005) \text{ pc}^{-1}$. Rousseau-Nepton et al. (2018) a obtenu une pente de $(-0.016 \pm 0.001) \text{ pc}^{-1}$ pour la galaxie spirale (SA(s)c) NGC 628, suggérant que la pente de la fonction de taille n'est pas universelle pour tous les types morphologiques de galaxies.

Le diamètre caractéristique obtenu ($2''.6 \pm 0''.3$) ne semble pas en accord avec celui obtenu par les autres études telles que celle de Valdez-Gutiérrez et al. (2002) : $1''.73 \pm 0''.1$, Fuentes-Masip et al. (2000a) : $1''.6$, van den Bergh (1981) : $3''.2$, Sabbadin & Bianchini (1979) : $6''.2$ et Hodge (1983) : $5''.5$. La définition de la taille d'une région H II et le *seeing* viennent grandement influencer cette mesure, ainsi, il est difficile de comparer justement les valeurs avec différentes études. L'excentricité des régions est aussi calculée, indiquant que les régions à l'extérieur de la galaxie semblent moins sphériques que celles dans le centre.

La corrélation entre la luminosité H α , la taille et la dispersion de vitesse des régions H II extragalactiques géantes est étudiée. Contrairement à d'autres études (p. ex. Arsenault & Roy 1988 ; Arsenault et al. 1990 ; Fuentes-Masip et al. 2000b ; Hippelein 1986 ; Melnick 1979 ; Melnick et al. 1987 ; Roy et al. 1986 ; Rozas et al. 1998 ; Terlevich & Melnick 1981), aucune corrélation n'est observée.

La distance médiane entre les centroïdes des régions voisines les plus proches est de $(42 \pm 3) \text{ pc}$. Cette valeur est plus petite que celle obtenue par Rousseau-Nepton et al. (2018) pour NGC 628 (110.0 pc). Puisque NGC 4449 est plus proche, il est possible de mieux résoudre les régions H II individuelles. La meilleure résolution spatiale des données explique aussi l'écart entre la distance de proximité médiane mesurée par Hunter (1982), soit 170 pc , entre les régions H II de NGC 4449.

Les rapports de raies pour la galaxie entière et les régions d'émission détectées sont calculés. Des diagrammes BPT sont réalisés, confirmant que la majorité des régions d'émission détectées sont des régions H II. Quelques zones de chocs sont aussi observées, majoritairement dans le gaz diffus ionisé. Il est aussi possible de remarquer que les régions avec les dispersions de vitesses les plus élevées se trouvent plus proche de la limite du régime des régions H II et du régime de transition. Ceci sous-entend que les régions ayant une grande dispersion de vitesse seraient probablement associées à des régions de chocs dans le gaz diffus ionisé.

Les amas stellaires sous-jacents sont étudiés en comparant le continuum des filtres SN1 et SN2 et le flux H α . Il est possible d'observer que certaines des régions d'émission détectées sont bel et bien associées avec une population stellaire jeune. Cependant, elles ne se trouvent pas toujours directement sous le centroïde de la région d'émission. Les régions d'émission détectées sont aussi comparées aux amas stellaires détectés par LEGUS. L'âge médian des

amas stellaires détectés par LEGUS qui se retrouvent dans des régions d'émission est de 5 Mans, comparativement à 10 Mans pour ceux qui ne se retrouvent pas dans des régions H II.

La métallicité moyenne des régions d'émission détectées est de 8.27 ± 0.03 . Cette valeur, obtenue avec l'indicateur $N2O2$ de (Pilyugin & Grebel 2016), est en accord avec les valeurs provenant des travaux de Berg et al. (2012), Cook et al. (2014), Engelbracht et al. (2008), Izotov et al. (2006), Kobulnicky et al. (1999), Marble et al. (2010), Martin (1997), Sabbadin et al. (1984) et Skillman et al. (1989) et Annibali et al. (2017), qui utilisent des indicateurs différents. Seule la valeur de Scowen (1992) (8.5 ± 0.1), obtenu avec la méthode de Edmunds & Pagel (1984), n'est pas en accord.

La pente du gradient de métallicité observé dans cette étude est de $(-4.8 \pm 0.4) \times 10^{-5} \text{ pc}^{-1}$. Cette pente montre un comportement inverse à la pente positive obtenue par Kumari et al. (2017). Ces deux comportements sont incohérents avec la pente nulle observée par Scowen (1992), à l'aide de son catalogue contenant 160 régions H II. L'influence importante du calibrateur de métallicité utilisé rend difficile de conclure avec certitude à quelque comportement que ce soit. Une étude plus poussée de la métallicité des régions H II de NGC 4449 est nécessaire pour comprendre les variations de métallicité au travers de la galaxie et des mécanismes qui les causent.

Un outil d'apprentissage machine, développé par Rhea et al. (in prep.), est utilisé pour prédire la catégorisation des régions d'émission détectées. Comme la technique classique (diagrammes BPT), l'outil confirme que la majorité des détections sont en effet des régions H II. 19 sont classifiées comme des nébuleuses planétaires et 5 comme des rémanents de supernovae. Ces objets méritent des études spectroscopiques plus poussées, puisqu'elles n'ont pas des rapports de raies classiques pour des régions H II.

La cinématique du gaz ionisé de la galaxie pixel à pixel et des régions d'émission est étudiée, montrant que le comportement global des deux est similaire. La vitesse moyenne des régions d'émission est de $(207.1 \pm 0.8) \text{ km s}^{-1}$ et la dispersion de vitesses est de $(20.4 \pm 0.7) \text{ km s}^{-1}$.

La présence d'une éjection de matière est suggérée par les doubles composantes observées dans le centre de la galaxie, comme mentionné par Summers et al. (2003) et Kumari et al. (2017). Valdez-Gutiérrez et al. (2002) observent aussi des composantes doubles dans cette région. Plus d'études sont nécessaires pour déterminer si ces doubles composantes correspondent réellement à une éjection de matière bipolaire au centre de la galaxie. Le lien entre cet afflux ou exode de gaz et les variations dans le gradient de métallicité mérite d'être étudié plus en profondeur.

Tout au long de l'étude, les régions d'émission détectées dans la barre du centre et dans le bras du nord sont comparées entre elles pour essayer de mieux comprendre les variations spatiales et temporelles de la formation stellaire. Pour la fonction de luminosité, une pente de -1.1 ± 0.4 est obtenue pour la barre et une pente de -0.8 ± 0.1 , pour le bras nord. Un

test statistique de Kolmogorov–Smirnov confirme que les populations sont statistiquement différentes. Au niveau de la fonction de taille, un diamètre caractéristique de $4''.7 \pm 0''.5$ et $2''.8 \pm 0''.3$ sont obtenus pour la barre et le bras nord, respectivement. Le rayon moyen des régions d'émission est respectivement (37 ± 3) pc pour la barre et (31 ± 2) pc pour le bras nord. Cependant, un test de Kolmogorov–Smirnov ne permet pas de conclure que les deux populations sont statistiquement différentes au niveau de leurs rayons. Une excentricité moyenne pour les régions d'émission de 0.62 ± 0.01 est obtenue pour la barre et de 0.56 ± 0.01 pour le bras nord. Il n'y a pas de relation claire entre luminosité $H\alpha$, la taille et la dispersion de vitesse pour les deux populations. La distance de proximité médiane est de (38 ± 3) pc et (42 ± 3) pc pour la barre et le bras nord, respectivement. Un test de Kolmogorov–Smirnov permet de confirmer que la distance de proximité dans les deux populations est statistiquement différente. Chimiquement, les populations de régions d'émission diffèrent légèrement. Sur le diagramme BPT $\log [OIII]/H\beta$ versus $\log [NII]/H\alpha$, les régions de la barre se situent plus près de la limite du régime des régions H II, indiquant que certaines de ces régions pourraient être plus contaminées par le gaz diffus ionisé. En ce qui concerne le diagramme BPT $\log [OIII]/H\beta$ versus $\log [SII]/H\alpha$, les régions de la barre semblent montrer moins de diversité dans leurs variations chimiques. L'âge médian des amas stellaires détectés par LEGUS se retrouvant dans des régions H II situés dans la barre est de 10 Mans, tandis qu'il est de 5 Mans pour les régions dans le bras nord. Un test de Kolmogorov–Smirnov permet de confirmer que les âges des populations dans les deux structures galactiques sont statistiquement différents. La métallicité moyenne dans la barre est de 8.32 ± 0.03 et de 8.24 ± 0.02 dans le bras nord. Un test de Kolmogorov–Smirnov confirme que les valeurs de métallicités sont statistiquement différentes. Cinétiquement, la vitesse de dispersion moyenne dans la barre du centre est de $(24.1 \pm 0.7) \text{ km s}^{-1}$, tandis qu'elle est de $(19.5 \pm 0.5) \text{ km s}^{-1}$ dans le bras du nord. Ces différences dans les populations basées sur leur localisation dans les structures galactiques pourraient indiquer une fonction de masse initiale différente ou des différences dans les échelles temporelles des processus de formation stellaire. Une étude plus poussée des historiques de formation stellaire dans ces deux structures permettrait de mieux comprendre le lien entre l'activité de formation stellaire et l'environnement dans la galaxie.

La majorité des différences entre les résultats obtenus dans cette étude et les précédentes peuvent être attribuées à l'utilisation d'une méthode systématique développée pour la détection de région d'émission avec les données SITELLE. Un échantillon statistique de la population de régions d'émission peut être obtenu, ce qui permet d'étudier des tendances à travers la galaxie de manière plus rigoureuse et fiable.

Ce catalogue de régions d'émission ne prétend pas être complet, cependant il est considéré comme suffisamment complet pour étudier de manière statistique le comportement des régions d'émission au travers de la galaxie. Une amélioration dans la méthode et un raffinement des paramètres de détection permettraient de détecter des régions H II ayant des luminosités plus

faibles et celles situées dans des régions avec une quantité de gaz diffus ionisés élevée. Il serait aussi intéressant de pouvoir discerner la nature des régions d'émission de manière plus sophistiquée pour mieux étudier les différences entre les sources d'émission, particulièrement entre les régions H II et le DIG.

Des paramètres morphologiques plus poussés, ne supposant pas que toutes les régions ont une distribution d'une gaussienne 2D, permettraient d'obtenir de l'information sur les variétés topologiques des régions H II. Il serait alors possible de catégoriser les différentes régions d'émission par leur morphologie (p. ex. symétrique, asymétrique, compacte, diffuse, filament, anneau, etc.) et, ainsi, de mieux comprendre les paramètres et l'origine de la diversité morphologique observée. Des corrélations avec d'autres propriétés intrinsèques, tel que l'âge de la région et les amas stellaires sous-jacents, pourraient être étudiées.

Une résolution spectrale plus élevée permettrait aussi de mieux comprendre le phénomène de super-vent galactique potentiel observé au centre de la galaxie. Une étude plus poussée de la cinématique du gaz du jet pourrait aider à identifier la direction du gaz (afflux ou exode), permettant de conclure sur l'origine et l'impact du jet sur NGC 4449. Par exemple, la résolution maximale pour le filtre SN3 de SITELLE ($R \approx 9000$) a été obtenue pour la nébuleuse du Crabe par Martin et al. (2021), un objet de nature et dynamique drastiquement différent que celle d'une galaxie. Cette résolution spectrale devrait être testée sur NGC 4449, pour résoudre la dynamique complexe à une échelle de distance totalement différente. Des données Fabry-Perot, permettant une résolution de $R \approx 20000$ pourraient aussi être une solution pour l'étude de la dynamique particulière dans NGC 4449.

Pour mieux comprendre le comportement du gradient de métallicité et son origine dans NGC 4449, il serait nécessaire d'utiliser la méthode directe pour obtenir des résultats plus fiables. Une mesure plus juste du gradient de métallicité aiderait à mieux comprendre la nature de l'afflux/exode potentiel de gaz dans le centre de la galaxie. Pour mesurer la raie d'émission [O III] $\lambda 4363$, des données SITELLE avec le filtre C2 sont nécessaires. Cependant, cette raie d'émission est très faible, donc elle risque d'être difficile à mesurer avec précision.

La méthodologie systématique développée pour détecter et étudier les régions d'émission sera appliquée sur les autres galaxies de l'échantillon SIGNALS. Des travaux similaires ont déjà été réalisés ou sont en cours sur les galaxies NGC 628 par Rousseau-Nepton et al. (2018), NGC 7479 par Savard et al. (in prep.) et NGC 1637 par Massé et al. (in prep.). Ces études et les futures études sur les galaxies de divers types morphologiques permettront d'analyser les différences entre les populations de régions d'émission. Ainsi, une meilleure compréhension des processus de formation stellaire pour des galaxies ayant des propriétés et des environnements différents sera acquise.

Bibliographie

- Adamo, A. et al. (2017). *ApJ* 841, p. 131.
- Adelman-McCarthy, J. K. et al. (2007). *ApJS* 172, p. 634-644.
- Aguirre, A. et al. (2001). *ApJ* 561, p. 521-549.
- Anderson, L. D. et al. (2014). *ApJS* 212, p. 1.
- Annibali, F. et al. (2008). *AJ* 135, p. 1900-1916.
- Annibali, F. et al. (2011). *AJ* 142, p. 129.
- Annibali, F. et al. (2012). *ApJ* 745, p. L1.
- Annibali, F. et al. (2017). *ApJ* 843, p. 20.
- Annibali, F. et al. (2016). *ApJ* 826, p. L27.
- Arsenault, R. et Roy, J.-R. (1988). *A&A* 201, p. 199-207.
- Arsenault, R., Roy, J.-R. et Boulesteix, J. (1990). *A&A* 234, p. 23.
- Auer, R. (1999). *A spiral galaxy model combining the density wave and self-propagating star formation.*
- Baade, W. et Mayall, N. U. (1951). « Distribution and Motions of Gaseous Masses in Spirals ». *Motion of Gaseous Masses of Cosmical Dimensions*. Paris, France, p. 165.
- El-Badry, K. et al. (2016). *ApJ* 820, p. 131.
- Bajaja, E., Huchtmeier, W. K. et Klein, U. (1994). *A&A* 285, p. 385-388.
- Balick, B. et Heckman, T. (1978). *ApJ* 226, p. L7-L10.
- Bendo, G. J., Galliano, F. et Madden, S. C. (2012). *MNRAS* 423, p. 197-212.
- Berg, D. A. et al. (2012). *ApJ* 754, p. 98.
- van den Bergh, S. (1981). *AJ* 86, p. 1464-1467.
- Bignell, R. C. et Seaquist, E. R. (1983). *ApJ* 270, p. 140-143.
- Binggeli, B., Sandage, A. et Tammann, G. A. (1988). *ARA&A* 26, p. 509-560.
- Blair, W. P., Kirshner, R. P. et Winkler Jr., P. F. (1983). *ApJ* 272, p. 84-91.
- Blair, W. P. et al. (1984). *ApJ* 279, p. 708-713.
- Böker, T. et al. (1999). *ApJS* 124, p. 95-126.
- Böker, T. et al. (2001). *AJ* 121, p. 1473-1481.
- Bomans, D. et Weis, K. (2014). *Astronomische Nachrichten* 335.1, p. 99-105.
- Bosma, A. (2017). « Hi in the Outskirts of Nearby Galaxies ». *Outskirts of Galaxies*. Astrophysics and Space Science Library. Cham : Springer International Publishing, p. 209-254.

- Bothun, G. D. (1986). *AJ* 91, p. 507-516.
- Böttner, C., Klein, U. et Heithausen, A. (2003). *A&A* 408, p. 493-498.
- Bournaud, F., Elmegreen, B. G. et Martig, M. (2009). *ApJ* 707, p. L1-L5.
- Bower, R. G. et al. (2006). *MNRAS* 370, p. 645-655.
- Buckalew, B. A., Kobulnicky, H. A. et Dufour, R. J. (2005). *ApJS* 157, p. 30-58.
- Burrows, D. N. et al. (2005). *Space Sci. Rev.* 120, p. 165-195.
- Calzetti, D. et al. (2015). *AJ* 149.2, p. 51.
- Capuzzo Dolcetta, R., Di Matteo, P. et Miocchi, P. (2005). *AJ* 129, p. 1906-1921.
- Carroll, B. W. et Ostlie, D. A. (2006). *An introduction to modern astrophysics and cosmology*.
- Ceverino, D., Dekel, A. et Bournaud, F. (2010). *MNRAS* 404, p. 2151-2169.
- Ceverino, D. et al. (2012). *MNRAS* 420, p. 3490-3520.
- Ceverino, D. et al. (2016). *MNRAS* 457, p. 2605-2612.
- Chyžík, K. T. et al. (2000). *A&A* 355, p. 128-137.
- Cignoni, M. et al. (2018). *ApJ* 856.1, p. 62.
- Cignoni, M. et al. (2019). *ApJ* 887, p. 112.
- Collaboration, P. et al. (2011). *A&A* 536, A7.
- Combes, F. et al. (2002). *Galaxies and cosmology*. 2nd. Astronomy and Astrophysics Library.
New York, NY, USA : Springer Berlin, Heidelberg.
- Cook, D. O. et al. (2019). *MNRAS* 484, p. 4897-4919.
- Cook, D. O. et al. (2014). *MNRAS* 445, p. 899-912.
- Cosens, M. et al. (2022). *ApJ* 929.1, p. 74.
- Cresci, G. et al. (2010). *Nature* 467, p. 811-813.
- Crillon, R. et Monnet, G. (1969). *A&A* 1, p. 449.
- Daddi, E. et al. (2010). *ApJ* 714, p. L118-L122.
- Dale, D. A. et al. (2009). *ApJ* 703, p. 517-556.
- Davé, R., Finlator, K. et Oppenheimer, B. D. (2011). *MNRAS* 416, p. 1354-1376.
- Dekel, A. et al. (2009a). *Nature* 457, p. 451-454.
- Dekel, A., Sari, R. et Ceverino, D. (2009b). *ApJ* 703, p. 785-801.
- Della Ceca, R., Griffiths, R. E. et Heckman, T. M. (1997). *ApJ* 485, p. 581-597.
- Denicoló, G., Terlevich, R. et Terlevich, E. (2002). *MNRAS* 330, p. 69-74.
- Diaz, A. I. (1989). *Abundance Gradients in Disc Galaxies and Chemical Evolution Models*.
- Dobbs, C. L., Burkert, A. et Pringle, J. E. (2011). *MNRAS* 417, p. 1318-1334.
- Dobbs, C. L. et al. (2014). *Formation of Molecular Clouds and Global Conditions for Star Formation*. eprint : arXiv :1312.3223.
- Dopita, M. A., Mathewson, D. S. et Ford, V. L. (1985). *ApJ* 297, p. 599-606.
- Dopita, M. A. et al. (2016). *Ap&SS* 361, p. 61.
- Dressler, A. (1980). *ApJ* 236, p. 351-365.
- Drissen, L. et al. (2019). *MNRAS* 485, p. 3930-3946.
- Edmunds, M. G. et Pagel, B. E. J. (1984). *MNRAS* 211, p. 507-519.

- Efremov, Y. N. et Elmegreen, B. G. (1998a). *MNRAS* 299, p. 588-594.
- Efremov, Y. N. et Elmegreen, B. G. (1998b). *MNRAS* 299, p. 643-652.
- Elmegreen, B. G., Bournaud, F. et Elmegreen, D. M. (2008). *ApJ* 688, p. 67-77.
- Elmegreen, B. G. et Elmegreen, D. M. (2005). *ApJ* 627, p. 632-646.
- Elmegreen, B. G., Zhang, H.-X. et Hunter, D. A. (2012). *ApJ* 747, p. 105.
- Elmegreen, D. M. et Elmegreen, B. G. (1980). *AJ* 85, p. 1325-1327.
- Elmegreen, D. M. et al. (2007). *ApJ* 658, p. 763-777.
- Elmegreen, D. M. et al. (2009). *ApJ* 701, p. 306-329.
- Elmegreen, D. M. et al. (2016). *ApJ* 825, p. 145.
- Engelbracht, C. W. et al. (2008). *ApJ* 678, p. 804-827.
- Epinat, B., Amram, P. et Marcellin, M. (2008). *MNRAS* 390, p. 466-504.
- Espinosa-Ponce, C. et al. (2020). *MNRAS* 494.2, p. 1622-1646.
- Fabbiano, G., Kim, D. .- et Trinchieri, G. (1992). *ApJS* 80, p. 531.
- Feng, H. et Soria, R. (2011). *New Astron. Rev.* 55, p. 166-183.
- Fisher, J. R. et Tully, R. B. (1981). *ApJS* 47, p. 139-200.
- Förster Schreiber, N. M. et al. (2011). *ApJ* 739, p. 45.
- Frei, Z. et al. (1996). *AJ* 111, p. 174.
- Fuentes-Masip, O., Castañeda, H. O. et Muñoz-Tuñón, C. (2000a). *AJ* 119.5, p. 2166.
- Fuentes-Masip, O. et al. (2000b). *AJ* 120.2, p. 752.
- Gallagher, J. S. et Hunter, D. A. (1983). *ApJ* 274, p. 141-151.
- Gallagher, J. S., Hunter, D. A. et Knapp, G. R. (1981). *AJ* 86, p. 344-356.
- García-Benito, R. et al. (2011). *AJ* 141, p. 126.
- Garnett, D. R. (1992). *AJ* 103, p. 1330.
- Gehrels, N. et al. (2004). *ApJ* 611, p. 1005-1020.
- Genel, S. et al. (2012). *ApJ* 745, p. 11.
- Genzel, R. et al. (2008). *ApJ* 687, p. 59-77.
- Genzel, R. et al. (2010). *MNRAS* 407, p. 2091-2108.
- Genzel, R. et al. (2011). *ApJ* 733, p. 101.
- Gerola, H. et Seiden, P. E. (1978). *ApJ* 223, p. 129-139.
- Gerola, H., Seiden, P. E. et Schulman, L. S. (1980). *ApJ* 242, p. 517-527.
- Giavalisco, M. et al. (2011). *ApJ* 743, p. 95.
- Grebel, E. K., Gallagher III, J. S. et Harbeck, D. (2003). *AJ* 125, p. 1926-1939.
- Guo, Y. et al. (2012). *ApJ* 757, p. 120.
- Gutiérrez, L. et Beckman, J. E. (2010). *ApJ* 710, p. L44-L48.
- Gutiérrez, L., Beckman, J. E. et Buenrostro, V. (2011). *AJ* 141.4, p. 113.
- Hartmann, L. W., Geller, M. J. et Huchra, J. P. (1986). *AJ* 92, p. 1278-1290.
- Heckman, T. M., Armus, L. et Miley, G. K. (1990). *ApJS* 74, p. 833.
- Heckman, T. M. et al. (2000). *ApJS* 129, p. 493-516.

- Hensler, G. (2011). « The Morphological Origin of Dwarf Galaxies ». *CRAL conference*. T. 48. EAS Publications Series, p. 383-395.
- Hill, R. S. et al. (1994). *ApJ* 430, p. 568.
- Hippelein, H. H. (1986). *A&A* 160, p. 374.
- Hodge, P. W. (1974). *PASP* 86, p. 845.
- Hodge, P. W. (1976). *ApJ* 205, p. 728-744.
- Hodge, P. W. (1983). *AJ* 88, p. 1323-1329.
- Hodge, P. W. et Kennicutt Jr., R. C. (1983). *AJ* 88, p. 296-328.
- Hodge, P. W. (1967). *AJ* 72, p. 129.
- Hodge, P. W. (1969a). *ApJ* 156, p. 847.
- Hodge, P. W. (1969b). *ApJS* 18, p. 73.
- Hopkins, P. F. et Hernquist, L. (2009). *ApJ* 694, p. 599-609.
- Hopkins, P. F., Narayanan, D. et Murray, N. (2013). *MNRAS* 432, p. 2647-2653.
- Huchra, J. P. (1977). *ApJ* 217, p. 928-939.
- Huchtmeier, W. K., Seiradakis, J. H. et Materne, J. (1981). *A&A* 102, p. 134-141.
- Humphreys, R. M. (1979). « The Distribution of Young Stars, Clusters and Cepheids in the Milky way and M33-A Comparison ». *The Large-Scale Characteristics of the Galaxy*. T. 84. College Park, Maryland, USA, p. 93.
- Hunter, D. (1997). *PASP* 109, p. 937-950.
- Hunter, D. A. (1982). *ApJ* 260, p. 81-103.
- Hunter, D. A., Gallagher, J. S. et Rautenkranz, D. (1982). *ApJS* 49, p. 53-88.
- Hunter, D. A. et al. (1986). *ApJ* 303, p. 171.
- Hunter, D. A. et Gallagher, J. S. (1986). *PASP* 98.599, p. 5-28.
- Hunter, D. A. et Gallagher III, J. S. (1990). *ApJ* 362, p. 480.
- Hunter, D. A. et Gallagher III, J. S. (1997). *ApJ* 475, p. 65-82.
- Hunter, D. A. et Thronson Jr., H. A. (1996). *ApJ* 461, p. 202.
- Hunter, D. A., Woerden, H. van et Gallagher, J. S. (1999). *AJ* 118, p. 2184-2210.
- Hunter, D. A. et al. (1998). *ApJ* 495, p. L47-L50.
- Hunter, D. A. et al. (2018). *ApJ* 855.1, p. 7.
- Immeli, A. et al. (2004). *ApJ* 611, p. 20-25.
- Izotov, Y. I. et al. (2006). *A&A* 448.3, p. 955-970.
- James, B. L. et al. (2014). *ApJ* 795, p. 109.
- James, B. L. et al. (2016). *ApJ* 816, p. 40.
- Jansen, F. et al. (2001). *A&A* 365, p. L1-L6.
- Jarrett, T. H. et al. (2003). *AJ* 125, p. 525-554.
- Karachentsev, I. D., Karachentseva, V. E. et Huchtmeier, W. K. (2007). *Astronomy Letters* 33, p. 512-519.
- Karczewski, O. L. et al. (2013). *MNRAS* 431, p. 2493-2512.
- Kennicutt Jr., R. C. (1979). *ApJ* 228, p. 394-404.

- Kennicutt, R. C. et Evans, N. J. (2012). *ARA&A* 50, p. 531-608.
- Kennicutt Jr., R. C. (1989). *ApJ* 344, p. 685.
- Kennicutt Jr., R. C. (1992). *ApJS* 79, p. 255.
- Kennicutt Jr., R. C. et Chu, Y.-H. (1988). *AJ* 95, p. 720.
- Kennicutt Jr., R. C. et De Los Reyes, M. A. C. (2021). *ApJ* 908, p. 61.
- Kennicutt Jr., R. C., Edgar, B. K. et Hodge, P. W. (1989). *ApJ* 337, p. 761.
- Kereš, D. et al. (2005). *MNRAS* 363, p. 2-28.
- Kewley, L. J. et Dopita, M. A. (2002). *ApJS* 142, p. 35-52.
- Kewley, L. J. et Ellison, S. L. (2008). *ApJ* 681, p. 1183-1204.
- Kewley, L. J. et al. (2010). *ApJ* 721, p. L48-L52.
- Klein, U. et al. (1996). *A&A* 313, p. 396-404.
- Knapen, J. H. et al. (1993). *AJ* 106, p. 56.
- Kobulnicky, H. A., Kennicutt Jr., R. C. et Pizagno, J. L. (1999). *ApJ* 514, p. 544-557.
- Kobulnicky, H. A. et Kewley, L. J. (2004). *ApJ* 617, p. 240-261.
- Kreckel, K. et al. (2016). *ApJ* 827, p. 103.
- Kroupa, P. (2001). *MNRAS* 322, p. 231-246.
- Kuchinski, L. E. et al. (2000). *ApJS* 131, p. 441-463.
- Kumari, N., James, B. L. et Irwin, M. J. (2017). *MNRAS* 470.4, p. 4618-4637.
- Kunth, D. et Östlin, G. (2000). *A&ARv* 10.1-2, p. 1-79.
- Lacey, C. K., Goss, W. M. et Mizouni, L. K. (2007). *AJ* 133, p. 2156-2162.
- Larson, R. B. et Tinsley, B. M. (1978). *ApJ* 219, p. 46-59.
- Lebouteiller, V. et al. (2008). *ApJ* 680, p. 398-419.
- Lee, J. C. et al. (2009). *ApJ* 706, p. 599-613.
- Leitherer, C., Robert, C. et Drissen, L. (1992). *ApJ* 401, p. 596.
- Lelli, F., Verheijen, M. et Fraternali, F. (2014a). *A&A* 566, A71.
- Lelli, F., Verheijen, M. et Fraternali, F. (2014b). *MNRAS* 445, p. 1694-1712.
- Lequeux, J. et al. (1979). *A&A* 80, p. 155.
- Leroy, A. K. et al. (2015). *ApJ* 814, p. 83.
- Lin, C. C. et Shu, F. H. (1964). *ApJ* 140, p. 646.
- López-Cobá, C. et al. (2020). *AJ* 159.4, p. 167.
- Mac Low, M.-M. et Ferrara, A. (1999). *ApJ* 513, p. 142-155.
- Maeder, A. (2009). *Physics, Formation and Evolution of Rotating Stars*.
- Marble, A. R. et al. (2010). *ApJ* 715, p. 506-540.
- Marino, R. A. et al. (2013). *A&A* 559, A114.
- Martin, C. L. (1997). *ApJ* 491, p. 561-583.
- Martin, C. L. (1998). *ApJ* 506, p. 222-252.
- Martin, D. C. et al. (2005). *ApJ* 619, p. L1-L6.
- Martin, T., Milisavljevic, D. et Drissen, L. (2021). *MNRAS* 502, p. 1864-1881.
- Martinez-Delgado, D. et al. (2012). *ApJ* 748.2, p. L24.

- Massé, E., Robert, C. et Drissen, L. (in prep.).
- Mateo, M. L. (1998). *ARA&A* 36, p. 435-506.
- Matteucci, F. (2012). *Chemical Evolution of Galaxies*. Springer. Italy.
- McCall, M. L., Rybski, P. M. et Shields, G. A. (1985). *ApJS* 57, p. 1-62.
- McConnachie, A. W. (2012). *AJ* 144.1, p. 4.
- McQuinn, K. B. W. et al. (2010). *ApJ* 721, p. 297-317.
- Melnick, J. (1979). *ApJ* 228, p. 112-117.
- Melnick, J. et al. (1987). *MNRAS* 226, p. 849-866.
- Menon, S. H. et al. (2021). *MNRAS* 507, p. 5542-5566.
- Meurer, G. R. et al. (1992). *AJ* 103, p. 60.
- Momose, R. et al. (2010). *ApJ* 721, p. 383-394.
- Morgan, W. W., Sharpless, S. et Osterbrock, D. (1952). *AJ* 57, p. 3-3.
- Mueller, M. W. et Arnett, W. D. (1976). *ApJ* 210, p. 670-678.
- Munoz-Tunon, C. (1994). « Supersonic Motions in Giant HII Regions ». *Violent Star Formation : From 30 Doradus to QSOs*. Cambridge : Cambridge University Press, p. 25-38.
- Munoz-Tunon, C., Fuentes-Masip, O. et Castañeda, H. (1998). *Publ. Astron. Soc. Australia* 15, p. 103-5.
- Murray, N., Quataert, E. et Thompson, T. A. (2010). *ApJ* 709, p. 191-209.
- Odenkirchen, M. et al. (2003). *AJ* 126, p. 2385-2407.
- Oey, M. S. et al. (2003). *AJ* 126, p. 2317-2329.
- Onodera, S. et al. (2010). *ApJ* 722, p. L127-L131.
- Osterbrock, D. E. (1989). *Astrophysics of gaseous nebulae and active galactic nuclei*. University Science Books.
- Ott, J., Walter, F. et Brinks, E. (2005). *MNRAS* 358.4, p. 1453-1471.
- Patnaude, D. J. et Fesen, R. A. (2003). *ApJ* 587, p. 221-226.
- Patton, D. R. et al. (2013). *MNRAS* 433, p. L59-L63.
- Peñarrubia, J. et al. (2009). *ApJ* 698, p. 222-232.
- Pettini, M. et Pagel, B. E. J. (2004). *MNRAS* 348, p. L59-L63.
- Phillipps, S. (2005). *The Structure and Evolution of Galaxies*.
- Pilbratt, G. L. et al. (2010). *A&A* 518, p. L1.
- Pilyugin, L. S. et Grebel, E. K. (2016). *MNRAS* 457, p. 3678-3692.
- Pilyugin, L. S. et Thuan, T. X. (2005). *ApJ* 631, p. 231-243.
- Ramya, S., Kantharia, N. G. et Prabhu, T. P. (2009). « A Radio Continuum and H I Study of Optically Selected Blue Compact Dwarf Galaxies : Mrk 1039 and Mrk 0104 ». *The Low-Frequency Radio Universe*. T. 407, p. 114.
- Reines, A. E., Johnson, K. E. et Goss, W. M. (2008). *AJ* 135, p. 2222-2239.
- Rhea, C. L. et al. (in prep.).
- Rich, R. M. et al. (2012). *Nature* 482.7384, p. 192-194.
- Roberts, W. W. (1969). *ApJ* 158, p. 123.

- Rosales-Ortega, F. F. et al. (2011). *MNRAS* 415, p. 2439-2474.
- Rousseau-Nepton, L. et al. (2018). *MNRAS* 477, p. 4152-4186.
- Rousseau-Nepton, L. et al. (2019). *MNRAS* 489, p. 5530-5546.
- Roy, J.-R., Arsenault, R. et Joncas, G. (1986). *ApJ* 300, p. 624.
- Roy, J.-R. et al. (1991). *ApJ* 367, p. 141.
- Rozas, M. et al. (1998). *A&A* 338, p. 15-26.
- Rupke, D. S., Veilleux, S. et Sanders, D. B. (2005a). *ApJ* 632, p. 751-780.
- Rupke, D. S., Veilleux, S. et Sanders, D. B. (2005b). *ApJS* 160, p. 87-114.
- Rupke, D. S., Veilleux, S. et Sanders, D. B. (2005c). *ApJS* 160, p. 115-148.
- Sabbadin, F. et Bianchini, A. (1979). *PASP* 91, p. 280-288.
- Sabbadin, F., Ortolani, S. et Bianchini, A. (1984). *A&A* 131, p. 1-8.
- Sacchi, E. et al. (2016). *ApJ* 830, p. 3.
- Sacchi, E. et al. (2018). *ApJ* 857.1, p. 63.
- Sánchez, S. F. et al. (2016). *A&A* 594, A36.
- Sánchez Almeida, J. et al. (2013). *ApJ* 767, p. 74.
- Sánchez Almeida, J. et al. (2014). *ApJ* 783, p. 45.
- Sánchez Almeida, J. et al. (2015). *ApJ* 810, p. L15.
- Sánchez-Menguiano, L. et al. (2016). *A&A* 587, A70.
- Sandage, A. et Binggeli, B. (1984). *AJ* 89, p. 919-931.
- Sandage, A. et Bedke, J. (1994). *The Carnegie atlas of galaxies*. T. 638. Carnegie Institution of Washington publication. Washington, D.C., USA : Carnegie Institution of Washington with the Flintridge Foundation.
- Sandage, A. et Tammann, G. A. (1974). *ApJ* 190, p. 525-538.
- Sasaki, M., Ohta, K. et Saito, M. (1990). *Publications of the Astronomical Society of Japan* 42, p. 361-369.
- Savard, G. et al. (in prep.).
- Schmidt, M. (1959). *ApJ* 129, p. 243.
- Schruba, A. et al. (2010). *ApJ* 722, p. 1699-1706.
- Scowen, P. A. (1992). Thesis. Rice University.
- Seaquist, E. R. et Bignell, R. C. (1978). *ApJ* 226, p. L5-L6.
- Searle, L. et Sargent, W. L. W. (1972). *ApJ* 173, p. 25.
- Sheth, K. et al. (2010). *PASP* 122, p. 1397.
- Silk, J. et Rees, M. J. (1998). *A&A* 331, p. L1-L4.
- Skillman, E. D., Kennicutt, R. C. et Hodge, P. W. (1989). *ApJ* 347, p. 875.
- Skrutskie, M. F. et al. (2006). *AJ* 131, p. 1163-1183.
- Sokal, K. R. et al. (2015). *AJ* 149, p. 115.
- Spitzer, L. (1978). *Physical processes in the interstellar medium*.
- Starkenburg, T. K., Helmi, A. et Sales, L. V. (2016). *A&A* 595, A56.
- Stierwalt, S. et al. (2017). *Nature Astronomy* 1, p. 0025.

- Summers, L. K. et al. (2003). *MNRAS* 342.3, p. 690-708.
- Swartz, D. A. et al. (2011). *ApJ* 741, p. 49.
- Taylor, V. A. et al. (2005). *ApJ* 630, p. 784-803.
- Terlevich, R. et Melnick, J. (1981). *MNRAS* 195, p. 839-851.
- Theis, C. et Kohle, S. (2001). *A&A* 370, p. 365-383.
- Theis, C. (1999). *Reviews in Modern Astronomy* 12, p. 309.
- Thronson Jr., H. A. et al. (1987). *ApJ* 317, p. 180.
- Toloba, E. et al. (2016). *ApJ* 824, p. 35.
- Tolstoy, E. et al. (1998). *AJ* 116, p. 1244-1262.
- Toomre, A. (1977). *ARA&A* 15, p. 437-478.
- Tremonti, C. A. et al. (2004). *ApJ* 613, p. 898-913.
- Tully, R. B. et al. (2006). *AJ* 132, p. 729-748.
- Turner, M. J. L. et al. (2001). *A&A* 365, p. L27-L35.
- Valdez-Gutiérrez, M. et al. (2002). *AJ* 124, p. 3157-3178.
- de Vaucouleurs, G. (1975). *Nearby Groups of Galaxies*. T. 9. Stars and Stellar Systems. Chicago, IL, USA : University of Chicago Press.
- de Vaucouleurs, G. et al. (1991). *Third Reference Catalogue of Bright Galaxies*. New York, NY, USA : Springer.
- Veilleux, S., Cecil, G. et Bland-Hawthorn, J. (2005). *ARA&A* 43.1, p. 769-826.
- Vogler, A. et Pietsch, W. (1997). *A&A* 319, p. 459-469.
- Walter, F. et al. (2008). *AJ* 136, p. 2563-2647.
- Werner, M. W. et al. (2004). *ApJS* 154, p. 1-9.
- Westmoquette, M. S. et al. (2013). *A&A* 550, A88.
- White, S. D. M. et Rees, M. J. (1978). *MNRAS* 183, p. 341-358.
- Whitmore, B. C. et al. (2020). *ApJ* 889, p. 154.
- Winter, L. M., Mushotzky, R. F. et Reynolds, C. S. (2006). *ApJ* 649.2, p. 730.
- van Woerden, H., Bosma, A. et Mebold, U. (1975). « Distribution and Motions of Neutral Hydrogen in the Giant Irregular Galaxy NGC 4449 ». *La Dynamique des galaxies spirales*. T. 241, p. 483.
- Woodward, P. R. (1976). *ApJ* 207, p. 484-501.
- Wright, E. L. et al. (2010). *AJ* 140, p. 1868-1881.
- York, D. G. et al. (2000). *AJ* 120, p. 1579-1587.
- Youngblood, A. J. et Hunter, D. A. (1999). *ApJ* 519, p. 55-68.
- Zamora-Avilés, M. et al. (2019). *MNRAS* 487, p. 2200-2214.
- Zaritsky, D., Kennicutt Jr., R. C. et Huchra, J. P. (1994). *ApJ* 420, p. 87.